



**ULTRA-HIGH PRECISION MACHINING OF RAPIDLY SOLIDIFIED ALUMINIUM
(RSA) ALLOYS FOR OPTICS**

By

PETER BABATUNDE ODEDEYI

(215391292)

December 2021

**ULTRA-HIGH PRECISION MACHINING OF RAPIDLY SOLIDIFIED ALUMINIUM
(RSA) ALLOYS FOR OPTICS**

by

PETER BABATUNDE ODEDEYI

Submitted in fulfilment/partial fulfilment of the requirements for the
Degree of Doctor of Philosophy: Mechatronics

in the

FACULTY OF ENGINEERING, THE BUILT ENVIRONMENT, AND INFORMATION
TECHNOLOGY

at the

NELSON MANDELA UNIVERSITY

Promoter/Supervisor: Prof. Khaled Abou-El-Hossein

December 2021


COPYRIGHT STATEMENT

The copy of this thesis has been provided on condition that anyone who accesses it understands and recognizes that its copyright rests with the Nelson Mandela University and that no information derived from it may be published without the prior consent of the Author unless appropriately referenced.

DECLARATION

In accordance with Rule G5.6.3, I, **Peter Babatunde Odedeyi**, student number 215391292 do hereby solemnly declare that:

- The work done in this thesis is my own.
- All sources used or referred to have been recognized and duly referenced; and
- This thesis has not been previously submitted in full or partial fulfilment of the requirements for an equivalent or lower qualification at any other educational institution.



Peter Babatunde Odedeyi

24_11_2021

Date:

DEDICATION

To God Almighty through my lord Jesus Christ in whom I live, I move and have my
being..... **Acts 17:28**

ACKNOWLEDGEMENT

First and foremost, I want to acknowledge the presence of the Holy Spirit of God all through my studies. My bible tells me in Job 32:8...*But there is a spirit in man, the breath of almighty gives him understanding (wisdom).....*

Secondly, my sincere and deepest appreciation goes to my indefatigable and amiable Supervisor, the one and only Prof. Khaled Abou-El-Hossein. I count it as a privilege to be a tutelage under your supervision. It is under this process you imbued in me the art of scientific investigation. Your guidance, unwavering supports, and patience all along starting from my master's days will never be forgotten in a hurry.

I want to thank the National Research Foundation (NRF) of South Africa and German Academic Exchange (DAAD), Germany for their financial supports. Also, my sincere and special appreciation goes to research capacity development (RCD) now Research Development (RD) at Nelson Mandela University for their financial supports for this research. I want to render my gratitude to the Centre for High Performance Computing (CHPC) South Africa and their staff Dr. Krishna Govender for providing a platform for large and fast Molecular Dynamics (MD) simulation. They also provided BIOVIA material studio 2020 software for the development and design of my unique molecular dynamic workpiece and cutting tool. I say thank you.

I seize this opportunity to thank all my co-researchers, friends within and outside Precision Engineering laboratory at Nelson Mandela University for their enormous supports and sincere encouragements. I want to say a big thank you to Dr. Lukman Abdulkadir, Dr. Abubakar Jumare, Dr. Liman Muhammad, Dr. Shahrokh Hatefi, Dr. Andrew Mkoko, Dr. Kunle Funsho, Kenny Adeniyi, Dr. Ayo Adeniran, Engr. Goodness Onwuka, Dr. Iruka, Mr. Tirimisiyun Abiola, Dr. Chinedu Ahia, Dr. Vitus Ejesieme. Special thanks also go to the entire eNtsa staffs at Nelson Mandela University.

I remain grateful to my family for their supports and prayers towards the success of this study. I want to thank my brother Pastor Funsho Williams, Sister Funmi Williams, Elizabeth Odedeyi and to my Late parents. I hope I made you proud.

Finally, I want to thank late Mrs Victoria Odedeyi a rare woman of virtue, I know you have gone to a better place, may your soul rest in peace. My biggest appreciation to my wife Mrs. Atinuke Odedeyi (my Queen) and my son Othniel Odedeyi, the strength of my youth. Bundle of joy and a gift from almighty God. Thank you for your endurance, patience, encouragement, supports and prayers. May God continue to preserve you for me.

ABSTRACT

ULTRA-HIGH PRECISION MACHINING OF RAPIDLY SOLIDIFIED ALUMINIUM (RSA) ALLOYS FOR OPTICS

ODEDEYI, P B

PhD., Mechatronics Engineering

Supervisor: Prof Khaled Abou-El-Hossein

Faculty of Engineering, the Built Environment, and Information Technology

P.O. Box 77000, Nelson Mandela University,

Port Elizabeth, South Africa

December 2020

The advancement of ultra-precision is one of the most adaptable machining processes in the manufacturing of very complex and high-quality surface structures for optics, industrial, medical, aerospace and communication applications. Studies have shown that single-point diamond turning has an outstanding ability to machine high-quality optical components at a nanometric scale. However, in a responsive cutting process, the nanometric machinability of these optical components can easily be affected by several factors. The call for increasing needs of optical systems has recently led to the development of newly modified aluminium grades of non-ferrous alloys characterized by finer microstructures, defined mechanical and physical properties. To date, there has been a lack of sufficient research into these new aluminium alloys.

In modern ultra-precision machining, the high demands for smart and inexpensive cutting tools are becoming more relevant in recent precision machines. In monitoring and predicting high-quality surface, cutting forces in single point diamond turning are believed to be as critical as other machining processes due to their potential effects on the quality of surface roughness. Undermining such an important factor is a compromise between the machining process's efficiency and the increased cost of production.

Therefore, a comprehensive scientific understanding of the Nano-cutting mechanics is critical, particularly on modelling and analysis of cutting force, surface roughness, chip

formation, acoustic emission, material removal rates, and molecular dynamic simulation of the rapidly solidified aluminium alloys to bridge the gap between fundamentals and industrial-scale application.

The study is divided into three essential sections. First, the development of a force sensor. Secondly, investigation of the effect of cutting parameters (i.e., cutting speed, feed rate, and cutting depth) on cutting force, acoustic emission (AE), material removal rate (MRR), chip formation, Nose radius, and surface roughness (Ra), which play a leading role in the determination of machine productivity and efficiency of single-point diamond turning of rapidly solidified aluminium alloys. Thirdly, a 3-D molecular dynamic (MD) simulation of RSA 6061 is also carried out to further understand the nanometric mechanism and characterization of the alloy. The experiment was mainly conducted using Precitech Nanoform ultra-grind 250 lathe machines on three different advanced optical aluminium alloys materials; these are RSA 443, RSA 905, and RSA 6061.

The developed self-sensor cutting force tool holder (SSCFTH) was implemented and validated against a commercial dynamometer (Kistler). The developed force sensor has a natural frequency of about 807.5 Hz and a sensitivity of 0.004592 v//N with R^2 of 99.6% from the sensor sensitivity curve during calibration.

Generally, the average cutting force was low during machining of all the three RSA alloys. However, the highest cutting force was observed for diamond turning of RSA 443. This could be as a result of high silicon content (40%) in the alloys. The best combination for cutting parameters to optimize the surface roughness during the cutting of RSA 6061, which predicts the best surface roughness at a rotational speed = 1976 rpm, feed rate = 5 mm/min, and depth of cut = 5 μ m with Ra as low as 1 nm.

Molecular dynamic simulation revealed that an increase in the depth of cut will lead to more material deformation ahead of the cutting tool. A constant increase in various stress components will lead to more energy requirement for material removal. Feed forces and tangential cutting forces were significantly high as the depth of cut keeps increasing.

TABLE OF CONTENTS

	Page
COPYRIGHT STATEMENT	i
DECLARATION	ii
DEDICATION.....	iii
ACKNOWLEDGEMENT	iv
ABSTRACT	vi
LIST OF FIGURES	xvii
LIST OF TABLES.....	xxxii
LIST OF EQUATIONS	xxxv
LIST OF ABBREVIATIONS.....	xxxviii
LIST OF PUBLICATIONS	xli

CHAPTER 1

INTRODUCTION

1.1	ULTRA-PRECISION MACHINING IN OPTICS APPLICATIONS.....	1
1.1.1	Single Point Diamond Machining (SPDM) for optical applications	2
1.2	PROBLEM STATEMENT	3
1.3	AIMS AND OBJECTIVES	5
1.4	THE SCOPE FOR THIS STUDY	6
1.5	MOTIVATION	7
1.6	METHODOLOGY	8
1.6.1	UHPM Methodology.....	8

1.6.2	MD Methodology	8
1.6.3	Structure of the Thesis	9

CHAPTER 2

LITERATURE REVIEW

2.1	ULTRA-HIGH PRECISION MANUFACTURING	10
2.2	ULTRA-PRECISION MACHINING (UPM)	11
2.3	DUCTILE-REGIME MACHINING.....	12
2.4	BRITTLE - DUCTILE REGIME DURING MACHINING.....	13
2.5	SINGLE POINT DIAMOND TURNING (SPDT).....	17
2.6	DIAMOND CUTTING TOOL	17
2.6.1	Anisotropy of Diamond.....	18
2.6.2	Cutting tool geometry.....	20
2.7	ATTRIBUTES OF ALUMINIUM	22
2.7.1	Aluminium alloys	23
2.8	GRADES OF RSA ALLOYS FOR OPTICAL USE	23
2.9	RAPID SOLIDIFICATION PROCESSING	24
2.10	PERFORMANCE OF RSA FOR MOULD	27
2.11	APPLICATIONS OF OPTICAL RSA	28
2.12	RECENT STUDIES IN ULTRA-PRECISION MACHINING OF RSA ALLOYS.....	31
2.13	SURFACE ROUGHNESS IN ULTRA PRECISION MACHINING	35
2.14	TECHNIQUES FOR SURFACE ROUGHNESS PREDICTION.....	40
2.15	ACOUSTIC EMISSIONS IN ULTRA-HIGH PRECISION MACHINING.....	43
2.16	REQUIREMENTS FOR SENSOR TECHNOLOGY AT PRECISION SCALE	46
2.17	MOLECULAR DYNAMICS SIMULATION AND ITS PRINCIPLE.....	48

2.17.1	Potential Energy Functions	50
2.17.2	Selection of potential energy function	52
2.17.3	Lennard-Jones potential energy function	54
2.17.4	Morse potential energy functions	55
2.17.5	Embedded atom method (EAM).....	56
2.17.6	Tersoff potential energy functions	57
2.17.7	Analytical Bond Order Potential (ABOP)	59
2.17.8	MEAM potential energy functions	60
2.17.9	ReaxFF	61
2.17.10	Steps in Molecular Dynamics.....	63
2.17.11	Model Selection	65
2.17.12	Choose an appropriate potential energy function.....	65
2.17.13	Choose the algorithm for the integration of the equations of motion .	65
2.17.14	Initialization of the model.....	66
2.17.15	Relax the model from its initial state to its dynamically equilibrium condition.....	66
2.17.16	Run the simulation and analyze the results.....	66

CHAPTER 3

CUTTING FORCES IN MACHINING

3.1	CUTTING FORCE PREDICTIONS AND MODELLING	68
3.2	CUTTING FORCES IN MICRO MACHINING	72
3.3	CUTTING FORCE MONITORING	73
3.4	CUTTING FORCES SENSING TECHNIQUES IN NANO MACHINING	75
3.5	CUTTING REGIME VERSUS CUTTING FORCES	80
3.6	CUTTING FORCES IN NANO MACHINING	82

3.7	DESIGN AND DEVELOPMENT OF SELF SENSING CUTTING FORCE (SSCF) TOOL HOLDER.....	85
3.8	THEORETICAL ANALYSIS	87
3.8.1	Analytical model.....	87
3.8.2	Finite Element Analysis of the design	88
3.9	MECHANICAL PART.....	89
3.9.1	Load cells and strain gauges	89
3.9.2	Strain gauge.....	90
3.9.3	Types of strain gauges:.....	90
3.9.4	Principle of strain gauges.....	91
3.10	INSTRUMENTATION USED FOR STRAIN GAUGE DEVICES	93
3.11	CHOICE OF MEASUREMENT SYSTEM (STATIC) E.....	94
3.12	CHOICE OF INSTRUMENTATION AND DATA COLLECTION	96
3.12.1	Electronics part	96
3.12.2	Electronics hardware.....	97
	3.12.2.1 <i>Arduino Micro atmega32u4</i>	97
	3.12.2.2 <i>HX711 Load cell amplifier</i>	99
3.12.3	Software.....	100
3.13	SELF-SENSING CUTTING FORCE TOOL HOLDER (SSCFTH) STRAIN GAUGE INSTALLATION	101
3.13.1	Procedures for strain gauge preparation and installation	101
3.14	DYNAMIC PROPERTIES OF THE SENSOR.....	107
3.15	CALIBRATION.....	108
3.15.1	Mechanical calibration of the load cell.....	108
3.15.2	Voltage calibration	111

3.16	CALIBRATION RESULTS OF SELF-SENSING CUTTING FORCE TOOL HOLDER.....	112
------	---	-----

CHAPTER 4

METHODOLOGY, MATERIALS AND EXPERIMENTAL SETUP FOR ULTRA PRECISION MACHINING

4.1	INTRODUCTION	116
4.2	DESCRIPTION OF THE EXPERIMENT	116
4.3	MACHINE TOOL AND MACHINE SET UP	116
4.3.1	Precitech Nano 250 has the following main features:	117
4.3.2	Explanation of components set up	120
4.4	WORKPIECE MATERIALS	121
4.5	DIAMOND TURNING CUTTING TOOL.....	124
4.6	DATA ACQUISITION SYSTEM - ACOUSTIC EMISSION (AE).....	127
4.7	RESPONSE SURFACE METHOD AND BOX BEHNKEN DESIGN	131
4.7.1	Design of Experiment.....	131
4.7.2	Box-Behnken Design (BBD).....	132
4.8	SURFACE ROUGHNESS MEASUREMENT.....	134

CHAPTER 5

DIAMOND TURNING OF RAPIDLY SOLIDIFIED ALUMINIUM (RSA) 905 ALLOY

5.1	ANALYSIS ON RSA 905	137
5.1.1	Force sensor comparison and analysis.....	137
5.1.2	Analysis for regression and ANOVA of force for RSA 905	140
5.1.3	Profile plot for Force sensor of RSA905.....	143
5.1.4	Machining Optimization.....	145

5.1.5	Graphical representation of cutting force characteristics during machining of RSA 905	147
5.2	AE ANALYSIS FOR RSA 905.....	153
5.2.1	Acoustic Emission (AE) Analysis for RSA 905	156
5.2.2	Summary output for regression and ANOVA analysis of AE for RSA 905	157
5.2.3	Profile plot for acoustic emission of RSA905	162

CHAPTER 6

DIAMOND TURNING OF RAPIDLY SOLIDIFIED ALUMINIUM (RSA) ALLOY

6.1	INTRODUCTION	165
6.2	CUTTING FORCE ANALYSIS ON RSA 443	165
6.3	GRAPHICAL REPRESENTATION OF CUTTING FORCE CHARACTERISTICS DURING MACHINING OF RSA 443	166
6.4	STATISTICAL ANALYSIS FOR CUTTING FORCES ACQUIRED DURING MACHINING OF RSA 443.....	173
6.5	PROFILE PLOT OF CUTTING FORCES FOR RSA443	177
6.6	OPTIMIZATION OF CUTTING PARAMETERS FOR FORCE DURING MACHINING PROCESS.....	179
6.7	AE ANALYSIS FOR RSA 443.....	179
6.8	STATISTICAL ANALYSIS FOR AE ACQUIRED DURING MACHINING OF RSA 443	180
6.9	PROFILE PLOT FOR ACOUSTIC EMISSION OF RSA 443	185
6.10	OPTIMIZATION OF CUTTING PARAMETERS FOR AE DURING MACHINING PROCESS.....	187

CHAPTER 7

DIAMOND TURNING OF RAPIDLY SOLIDIFIED ALUMINIUM (RSA) ALLOY 6061

7.1	INTRODUCTION	188
-----	--------------------	-----

7.2	FORCE ANALYSIS FOR RSA 6061 AT NOSE RADIUS (NR) 0.5MM	188
7.2.1	Statistical analysis of cutting forces for RSA 6061 at nose radius = 0.5mm	196
7.2.2	Profile plots of cutting force for RSA6061 at nose radius = 0.5mm.....	203
7.3	ANALYSIS OF CUTTING FORCES FOR RSA 6061 AT NOSE RADIUS = 1.0MM	205
7.3.1	Statistical analysis of cutting forces for RSA 6061 at nose radius = 1.0mm	207
7.3.2	Profile plot of cutting forces for RSA6061 at NR = 1.0	211
7.3.3	Optimization of cutting parameters for RSA 6061 at nose radius = 1.0mm	213
7.4	FORCE ANALYSIS FOR RSA 6061 AT NOSE RADIUS OF 1.5MM.....	214
7.4.1	Statistical analysis of cutting forces for RSA 6061 at nose radius = 1.5mm	217
7.4.2	Profile plot of cutting parameters for force on RSA6061 at nose radius 1.5mm.....	221
7.4.3	Optimization of cutting parameters for RSA 6061 at nose radius = 1.5mm	224
7.5	THE EFFECTS OF TOOL GEOMETRY AND MACHINE PARAMETERS ON CUTTING FORCE DURING MACHINING OF RSA 6061.	225
7.5.1	Effects of speed and varied nose radius (NR) on cutting force	225
7.5.2	Effects of feed rate and varied nose radius on cutting forces.....	227
7.5.3	Effects of depth of cut and varied nose radius (NR) on cutting forces	228
7.6	SURFACE ROUGHNESS ANALYSIS OF RSA 6061	230
7.6.1	Introduction	230

7.6.2	Statistical analysis of Ra for RSA 6061	235
7.6.3	Profile plot for Surface Roughness (LnRa) of RSA6061	240
7.6.4	Cutting process Optimization for surface roughness of RSA 6061	242
7.7	ANALYSIS OF MATERIAL REMOVAL RATE (MRR) ON RSA 6061	243
7.7.1	Statistical analysis of MRR for RSA 6061	244
7.7.2	Profile plot for Material Removal Rates (Ln MRR) of RSA6061	249
7.7.3	Statistical analysis of chip formation for RSA 6061	253
7.7.4	Profile plotting for effective chip formation of RSA6061	256
7.7.5	Effective chip morphology during machining of RSA6061.....	258
7.8	ACOUSTIC EMISSION ANALYSIS DURING MACHINING OF RSA6061 ..	264
7.8.1	Statistical analysis of AE for RSA 6061.....	266
7.8.2	Profile plot for acoustic emission of RSA 6061	271

CHAPTER 8

MOLECULAR DYNAMICS SIMULATION OF RSA 6061

8.1	METHODOLOGY OF MOLECULAR DYNAMICS SIMULATION OF RSA 6061	274
8.1.1	Pre-Processing phase.....	274
8.1.2	Processing phase	278
8.2	INTERATOMIC POTENTIALS AND PARAMETER SETTING FOR SIMULATION.....	279
8.3	SELECTION OF INTERATOMIC POTENTIALS AND PARAMETERS SETTING	282
8.4	MD ANALYSIS OF STRESSES, CUTTING FORCES, CUTTING KINETIC FRICTION, TEMPERATURE AND SPECIFIC CUTTING ENERGY IN THE CUTTING ZONE.....	284

8.4.1	Effect of depth of cut on stresses.....	285
8.4.2	Analysis of cutting forces during MD simulation of RSA 6061.....	293
8.4.3	Analysis of Cutting Energy.....	298
8.4.4	Specific Cutting Energy (SCE).....	300
8.4.5	Analysis of Temperature.....	301

CHAPTER 9

CONCLUSIONS AND RECOMMENDATION

9.1	CONCLUDING REMARKS ON THE DEVELOPED SSCFTH	305
9.1.1	Concluding remarks on ultra-precision machining of RSA Alloys (RSA 443, 906 and 6061)	306
9.1.2	Concluding remarks on MD simulation of RSA 6061	308
9.2	RECOMMENDATION FOR FUTURE INVESTIGATION	309
	REFERENCES	311

LIST OF FIGURES

	Page
Figure 2.1:	The development of achievable machining accuracy [23]..... 10
Figure 2.2:	Ultra-precision diamond turning 11
Figure 2.3:	Complexities involved in ductile-regime machining [23]..... 13
Figure 2.4:	Schematic of ductile-regime machining [35] 14
Figure 2.5:	Analytical model of ductile regime machining and 2D representation of the 3D condition showing nose radius of the tool [23, 47, 48]..... 16
Figure 2.6:	Mono-crystalline synthetic diamonds for requiring an ultra-high-quality surface finish (a) manufactured in HTHP processing (b) inserted with mono-crystalline natural diamond cutting edge..... 19
Figure 2.7:	Single-point diamond tools for ultraprecision machining by Rudrali Hi Tech Tools Pvt. Ltd [58]..... 20
Figure 2.8:	Typical cutting-edge preparation geometry [62] 21
Figure 2.9:	Required steps in Rapid solidification process [4, 85]..... 25
Figure 2.10:	Microstructure of conventional alloy AA6061 and RSA 6061 alloy [6].. 26
Figure 2.11:	Mould after diamond turning process b) sunglass design from RSA Mould [6]..... 28
Figure 2.12:	A lens mold and the injection-molded camera lenses for mobile phones [87] 29
Figure 2.13:	Application of Mould in the making of precision optics[88] 30

Figure 2.14:	Mould manufacturing [88]	30
Figure 2.15:	Other applications of RSA alloys apart from its optic application [89] ..	31
Figure 2.16:	Roughness and waviness in a surface [100, 101].....	35
Figure 2.17:	Features of machined surface [103].....	36
Figure 2.18:	Details of workpiece surface texture [128]	39
Figure 2.19:	Arithmetic surface roughness average, Ra and geometric root mean square (RMS) [130].....	40
Figure 2.20:	Structure of a neural network system [140].....	41
Figure 2.21:	Diagram showing various AE source during cutting process [153]	44
Figure 2.22:	Schematic diagram of the AE test system [156].....	45
Figure 2.23:	Characteristics of acoustic emission signal [157].....	45
Figure 2.24:	Sources of AE at varying stages of material removal [150].....	47
Figure 2.25:	Principle of molecular dynamics simulation [172].....	49
Figure 2.26:	Variation of the attractive, repulsive and net forces (a) and the attractive, repulsive and net potential energies (b), as a function of the interatomic distance r between two atoms [173]	51
Figure 2.27:	Potential energy function for molecular dynamics simulation [177].....	52
Figure 2.28:	Lennard-Jones potential function and the effect of atomic distance [182, 184, 185].....	54
Figure 2.29:	Morse potential function and the effect of atomic distance on intermolecular force [188]	55
Figure 2.30:	General Flow chart for MD simulation.....	64

Figure 3.1:	Modelling approach adopted for machining processes[235]	69
Figure 3.2:	Cutting force measurement with embedded sensor [301].....	76
Figure 3.3:	Cutting force measurement using Dynamometer [297].....	77
Figure 3.4:	Effect of tool geometry on performance parameters in turning [339] ...	83
Figure 3.5:	Variation of tangential cutting force with tools of different edge radius [247]	84
Figure 3.6:	Cantilever beam before and after deflection	87
Figure 3.7:	Von mises stress.....	89
Figure 3.8:	Principal stress.....	89
Figure 3.9:	Typical T-rosette strain gauges.....	93
Figure 3.10:	Full Wheatstone bridge configuration.....	94
Figure 3.11:	Half bridge setup.....	96
Figure 3.12:	Schematic diagram of self-force sensor tool holder	97
Figure 3.13:	(A) Pin mapping of the Arduino Micro displays (B) Arduino Micro Front side	99
Figure 3.13:	HX711 load cell amplifier module.....	100
Figure 3.14	Arduino IDE.....	101
Figure 3.15:	Contour [®] Tool holder	103
Figure 3.16:	Installation set up table	103
Figure 3.17:	Top installation showing T-rosette (strain gauge) for tensile stress ...	104

Figure 3.18:	Bottom installation showing T-rosette (strain gauge) for compression stress	104
Figure 3.19:	Design and dimensions for the tool holder	105
Figure 3.20:	Structural diagram of the developed self-force sensor tool holder	107
Figure 3.21:	Schematic design application.....	109
Figure 3.22:	Schematic linear relationship for calibration.....	110
Figure 3.23:	Load samples for calibration	113
Figure 3.24:	Calibration with 98g	113
Figure 3.25:	Calibration with 125.5g	114
Figure 3.26:	P3 static strain indicator	114
Figure 3.27:	Sensor sensitivity curve	115
Figure 4.1:	Precitech nanoform 250 ultra-grind lathe machine.....	118
Figure 4.2:	Set up for diamond machining of RSA alloys	118
Figure 4.3:	Spindle balancing and monitoring platform	119
Figure 4.4:	Cutting tool alignment display	119
Figure 4.5:	Optical tool setter for tool adjustment and alignment	120
Figure 4.6:	Surface of diamond turned RSA 6061	123
Figure 4.7:	Surface of diamond turned RSA 905	123
Figure 4.8:	Surface of diamond turned RSA 443	124
Figure 4.9:	Typical tool holders and inserts for diamond turning.....	125

Figure 4.10:	Typical set up for acoustic emission measurement during diamond turning [366]	127
Figure 4.11:	National Instruments NI PXIe-1071.....	128
Figure 4.12:	NI BNC-2110.....	129
Figure 4.13:	AE-Piezotron Sensor – Kistler 8162B	129
Figure 4.14:	AE Piezotron Couper – Kistler 5125B	129
Figure 4.15:	Live display LabView front panel of AE acquisition	130
Figure 4.16:	Display of LabView block diagram for AE acquisition	130
Figure 4.17:	The design for three factors in Box-Behnken	133
Figure 4.18:	Taylor Hobson PGI dimension XL surface profilometer	135
Figure 4.19:	Surface Profilometer display sample measured.....	136
Figure 4.20:	Surface profile chart.....	136
Figure 5.1:	Comparison between the data acquired by SSCFTH designed and industrial Kistler sensor	140
Figure 5.2:	Validation of the experiment carried out by self-sensor (SSCFTH) a well scattered plot	142
Figure 5.3:	Comparison between experimental and predicted data of self-sensor cutting force tool holder and predicted data	142
Figure 5.4:	Profile plot for speed against natural log of cutting force	143
Figure 5.5:	Profile plot for feed rate against natural log of cutting force	144
Figure 5.6:	Profile plot for Depth of cut against natural log of cutting force	144

Figure 5.7:	Interaction plot between depth of cut and speed on cutting force for RSA 905	145
Figure 5.8:	Contour plot between depth of cut and speed against natural log of cutting force.....	146
Figure 5.9:	3D plot between Depth of cut and speed against natural log of cutting force	147
Figure 5.10:	Filter design and its parameters for AE of RSA 905	154
Figure 5.11:	Frequency domain representation for Experiment 2 feed rate = 25mm/min, depth of cut = 5mm, speed = 1750rpm	155
Figure 5.12:	Frequency domain representation for Experiment 7 feed rate = 15mm/min, depth of cut = 25mm, speed = 500rpm	155
Figure 5.13:	Frequency domain representation for Experiment 15 feed rate = 15 mm/min, depth of cut = 5 mm, speed = 500rpm	156
Figure 5.14:	Validation plot for acoustic emission model on RSA 905	159
Figure 5.15:	Comparison graph between experimental acoustic emission value and the predicted value.....	160
Figure 5.16:	Interaction plot between speed and feed rate on inverse of AE	161
Figure 5.17:	3D plot between feed rate and speed on inverse of AE	161
Figure 5.18:	Shows 2D effect of speed and feed rate on the inverse of AE acquired during machining of RSA 905.....	162
Figure 5.19:	Profile plot for speed against inverse of AE	163
Figure 5.20:	Profile plot for Feed rate against inverse of AE.....	163
Figure 5.21:	Profile plot for depth of cut against inverse of AE	164

Figure 6.1:	Validation plot for cutting force from the model on RSA 443.....	174
Figure 6.2:	Comparisson between experimental value and predicted value for cutting force on RSA 443	175
Figure 6.3:	Interaction plot between cutting speed and depth of cut	176
Figure 6.4:	2D plot for depth of cut and speed	176
Figure 6.5:	3D plot between cutting speed and depth of cut	176
Figure 6.6:	Effect of speed on cutting force during diamond turning of RSA 443	177
Figure 6.7:	Effect of feed rate on cutting force during diamond turning of RSA 443	178
Figure 6.8:	Effect of depth of cut on cutting force during diamond turning of RSA 443	178
Figure 6.9:	Scattered validation plot for AE on RSA 443	182
Figure 6.10:	Comparison between experimental value and predicted value for AE on RSA 443.....	182
Figure 6.11:	Interaction plot between feed rate and depth of cut against Inverse of AE	183
Figure 6.12:	2D response surface plot for AE on RSA 443.....	184
Figure 6.13:	3D response surface plot for AE on RSA 443.....	184
Figure 6.14:	Profile plot for feed rate against Inverse AE.....	185
Figure 6.15:	Profile plot for feed rate against Inverse AE.....	186
Figure 6.16:	Profile plot for depth of cut against Inverse AE	186

Figure 7.1:	Validation plot for RSA 6061 with Nose radius 0.5mm.....	198
Figure 7.2:	Comparison between experimental and predicted values for RSA 6061 with Nose radius = 0.5mm	199
Figure 7.3:	Contour plot for feed rate and depth of cut against inverse of cutting force at NR =0.5 mm	200
Figure 7.4:	Contour plot for speed and depth of cut against inverse of cutting force at NR =0.5 mm.....	200
Figure 7.5:	Interaction plot between feed rate and depth of cut against inverse of cutting force at NR =0.5 mm	201
Figure 7.6:	Interaction plot between speed and depth of cut against inverse of cutting force at NR =0.5 mm	201
Figure 7.7:	3D plot between depth of cut and feed rate against inverse of cutting force at NR =0.5 mm	202
Figure 7.8:	3D plot between depth of cut and speed against inverse of cutting force at NR =0.5 mm	202
Figure 7.9:	Profile plot for speed at nose radius 0.5 mm	203
Figure 7.10:	Profile plot for feed rate at nose radius 0.5mm.....	204
Figure 7.11:	Profile plot for depth of cut at nose radius 0.5mm	204
Figure 7.12:	Scattered plot for cutting force on RSA 6061 at nose radius 1.0mm.....	208
Figure 7.13:	Comparison between experimental and predicted value at nose radius = 1.0mm	209
Figure 7.14:	2D Contour plot for RSA 6061 at nose radius 1.0mm	210
Figure 7.15:	3D Contour plot for RSA 6061 at nose radius 1.0mm	210

Figure 7.16:	Interaction effect between speed and feed rate on cutting force at nose radius = 1.00mm	211
Figure 7.17:	Effect of speed on cutting forces at nose radius 1.0mm.....	212
Figure 7.18:	Effect of feed rate on cutting forces at nose radius 1.0mm	212
Figure 7.19:	Effect of depth of cut on cutting forces at nose radius 1.0mm.....	213
Figure 7.20:	2D contour plot for feed rate and speed on RSA 6061 at nose radius 1.5mm	214
Figure 7.21:	Scattered plot for RSA 6061 at nose radius 1.5mm	218
Figure 7.22:	Comparison between experimental and predicted value for RSA 6061 at nose radius 1.5mm.....	219
Figure 7.23:	2D contour plot speed and feed rate for RSA 6061 at nose radius 1.5mm	219
Figure 7.24:	3D contour plot between speed and feed rate for RSA 6061 at nose radius 1.5mm.....	220
Figure 7.25:	2D contour plot between speed and depth of cut for RSA 6061 at nose radius 1.5mm.....	220
Figure 7.26:	3D contour plot between speed and depth of cut for RSA 6061 at nose radius 1.5mm.....	221
Figure 7.27:	Effect of Speed on cutting forces at nose radius 1.5mm	222
Figure 7.28:	Effect of Speed on feed rate at nose radius 1.5mm	223
Figure 7.29:	Effect of Speed on depth of cut at nose radius 1.5mm	224
Figure 7.30:	Effect of speed on cutting force at constant feed rate = 5mm/min, Depth of cut = 5 μ m and varied nose radius (0.5 – 1.5) mm	225

Figure 7.31: Effect of speed on cutting force at constant feed rate = 15mm/min, Depth of cut = 15 μ m and varied nose radius (0.5 – 1.5) mm	226
Figure 7.32: Effect of speed on cutting force at constant feed rate = 25mm/min, Depth of cut = 25 μ m and varied nose radius (0.5 – 1.5) mm	226
Figure 7.33: Effect of feed rate on cutting force at constant speed = 500rpm, Depth of cut = 5 μ m and varied nose radius (0.5 – 1.5) mm	227
Figure 7.34: Effect of feed rate on cutting force at constant speed = 1750rpm, Depth of cut = 15 μ m and varied nose radius (0.5 – 1.5) mm	227
Figure 7.35: Effect of feed rate on cutting force at constant speed = 3000rpm, Depth of cut = 5 μ m and varied nose radius (0.5 – 1.5) mm	228
Figure 7.36: Effect of Depth of cut on cutting force at constant speed = 500rpm, feed rate = 5mm/min and varied nose radius (0.5 – 1.5) mm	228
Figure 7.37: Effect of Depth of cut on cutting force at constant speed = 1750rpm, feed rate = 15mm/min and varied nose radius (0.5 – 1.5) mm	229
Figure 7.38: Effect of Depth of cut on cutting force at constant speed = 3000rpm, feed rate = 25mm/min and varied nose radius (0.5 – 1.5) mm	229
Figure 7.39: Profile chart for Experiment 1, speed = 1750rpm, feed rate = 25mm/min and depth of cut = 25 μ m. $R_a = 0.3$ nm	232
Figure 7.40: Profile chart for Experiment 3, speed = 3000rpm, feed rate = 5mm/min and depth of cut = 15 μ m. $R_a = 2.1$ nm	232
Figure 7.41 Profile chart for Experiment 4, speed = 1750rpm, feed rate = 15mm/min and depth of cut = 15 μ m. $R_a = 3.6$ nm	233
Figure 7.42: Profile chart for Experiment 10, speed = 500rpm, feed rate = 25min and depth of cut = 15 μ m. $R_a = 132.2$ nm	233

Figure 7.43:	Profile chart for Experiment 13, speed = 1750rpm, feed rate = 5mm/min and depth of cut = 5 μ m. R_a = 1.8nm.....	234
Figure 7.44:	Profile chart for Experiment 17, speed = 500rpm, feed rate = 15mm/min and depth of cut = 5 μ m. R_a = 37.1nm.....	234
Figure 7.45:	Scattered plot for surface roughness on RSA 6061	237
Figure 7.46:	Comparison between experiment and predicted R_a	237
Figure 7.47:	2D contour plot for surface roughness of RSA 6061	238
Figure 7.48:	3D plot for surface roughness of RSA 6061	239
Figure 7.49:	Interaction plot between feed rate and speed for surface roughness of RSA 6061	239
Figure 7.50:	Effect of speed on surface roughness at varied feed rates and depth of cut	240
Figure 7.51:	Effect of feed on surface roughness at varied speed and depth of cut	241
Figure 7.52:	Effect of depth of cut on surface roughness at varied feed rates and speed	242
Figure 7.53:	Scattered plot for MRR on RSA 6061	246
Figure 7.54:	Comparison between experimental values and predicted values	247
Figure 7.55:	2D contour plot showing effect of speed and feed rate on MRR on RSA 6061	247
Figure 7.56:	3D-plot showing effect of speed and feed rate on MRR on RSA 6061	248
Figure 7.57:	Interaction plot between feed and speed	248

Figure 7.58:	Effect of speed on MRR at varied feed rates and depth of cut.....	249
Figure 7.59:	Effect of feed on MRR at varied speed and depth of cut.....	250
Figure 7.60:	Effect of depth of cut on MRR at varied feed rates and speed 7.8 Effective chip formation during machining of RSA6061	250
Figure 7.61:	Scattered plot for effective chip formation on RSA 6061	255
Figure 7.62:	Comparison between experimental values and predicted values	256
Figure 7.63:	Effects of speed on chip formation at constant feed rates and depth of cut	257
Figure 7.64:	Effects of feed rate on chip formation at constant speed and depth of cut	257
Figure 7.65:	Effects of depth of cut on chip formation at constant feed rates and speed	258
Figure 7.66:	Scattered plot for AE model validation	268
Figure 7.67:	Comparison between AE experimental values and predicted values...	268
Figure 7.68:	2-D contour graph showing the effects of speed and feed rates on AE	269
Figure 7.69:	3-D graph showing the effects of speed and feed rates on AE	270
Figure 7.70:	2-D contour graph showing the effects of depth of cut and feed rates on AE	270
Figure 7.71:	3-D contour graph showing the effects of depth of cut and feed rates on AE	271
Figure 7.72:	Effect of speed on AE at constant feed rates and depth of cut	271

Figure 7.73:	Effect of feed rates on AE at constant speed and depth of cut	272
Figure 7.74:	Effect of depth of cut on AE at constant feed rates and speed	273
Figure 8.1:	The structure of Diamond.....	276
Figure 8.2:	The schematic representation of the MD simulation model.....	277
Figure 8.3:	Flow chart of processing phase of MD simulation system.....	281
Figure 8.4:	Machining simulation development showing increase in depth of cut with tool travel	287
Figure 8.5:	Machining simulation displaying dislocations of RSA 6061 as tool travels	288
Figure 8.6:	Change in stresses with distance in RSA 6061 at depth of cut = 0.5nm	289
Figure 8.7:	Change in stresses with distance in RSA 6061 at depth of cut = 1.0 nm	290
Figure 8.8:	Change in stresses with distance in RSA 6061 at depth of cut = 1.5nm	290
Figure 8.9:	Average thrust, tangential and axial stresses against depth of cut	291
Figure 8.10:	Maximum thrust, tangential and axial stresses against depth of cut	291
Figure 8.11:	Change in hydrostatics stresses with distance in RSA 6061 at different depth of cuts.....	292
Figure 8.12:	Average Hydrostatics stress against depth of cut	293
Figure 8.13:	Orthogonal machining nomenclature [454]	294
Figure 8.14:	Cutting force against time steps at depth of cut = 0.5 nm	296

Figure 8.15:	Cutting force against time steps at depth of cut = 1.0 nm	296
Figure 8.16:	Cutting force against time steps at depth of cut = 1.5 nm	297
Figure 8.17:	Average cutting forces	297
Figure 8.18:	Maximum cutting forces	298
Figure 8.19:	Average kinetic Friction.....	298
Figure 8.20:	Total Energy.....	299
Figure 8.21:	Average total energy.....	300
Figure 8.22:	Maximum total energy.....	300
Figure 8.23:	Specific cutting energy against depth of cut.....	301
Figure 8.24:	Temperature against depth of cut	303
Figure 8.25:	Average Temperatures versus depth of cut	303
Figure 8.26:	Maximum Temperature versus depth of cut.....	304

LIST OF TABLES

	Page
Table 2.1: The alloy composition of conventional aluminum 6061 and RSA 6061 chemical composition	26
Table 2.2: Comparison of physical and mechanical properties of selected newly graded RSA	27
Table 2.3: Comparison of some interatomic potential	63
Table 3.1: Capabilities and limitations of modelling approaches [235].....	71
Table 3.2: Reaction force and moment on constraints	88
Table 3.3: Arduino Micro atmega32u4 Features	98
Table 3.4: Weight results during static calibration.....	115
Table 4.1: Physical properties of workpiece.....	122
Table 4.2: Chemical composition of the workpiece [363]	122
Table 4.3: Properties of Diamond [365]	125
Table 4.4: Geometry of diamond tools	126
Table 4.5: Machining Parameters or domain for the experiment	134
Table 5.1: Cutting force data for self-sensing sensor and Kistler sensor	138
Table 5.2: Regression and ANOVA summary output of force for RSA 905	140
Table 5.3: Optimization of cutting parameter for RSA 905.....	145
Table 5.4: Cutting force characteristics of RSA 905.....	148
Table 5.5: Acoustic emission data for RSA 905.....	157

Table 5.6:	Regression and ANOVA analysis of AE for RSA 905	158
Table 6.1:	Cutting force description for RSA 443	166
Table 6.2:	Experimental forces acquired for RSA 443	172
Table 6.3:	Regression and ANOVA output summary for cutting forces of RSA 443.....	173
Table 6.4:	Optimization conditions for cutting force of RSA 443	179
Table 6.5:	Experimental AE acquired for RSA 443	180
Table 6.6:	Regression and ANOVA output for AE of RSA 443	181
Table 6.7:	Optimization conditions for AE of RSA 443.....	187
Table 7.1:	Force characteristics during machining of RSA 6061	189
Table 7.2:	Experimental result of cutting forces for RSA 6061 during diamond turning using nose radius = 0.5mm	195
Table 7.3:	Summary of variance inflation factor	195
Table 7.4:	DoF for evaluation.....	196
Table 7.5:	Regression and AVONA output of cutting forces for RSA 6061 at nr = 0.5mm.....	197
Table 7.6:	Experimental results for cutting forces of RSA 6061 during diamond turning using nose radius = 1.0mm	205
Table 7.7:	Summary of VIF	206
Table 7.8:	DoF for evaluation.....	206
Table 7.9:	Regression and ANOVA output of cutting forces for RSA 6061 at nr =1.0mm.....	207

Table 7.10:	Optimization for RSA 6061 at nose radius 1.0mm	214
Table 7.11:	Experimental cutting forces for RSA 6061 during diamond turning using nose radius = 1.5mm	215
Table 7.12:	Summary of VIF	216
Table 7.13:	DoF for evaluation.....	216
Table 7.14:	Regression and ANOVA output for cutting forces for RSA 6061 AT NR = 1.5mm	217
Table 7.15:	Optimization conditions for RSA 6061 at nose radius 1.5mm	224
Table 7.16:	Experiment results for surface roughness (Ra).....	231
Table 7.17:	Summary output for regression and ANOVA Oof Ra for RSA 6061	235
Table 7.18:	Surface roughness optimization for RRSA 6061	242
Table 7.19:	Experimental results for MRR of RSA 6061	244
Table 7.20:	Summary output for regression and ANOVA of MRR for RSA 6061	245
Table 7.21:	Experimental results of chip formation for RSA 6061	253
Table 7.22:	Regression and ANOVAL analysis of chip formation	254
Table 7.23:	Chip morphology characterization for RSA 6061	259
Table 7.24:	Experimental results for AE during diamond turning of RSA 6061	265
Table 7.25:	Variance of inflation.....	266
Table 7.26:	Regression analysis and ANOVA for AE of RSA 6061	266
Table 8.1:	Chemical constituents of RSA 6061	275
Table 8.2:	Physical properties of Diamond	276

Table 8.3:	2D and 3D representation of tool geometry	277
Table 8.4:	MD simulation parameters	280
Table 8.5:	Mores Potential parameters for constituent elements of RSA 6061	283
Table 8.6:	Tersoff Potential Parameters	284

LIST OF EQUATIONS

	Page
Equation 2.1	38
Equation 2.2	39
Equation 2.3	42
Equation 2.4	42
Equation 2.5	42
Equation 2.6	42
Equation 2.7	43
Equation 2.8	43
Equation 2.9	46
Equation 2.10	49
Equation 2.11	50
Equation 2.12	53
Equation 2.13	53
Equation 2.14	54
Equation 2.15	56
Equation 2.16	56
Equation 2.17	57
Equation 2.18	60

Equation 2.19	60
Equation 2.20	61
Equation 3.1	87
Equation 3.2	88
Equation 3.3	88
Equation 3.4	88
Equation 3.5	88
Equation 3.6	94
Equation 3.7	95
Equation 3.8	95
Equation 3.9	95
Equation 3.10	96
Equation 3.11	106
Equation 3.12	106
Equation 3.13	107
Equation 3.14	107
Equation 3.15	108
Equation 3.16	110
Equation 3.17	111
Equation 3.18	111

Equation 3.19	112
Equation 5.1	139
Equation 5.2	139
Equation 5.3	139
Equation 5.2	141
Equation 5.3	159
Equation 7.1	198
Equation 7.2	208
Equation 7.3	218
Equation 7.4	230
Equation 7.5	235
Equation 7.6	245
Equation 7.7	252
Equation 7.8	254
Equation 7.9	267
Equation 8.1	279
Equation 8.2	283

LIST OF ABBREVIATIONS

2D	2-Dimensional
3D	3-Dimensional
ACF	Auto Correlation Function
ABOP	Analytical Bond Order Potential
ADC	Analog to Digital Converter
AE	Acoustic Emission
AFS	Atomic Force Microscopy
AMS	Atomic Mass Spectroscopy
ANFIS	Adaptive Neuro Fuzzy Inference System
ANN	Artificial Neural Network
ANOVA	Analysis of Variance
AVDD	Analogue Voltage Drain Drain
BBD	Box-Behnken Design
BUE	Built-Up Edge
CAD	Computer-Aided Diagram
CBN	Cubic Boron Nitride
CNC	Computer Numerical Control
COM	Communication
COMB	Combination
DAQ	Data Acquisition System
DBT	Ductile Brittle Transition
Dof	Degree of Freedom
DOE	Design of Experiment
DRM	Ductile Regime Machining
EDM	Electro Discharge Machining
FAN	Fuzzy Adaptive Network
FBG	Fibre Brag Grating
FEM	Finite Element Modeling
HIP	High Isolation Pressure

HPHT	High Pressure High Temperature
ICSP	In Circuit Serial Programming
IDE	Integrated Development Environment
IR	Infrared
KF	Kelman Filter
LAMMPS	Large-scale Atomic/Molecular Massively Parallel Simulation
LJ	Lenard Jones
MAPE	Mean Absolutely Percentage Error
MD	Molecular Dynamics
MEAM	Modified Embedded Atom Method
MOI	Moment of Inertia
MRF	Magnetorheological finish
MRR	Material Removal Rate
PGA	Programmable Gain Amplifier
PVDF	Poly Vinylidene Fluoride
PWM	Pulse Width Modulation
PCB	Printed Circuit Board
REBO	Reactive Empirical Bond Order
RF	Radio Frequency
RMS	Root Mean Square
RMSE	Root Mean Square Error
RPM	Revolution Per minute
RSA	Rapidly Solidified Aluminium
RSP	Rapidly Solidify Process
SCD	Single Crystalline Diamond
SCE	Specific cutting Energy
SDO	Simulation Driven Optimization
SEM	Scanning Electron Microscopy
SPDM	Single Point Diamond Machining
SPDT	Single Point Diamond Turning
SSCFTH	Self-Sensor Cutting Force Tool Holder

STM	Scanning Tunneling Microscopy
SVM	Support Vector Machine
SW	Stillinger Weber
TCM	Tool Condition Monitoring
TIS	Total Integration Scattering
UHPM	Ultra-High Precision Machining
UPM	Ultra-Precision Machining
US	United States
UV	Ultra-Violet

LIST OF PUBLICATIONS

1. **Odedeyi P B**, Abou-El-Hossein Khaleda, Abdulkadir Lukman N “Acoustic Emission and Surface Roughness in Ultra-Precision Diamond Turning of RSA 6061 for Optics Applications” Universal Journal of Mechanical Engineering 9(2): 11-20) September 2021. <http://dx.doi.org/10.13189/ujme.2021.090201>.
2. **Odedeyi Peter Babatunde** and Abou-El-Hossein Khaled, “A model for prediction and optimization of flank wear in End Milling of AISI 316 stainless steel”, The 8th International Conference on Fracture Fatigue and Wear (FFW 2020) Published: 13 January 2021. http://dx.doi.org/10.1007/978-981-15-9893-7_42
3. Lukman N. Abdulkadir, Khaled Abou-El-Hossein, **Peter B. Odedeyi**, Muhammad M. Liman & Abubakar I. Jumare, “RSM and MD—a roughness predictive model and simulation comparison of monocrystalline optical grade silicon” The International Journal of Advanced Manufacturing Technology, (2021) 112:437–451. <https://doi.org/10.1007/s00170-020-06277-8>
4. **Peter Babatunde Odedeyi**, Khaled Abou-El-Hossein “Tool Wear Progression and Optimization in End Milling of AISI 316 Stainless Steel” Materials Science Forum (Volume 1013) October 2020, <https://doi.org/10.4028/www.scientific.net/MSF.1013.33>
5. **Peter Babatunde Odedeyi**, K. Abou-El-Hossein, F. Oyekunle, and A. K. Adeleke, “Effects of Machining Parameters on Tool Wear Progression in End Milling of AISI 316”, Progress in Canadian Mechanical Engineering. Volume 3, Jun. 2020, doi: 10.32393/csme.2020.53. <https://library.upei.ca/islandora/object/csme2020%253A133>
6. **Odedeyi, P. B.**, K. Abou-El-Hossein, M. M. Liman, A. I. Jumare, and A. N. Lukman, "Acoustic Emission in Stainless Steel End Milling with Carbide Tools," in Key Engineering Materials, 2017: 206-210. <https://doi.org/10.4028/www.scientific.net/KEM.753.206>
7. **Odedeyi Peter Babatunde** and Abou-El-Hossein Khaled, “A model for prediction and optimization of flank wear in End Milling of AISI 316 stainless steel”, The 8th International Conference on Fracture Fatigue and Wear (FFW 2020) August 26 – 27, 2020, Online conference. <http://www.ffwconf.org/2020/>

8. **P B Odedeyi**, Abou-El-Hossein K, Liman M. "An experimental study of flank wear in the end milling of AISI 316 stainless steel with coated carbide inserts," in Journal of Physics: Conference Series, 2017, p. 012058.
[doi:10.1088/1742-6596/843/1/012058](https://doi.org/10.1088/1742-6596/843/1/012058)
9. Onwuka, G. R., **Odedeyi, P. B.**; Abou-El-Hossein, K.; Abdulkadir, L. N "Ultra-high Precision Grinding of Optical Glass Using Acoustic Emission Monitoring Technique" ASPE Proceedings 2018, pp. 321– 324,
<http://aspe.net/resources/aspe-proceedings-archive/>.
10. Abdulkadir, L. N., K. Abou-El-Hossein, A. I. Jumare, **P. B. Odedeyi**, M. M. Liman, and T. A. Olaniyan, "Ultra-precision diamond turning of optical silicon—a review," The International Journal of Advanced Manufacturing Technology, 2018; 96: 173-208.
<https://doi.org/10.1007/s00170-017-1529-x>
11. Liman, M. M., K. Abou-El-Hossein, A. I. Jumare, **P. B. Odedeyi**, and A. N. Lukman, "Modelling of surface roughness in ultra-high precision turning of an RGP contact lens polymer," in Key Engineering Materials, 2017: 183-187.
<https://doi.org/10.4028/www.scientific.net/KEM.753.183>
12. Jumare, A. I., K. Abou-El-Hossein, W. E. Goosen, Y.-C. Cheng, L. N. Abdulkadir, **Peter. B. Odedeyi**, et al., "Prediction model for single-point diamond tool-tip wear during machining of optical grade silicon," The International Journal of Advanced Manufacturing Technology, July 11, 2018.
<https://doi.org/10.1007/s00170-018-2402-2>
13. Muhammad Muktar Liman, Abou-El-Hossein K, **Peter Babatunde Odedeyi**. "Modeling and Prediction of Surface Roughness in Ultra-High Precision Diamond Turning of Contact Lens Polymer Using RSM and ANN Methods," in Materials Science Forum, 2018, pp. 139-143.
<https://doi.org/10.4028/www.scientific.net/MSF.928.139>
14. Abdulkadir, L. N., K. Abou-El-Hossein, A. I. Jumare, M. M. Liman, T. A. Olaniyan, and **Peter. B. Odedeyi**, "Review of molecular dynamics/experimental study of diamond-silicon behavior in nanoscale machining," The International Journal of Advanced Manufacturing Technology, June 09, 2018
<https://doi.org/10.1007/s00170-018-2041-7>

15. Muhammad Mukhtar Liman*, Khaled Abou-El-Hossein, Lukman Niyi Abdulkadir, **Peter Babatunde Odedeyi** and Abubakar Is'haq Jumare "Effect of cutting parameters on surface roughness in ultra-high precision turning of a contact lens polymer", Int. J. Computational Materials Science and Surface Engineering, Vol. 8, Nos. 3/4, 2019.
[doi/abs/10.1504/IJCMSSE.2019.104696](https://doi.org/10.1504/IJCMSSE.2019.104696)
16. Lukman N. Abdulkadir, Khaled Abou-El-Hossein, Abubakar I. Jumare, Muhammad M. Liman, **Peter B. Odedeyi**, "Predictive model for surface accuracy in ultra-high precision single point diamond machining of monocrystalline silicon using RSM and MD" International Journal of Computational Materials Science and Surface Engineering, 11th Sept 2020, **<https://doi.org/10.1504/IJCMSSE.2020.109559>**
17. Lukman N. Abdulkadir, Khaled Abou-El-Hossein, Abubakar I. Jumare, Muhammad M. Liman, **Peter B. Odedeyi**, "Predictive model for surface accuracy in ultra-high precision single point diamond machining of monocrystalline silicon using RSM and MD" International Journal of Computational Materials Science and Surface Engineering, 11th Sept 2020,
<https://doi.org/10.1504/IJCMSSE.2020.109559>
18. Liman M M, Khaled Abou-El-Hossein, **Odedeyi P. Babatunde** and Abubakar I. Jumare
"Ultra-High Precision Diamond Turning of Contact Lens Polymer", Proceedings of the 1st
International Conference of Institute of Polymer Engineers, Abuja, Nigeria, 15th-17th December 2016. PP 8-10.

CHAPTER 1

INTRODUCTION

In the early 1970s, Ultra-Precision Machining (UPM) emanated from US government weapons labs. Traditionally, ultra-precision machining using a single-point diamond tool has been used in the manufacturing of high-quality parts and components. It is one of the most efficient fabricating approach to produce optical and dimensional parts for systems in a range of applied research, defence, aerospace, and technology applications such as silicon wafers. Since the 1980s, this method has been extended to the production of a range of optical components for its high precision, flexibility, and lower average production costs. Therefore, ultra-precision machining is defined as a method for material removal using diamond turning, precision grinding, fly cutting and precision polishing to achieve high surface quality for optics and precision purposes.

Using geometrically specified diamond cutters, Diamond turning is an ultra-precision machining technology used to produce intricate functional surfaces and extremely fine microstructures. Diamond turning is currently applied to a wide variety of precious crystals, metallic alloys, and polymeric materials [1].

Single-point diamond turning (SPDT) based ultra-precision machining is a method that utilizes a nanocrystal diamond cutting tool with nanometric edge sharpness for reproducibility of shape and wear resistance [2]. The depth of cut being used is in the order of a micrometers or less. This process produces components with micrometers to sub-micrometers form precision and surface roughness within the nanometre scale. This ultimately makes it possible to directly machine non-ferrous materials (such as aluminium, copper alloy, silver, gold, electroless nickel and plastics) to optical quality without the need for subsequent post-polishing [3].

1.1 ULTRA-PRECISION MACHINING IN OPTICS APPLICATIONS

The superior surface finish and the precision form of ultra-precision diamond turning enable the technology to be widely adopted for the manufacture of a wide range of precision mechanical and optical components. Examples can be found in the production of optical components such as photoconductor drums, scanner mirrors, compact camera lenses, contact lenses, magnifiers, telescopes, injection moulding

inserts for plastic camera lenses and memory disk substrates, etc [4, 5]. In the other hand, by adding elements of aspherical and diffractive optics, the number of spherical lenses can be greatly decreased in complicated optical systems. However, with all materials using traditional machining techniques, aspheres and diffractive optic components are exceedingly difficult to manufacture to a high precision. Hence, ultra-precision machining based on SPDT has since become an economically feasible option for the manufacture of diffractive optics and aspheres. With the aid of tool path generation tools, the use of numerical control enables precise turning of aspherical and diffractive optical surfaces to the intricate details.

1.1.1 Single Point Diamond Machining (SPDM) for Optical Applications

Over the last few years, the SPDM of aluminium optics has rapidly improved. High-quality optics can currently be developed with unique aspherical shapes that meets with strict consumer requirements using this technology [6]. Special to the state of the art, with a micro-roughness of a few nanometres, SPDM has the potential to produce aspherical surfaces. High surface finishing precision is often considered to minimize surface dispersion to an appropriate degree for optical systems operating in the visible spectrum region. Although this technology has been confined to infrared applications in the past. Recent experiences by [7, 8], have demonstrated that by using amorphous material alloys produced by Rapid Solidification Processing (RSP), surface roughness can be greatly enhanced.

Due to the extremely high fidelity in the transition of the machine motion and the tool profile to the workpiece, the superior surface finish is formed in SPDT [3]. Ultra-precision machining technology's success depends not only on advanced machine design and control, but also on its associated metrology. Extremely high precision metrology tools are needed to inspect the quality of the machined surfaces for a nanometre level surface roughness and sub-micrometers level form precision [2].

For the success of an ever-increasing number of new optical products used for business, commercial, industrial, medical, and military applications, the availability of highly accurate optics is essential. Materials used in the production of optical moulds include optical aluminium alloys, nickel-phosphorous (Ni-P) plated steels and copper alloys. Aluminium alloys, which have proved to be advantageous and are most used

in mould making over other materials. It is one of the outstanding among these materials. In contrast to Ni-P steels and copper alloys, aluminium alloys exhibit less tool wear and are relatively cheaper.

The call for increasing optical system requirements has recently led to the development of newly modified grades of non-ferrous alloys characterized by finer microstructures. Its defined mechanical and physical characteristics have become a preferred material in the field of optical mould making.

1.2 PROBLEM STATEMENT

Although ultra-precision machining has outstanding ability to fabricate high-quality components with surface roughness at a nanometric level. But the nanometric surface roughness can easily be affected by a lot of different factors in a sensitive cutting process. Recently, researchers have been dedicated to investigating the effects of factors on surface roughness progress in ultra-precision machining. Some of these general factors are tool geometry [9], machine tool [9], cutting conditions[10], material property [11], tool wear [12], chip formation [13], vibration [14], environmental conditions [15, 16] etc. However, it is worth noted that these factors are still lacking enough investigations especially on newly graded aluminium alloys used for optics purposes. Therefore, some of the optimum conditions of these factors are demanded to be examined to achieve better surface finish for optical aluminium alloys.

In order to support the need for this task, given the increasing demand for higher precision requirements in the optical components industry, surface roughness plays an important role in the ultra-high precision machining of Rapidly Solidified Aluminium (RSA) alloys using the SPDT process [17]. It is known that traditional aluminium alloys can be machined with diamond tools for optical components such as mirrors and mould inserts. However, by replacing traditional 6061 with RSA-6061, surface roughness can be improved by a factor of 4 [18].

From literature, generally, a lot of data has been gathered for Traditional aluminium materials. Even though commercially available aluminium alloy such as traditional 6061 grade can be diamond turned to best surface roughness (R_a) values of approximately 4-8 nm because it was produced only by powder metallurgy. Hence, the homogeneity in the constituent alloys is lacking [17]. In addition, the fact remains

that this R_q value is only appropriate for the infrared spectral range, but it cannot be used in the visual spectral range because of the Total Integration Scatter (TIS) equation used for the visual spectral range design. TIS is also dependent on Surface Roughness R_q of certain value which must be less than what is used in wavelength i.e. ($R_q \ll \lambda$). According to Horst et al [6], using 300nm as the shortest visual wavelength, diamond turning of traditional or commercially available Aluminium alloys cannot deliver such a very low surface roughness value. Therefore, it can be suggested that ultra-high precision machining of the modified optical aluminium grades with fine and smaller grains could be a possible solution. It is also noted that not enough assessment has been carried out on these materials compare to traditional optical aluminium. There is therefore an increasing need to investigate the machinability and surface quality of newly developed aluminium grades developed during spinning melting by the rapid solidification process.

Furthermore, in modern manufacturing, there is a growing need for inexpensive and less cumbersome cutting tools. As a critical trend in the design of revolutionary smart cutting tool, cutting-edge sensor technologies have been adopted. An easy customized force sensor where the force information is very important for high-precision measurements is required. Sensors focused on surface finish monitoring have also become a major part of the sensor family over the last decade or so. These have seen numerous applications ranging from identification of gas and vapor to measurement of strain, pressure, and temperature [8-11].

Cutting forces in single point diamond turning is believed to be of more significant than other machining processes in monitoring and predicting high quality surface finish due to their resulting effects on the surface roughness quality. It is worth noted that cutting forces have direct influence on cutting pressure and power consumption, tool wear, and heat generation during machining. Therefore, undermining such an important characteristic is to compromise quality machining process and enhanced production cost. Currently, dynamometer is used conventionally to measure cutting forces, however, it is quite expensive and difficult to mount on a lathe machine than even an accelerometer. Hence, in this study, the researcher presents the development and implementation of self-sensor cutting force tool holder (SSCFTH) using strain gauges

to capture the applied cutting forces in real time during single point diamond turning of RSA alloys.

Nanotechnology includes two aspects, which are structures and materials at Nano scale. It also includes studying and applying special Nano scale phenomena to create new or improved functionality features [19, 20]. Nano scale typically refers to lengths ranging from 1 nm to 100 nm, while nanoscale cutting involves adjustments near the workpiece surface in only a few atomic layers that need to be studied from an atomic point of view. The continuum description of the subject becomes uncertain on such a limited governing longitude scale. On the nanoscale, this makes the material removal mechanisms not fully known. Therefore, more insight is still needed in order to be able to accurately predict industrial nanomachining processes. Atomic simulation is therefore necessary for this newly developed optical RSA alloy to fill another huge gap.

This study therefore addresses some aspects of the molecular dynamic simulation of RSA 6061 alloy material that may be attributed to the lack of adequate data on the microstructure and the interatomic potential limitations of the same RSA alloy.

1.3 AIMS AND OBJECTIVES

The aim of this research is derived from the general competitive perspective of today's manufacturing industries, which is to produce products at a low cost and at high quality within a short time. Therefore, this study is to:

- Investigate the ultra-precision machining of optical aluminium alloys such as RSA 905, 443 and 6061 for the manufacture of optical components by identifying machining parameters that will help to replace traditional aluminium alloy grades leading to ultra-high surface quality.
- Understand the atomistic and dynamics of nanometric cutting of RSA 6061 using a will be developed molecular dynamics simulation model to deliver and provide accurate and clear understanding of the influence of cutting parameters characteristics, thermal effect, stress impacts and cutting force characteristics during cutting and sub-surface deformation underneath the machined surface of RSA 6061.

To achieve the above aims, the following specific objectives have been outlined:

- To review the existing literature to gain clear understanding of the previous investigations and simulation works on UHPM of RSA alloys.
- To design, develop, implement, and validate a monitoring sensing tool holder for cutting force using first principle during diamond turning of RSA alloys.
- To study the effect of cutting force generated from SSCFTH and develop cutting force models for RSA alloys during diamond turning process.
- To study the effect of cutting parameters such as spindle speed (rpm), Feed rate (mm/min), depth of cut (μm) on RSA alloys.
- To study the acoustic emission during ultra-precision machining of RSA alloys
- To study the effect/influence of tool geometry such as tool nose radius (mm) during machining of RSA 6061.
- To develop a material removal rate for machining process and evaluation chip morphology and formation of RSA 6061
- To develop response surface models that predicts the surface roughness with their relationship to cutting parameters of RSA 6061
- To develop an atomistic tool-workpiece model for nanomachining.
- To simulate nanomachining process mechanisms using the Molecular Dynamics (MD) method

1.4 THE SCOPE FOR THIS STUDY

This study is expected to provide a data guide for the anticipated surface quality in ultra-high precision machining of rapidly solidified aluminium alloys and conventional aluminium alloys over a variety of machining parameters. The following limitations are included in the research:

- Strain gauge (T-rosette type) is used to develop the self-sensing cutting force tool holder (SSCFTH)
- The machining process will be ultra-precision single-point diamond turning (SPDT) of optical aluminium alloys - the workpiece materials used in the study shall be RSA 443, 905 and 6061.

- The nature and surface of the workpiece will be cylindrical and flat respectively
- The cutting parameters to be accommodated will be cutting speed, feed rate, and depth of cut.
- The tool geometries to be controlled for RSA 6061 will be tool nose radius (0.5 – 1.5) mm and for RSA 905 and RSA 443 will be 0.5 mm.
- The tool will be monitored online during cutting by studying the Acoustic Emission (AE) signals.
- The nature and surface of the workpiece during atomistic simulation will be rectangular and flat, respectively.
- The cutting parameter that will be varied during atomistic simulation will be depth of cut

1.5 MOTIVATION

According to market research by Arizton [21], the study expects the size of the global precision market to reach \$225 billion by 2022, rising at a compound annual growth rate (CAGR) by more than 11 per cent in 2016-2022. In-depth market analysis, share, market size and segment forecasts are presented in this industry analysis report. End-users (such as vehicles, watches, healthcare, aerospace, electronics and semiconductors) evaluate the segments given in the report by geographical location (e.g. Europe, North America, Middle East & Africa, and Latin America) [21].

The need for precision components in the end-user segments such as semiconductor production, equipment design, automotive assembly and machinery is supported by a faster technology curve. Engineering has now developed into a specialized market with considerable experience in the hands of small and medium-sized businesses who can quickly develop expertise propelled by open design architectures and the growth of CAD applications focused on subscriptions system.

This new technology is critical because of the decrease in processing time and high surface quality which has many manufacturing and economic advantages. According to [17], Rapidly Solidified Aluminium (RSA) is becoming more recognized as an alternative material. As described earlier, it is developed during casting by rapid solidification. This leads to fine microstructures with better mechanical and physical properties, making it preferable than conventional aluminium alloy grades. AA 6061 is

for instance, is produced by traditional foundry processes involving slow solidification. They, therefore, made up of a coarse microstructure and comparatively broad sizes of grain. This provides medium to high strength, although outstanding resistance to corrosion and very good weldability, but poor surface finish [22-24]. In the photonics industry, ultra-high precision machining (UHPM) is used intensively in the manufacture of parts for optical instruments and measuring devices. Optical aluminium alloys are among the materials used in the manufacture of optical mould inserts that produce a surface finish at Nano level and form.

1.6 METHODOLOGY

The methodology used in this research can be divided into two, i.e., the experimental part using the Ultra-High Precision Machining (UHPM) process and the simulation part using the Molecular Dynamics method.

1.6.1 UHPM Methodology

Experimental testing will be conducted on the Precitech Nanoform 250 Ultra-grind system in the Precision Laboratory at Nelson Mandela University. High-performance ultra-precision machine for the most difficult turning and grinding applications. The cutting parameters investigated were cutting speed, feed rate, and depth of cut while the tool geometries to be manipulated are tool nose radius and rake angles. Cutting force, acoustic emission, material removal rate, chip formation, and surface roughness are the main responses examined. Statistical approach is used to construct a mathematical model of experiments and investigate their effects on the responses. As a workpiece, cutting would be done on a circular RSA 6061 and the responses of surface generated would be investigated. A statistical model was created from the data, the impact of cutting parameters was established. A surface roughness map and corresponding cutting force and acoustic emission data are produced to classify areas that provide optimal results.

1.6.2 MD Methodology

An atomistic tool-workpiece model for nanomachining would be developed and Molecular Dynamics (MD) using Large-scale Atomic/Molecular Massively Parallel Simulator (LAMMPS) simulation of the nanomachining process is done. The results of

the simulation would be analyzed to observe the phenomena of temperature, depth of cut, cutting force, hydrostatic force, specific cutting energy, total energy, plastic deformation, and chip formation considering different depth of cuts during molecular dynamic simulation.

1.6.3 Structure of the Thesis

The thesis is divided into 9 chapters as described:

- Chapter 1: offers an overview of ultra-precision machining in optics applications and of the importance of research in terms of ultra-precision manufacturing. The chapter specifies the purpose of the analysis, the goals, the hypothesis, and scope of the research.
- Chapter 2: provides literature reviews on UHPM, machining of aluminium grades with highlights on the various issues such as applications of optical RSA, surface roughness in ultra-precision of RSA, molecular dynamics simulation and its principle
- Chapter 3: focuses on the cutting forces in ultra-precision machining, design and development of self-sensing cutting force (SSCF) tool holder.
- Chapter 4: offers methodology, materials, and experimental setup for ultra-precision machining of RSA.
- Chapter 5: presents tests of SSCFTH on RSA 905, analysis, and modelling of cutting force and acoustic emission during diamond turning of rapidly solidified aluminium (RSA) 905 alloy
- Chapter 6: presents tests of SSCFTH on RSA 443, analysis, and modelling of cutting force and acoustic emission during diamond turning of rapidly solidified aluminium (RSA) 443 alloy
- Chapter 7: presents analysis, modelling, and process optimization of cutting force, effects of tool geometry, acoustic emission, surface roughness, and chip formation during diamond turning of rapidly solidified aluminium (RSA) 6061 alloy.
- Chapter 8: provides MD simulation of RSA 6061 and the analysis of the MD results.
- Chapter 9: Conclusion and recommendations for future work.

CHAPTER 2

LITERATURE REVIEW

2.1 ULTRA-HIGH PRECISION MANUFACTURING

The focus of manufacturing research has changed from micro-to-nano-scale methods over the last couple of decades [25]. For the manufacture of optical, precision, and micro parts and precision structured surfaces, this advanced technology has been developed. Mechanical processes for ultra-precision machining are almost universal and have a long technological tradition [26]. In the year 1980s, Taniguchi [27, 28] provided a predictive development map for ultra-precision manufacturing in **Figure 2.1**. This pattern is becoming more probable as we reach 2020 and beyond. This is due to a large variety of engineering products that can be processed, such as metals, semiconductors, ceramics, optical glasses, and plastics. Hence a wide range of surfaces with optical, mechanical, or other properties can be made.

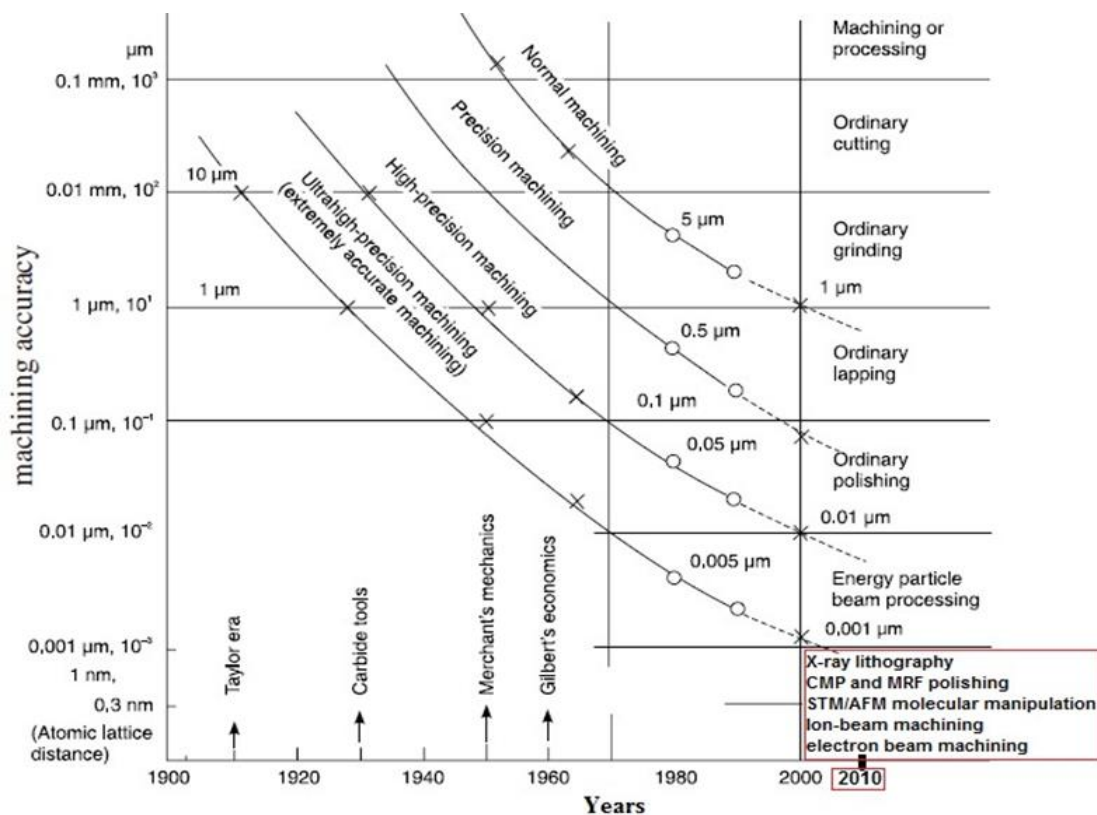


Figure 2.1: The development of achievable machining accuracy [25]

Ultra-precision development has now become an efficient method for monitoring surface properties and the integrity of the sub-surface of mainly optical and other practical components [25, 26].

2.2 ULTRA-PRECISION MACHINING (UPM)

As seen in **Figure 2.2**, ultra-precision machining can be defined as the best processing capabilities of the production process at the lowest point or before the atomic size is reached. For the generation of free-form surfaces and complex micro-structured surfaces with specific precision and cost-effectiveness, ultra-precision machining has produced deterministic techniques over the last few decades. The enormous variety of shapes that can be created today in optical or near-optical quality by multi-axis machining has inspired the design of complex optics. Ultra-precision production applications range from aerospace, medical, lighting, astronomy, optics, and metrology [26].

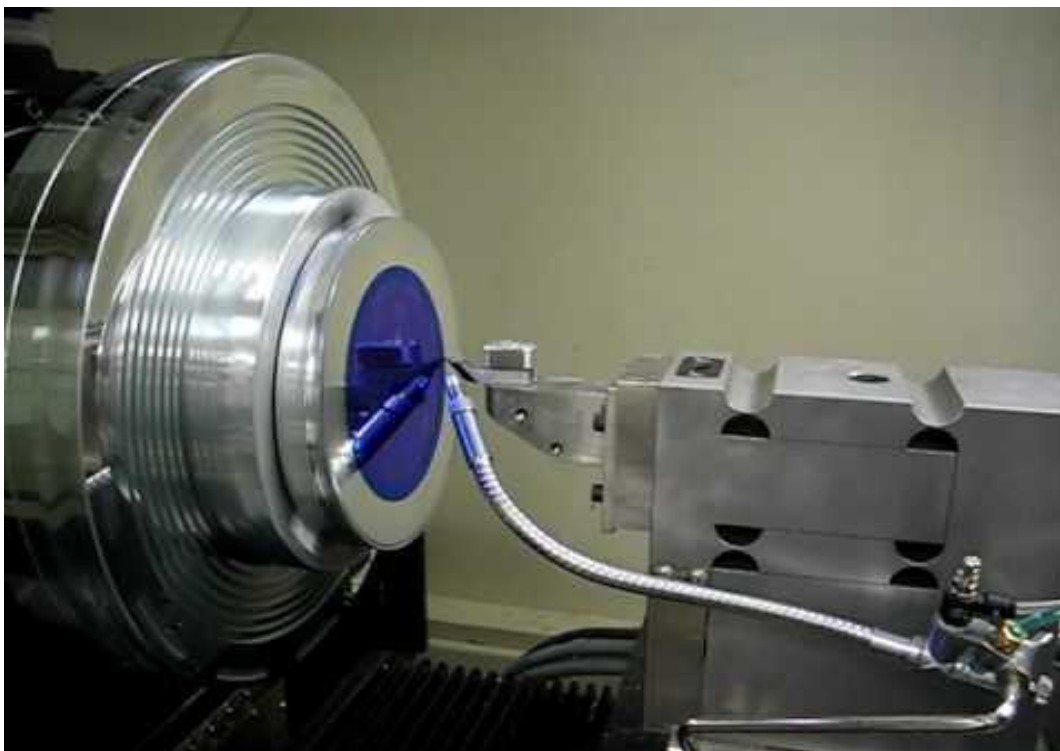


Figure 2.2: Ultra-precision diamond turning

The ability of machines to manufacture or operate machined surfaces or features that are subsequently sufficient for the performance of optical and mechanical functions can be described as ultra-high precision turning machines [29].

According to Siva, [30], ultra-precision machining characteristics usually range from 0.1 to 100 nm, according to Siva [28]. These include processes such as single-point diamond turning, cutting of cubic boron nitride, abrasive processes such as multi-point fixed (e.g. grinding, honing, belt polishing), free abrasive processes (e.g. lapping, polishing) and chemical processes (e.g. etch machining) [31]. Single point diamond turning has been an efficient process for optical and semiconductor industries to manufacture mirror-like surface finishes in components.

2.3 DUCTILE-REGIME MACHINING

According to Yu et al. [32], aluminium alloy was subjected to ductile and brittle fracture tests. It was discovered that aluminium alloy was more brittle than ductile probably because of the presence of silicon, iron, and other elements. Ductile element is suitable for machining brittle materials such as silicon, germanium, RSA alloys, silicon carbide, silicon nitride, glass, etc. so as to produce high-quality surfaces by removing chips in a ductile manner. This process is known as ductile-regime machining. An alternative approach to machine brittle materials aimed at achieving a high-quality crack-free surface finish through the ductile regime machining (DRM) technique using a plastic material removal operation [33].

In DRM, the material removal process is distinct from the brittle micromachining regime. During material removal, the chip form undergoes plastic deformation in the DRM, leaving a crack-free surface. The chip forming for brittle process micromachining, however, undergoes a deformation of the brittle fracture mode, leaving behind a surface with broken cracks. According to Griffith principle, the propagation of brittle fracture will take place when elastic energy concentration releases energy around the crack tip, overwhelming the lowest amount of energy-related to the presence of a free surface. Therefore during ductile-regime machining, plastic deformation becomes the dominant chip formation mechanism [25, 34]. Furthermore, Griffith also observed that the energy needed to propagate a crack is higher than the energy required for plastic yielding when at low feed rates. Therefore, during ductile regime machining, plastic deformation becomes the main procedure for chip formation. Also, it has been observed that the volume of material removed is directly proportional to the energy required for plastic deformation. Meanwhile, brittle crack energy is strictly proportional to the crack's surface area. The method of brittle

machining can, therefore, be seen in terms of minimal energy [35]. Therefore, brittle-ductile transformation would also need more specific cutting energy (SCE) than brittle-fracture-controlled machining to perform ductile regime machining. **Figure 2.3** represent complexities experienced in ductile-regime machining.

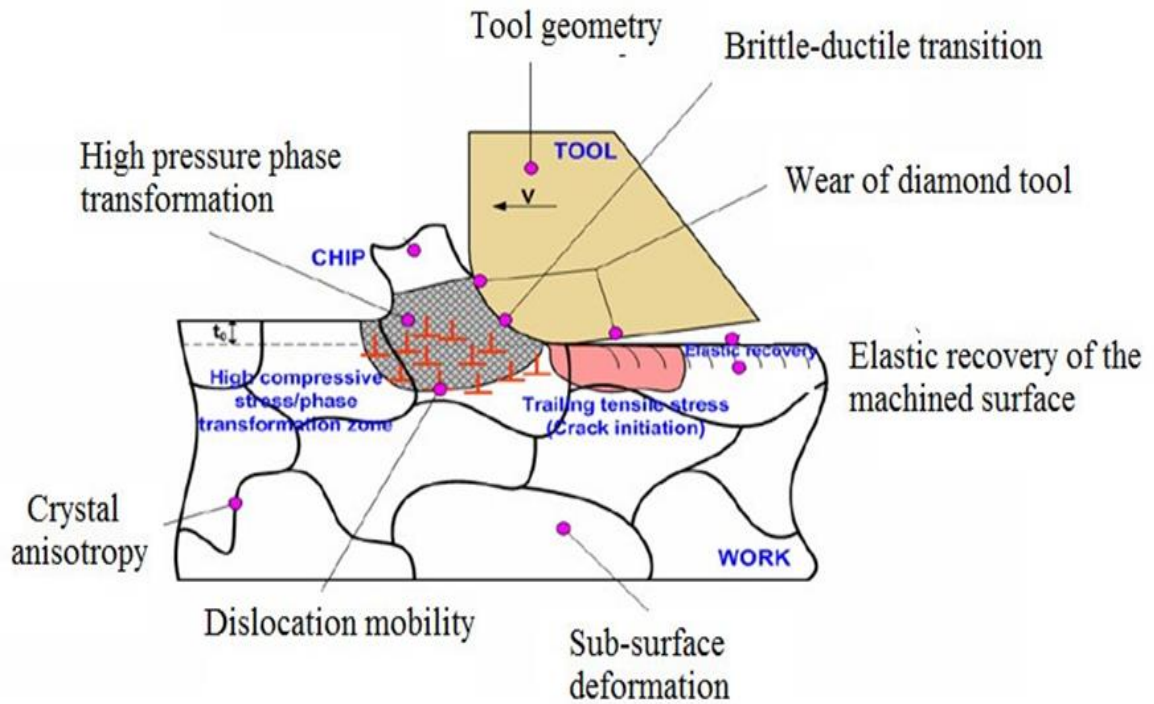


Figure 2.3: Complexities involved in ductile-regime machining [25]

2.4 BRITTLE - DUCTILE REGIME DURING MACHINING

The process of brittle-ductile regime machining is carried out on an ultraprecision diamond turning machine and can be described in **Figure 2.4**. The depth of cut is increased in a plunge cut from left to right in Figure 2.4; the surface quality and chip formation are observed [36]. As the tool crosses the workpiece, there are three distinct zones: first, a ductile zone where the chip formation is continuous and the surface is free of any defects such as micro-cracks, craters, etc. secondly, a brittle-ductile transition zone featuring a fractured semi-brittle surface and thirdly, a fractured surface with holes, cracks and severe surface damage [37]. It can be observed that there is a certain depth at which a ductile to brittle transition occurs, and the depth depends on process parameters, workpiece material properties, and tool geometry.

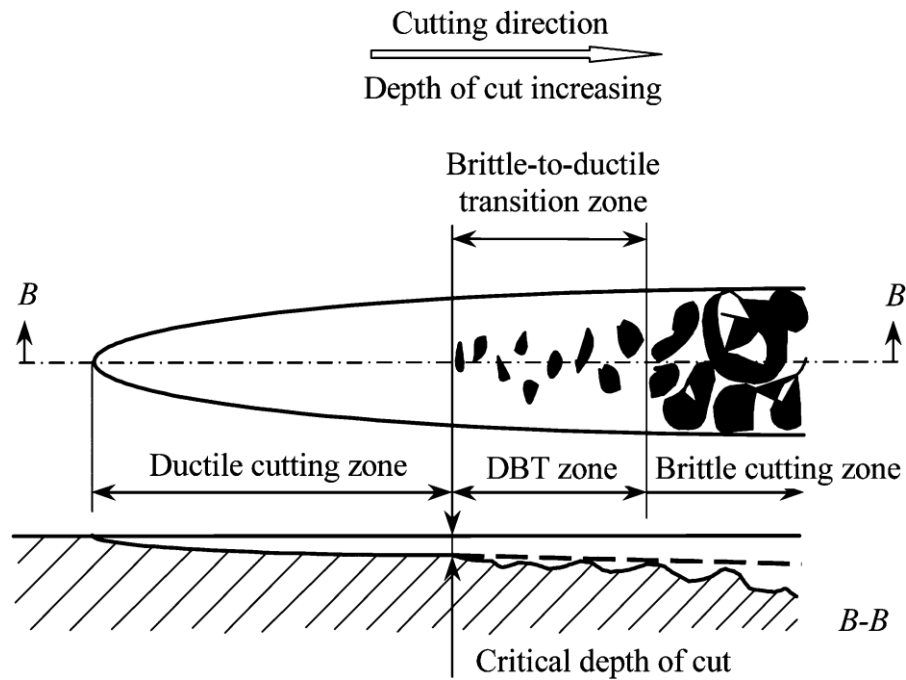


Figure 2.4: Schematic of ductile-regime machining [37]

The applications of brittle-ductile machining range from producing micro wafers, aspherical lenses for camera equipment, and optical instruments to manufacturing no replacements using ceramics. In comparison to other ultraprecision machining processes such as polishing, lapping, etc., ductile-regime machining is both cost-effective and less time consuming [36, 38, 39]. In order to develop the proposed predictive model, several aspects of machining are required, which would aid in a better understanding of the mechanics of ductile-regime machining. Some of the aspects can include force modelling, the process of ductile-regime machining, effects of microstructure on flow stress, material constitutive model, and high-pressure phase transformation [30].

The process of ductile cutting of polycrystalline materials has not been widely reported as single-crystal materials. The obvious reason for this trend is the fact that single-crystal materials are homogeneous in their structure and more amenable to cutting. Bifano et al. [40], noted that brittle materials could be machined under a ductile regime at a lower critical depth of cut. Consequently, with no surface pitting or cracking, it generates a good surface finish. And in micro machining, the chip thickness may be on the order of the critical depth of cut. However, in brittle materials, micro machining can serve as a novel means of producing special requirements.

Liu [41], researched ductile carbide (WC) cutting and showed that the undeformed chip thickness was growing from the ductile cutting to the brittle mode technically. Yan et al. [42], carried out ductile cutting tests on polycrystalline germanium using a sharp nose diamond tool. The cutting process was carried out on three grains. Surface finish and forces have been recorded. The force and surface roughness of the three grains were discovered as the tool went through the workpiece. It has also been documented that even ductile-cut surfaces have been developed using an unparalleled, incredibly small chip thickness of about 80 nm. Ductile machining on polycrystalline silicon carbide was carried out by Bhattacharya et al. [43] and a transformation of a substance under the tool was recorded. Furthermore, the authors report that polycrystalline carbide ductile cutting is possible at penetration depths of between 10 and 25 nm.

From the deliberation on laboratory studies, it is apparent that many brittle materials have been treated effectively by ductile regime machining, which for the future of this process is appropriate. While experiments are an efficient way to analyze material reaction, a simple understanding of process dynamics is required if process technology is to be translated from the laboratory to a large-scale manufacturing set-up successfully.

Moreover, literature findings have shown that several diverse materials have experimentally checked the method of ductile die machining. The most studied material was single crystal (Si) since it is the cornerstone of the semiconductor industry. The remaining materials tested are germanium (Ge), silicon carbide (SiC), glass, etc.

In Fang and Zhang [38], the effect of a tool edge radius on the cutting of single crystal silicon was examined. The findings demonstrate that ductile cuts can be accomplished by adjusting the advanced radius and undeformed chip thickness, which varies the effectiveness of the rake angle. Yan et al. [44] developed a ductile device based on the direct line enveloping process to produce rough, brittle convex axisymmetric aspherical surfaces. A surface was generated using a straight nosed diamond tool on single crystal silicon and the roughness value of $R_a = 16$ nm was obtained.

Yoshino et al. [45], developed a machining device to carry out precision machining experiments under external hydrostatic pressure. The authors performed cutting

experiments on soda glass, quartz, and silicon under hydrostatic pressure. According to Patel and Mir [46, 47], claim that machining of energy mode is transported by some undeformed chip thicknesses from plastic deformation to fracture deformation. Machining energy is also an important element in the characterization of material removal mode in a delicate regime.

Research conducted by Fang et al. [48], shows that the energy needed for breaking up is typically higher at a limited infeed rate than the energy needed for plastic yield. Furthermore, fragile materials undergo a spring-ductile transition. **Figure 2.5** displays the analytical model of machining of the ductile regime.

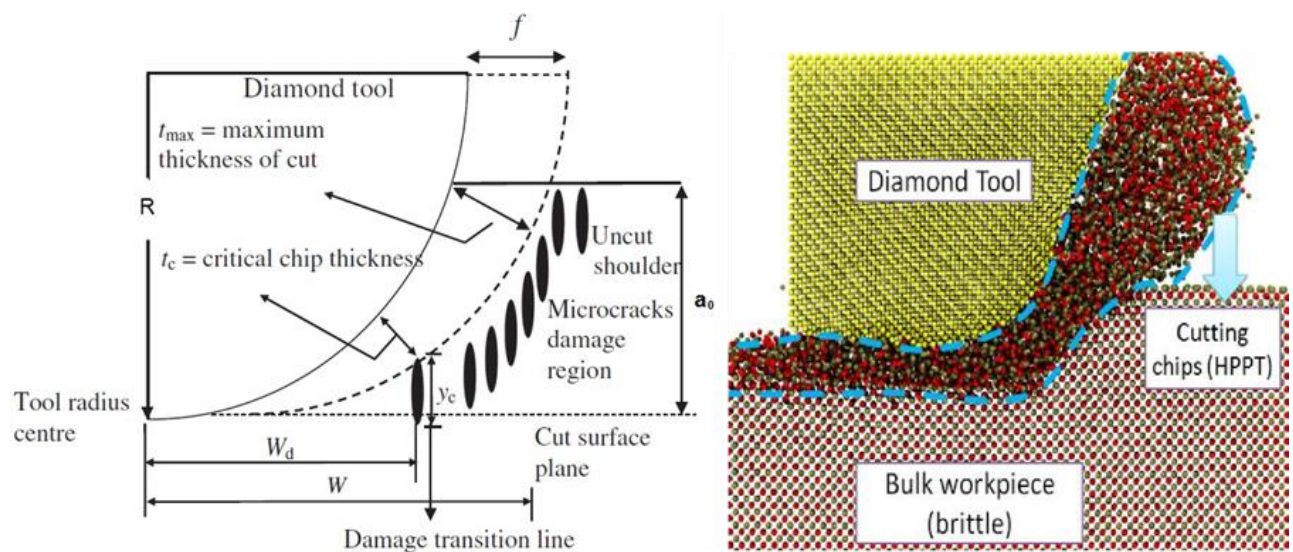


Figure 2.5: Analytical model of ductile regime machining and 2D representation of the 3D condition showing nose radius of the tool [25, 49, 50]

The application of external hydrostatic pressure suppresses the brittle response in ductile mode cutting as it minimizes cracking tendency and chipping. Yan et al. [51] demonstrated single point diamond turning of calcium fluoride (CaF_2) to produce surfaces with nanometric finish. Diamond turning of brittle materials such as silicon, germanium and lithium niobate was carried out by Nakasuji et al. [52]. They found transformation in some areas but with no clear lithium niobate orientation but concluded that a vibration-free machine tool and low cutting thickness were sufficient for ductile cutting of this highly brittle material. Indentation and diamond turning experiments have been documented by Jasinevicius [53] for materials such as gallium arsenide (GaAs) and indium antimonide (InSb). For ductile cutting at feed rates

ranging from 1.25 to 7.5 $\mu\text{m}/\text{rev}$, these materials were very desirable. However, GaAs showed only the lowest feed rate with a predominantly ductile response. Bifano et al. [40], reported ductile regime grinding results for various materials such as fused silica, soda lime glass, zerodur, quartz, zirconia, germanium, silicon, and silicon carbide.

2.5 Single point diamond turning (SPDT)

There are two major groups of tools according to the number of main cutting points. These are single-point and multiple cutting-edge tools. The former is referred to as such because it makes use of one single edge contact with the workpiece during machining. While the later, uses many cutting edges usually found in the application of drilling, milling, grinding, reaming, tapping, and sawing operations. The main feature of SPDT is its ability to produce high-quality, nanometer-size surface finish while maintaining tight micrometer-order form tolerances [30, 54]. When it comes to products, a crucial index for product quality and the technical requirement is surface roughness. The surface roughness is to be kept within a certain range in place of the possible lowest value in certain circumstances especially for precise mould inserts of optical parts used for injection moulding processes. The investigation into predicting surface roughness in SPDT is consequently important and necessary in order to quickly and effectively control the desired surface roughness of the product [54].

2.6 DIAMOND CUTTING TOOL

The cutting tool often used in SPDT is diamond. Two types of diamonds are currently available commercially; these are traditional and synthetic diamonds. The diamonds which the former process can obtain are known as natural diamonds and those obtained by the latter are known as synthetic diamonds. When synthetic diamonds are produced in industry, the use of high pressure and high temperature (HPHT) presses graphite to the same or similar conditions as diamonds formed in natural diamonds formed in the crust of the earth. Under such conditions, the diamond produced has a fine crystalline structure. Natural diamonds can be classified in four kinds, namely due to the existence of nitrogen in the crystal and certain other properties (Ia, Ib, IIa, IIb). The majority of natural diamonds are of type Ia, with a high concentration of nitrogen in various crystal aggregates [55].

Over the years, with high pressure and high temperature (HPHT), type Ib changes to type Ia, in which nitrogen spread and coalesced into aggregates. Synthetic diamonds can also be classified as natural diamonds according to the same arrangement. Nearly all synthetic diamonds are type Ib, with an even distribution of nitrogen atoms replaced with carbon atoms (up to about 500 ppm). Type IIa and Type IIb are very rare in nature but can be combined for industrial applications [55]. There are many impurity elements in natural diamonds such as nitrogen, hydrogen, boron, and oxygen. Nitrogen and boron can be found in the crystal grid as substitutes for carbon. These impurities can be found in small amounts. Synthetic diamonds, on the other hand, do not have a great variety of impurities [55, 56].

2.6.1 Anisotropy of Diamond

For polishing process, manufacturers normally choose crystallography orientation for diamond tool design. **Figure 2.6** highlights the three most frequently used planes of a diamond crystal. The octahedrons (111), cubes (100) and dodecahedrons are (110). The crystallographic (110) or (100) planes are often chosen as the instrument rake face with the tool axis and the tool shank parallel to $\langle 110 \rangle$ direction.

As regards the crystallographic orientation of single point diamond turning, it has been established that single crystal diamonds are used as cutting tools, especially for ultra-precision machining because of its excellent mechanical and physical properties. Due to its properties such as strength, abrasion or wear resistance, the use of a single crystal diamond tool is very complex. Friction coefficient is critically dependent on its crystallographic orientations [55] because according to Jayesh et al. [57] and Buckley [58]. In order to obtain the best possible performance from a cutting tool, however, flanks and rake face must be polished and smoothed to minimize friction and ensure that the cutting edge is sharp and clean [25, 59]. In addition, the performance of a cutting tool depends on the cutting edge's strength and quality. There are two classic rules for the orientation of the diamond cutting tool. First the diamond cannot be positioned so that the orientation of the cleavage planes promotes the work stress placed in the tool to cut or to chip the tip of the tool. Secondly, the polishing direction must be placed towards and not away from the edge of the diamond when polishing the tool close to the cutting edge. This prevents tensile stresses in which the diamond is most sensitive [59]. A good polish on the flat side of the rake is easier than on the

curved flank. The final step in the development of a cutting tool is to give the rake a fine finish to produce a good edge.

Due to its excellent mechanical, chemical, thermal, and electrical properties, Diamond is a perfect material for cutting tools. The benefits of diamond cutting tools are that they are used because of their ultra-high wear resistance hardness, which allows hard and ceramic materials to be machined in most of the early micro machining research. Ultra-small sharp cutting-edge radius could also easily be produced, enabling programming of smaller undeformed chip thickness and thus ultra-precision machining. Diamond tools also have the ability, due to their mechanical and chemical properties, to retain an incredibly sharp cutting edge. It is possible to separate diamonds into single crystals and polycrystals. The only tool material that can be used for ultra-precision machining is single-crystal diamond (SCD), since only on SCD can an incredibly sharp cutting edge be obtained. The approximate edge sharpness (edge sharpness) is a few nanometers up to a few tens of nanometers.



Figure 2.6: Mono-crystalline synthetic diamonds for requiring an ultra-high-quality surface finish (a) manufactured in HTHP processing (b) inserted with mono-crystalline natural diamond cutting edge.

The reinforced diamond, i.e. SCD, has recently been marketed as cutting tool material for ultra-precision cutting instead of natural diamond [60]. In the industry, SCD tool were used for many years to produce optics and precision parts by diamond turning or fly cuts. While the cutting edge radius of the single-point diamond tools can be sharpened to 20 nm [61]. The edge wave can be reached at 50 nm. For this reason, diamond turning tool are used for the clearance angle in single point diamond tools

(see Figure 2.7). However, simple convex microparts or microstructures can limit the generation of concave shapes of deep or steep cavities.



Figure 2.7: Single-point diamond tools for ultraprecision machining by Rudrali Hi Tech Tools Pvt. Ltd [62]

Due to hard and excellent tool properties, tools can produce high precision, efficiency, and low tool wear rates etc., and particularly for the machining of hard and brittle materials see **Figure 2.8**. Diamond is, therefore, the perfect material for the machining of materials with inclusions, hard-to-cut materials, glass, or the machining of other tool materials such as cemented carbides. Typical processes using diamond methods include micro-turning, frying and boiling, and grinding [63]. The drawbacks of diamond tools, however, are that they are very similar to iron. In particular micro-cutting is limited to machining materials like brass, aluminium, copper and nickel, etc., [60]. Hard materials, such as single crystal silicone, titanium and other brittle materials are now difficult to machine with ultra-precision machining, using diamond cutting tools.

2.6.2 Cutting tool geometry

Tool geometry can be considered at a cutting point as the basic angles or slopes of the tools' faces and edges [64]. It defines the nose radius of the tool and other angles that completely define the tool features [65]. Several parameters can be described in the geometry of the instrument, namely: angles for back and side rake, angles for end

and side relief, angles of the end and side cut and ultimately the radius of the nose.

Figure 2.8 displays the tool geometry forms.

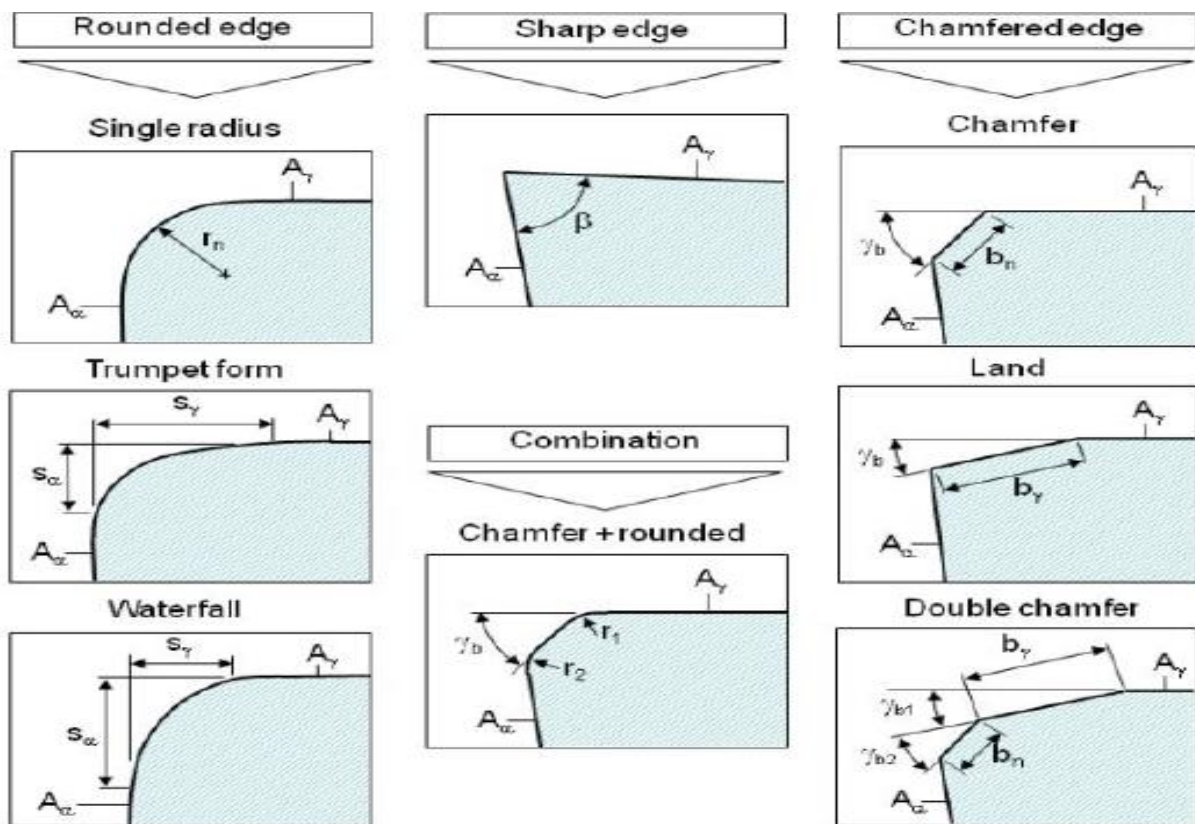


Figure 2.8: Typical cutting-edge preparation geometry [66]

Surface roughness, tool life, tool wear, ductile to brittle limits, depth of cuts, and general tool material are crucial issues to be considered when developing cutting tool geometry because of the major role it plays. Although, the effective tool condition monitoring (TCM) systems have been developed by many researchers [67, 68] in order to increase diamond cutting tool performances, it is still challenging due to diamond tool wear mechanism that is quite complicated and difficult to characterize which makes it different from other cutting tools. Thus, the optimum diamond tool geometries associated with effective TCM systems remain in requirements. A key criterion is to choose the tool with the lowest edge radius and least edge waviness when choosing diamond cutting tools for micro machining.

Ultra-precision machining is extensively utilized in surface finishing due to the high need for low surface roughness, complex characteristics, and little crack layers in the subsurface [69]. However, researchers have done few investigations into the effects of tool geometry on the state of the workpiece during diamond turning. According to

the investigation carried out by Yue et al. [70], on optical material, one of the major important parameters that will affect final surface roughness of the workpiece is cutting edge radius. Generally, cutting edge radius and rake angle are the two major geometric consideration evaluated when developing tool geometry for ultra-precision machining.

Findings have shown that the cutting-edge radius has an important effect on the material's ductile to brittle transition. According to Fang et al. [71], the state-of-the-art radius is considered to be sharp when the edge radius is less than the cutting depth or vice versa. If the cutting depth is less than the leading radius, an efficient rake is created [72], further research showed that an extreme rake angle would produce higher forces which would in turn deform further. The nose radius is one of the key parameters of tool geometry that was not systematically studied, perhaps because of its intuitive impact on component surface finishes.

It was also found that the greater the nose radius of the tool, the better the surface finish [73-75], which was confirmed in this current study. Shintani and Fujimura study [76], they confirmed that the tool life based on flank wear would increase just as the nose radius increases. However, findings confirmed that that at large nose radii, a serious groove wear will be unavoidable. Therefore, the poor surface quality will be evident. Apart from effects of tool nose radius on surface finish, it also impacts the uncut chip geometry in such a way that the ratio of edge radius to the uncut chip thickness may affect the forces generated during ploughing in hard-turning process [35]. In this current study, the tool nose radius used are 0.5 mm, 1.0 mm, and 1.5 mm.

2.7 ATTRIBUTES OF ALUMINIUM

Aluminium as an element was discovered about 160 years ago. A viable production process began [77] about 100 years ago. Currently, about 63,697 metric tons of aluminium was produced in 2019 [78]. More aluminium is produced each year than all other nonferrous metals altogether. Aluminium is accounted for as the third-largest abundant element consisting of almost 8% of the earth's crust. Because aluminium is not found naturally in metallic form. It is found mostly in rocks, soil, clay, and vegetation combined with oxygen and some other elements. Aluminium is a corrosion-resistant element, it has an atomic number of 13, i.e., 13 electrons, 13 protons and 14 neutrons.

The electron configuration at ground state for aluminium is [Ne] 3s² 3p¹. Aluminium also has three oxidation states which are +3, +2, +1 but the most common is +3.

2.7.1 Aluminium alloys

Aluminium in its alloy is one of the most versatile, attractive, and economical material for a wide variety of applications because of its special ability to combine with other elements. Apart from steel, aluminium alloys are second in usage globally as a structural metal. There are two types of aluminium alloys that are common; the first is cast alloys and the second one is wrought alloys the main classes of aluminium alloys classified into series such as 1xxx – 9xxx series [79].

According to [79, 80], the 4 digits signifies the type of main elements added to the aluminium such as 2xxx. This means copper is the major element added to aluminium. 4xxx means silicon is the major element added to aluminium. Also, alpha numeric suffix is sometimes included in the alloy name, which can also mean that certain heat treatment or fabrication process has been gone through for production to take place. For example, 6061-T6 and RSA 6061, represents the degree of hardness or tempering which occurred during production and the later was achieved by means of rapidly solidified means [81].

Aluminium in its alloy is a chemical composition that contains additional elements in a well-controlled proportion. The reason for the additional regulated elements is to improve its mechanical strength, optical ability, and machinability to achieve a particular aim. Some of the common elements that can be added to pure aluminium are iron, silicon, magnesium, chromium, copper, manganese, zinc, zirconium, titanium. Aluminium alloys are found useful in the area of aerospace, electronics, astronomy, medicine, telecommunication, manufacturing of house-hold utensils and shipbuilding [80, 81].

2.8 GRADES OF RSA ALLOYS FOR OPTICAL USE

Aluminium alloys for various precision and optical components such as mirrors and hard disks are commonly used. For high-quality infra-red optics that are diamond-turned and gold-plated, aluminium forgings are used to give a surface finish in the order of one Angstrom [82]. In the production of traditional grades of aluminium alloy

through conventional foundry processes, slow solidification is commonly used. This process causes a coarse microstructure and relatively broad grain size of aluminium alloy. Traditional aluminium alloy surface ruggedness such as AA 6061 is approximately about 5-8 nm [83].

Among all the traditional aluminium alloys, the most utilized traditional aluminium alloys are AA6061 because it offers good corrosion resistance, high strength, and good welding ability [84]. Recently, 6082 aluminium alloy is well-known over AA 6061, since it has about the same physical features as AA6061 aluminium alloy grade and has stronger mechanical properties when tempered. The intensity was related to the presence of more manganese in AA 6082 [85]. While aluminium alloy 6082 offers good resistance to corrosion, formability, weldability, braze capacity with excellent finishing characteristics [86]. T6 tempers are ideal for optical work applications according to tempering designations and definitions of aluminium alloys because they provide the best machinability and the highest strength and result in a better surface quality.

2.9 RAPID SOLIDIFICATION PROCESSING

Currently, the rapid solidification melt spinning technology is used for the manufacture of aluminium alloys for optical mould making. In efficiency, the foundry method of melt spinning is the best way to rapidly solidify, not only by having one of the fastest cooling speeds (10^6 K / s), but also the finest micro-structure [87]. **Figure 2.9** demonstrates the steps in the process of rapid solidification. Aluminium is melted along with all the elements in one furnace container in the first step. The liquified alloy is then moved to a high-speed copper spinning wheel to produce a rapidly solidified ribbon. The fine nanostructure alloys with improved physical and mechanical properties are manufactured by [8, 23, 24, 88-91]. This ribbon is cut and placed in a container. Finally, the flakes are revealed to create a mixed, condensed rapidly solidified aluminium alloy (RSA) material and are subjected to heat isostatic pressure (HIP) processing. Most of the diameter is 1 mm of billet sizes. However, if the need arises, the billets may be forged or extruded into different sizes [6, 91].

Figure 2.10 shows clearly that quick solidified aluminium RSA alloys have an advanced finer grain structure than conventional aluminium alloys. The size of the grain in RSA is approximately 1 μ m. This shows that a very good surface quality can

be obtained when all machining processes are tracked and observed. **Table 2.1** displays the chemical composition of the current research alloy, AA 6061, and RSA 6061. The physical and mechanical properties of selected RSA used for the analysis are also shown in **Table 2.2**. According to Newsander et al. [92], the heat treatment temperature of RSA-6061 was significantly higher than traditional AA-6061, but still in compliance with the AMS 2772 requirements. For RSA-6061, the 1-hour solution treatment period varies in the short term from AMS 2772. AMS 2772 is supposed to soak at the solution treatment temperature for a 15 cm thick portion for three hours. The quench delay of the RSA-6061 was also set to be very short for a maximum of 5s and stated a maximum of 15 s within the AMS 2772. The artificial RSA-6061 age was, therefore, achieved at a slightly higher 185°C temperature compared to 177°C specified by AMS 2772. These variations are based on RSP technology, previous studies and the heat treatment experience of the RSA material solution have been shown in [6, 92].

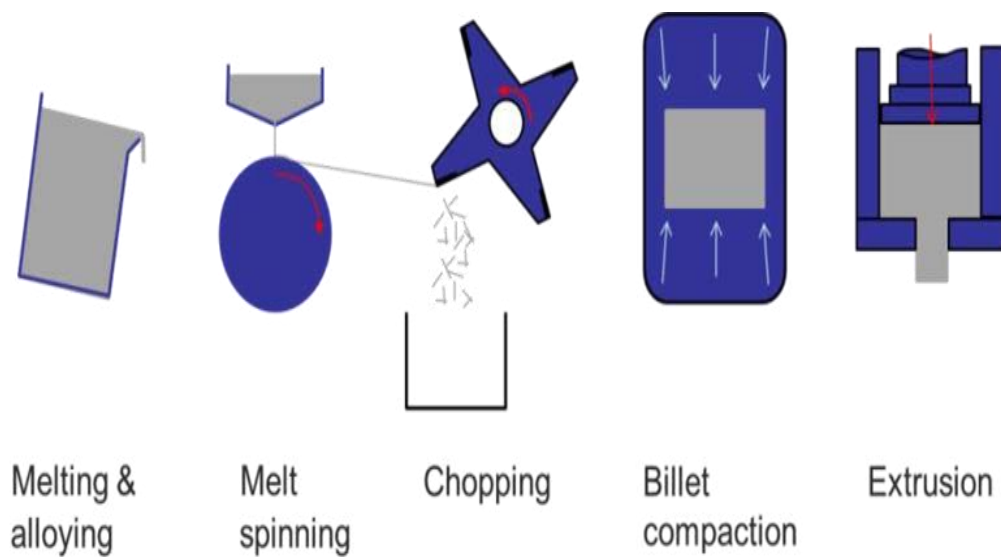
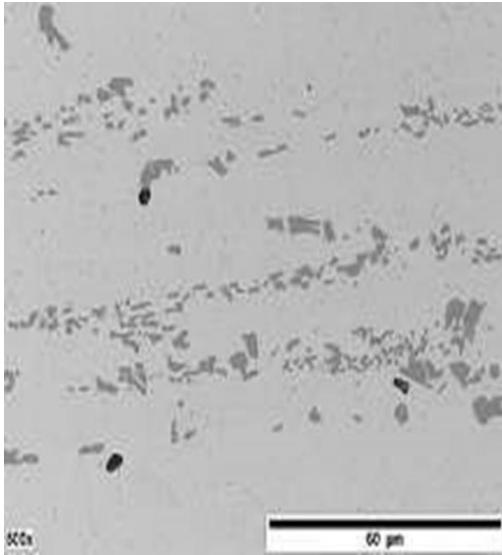
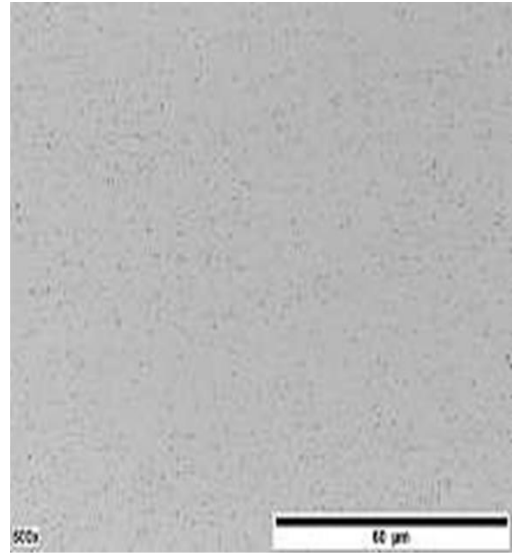


Figure 2.9: Required steps in Rapid solidification process [6, 92]



AA6061



RSA 6061

Figure 2.10: Microstructure of conventional alloy AA6061 and RSA 6061 alloy [8]

Table 2.1: The alloy composition of conventional aluminum 6061 and RSA 6061 chemical composition

Wt%	Si	Fe	Mg	Cu	Zn	Cr	Mn	Zr	Ti
Chemical Composition of 6061	0.4-0.8	0.0-0.7	0.8-1.2	0.15-0.4	0.0-0.25	0.04-0.35	0.0-0.15	0.0-0.05	0.0-0.15
RSA 6061	0.6	0.3	1.0	0.3	0.0	0.2	0.1	0.05	0.1
Conventional 6061	0.744	0.215	1.0	0.340	0.034	0.085	0.033	<0.001	0.027

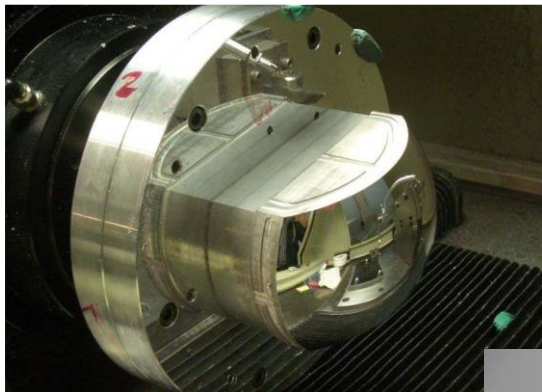
Table 2.2: Comparison of physical and mechanical properties of selected newly graded RSA

		RSA 905	RSA 443	RSA 6061
Physical Properties	Density [gm/cm ³]	2.95	2.54	2.70
	Thermal expansion [10 ⁻⁶ /°]	19.0	13.6	22.6
	Young's modulus [GPa]	90	102	70
	Specific Stiffness [GPa/(g/cc)]	31	40	26
	Thermal Conductivity k [W/m. K]	115	135	165
Mechanical Properties	UTS [MPa]	600	225	340
	Ys [MPa]	475	155	315
	Elongation [%]	5	1.5	16
	Hardness [HB]	180	105	110

2.10 PERFORMANCE OF RSA FOR MOULD

When rapidly solidified grades (RSA) are used as a mould material, they demonstrated excellent performance [83] see **Figure 2.11**. The performance of mould inserts made from beryllium copper and AA6061 compared to RSA was studied by Zhong et al. [93]. They found that RSA's diamond turning provided a better surface finish for the mould insert. The result was due (as previously stated) to the fine RSA microstructure that resulted in finer cutting stripes on the insert's machined surface. In subsequent investigations carried out by Gubbels et al. [7], they performed single point diamond turning experiments on RSA 6061 using tool geometry with a rake angle of 0°. Within shorter machining steps, diamond machining of RSA 6061 produced small surface roughness values ranging from 2-3 nm. The optimization of the machining process has not, however been carried out. In the meantime, the surface roughness produced

by RSA 6061 was not only lower than other conventional mould materials e.g., plated materials, but also did not require lengthy processing, such as grinding and polishing.



Mould after diamond turning process

Sunglass design



Figure 2.11: Mould after diamond turning process b) sunglass design from RSA Mold [8]

The study [24, 89] failed to expand on the efficiency of RSA in terms of tool life and tool wear. The research instead concentrated on evaluating the consistency of the machined surface. In addition, a significant number of researchers have studied the ultra-high-precision machining of optical grades of aluminium alloys such as AA6061. Therefore, there is a need to look at precision diamond machining and tool wear features because of turning of those new aluminium grades changed by rapid solidification.

2.11 APPLICATIONS OF OPTICAL RSA

Injection moulding continues to play a crucial role in the manufacturing sector of various optical plastic products. Polymer injection moulding is used for the manufacture of optical components such as contact and intraocular lenses, as shown in **Figures 2.12 - 2.15**. In addition to other materials such as beryllium copper alloys, conventional aluminium grades such as 6016-T6 are also used to produce mould

inserts for plastic optics injection. Conventional aluminium is distinguished by its high machinability, and low cost at the expense of its comparatively low strength compared to other mould materials. However, with enhanced intensity, the industry has witnessed the production of unique and modified aluminium grades. This is due to advanced casting and melting technologies that have recently been developed.

According to Guido et al. [7], even though gold coating has the highest reflectivity in the spectral range, when it comes to visual range, RSA alloy is much better. Similarly, when compared with nickel coating in terms of reflectance in visual spectral range for optical systems, RSA is twice better than nickel coating, despite its fair surface roughness which ranges between 1-2 nm. Furthermore, Guido et al. [7], was able to diamond-turned RSA 6061 alloy used for star separator M10 Mirror that attained a sharp edge $< 30 \mu\text{m}$ and surface roughness as low as possible which is not achievable by nickel coating. RSA 6061 was also found useful in the manufacturing study for Bepi Colombo baffle vane.

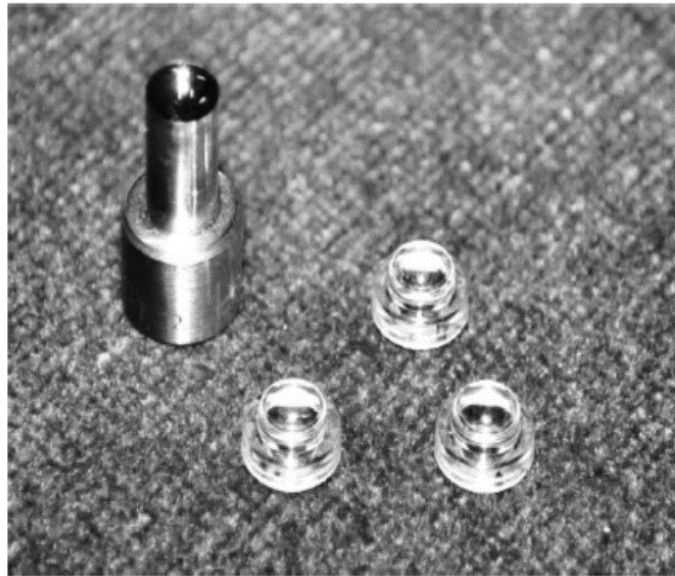


Figure 2.12: A lens mold and the injection-molded camera lenses for mobile phones [94]

Manufacturing process flow for micro plastic lenses



Figure 2.13: Application of Mould in the making of precision optics[95]

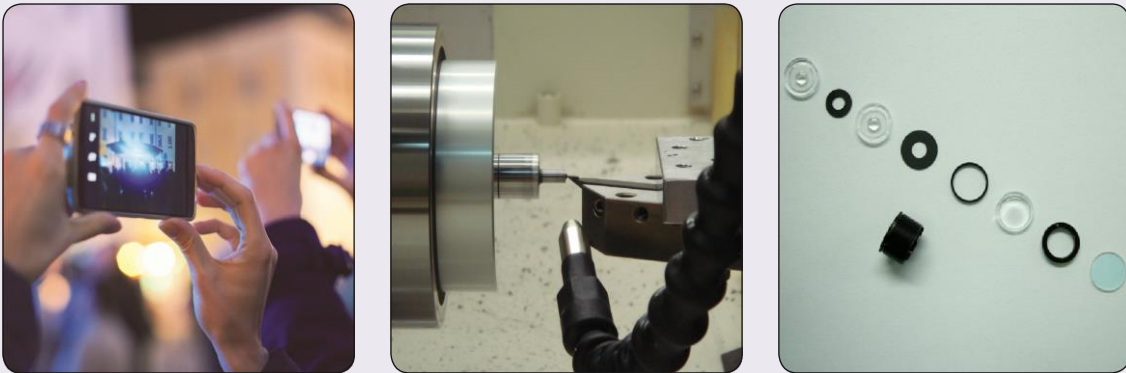


Figure 2.14: Mould manufacturing [95]



Figure 2.15: Other applications of RSA alloys apart from its optical application [96]

2.12 RECENT STUDIES IN ULTRA-PRECISION MACHINING OF RSA ALLOYS

Few researchers have carried out studies on some of the newly graded aluminium alloys. Although since these materials are new, extensive investigations/ experiments are yet to be conducted on the RSA alloys. The author also noticed that researchers have compared their machinability findings with other materials that can be used for optical applications. Abou-EI-Hossein et al. [97], carried out investigations on the performance of SPDT with grooving two RSA (443 and 905) alloys grades. They used two series of experiments to create radial micro-grooves on surface roughness of the two different alloys. The first method was to use the same combination of cutting parameters to measure surface roughness and the second method was to vary the cutting speed and keep the depth of cut and feed rate constant. The result shows that RSA 905 produced better groove surface roughness than RSA 443. Also, increase in cutting speed reduces the grooving surface roughness, which is more pronounced in RSA 905 than RSA 443.

Abou-EI-Hossein et al. [98], did a study on tool wear mechanisms encountered during diamond turning of rapidly solidified aluminium alloys grade using monocrystalline diamond tool. Acoustic emission system was employed to monitor the tool wear state while the cutting speed and depth of cut were set at 2000 rpm and 25 μm , respectively.

It was reported that because RSA 905 has a high ultimate strength, the tool wear was absolutely very low even at long distance of machining.

Cheng et al. [99], carried out studies on RSA that are subjected to MRF and SPDT and compared their result with conventional 6061. They used white light interferometer to analyze the surface roughness of the two RSA. The result corroborated the fact that RSA 6061 which was manufactured through melt-spun, is more suitable for optical applications than conventional 6061 alloy. Also, feed rate has shown to be more influential on the surface roughness generation during SPDT. The surface finish produced by RSA 6061 is approximately < 1.5 nm which enhances its suitability for UV wavelength application.

In another study by Cheng et al. [17], they investigated tool wear by varying the feed rate (5, 15 and 25 mm/min) during diamond turning of RSA 905. The dimension of the workpiece machined was to create convex platform of 100 mm radius for convex shape. A tool geometry that has a clearance angle and rake angle of 5° was employed. During cutting process, depth of cut and cutting speed were made constant at $25\mu\text{m}$ and 2000 rpm, respectively.

The machining tests were stopped after cutting 17 km. SEM analysis was carried out on the diamond tool to observe the wear mechanism and chip formation. Similar tool wear mechanism was observed for the feed rates. The result shows that an increase in feed rate leads to an increase in tool wear, i.e., tool wear of $3\ \mu\text{m}$, $12\ \mu\text{m}$ and $10\ \mu\text{m}$ for 5 mm/min, 15 mm/min and 25 mm/min were recorded, respectively. The results revealed that the most dominant wear mechanism during machining was caused by abrasive effect.

It was found that the abrasion was less damaging and low at lower feed rates. No chipping, grooving structures, and consistent wear were presented in the SEM study. It was noted that the absence of notch wear showed that RSA was almost free of built-up edge and chip morphology. The chips produced from all three feed rates were continuous, which meant that they were flowing smoothly during machining. This is because of RSA's fine microstructure. In contrast, this study finds that RSA has better wear efficiency of the tool than conventional aluminium alloys (AA 6061) [17].

Gubbles et al. [7] examined single point diamond turning of three different optical alloys (melt-spun RSA 6061, nickel-plated RSA, and traditional AA 6061). The three workpiece samples are flat with 40 mm diameters. Three different inserts the same geometry was used. The machining parameters were kept constant at cutting speed of 3000 rpm, feed rate of 5 mm/min, and depth of cut of 5 μ m. The result of the surface roughness shows that nickel-plated RSA has the lowest surface roughness of 1.7 nm, followed by melt-spun of 2.3 nm, and AA6061 with Ra of 3.8 nm. Gubbles et al. later explained that nickel-plated RSA 6061 was able to achieve that small Ra because of its hardness that called for surface polishing after diamond turning. Hence, this demanded more manufacturing process, cost, and time.

According to diamond turning and polishing investigation carried out by Horst et al. [6], on AA 6061, RSA 6061, and RSA 905, they compared the attainable surface roughness of these three mentioned alloys and concluded that RSA 905 and RSA 6061 attained 3.5 nm, and AA6061 achieved 5 nm. It was observed that this study was conducted under the same cutting conditions such as workpiece sample at 60 mm diameter each, feed rate of 2 mm/min, depth of cut of 4 μ m and cutting speed of 2500 rpm.

In addition, different heat-treated samples of these alloys were diamond turned and compared billet and extrusion. It was discovered that the extruded samples performed slightly better than the billet samples under these machining conditions. The machining conditions were then optimised using statistical methods to determine the effect of various parameters on the resulting surface roughness. The following factors were investigated: machine, operator, tool wear, spindle speed, feed rate, diamond crystal orientation, tool nose radius, Plano/spherical workpiece, lubricant application pressure, lubricant quantity, rake angle of the tool and material. It was found that tool angle, tool sharpness, speed, feed rate, and machine were the only ones that were statistically relevant. For minimum surface roughness, the tool should be sharp and have a 0° rake angle [91].

Guo et al. [100], presented a study on analytical and experimental magnetic-field assisted finishing on surface roughness of RSA 905. Scanning electron microscope was used to examine the surface and subsurface quality of the material. The result shows low surface roughness achieved when SiC abrasive was used with grit size of

12 μm at polishing speed of 400 rpm. Belgraver et al [101], examined diamond turning of several RSA alloys and compared the results obtained from tool wear and surface roughness with conventional aluminium alloys. The results followed a general trend with low tool wear and surface roughness for RSA alloys as compared with conventional aluminium alloys. Onwuka et al [102], did a study on RSA alloy, using acoustic emission (AE) signal to monitor surface roughness and tool wear during ultra-precision grinding of RSA 443 alloy. They noticed an increasing trend in raw AE spikes and peak -to - peak signal was associated with high surface roughness and tool wear [102].

These are usually normal settings. The best machine, tool setup and tool sharpness should therefore be selected. The spindle speed and feed rate can be adjusted for the optimal outcome. In order to achieve a minimum surface roughness, an optimizing feed rate to spindle rate ratio of 1.3 $\mu\text{m}/\text{rev}$ was measured. In optimized conditions of machining a surface roughness within 1 nm for RSA 6061 and around 2 nm for RSA 905 was then achieved. Under optimized machining conditions, no difference in surface roughness was made between billets and extruded samples. In these optimum conditions, all of the samples were turned with the same tool for a total distance of approx. 35 km, and no noticeable wear of the tool was observed. The unoptimized resulting samples were polished and both normal as well as modified alloys obtained surface ruggedness of approximately 1 nm. This shows that AA 6061 required more polishing distance [91].

Guo et al. [103] presented analytical and experimental studies on diamond turning of V-groove structures of rapidly solidified aluminium alloy 905, a model that explained chip flow and material removal characteristics was developed. Under the best machining conditions, the result revealed that less than 1 μm peak-to-valley form accuracy and 15 nm surface roughness were achieved on V-groove surface. A typical smooth chip morphology and tool wear established machinability of RSA 905 was also noticed.

Otieno and Abou-El-Hosseini [104], further investigated machinability of RSA 905 by varying feed rate, cutting speed, and depth of cut. They also conducted surface roughness measurement of over 4 km cutting distance. They developed a predictive model for surface roughness, and the experimental study revealed that an increase in

the cutting distance leads to a decrease in surface roughness. At a cutting distance of 4 km, feed rate of 5 mm/min, depth of cut of 25 μm , and rotational speed of 1759 rpm, the lowest surface roughness of 3.2 nm was obtained [104]. Mkoko and Abou-El-Hossein [105], reported wear mechanisms of monocrystalline diamond tool during machining of RSA 443. They conducted SEM on the inserts and found out that at 4 km, diamond tool wear was sensitive to cutting speed than other parameters. The study also established that at the low speed (500 rpm), high tool wear rate (12 μm) was recorded. Conversely, at high speed (3000 rpm), low edge wear was observed at 3 μm [105].

2.13 SURFACE ROUGHNESS IN ULTRA PRECISION MACHINING

Before conducting further research on surface roughness, the author briefly introduces some aspects of machined surface form in ultra-precision machining, such as surface topology, surface integrity, surface metallurgy, surface finish, and surface roughness.

Surface topology can be regarded as the combination of three factors of irregularities such as high-frequency irregularity called surface roughness, medium-frequency irregularity called surface waviness and lay irregularity. Lay is the direction of the prevalent surface form due to the machining process see **Figure 2.16** [106].

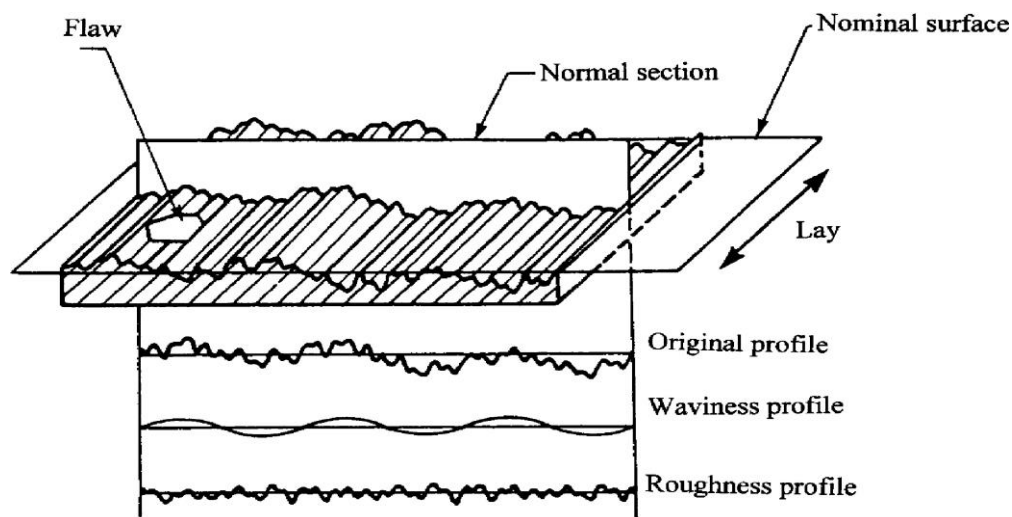


Figure 2.16: Roughness and waviness on a surface [107, 108]

The surface form of a machined workpiece after being altered by a machining process can be called surface integrity [109]. There are three categories that have been recognized during processes by which surface integrity can be altered. These are

traditional machining, which includes grinding, milling, turning, non-traditional machining, which includes EDM, electrochemical, and surface finishing operations. However, researchers have seen improved surface finish operation or damaged surfaces; in fact, they can be useful in the removal of burrs or imperfections. Surface metallurgy is described as the nature of engineered layers below the machined surface with respect to base materials as seen in **Figure 2.17**. However, as a result of the machining process, all the above forms are sometimes not lacking. So, when you have all the surface forms to deal with in a process, then surface finish will be considered and researched.

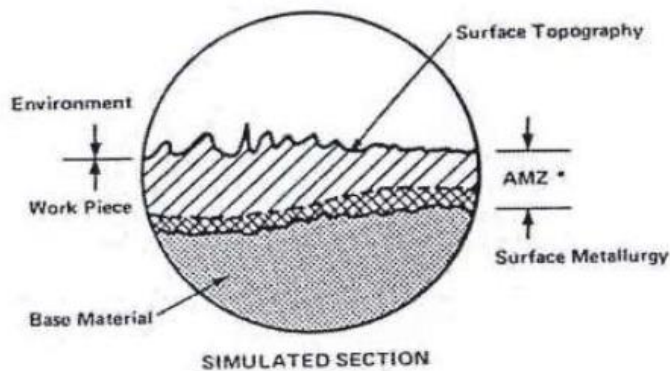


Figure 2.17: Features of machined surface [110]

Machined surface is normally described as a newly generated surface sometimes, ahead of the cutting edge during the process; material separation has to occur [111]. Thus, the surface quality of machined components has become one of the most important criteria for assessing turning processes. In UPM process, surface features are generated by the relative motion between the tool and workpiece in addition to the mechanism of material removal [94]. That is to say, surfaces in UPM are characterized by tool marks, material swelling [112, 113], material swelling and recovery [113, 114], spindle-induced vibration [115], wavy surface [116], material pile-up [117], and material crack/pit/surface wrinkle/fracture/defect/dimple [118, 119].

Thus, the characterization of surfaces generated by SPDT of SCSi is an essential aspect of the UHPM technique. The product performance is, among other factors, determined by the surface integrity of the machined surfaces. Machining of hard and brittle materials like Si without causing surface and subsurface damage is extremely

challenging due to their high hardness, brittleness, and poor machinability. They can only be machined by DRM process by providing sufficient compressive stress and thorough scrutiny of the cutting process and parameters [35], as they influence surface quality generation in SPDT [120].

Surface roughness is the generally used as the primary measure of the consistency of the surface finish [121]. Among the many methods for quantifying and qualifying surface integrity. It is one of the components of the surface finish which, because of its definitive influence on the physical and mechanical properties of a machined component [122]. It is mainly considered to be an important feature of a machined surface. It is an indicator of a product's technical quality and a factor that highly influences the cost of production [123]. The other two components are the waviness induced by the vibration or deflection of the tool in the workpiece and form surface defects or flaws caused by worn off machine table and other variables [65]. However, all three elements of the surface finish occur concurrently, with some overlap. In addition, the geometry of the machined surfaces coupled with the surface texture is defined by surface roughness. Surface roughness refers to the third to sixth order deviation from the nominal surface and is often used as an index in the machining method for evaluating the surface finish [124]. In other words, it is quantified over the entire sampling length by the vertical deviations of a real surface from its ideal form [125].

For several years, serious attention has been paid to surface finishing issues [126], with the common use of product quality indices and in most cases, technical specifications for mechanical products. The allowed aberration from a perfectly smooth surface formed by certain manufacturing processes is the surface finish [127]. A faithful signature of the cutting process and the variation of material properties are given by the surface roughness profile of a machined surface [127]. Whereas the generation of super-smooth surfaces (as needed for IR optical lenses) is heavily dependent on the machining environment (such as vibration isolation, temperature stability), machine tool performance, process parameters (spindle speed, depth of cut and feed rate), geometry of the tool (nose radius, rake, face and clearance angles), cutting edge radius, physical and chemical parameters [128-130].

In the past, both theoretical and practical studies have been carried out in order to characterize surface roughness of machined surfaces [131], and various methods for measuring surface roughness have also been developed. This includes the stylus (contact) method [132] and the optical (non-contact) profiler method [133] with 2D Fourier analysis [134] since roughness is based on the physical texture of a given surface. Other methods are low-power optical microscopy, scanning tunnelling microscopy (STM) and much recently, the atomic force microscopy (AFM) are other techniques for measuring surface roughness. However, All the approaches, however, are based on documenting the profile of surface height [133], and each of these techniques have their own merits and demerits.

Similarly, for the characterization of surface roughness, several parameters are used in **Figure 2.18**, but the most commonly used metric is the mean roughness, R_a , which represents the arithmetic mean of absolute ordinate values $f(x)$ within the sampling length (L), as shown in **Equation 2.1** [133]:

Equation 2.1

$$R_a = \frac{1}{L} \int_0^L \frac{f(x)}{dx}$$

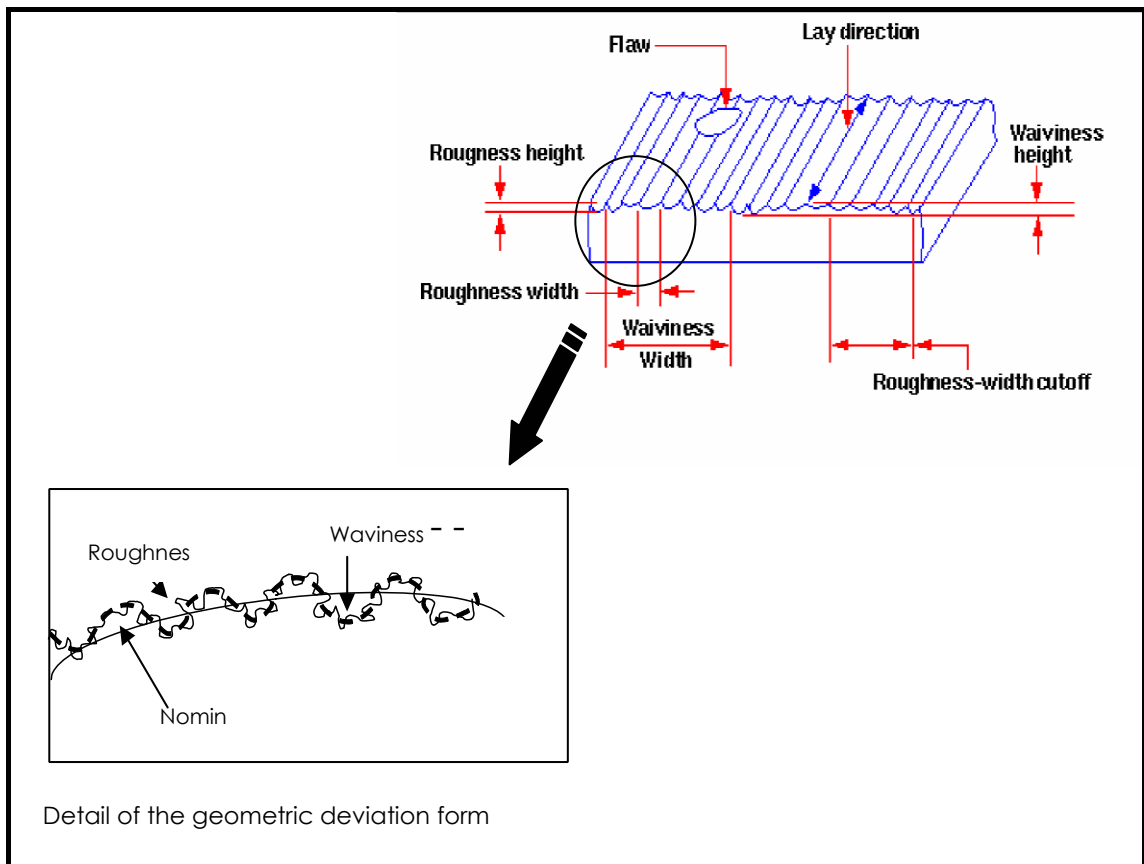


Figure 2.18: Details of workpiece surface texture [135]

Arithmetic mean: is the value obtained by calculation (see **Equation 2.2**) of the mean difference between the peaks and the central line of a track **Figure 2.19**. The centreline is the line between two lines that have an equal area between them, one above and the other below. Shaw [136], predicted surface roughness as:

Equation 2.2

$$R_a = \frac{Y_1 + Y_2 + Y_3 + \dots + Y_n}{n}$$

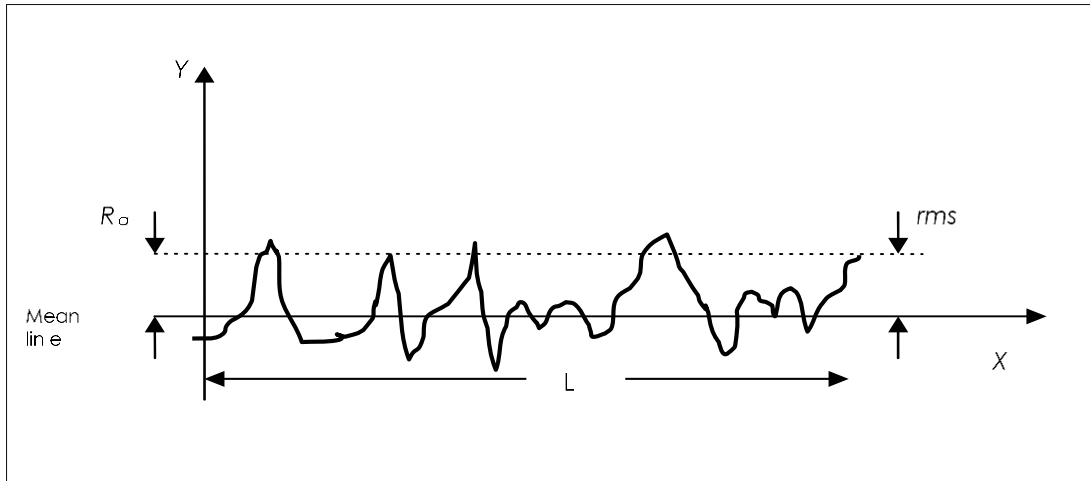


Figure 2.19: Arithmetic surface roughness average, R_a and geometric root mean square (RMS) [137]

2.14 TECHNIQUES FOR SURFACE ROUGHNESS PREDICTION

As it defines their functional behaviour, surface roughness is commonly used as a measure of the quality of a machined product and as a technical condition for mechanical products. Many researchers are especially interested in predicting surface roughness using different methods to calculate the parameter [138]. With this understanding, Lu [139], categorizes surface roughness prediction methods into three major groups: pure modelling-based approach, signal-based approach [140], and Artificial Intelligence (AI)-based approach [141].

However, Sujuan [122], shows that the method of predicting surface roughness in machining is based on the theory of cutting mechanics or machining for advancing analytical models or computer programs to denote machined surface characteristics. Nevertheless, it is suggested that factors such as cutting kinematics, cutting force and tool material properties, vibration, tool runout [142], back cutting effects, and chip forming mechanism should be integrated into the model [143], in order to build stronger and precise model for prediction.

Another model for prediction of tool wear and surface quality was proposed in the study conducted by Özelet al. [144], using artificial neural network (ANN) to predict surface roughness and tool flank wear under different cutting conditions in finished hard turning, **Figure 2.20**. Similarly, in terms of cutting parameters, Ali et al. [145] used an ANN model for tool wear and surface roughness predictions, while Zeng et al. [146]

used a real auto-correlation function (AACF) and pattern analysis to track and predict the effect of tool wear on a workpiece's surface finish. A surface roughness generation model was developed by Xu et al. [147], which took into account the static and dynamic properties of the machine tool in the end milling process during design.

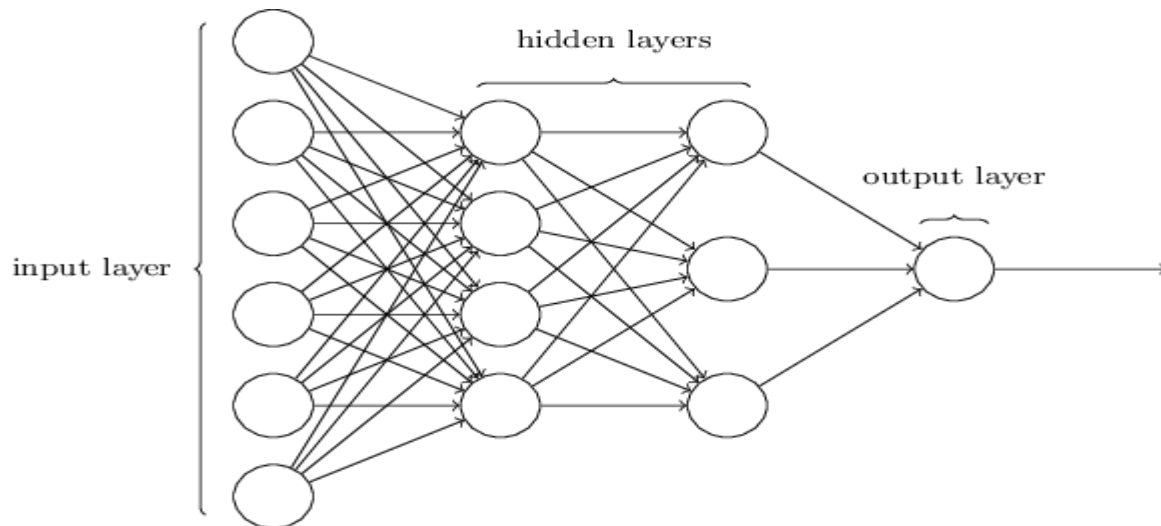


Figure 2.20: Structure of a neural network system [147]

Abburi and Dixit [148] have recently investigated the combination of NNs and the framework of fuzzy-nets as a prediction method. The result indicates that the combination of fuzzy logic and NNs is best suitable and handier than NNs alone. They implemented a fuzzy adaptive network (FAN). In Jiao and Lei work [149], to generated a prediction model using the three cutting parameters such as speed, feed rate and depth of cut. The outcome shows a lot of improvements, particularly in turning operations, over regression modelling. Meanwhile the support vector machine (SVM) has recently been introduced as an alternative for traditional ANN and has created less prediction model errors than NN [150].

The author also reported other approaches to surface roughness prediction in UPM as a mechanistic process-based modelling investigation [150]; MD models, finite element methods (FEMs), and multiple regression [151-153]. Multiple regression is a statistical technique that enables the purpose of the association between a continuous dependent variable and two or more continuous or discrete independent variables which can be used for analyzing the experimental results [154]. All the techniques listed are defined as techniques of soft computing or Artificial Intelligent Systems [155].

In single point diamond turning process, the cutting parameters and tool parameters significantly influence the surface roughness. It is possible to express the relationship as:

Equation 2.3

$$R_a \approx \frac{0.032f^2}{RV^2}$$

Where R_a is surface roughness, f is the feed rate, R is the radius of the nose of the tool, and V is the speed of the rotational spindle. Taylor's tool life equation can be borrowed in metal cutting, where an established functional correlation between surface roughness and independent variables such as velocity, feed rate, depth of cut and nose radius is hypothesized as **Equation 2.4**:

Equation 2.4

$$R_a = cf^m r^n v^p d^q$$

where R_a is the surface roughness, c the constant, f the feed rate (mm/rev), r the tool nose radius (mm), v the cutting speed (m/min), d the depth of cut (mm), m , n , p , q are the constant that is to be derived.

A logarithmic transformation of **Equation 2.5** can be used to translate the non-linear form of **Equation 2.4** to arrive at the following linear form.:

Equation 2.5

$$\ln(R_a) = \ln c + m \ln(f) + n \ln(r) + p \ln(v) + q \ln(d)$$

This is one of the data transformation methods used in empirical model building **Equation 2.6** can be rewritten as a linear model:

Equation 2.6

$$\eta = \beta_0 + \beta_1 x_1 + \beta_2 x_2 + \beta_3 x_3 + \beta_4 x_4$$

where g is the true value of surface roughness on logarithmic scale. For simplicity **Equation 2.7** can be written as:

Equation 2.7

$$y = b_0 + b_1x_1 + b_2x_2 + b_3x_3 + b_4x_4$$

where y is the predicted surface roughness value after logarithmic transformation and $b_0, b_1, b_2, b_3,$ and b_4 are estimates of the parameters $\beta_0, \beta_1, \beta_2, \beta_3, \beta_4,$ respectively. With the experimental results, for a first order model, the study consisted of estimating these four parameters.

However, a second-order model can then be created when the first-order model shows some statistical lack of fit. Once the actual response function is uncertain and non-linear, a second-order model involves empirical regression. It is possible to use the second-order regression Equation 2.8 to estimate surface roughness [156].

Equation 2.8

$$y = b_0 + b_1x_1 + b_2x_2 + b_3x_3 + b_4x_4 + b_{12}x_1x_2 + b_{13}x_1x_3 + b_{14}x_1x_4 + b_{23}x_2x_3 + b_{34}x_3x_4 + b_{11}x_1^2 + b_{22}x_2^2 + b_{33}x_3^2 + b_{44}x_4^2$$

2.15 ACOUSTIC EMISSIONS IN ULTRA-HIGH PRECISION MACHINING

Recent demands in high-technology industries such as semiconductors, optics, MEMS, automotive, biomedical, etc. have anticipated the need for manufacturing processes that can produce increasingly smaller features that at very high tolerances reliable. The on-site monitoring device is a non-destructive measurement tool, the process is used to characterize, manage, and develop the manufacturing of these smaller features. Therefore these methods are important to meet growing demands in terms of accuracy and quality [157]. Acoustic emission (AE) may usually be characterized as transitory elastic waves that discharge localized stress-energy into the material [158]. During metal cutting, the workpiece is subjected to severe plastic deformation linked to acoustic emission generation. AE is related to the plastic deformation process during chip formation due to the contact between the workpiece and cutting tool [159]. **Figure 2.21** shows several locations where signals can be obtained by AE during normal machining

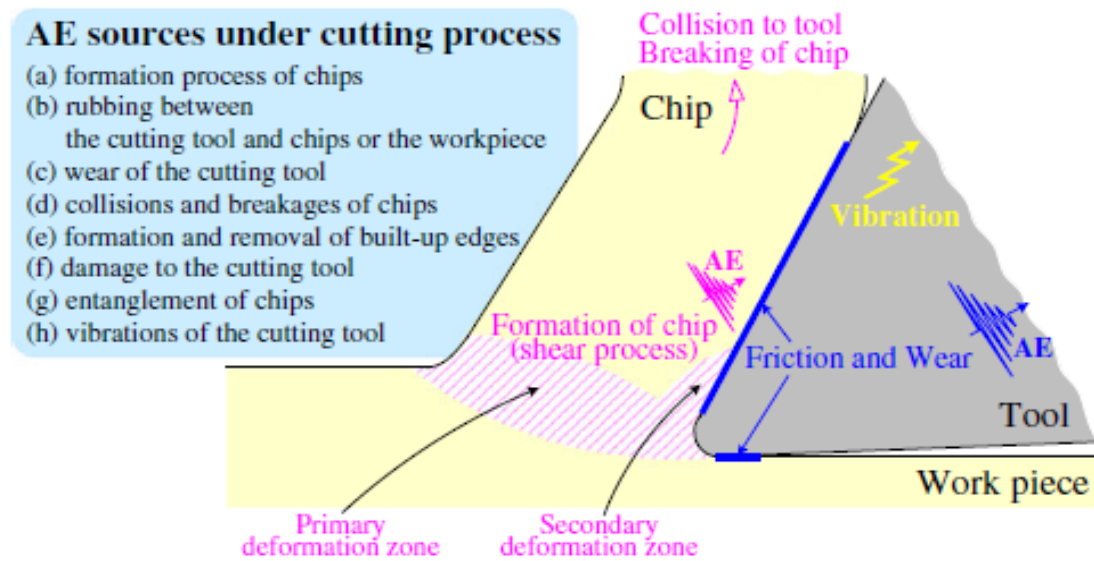


Figure 2.21: Diagram showing various AE source during cutting process [160]

AE signals are considered to have high-frequency bandwidth range between 10 Hz and 50 MHz infrasound by ultrasound with low amplitude and ultrasonic wave propagation [157]. AE is a physical phenomenon which involves the formation of elastic transient waves within or within a parent physical centre and is caused by disturbances in the atomic level see **Figure 2.22** [161]. Based on localized dynamic changes in the structure of the material, elastic waves are produced and propagated from the source of the change. The elastic waves spread through the material structure, where their energy is mainly used for the mechanical work and heat generation at the local level [162]. An integral part of the energy radiates to the edge of the device, and a sensor senses it as an EA. The features of an explosive signal during machining are shown in **Figure 2.23**.

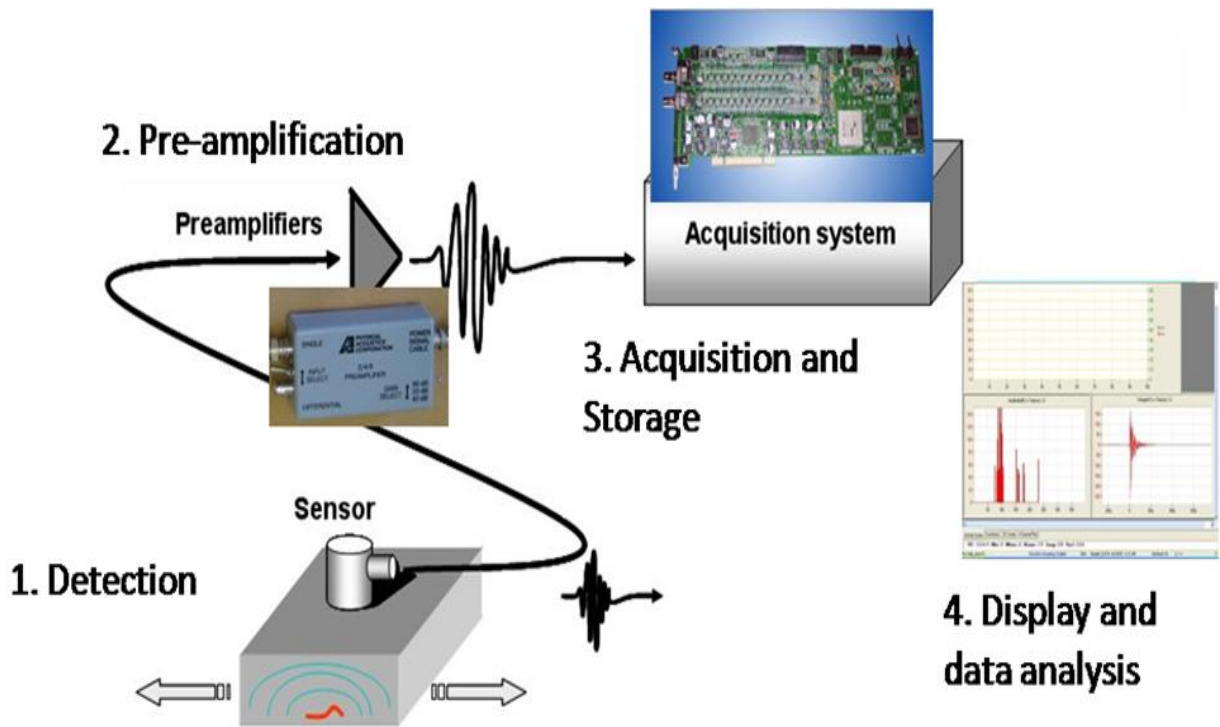


Figure 2.22: Schematic diagram of the AE test system [163]

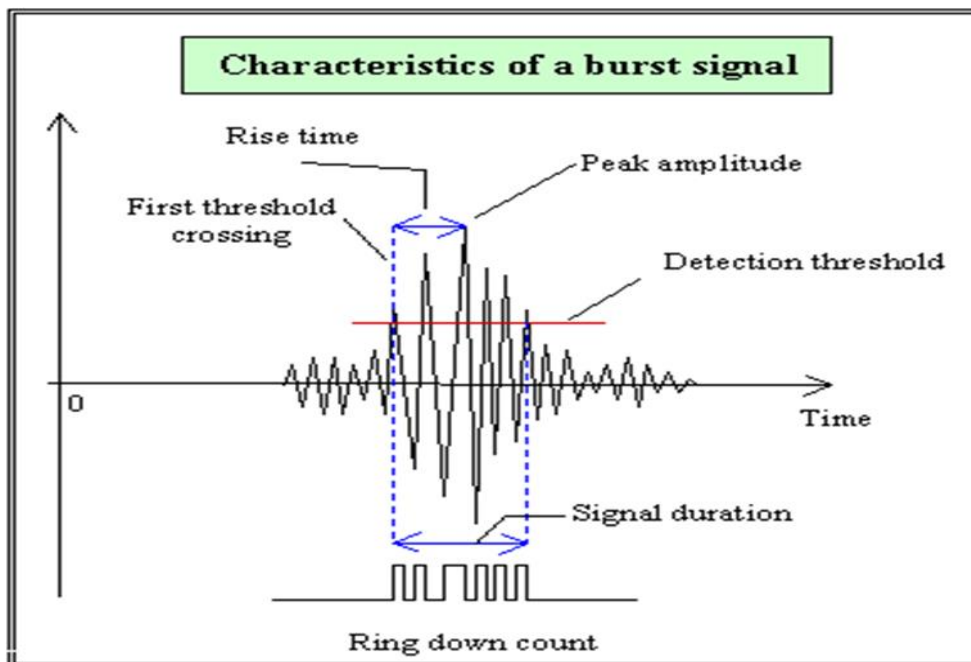


Figure 2.23: Characteristics of acoustic emission signal [164]

Root mean square: Lindberg described RMS as being sensitive to occasional highs and lows, making it more reasonable to complement R_a in **Equation 2.9** [165]:

Equation 2.9

$$RMS = \sqrt{\frac{Y_1^2 + Y_2^2 \dots + Y_n^2}{n}}$$

2.16 REQUIREMENTS FOR SENSOR TECHNOLOGY AT PRECISION SCALE

During the material removal process, the undeformed chip thickness can be as little as a few microns. In reality, it can hit the nanoscale, or it can be less than that. At this stage, the microstructure and material make-up of the workpiece, such as the crystallographic positioning of the material at the tool-chip interface, ductile-brittle performance, and micro-topography characteristics, are closely affected by the subsurface, and surface edge condition of machined features and critical mechanism for chip morphology [157, 166].

Many studies have been devoted to estimating the use and essence of sensors in various production processes, which were previously examined by Dornfeld et al. [[166, 167] with an emphasis on the new sensing techniques with regard to potential production requirements. The role of cutting force and AE as a means of condition monitoring and adaptive control was studied by Tlustý et al. [168]. Tonshoff et al. [169] suggested methods for condition monitoring strategies such as smart machining and multi-sensor systems.

One of the most detailed reviews was performed by Byne et al. [170] on sensor technology and approaches to data processing for automated machining. Similarly, Iwata [171], investigated the conditions of the Japanese advanced manufacturing for sensors and process monitoring. One notable thing in the above articles, however, was that all of them stressed monitoring at the conventional level and not at the level of ultra-precision.

The influence of machining parameters on the total AE signal has been emphasized in recent studies. According to Liu [172], he found a perfect relationship for diamond turning between modelling and experimental AE root-mean-square (RMS) signal, so he developed a clear connection between chip thickness, cutting speed, and AE and RMS. Chen [173], performed additional studies on the subject where an exponential decrease in specific AE and RMS (analogous to specific cutting energy, energy

density, or volume of energy/chip) vs. chip thickness was established. The sensitivity of AE was so poor that a chip thickness of 0.01 mm was observed, with a sharp difference between worn and sharp tools in the same AE RMS.

Acoustic emission (AE) has shown a high degree of certainty in the explanation of several trends related to material removal in the previous review papers by Dornfeld et al. [166]. **Figure 2.24**, especially on the microscale, thus providing confidence in its suitability for monitoring of production processes [157, 166].

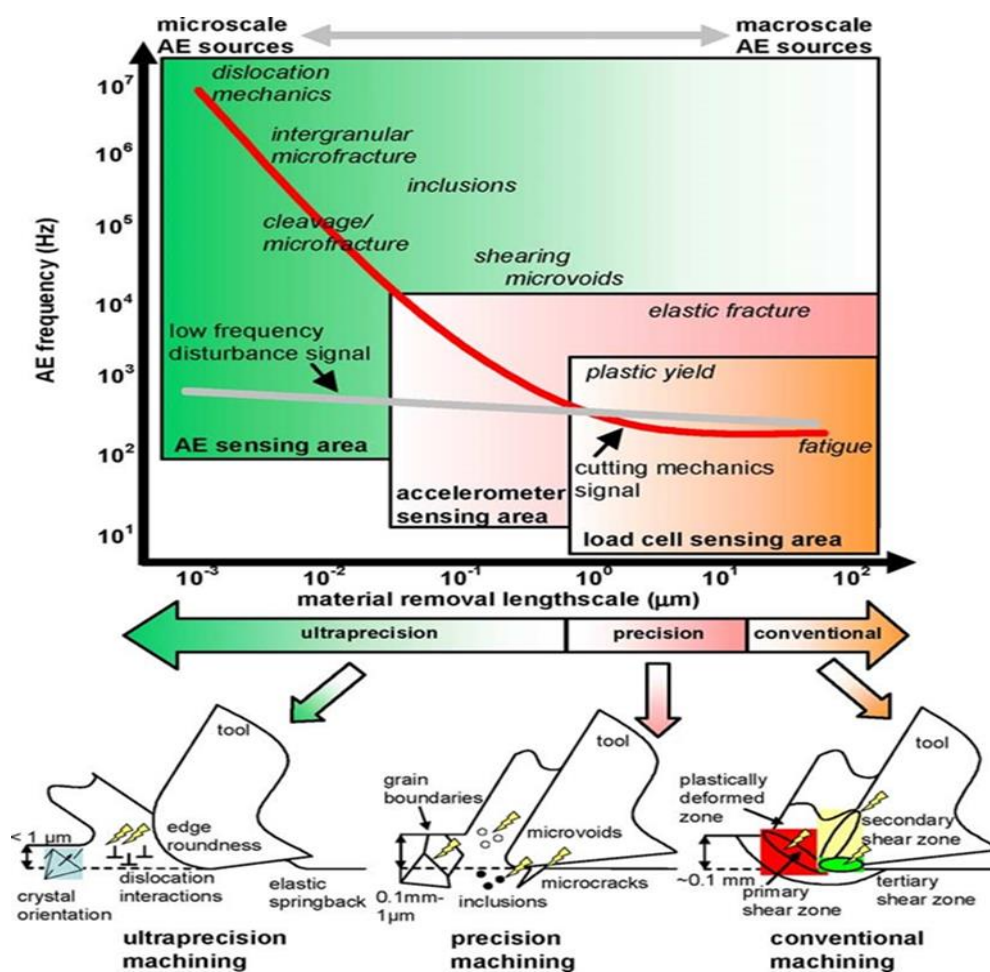


Figure 2.24: Sources of AE at varying stages of material removal [157]

According to the investigations conducted by Bifano et al. [40], They suggested that acoustic emission energy produced in the glass grinding process can be used to indicate the brittle-ductile transition for DRM. In DRM, the acoustic emission energy is stated to be greater than in brittle machining processes. This is due to DRM's greater material bond-breaking than brittle device machining. By using this acoustic emission indicator for DRM, a critical cut depth can be monitored. When machining RSA 905,

Olufayo in [174], used AE as a precision sensing technique and further processed it to compare AE RMS features with the output of the process.

2.17 MOLECULAR DYNAMICS SIMULATION AND ITS PRINCIPLE

In general, molecular dynamics (MD) can be defined as a technique used for computational assessment of the thermodynamic and transfer properties of materials by solving classical molecular motion equations [175]. MD simulation is also seen as a combination of three different procedures, which includes: molecular modelling, computer simulation, and statistical mechanics.

MD simulation is a scientific collection of rules by which atoms or molecules are assembled for a given time in each set of intermolecular interactions to yield a trajectory of their motion. An example of MD cutting is shown in **Figure 2.25** where the atoms between the workpiece and the cutting tool are at certain locations at time t . As the tool travels in the time interval Δt over a certain distance, atom i acting on by force F_{ij} , changes its location in the time interval $t + \Delta t$. Therefore, classical Newtonian mechanics can be used to predict the new position of the atom i [176] .

One of the essential considerations to bear in mind during the MD simulation procedure is to realize that the sufficient potential energy function of the material is very important. The principle of classical Newtonian mechanics was developed by Rapaport in the 18th century, and he found that a known potential and initial position of a system would effectively improve molecular motion [177]. Later on, during experiments on the interactions of hard spheres, the implementation of MD simulation was then first introduced through the ground breaking work of Alder and Wainwright in the late 1950s [178].

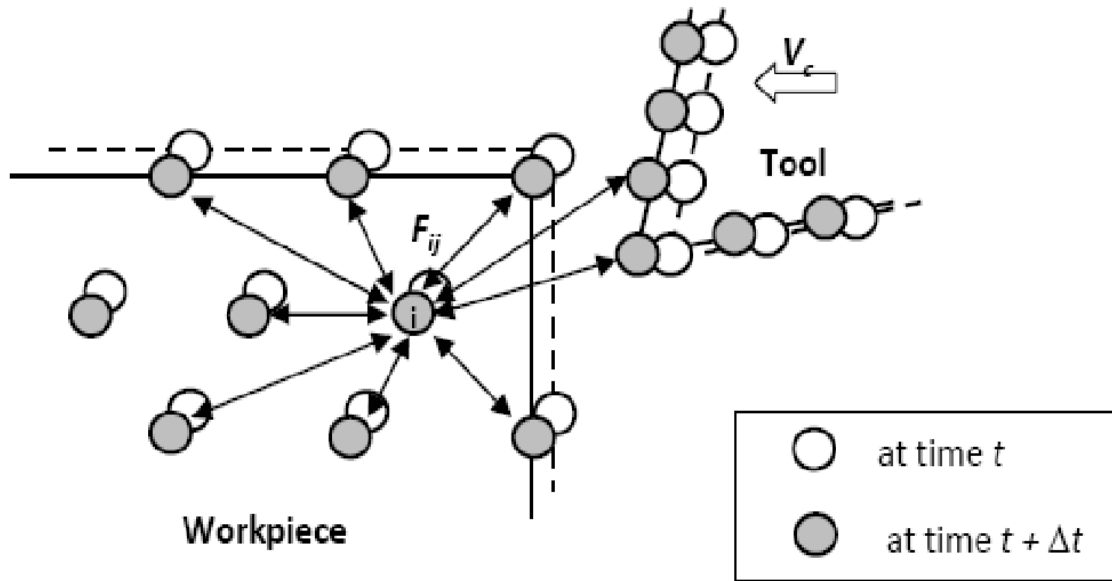


Figure 2.25: Principle of molecular dynamics simulation [179]

They also pointed out that the concept of the interatomic energy of materials includes the theory of molecular dynamics. Hence, we may derive the interatomic force based on the potential energy function. This will allow researchers to obtain each atom's acceleration according to Newton's motion equation in Equation 2.10. Therefore, when the initial position and velocity of each atom is given, it is possible to determine the new position of each atom. The purpose behind the MD simulation method is to decide how an ensemble of atoms can be used for the mathematical solution of Newton's equation of motion [180, 181].

These equations are combined by computational techniques for extremely short time intervals (on fs scale, $1 \text{ fs} = 10^{-15} \text{ s}$), and statistical averages, such as temperature, stress, etc., measured as time averages over the time of observation, as defined in the Newton law equation below [180]:

Equation 2.10

$$F_i = m_i a_i$$

$$F_i = m_i \frac{d^2 r_i}{dt^2} \quad i = 1, 2, \dots, n$$

where m_i is the mass of particle, i and F_i is the force acting on it. This equation can also be obtained from Lagrange's equation of motion, which provides a more general framework for deriving equations of motion for systems of particles evolving under constraints [176, 181].

To derive a function for all atomic positions, the resultant force F_i **Equation 2.11**, can be obtained from potential energy function $U(r)$ [182]:

Equation 2.11

$$F_i = - \frac{\partial u(r)}{\partial r}$$

2.17.1 Potential Energy Functions

The potential energy function, as described earlier, is the main platform for MD simulation as it is important to consider the interaction forces between the atoms during MD simulation and it is the duty of these forces to determine the bulk of what happens in any physical case. In addition, the potential energy functions decide these forces. While the simulation results are determined by the accuracy of the possible function, the time needed for a given computer system is determined by its functional complexity.

There is no potential energy mechanism that can fulfil all materials or atoms, it is important to remember. Each substance or atom must therefore establish its own potential energy feature. Empirical potential is usually used. Simple mathematical terminology is the basis of scientific potential, usually used for the interaction of two ions or atoms. It can be technically supported or cannot be supported and requires one or more parameters changed to the experimental data. For a variety of features, the stability of the crystal and the validity of the function for a certain material, including cohesion energy, grid constants, compression, elastic constants, and state equation, are examined. These potentials can then be relative to simple cubic crystals.

The dependency between attractive, repulsive and net forces is shown in **Figure 2.26** [180]. The attractive force holds the atoms together while they are prevented from uniting by the repulsive force. A rise in the magnitude of the two forces would contribute to a decrease in the distance between the two forces, as the repulsive force increases faster than the attractive force [181, 183].

The repulsive force is used primarily to determine the curvature of the probable energy function, thereby deciding the solid's elastic behaviour. Where r is the bond length, the center-to-center distance between the binding atoms. Strong bonds will carry the atoms together, so smaller bond lengths run counter to weak bonds. At r_0 , desirable and repulsive force balance, and net force is null. The system thus achieves stable equilibrium and minimum potential energy, and the bond energy is the magnitude [181].

MD simulation requires a fundamental description of the concepts in a simulation framework in particles. The potential energy function governs this interaction of the simulation method, representing the quantum interactions between the electron shells, and characterizes the physical properties of the simulated atoms, such as their elastic constants and grids parameters [184].

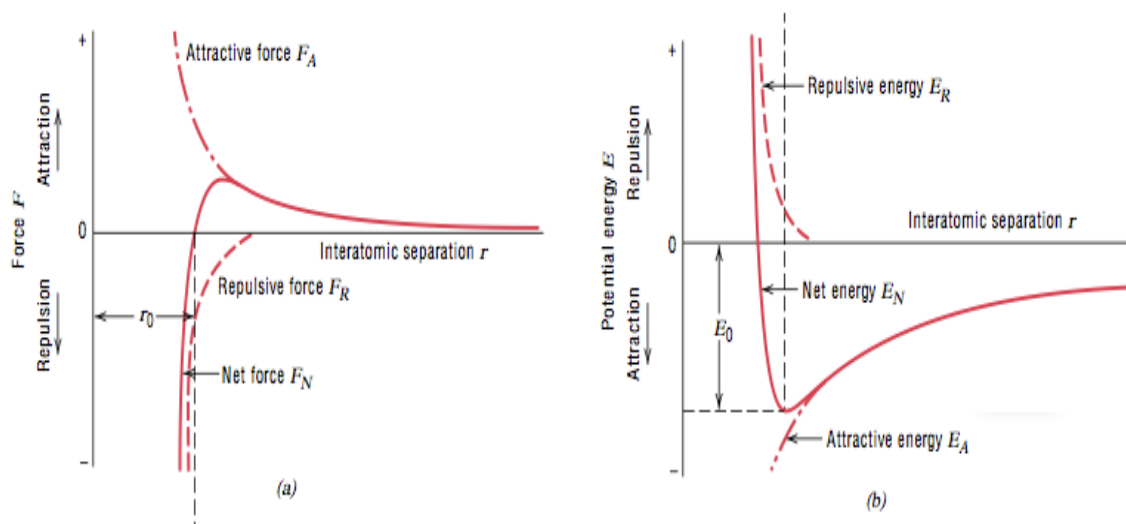


Figure 2.26: Variation of the attractive, repulsive and net forces (a) the attractive, repulsive and net potential energies (b) interatomic distance r between two atoms [180]

Potentials are considered for those used in material physics. In chemistry, most force fields are empirical and consist of a summary of forces associated with chemical bonds, bond angles, dihedrals, Van Der Waals forces-related nonbonding forces, and electrostatic forces. The potential energy function V_p is the product of accuracy of the MD simulation and comprises Van Der Waals interaction, electrostatic interaction, bonds, angles, and dihedral/torsion [180, 184], as illustrated in **Figure 2.27** via ball and spring systems.

$$\begin{aligned}
U = & \sum_{i < j} \sum 4\epsilon_{ij} \left[\left(\frac{\sigma_{ij}}{r_{ij}} \right)^{12} - \left(\frac{\sigma_{ij}}{r_{ij}} \right)^6 \right] \\
& + \sum_{i < j} \sum \frac{q_i q_j}{4\pi\epsilon_0 r_{ij}} \\
& + \sum_{\text{bonds}} \frac{1}{2} k_b (r - r_0)^2 \\
& + \sum_{\text{angles}} \frac{1}{2} k_a (\theta - \theta_0)^2 \\
& + \sum_{\text{torsions}} k_\phi [1 + \cos(n\phi - \delta)]
\end{aligned}$$

Figure 2.27: Potential energy function for molecular dynamics simulation [184]

2.17.2 Selection of potential energy function

A significant feature of the interatomic potential is that it is the mathematical function used for the measurement of the potential energy of space-positioned atoms [185-187]. Therefore, determining this energy and interatomic forces as a function of the atomic location in a system is necessary since the interaction between atoms originates from electronic structures. In order to explain the interaction, the application of empirical formula is always used, and thus the reliability of simulations depends entirely on the accuracy and reality of the interatomic potentials [187].

The selection of an effective potential energy function is often dependent on the type of material, and this determines both the precision of the MD simulation and the computational time frame. Lennard-Jones potential, Morse potential, Born-Mayer potential et cetera are some of the potentials that are widely used. In addition, such as Tersoff and Embedded-Atom Method (EAM) potentials are multi-body potentials [188].

It is also necessary to remember that the interatomic potential should be versatile enough to accommodate a wide variety of suitable data during molecular dynamic analysis. It should be capable of reproducing a suitable database accurately.

Structures not included in the fitting database should also be defined and the capacity should be evaluated efficiently (i.e., it should be Scalable, Reliable, Transferable and Computationally Efficient) [189, 190].

Since there is always a difficulty in MD simulation to measure all the interactions between one atom and the other simulated atoms, only the closest neighbours of each atom are taken into account in order to minimize the computation power instead of the immeasurable set of possible functions. A cut-off radius, which will act as the maximum point of the modulus of the radius vector, must be followed to achieve this principle. This means that **Equation 2.12** only considers the interactions between atoms separated by less than R_c . A skin factor F_c must be established to accomplish this, which will ease the transition when the value r approaches R [191].

Equation 2.12

$$V(r) = \begin{cases} \phi_{LJ}(r) - \phi_{LJ}(R_c), & \text{if } r \leq R_c \\ 0, & \text{if } r > R_c \end{cases}$$

The selection of appropriate time steps is an additional challenge that might be faced during MD simulation study. It has been noted that at the same time, a very small-time step will draw a high computational cost and a very large time step will yield undependable performance. For the numerical integration of the motion equations of individual atoms, proper time steps are required to be less than 10 percent of the vibration duration of an atom. An ideal time step is therefore dependent on the material as well as the potential feature used. For example, given the Tersoff potential, every individual silicon or diamond atom may be forced to migrate in a direction to display the corresponding stiffness k to calculate the vibration time of the atom in the direction T by the following **equation 2.13**:

Equation 2.13

$$T = 2\pi\left(\frac{m}{k}\right)^{\frac{1}{2}}$$

where m , is the mass of the atom[181].

2.17.3 Lennard-Jones potential energy function

One of the best mathematical models suitable for rare gases is the potential energy function of Lennard-Jones. This potential energy mechanism is sufficient for non-bonded and uncharged atoms to interact with each other (pair of neutral atoms or molecules). Van der Waal achieved this equation by adapting experimental data due to the weak Van der Waal forces [189]. The following equation gives this potential:

Equation 2.14

$$V_{ij} = 4 \epsilon \left[\left(\frac{\sigma}{r_{ij}} \right)^{12} - \left(\frac{\sigma}{r_{ij}} \right)^6 \right]$$

Where V_{ij} is the bond energy of all atomic bonds, ϵ is the minimum potential showing the bonding/dislocation energy that occurs when the distance r_{ij} is equal to $2^{1/6}\sigma$, r_{ij} is the distance between particle i and particle j , σ is the length between particles at an intermolecular potential value of zero (as shown in Figure 2.28) and is determined by the physical characteristics of the material. The maximum distance of two nonbonding particles, also known as the Van Der Waals radius is also indicated [181].

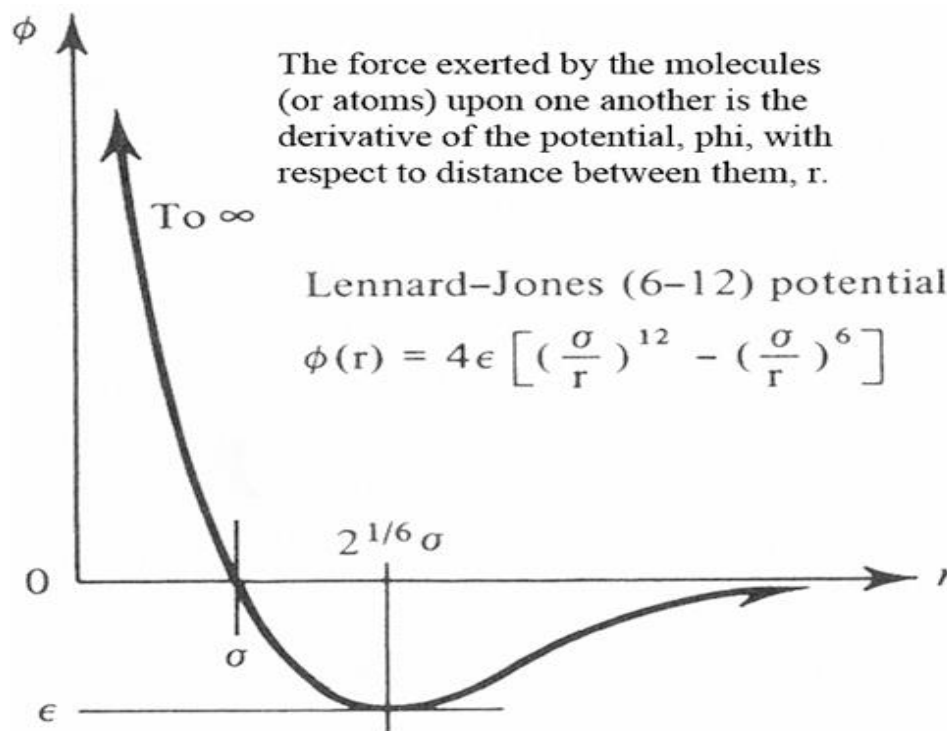


Figure 2.28: Lennard-Jones potential function and the effect of atomic distance [189, 191, 192]

The potential of Lennard-Jones is strongly repulsive at small distance, but after reaching the minimum about $1,122\sigma$, it becomes desirable for bigger r . Because of the Paulie theory, the repulsion between atoms at close range is modelled by the term $\sim \frac{1}{r^{12}}$ due to the increase in system energy when electronic clouds covering the atoms overlap. The attractive portion expressed by $\sim \frac{1}{r^6}$ is dominated by weak Van Der Waals forces at a considerable distance. However, due to the formation of strong localized bond or delocalized electron sea, LJ potential is not adequate to characterize covalent bond or metal interaction. This ability focuses on fundamental problems rather than the analysis of the characteristics of a particular material [191]. It is necessary to remember that the deeper the depth (ϵ), the greater the relationship between the two particles. If the potential bonding energy is equal to zero, then the separation frequency, r , is equal to the distance between the particles (σ) [181].

2.17.4 Morse potential energy functions

A pairwise potential energy function for bonded interactions is Morse potential. Many authors have given various constants for different materials for the Morse potential [193, 194]. The potential trails the energy reaction curve to the distance between atoms see **Figure 2.29**, yielding a repulsive force along the curve in the short-range, enticing force along the medium-range growing curve and smoothly decaying to zero in the long-range of atomic force energy [181, 195].

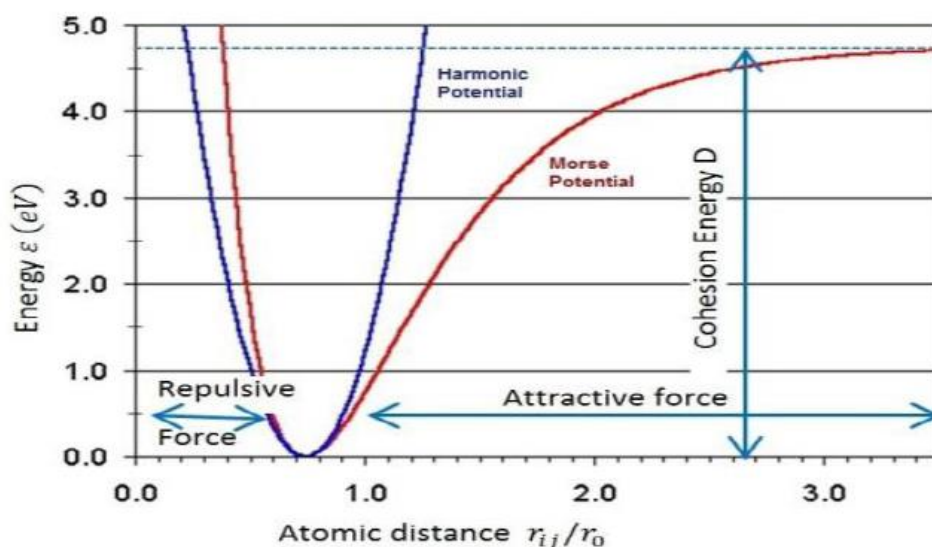


Figure 2.29: Morse potential function and the effect of atomic distance on intermolecular force [195]

The Morse potential function is therefore given as:

Equation 2.15

$$V_{ij}(r_{ij}) = D(\exp[-2\alpha(r_{ij} - r_0)] - 2 \exp[-\alpha(r_{ij} - r_0)])$$

The function $V_{ij}(r_{ij})$ is a function of pair potential, while the cohesion energy, elastic modulus, and atomic distance at equilibrium are D , α and r_0 respectively. For alloys and cubic metals, the Morse potential is most appropriate. This potential role restricts the exploration of atomic interaction between the workpiece and the cutting tool, which is a significant restriction of Morse potential and all potential functions of pairs since this weakness triggers their inability to replicate a material's Cauchy pressure [25]. This potential function is employed in the MD simulation section in this study.

2.17.5 Embedded atom method (EAM)

The embedded atom approach is one of the multi-body potentials that are also ideal for metallic structures (EAM). Each atom's EAM is embedded in an electron gas formed by all neighbouring atoms, and the amount of energy required to inject an electron gas of a given density into an atom is referred to as the embedding function [191]. The potential energy of an atom, i , is given in a simulation by:

Equation 2.16

$$E_i = F_\alpha \left(\sum_{t \neq j} \rho_\beta(r_{ij}) \right) + \frac{1}{2} \sum_{t \neq j} \phi_{\alpha\beta}(r_{ij})$$

where r_{ij} is the distance between atoms i and j , $\phi_{\alpha\beta}$ is a pair-wise potential function, ρ_β is the contribution to the electron charge density from atom j of type β at the location of atom i , and F is an embedding function that represents the energy required to place atom i of type into the electron cloud.

The mean value of the pair interaction between individual species is the pair interaction of two species and is strictly repugnant. In EAM, three scalar functions are required for the single element atom framework to be stipulated: an electron cloud contribution function, a pair-wise interaction, and an embedding function. Although three pair-wise interactions (P-P, P-Q, Q-Q) are needed for a binary alloy, two embedding functions,

one for each atom form, and two-electron cloud contribution functions are required [181, 191]. This technique has been used to study fractures and defects, grain boundaries, and other metallic processes and structures.

2.17.6 Tersoff potential energy functions

The "Tersoff-Abell" formalism is actually the most frequently used bond order potential [25]. Tersoff [196] models the overall energy of a system as a total amount of pair-like interactions, based on the idea of bond order, an interatomic environment-dependent potential consisting of interactions of several bodies that was included in the bond order term [197]. Since the strength of the bond is defined by where the electronic charge is centred instead of the coordination of the atoms in covalent bonding [198]. It is environmentally dependent since, at the tetrahedral angle, the force of attraction between two atoms is not stable and has no minimum amount. The surface and defect characteristics of silicon crystals and nanostructures and their convective heat transfer properties are well defined by Tersoff. It has been used in the investigations of lattice dynamics [199], thermomechanical properties [200] point defects [201], the liquid and amorphous phases [202]. Therefore, the potential energy is in the form in the **Equation 2.17 below** [181, 190]:

Equation 2.17

$$E(r) = \sum_i E_i = \frac{1}{2} \sum_i \sum_{i \neq j} V_{ij}$$

$$V_{ij} = f_c(r_{ij})[a_{ij}f_R(r_{ij}) + b_{ij}f_A(r_{ij})]$$

$$\text{repulsive part } f_R(r) = A \exp(-\pi_1 r)$$

$$\text{attractive part } f_A(r) = B \exp(-\pi_2 r)$$

The potential cutoff function is given as:

$$f_c(r) = \begin{cases} 1 & \\ \frac{1}{2} - \frac{1}{2} \sin\left(\frac{\pi}{2} \frac{(r-R)}{D}\right) & \\ 0 & \end{cases}$$

$$\begin{aligned}
r &\leq R - D \\
R - D &< r < R + D \\
r &\geq R + D
\end{aligned}$$

$$b_{ij} = (1 + \beta^n \zeta_{ij}^n)^{-\frac{1}{2n}}$$

$$\zeta_{ij} = \sum_{k \neq i, j} f_c(r_{ij}) g_{\theta_{jik}} \exp(\lambda_3^3 (r_{ij} - r_{ik})^3)$$

$$g(\theta) = 1 + \frac{c^2}{d^2} - \frac{c^2}{[d^2 + (h - \cos\theta)^2]}$$

$$a_{ij} = (1 + \alpha^n \eta_{ij}^n)^{-\frac{1}{2n}}$$

$$\eta_{ij} = \sum_{k \neq i, j} f_c(r_{ik}) \exp(\lambda_3^3 (r_{ij} - r_{ik})^3)$$

$E(r)$ and E_i are the interacting energy of atoms, V_{ij} is the pair potential, R and D are cut-off parameters, and b_{ij} is a cut-off radius function. ζ_{ij} is the atom effective coordination number, i.e., it counts the number of other bonds to atom i besides the i - j bond, f_c represents a smooth cut-off function to limit the range of the potential, r_{ij} is the distance between atoms i and j while θ_{jik} is the angle between ij and ik .

Over the years, Tersoff refined his formalism and proposed a few modifications to describe both Si and C along with their alloys [176]. The Si(B) and Si(C) originally suggested by Tersoff for pure Si adequately describes the Silicon's surface and elastic characteristics [203]. One major limitation of Tersoff's potential is that the transformation of graphite into diamond is poorly defined, a shortcoming which can be improved by increasing the potential S parameter to 2.46 [204]. There is also a lack of a correct definition of silicon dimer (which was also solved by ABOP) [176].

Another of Tersoff's anomalies is his weak estimation of silicon melting point; however, it was also taken care of to change three parameters of this ability [205]. The determination of the next nearest neighbour atoms through a limited distant dependent cut off is another downside to the original Tersoff formula. This has brought about an artificial shift in the energy-distance relationship (short range), also leading to an

overestimate of bonding forces, which has caused silicone to show ductile behaviour rather than brittle nature. Pastewka et al. [206], have established a better screening cut-off scheme that extends Tersoff's ability to resolve the limits stated [181, 207].

Regarding the accuracy of the possible thermal functions of Tersoff in the silicon description. Some authors [59], believed Tersoff is confined to thermal silicon description, which could restrict the study of high-temperature processes. This is because the initial Tersoff parameters of 1989 [196], yielded a melting transition temperature of $T_m = 3300 \text{ }^\circ\text{K}$ [208], which is too high and greatly exceeds the experimental value of $1687 \text{ }^\circ\text{K}$ [209] and that yielded by Stillinger Weber (SW) potential $T_m = 2340 \text{ }^\circ\text{K}$ [210]. To correct the temperature gap, Tersoff-ARK potential was suggested by Komanduri, Agrawal and Raff in 2005 [211], to correct this temperature difference, which included adding alternative parameters to the potential functions of Tersoff. The measured silicon melting point was therefore, closer to the experimental value than that obtained by the SW potential.

The potential of Tersoff-ARK has attracted and re-interest in studying the formation of melting of silicon nanostructures [212] and crystalline silicon due to its performance [213]. Some aspects in which Tersoff seems to have some limitations include the ductile-brittle transition during nanometric cutting of silicon and silicon carbide (a field where it has achieved extensive use the process of cleavage on some crystal orientations of brittle materials which is unfortunately an aspect that is not captured by all the potential energy functions [59].

However in the prediction of mechanical behaviour of silicon, Tersoff potential has been extensively adopted and verified [214], and it can improve the definition of amorphous phases and correctly describe the response of brittle materials according to prior research [215]. Additionally, the refined Tersoff potential function of Agrawal et al. [216] is robust in predicting both thermal softening activity and the melting point of silicon at high temperatures [217].

2.17.7 Analytical Bond Order Potential (ABOP)

With the refined Tersoff function, ABOP [218], has almost the same formalism. Which was suggested to resolve the silicon dimer problem and bulk properties such as binding energy, D_0 , equilibrium bonding distance, r . ABOP [218], can now accurately

address and specify the wave number, k , of the ground-state oscillation that Tersoff does not explain entirely. ABOP is given as follows:

Equation 2.18

$$E = \sum_{i>j} f_c(r_{ij}) [V_R(r_{ij}) - \frac{b_{ij} + b_{ji}}{2} V_A(r_{ij})]$$

$$V_R(r) = \frac{D_0}{S-1} \exp[-\beta \sqrt{2S(r - r_0)}]$$

$$V_A(r) = \frac{SD_0}{S-1} \exp[-\frac{\beta\sqrt{2}}{S(r - r_0)}]$$

$$f_c(r) = \begin{cases} 1, & r < R - D \\ 0, & r > R - D \\ \frac{1}{2} - \frac{1}{2} \sin(\frac{\pi}{2} \frac{r - R}{D}), & |R - r| \leq D \end{cases}$$

where the parameters R and D specify the position and the width of the cut off region. The bond order is given by:

Equation 2.19

$$b_{ij} = (1 + \chi_{ij})^{-\frac{1}{2}}$$

$$\chi_{ij} = \sum_{k(\neq i,j)} f_c(r_{ik}) \exp[2\mu(r_{ij} - r_{ik})g\theta_{ijk}]$$

And the angular function is given by:

$$g(\theta) = \lambda(1 + \frac{c^2}{d^2} - \frac{c^2}{d^2 + (h + \cos\theta)^2})$$

2.17.8 MEAM Potential Energy Functions

Angular terms have been incorporated into the EAM potential energy expression for updated EAM (MEAM) to accurately model the fine details of the structure, thermodynamics and dynamics of transition metal systems [218]. The mathematical structure of MEAM potential is similar to that of EAM. Except that the electron density is given by a complex expression involving sums of three-body contributions depending on the angle θ_{ijk} subtended by atoms j and k at a central atom i . EAM modification may also be accomplished by using a chemically precise potential bond-

order model that involves the directionality of electron orbitals d and f and the distinction between orbitals σ , π , δ , bonding, anti-bonding, and non-bonding. An interatomic potential formalism that is applicable to a broad range of material systems such as bcc, fcc, hcp, gaseous elements, and diamond-structured using popular formalism is a modified embedded-atom process [218]. In order to understand the directionality of bonding, Baskes in [219], created MEAM by developed modifying embedded-atom method (EAM) to consider the directionality of bonding.

The original MEAM, which only considers interactions between the first nearest atoms, was later updated by Baskes in order to partly take into account interactions between the second nearest atoms. These also helped to overcome some of the initial MEAM's critical limitations.

Generalized MEAM (i.e., the second closest neighbour to MEAM) has indeed been utilized on materials such as bcc, fcc, hcp metals, and manganese. Covalent bonding elements namely carbon, silicon, germanium, and their alloys are also diamond-structured has also investigated using the same MEAM [220]. MEAM is more difficult to use than EAM, however. This is possibly the reason why it has been less commonly used. Furthermore, there is no evidence of the capacity to address quantitatively the limitations of the simplified model. The total energy of the device is approximated in the MEAM as:

Equation 2.20

$$E = \sum_i \left[F_i(\rho_i) + \frac{1}{2} \sum_{j(\neq i)} S_{ij} \phi_{ij}(R_{ij}) \right]$$

where F_i is the embedding function, ρ_i is the background electron density at site i . S_{ij} and $\phi_{ij}(R_{ij})$ are the screening factor and the pair interaction between atoms i and j separated by a distance R_{ij} , respectively.

2.17.9 ReaxFF

ReaxFF has become one of the possible reactive force fields available and is often used to examine corrosion and failure of surfaces. Other developed potential reactive force fields include REBO and COMB. Sadly, there are few MD studies of silicon corrosive behaviour and most of the available ones used non-reactive force fields in their research, but both the transition states and chemical reactions of silicon are not

completely explained. Finally, empirical potentials such as Stillinger Weber, Tersoff, etc. replicate to a very large degree the properties of bulk and point defect, while surface and in particular cluster properties are comparatively less satisfactory [221]. In short: for metals, the potential for EAM and MEAM is sufficient. Suitable usable LJ and Morse potentials can be used with caution for covalent materials; Tersoff and MEAM should be used and for the interface of materials where sufficient potentials have not yet been developed [189]. **Table 2.3** highlights some of the interatomic potentials, their models and functional application areas.

Table 2.3: Comparison of some interatomic potential

Name	Model	Application
<i>Lennard-Jones Potential</i>	$V_{ij} = 4\epsilon \left[\left(\frac{\sigma}{r} \right)^{12} - \left(\frac{\sigma}{r} \right)^6 \right]$ <p>σ and ϵ are constants which are dependent on the physical property of the materials.</p>	Mostly suitable for rare gases
<i>Morse Potential</i>	$V_{ij} = D \{ \exp[-2\alpha(r_{ij} - r_e)] - 2 \exp[-\alpha(r_{ij} - r_e)] \}$ <p>r_{ij} and r_e are instantaneous and equilibrium distances between atoms i and j respectively α and D are constants determined on the basis of the physical properties of the material</p>	Mostly suitable for cubic metals
<i>Born-Mayer Potential</i>	$V_{ij} = A \{ \exp[-2\alpha(r_{ij} - r_0)] \}$ <p>A and r_0 are constants dependent on the material (Born & Mayer, 1932)</p>	Mostly suitable for ceramics
<i>Tersoff Potential</i>	$V_{ij} = V_r(r_{ij}) - B_{ij} V_a(r_{ij})$ <p>V_r and V_a are the potentials due to repulsive and attractive forces between atoms i and j and B_{ij} is a parameter that provides the information for the direction and the length of the bond.</p>	Mostly suitable for covalently bonded materials
<i>Embedded-Atom Potential (EAM)</i>	$E_{tot} = \sum_i G_i(\rho_{h,i}) + \frac{1}{2} \sum_{i,j} V_{ij}(r_{ij})$ <p>$\rho_{h,i}$ is the total electron density at atom i due to the rest of the atoms in the system. G_i is the embedding energy for placing an atom into the electron density $V_{i,j}$ is the short range pair interaction representing the core-core repulsion r_{ij} is the separation of atoms i and j</p>	Mostly suitable for a wide range of metals

2.17.10 Steps in Molecular Dynamics

Generally, a molecular dynamics analysis involves a set of procedures that can be systematically organized into domain construction, equilibrium and relaxation, objective run, and post-processing **Figure 2.30**. For different models or different

simulations, these steps are usually repeated. The third step, or objective run, can be repeated with different kinds of loading conditions, followed by a post-processing session, which allows us to commence each simulation at the same exact domain configuration.

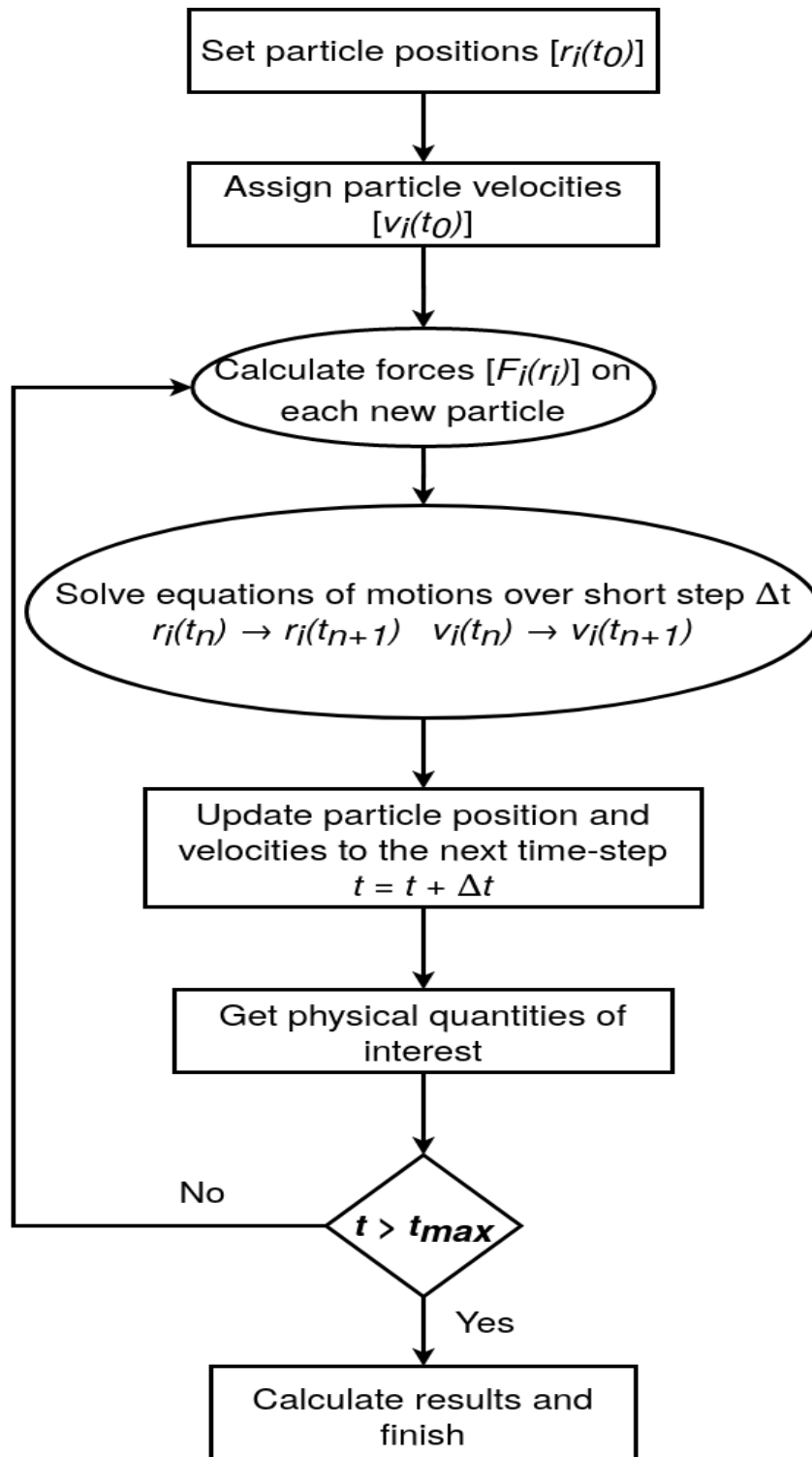


Figure 2.30: General flow chart for MD simulation

Potential energy functions are complex in nature, there is no analytical solution to the integration of Newton's equation. Therefore, time integration algorithms are used. The algorithm functions to solve for positions and velocities at a time, t and later, $(t + \Delta t)$. This is done by dividing time into discrete time steps, no more than a few femtoseconds (10^{-15} s) each at which the forces acting on each atom is computed using a molecular mechanics force field [222]. The movement of the atoms can start from their initial positions; their new positions and velocities are then updated using Newton's laws of motion. Huge time step reduces the computational time, in addition, when the time step is too large, this also causes instability and inaccuracy in the solution[188]. It is necessary to remember that the MD program has already selected the algorithm that would be used for the simulation. The MD simulation description is as follows [188]:

- Selection of the model
- Select a suitable potential energy function
- Select the algorithm for integrating the equations of motion
- Initialize the model
- Relax the model from its initial state to its dynamical equilibrium condition
- Run the simulation and analyze the outcomes.

2.17.11 Model Selection

To recreate a well-expected 2D or 3D simulation model, a good selection with a high level of details and accuracy are needed to guide through for the MD model.

2.17.12 Choose an appropriate potential energy function

Another very important step is how to choose a suitable potential energy function for the simulation. However, different types of possible potential energy function have been described in detail under 2.17.

2.17.13 Choose the algorithm for the integration of the equations of motion

The next thing is a suitable algorithm for the purpose of integrating Newton's equation of motions once the interatomic potential is defined. This is however, numerically solved for positions and velocity at a time, t and change of position at a time $(t + \Delta t)$. For the integration of the equation of motion, a lot of mathematical systems were

developed. The Verlet algorithm, the predictor-corrector algorithm and the Beeman algorithm are some of the popular algorithms often used [223-227]. When selecting an integrator algorithm, the following factors need to be considered [223]:

- Accuracy – it should produce an approximate result close to the exact solution
- Memory requirement – it should require little memory
- Efficiency – it should be fast and computationally efficient
- Time Step – it should permit long time step Δt for the integration

2.17.14 Initialization of the model

To initialize the molecular dynamic simulation, few systems must be set up or defined such as the controlled volume(MD box), initial positions, and velocities of the atom can be randomly assigned, positions of the atoms, assume particular crystal structure with initial velocities randomly assigned [223].

2.17.15 Relax the model from its initial state to its dynamically equilibrium condition

To mimic true materials, the model must be relaxed from its temporal assigned initial conditions to its natural, dynamically equilibrium state. This can be accomplished by running the molecular dynamic model at constant temperatures for pre-determined time stages, so that the velocities of atoms initially allocated randomly or on the basis of a normal distribution are progressively balanced at the defined simulation temperature. These relaxation time steps are not always the same, all depending on the time needed for the model to reach its natural and dynamic equilibrium state, which must be compatible with the ambient temperature [223, 228].

2.17.16 Run the simulation and analyze the results

The last segment is left to run the simulation and evaluate the effects. As in the case of macro or nano machining, variables of interest may be determined. Examples of such variables are depth of cutting, speed, feed rate, cutting edge, or other machining parameters that can be specified for simulation purposes. The simulation of MD made it easy to vary the properties of work materials and cutting tools [180]. The result of the simulation can be a few quantities that can also be extracted from nano-machine

predictions. This involves the effect of cutting forces, temperature reduction, total energy, potential and kinetic energy, friction, special energy cutting, etc [223].

CHAPTER 3

CUTTING FORCES IN MACHINING

In general, cutting forces can be defined as the force produced by the cutting tool, as the cutting tool cuts through the workpiece [229]. The cutting force is classified into main and secondary cutting forces. According to [229], the primary feed force are defined as the forces created in the same direction as the cutting tool moves during cutting; thus the force is directly produced by the relative movement of the cutting tool in relation to the workpiece during machining. Consequently, the secondary cutting force is then produced as a result of the impact of primary cutting forces, such as vibration in machining [229-232].

3.1 CUTTING FORCE PREDICTIONS AND MODELLING

Smith and Tlustý [233] developed and reviewed a few numbers of cutting forces predictions that are modeled based on theoretical assumptions and experimental observations. They also revealed that for the past decades, enhanced cutting force models had been developed [234-240].

There are currently four major ways (**Figure 3.1**) to predict cutting forces in machining: empirical/semi-empirical, simulation/FEM, analytical methods, and hybrid models [241, 242]. Experimental empirical approaches include the modelling of a statistical equation, such as the exponential model, the second-order model, etc., between the cutting forces and cutting parameters [241, 243]. In semi-empirical method, the relationship between uncut chip thickness and cutting forces is established where the uncut chip thickness is analyzed and modelled [244]. According to Li et al. they focused on mechanistic ball end milling modelling and found in their experiments that cutting forces under such cutting conditions are proportional to uncut chip thickness and the ratios are called force component coefficients [241].

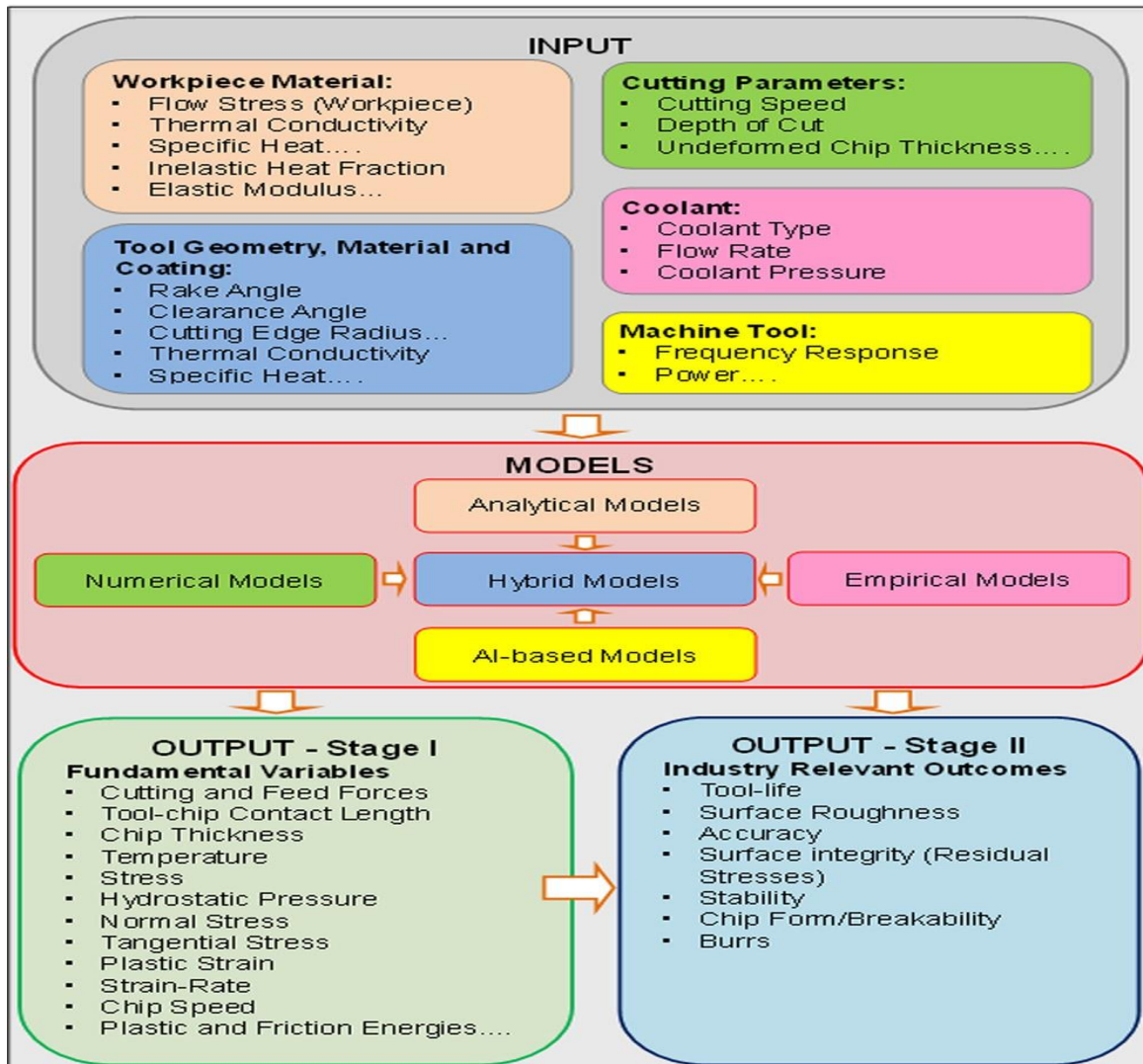


Figure 3.1: Modelling approach adopted for machining processes[242]

Simulation method is an important means to study complex level of cutting process. This method often becomes very difficult to study by experimental measurement. Example of such simulation is FEM, molecular dynamics (MD). FEM is often and popularly known in 1980s till the 90s. But as the machining process moves from micro to nano cutting level, MD became popular for simulation. These methods can be utilized to calculate cutting forces [245], cutting temperature [246], stress distribution [247], tool design [241] and cutting force optimization both in macro, micro and nano-level of machining [248, 249]. Examples of software used for FEM are ABACUS, Autodesk software, ANSYS, COSMOS, LS-DYNA, NASTRAN, etc. [249-252]. Example of software for MD are: lammmps, namds/vdm, charmms, gromacs, gromos etc [183, 189, 195, 253-256].

Analytical methods are often taken as the analysis in the cutting processes, which includes but not limited to, material flow, material deformation, contact action, and so on. It is commonly well-thought-out that the cause of subsequent cutting forces are friction and shearing in the cutting processes [257]. According to Haoqiang et al. mathematical modelling to predict cutting forces in micro drilling was established, while the geometric features of microdrill were taken into consideration in force models. Thrust was modelled in three stages: main cutting edges, secondary cutting edges, and indentation zone. The primary cutting edges and secondary cutting edge are further separated into components using slip-line field theory. Where the force factor is measured using an oblique cutting model and an orthogonal model respectively [258].

Kim et al. [259], proved analytically the differences between the cutting forces in micro-machining and macro-machining processes. They established that shear occurs along a shear plane in macro-model, while in micro-machining, the shear stress grows uninterruptedly around the cutting edge. They further claimed that the orthogonal micro-cutting force analytical model considered the elastic recovery of the workpiece along the clearance face of the tool and the radius of the tool edge plowing effect. They model the cutting forces based on four distinct regions to test the elastic results. According to Fetecau and Stan, the purpose of generating mathematical models in machining operations is to have a good understanding of the effects of the parameters involved in the machining process on different machinability aspects [260].

Table 3.1: Capabilities and limitations of modelling approaches [242]

	Analytical	Numerical	Empirical	Hybrid
Principle	Slip-line theory or minimum energy principle	Continuum mechanics using FEM, FDM & meshless FEM	Curve fitting of experimental data	Combines the strengths of other approaches
Capabilities	Predicts cutting forces, chip geometry, tool–chip contact length, average stresses, strains, strain-rates and temperatures	Predicts forces, chip geometry, stresses, strain, strain-rates, and temperatures	Applicable to most machining operations for measurable process variables only	Provides meta-models for a family of models to be integrated
Limitations	Usually limited to 2-D analysis with single and multiple cutting edge, but some 3-D models exist	Material model, friction as input, computational limitations: e.g., meshing	Valid only for the range of experimentation	Limited to the strength of the base model: i.e., analytical, numerical, empirical, etc.
Advantages	Ability to develop fast practical tools	Opportunities to connect to industry-relevant parameters	Practical, fast and direct estimation of industry-relevant parameters	Improves the capabilities and accuracies of the base models
Disadvantages	Unique to each machining problem	Long computation time	Extensive experimentation, time-consuming and costly	Need for extensive data from experiments and/or simulations

3.2 CUTTING FORCES IN MICRO MACHINING

Kim et al. [259], investigated the process involved between micro-machining and macro-machining. They pointed out that in micro-model, the shear stress constantly increases across the cutting edge, whereas shear stress grows along a shear plane in micro-machining [259]. Hence in this light, tool deflection and bending stress are determined by cutting forces, limiting the feed rate in micro-machining [261-263].

For an operator to choose the right cutting conditions for operating system, a well-established cutting force model is required. Some of these existing models can be accessed through literature. Shearing forces and plowing forces are the two major components of cutting forces. Also noted that because the size of the edge radius of the tool in micromachine applications is comparable to chip thickness size, it becomes difficult to apply the normal sharp-edge theorem in the micromachining process because of their larger negative rake angle. Also, because elastic-plastic deformation of the chip thickness, that leads to chatter.

Kim et al. [264], explored the effect of deflection on static tools by using a cutting tool as a simple cantilever beam. The model increased the real cutting depth by deducing the deflection of the cutting tool from the regulated depth of cut [68]. Through predicting the cutting and thrust forces, Dow et al. [263] addressed the issues associated with deflection errors in micro-tools. At the micro-level, cutting force and tool deflections affect each other in vice versa. This mixture should be used in the templates for cutting forces in machining [68].

Bao et al. [265] performed analytical micro-machining by designing a cutting force model to measure the thickness of the chip by considering the path of the tool. However, the negative angle of the rake, the deflection of the tool, and the elastic-plastic workpiece have not been taken into consideration. But it was noticed that they used a reasonably large tool diameter. According to Kim et al. [68], it is not recommended that a standard macro-model be applied to the micro-machine process, particularly when the ratio of feed per tooth to tool edge radius is greater than 0.1 [266, 267]. Therefore when it comes to micro-machining activities, conventional sharp-edge macro-cutting in micro-machining would not be the ideal model for predicting cutting forces [68].

In Yigit et al. [268] investigation, they used an approach described as multi-response optimization of turning process parameters where two optimization methods were identified as Taguchi and Grey Relation Analysis (GRA). This combination yielded a maximum material removal rate, absolute minimum surface roughness, and applied cutting force during machining. This study went on to conclude that when cutting parameters are properly selected, it generates a low cutting force, better surface roughness, and a high rate of material removal.

In Santos et al. work, they established that during the machining of non-ferrous metal such as aluminium alloys, cutting forces of non-ferrous metals are often low when compared with ferrous alloys because of their low mechanical strength, which had resulted in specific cutting pressures to be 70% lower than the machining of metal such as steels. Although this difference is minimal among aluminium alloys, they further stressed that it is depending on their chemical composition and physical properties [269].

3.3 CUTTING FORCE MONITORING

The relevance of monitoring cutting force in the single-point diamond turning process has been well established in both industry and open literature. Of all the variable quantities observed in the machining process, one of the most critical measurements is cutting force, which is closely associated with cutting situations, such as measuring the wear of the cutting tool [270, 271], machining vibration [272], and surface integrity [271]. This is because machining process is prone to any slight effect of applied force due to a short time of forced vibrations which when not properly managed, may develop to high amplitude, oscillations, instability, and poor quality of machined part [273].

Thus, cutting force requires competent condition monitoring in the machining process. In this review, the authors have identified a few methods of monitoring cutting forces, such as direct and indirect methods. of monitoring cutting forces, which is during the machining process, and this can be achieved by using dynamometers. In Stein and Huh [274] investigations, they established a monitoring method that did not make use of dynamometer but instead they adopted an approach that evaluates cutting force based on the spindle motor current and speed as well as a model that relates to all

these measured quantities to the cutting force. This method was verified on a CNC lathe.

To be specific, researchers such as Inasaki and suk vittayawong [275], Tlustý and Andrews [266], and Weck [276] established that some cutting forces information extracted in real time and on-line can be linked to the prediction of tool wear breakage detection and other glitch inspections [274]. Stein and Huh [274], further stated that sometimes it depends on the sensors, models, and estimate of the algorithm used. Several model-based monitoring systems can be designed to evaluate the cutting force.

Spiewak [277], has also developed another indirect force sensor based on the analysis of 3-axis spindle acceleration and spindle deflection. Sharaish and Aoshima [278], Sharaish and Aoshima [271], used a state observer and a displacement transducer to measure the cutting force. Another approach with no additional sensor is recommended by Stein and Huh in [279, 280] and Huh et al. in [280] where they demonstrated a number of cutting force monitoring systems by taking into account the cutting force as transducer input to the spindle drive. A method for cutting force control was developed by Kurihara et al. [281], who proposed a sensor using a parallel disruption observer with a lower cutting force control technique. Via simulation and experimentation using a linear motor drive bench, the implementation of this proposed approach was estimated.

The use of laser interferometer in ultra-precision machining to evaluate cutting force was proposed by Shinno et al. [282]. During milling process, Matsubara and Ibaraki et al. [283], assessed cutting forces by using servo and spindle motor current that are correlated to cutting force. In Xaoli et al. [284] study, they proposed a system that made use of signals from motor current and an adaptive neuro-fuzzy inference system (ANFIS) for online estimation of cutting forces. Chang [285] used a neural network to develop a spindle motor model, and subsequently conducted a cutting force evaluation based on the current generated by the spindle motor. They concluded that the cutting power of the feed force was measured using neuro-fuzzy techniques for the current of the feed motor.

3.4 CUTTING FORCES SENSING TECHNIQUES IN NANO MACHINING

Different cutting force sensing systems can usually be divided into two categories that are primary or indirect techniques. With indirect sensing methods, it identifies and sense parameters that respond to change to certain degree with cutting force. Such parameters are Voltage, acceleration, acoustic emission, spindle motor current and vibration, etc. [286-295]. whereas the direct method of sensing adopts the use of certain effects instigated precisely by cutting force. According to literature [296-302] direct effects include mechano-magnetic, mechano-electric, and mechano-optic conversions, etc.

According to Liu et al. [303], it is easy to apply direct method of sensing for measurement systems because it produces more accurate measurement results. Some drawbacks, however, such as low durability, high cost, overload fragility, etc., have prevented such techniques from being widely adopted in machine shops [303, 304]. Some available researched approaches have been adopted in machining, this is where multi-component cutting force sensing systems (**Figure 3.2**) can be used to sense cutting forces along various axes [304]. These techniques are based on experimental models, current sensors, strain gauge, capacitive, optoelectronic and piezoelectric processes [305, 306]. The outcome of any of the above-mentioned techniques depends on proper selection of cutting force sensing systems applied. Example of cutting force measurement using strain gauge in **Figure 3.3**.

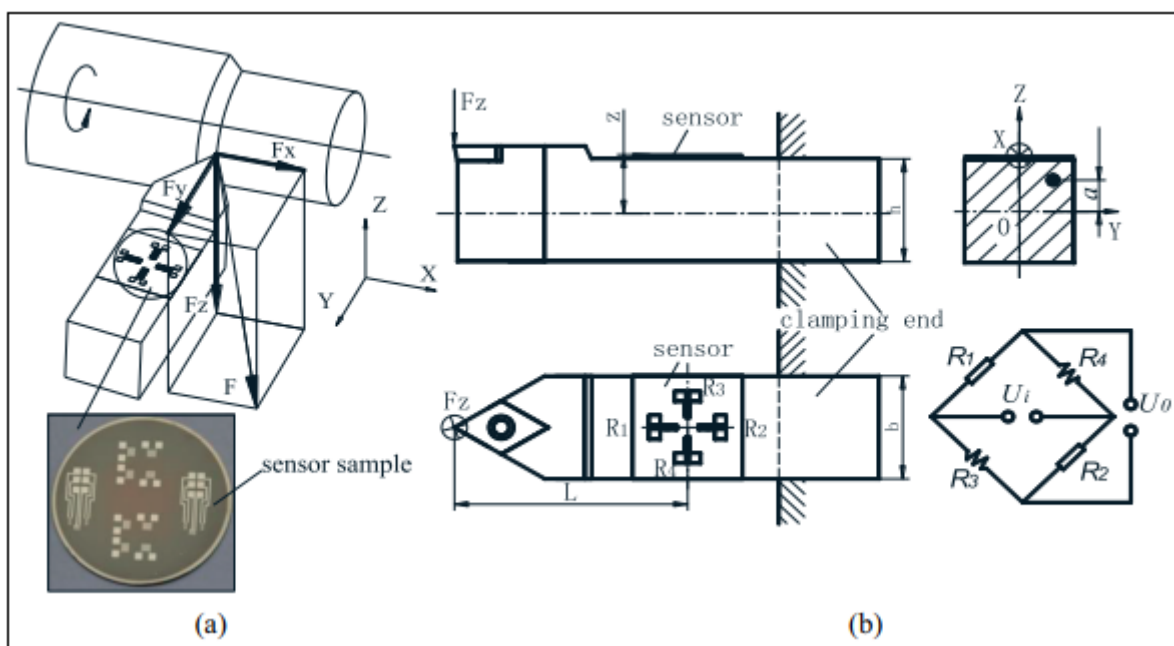


Figure 3.2: Cutting force measurement with embedded sensor [307]

Shin et al. [287] investigation came up with a technique that can be employed to predict cutting forces in end-milling process using an accelerometer and Hall-effect current sensors [305, 306]. Stein et al. [308] came up with an idea of how to predict the current of a direct current (DC) of a CNC machine tool by developing a dynamic lumped parameter; they evaluated cutting force by correlating the electric current and associated forces that run the system components. In Altintas studies, they calculated cutting force and predicted the tool failure in milling based on a proposed model of a vertical milling machine feed drive control [305, 306, 309, 310]. They further carried out feasibility work on armature current measurement using cutting force prediction method.

Kim et al. presented an investigation to show viability of in-process multiple-axis machining force. This investigation used Artificial Neural Network (ANN) approach; the results of the experiments reveal that the cutting force forecast by using the recommended ANN methodology concurred with original cutting force known. The results also agreed with Kalman Filter (KF) when they were compared [305, 306, 311, 312]. They further established a design for ANN that has four-layers i.e., an input layer, two hidden layers, and an output layer which was implemented in the same study. A unique approach to identify cutting force via control voltages acquired from electro-magnetic bearing was explained by Auchet et al. [288, 305, 306], according to their experimental outcomes, it shows that the estimated cutting forces yielded good results similar to what was acquired in an industrial Kistler instrument.

Liang et al. discovered that the projected measurement system for the accuracy of static and bandwidth are around 8% and roughly 62 Hz, correspondingly [305, 306]. The first combined strain gauge sensor system to monitor cutting force in diamond turning machining was described by Santochi et al. They described how strain gauges can be mounted and arranged at precise locations on tool with full sensor configuration arrangement to enhance sensor responsivity. They also described connections of data acquisition system between input data from infra-red and output data of the bridge. The results showed the entire system repeatability and sensitivity were recorded to be less than $\pm 3\%$ F.S. and 0.24 mV/N, respectively, under different machining conditions [305, 306, 313].

Yaldız and Ünsaşar [304] illustrated a dynamometer designed specifically from strain gauge principle and piezo-electric from acceleration-based principle (accelerometer) to detect dynamic and static measurements of many-sided cutting forces in diamond turning see **Figure 3.3**. The anticipated dynamometer consists of an elastic material with four ring shapes in an octagonal way, in which strain gauges are attached to and later connected to form Wheatstone bridges. Experimental tests were carried out by adopting various cutting parameters, and the outputs showed that the strain gauge designed to acquire cutting force was suitable to carry out turning operations [305, 306].

Zhao et al. developed a half-bridge strain gauge configuration for the cutting-edge sensor system which was integrated and connected to the cutting tool to achieve a 2D cutting force. The new elastic component, which has two nearly perpendicular rings, is placed on the cutting tool, thereby forming the tool post. This design was chosen to define the cutting force with a high sensitivity and a high natural frequency. This is because this approach has put in place an advanced elastic material and a MEMS production technique. The maximum detected sensitivity is 0.31 mV/N, while the natural frequency is 771 Hz for this proposed device [305, 306, 314].

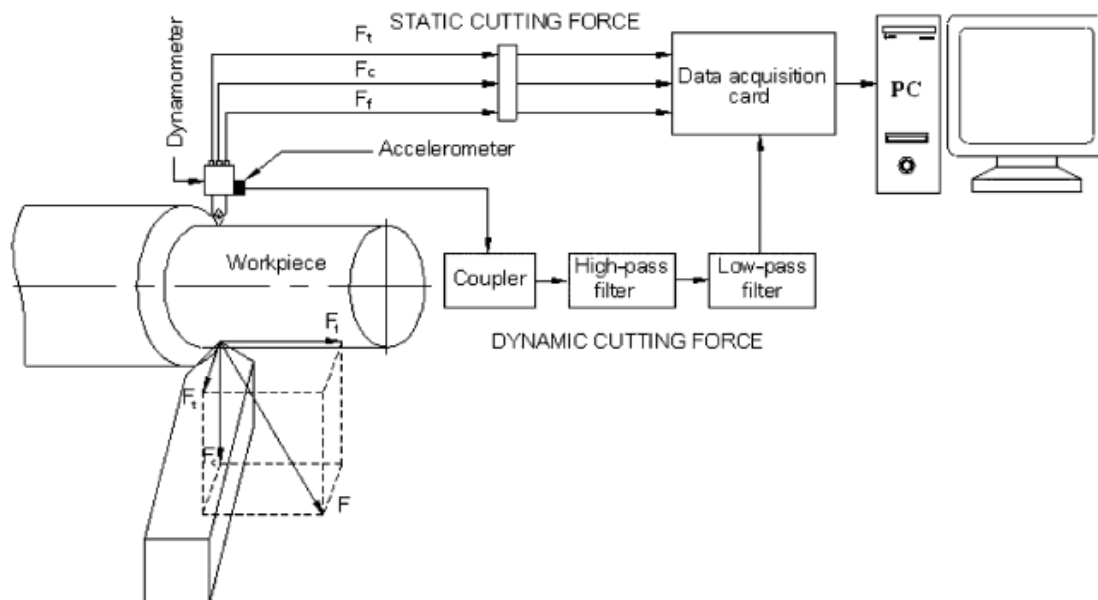


Figure 3.3: Cutting force measurement using Dynamometer [304]

In another study, Zhao et al. introduced a 3-D cutting force sensor that generated high-performance during diamond turning operations. They designed the sensitive part of

the sensor to be in form of two octagonal rings that are mutually perpendicular. To test functionality of the sensor developed, they carried out a study on static calibration and the results showed the accuracy of the proposed sensor was between 0.38% and 0.83%. At the same time, the natural frequency was 1122 Hz [305, 306, 315].

To further advance Zhao et al's. [305, 306] work, they designed and developed cutting force sensor that measures six-axis cutting force for turning operation. With an innovative elastic component (**as shown in Figure 3.2**) and a new strategic arrangement on how to mount strain gauges on the sensing system, it could sense tangential, normal forces and the moments along three axes simultaneously. They also adopted Simulation-Driven Optimization method (SDO) and an ANN-based decoupling algorithm to process all the multiple dimensions of cutting forces. They observed a maximum coupling error of 1.47% F.S and a nonlinearity error. and 1.94% F.S during testing [305, 306].

It was recently revealed that one of the most sensitive ways to monitor cutting forces in cutting force sensing systems is the use of capacitive sensor which had yielded moments at Micro-Nano even at Pico-Nano resolutions [305, 306]. Liang et al, further stressed that the output of capacitor sensor system are obtained through switched-capacitor circuits, capacitive ac-bridges, and capacitance to frequency converters [305, 306]. Albrecht et al, presented a study whereby a capacitance displacement measurements principle was used to develop indirect cutting force sensing system. They explained how a high-resolution capacitive sensor from Lion Precision manufacturer was clamped on the machine spindle to sense the gap variation between the spindle shaft and the sensor [305, 306, 316].

They used industrial piezoelectric dynamometer to calibrate the system and the gap variation was found to be directly proportional to the applied cutting force. A satisfying linearity performance was also observed for cutting force when static calibration was carried out experimentally [305, 306]. This is one of the most widely used approach to sense cutting force for micro or macro machining. Another method to detect cutting force during machining can also be based on optoelectronic sensing systems. This technique is good for manufacturing companies that operates in harsh manufacturing environments because its multiple modules of optoelectronic cutting force sensing system remain an added advantage to concern operators.

Liu et al. [303, 306, 317] presented their studies on the technique that operate on Fiber Bragg grating sensor examined three perpendicular force measurement in machining operations. They designed and used an elastic material that was retrofitted by fibre Bragg grating sensors that contains four rings in a ring-like shape with pre-constricting mechanism. The experiment was verified and validated, and the results revealed that the idea could be implemented for turning and milling processes [306].

Jin et al. [296] described a similar method to measure cutting force using an optical fiber sensor. The experiment was calibrated, and the test results showed that the illustrated method has competitive benefit. The natural frequency, sensitivity and linearity of the system were recorded to be 950 Hz, 2.51 mV/N and 1.2% F.S.[305, 306], respectively. This application is also dynamic in machining process. In a study by Bartow et al. [318], they came up with similar idea like Liu et al for sensing system that operates based on the principle used in Fibre Bragg Grating (FBG) sensors. The FBG sensors operation methodology was such a way that sensors were attached to the cutting tool body. In contrast, an accurate estimation of tool tip motion was computed by comparing it with a piezoelectric accelerometer. Real time cutting was carried out on a lathe machine. Outcome of the results shows high reliability and feasibility of the proposed force sensing system.

Totis et al. set up a force sensing technology for turning process based on piezoelectric sensor that utilizes three-component cutting force instruments. An industrial 3-axes piezoelectric force sensor from Kistler was fitted into the sensing system. They carried out static calibration experiments and dynamic response tests using one modern CNC lathe machine. They recorded highest relative error of 6.6% and static crosstalk disturbances of 3% [305, 306, 319, 320].

Rao et al., built a sensing system based on integrated piezoelectric dynamometer for cutting force with a resolution of 0.44 mN and a sensitivity of 7 mV/gm. A theoretical model was proposed from this study which generated a relationship between geometry dimensions. The observed cutting force signals have predicted the cutting depth and width of the experiment. They established that experimental results presented that their proposed predicted method has the capability to measure cutting geometry with the maximum relative error of 10%. [293, 305, 306]

3.5 CUTTING REGIME VERSUS CUTTING FORCES

Cutting regime can be defined as the effect on cutting forces during the cutting process of tool geometry, cutting parameters, cutting environmental conditions, and workpiece. Over the years, experiments have been performed on the effect of the cutting regime on cutting forces. The cutting force is a critical parameter of the cutting mechanism in the cutting process. There is a need to include both processing operations and technological possibilities for maximum utilization or the implementation of all accessible manufacturing facilities in order to improve productivity. During the micro cutting process, the uncut chip thickness is close to the cutting-edge radius of the tool. Therefore, as the uncut chip thickness exceeds the edge radius of the tool, the effect will play a major role in cutting force over the nominal angle of the rake during micro-machining [321-323].

In addition, the effect of a combination of cutting parameters, such as feed rate, cutting speed, and depth of cut, on different workpiece materials has also been shown to determine the cutting force during machining. An analysis was carried out by Vikas et al. [324], concerning the effect of the feed rate on the cutting force of EN 8 carbon steel during the turning process. The investigation examines the measurement of the cutting force components produced by the turning at different cutting parameters with different tools at different feed rates. The cutting depth and cutting speed were kept constant during the experiments. Each test was performed using a sharp tool. They analyzed the effects of cutting parameters and feed rates on cutting forces. The results showed that, regardless of the feed rate, the thrust force (F_t) is greater than the feed force (F_f). With the rise in feed rate, the cutting forces have been demonstrated to increase. By conducting 24 experimental runs on AISI 1020 steel, Baldoukas et al. [325] analyzed the effect of feed rate and tool rake angle and provided findings that indicate an increasing trend in the main cutting forces as the feed rates rise while the feed rates and cutting force decrease dramatically as the rake angle rises.

According to Gunay et al. [326], by conducting experiments on AISI 1040 as a workpiece, they examined the effect of the rake angle on the major cutting force. The findings were contrasted with the experimental results provided by the Kienzle method. They discovered that as the rake angle increases from negative angle to positive values, there is a declining pattern in cutting forces. The measured deviation found

was in the order of 10-15% between empirical method and experiments. In literature, several researchers have proposed cutting force models using the effect of the tool edge radius on the cutting force. Slip-line models have been suggested in some previous studies to understand the effect of the tool edge radius [39, 323, 327]. To consider the influence of tool edge radius on cutting force, Vogler et al. [323, 328] used the minimum chip thickness concept in their model

Liu et al. [329], developed a cutting force model of micro-end milling to explain the effect of minimal chip thickness and elastic recovery. They assumed that a solid built-up-edge remained during the cutting process. Bissacco et al [323, 330], used an analogous rake angle to understand the influence of tool edge radius on cutting force. Huang et al. [323], developed and presented an algorithm that predicts cutting force for ultra-precision diamond turning, that takes into account the effect of tool edge radius. For cylindrical diamond turning procedures such as fast tool or slow servo assisted diamond turning, the algorithm is most used to predict cutting force. Experiments were further used to validate the developed algorithm [331].

The effect of feed rate and cutting speed on cutting forces, surface roughness, and tool-chip contact duration during machining was investigated by Korkut et al [332]. The cutting force measurements were carried out using a dynamometer designed based on strain gauge. Using a certain set of cutting parameters, there is an increase in cutting speed and an increase in cutting forces, whereas the pattern of cutting tool BUE formation increased at lower and intermediate cutting speeds.

Bartyra et al. [333], proposed an attempt to build a model for estimating cutting force using the hone edge uncoated CBN method during finishing machining of EN31 steel hardened to 60 ± 2 HRC. The combination of cutting parameters was tested to achieve improved performance with a specified set of cutting conditions. To develop a regression model for cutting force and surface roughness within the range of parameters selected, a complete factorial design of experiments (DOE) process was used. The regression model developed demonstrates a strong effect on cutting forces of machining parameter dependence, such as cutting, radial, and axial forces. Therefore, cutting forces can serve as a good factor for predictions. Further studies have also been carried out to explore the influence of cutting and tool parameters on the ultra-precision machining of the metals [334-337].

3.6 CUTTING FORCES IN NANO MACHINING

Ductile-regime machining has been recognized as a feasible and practicable technique for efficiently processing brittle materials. While it has been extensively studied, less study has been performed on the cutting forces in the ductile-regime processing of brittle materials. It was noted, according to DeVries [338], that cutting forces could cause deflections that can lead to geometric errors and challenges in reaching requirements of tolerance.

The proper understanding of cutting forces is one of the most common foundations for modelling the machining process. Huang et al. [339], have developed a model of cutting force for ductile-regime machining of brittle materials. The prediction was used in the manufacturing of crystal MgF_2 (100). With less than 5.5 percent prediction error, the predicted cutting forces aligned with the experimental forces. The study indicates that with the rise in feed rate or depth of cut, overall cutting forces increased. They concluded that the cutting forces generated by the brittle materials are most important in the overall cutting forces under cutting conditions of large feed rate and depth of cut.

According to Ma et al. [340, 341], they proposed a theoretical model for cutting force in turning Lithium disilicate glass-ceramic. During machining process, they considered the principle of energy conservation. The work done on the shear plane by the force component of the main cutting force equals the energy changes of the crack mechanism [340]. However, as fracture mechanics are considered, different energy models for the crack system are applied. Another theoretical cutting force model was derived for the turning of hard-brittle materials. The experimental part of turning indicated that with an increase in cutting speed, the main cutting force decreases. Also, an increase in speed causes an increase in feed rate but a decrease in depth of cut. The predicted values of the theoretical cutting force model then have the same effects as the experimental values when turning hard-brittle materials [340, 342].

DEFORM-3D FEM simulation and experimental validation were presented in the analysis of Ezilarasan [342, 343] when turning Nimonic C-263 super alloy material using a cemented carbide cutting process. They noticed that the tangential cutting force must also be simulated to use the machining model effectively. The propagation of temperature was around the tip of the tool. The findings revealed that the results

expected were well in line with what was recorded from experimental data. Diana et al. [344], worked on prediction of cutting forces at 2D titanium machining. They found in their studies that the coefficient of cutting force increased with the reduction in depth of cut. They also reported that the coefficient of cutting force increased with the decrease of one of the chip's performance criteria, i.e. either the feed rate or the depth of cut [344, 345]. **Figure 3.4** shows the effect of geometry of the tool on the process variables of the turning.

Duong et al. [346], carried out studies to show any correlation between the tool rake angle and cutting force in ultraprecision machining of electroless nickel. They compared and investigated the cutting force at different tools rake angles on micro machining of electroless nickel by using theoretical and experiment analysis. They concluded that diamond cutting tool with rake angle of 10° caused the smallest cutting force theoretically, but experimentally diamond tool with rake angle of 0° degree induced smallest cutting force.

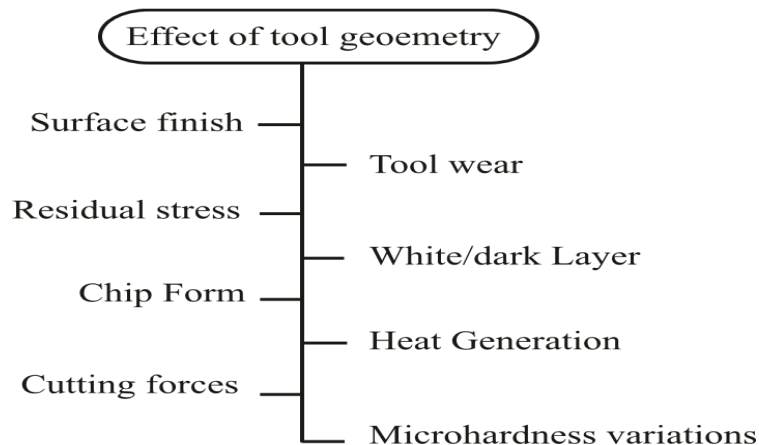


Figure 3.4: Effect of tool geometry on performance parameters in turning [345]

According to [347, 348], it was known that there was a relationship between cutting forces and tool rake angle variance, which implies that the optimal value of the rake angle caused an increase in cutting machinability and a decrease in cutting forces. Cerattia et al. [349], have shown the feasibility of tailored FEM modelling in predicting chip forms. They estimated that the influence of the cutting conditions would have influenced the predicted cutting forces and process parameters. In the same manner, the critical value for the simulation for either a positive or a negative angle of the rake was somewhat different.

According to Ekkard Brinksmeier et al., a face turning of aluminium alloy (AlMg5) experiment was carried out with a steady material removal rate, where measurement of cutting forces as a continuous function of cutting speed were used for the thrust force exceeded cutting force concluding that this indication may be due to amplified bond between the hot aluminium chip and the rake face of the diamond tool in the HSC domain. The cutting force is directly associated with chip formation. They also discovered that thin depths of cut can generate little cutting forces with inappropriate signal-to-noise ratio [175, 178]. Meanwhile, literatures have revealed that most low cutting forces during machining are often due to increase in the cutting speed, irrespective of how hard and strong the aluminium alloy [179-181].

The cutting force in the cutting direction is the overall force generated by the cutting tool [350, 351]. Computation of cutting force can be done in molecular dynamics by summing up the combined force of all atomic forces in the X-direction exerted by the workpiece atoms on the tool atoms [351]. According to Abdukadir et al., the tangential cutting force's mean value was determined for all the edge radius due to the observed pattern of cutting forces during MD simulation of silicon see **Figure 3.5**. They agreed to use two edge radius 5 Å and 20 Å and discovered that 5 Å edge radius had the least value of 42.39 Nn while 20 Å radius had the highest value of 65.78Nn [253, 351]

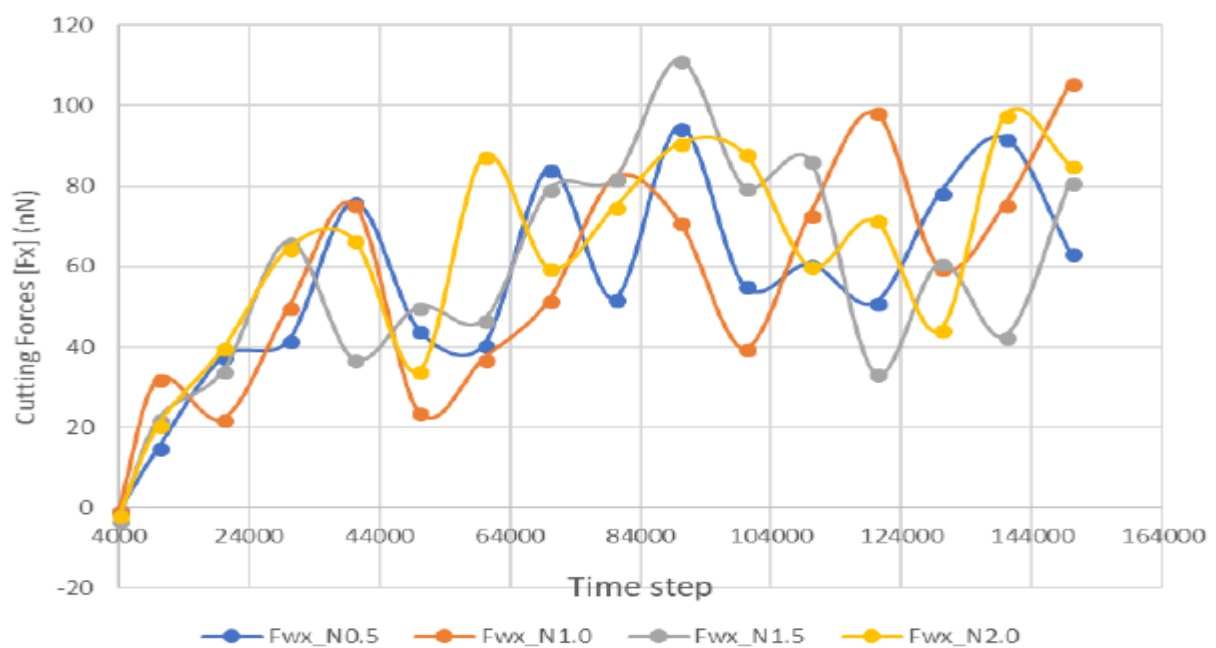


Figure 3.5: Variation of tangential cutting force with tools of different edge radius [253]

They further analyzed and concluded that the cutting force often increases as the thrust force decreases, just as the ratio of uncut chip thickness to edge radius decreases. It has also been found a decreased cutting force is important for a high quality surface roughness in nanometric cutting [351, 352]. The magnitude of the cutting force on rapidly solidified aluminium alloy RSA 905 was investigated by Otieno and Khaled, an increase in cutting force with increasing cutting distance was discovered. They also recommend that cutting conditions that produce lower forces would be more beneficial and would reduce negative impacts on the tool and machined surface.

Therefore the lowest forces were associated with high cutting speed, low feed rate, and low depth of cut [353]. Jang et al. [354], carried-out studies on MD simulation of aluminium 7075 alloys. They proposed a potential model that will consider all the components of the alloy, particularly with and without Zinc. They analyzed the mechanical behaviour under different strain rates and discovered that the Zinc constituent model has higher yield stress and tensile strength than the Zinc-free constituent model.

3.7 DESIGN AND DEVELOPMENT OF SELF SENSING CUTTING FORCE (SSCF) TOOL HOLDER

Due to the constraints of current commercial sensor systems, reconfigurability, and some related flexibility challenges, sensor integration techniques are recognized [355]. Byrne [356] has suggested an integrated force sensor solution for drilling operations by integrating two piezoelectric force sensing rings into a direct driven motor spindle. Jun et al. [357], who incorporated a force ring into the spindle housing for triaxial cutting force measurement and completed the evaluation work on the sensor performance [355]. Totis et al. [320] have developed a rotating dynamometer for the milling process by installing commercial piezoelectric triaxial force sensors between the modular cartridge and the cutter body. In addition, during the milling process, Ma et al. proposed a variety of integrated sensor techniques for measuring feed and transverse forces [358] and torque [359] a piezoelectric thin film polyvinylidene fluoride (PVDF) strain sensor was installed on the shank of the cutting tool and all the electronics and batteries were positioned mechanically connected to the tool holder in a metal housing [355].

Several manufacturers have already designed some types of commercial piezoelectric rotating dynamometers, such as Kistler Instrument Corporation [360], and some of these devices can simultaneously recognize four-component cutting forces with good dynamic performance. However, these instruments are also very expensive. Albrecht et al. [316] developed a method of measuring only the radial cutting force by integrating capacitive sensors into the spindle in order to measure the static and dynamic variation of the distance between the sensor head and the rotating spindle shaft [355].

Rizal et al. [361] introduced the force sensing element on which strain gauges were mounted, and then integrated it into a tool holder to calculate three cutting forces during milling. Similar work was done by Suprock [362] and Nichols [363], who built a strain gauge-based torque measurement tool holder, which was known as a smart tool holder in their studies carried out similar work. In order to measure cutting force, all the rotating dynamometers developed by these researchers have been checked and confirmed to have good performance [355].

However, only two or three-axis cutting force or torque can be measured by most current devices based on capacitive sensors or strain gauges, to the best of the knowledge of the authors. Too many strain gauges are needed if they are used to measure more axis forces, just like the dynamometer designed by Rizal et al [361, 363]. in which three full Wheatstone bridge circuits were constructed and 24 strain gauges were integrated in total, which undoubtedly increases the device's complexity and reduces reliability [355].

This current study contributes further to solving the problems of designing and creating an integrated tool holder system designed to measure the cutting force in diamond turning operations. The standard commercial tool holder is reengineered in order to form deformable beams and to render itself a force sensing element. Two T-rosette strain gauges are used and inserted into the force sensing tool holder to define the deformation of the beams and then determine the cutting force.

The rotary dynamometer is designed to measure forces not exceeding 10 N of cutting and 100 Nm of torque with up to 3000 rpm of spindle speed using a monocrystalline diamond cutting tool. In addition, the device has the advantages of simple construction and low cost, making it simple to produce and suitable for industrial use. A series of

studies have been performed and the results indicate that accurately calculating the cutting force in diamond turning processes is safe and practical.

3.8 THEORETICAL ANALYSIS

This deals with mathematics behind the simple cantilever principle employed in the design and the brief finite element analysis of the cantilever beam when loaded with 1N.

3.8.1 Analytical model

Cantilever beam:

In this study, the principle of a cantilever beam was adopted for the force-based strain gauge sensor cutting tool holder. Cantilever which can be referred to as the beam in which one end is fixed and another end is free. If load is applied to the free end, then deflection occurred.

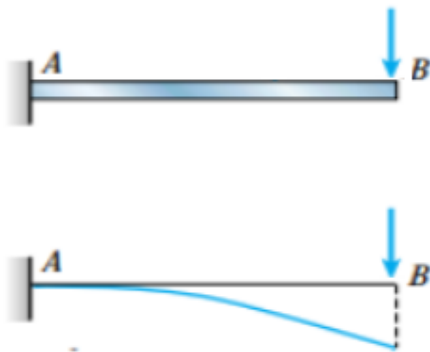


Figure 3.6: Cantilever beam before and after deflection

For the experiment of the clamped beam at one end and free at the other the following expression for the tension at the surface of the beam,

Equation 3.1

$$\sigma = \frac{M\rho}{I}$$

where M is the resulting bending moment, I is the moment of inertia of the cross-sectional area, and p is the distance from the neutral line to the point of interest. The moment of inertia is given by

Equation 3.2

$$I = \frac{bh^3}{12}$$

where b is the width of the beam and h is its thickness. Substituting Equation (3.2) into Equation (3.1) and c for h/2 we have

Equation 3.3

$$\sigma_{max} = \frac{6M}{bh^2}$$

which corresponds to the tension σ_{max} on the surface of the beam when subjected to a bending moment M. It is known that the deformation ϵ can be obtained by means of the Equation 3.4, known as the Hooke's Law, where E is the modulus of elasticity of the material.

Equation 3.4

$$\epsilon = E\sigma$$

Substituting Equation 3.3 into Equation 3.4 gives the equation for the deformation at the beam surface when subjected to bending, Hence equation 3.5.

Equation 3.5

$$\epsilon = E \frac{6M}{bh^2}$$

3.8.2 Finite Element Analysis of the design

Table 3.2: Reaction force and moment on constraints

Constrain Name	Reaction Force		Reaction Moment	
	Magnitude	Component(X,Y,Z)	Magnitude	Component(X,Y,Z)
Fixed Constarint:1	1N	0N	0.0467517Nm	0.0467517Nm
		1N		0N
		0N		0N

Von Mises Stress

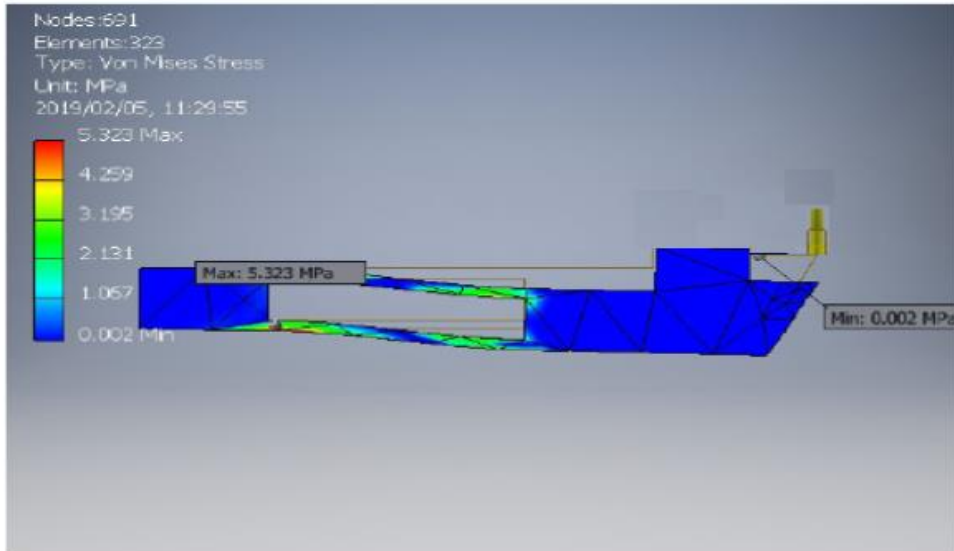


Figure 3.7: Von mises stress

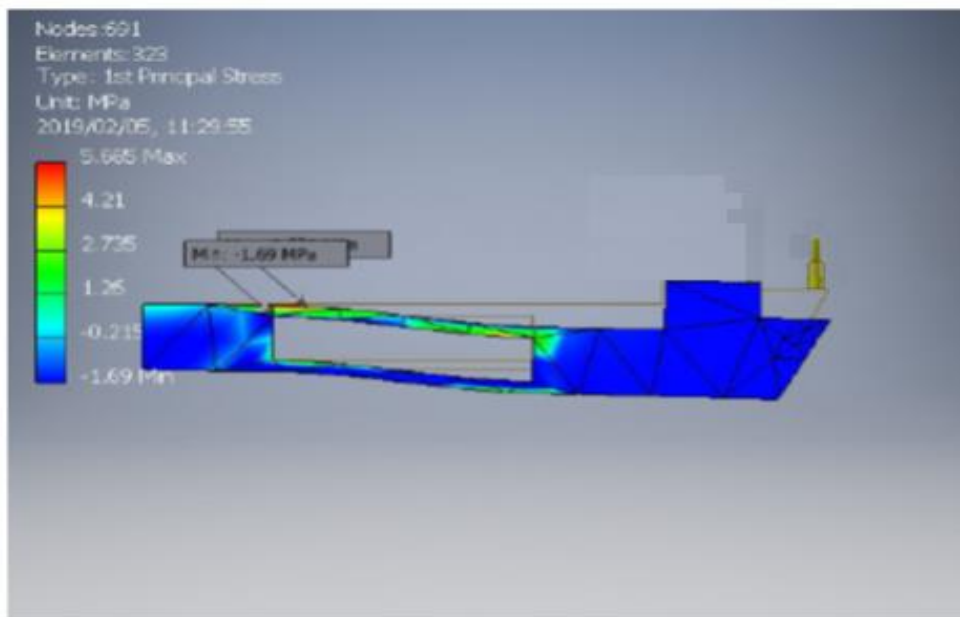


Figure 3.8: Principal stress

3.9 MECHANICAL PART

3.9.1 Load cells and strain gauges

Load is a term generally used in engineering to mean the force exerted on a surface or body. Usually, a load cell is a load transducer that transmits electrical signals to the load, weight or force that acts on it. The load cell is referred to as the cantilever beam assembly in such a way that the strain gauge is used in either one or more axes as a

force indicator. Therefore, the strain gauge is the transducer that translates force in this case to change electrical parameters, altering resistance (and/or resistivity, if semiconductor strain gauges are used). The outer assembly that houses the strain gauges and distributes the strain gauge can also be called the load cell.

Load cells are the most effective, reliable, and fast system for industrial weighing and for tracking strain on structural supports. Strain gauge load cells are connected to industrial-scale platforms, vessel mounting legs, support columns, wire rope, cranes and more to determine the amount of force applied. The force deforms the load cell to a small degree, turning the mechanical force into an electrical proportional signal that can be calculated by several types of electronics. This data is very useful for batching, process control and material use control systems, as well as for a host of other applications. In many industrial settings, load cells have become the preferred weighing sensor due to the precision and speed with which they return data.

3.9.2 Strain gauge

A strain gauge is a transducer device commonly referred to as a sensor whose resistance varies with the force applied; it can be used to convert force, pressure, tension, weight, etc., into a measurable change in electrical resistance. Stress and strain are the outcome if external forces are applied to a stationary object. Stress is defined as the internal resisting forces of the object, and strain is defined as the occurrence of displacement and deformation.

3.9.3 Types of strain gauges:

There are different types of strain gauge:

- Acoustical strain gauges
- Electrical strain gauges
- Optical strain gauges
- Pneumatic strain gauges
- Mechanical strain gauges

Acoustic Strain gauge: The difference in the length of a wire stretched between two-gauge points in an acoustic strain gauge is measured, which affects the wire's natural

frequency. For a strain gauge, the magnitude of frequency change may be increased by reducing the wire length or wire tension. These gauges are extremely precise and are accurate in the long term.

Electrical Strain gauge: The displacement or strain is measured as a function of the change in resistance caused by the displacement in the gauging circuit in the electrical resistance strain gauge. Its length will increase as the conductor is extended, and the area of the cross section will decrease, resulting in a resistance change. The Gauge Factor is defined as the change in resistance per unit strain. The sensitivity of the strain gauge is indicated by the Gauge Factor.

Optical Strain gauge: To achieve optical magnification, there are two types of optical strain gauges that use a variety of mirror systems. Marten 's optical gauge is another well-known optical device used in a strain gauge on a single mirror system, Tuckerman Optical Gauge, which has relative rotation with autocollimator between the fixed mirror and the movable mirror. The autocollimator consists of a lamp source for the creation of parallel ray beams and a scale for the measurement of reflected ray deflection.

Pneumatic strain gauge: A pneumatic gauge principle of operation relies on the relative discharge of air between a fixed orifice and a variable orifice. Magnification of up to 100,000 times and the length of the gauge as small as 1 mm can be achieved with these gauges. Both static and dynamic strain measurements are acceptable for these gauges.

Mechanical strain gauge: It is also known as Extensometers to calculate conditions of static or gradually varying load. Two knife edges are typically provided for these gauges, which are clamped firmly in contact with the test part by means of a clamping spring at a precise gauge length distance.

3.9.4 Principle of strain gauges

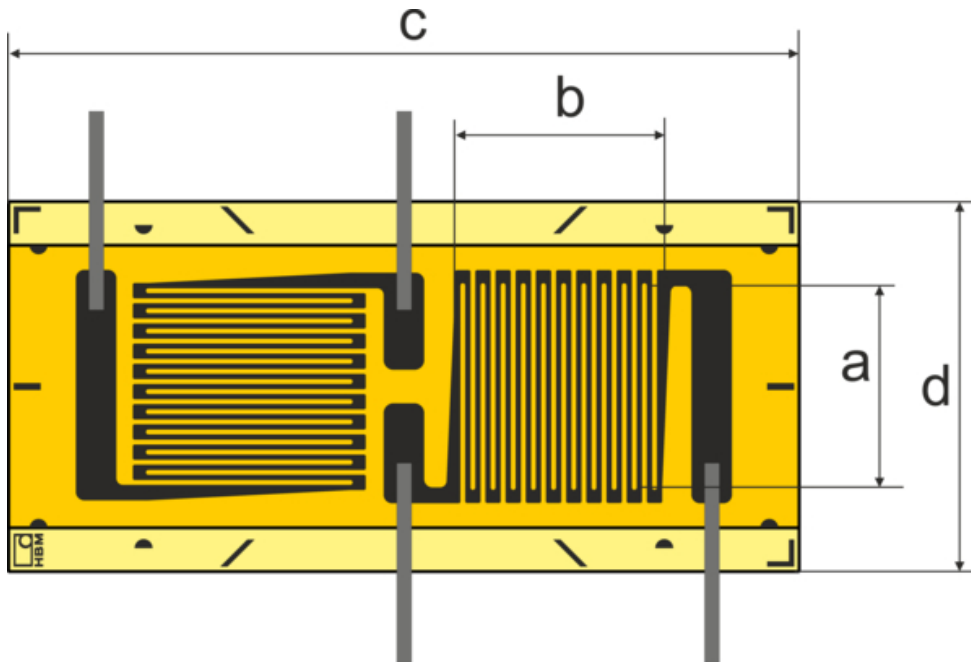
A strain gauge is a system that is used to measure an object's strain. Edward E. Simmons and Arthur Ruge invented the system in the year 1938. The system is still used mainly as the key sensing factor for sensors such as torque sensors, pressure sensors, load cells and so on in many electronic circuits.

Only one application of strain gauges is load cells. In the case of load cells, either in one or many axes, this application happens in case of force measurement. The strain gauge is the transducer that translates force to adjust electrical parameters, changing resistance (and/or resistivity, if semiconductor strain gauges are used) in this case. The load cell is the outside assembly which houses the strain gauges and distributes the strain.

As an integral part of a structure or system, a force transducer is often built in, and many force calibration devices themselves are machines. Therefore, the force measurement device is also difficult to understand independently from the application and this has many implications on the processes for system design, calibration, and operation.

The strain gauge load cell is the most common type of force transducer, and one which is a simple example of an elastic system. Each cell is based on an elastic element to which a variety of strain gauges of electrical resistance are bonded. The magnitude of the strain field created by the action of the force is determined by the geometric shape and elasticity modulus of the product. Each strain gauge reacts at its position to the local strain, and the force measured is determined from a combination of these individual strain measurements.

Standard strain gages for electrical resistance consist of a thin film used as a backing material. As an insulator and carrier for strain on a given object. For lead wire connections, strain gages provide terminals. A strain sensing element is placed on top of the backing film, which is constructed from different metals, as seen in **Figure 3.9**. To obtain required resistance values for a given experiment according to Khan and Wang [364], the metallic material is looped into a 'grid pattern' in an orientation. Usually, the rated capacities of strain gauge load cells range from 1N to more than 50 MN and have become the most widespread of all transducers of force measurement. They can be used as force transfer standards with high resolution digital indicators. In section 3.6 below, the calibration and checking of load cells for strain gauges will be addressed in detail.



a = grid width, b = grid length, c = base length, d = base length

Figure 3.9: Typical T-rosette strain gauge

For different applications, there are number of resistance strain gauges available, some of which are: foil strain gauges, thin-film strain gauges, and wire strain gauges. In this research, because of the following characteristics, foil strain gauges were classified as most appropriate: widely used materials that can be found Nickel, Chromium, Iron, Aluminium Gage, better suited to low temperature environments (as low as -265 °C), more durable over prolonged strain periods, not very difficult to solder. With the design and application, the nominal resistance of the strain gauge varies. The wire gauge resistance ranges usually range from 60 Ω to 350 Ω , 120 Ω to 5k Ω of foil and semiconductor gauges, and around 10 k Ω of thin film types.

3.10 INSTRUMENTATION USED FOR STRAIN GAUGE DEVICES

It is common to link one or more strain gauges aligned to respond to the maximum compressive strain and another set aligned to the maximum tensile strain to optimize the response of the load cell. This has the added benefit of minimizing the effects of environmental changes such as temperature, which work on all gauges equally, when linked electrically in a Wheatstone bridge configuration (see **Figure 3.10**). By evaluating the differential voltage across the bridge, the resistance change is observed. When excited by an input voltage, the voltage output from the bridge is

connected linearly to the resistance change of the strain gauges and is a function of the force applied to the element. Mathematically this is the product of the strain and the excitation voltage. The rated output of a load cell may be standardized to a nominal level, usually 2 mV/V (2 mV output per volt applied) but this may range from 1 mV/V to 4 mV/V.

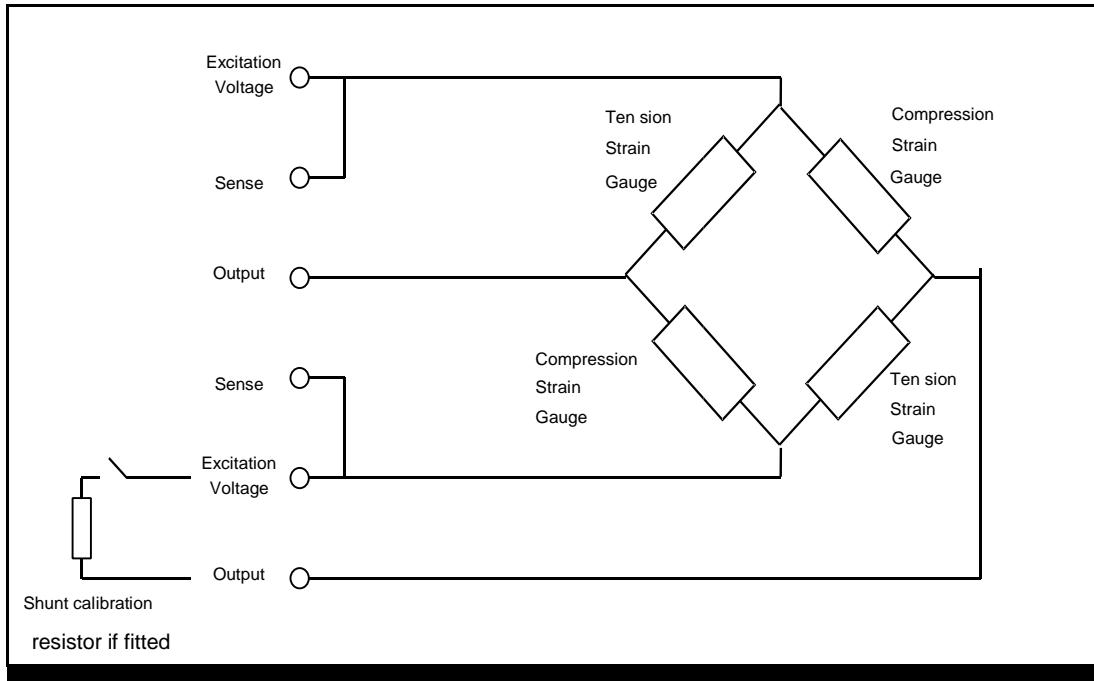


Figure 3.10: Full Wheatstone bridge configuration

3.11 CHOICE OF MEASUREMENT SYSTEM (STATIC) E

The metal foil strain gauges used in this research are resistors with a nominal (unstrained) resistance of 350 Ohms. It has 2 separate strain gages with perpendicular grids on a single carrier both make up a full bridge when attached to the metal on top and beneath **Figure 3.11**.

The fundamental formula for the resistance of a wire with uniform cross section, A , and resistivity, ρ , can be expressed as:

Equation 3.6

$$R = \rho \frac{L}{A}$$

the resistance changes per unit resistance ($\Delta R/R$)

Equation 3.7

$$\frac{dR}{R} = \frac{d\rho}{\rho} + (1 + 2V)\varepsilon$$

A measure of the sensitivity of a material (or its resistance change per unit applied strain) is defined as the Gage Factor:

Equation 3.8

$$GF = 1 + 2V + \frac{d\rho}{\rho \varepsilon}$$

The expression of gauge factor above includes effects from two sources. The first term on the right directly represents the Poisson effect, i.e., the tendency in an elastic material to contract laterally in response to axial stretching. The second term represents the contribution due to changes in resistivity of the material in response to applied strain. In the absence of a direct resistivity change, then, the maximum and minimum values expected for the Gage Factor would be:

Equation 3.9

$$1 \ll GF \ll 2$$

Standard values related to strain gauge:

- Base resistance like 120 Ω , 350 Ω , 500 Ω , 1000 Ω are available.
- Gauge length ranges from [0.2-100 mm] for different cases.
- Gauge factor that is supplied by most manufacturers is usually 2 as earlier indicated.

For the sensor that was adopted in this study, the strain arrangement used is presented in Figure 3.11, in which the output is a linear function of strain. The half bridge was preferred to the quarter bridge, as automatic temperature compensation was ensured by using two gauges having well-matched temperature/ resistance characteristics. The full bridge would have been a better alternative to the half bridge arrangement as far as the sensitivity of the device is concerned but owing to the fact that the elastic beam used was not very wide (0.0135 m), it would not have been

practical to install and wire two gauges on the same side of the beam. Hence the half bridge arrangement as preferred and chosen.

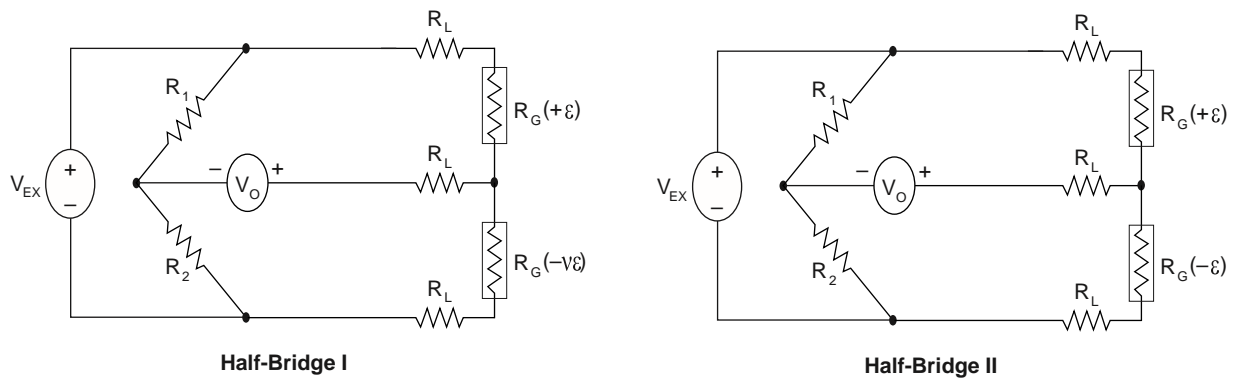


Figure 3.11: Half bridge setup

Equation 3.10

$$strain (\epsilon) = \frac{-4v_f}{GF[(1+v)-2v_f(v-1)]} * \left(1 + \frac{R_L}{R_G}\right)$$

$$strain (\epsilon) = \frac{-2v_f}{GF} * \left(1 + \frac{R_L}{R_G}\right)$$

3.12 INSTRUMENTATION AND DATA COLLECTION

3.12.1 Electronics part

From the diagram shown in **Figure 3.12**, the electronics part of the self-force sensor tool holder is divided into two sections which are electronics hardware and software. The electronics hardware comprises of Arduino microcontroller board called ATmega32U4, HX711 load cell Amplifier and Software part is the IDE Arduino software.

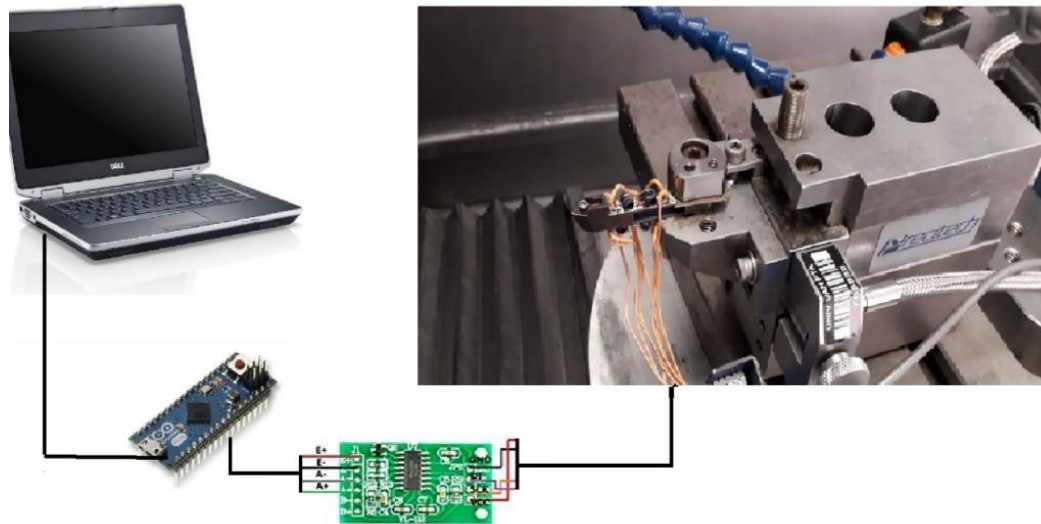


Figure 3.12: Schematic diagram of self-force sensor tool holder

3.12.2 Electronics hardware

3.12.2.1 *Arduino Micro atmega32u4*

The Arduino Micro is an ATmega32u4 (datasheet) based microcontroller module, built in partnership with Adafruit. It has 20 digital input/output pins, a 16 MHz crystal oscillator, a micro-USB link, an ICSP header and a reset button (of which 7 can be used as PWM outputs and 12 as analog inputs). It includes everything necessary to support the microcontroller; to get started, it can easily be connected to a computer with a micro-USB cable. It has a shape factor that allows it to be put easily on a breadboard. The Micro is like the Arduino Leonardo in that USB connectivity is built-in to the ATmega32u4, removing the need for a secondary processor. This enables the Micro, in addition to a virtual (CDC) serial/COM port, to appear to a connected device as shown in **Figure 3.12** above to provide a mouse and keyboard. It also has other consequences for the board's behaviour; it can be operated by a micro-USB or an external power supply link. The source of power is automatically chosen.

The Micro PCB's maximum length and width are 4.8cm and 1.77cm respectively, see **Figure 3.13**, with the USB connector extending beyond the previous dimension. The layout enables simple positioning on a solderless breadboard as well. A0-A5, A6 - A11 Analog Inputs: (on digital pins 4, 6, 8, 9, 10, and 12). The Micro has a total of 12 analog inputs see **Table 3.3**, pins from A0 to A5 are numbered directly on the pins and pins 4, 6, 8, 9, 10 and 12 are shared on digital pins 4, 6, 8, 9, 10 and 12 respectively on the

other pins that you can access in code using the constants from A6 to A11. All of which can be used as digital I/O as well. Each analog input provides a resolution of 10 bits (i.e., 1024 different values). The researchers used pins A5, A4, GND and 5V for this research work.

Table 3.3: Arduino Micro atmega32u4 Features

Operating Voltage	5V
Input Voltage (recommended)	7-12 V
Input Voltage (limits)	6-20 V
Digital I/O Pins	20
PWM Channels	7
Analog Input Channels	12
DC Current per I/O Pin	40 Ma
DC Current for 3.3V Pin	50 Ma
Flash Memory	32 KB (ATmega32u4)
SRAM	2.5 KB (ATmega32u4)
EEPROM	1 KB (ATmega32u4)
Clock Speed	16 MHz

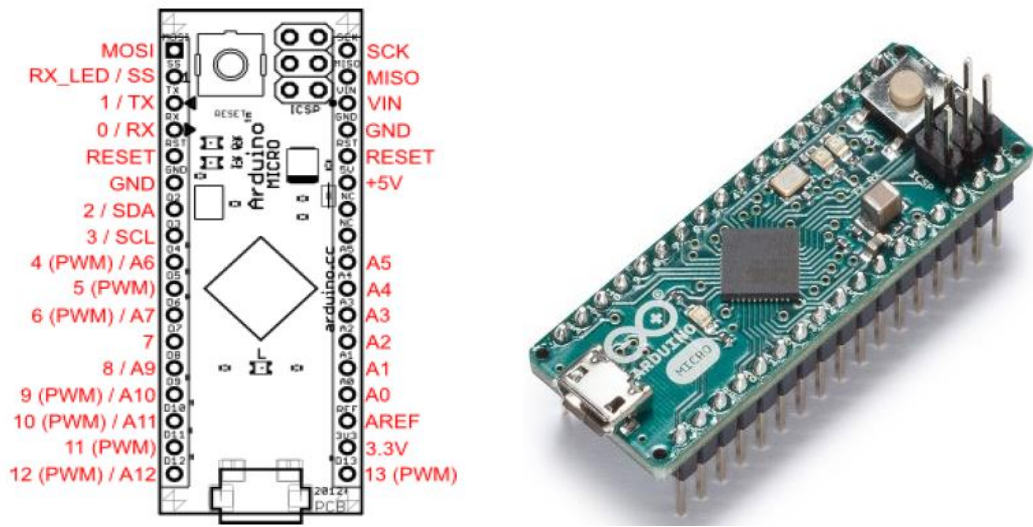


Figure 3.13: (A) Pin mapping of the Arduino Micro displays (B) Arduino Micro Front side

3.12.2.2 HX711 Load cell amplifier

The HX711 Load Cell Amplifier is a precise 24-bit analog to digital converter (ADC) designed to interface directly with a bridge sensor for weighing scales and industrial control applications. When low force (1N) is applied to the tool tip of a self-sensor tool holder during the ultra-precision machining process, it will experience a resistance shift that can be reported as a low electrical voltage. It requires amplification of this low voltage. The concept of using the HX711 Load Cell Amplifier is therefore considered to be valid in this research work. The input multiplexer chooses the differential input of either Channel A or B to the programmable low-noise gain amplifier (PGA). Channel A can be programmed with a gain of 128 or 64, corresponding to a full-scale differential input voltage of ± 20 mV or ± 40 mV, respectively, when an AVDD analog power supply pin is connected to the 5 V supply. A fixed gain of 32 is available for Channel B. The on-chip power supply regulator removes the need for an external power supply regulator to supply the ADC and sensor with analog power. The input of the clock is adjustable. It may be from an external source of the clock, a crystal, or an oscillator on the chip that does not need an external component. On-chip power on reset circuits simplifies initialization of the digital interface. For the internal registers, no programming is required. All the control of the HX711 is through the pins.

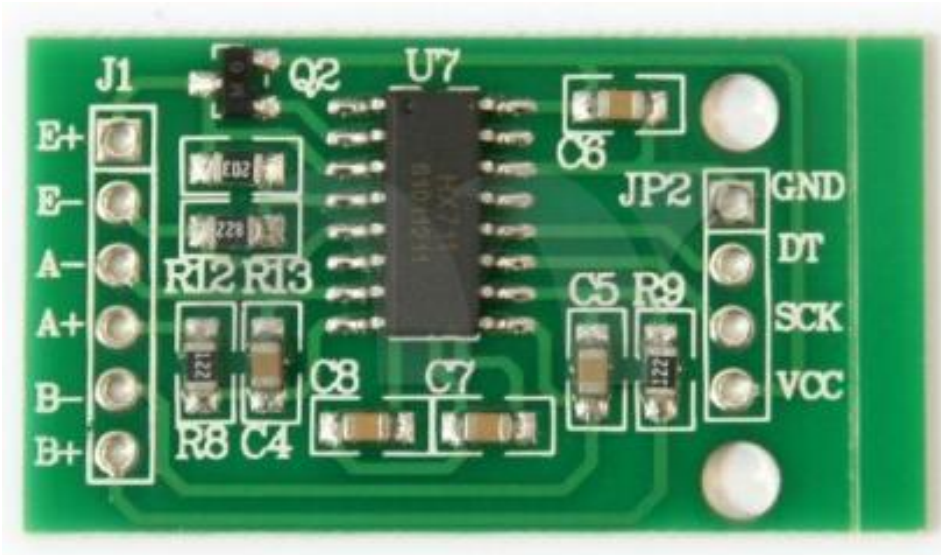


Figure 3.13: HX711 load cell amplifier module

3.12.3 Software

An Arduino Integrated Development Environment (IDE) is an official software introduced by Arduino.cc that is used to write, edit, compile and upload Arduino sketches to the Arduino boards. A Sketch is the main code created on the IDE platform that ultimately generate a Hex File which is then transferred and uploaded in the controller on the board such as Arduino Micro. The IDE environment contains two basic parts which are the Editor and Compiler. Editor is used for writing the required code and compiler is used for compiling and uploading the code into the given Arduino Module. This environment supports both C and C++ languages.

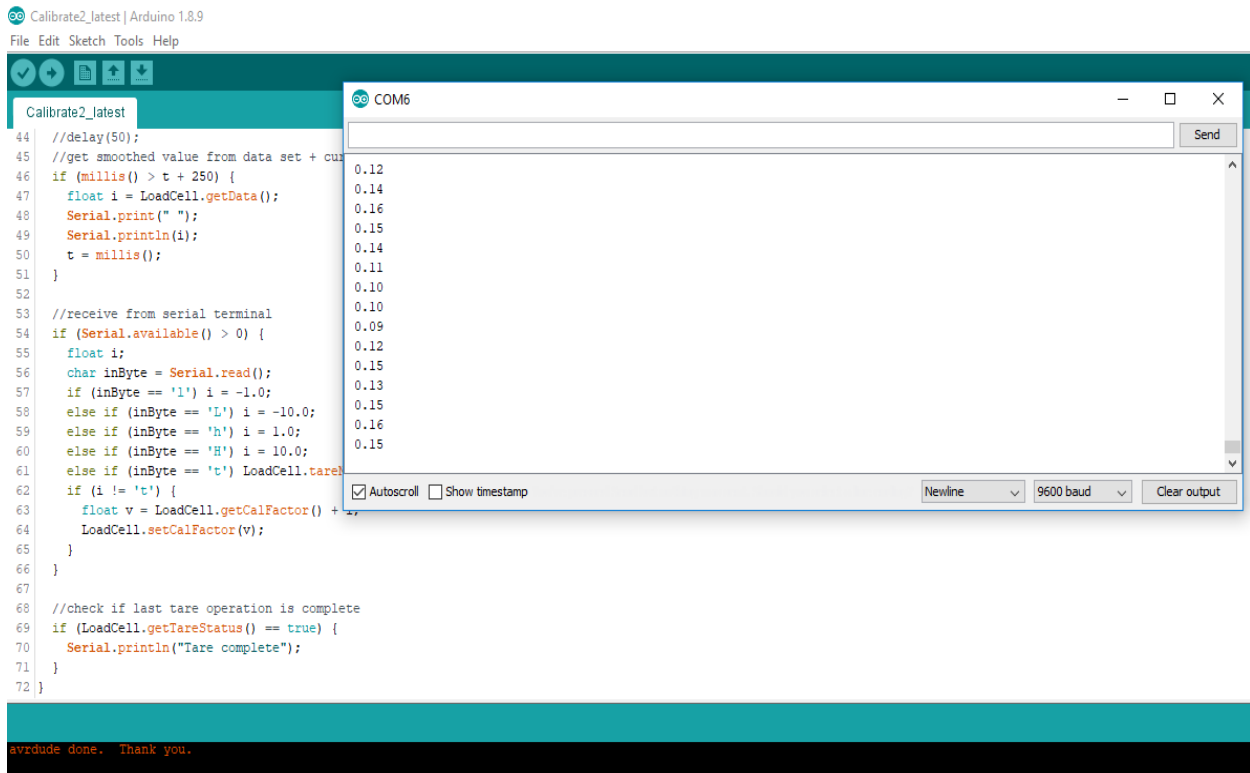


Figure 3.14: Arduino IDE screen shot during data acquisition

3.13 SELF-SENSING CUTTING FORCE TOOL HOLDER (SSCFTH) STRAIN GAUGE INSTALLATION

3.13.1 Procedures for strain gauge preparation and installation

The method and procedure applied in order to install strain gauge to the surface of the tool holder is explained step by step below.

- Degrease the surface of the titanium tool holder by subjecting it to heating process up to 120⁰. Clean the surfaces of the metal (Titanium). I mean the surface areas where the strain gauge will be positioned.
- Some suggestions on how to clean the surface. This is to be done by sandpaper with a fine coarse grit sandpaper, rinse the surface with a degreasing agent or rinse it with a neutralizer afterwards.
- Wipe the surface clean with gauze (gauze is a lint-free fabric).
- Heat the surface slightly to dry up the subsurface. This allows the glue to attach and bond with gauges adequately.
- To glue the strain gauge to the surface, the following steps are to be followed:

- Select the type of glue to be used (glue used in this research is M-Bond 200 from Micro Measurement. This is a cold curing type of adhesive).
 - Clean the surface with a wiper clothing until you hear a slicking clung sound.
 - Put the strain gauge face down on a piece of tape
 - If your bonding agent requires a catalyst, brush it on the exposed side of the strain gauge
 - Apply a single drop of superglue/bonding agent (M-Bond 200) to the clean surface of the titanium metal
 - Tape the gauge to the titanium metal so that the superglue touches the gauge
 - Apply pressure with your finger for at least three minutes.
 - Peel the tape off after a while and allow for curing for 24 hours.

- To solder the wires to the terminals on the strain gauge. This can probably be the trickiest step because the strand of the T-Rosette could be confusing. Hence handle gently with care. Otherwise, if care is not taken, this causes the solder to cool too quickly and form a bead shape on the strain gauge leads rather than coating the surface. Just do the best you can.

Figure 3.16 shows the holder of the diamond turning tool which was created by fine tooling of the contour. The tool holder was made of Titanium alloy giving it a very high mechanical strength to withstand sudden impacts. The only expected downside, however, could be the deflection sensitivity, but as you can see a slot was added to the unit to improve and increase the deflection potential at the point where the strain gauge will be glued to the holder of the instrument. Otherwise, it could be difficult for strain gauges to feel compression and tensile tension during the cutting process. The installation table in **Figure 3.17** consists of some of the devices required for installation. **Figures 3.18 and 3.19** demonstrate the gluing of the strain gauge to the upper and lower beams of the tool holder.



Figure 3.15: Contour[®] Tool holder

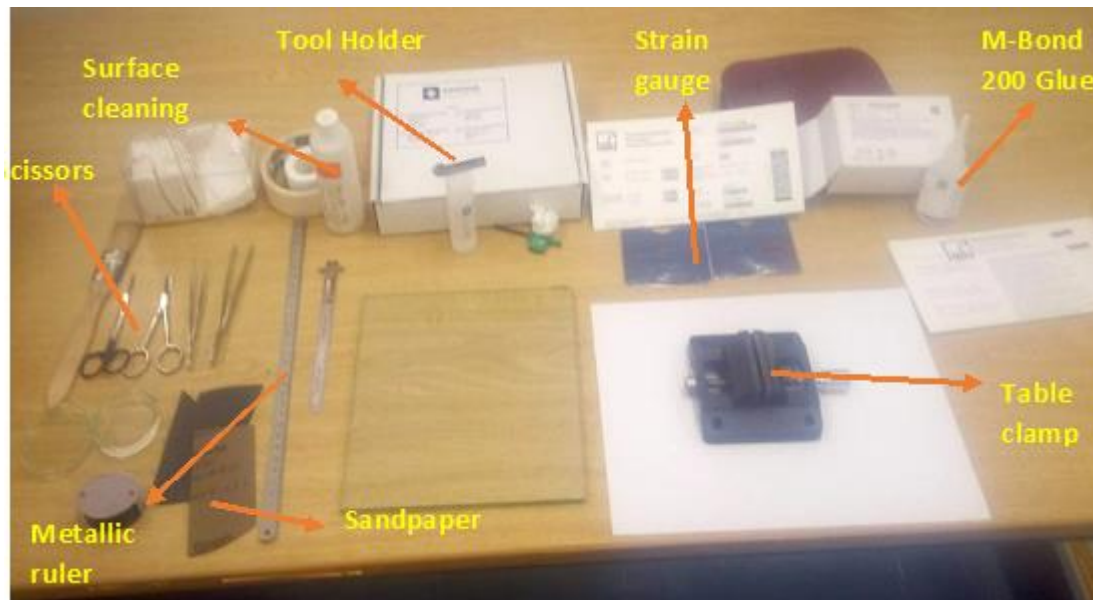


Figure 3.16: Installation set up table

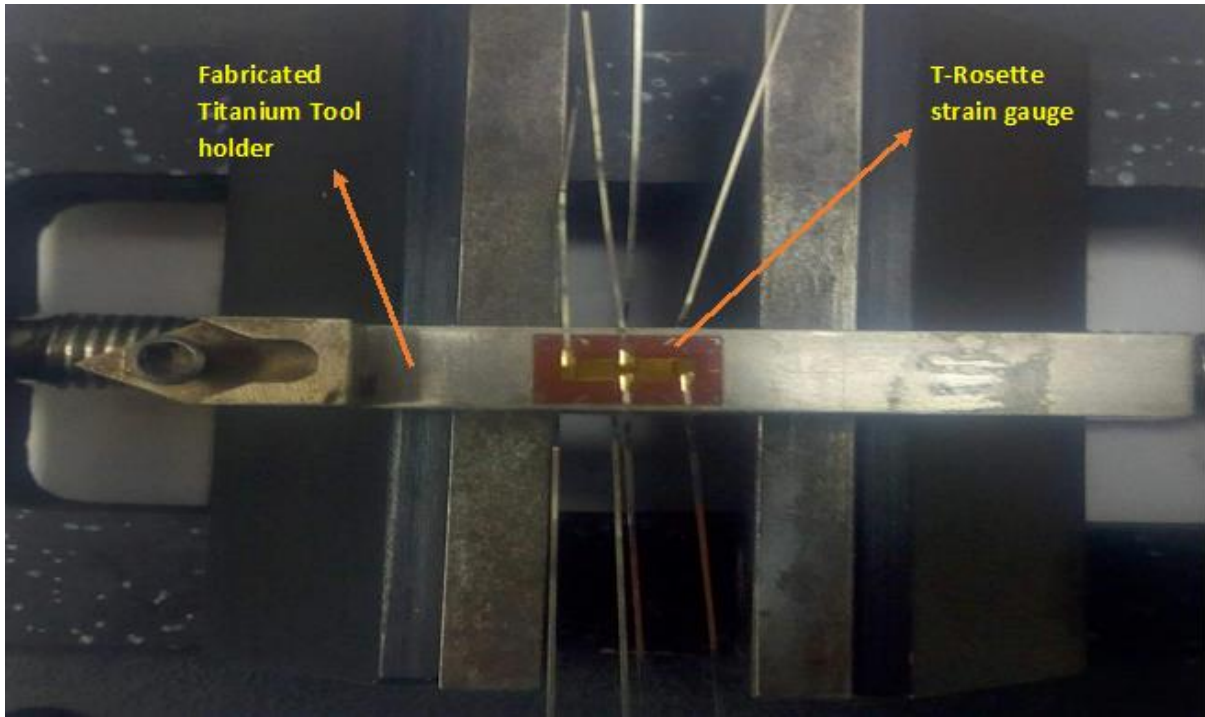


Figure 3.17: Top installation showing T-rosette (strain gauge) for tensile stress

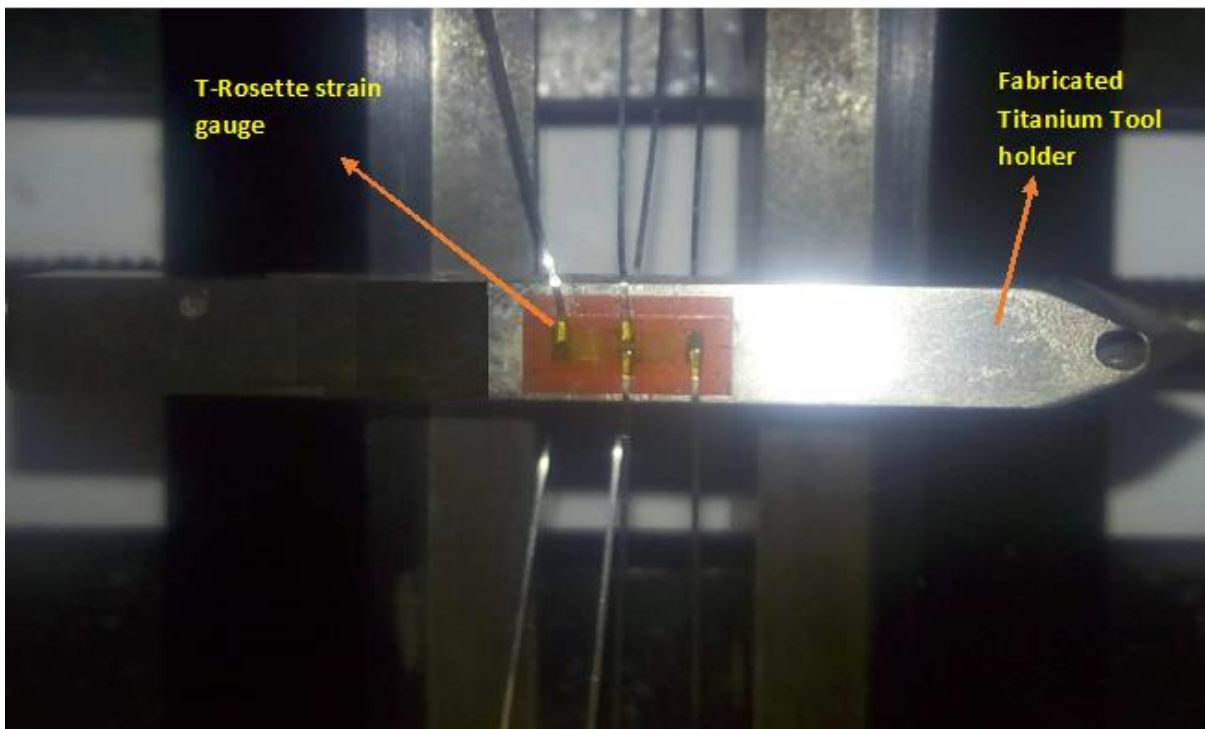


Figure 3.18: Bottom installation showing T-rosette (strain gauge) for compression stress

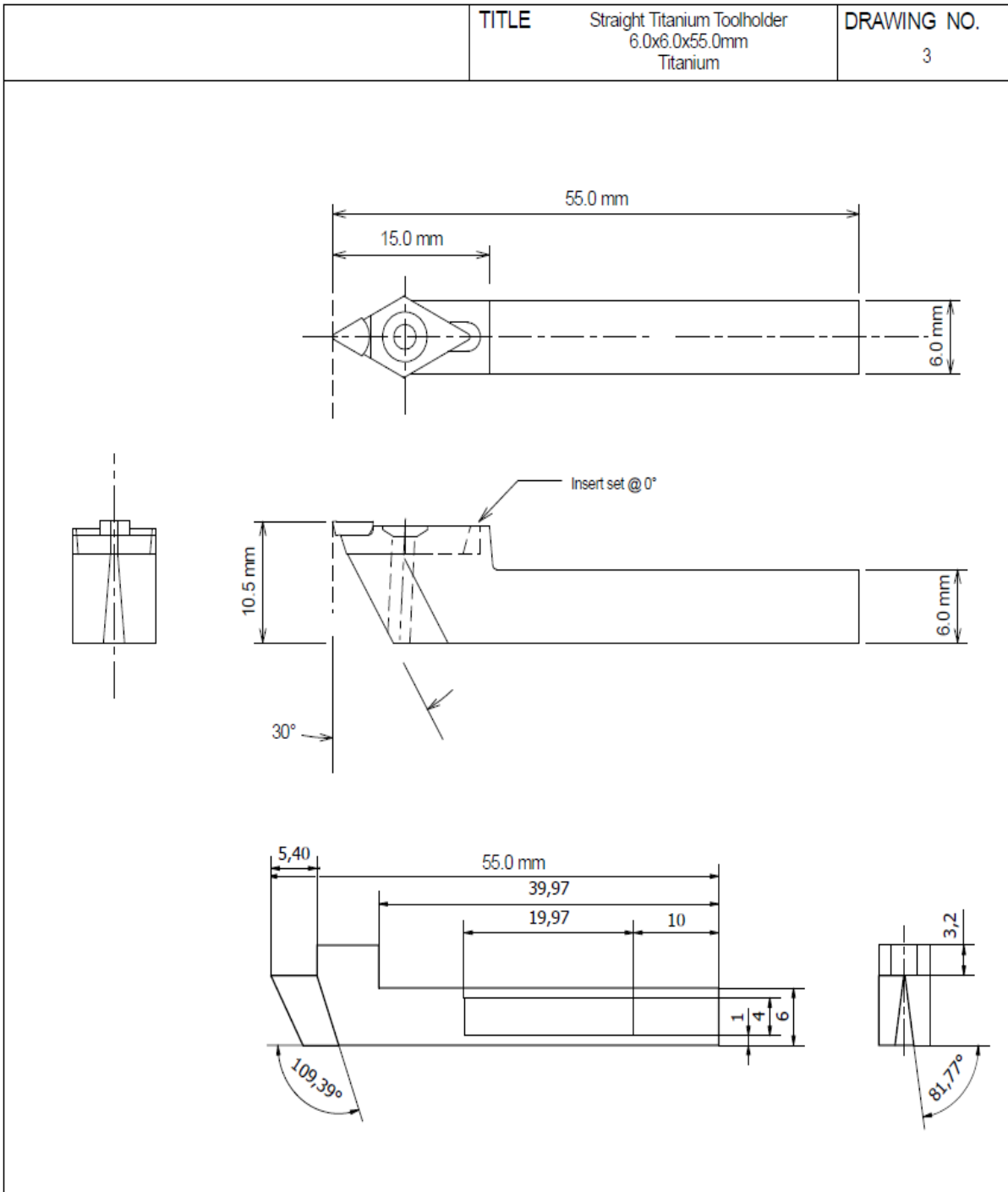


Figure 3.19: Design and dimensions for the tool holder

The material used for the cutting tool holder is a special titanium material with a very high tensile strength therefore, a possible low stiffness may occur. Due to this possibility, deflection on this material used for cantilever is worthwhile find out. The Moment of Inertial (MOI) of the structure designed can be calculated thus:

From Figure 3.20, Calculate moment of inertia:

Equation 3.11

$$MOI_{x1} = \frac{bh^3}{3} = 21223.125 \text{ mm}^4$$

$$MOI_{x2} = I'_{x2} + Ad_y^2 = 675.3 \text{ mm}^4$$

$$MOI_{x3} = \frac{bh^3}{12} + Ad_y^2 = 12251.25 \text{ mm}^4$$

$$MOI_{x4} = \frac{bh^3}{12} + Ad_y^2 = 826.7 \text{ mm}^4$$

$$I_{total} = 21223.125 - (675.3 + 12251.25 + 826.7) = 7469.88 \text{ mm}^4$$

Calculate maximum deflection (δ) of the tool holder at $L = 55 \text{ mm}$,

Equation 3.12

deflection (δ) at $L = 55 \text{ mm}$,

$$\delta_{max} = \frac{PL^3}{3EI} = 0.00009 \text{ mm}$$

Where $I = 7469.88 \text{ mm}^4$, $W = 1\text{N}$, $L = 55 \text{ mm}$, $E = 120 \times 10^9$, $h = 6 \text{ mm}$.

But the deflection at $L = 27 \text{ mm}$, from the centre of the sensor as seen in **Figure 3.22**.

$$\delta = 0.0000371 \text{ mm}$$

This shows that when a load of 1g which is approximately 1N is applied, a deflection of about 37.1 μm probably from tension is experienced by the tool holder which can also be sensed by stain gauge (sensor). It should be noted that a weight of 5N is designed for in this study because most times cutting force in diamond turning or Ultra-precision machining is often less 3N [323, 353, 365, 366].

Therefore, the strain (ϵ) is,

Equation 3.13

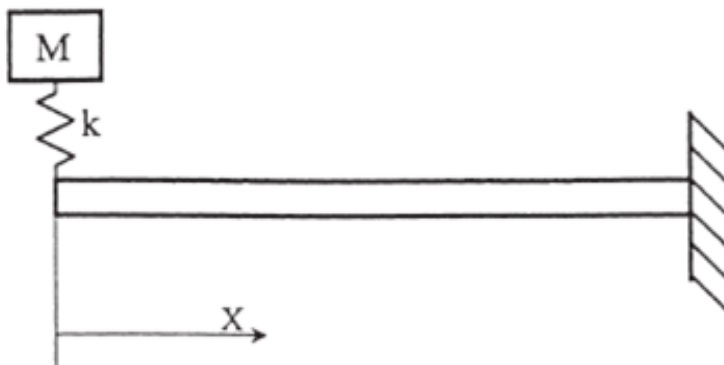
$$\varepsilon = \frac{MC}{EI} = \frac{WL \left(\frac{h}{2}\right)}{EI}$$

3.14 DYNAMIC PROPERTIES OF THE SENSOR

Any mechanical device capable of measuring force can be called a dynamometer. The vibration frequency of the machine tool on which the self-sensor cutting force is placed for the monitoring of the cutting force must be consistent with the natural set-up frequency. The normal frequency of a standard dynamometer should be as high as possible, according to literature [367]. The frequency of vibration of the machine tool is close to the speed of spindle of the machine tool. The holder of a self-sensor cutting tool representing a dynamometer should have a natural frequency at least four times greater than the vibration frequency of the machine tool [304, 320, 355, 367, 368]. The machine tool's vibration frequency is obtained from the relation:

Equation 3.14

$$f_m = \frac{n}{60} \frac{rev}{s}$$



Where M = mass, K = stiffness and X = length.

Figure 3.20: Structural diagram of the developed self-force sensor tool holder

If the maximum spindle speed of the machine for the experiment is 3000 rpm, then frequency of the machine tool (F_m) is 50 Hz. Therefore, the natural frequency of the tool holder sensor should be:

Equation 3.15

$$f_n \geq 4 \times \frac{n}{60} \frac{rev}{s}$$

$$f_n = \frac{1}{2\lambda} \sqrt{\frac{K}{M_t}}$$

$$k = \frac{3EI}{L^3}$$

$$M = \rho bdl$$

Where F_m is frequency of machine tool, n is spindle speed (rpm), F_n is the natural frequency of the tool holder, K is the stiffness, M is the total mass of the tool holder and strain gauges. From the design, $I = 5942.125$, $E = 120$ GPa, Density (ρ) of the tool holder material (Titanium) = 4420 kg/m³, area (A_0) of the tool holder designed ($b \times d \times L$) = 1350 mm². So, to fulfil the requirement as stated above in equation (1), if the frequency of the machine tool is 50 Hz, and the computed natural frequency of the tool holder is 807.5 Hz based on the relations in **Equations 3.15**, hence $F_n \geq 4F_m$.

3.15 CALIBRATION

3.15.1 Mechanical calibration of the load cell

The strain gauge used in this research is T- Rosette of metallic foil shown **Figure 3.9** above can be seen attached in **Figure 3.21**.

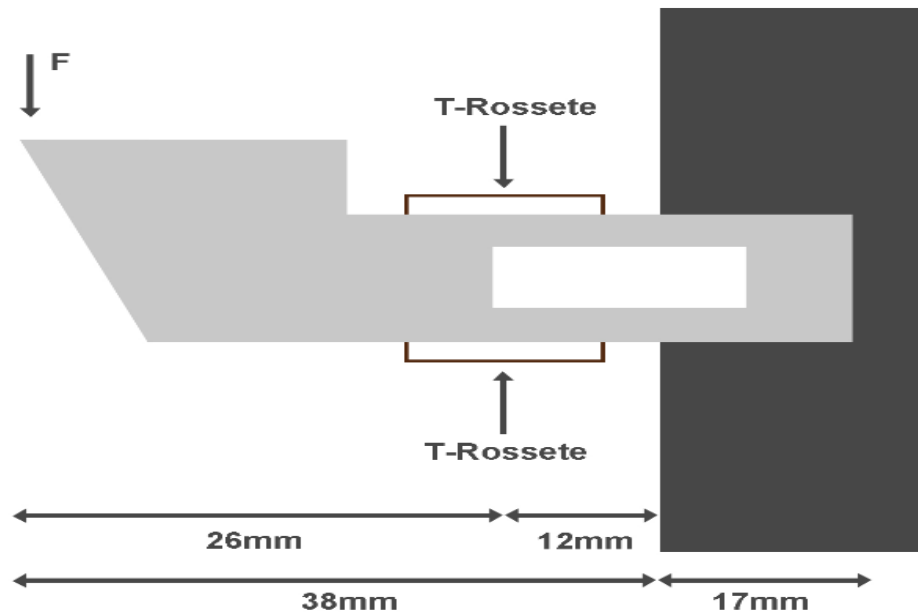


Figure 3.21: Schematic design application

Based on this design, As stated previously that the maximum deflection the designed tool holder can have is $\delta_{\max} = 3.71 \times 10^{-5}$ mm. However, it is advisable to position the strain gauge at the region where maximum stress is observed on the material because the plastic deformation activities due to loading (stress) can be sensed at this point. Based on the design above, if the strain gauges are placed at the high zones of stress (**Figures 3.7 – 3.8**) as depicted from FEA simulation analysis for sensitive to plastic deformation. Then, the deflection δ , will shift to where F is and becomes 0.153×10^{-4} mm and moment of inertial of the tool holder (I) remain as 5942.125 mm^4 .

Next, the author discusses the linear relationship of how the Arduino analog converter can be used to calibrate the load cell if other means cannot be dimmed. In most cases calibration of measuring instruments can be attained by comparing measurement results to a measurement standard. As shown in **Figure 3.22**, two T-rossettes were attached to the design representing four strain gauges on the cantilever beam. With relatively know resistance also with some normal possible uncertainty. Considering linear relationship on how to calibrate load cell, when a load M is applied to the beam causing the resistance to change. This causes the excitation V_e in **Figure 3.22**, to change. However, the measured V_m will be very small. Therefore, an amplifier HX711 is required to improve the voltage measured, V_m by increasing its magnitude to produce an output voltage V_a which goes to Arduino in figure (iv):

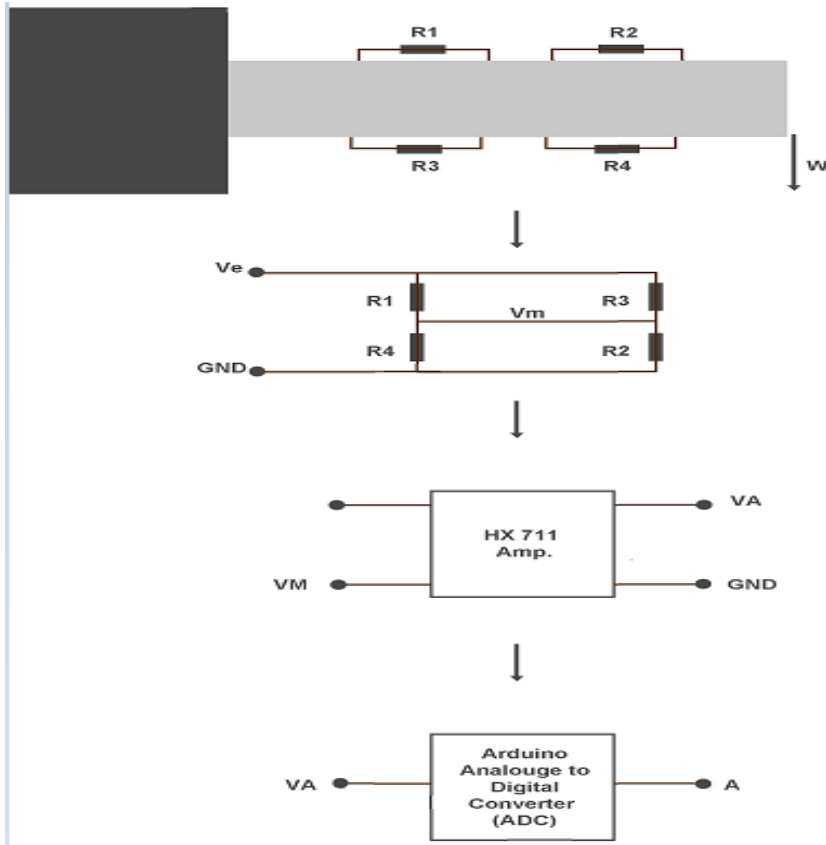


Figure 3.22: Schematic linear relationship for calibration

Where $R_1, R_2, R_3,$ and R_4 = Resistance, G_i = length of the beam (constant), V_e = Excitation voltage, V_a = output voltage, V_0 = at no load voltage, A = analogue read value, change in Resistance when load applied (R), R_i = resistance when load is applied, V_m = measured voltage, and W = weight.

Considering resistors R_1, R_2, R_3, R_4

Equation 3.16

$$A_{ri} = G_i M$$

$$V_m = V_0 + AV$$

$$AV = AV(A_{ri}, R_i, V_e)$$

Therefore,

$$V_a = P + GV_m$$

$$A = A(V_a, V)$$

This makes our design a little bit difficult. But looking at the linear process, it can be reversed if we go from analogue value (A), back to the Mass (M) applied to our beam in the system.

Electronic calibration can be obtained thus,

Equation 3.17

$$A_0 = A(M = 0)$$

$$A_{ref} = A(M = M_{ref})$$

$$M = \frac{(A - A_0)}{(A_{ref} - A_0)} * M_{ref}$$

M can also be determined using simple linear equation:

Equation 3.18

$$y = mx + b$$

$$m = \frac{(y - b)}{x}$$

This is m that represent our slope in **Figure 3.28**.

3.15.2 Voltage calibration

T Rosette Parameters

- Excitation voltage of the load cell (T-Rosette) = 4.5 V
- Resistance of the strain gauge (T-Rosette) = 350 Ω
- Gauge factor also known as strain gauge sensitivity = 1.95
- Rated output = 1 Mv/v
- Rated capacity designed = 300 g = 2.94 N
- So, if rated output is 1 Mv/v with known excitation of 4.5 V,
- Load cell output

Equation 3.19

$$\text{load cell output} = \frac{1Mv}{v} \times 4.5V = 4.5MV$$

To display for minimum of 1g,

$$1g = \frac{4.5Mv}{0.1 \times 9.81}$$

4.592 mv/N or 0.004592 v/N

This represents the sensitivity of the self-sensing cutting force tool holder (SSCFTH) designed. However, since data acquisition approach is implemented in the research, a multiplier is required for our serial monitor during machining. Hence, **Equation 3.17** applies.

3.16 CALIBRATION RESULTS OF SELF-SENSING CUTTING FORCE TOOL HOLDER

After the installation and mounting of the SSCFTH design, various known weights (**Figure 3.23**) were used to calibrate the multiplier factor of the voltage output. **Table 3.4** shows the weights and the voltage outputs. During calibration, sensors are subjected to known quantities (**Figure 3.24 - 25**) of physical measurand such as force and the corresponding values of the output variable are recorded. The magnitude of this load is accurately known, as it is measured with a traceably calibrated against factory standard (Kistler force sensor) at the same time. Depending on the method, sensors are calibrated either across the entire measuring range or in a partial range: at a single point, continuously, or stepwise at several different points. The method adopted in this study is continuous although certain literature prefers step by step method. During continuous calibration, the load is continuously increased to a certain level within a defined capacity of the strain gauge and then reduced to zero within the same time. A best straight line passing through the origin is defined for the resultant characteristic. It should be noted that it is never always easy to get a perfect straight or exactly linear line. The gradient of this line corresponds to the sensitivity of the sensor within the calibrated measured range. A 99.6% accuracy was achieved for this study.

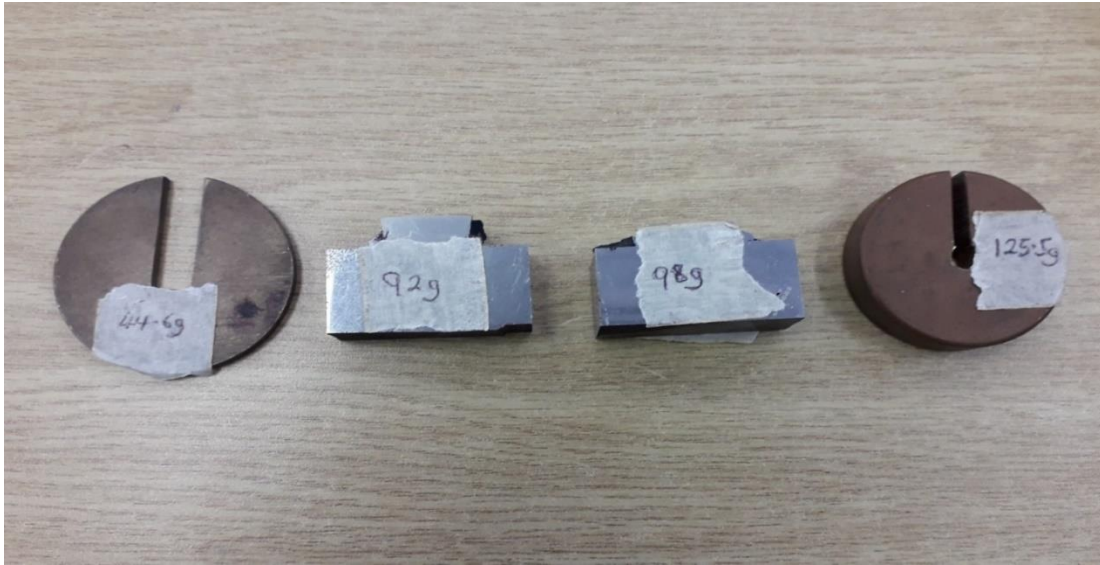


Figure 3.23: Load samples for calibration

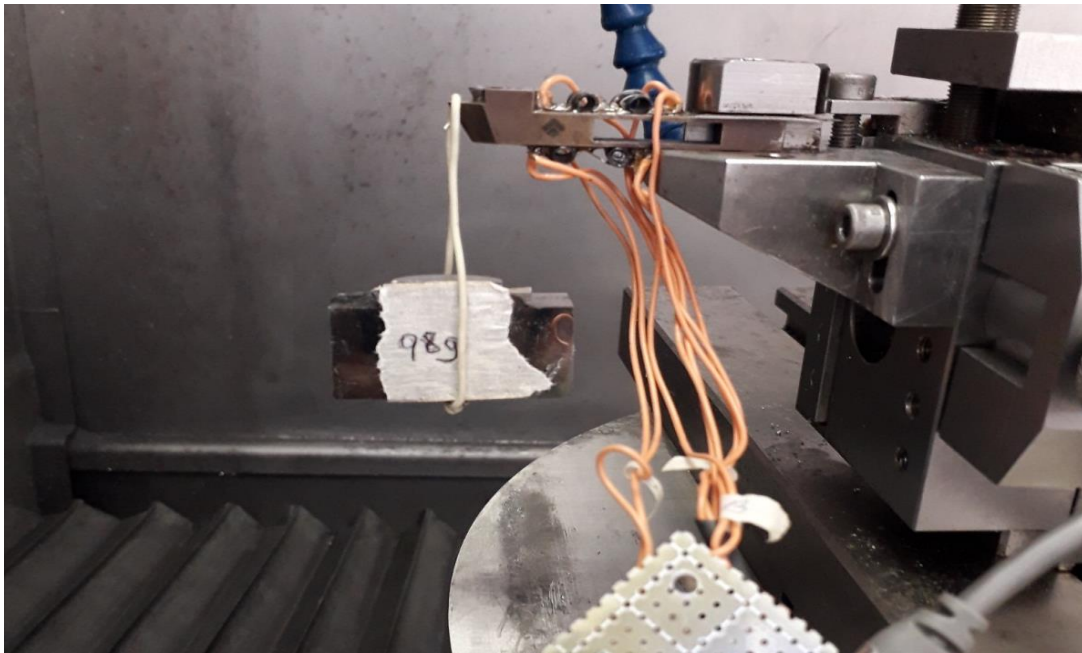


Figure 3.24: Calibration with 98g

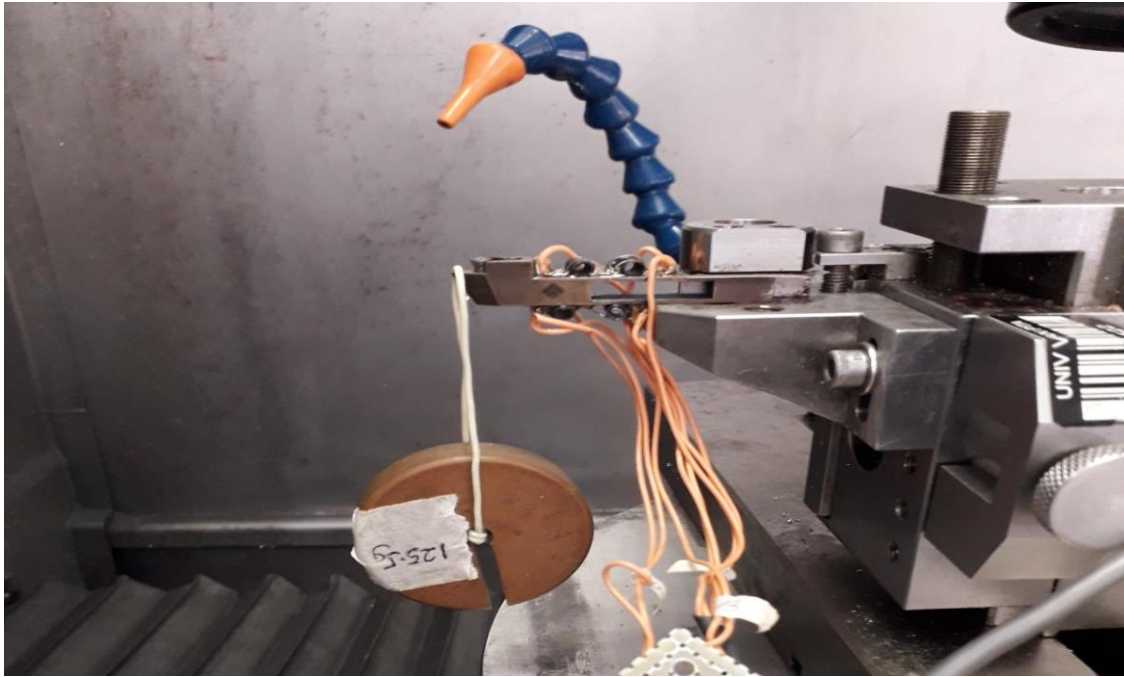


Figure 3.25: Calibration with 125.5g



Figure 3.26: P3 static strain indicator

Table 3.4: Weight results during static calibration

Known weight (g)	Known Weight (N)	Voltage output (mv/V)
0	0.000	0.00
44.6	0.438	0.61
92	0.903	1.22
98	0.961	1.41
125.5	1.231	1.76

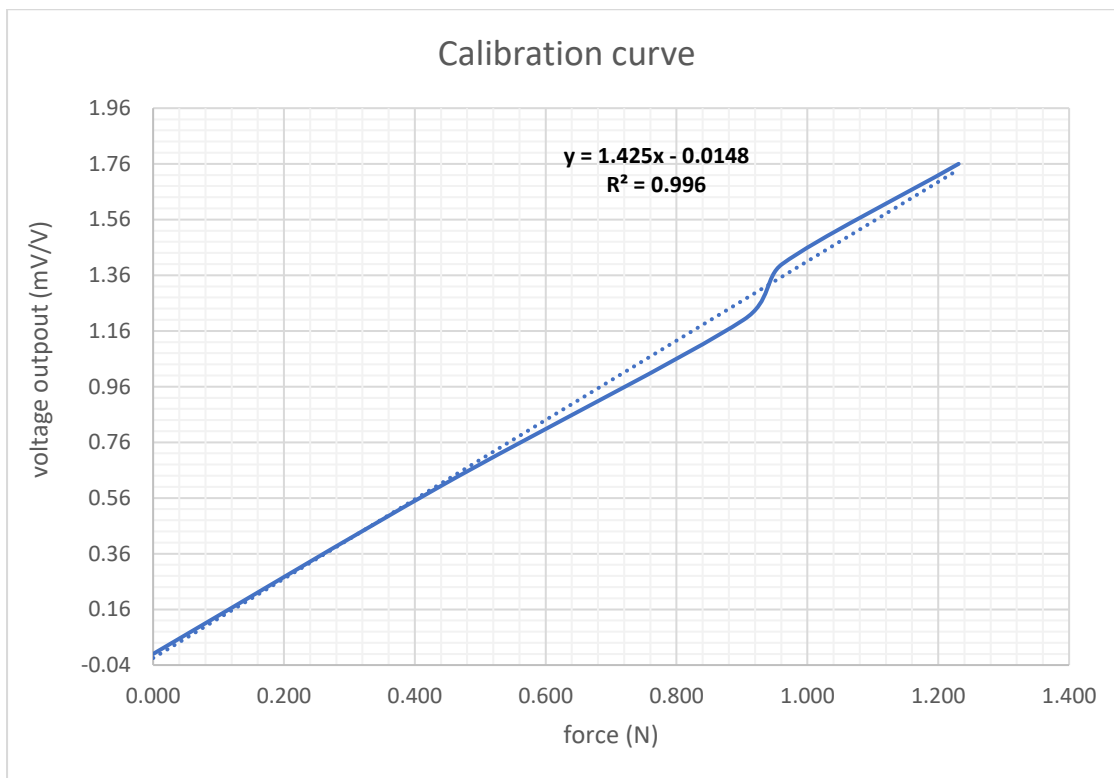


Figure 3.27: Sensor sensitivity curve

CHAPTER 4

METHODOLOGY, MATERIALS AND EXPERIMENTAL SETUP FOR ULTRA PRECISION MACHINING

4.1 INTRODUCTION

The goal of this section is to set up a machining system that will attain a surface finish at nano level since the removal actions of machining process is around this neighbourhood or less than 10 nm; thus, this chapter introduces and explains all the components, the set up and procedures that are involved in ultra-precision machining of optical aluminium alloys, errors in data acquisition may pose a challenge when all the set up and machining procedures are not properly followed.

4.2 DESCRIPTION OF THE EXPERIMENT

The research experiments were carried out in such a way that the Ultra-precision machine called Precitech Nanoform 250 Ultra grind lathe machine was used to machine three different cylindrical optical aluminium alloys RSA 905, 443, and 6061. National Instruments PXIe-1071 chassis was used as data acquisition system, LabVIEW was used as acquisition programme. Acoustic emission sensor system was attached to the tool holder table to monitor acoustic emission activities during machining. Furthermore, force, a very important parameter is to be monitored during machining, force sensor system was also attached to the tool holder to capture and monitor cutting force activities. Taylorsurf surface roughness measuring equipment a Taylor Hobson instrument was used to measure the surface roughness at the end of each experimental run. Finally, the author will briefly explain the method used for the evaluation of diamond turning of optical aluminium alloys, i.e., statistical modelling method using response surface methodology (RSM) based on Box-Behnken design approach.

4.3 MACHINE TOOL AND MACHINE SET UP

The experiments were performed on Precitech Nanoform[®] 250 Ultra grind machine (see **Figure 4.1**) is a flood coolant compatible. This machine was set up in such a way that acoustic emission sensor was attached to the tool holder table which was

connected to NI PXI - 1071 and a force sensor was also attached to the tool holder table to monitor the machining process (see **Figure 4.2**). Spindle was balanced at 1000 rpm and feed of 500 mm/min in clockwise direction to reach a spindle error cancelled out of -0.701 μm high -0.710 μm low and 0.009 μm P-V. This balancing was carried out using Precitech DIFFSYS monitoring platform (see **Figure 4.3**) to certify the vacuum chuck was well fixed and positioned to avoid any unexpected oscillation forms on the surface of the workpiece which would worsen the surface roughness of the workpiece and to guarantee contact all through wheel tip and workpiece surface. **Figures 4.4 and 4.5** are necessary for tool alignment and optical tool setter for adjustment of tool.

4.3.1 Precitech Nano 250 has the following main features:

- Axes in X, Y, Z for diamond turning and B direction for grinding
- Surface roughness of 1nm accuracy
- SP-150 up to 700 rpm of spindle speed
- It has Turning and grinding capabilities
- swing capacity between 440/220 mm over option B -axis
- slide travel up to 220 mm
- Max Feed rate up to 4000 mm/min
- Operating system that is up to 0.001 mm nanometre programming resolution.
- Diamond turning form accuracy that less than 0.15-micron ($\lambda/4$) PV
- Air bearing HS-75 work spindle



Figure 4.1: Precitech nanoform 250 ultra-grind lathe machine

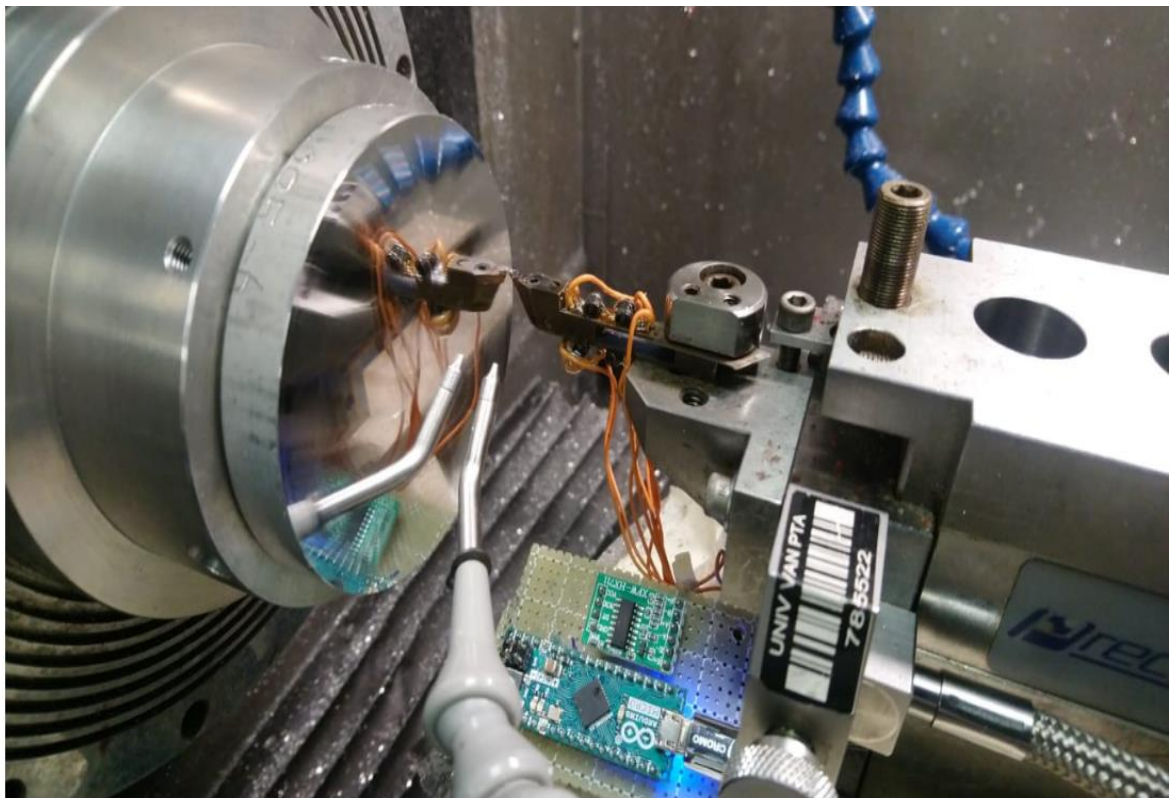


Figure 4.2: Set up for diamond turning of RSA alloys

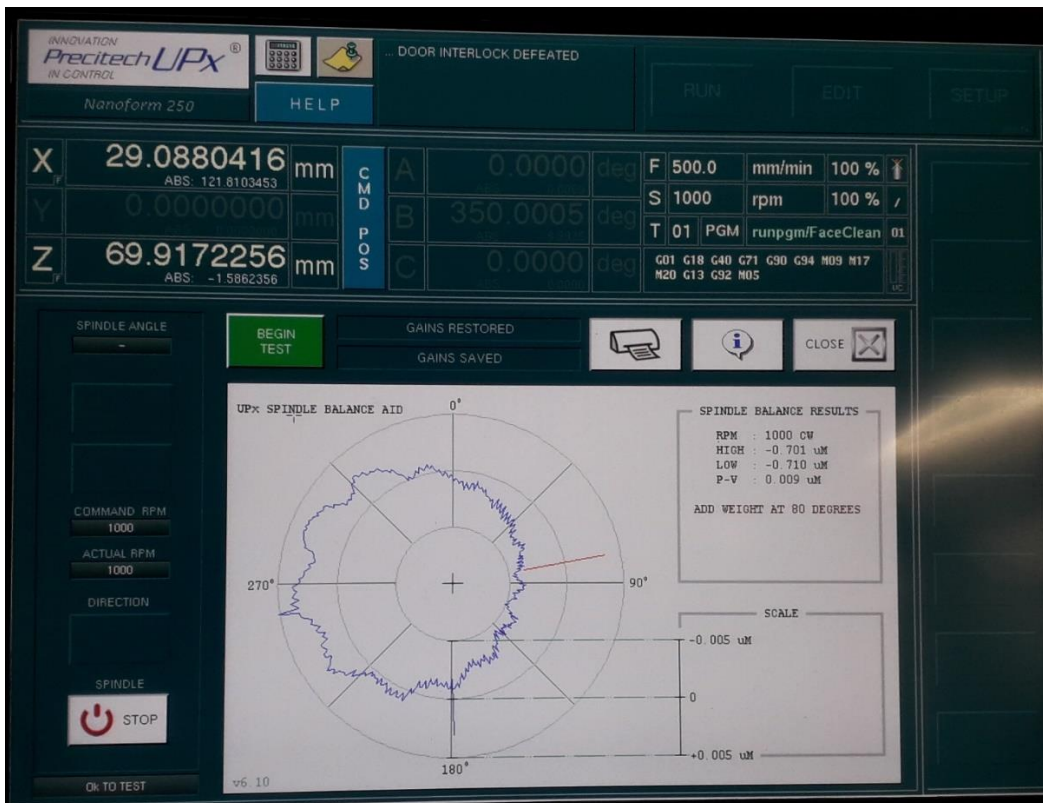


Figure 4.3: Spindle balancing and monitoring platform

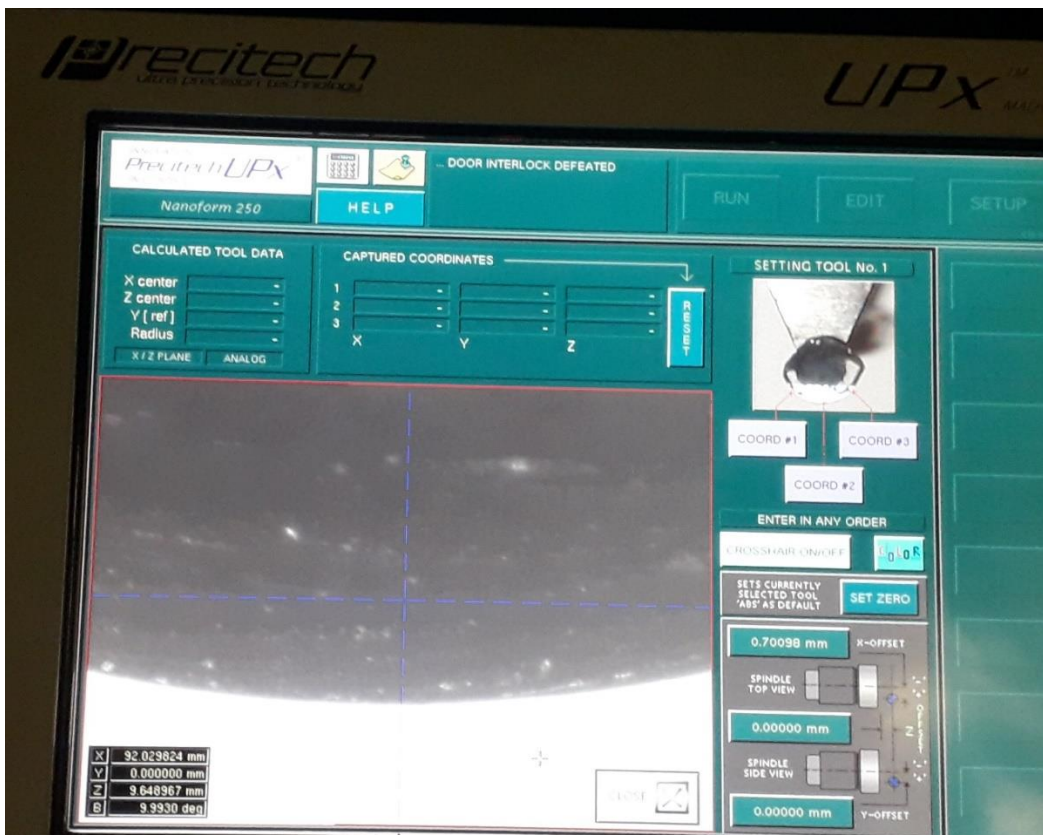


Figure 4.4: Cutting tool alignment display

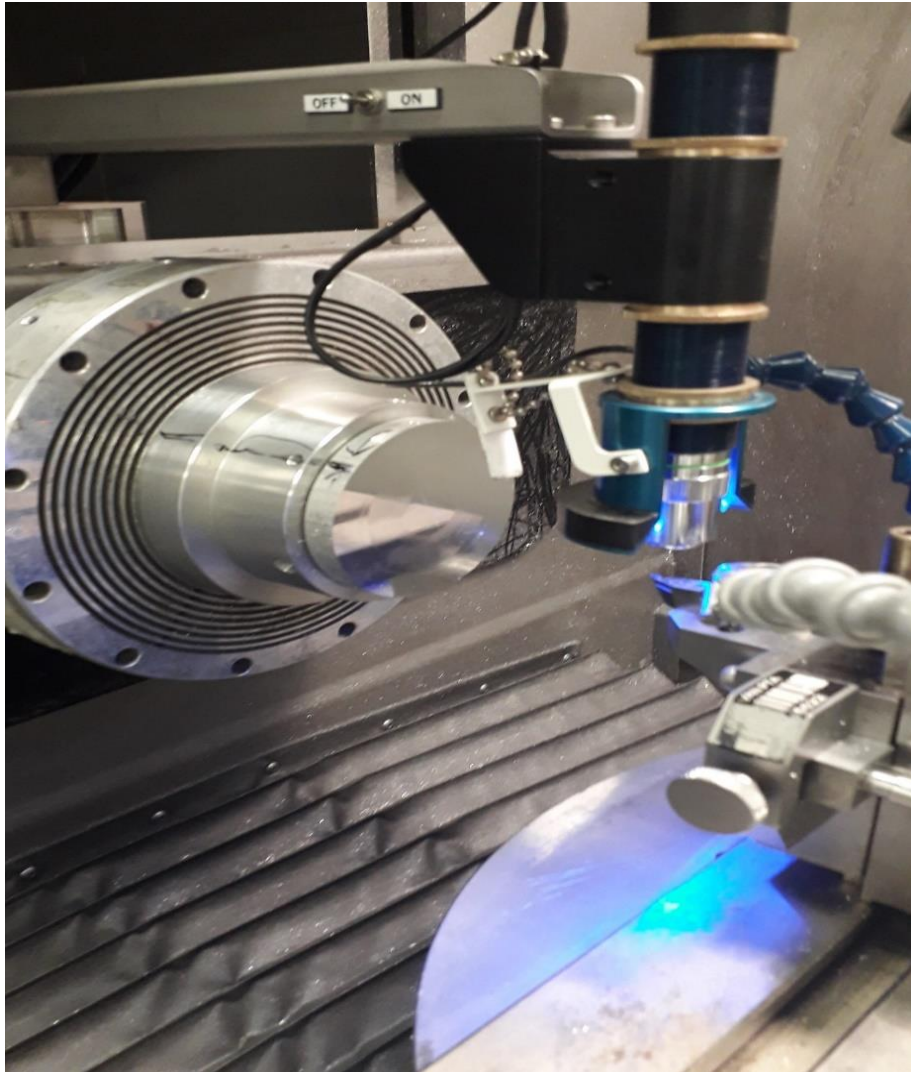


Figure 4.5: Optical tool setter for tool adjustment and alignment

4.3.2 Explanation of components set up

Step 1. An experimental pre-run tests were carried out at a feed rate of **6 mm/min** and workpiece spindle speed of 1000 rpm then the work spindle speed was reduced to 500 rpm. This was done to clean the surfaces of each of the three workpieces to achieve an evenly flat surface on the workpiece.

Step 2. Each workpiece was mounted on the chuck for SPDT one after the other during experimental machining.

Step 3: The program was loaded onto the single point diamond turning machine interface with the updated parameter values for speed, feed, and depth of cut.

Step 4: The LabVIEW program was initialized with continuous sample measurement and 10000 samples to read at a rate of 1000 kHz to adequately monitor and capture the acoustic emission data which was saved as a text file in Microsoft excel. During each cutting test, AE data were acquired using National Instruments PXIe-1071 data acquisition system (DAQ).

Step 5: Additional experimental passes were run to ensure repeatability. After each experiment, the workpiece was removed from the single point diamond turning machine and transferred to the Profilometer for surface profile measurements (Taylor Hopson PGI Dimension XL).

Step 6. All the forces and acoustic emissions data captured are further processed offline.

4.4 WORKPIECE MATERIALS

The workpiece materials used in this research work were RSA 6061, 905, and 443 produced by RSP Technology Ltd. RSA productions underwent the process called melt spinning solidification at a rate of $106\text{ }^{\circ}\text{K/s}$ in order to produce an ultra-fine microstructure composition that has optical capabilities. See **section 2.8** for full explanations on RSA. **The tables 4.1 and 4.2** show physical and chemical properties of the optical aluminium alloys while **Figures 4.6 - 4.8** show the diamond turned surfaces of RSA 6061, 905, and 443 respectively during machining.

Table 4.1: Physical properties of workpiece

Properties	RSA 6061	RSA 905	RSA 443
Density	2.70 g/cm ³	2.95 g/cm ³	2.54 g/cm ³
Thermal expansion	23. 4 x 10 ⁻⁶ /K	19 x 10 ⁻⁶ /K	13.6 x 10 ⁻⁶ /K
Thermal conductivity	160 W/m-K	100 W/m. K	135 W/m. K
Modulus of Elasticity	70 GPa	90 GPa	102.1 GPa
Ultimate tensile strength	330 MPa	600 MPa	240 MPa
Yield strength	300 MPa	475 MPa	150 MPa
Elongation	14%	7%	1.5%
Hardness	110 HB	180 HB	1110 HB
Workpiece Diameter	80 mm	60 mm	60 mm

Table 4.2: Chemical composition of the workpiece [369]

Alloys	% CHEMICAL COMPOSITION											
	Si	Fe	Cu	Mg	Zn	Cr	Mn	Ti	Ni	Mo	Zr	Al
RSA 905	-	2.5	2.5	0.6	-	-	1	0.6	5	0.8	0.8	86.2
RSA 6061	0.6	0.2	0.3	1	0.1	0.2	0.1	0.1	-	-	-	97.4
RSA 443	40	-	-	-	-	-	-	-	-	-	-	60

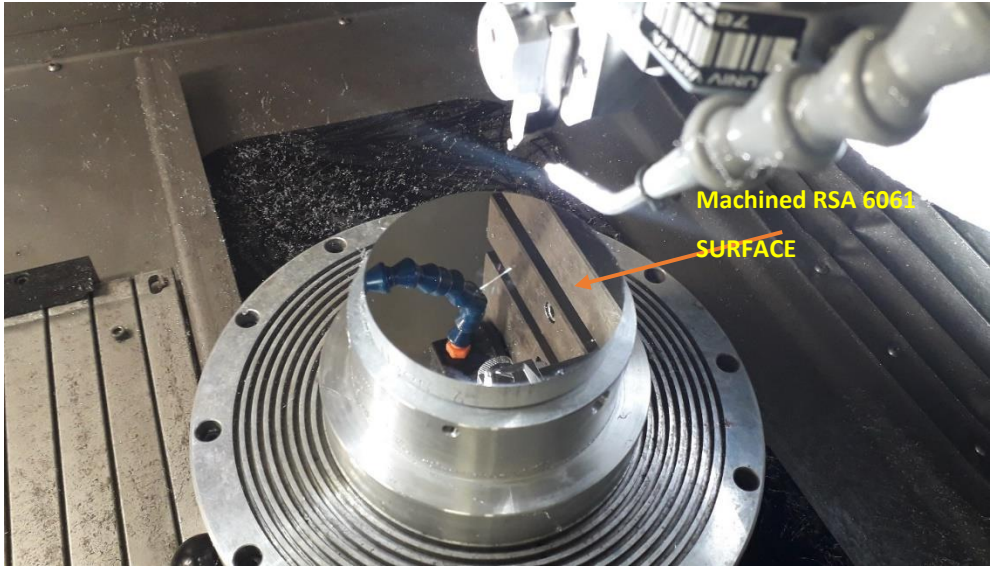


Figure 4.6: Surface of diamond turned RSA 6061



Figure 4.7: Surface of diamond turned RSA 905

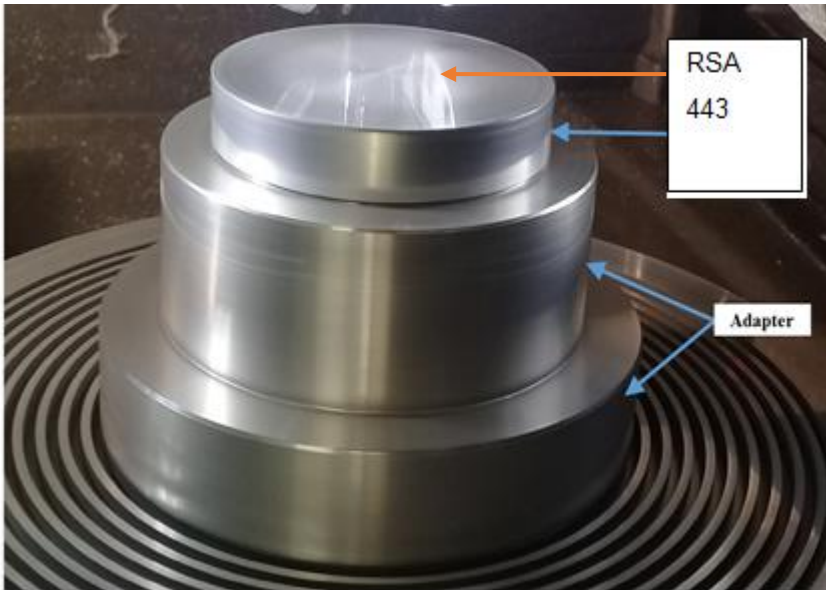


Figure 4.8: Surface of diamond turned RSA 443

4.5 DIAMOND TURNING CUTTING TOOL

The choice and selection of the geometry of the cutting tool is critical in SPDT as it impacts the overall surface finish. There are typically two kinds of diamond tools: mono-crystalline and poly-crystalline diamond tools. Mono-crystalline tools are favoured over poly-crystalline tools because they can be designed with sharper and more precise cutting-edge radii, according to Gubbels et al. This type of diamond tool can be manufactured with edge radii of approximately 20-75 nm, while poly-crystalline diamond tools consist of small grains with radii of approximately 2 μm . [370]. Due to high hardness, stiffness, thermal conductivity, honed sharp edge, and ability to hold on to the edge when cutting, single crystal natural diamond tool is usually the selected cutting tool. When working with aluminium, the tool also has low friction and relative inertness.

While diamond has its weaknesses affecting the surface finish and precision of machined components, the chemical reaction with elements such as carbon and iron, which has restricted it to non-ferrous alloys and cubic materials that are face centred. Another source of weakness is the breakout when machining at high temperatures, but this can be managed during turning by the appropriate selection of machining parameters such as feed, speed, and cut depth. For this experiment, a mono-crystalline diamond cutting tool manufactured by Contour Fine Tooling is used for the single-point turning of RSA-6061, 905, and 443. The selection of suitable tool

geometry used in this research was influenced by previous literatures, workpiece manufacturer's suggestions, past experiments on RSA alloys and experience to ensure that the turning parameters can be optimized. The monocrystalline diamond tool inserts (**Figure 4.9**) with properties shown in **Table 4.3** were mounted on a tool holder by means of M5 screws. A new diamond tool is used for each workpiece in the experiment and the same tool is used for all the experimental runs for each workpiece cutting combinations:

Table 4.3: Properties of Diamond Tool [371]

Symbol	C
Atomic Number	6
Atomic Weight	12.011
Hardness	7000 Knoop Hardness (W = 2100 Knoop Hardness)
Density	3.51 g/cm ³
Most Common Valence	+4
Electron Configuration	1s ² 2s ² 2p ²
Melting Point	> 3550 °C
Bonding Type and Energy	Covalent; 713 kJ/mol
Mechanical Properties	E = 1035 GPa
Electrical Conductivity	10-14 [(Ω-m) ⁻¹]
Thermal Conductivity	2000-2500 W/m ⁻⁰ K

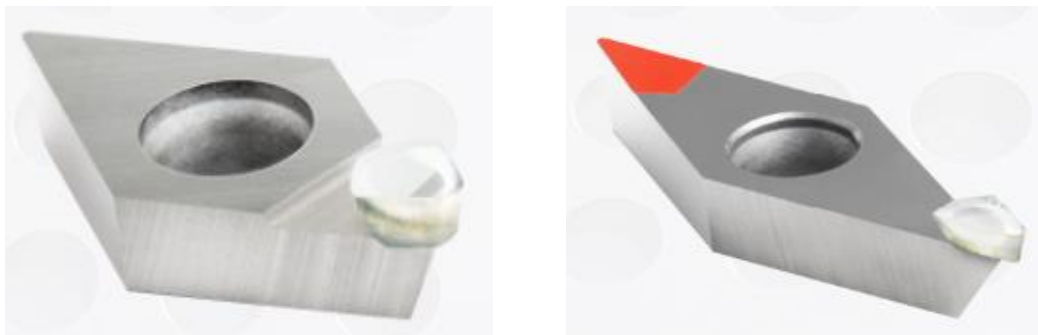


Figure 4.9: Typical tool holders and inserts for diamond turning

Table 4.4 represents the geometry information of the Diamond tools used in this research

Table 4.4: Geometry of diamond tools

S/N	Tool#	Nose Radius (mm)	Rake angle (°)	Clearance angle (°)	SCEA (°)	Factory info
1	SA79085	0.5	0	15° cylindrical	1 - 4°	 <p>CONTOUR FINE TOOLING SA79085 Type: N0.50mWEi Radius: 0.504mm Height: 3.147mm</p>
2	SA97066	1.0	0	15° cylindrical	1 - 4°	 <p>CONTOUR FINE TOOLING SA97066 Type: N1.00mWEi Radius: 1.005mm Height: 3.006mm</p>
3	SA79093	1.5	0	15° cylindrical	1 - 4°	 <p>CONTOUR FINE TOOLING SA79093 Type: N1.50mWEi Radius: 1.505mm Height: 3.006mm</p>

4.6 DATA ACQUISITION SYSTEM - ACOUSTIC EMISSION (AE)

Figure 4.10 is a typical representation of acoustic emission set up for diamond turning process carried out in this study. The LabView display has dual screens called front panel and block diagram. Both works simultaneously for efficient monitoring of data acquisition during machining. National Instruments, NI PXIe-1071 chassis as shown in **Figure 4.11** was used in conjunction with the NI BNC-2110 **Figure 4.12**. The BNC-2110 serves as an attachment point for instruments with BNC connections. PXIe-1071 operates at +/- 12V DC with an accuracy of 0.008 V and can sample at a maximum of 200kS/sec This system is attached to a PC installed with the NI LabView 2019 software. National Instruments (NI) LabVIEW is an acronym for Laboratory Virtual Instrument Engineering Workbench. It is a visual programming language used in this study for acoustic emission data acquisition and monitoring. **Figure 4.10** shows the experimental workflow of acoustic emission for this study.

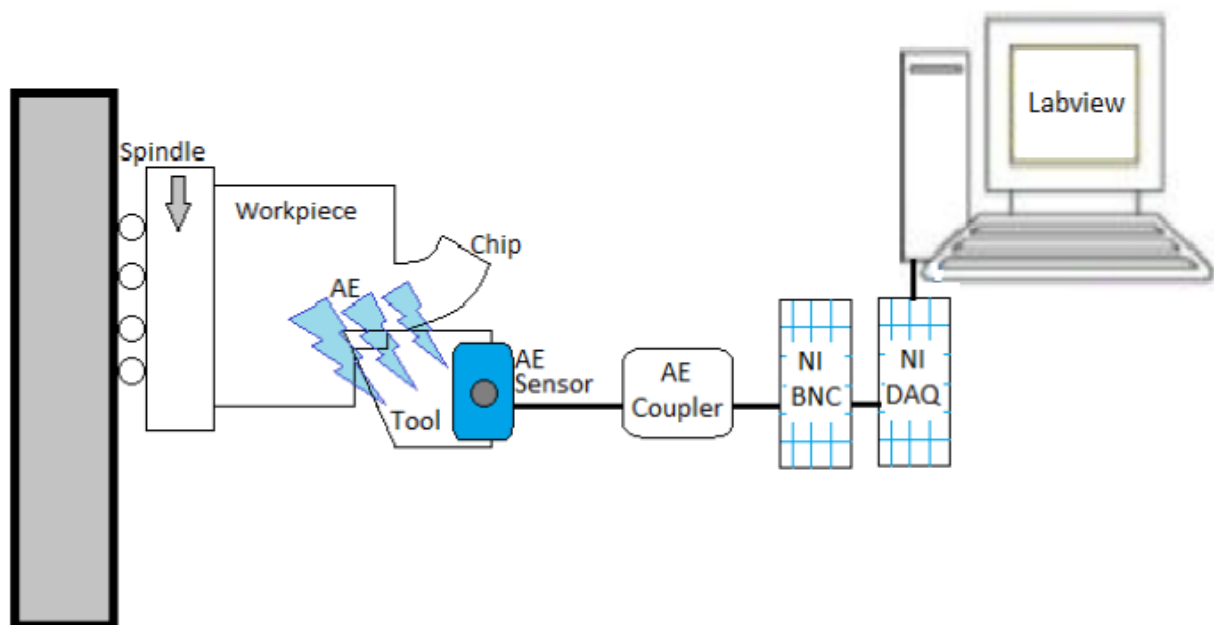


Figure 4.10: Typical set up for acoustic emission measurement during diamond turning [366]

In this experiment, the acoustic emission signals are acquired and monitored using an AE-Piezotron Sensor (Kistler 8152B) **Figure 4.13** which is mounted on the tool holder and is connected to AE Piezotron Coupler (Kistler 5125B) **Figure 4.15** which gives the AE signals and the RMS of the AE signals. The continuous and burst type AE signals

are acquired by Kistler 8152B AE piezotron sensors. The coupler (**Figure 4.14**) is used for signal pre-processing and conditioning, the input of the power supply was set at 220 V, with the output voltage stepped down to 24 V which was grounded. This was used to power and regulate the amount of current that goes into the energizer of the sensor. The NI LabVIEW consist of a front panel (**Fig 4.15**) for viewing the AE signal output in real time and a block diagram (**Figure 4.16**) section for developing the data acquisition. The programs created by LabVIEW usually called virtual image, (VI).



Figure 4.11: National Instruments NI PXIe-1071



Figure 4.12: NI BNC-2110



Figure 4.13: AE-Piezotron Sensor – Kistler 8162B



Figure 4.14: AE Piezotron Couper – Kistler 5125B

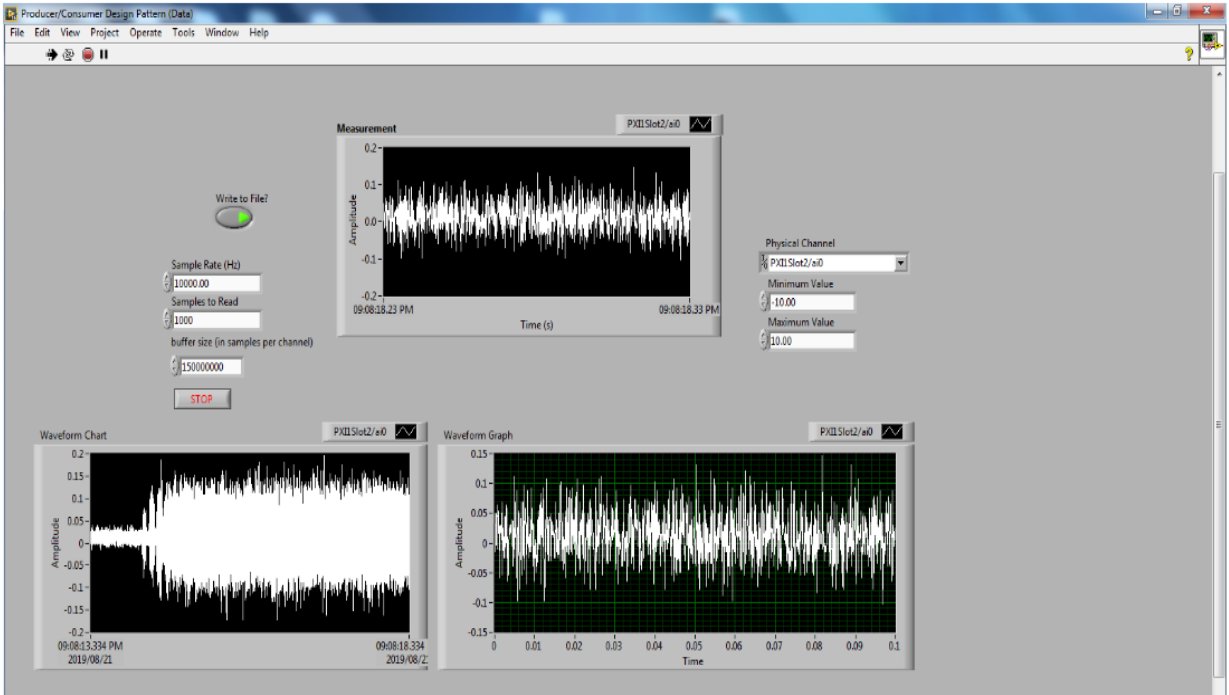


Figure 4.15: Live display LabView front panel of AE acquisition

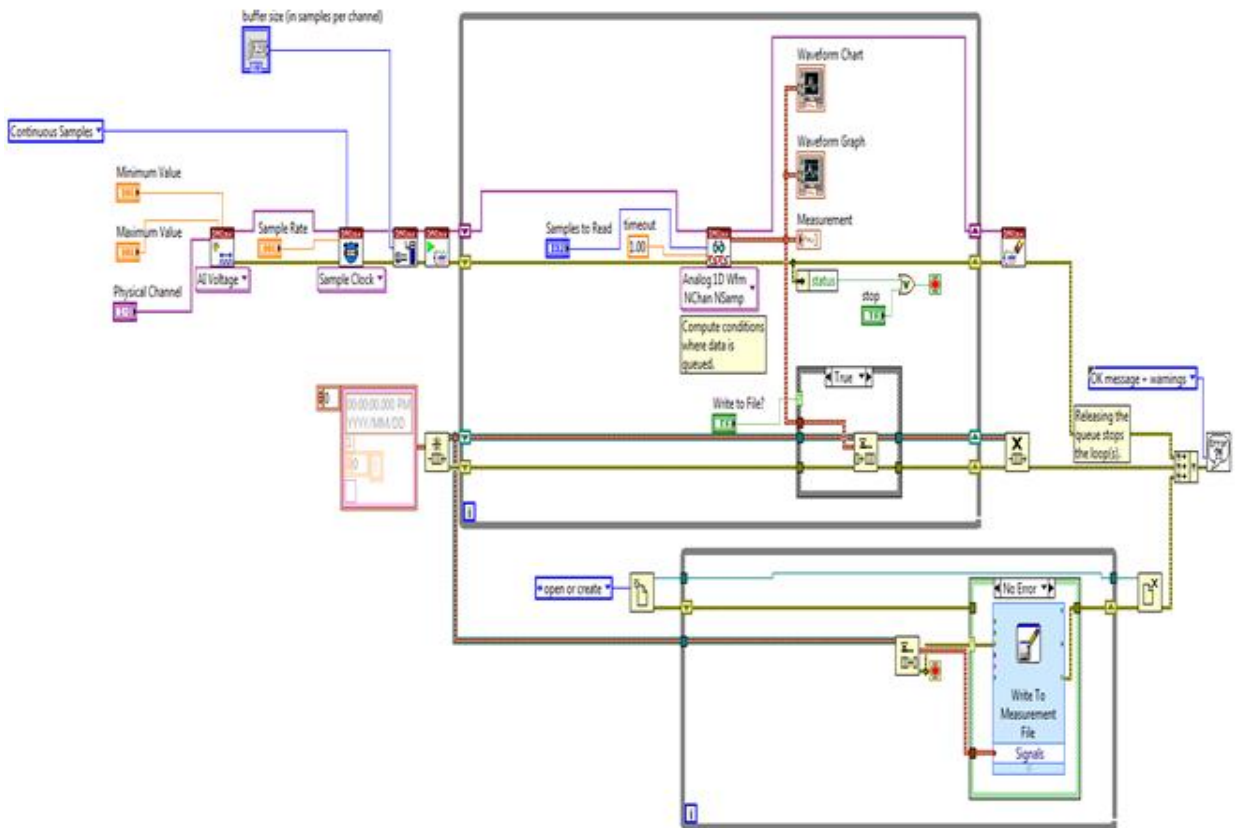


Figure 4.16: Display of LabView block diagram for AE acquisition

4.7 RESPONSE SURFACE METHOD AND BOX BEHNKEN DESIGN

A mathematical or statistical technique called response surface methodology (RSM) is used for modelling the relationship between experimental input variables and output responses. Often in Ultra precision machining, the cutting conditions such as cutting speed, feed rate and depth of cut, are the input parameters. The output responses are surface roughness, tool wear, acoustic emission (AE), RMS, MRR and force. RSM also provides a means of determining the most influential input parameter and the effect of the interactions of the parameters on the response. RSM reduces the required number of experiments for analysis saving time and cost.

4.7.1 Design of Experiment

Design of experiment (DoE) is a method being used widely in the industry and research field for process optimization [65, 372]. Its primary objective is to offer an effective means of experimental method and analysis of experimental results [65, 373]. The theory of DoE has been fully covered in many fundamental works [65, 374, 375] and its application to machining studies has also been discussed by many researchers [65, 374]. The DoE techniques enables designers to determine simultaneously the individual and interactive effects of many factors that could affect the output results in any design. It also provides a full insight of interaction between design elements. Experimental design is an effective tool for maximizing the amount of information gained from a study while minimizing the amount of data to be collected and is applicable to both physical processes and computer simulation models[65, 376, 377].

The DoE techniques enables designers to determine simultaneously the individual and interactive effects of many factors that could affect the output results in any design. It also provides a full insight of interaction between design elements. Experimental design is an effective tool for maximizing the amount of information gained from a study while minimizing the amount of data to be collected and is applicable to both physical processes and computer simulation models [376, 377].

In machining processes, DoE is used to generate the necessary combination of the machining parameters or conditions as inputs or independent variables and the corresponding surface roughness as output or dependent variable. By selecting the

best subset of experiments, it reduces the large number of potentially important parameters to those that are most significant.

4.7.2 Box-Behnken Design (BBD)

An efficient RSM that is often preferred is Box-Behnken. Because it involves fewer experiments, this method is popular in machining research. It was chosen because it is economical (fewer runs), nearly rotatable (accuracy varies with distance from the origin) and has no corner points or no unnecessary requirements). It is commonly used in non-sequential experimentation, and it provides efficient assessment for first and second order models. Since interaction parameter estimates are not completely confounded and, in many cases, these designs are considerably smaller than $3p-s$ fractional factorial designs [378]. In this research the author used Box-Behnken to generate the of runs in Design of Experiment **Figure 4.17**. A BBD also requires only three-levels and is a more efficient alternative to the full three-level factorial.

In other words, RSM is a sequential procedure and a collection of statistical techniques used for modelling and analysis of processes in which a response of interest is correlated with several input variables. It examines the relationships between one or more response parameters and a set of experimental input parameters [379]. RSM consists of three stages: design of experiment, regression analysis and statistical inferences [150] with primary objective of determining the optimum operating condition in terms of a region of factor space in which output requirements are satisfied [380]. RSM is widely applied in typical industrial conditions where numerous independent variables (input) have probable effect on the performance measures or quality characteristics of a product or process. The figure below shows the sample locations for the three factors.

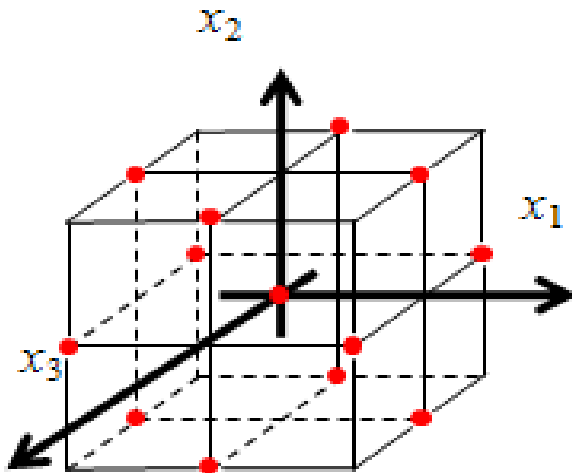


Figure 4.17: The design for three factors in Box-Behnken

RSM based on Box-Behnken design and ANOVA was employed in this study to statistically develop a model that would describe the extend of surface roughness dependence on the cutting parameters and their interactions. RSM is a group of statistical and mathematical methods suitable for developing, improving and optimizing processes [381]. RSM is a mixture of regression analysis and experimental design meant for response optimization. Response surface method (RSM) designs support in computing the relations between output responses and the independent input parameters. The factors that will be used for RSM has to be continuous and quantitative variables. The reason is to identify a required point in the design space. This sometimes can be found at a maximum, a minimum or even an area where the response is steady upon a range of the factors [379].

The general goal is to find a set of conditions for various responses at the same time. Box-Behnken designs (BBD) are response surface designs, specially made to require only 3 levels, coded as -1, 0, and +1. Bosques-Sendra et al. [382] described the advantages of BBD as response surface methodology for obtain second order models in full detail. Another advantage of BBD is that it does not contain combination for which all factors are simultaneously at their highest or lowest levels [383]. BBDs are obtainable for factors between 3 and 10 variables. They are designed by combining 2-level factorial designs using partial block designs.

This process generates designs with required statistical properties in which most of the time only one fraction of the experiments is obligatory for a three-level factorial due to only three levels of the quadratic model is appropriate. The effect of cutting

parameters were also carefully analyzed with the help of regression analysis to optimize the diamond turning process [379, 383]. In this study, **Table 4.5** present the cutting parameters for the experimental runs during diamond turning of RSA alloys.

Table 4.5: Machining Parameters or domain for the experiment

Standard Order	Experiment No.	Cutting Speed v (rpm)	Feed Rate f (mm/min)	Depth of Cut d (μm)
12	1	1750	25	25
10	2	1750	25	5
2	3	3000	5	15
13	4	1750	15	15
15	5	1750	15	15
11	6	1750	5	25
7	7	500	15	25
4	8	3000	25	15
8	9	3000	15	25
3	10	500	25	15
6	11	3000	15	5
1	12	500	5	15
9	13	1750	5	5
14	14	1750	15	15
5	15	500	15	5

4.8 SURFACE ROUGHNESS MEASUREMENT

Surface roughness is a guide used to determine the quality of machined products during ultraprecision machining. Therefore, there is a need for effective and reliable means to measure surface roughness. In this research, roughness measurements of diamond-turned RSA alloys were carried out after each experimental run using Taylor

Hobson PGI Dimension XL surface Profilometer at the Precision Engineering Laboratory, Nelson Mandela University (**Figure 4.17**). The surfaces were measured intermittently, and the average roughness values of the machined surfaces were obtained in each case and recorded accordingly.

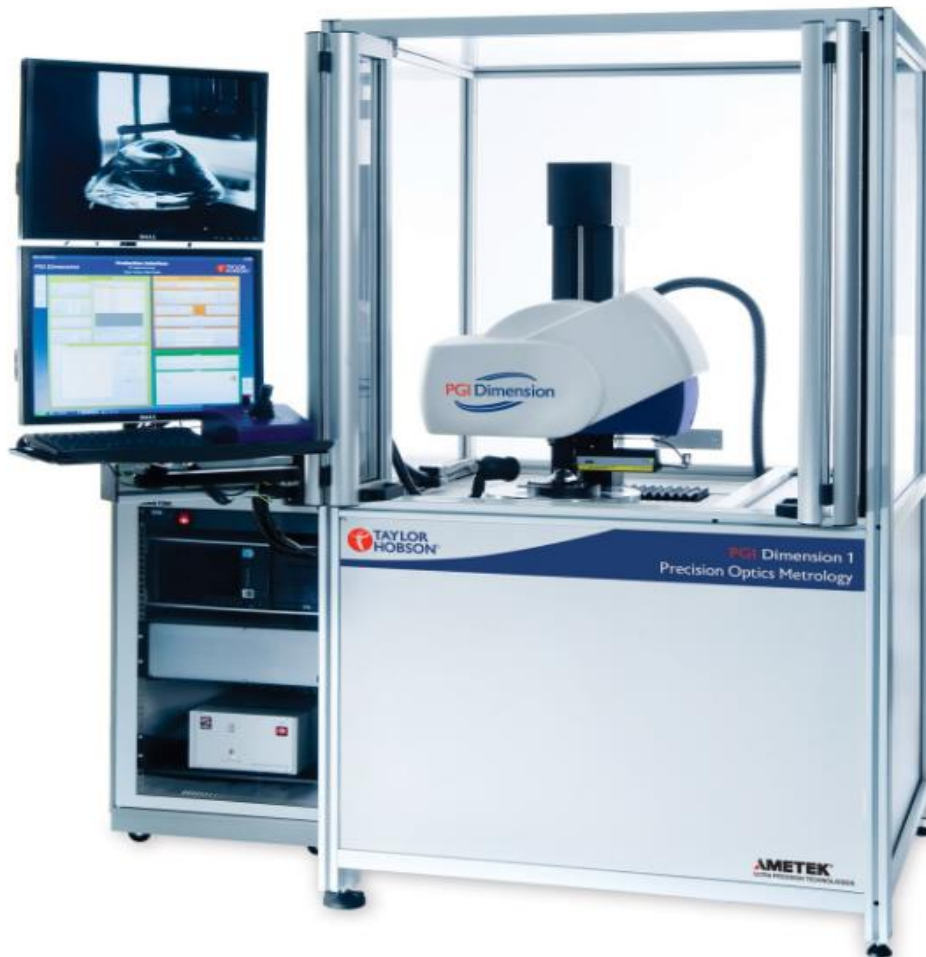


Figure 4.18: Taylor Hobson PGI dimension XL surface profilometer

The procedure is carried out in such a way that each workpiece was placed on the Taylor Hobson PGI Dimension XL Surface Profilometer air-bearing spindle table (**Figure 4.18**) and this process is a contact-based technique hence making the stylus of the profilometer is allowed to drag across the surface. The measured profile was processed and digitalized through an advanced surface finish analyzing software, which evaluates the roughness parameter seen in **Figure 4.19**. The roughness parameter utilized to accomplish the study on surface roughness is the average roughness or centreline average or arithmetic average (Ra), which is defined as the mean deviation of the surface height from the mean profile line see **Figure 4.20**.

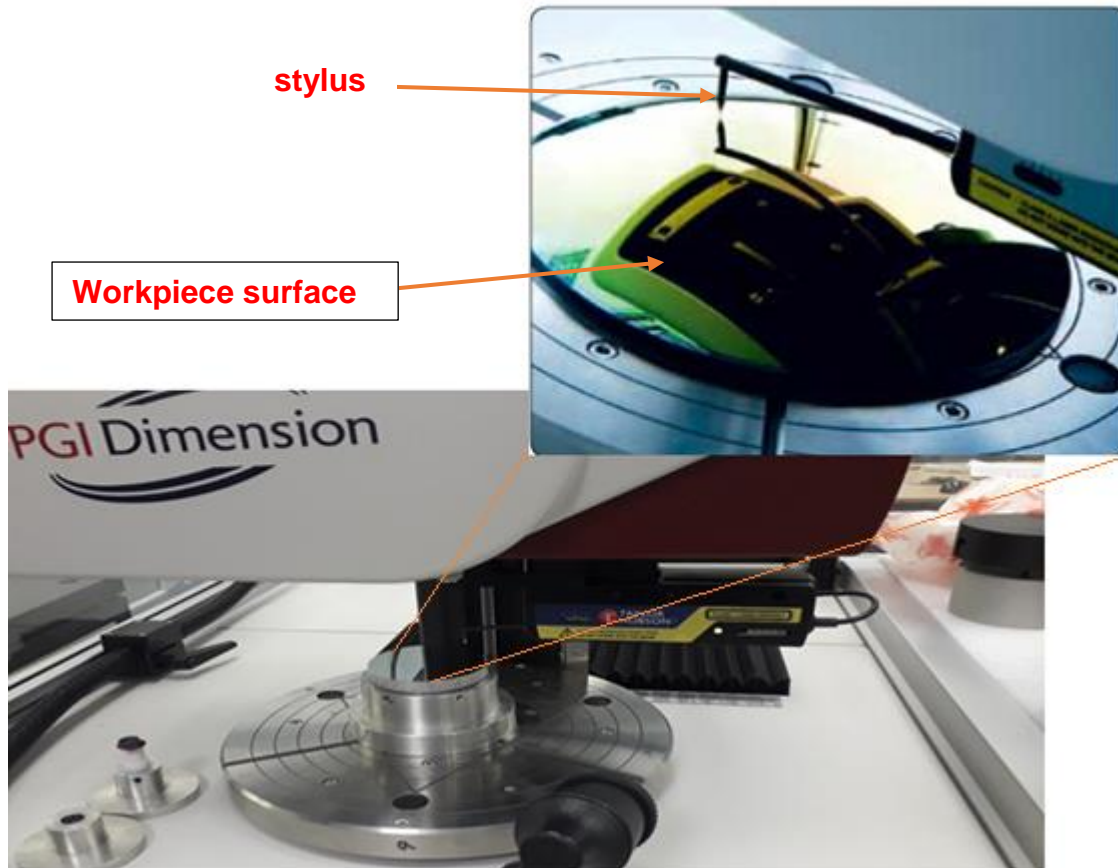


Figure 4.19: Surface Profilometer display sample measured

5.23.15.102

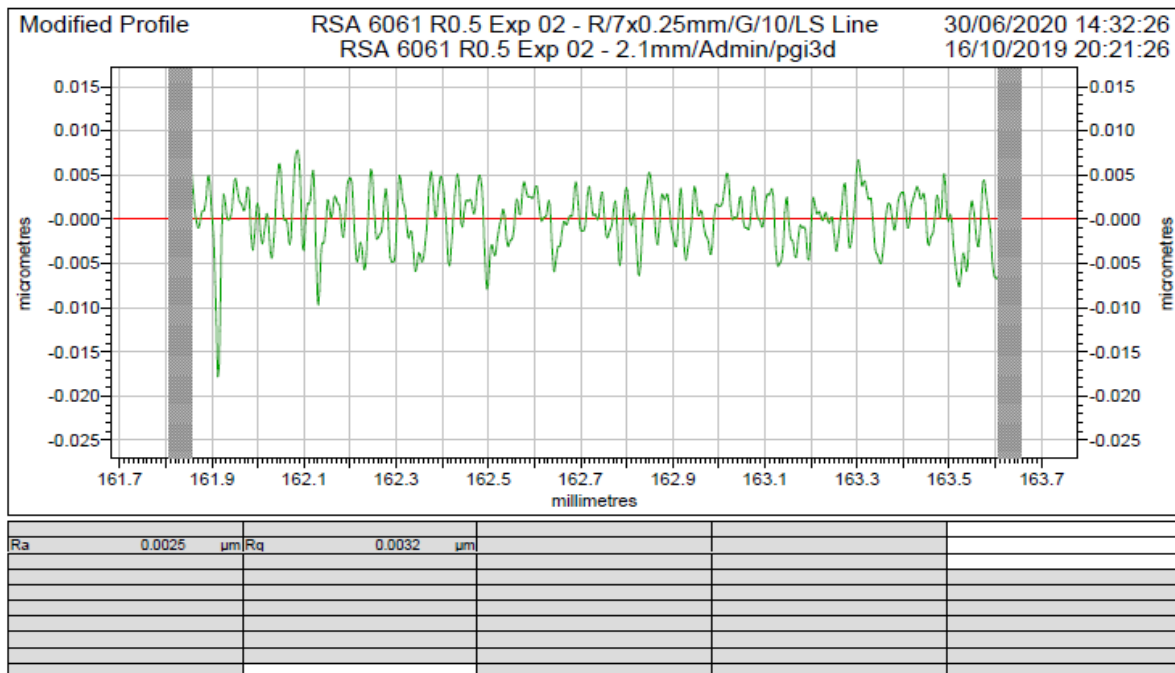


Figure 4.20: Surface profile chart

CHAPTER 5

DIAMOND TURNING OF RAPIDLY SOLIDIFIED ALUMINIUM (RSA) 905 ALLOY

This section presents the cutting force measurement, acoustic emission, and their effects on machinability of optical RSA 905 alloys. It is very crucial to understand the mechanism of how to achieve high-quality cutting process for this material due to its applicability in optical industry. The approach consists of conducting turning process for different cutting parameters, the force acquired using SSCFTH was compared with industrial data just to check for validity of the system. Thereafter, necessary statistical analysis and models were drawn from the experimental data captured on force and AE. Profile plots for cutting parameters and machining optimization are also presented.:

5.1 ANALYSIS ON RSA 905

5.1.1 Force sensor comparison and analysis

Table 5.1 shows the comparison between acquired force data using Kistler, a standard industrial force measurement sensor and the self-sensing cutting force tool holder (SSCFTH) that was designed.

Table 5.1: Cutting force data for self-sensing sensor and Kistler sensor

Run	V(rpm)	F (mm/min)	D(μ m)	F(N)	Kistler (N)
Exp1	1750	25	25	0.6623	0.7498
Exp2	1750	25	5	0.1490	0.2329
Exp3	3000	5	15	0.1060	0.4449
Exp4	1750	15	15	0.7114	0.6436
Exp5	1750	15	15	1.0114	0.6436
Exp6	1750	5	25	0.1799	0.6389
Exp7	500	15	25	0.9803	0.8584
Exp8	3000	25	15	0.2705	0.4737
Exp9	3000	15	25	0.3895	0.5701
Exp10	500	25	15	1.0548	0.9379
Exp11	3000	15	5	0.2581	0.1363
Exp12	500	5	15	0.3298	0.1489
Exp13	1750	5	5	0.0437	0.0757
Exp14	1750	15	15	1.0114	0.6436
Exp15	500	15	5	0.0760	0.1003

An outlier can be detected in experiment 7 by statistically looking at the data acquired from the self-sensor tool. This may be one of the random errors during the experiment. However, statistical parameters are used to check data reliability, such as percentage error, mean absolute percentage error (MAPE), root mean absolute error (RMSE), to verify that the established sensor is reliable.

Percentage error: this is often referred to as fractional difference which measures the accuracy of a measurement by the difference between a measured or experimental value E and true value of accepted value or sometimes predicted value A.

Equation 5.1

$$\% Error = \left(\frac{E - A}{E} \right)$$

Mean absolute percentage error (MAPE) is a statistical measure of how accurate a forecast is. Measured accuracy is expressed as percentage, it is calculated as the average absolute percentage error for each time subtracted from the actual value divided by actual value.

Equation 5.2

$$MAPE = \frac{1}{n} \sum_{t=1}^n \frac{A - P}{A} * 100$$

Where A is the actual value and P is the predicted value.

Root mean square error (RMSE) is the standard deviation of the residuals of predicted error. It can also be described as the standard way to measure the error of a model mostly in predicting experimental data. It is useful in regression analysis for predictions and to verify experimental results.

Equation 5.3

$$RSME = \sqrt{\sum_{i=1}^n \frac{(P - A)^2}{n}}$$

In this study, the values for these three statistical indicators are: % error is 2.19, MAPE is 17.57% and RMSE is 0.43.

The **Figure 5.1** shows the forces acquired when diamond turning RSA 905 with SSCFTH. This was verified with the same machining condition using an industrial scale force sensor from Kistler. Only experiment 7 bets to differ due to low speed and high depth of cut.

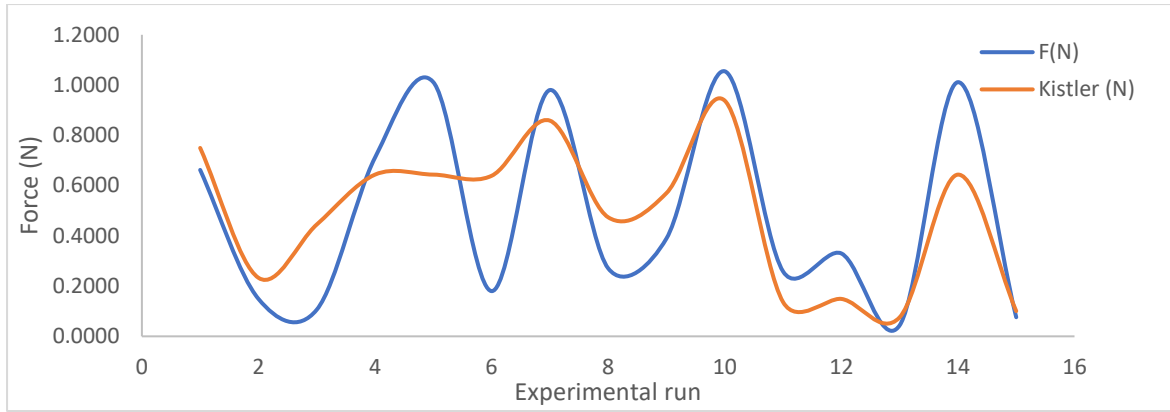


Figure 5.1: Comparison between the data acquired by SSCFTH designed and industrial Kistler sensor

5.1.2 Analysis for regression and ANOVA of force for RSA 905

Table 5.2 presents the summary output of statistical analysis for cutting force F(N) data during diamond turning of RSA 905.

Table 5.2: Regression and ANOVA summary output of cutting force for RSA 905

SUMMARY OUTPUT						
<i>Regression Statistics</i>						
Multiple R	0.983916					
R Square	0.968091					
Adj R Square	0.94416					
Stand Error	0.279756					
Observations	15					
ANOVA						
	<i>df</i>	<i>SS</i>	<i>MS</i>	<i>F</i>	<i>Significance F</i>	
Regression	6	18.99575	3.165958	40.4525	1.48E-05	
Residual	8	0.626109	0.078264			
Total	14	19.62186				
	<i>Coefficients</i>	<i>Standard Error</i>	<i>t Stat</i>	<i>P-value</i>	<i>Lower 95%</i>	<i>Upper 95%</i>
Intercept	-7.46354	0.536434	-13.9132	6.89E-07	-8.70056	-6.22652
v(rpm)	0.000674	0.000186	3.631807	0.006668	0.000246	0.001102
f (mm/min)	0.360953	0.044657	8.08284	4.05E-05	0.257974	0.463931
d(μm)	0.438701	0.048762	8.996829	1.86E-05	0.326256	0.551146
vd	-6.8E-05	1.12E-05	-6.06829	0.0003	-9.4E-05	-4.2E-05
f^2	-0.0101	0.001452	-6.96002	0.000117	-0.01345	-0.00676
d^2	-0.00769	0.001452	-5.30018	0.000728	-0.01104	-0.00435

Looking at the ANOVA table, the effects of the machining parameters can also be seen from the coefficient and P-value columns. Statistically, 'P' values < 0.0500 imply that all visible terms are significant. In this case, v, f, d, vd, f² and d² in this experiment are significant model terms. Meanwhile, values larger than 0.1000 imply that the terms of the model are not significant. The p-values of depth of cut and feed rate show higher influence on the cutting force applied. However, stepwise backward regression analysis was carried out to further ascertain the validity of sensor designed. The R² from regression shows 0.9681 which simply indicates that the model explains 96.81% of variability in cutting force applied during machining is explained by the model. It is worth noted that this percentage of variability, also confirmed the accuracy of the self-sensor tool holder to be (99.6%) in **Figure 3.28** during calibration process. Hence, equation 5.2 represents this model as:

Equation 5.2

$$\ln(F) = -7.46 + 6.74 \times 10^{-3}V - 0.36F + 0.4387D - 6.8 \times 10^{-5}VD - 0.0101F^2 - 7.69 \times 10^{-3}D^2$$

or

$$F = e^{(-7.46+6.74 \times 10^{-3}V-0.36F+0.4387D-6.8 \times 10^{-5}VD-0.0101F^2-7.69 \times 10^{-3}D^2)}$$

Where *V* is the speed in rpm, *F* is feed rate in mm/min and *D* is the depth of cut in μm and Force is the average cutting force in Newton.

From this model, the effect of positive and negative coefficient of cutting parameters is cleared and this will be further explained into details below. The author also saw an interaction effects between the spindle speed and dept of cut even though their contributions with this effect are very small but still counts. Another statistical tool used to validate this experimental model or design is scattered plot shown in **Figure 5.2**. **Figure 5.3** presented a plot showing the comparison between experimental data and the predicted data. This plot indicates that there was no deviation in experimental data and predicted data which can also serve as confirmation to reliability of the self-sensor tool holder.

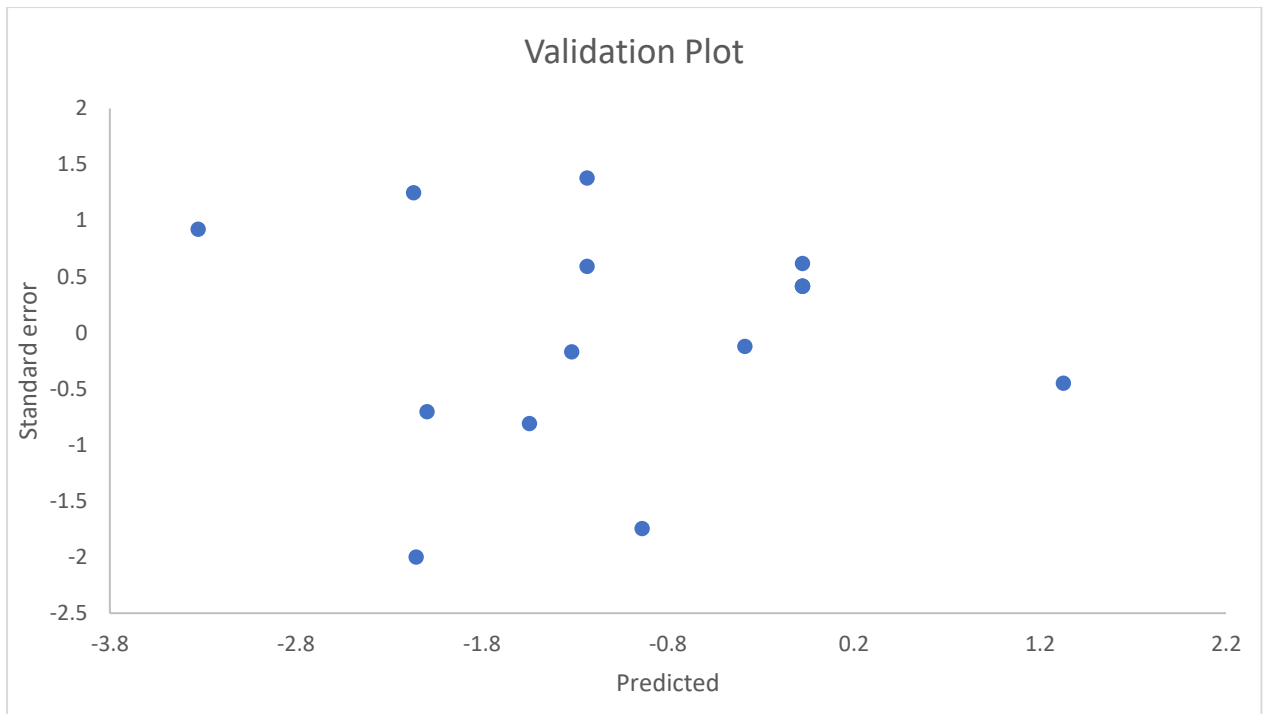


Figure 5.2: Validation of the experiment carried out by self-sensor (SSCFTH) a well scattered plot

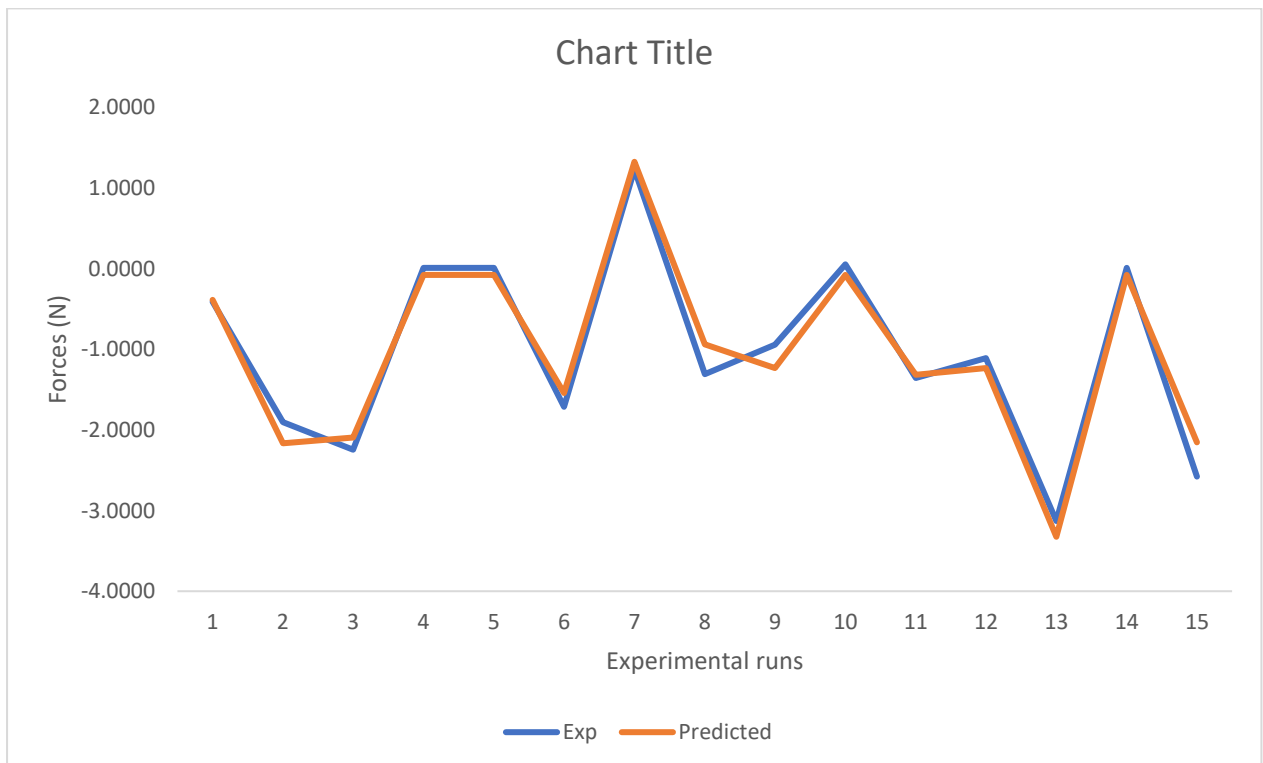


Figure 5.3: Comparison between experimental and predicted data of self-sensor cutting force tool holder and predicted data

5.1.3 Profile plot for force sensor of RSA905

Figures 5.4 - 5.6 show the effects of cutting speed, feed, and depth of cut on RSA 905, as previously indicated. **Figure 5.4** shows that, at a low feed rate of 5 mm/min and a cutting depth of 5 μm , the higher the cutting speed, the greater the force applied. Conversely, where the feed rate and the cutting depth have increased, the reverse is the case. It showed that the higher the spindle speed, the lower the force applied to cut the workpiece surface in this condition. For a robust model, the force acquired from $F(N)$ requires transformation. Therefore, the best statistical transformation that can model the sensor force has been identified to be natural log of force ($\ln F$).

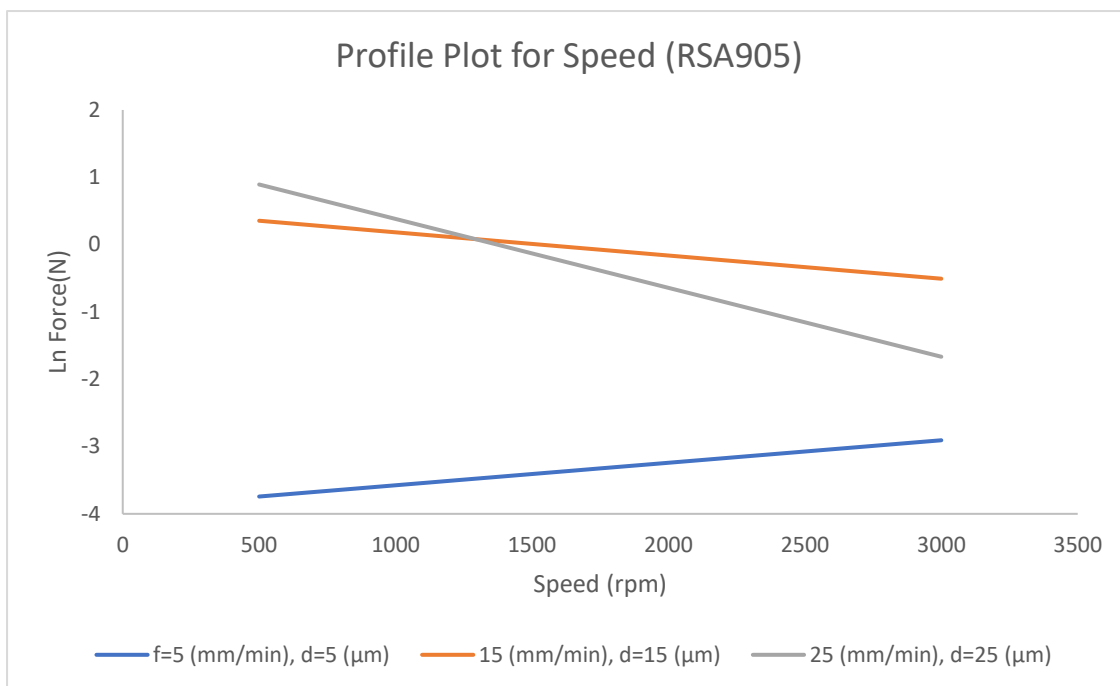


Figure 5.4: Profile plot for speed against natural log of cutting force

Figure 5.5 shows the effects of feed rate at various machining conditions on speed and depth of cut. Although the same pattern was observed for this effect but various level of force was applied at low, moderate, high Spindle speed and depth of cut. However, we have observed low force at low feed rate equally relatively high force at very high feed rate.

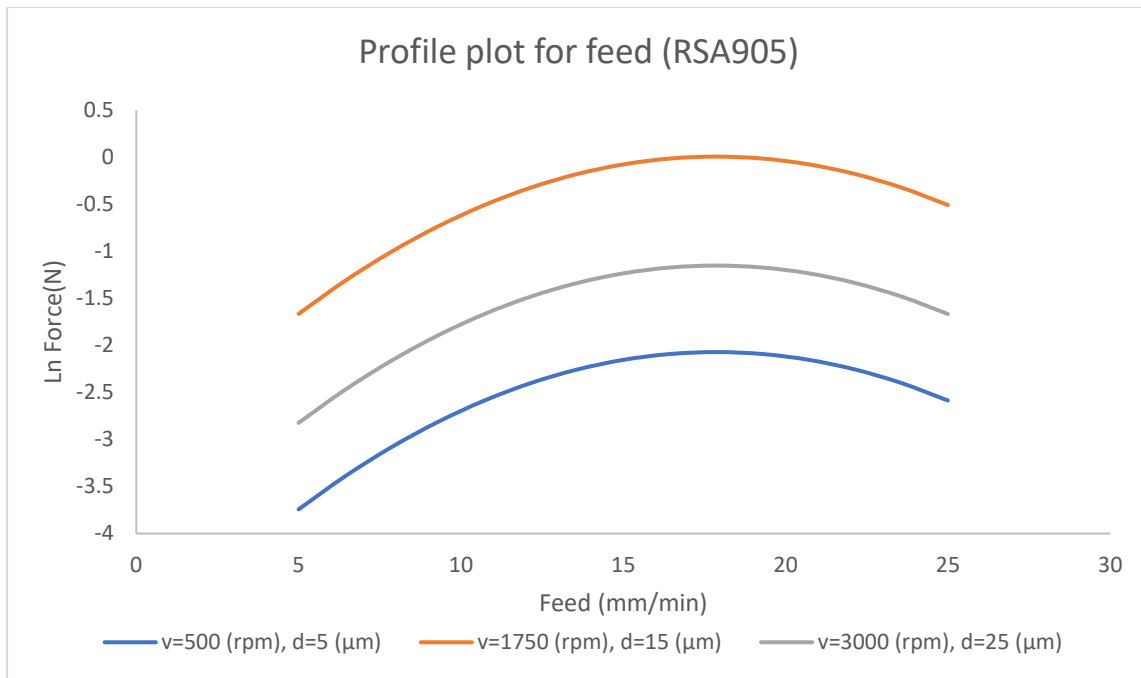


Figure 5.5: Profile plot for feed rate against natural log of cutting force

Figure 5.6 shows a unique pattern. During machining, it was observed that at a very low speed and low depth of cut, the force required was also low. The trend continues to increase as the depth of cut increases. In the case of high speed and feed, it seems there is a promise that the force applied may reduce to the nearest minimal.

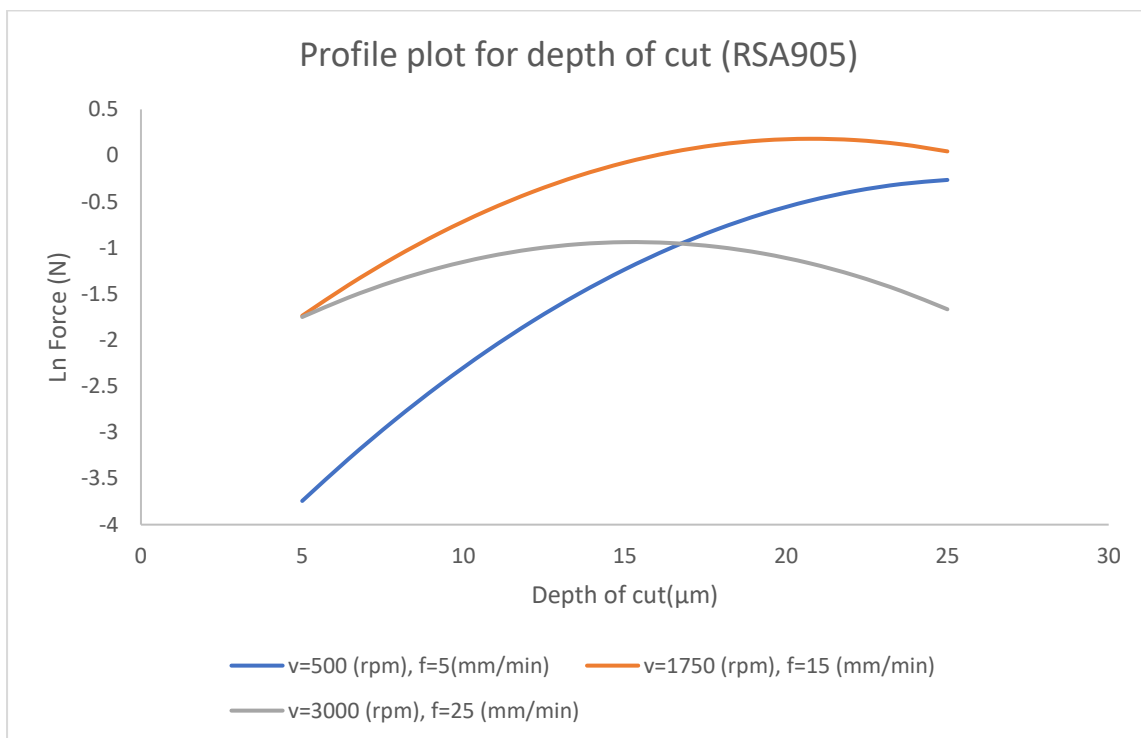


Figure 5.6: Profile plot for Depth of cut against natural log of cutting force

5.1.4 Machining Optimization

Table 5.3 shows optimization of the cutting parameters. It can be deduced here that at minimum speed (500rpm) and depth of cut (5 μm), a very low cutting force is required.

Table 5.3: Optimization of cutting parameter for RSA 905

	V (rpm)	F (mm/min)	D (μm)	Predicted Force (N)	Actual Force (N)
Max	500	17.86353	25	1.407547	4.08592
Min	500	25	5	-2.58576	0.07533

From **Equation 5.2** above, the model indicates an interaction between cutting speed and depth of cut hence, **Figure 5.7** shows interaction plots at feed rate 15 mm/min.

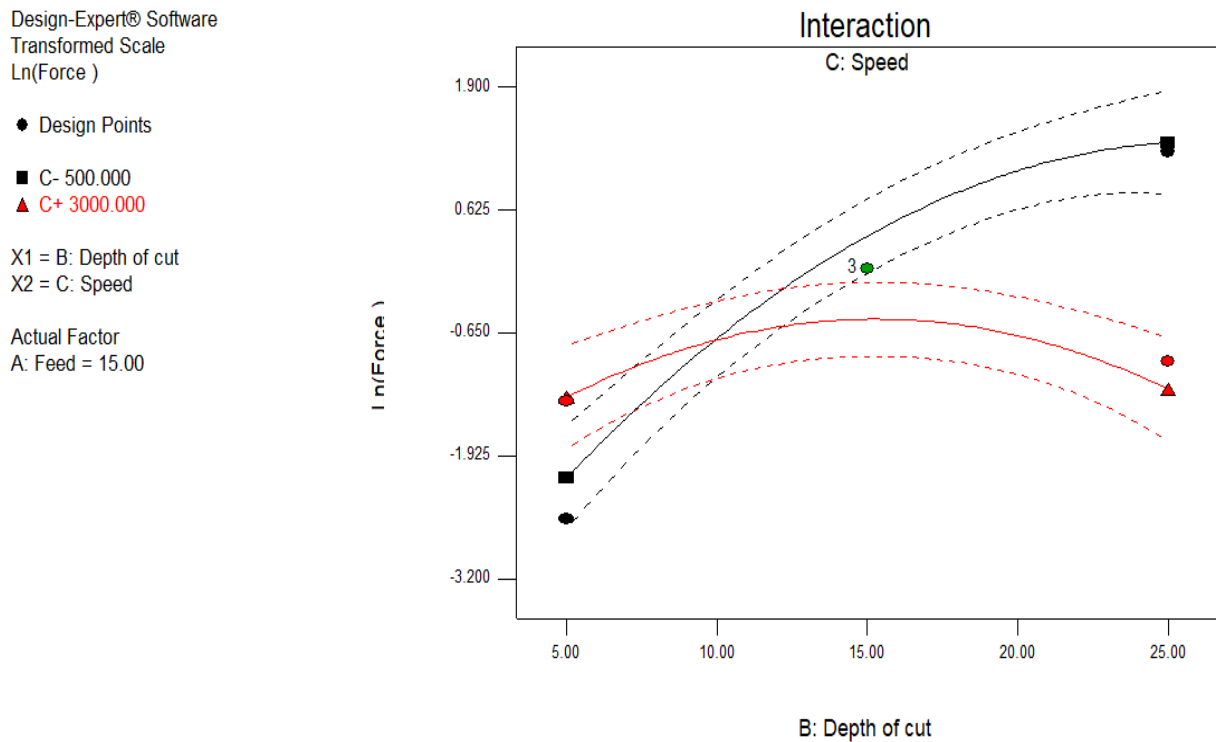


Figure 5.7: Interaction plot between depth of cut and speed on cutting force for RSA 905

The most significant factors in the contour plot are shown in **Figure 5.8**. At feed rate of level 15 mm/mins, a 2D contour plot was generated. This presented the effects of high depth of cut at 25 μm and low speed of 500 rpm resulting in a very high force being applied (Red zone) during machining RSA 905. This revelation also confirmed the computation under the optimization process in **Table 5.3** where at the same cutting condition, the force applied was maximised. The 3-D response surface plot in **Figure 5.9** under the same cutting parameters also depicts the same results.

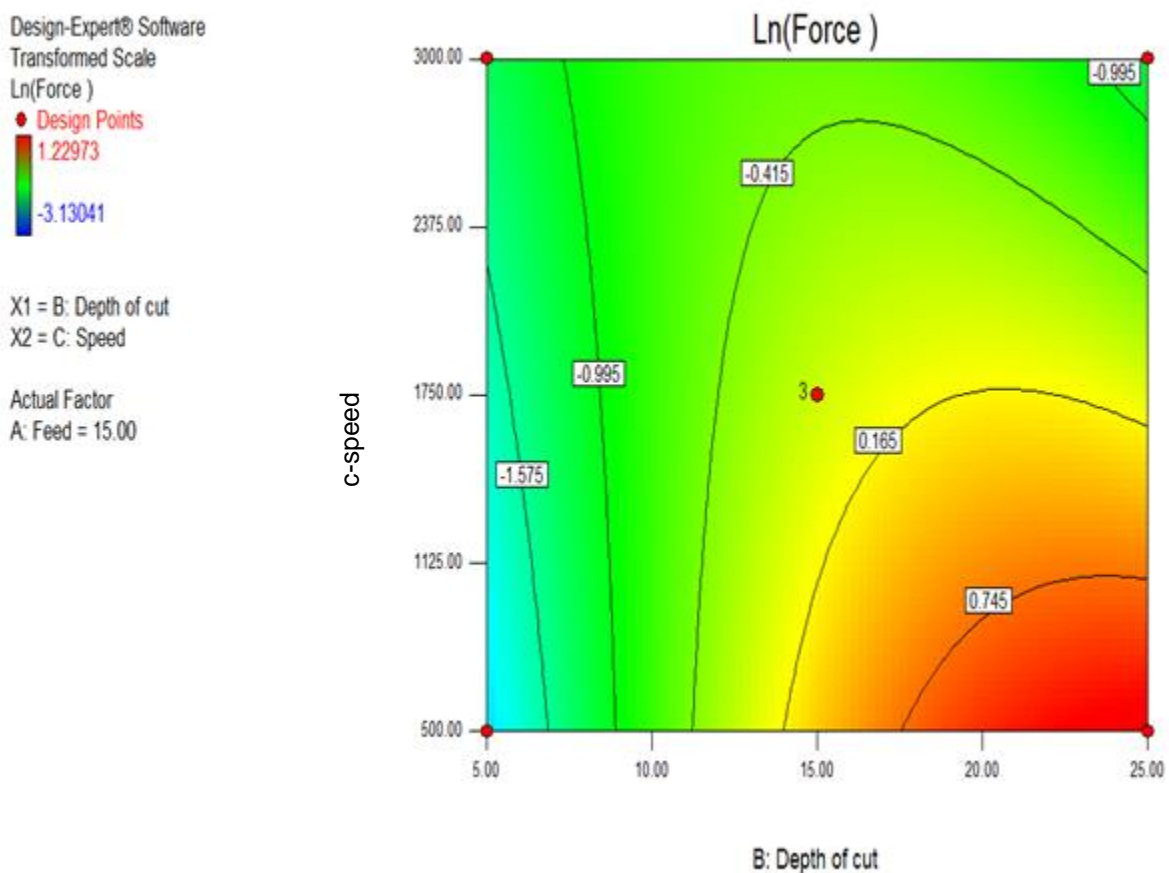


Figure 5.8: Contour plot between depth of cut and speed against natural log of cutting force

Design-Expert® Software
Transformed Scale
Ln(Force)

● Design points above predicted value

○ Design points below predicted value

1.22973

-3.13041

X1 = B: Depth of cut

X2 = C: Speed

Actual Factor

A: Feed = 15.00

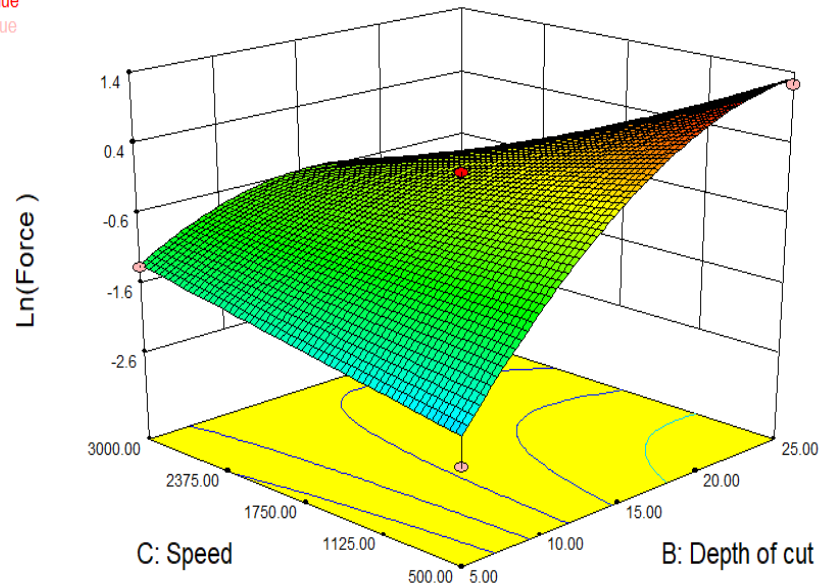


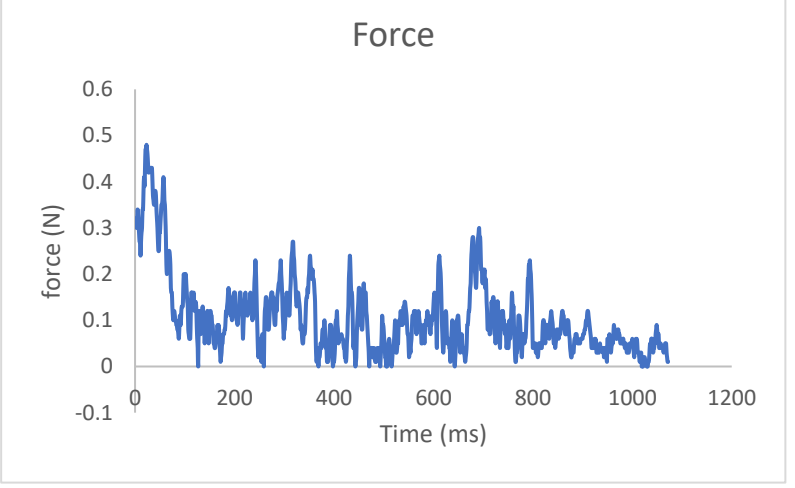
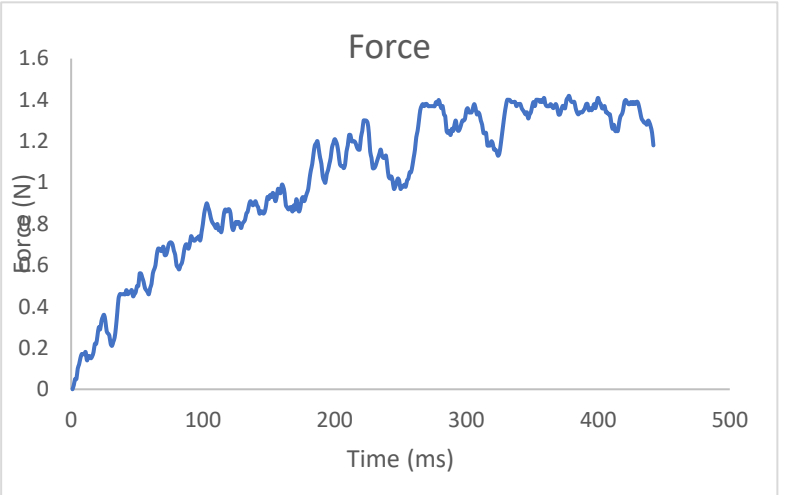
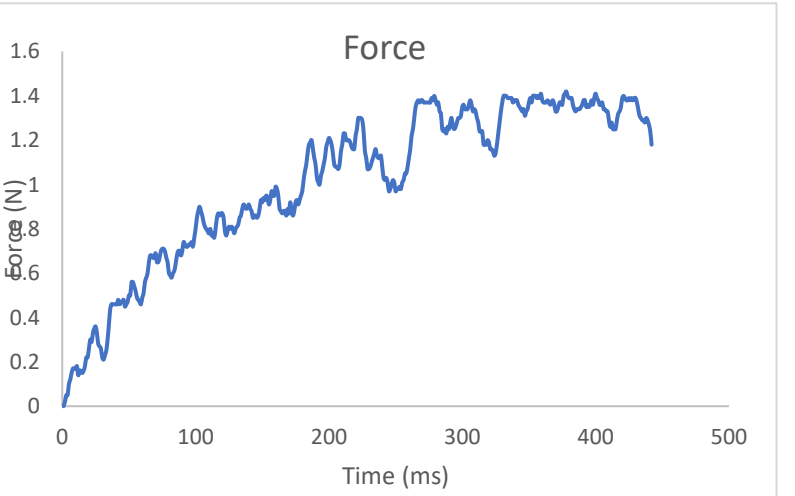
Figure 5.9: 3D plot between Depth of cut and speed against natural log of cutting force

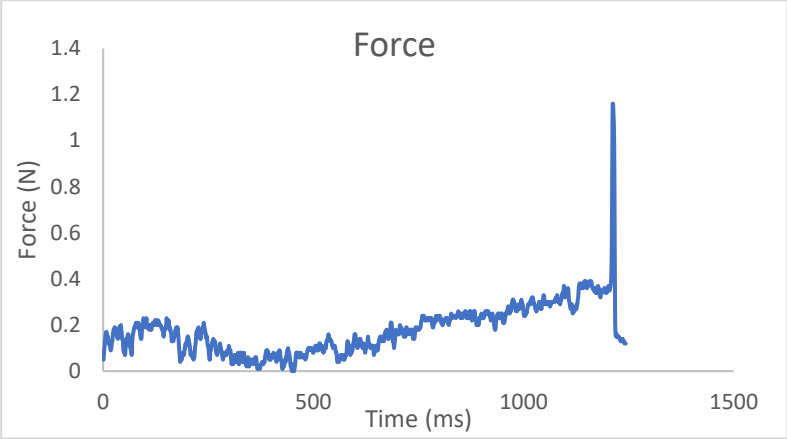
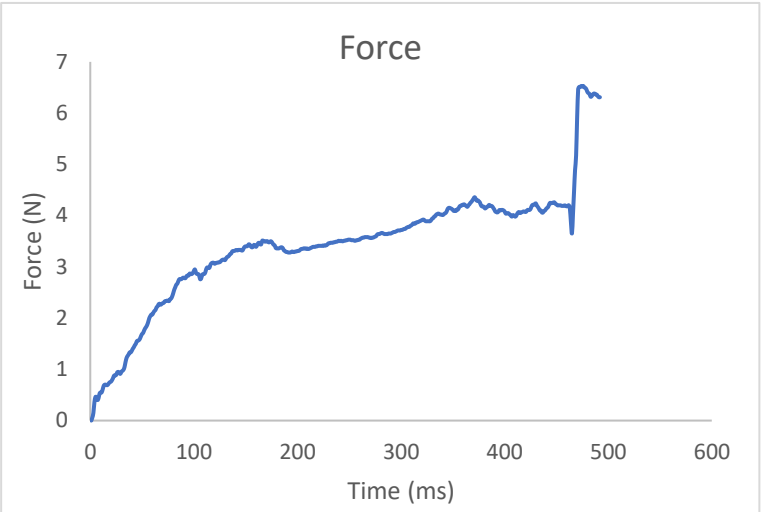
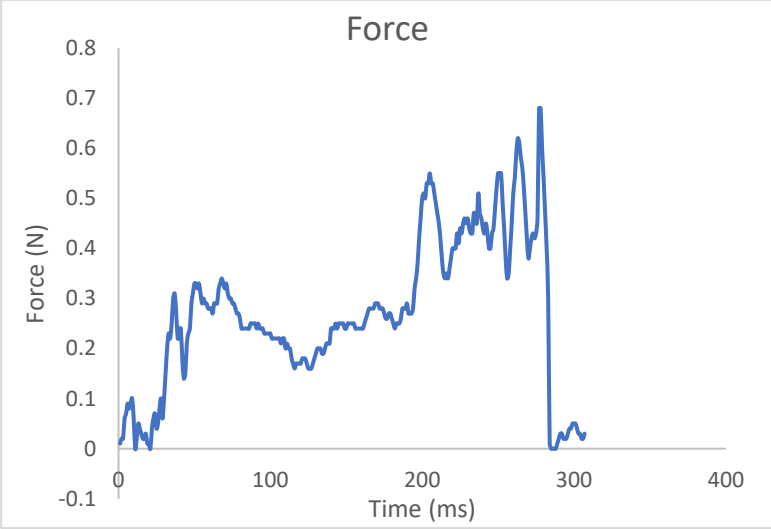
5.1.5 Graphical representation of cutting force characteristics during machining of RSA 905

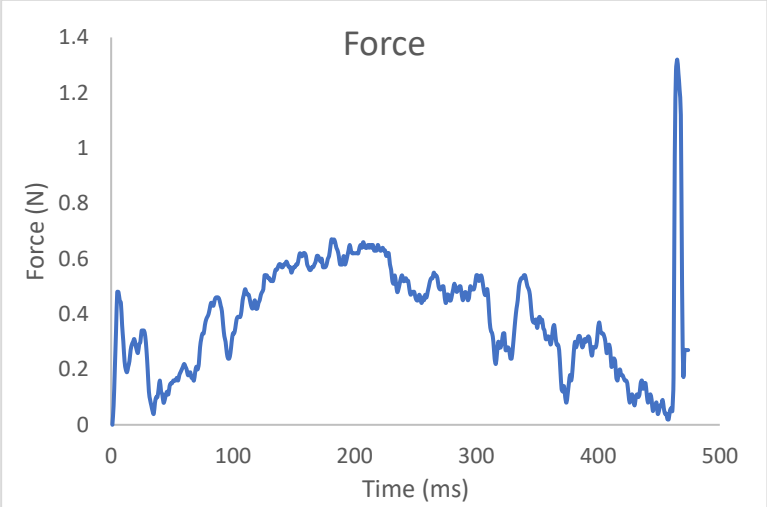
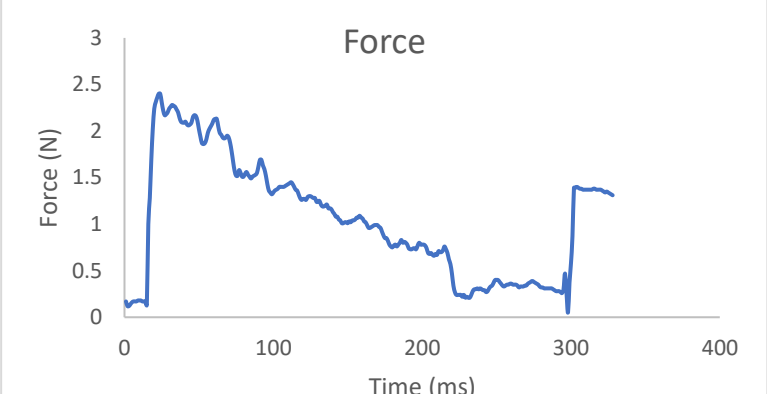
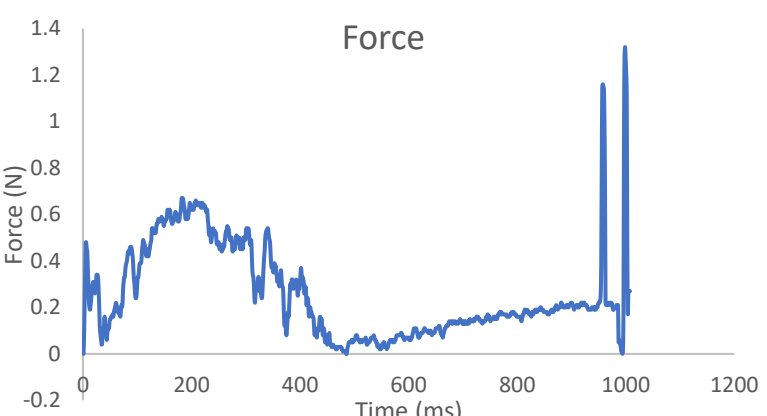
As earlier pointed out that a self-sensing cutting force tool holder was designed from first principle which was used to capture and monitor cutting forces during diamond turning of three different RSA alloys, **Table 5.4** presented graphical representation of force characteristics during ultra-precision diamond turning of RSA 905. It can be observed in Table 5.4 that the higher the feed rate at low cutting speed the higher the cutting force experienced. Looking at experiment 10 (feed rate = 25 mm/min, speed = 500 rpm), the cutting force applied is high. This is due to strain rate exerted during machining, leading to a large shear strength. However, this can be compensated for with a high cutting speed.

Table 5.4: Cutting force characteristics of RSA 905

Run	V rpm	F mm/min	D μm	Force characteristics
Exp1	1750	25	25	
Exp2	1750	25	5	

Exp3	3000	5	15	 <p>The graph for Exp3 shows force (N) on the y-axis ranging from -0.1 to 0.6 and time (ms) on the x-axis ranging from 0 to 1200. The force starts at approximately 0.45 N at 0 ms, drops to about 0.1 N by 100 ms, and then fluctuates between 0 and 0.3 N for the remainder of the 1200 ms period.</p>
Exp4	1750	15	15	 <p>The graph for Exp4 shows force (N) on the y-axis ranging from 0 to 1.6 and time (ms) on the x-axis ranging from 0 to 500. The force starts at 0 N at 0 ms and increases steadily to approximately 1.4 N by 450 ms, with some fluctuations.</p>
Exp5	1750	15	15	 <p>The graph for Exp5 shows force (N) on the y-axis ranging from 0 to 1.6 and time (ms) on the x-axis ranging from 0 to 500. The force starts at 0 N at 0 ms and increases steadily to approximately 1.4 N by 450 ms, with some fluctuations.</p>

Exp6	1750	5	25	
Exp7	500	15	25	
Exp8	3000	25	15	

Exp9	3000	15	25	
Exp10	500	25	15	
Exp11	3000	15	5	
Exp12	500	5	15	

Exp13	1750	5	5	
Exp14	1750	15	15	Same as Experiment 4 and 5
Exp15	500	15	5	

5.2 AE ANALYSIS FOR RSA 905

Acoustic emission (AE) is a transient elastic wave that are released within a material caused by the discharge of localized stress energy. This technology has been discovered to be among the most suitable method to detect the rates of a very small energy release [70] [59]. AE has a very high sensitivity in detecting the loss of mechanical reliability when compared to the well-known vibration monitoring methods. Because AE can provide effectiveness and superiority of a detectable indication from a minor defect, it has capability of giving early warning of emerging problems in order for proactive maintenance to be conveniently scheduled and carried out [59].

During acoustic emission process, the emissions generated on the surface of the material is presented as Rayleigh waves and as such can be measured with an AE sensor [59]. Other types of waves that can be found associated with this propagation are: Longitudinal, Lamb and shear waves [98].

There are two types of AE signals, transient(burst) and continuous signal. In AE burst signal, signal diverge completely from the background noise while in continuous AE signals, clear distinctions of amplitude and frequency can be seen and there is no ending for the signals [59]. The idea of AE technology is based on processing and detecting of these high frequencies' elastic waves into electrical signals which can be applied by connecting sensitive AE sensors on the surface structure [59] under test and applying an external inducement. Further processing can be done by amplifying sensor outputs using low-noise preamplifier then carry out filtering possible unwanted noise.

The set up for acoustic emission in this study has been explained in section 4.4. The AE raw data acquired were further processed using MATLAB software. Where unwanted signal such as associated noise with the AE raw data during machining were filtered. **Figure 5.10** shows the parameters used for filter during the analysis of frequency domain. Generally, the range of frequency for the acoustic emission during diamond turning of RSA 905 is observed to be between 0.5k and 1k Hz. The amplitude and the sharp spike of the acoustic emission is a good indication to monitor ultra-precision cutting process. Hence, the amplitudes that falls between the above-mentioned frequencies are considered as significant parameters to monitor machinability of RSA 905 in this study. Hence, experiments 2, 7, and 15 are examples

of displayed acoustic emissions in frequency domain **Figures 5.11 -5.13**. As can be seen, the amplitudes of the frequency features can be related to the effects of cutting parameters during machining. In **Table 5.4** above, feed rates and cutting speed are most influential or sensitive to high amplitudes in the experiment. This pattern can be confirmed in cutting force which are related to high cutting force perhaps poor surface quality and indication of a potential tool failure.

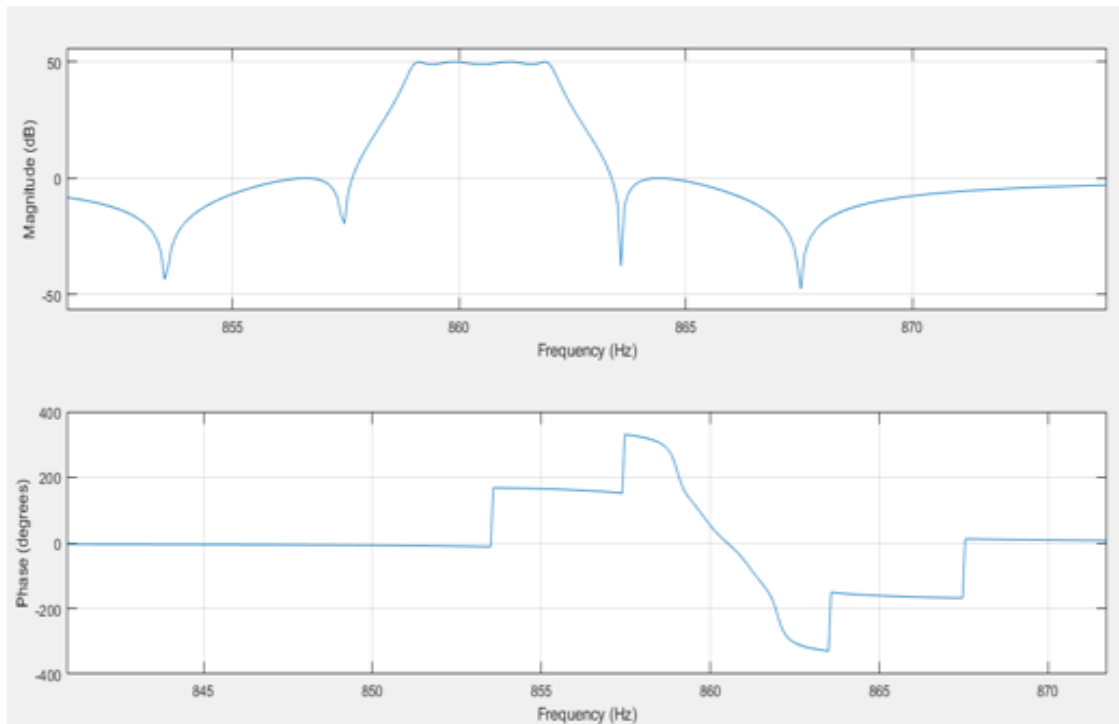


Figure 5.10: Filter design and its parameters for AE of RSA 905

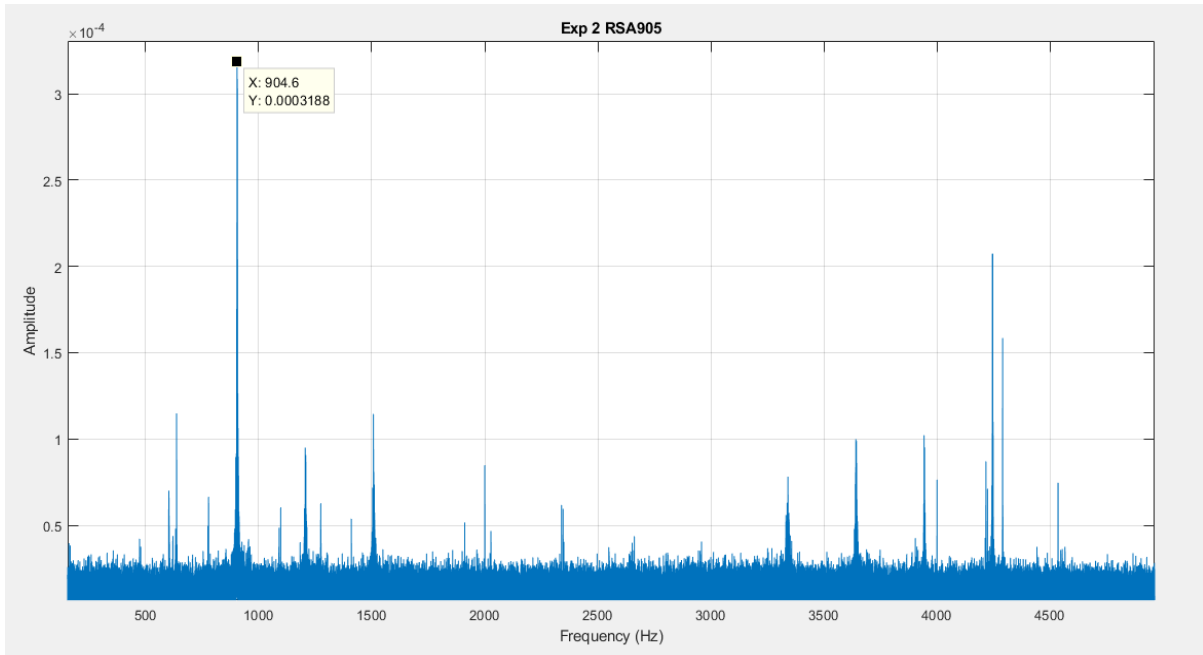


Figure 5.11: Frequency domain representation for experiment 2 feed rate = 25 mm/min, depth of cut = 5 μ m, speed = 1750 rpm

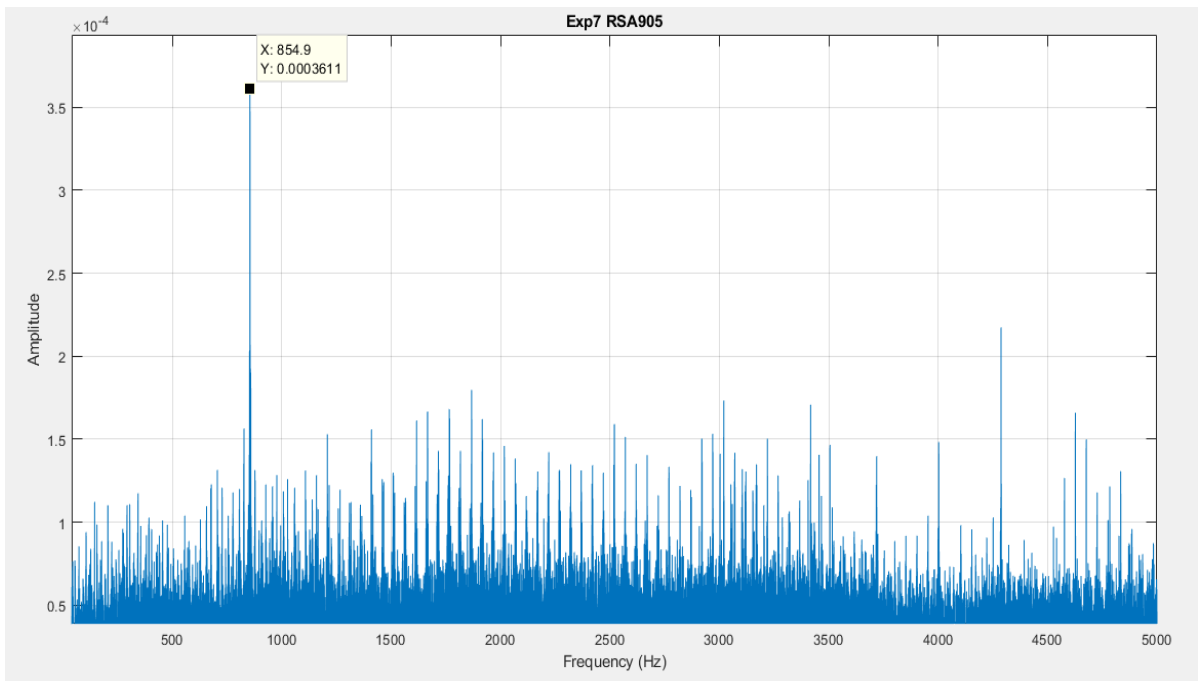


Figure 5.12: Frequency domain representation for experiment 7 feed rate = 15 mm/min, depth of cut = 25 μ m, speed = 500 rpm

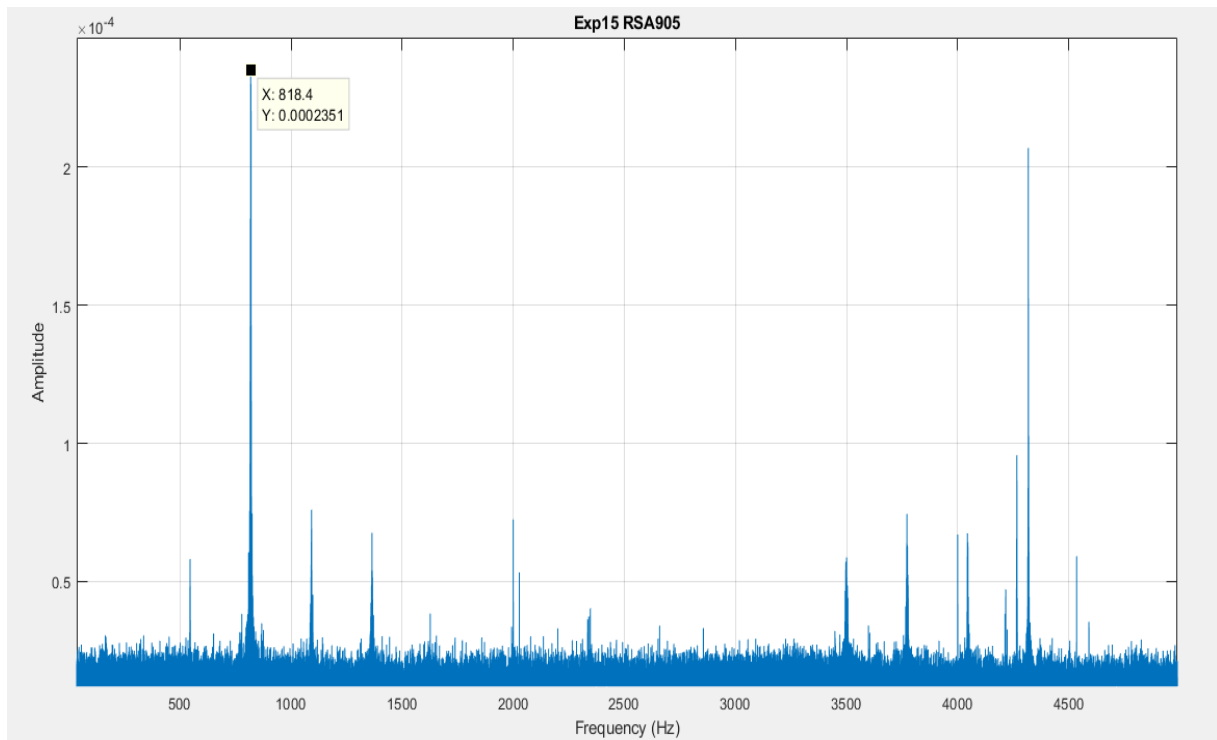


Figure 5.13: Frequency domain representation for experiment 15 feed rate = 15 mm/min, depth of cut = 5 μm , speed = 500 rpm

5.2.1 Acoustic Emission (AE) Analysis for RSA 905

Table 5.5 presents the acoustic emission data acquired during ultra-precision machining of RSA 905. Looking closely at raw data, among the three cutting parameters, it can be deduced that feed rates play the most significant role in the AE signal during machining. The effects of speed and depth of cut on applied force depends on the feed rate. Further statistical analysis revealed that a transformation is required for the AE raw data. Hence, an inverse transform is best suitable for the step wise regression analysis. Detailed statistical analysis on this data was presented in **Table 5.6**.

Table 5.5: Acoustic emission data for RSA 905

Run	V (rpm)	F (mm/min)	D (μm)	AE (v) $\times 10^{-3}$	1/AE (v^{-1})
Exp1	1750	25	25	3.0912	0.3235
Exp2	1750	25	5	3.1875	0.3137
Exp3	3000	5	15	3.2615	0.3066
Exp4	1750	15	15	2.4325	0.4111
Exp5	1750	15	15	2.4325	0.4111
Exp6	1750	5	25	1.2589	0.7943
Exp7	500	15	25	3.6105	0.2770
Exp8	3000	25	15	7.8113	0.1280
Exp9	3000	15	25	2.6945	0.3711
Exp10	500	25	15	5.8615	0.1706
Exp11	3000	15	5	2.9305	0.3412
Exp12	500	5	15	1.0999	0.9092
Exp13	1750	5	5	1.1599	0.8621
Exp14	1750	15	15	2.4325	0.4111
Exp15	500	15	5	2.3513	0.4253

5.2.2 Summary output for regression and ANOVA analysis of AE for RSA 905

Table 5.6: Regression and ANOVA analysis of AE for RSA 905

Regression Statistics						
Multiple R	0.926263					
R Square	0.857962					
Adj R Sq	0.779053					
Stdr Error	0.1112					
Observations	15					
ANOVA						
	df	SS	MS	F	Significance F	
Regression	5	0.672233	0.134447	10.87271	0.001319	
Residual	9	0.11129	0.012366			
Total	14	0.783522				
	Coefficients	Standard Error	t Stat	P-value	Lower 95%	Upper 95%
Intercept	1.0352	0.17659	5.862165	0.00024	0.635725	1.434674
v(rpm)	7.7E-05	0.000149	0.518518	0.616603	-0.00026	0.000413
f (mm/min)	-0.0438	0.008721	-5.02315	0.000716	-0.06353	-0.02408
d(μm)	-0.00221	0.003932	-0.56106	0.588453	-0.0111	0.006688
VF	1.12E-05	4.45E-06	2.517894	0.032882	1.14E-06	2.13E-05
V^2	-8.8E-08	3.68E-08	-2.39314	0.040349	-1.7E-07	-4.8E-09

From **Table 5.6**, the F-value of 0.001319 confirmed the model is highly significant at P-value of 0.00024 for intercept. P-values of depth of cut and feed rate show highest significance to the AE. which corroborate with predictions from cutting force model. Stepwise backward Regression analysis was carried out to further ascertain the validity of AE signal. The R^2 from ANOVA shows 0.8579, simply indicates that the model explains 85.79 per cent of the acoustic emission variability during the experiment. The most significant cutting parameter is feed rate that has a P-value of 0.000716 which contributed about 60.4% to the signal. The interaction effects between the speed and feed rate which is also significant at p-value of 0.03288 this effect contributed exactly by 10%. The effects of square of speed also contributed 9%. Meanwhile, from **Table 5.6**, speed and depth of cut made a total contribution of 1% and 7% respectively. However, the model equation revealed that speed contributes positive effect to signal acquired but both feed rate and depth of cut contribute negative effects. **Figures 5.14 and Figure 5.15** show the scattered plot and comparison between measured and predicted values for this experiment which further validate the

model standard. Equation 5.3 represent the acoustic emission model generated for the experiment conducted on RSA 905 is:

Equation 5.3

$$AE = (1.03 + 7.7 \times 10^{-5}V - 0.0438F - 2.21 \times 10^{-3}D + 0.0000112VF - 8.8 \times 10^{-8}v^2)^{-1}$$

Where v is the speed (rpm), f is the feed rate in (mm/min) and d is the depth of cut in (μm)

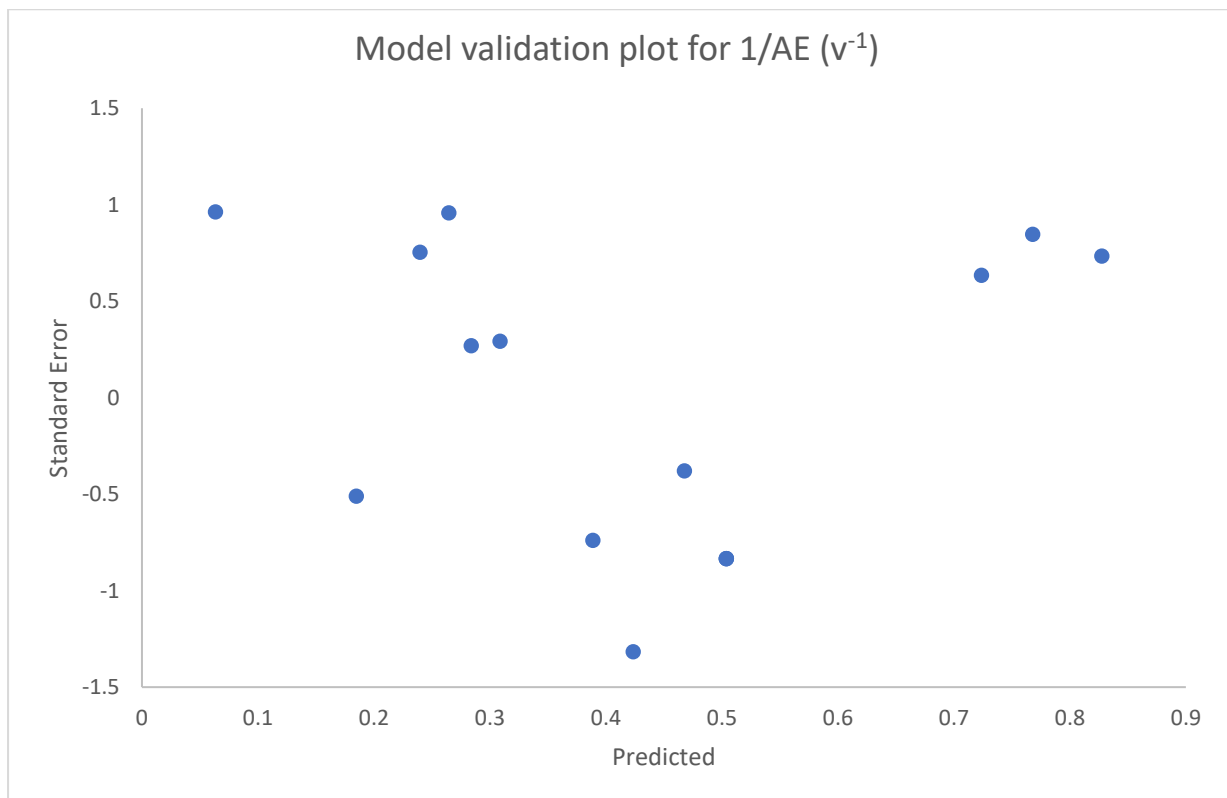


Figure 5.14: Validation plot for acoustic emission model on RSA 905

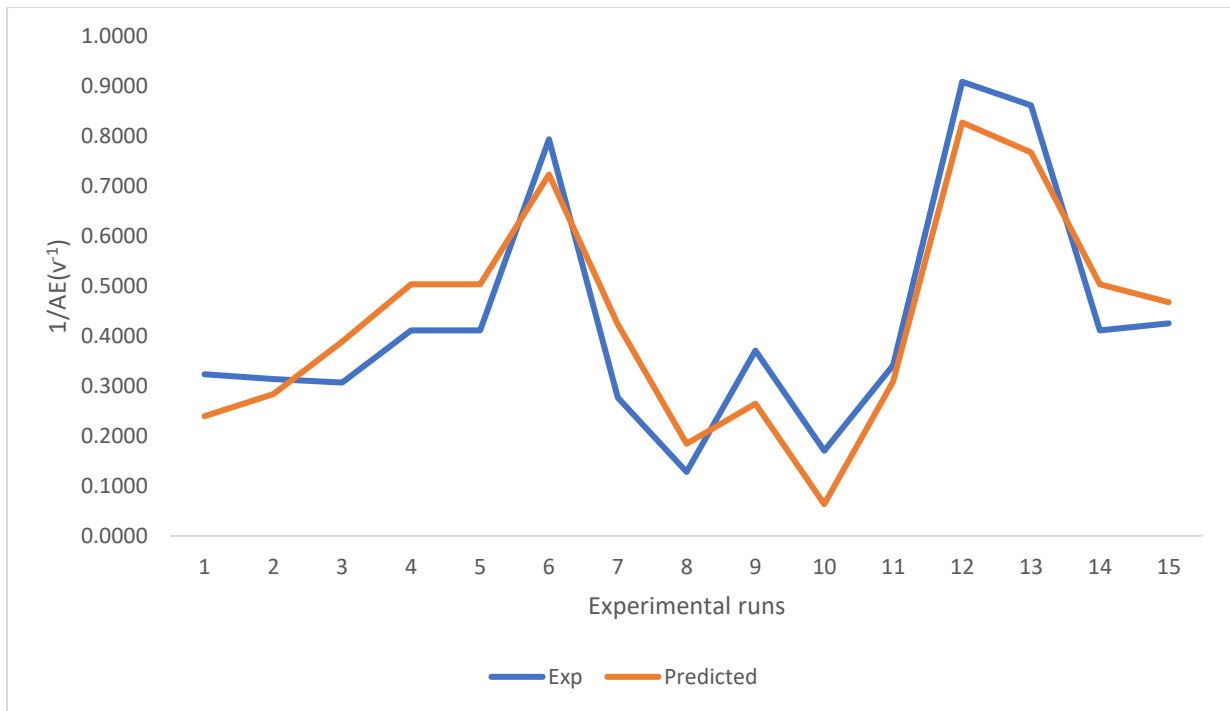


Figure 5.15: Comparison between experimental acoustic emission value and the predicted value

Figures 5.16 – 5.18 represent the interaction between feed rate and speed. At a high feed rate and high speed, there is a projection that a convergence of interaction between the two cutting parameters which may result in low inverse of acoustic emission being experienced during machining. **Figure 5.16** gave a clearer situation of the effects of this cutting parameter on RSA 906, it was observed that at high feed and low speed, the signal of the acoustic emission became very high. This could indicate an effect on surface of the machined part or result in cutting tool damage.

Design-Expert® Software
Transformed Scale
1/(AErms)

◆ Design Points

■ A- 5.000
▲ A+ 25.000

X1 = C: Speed
X2 = A: Feed

Actual Factor
B: Depth of cut = 15.00

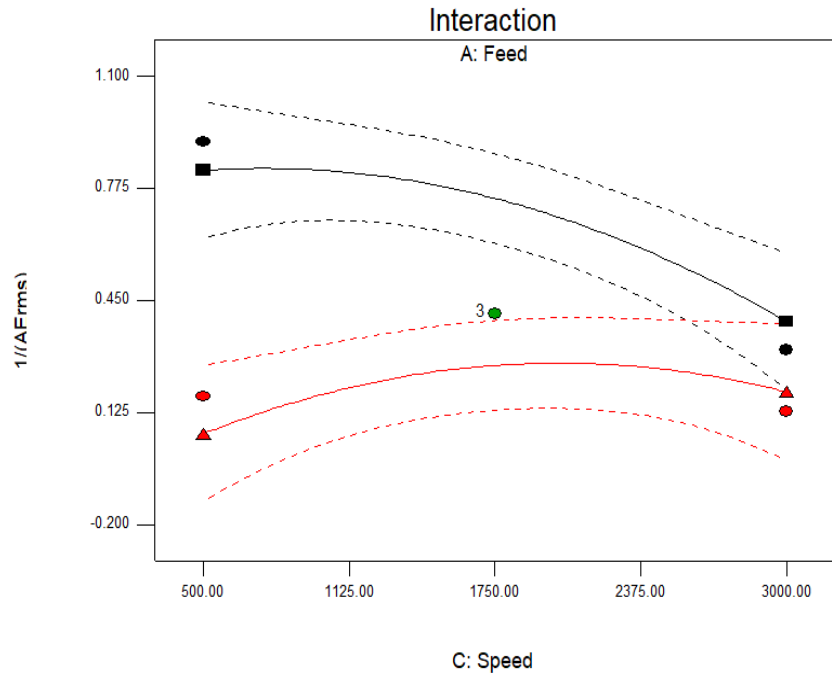


Figure 5.16: Interaction plot between speed and feed rate on inverse of AE

Design-Expert® Software
Transformed Scale
1/(AErms)

◆ Design points above predicted value
○ Design points below predicted value

0.12802
0.909174

X1 = A: Feed
X2 = C: Speed

Actual Factor
B: Depth of cut = 15.00

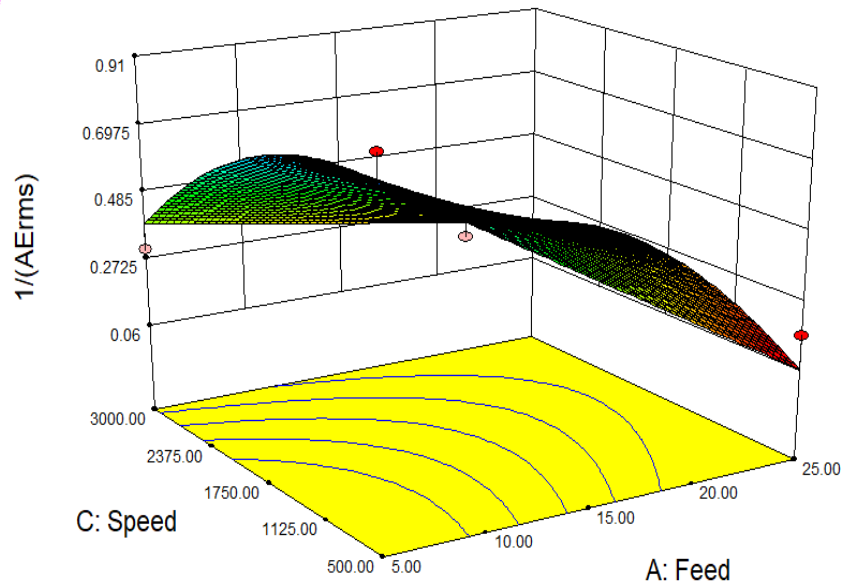


Figure 5.17: 3D plot between feed rate and speed on inverse of AE

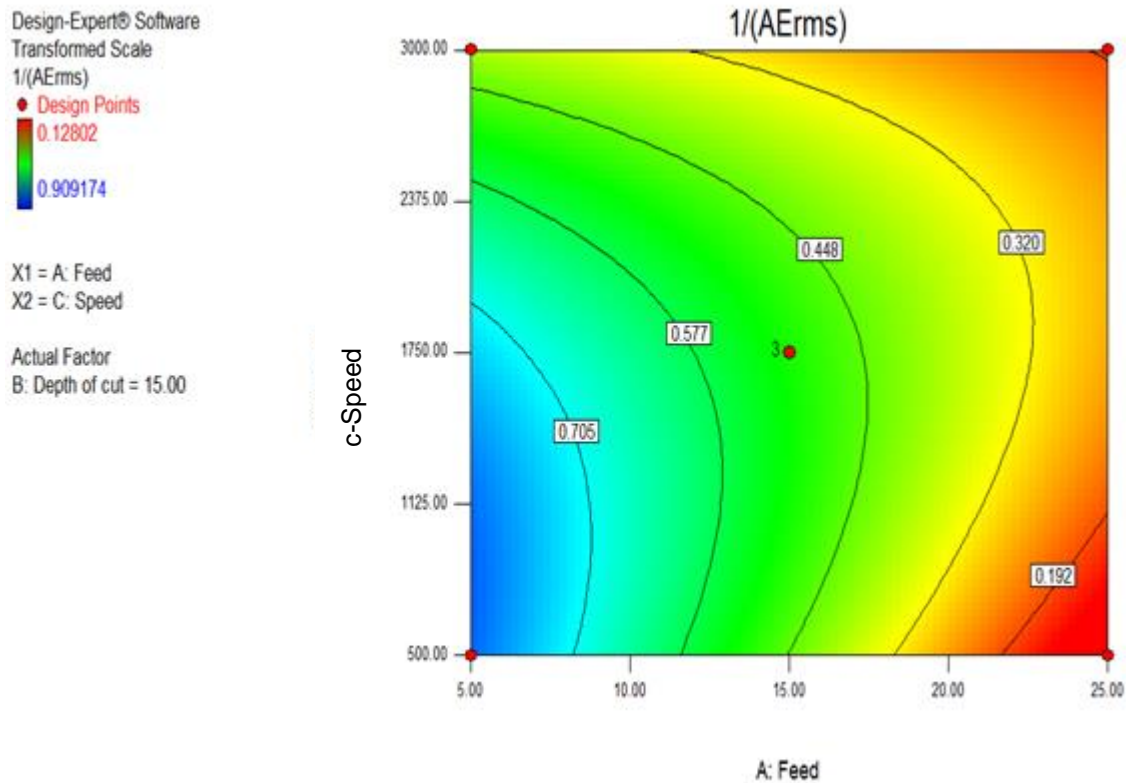


Figure 5.18: Shows 2D effect of speed and feed rate on the inverse of AE acquired during machining of RSA 905

5.2.3 Profile plot for acoustic emission of RSA905

Profile plot was thoroughly examined on the effects of each parameter on AE of RSA 905. **Figures 5.19 – 5.21** show the effects of speed at various machining conditions for feed rate and depth of cut. However, at low feed 5 mm/min, depth of cut 5 mm and low speed, a high inverse of AE was recorded. But at high cutting conditions of feed at 25 mm/min, depth of cut at 25 μ m and same low cutting condition for speed, a low inverse of AE was observed. Overall, looking at the profile plots, the higher the speed the lower the inverse of AE observed becomes. Meanwhile, the most significant cutting parameter during acoustic emission of RSA 905 is feed rate. At low cutting parameters, high inverse of AE was recorded. It can also be seen that the higher the feed rates, speed, and depth of cut, the lower the inverse of AE. However, it can also mean that the higher the feed rates, the lower the inverse of AE. This confirms the statistical model generated for the experiment. As earlier deduced from the model, depth of cut has very low significance in this experiment the profile plot for depth of cut looks seemly parallel as can be seen in **Figure 5.21**.

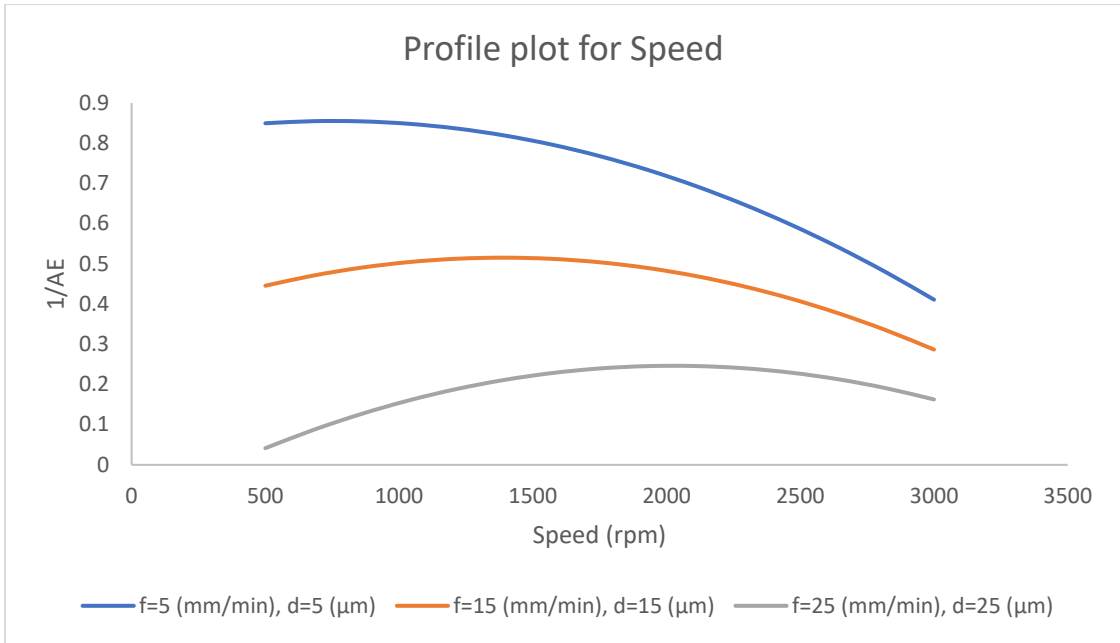


Figure 5.19: Profile plot for speed against inverse of AE

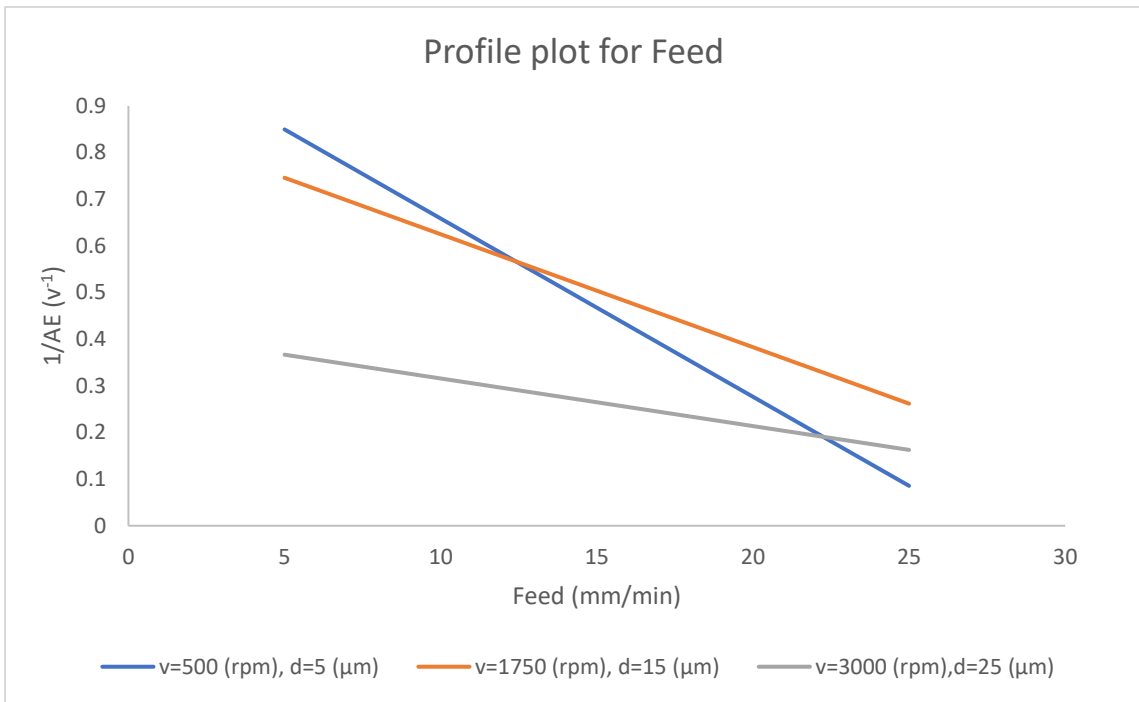


Figure 5.20: Profile plot for feed rate against inverse of AE

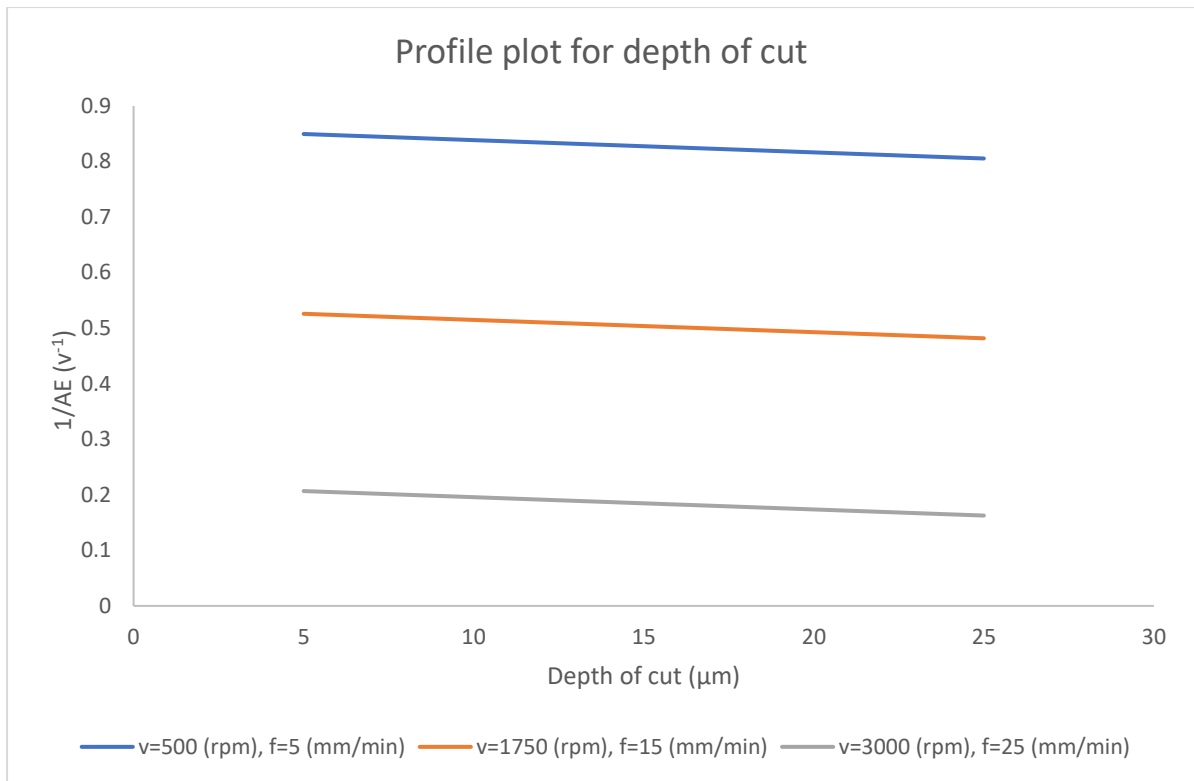


Figure 5.21: Profile plot for depth of cut against inverse of AE

CHAPTER 6

DIAMOND TURNING OF RAPIDLY SOLIDIFIED ALUMINIUM (RSA) ALLOY 443

6.1 INTRODUCTION

This chapter presents diamond turning of RSA 443 alloy. which is a commercially available alloy. It has a high silicon content about 40% with high thermal and mechanical properties. During the diamond turning, the SSCFTH and AE were used to monitor machining process. The data captured were analytically and statically processed to see any trend and effect of cutting parameters. Cutting force features were characterized while amplitude of filtered signal in frequency domain of acoustic emission was careful examined. Regression analysis and ANOVA on both cutting force and AE were conducted. Cutting models, profile plots, 2D & 3D contours and machining optimization were presented.

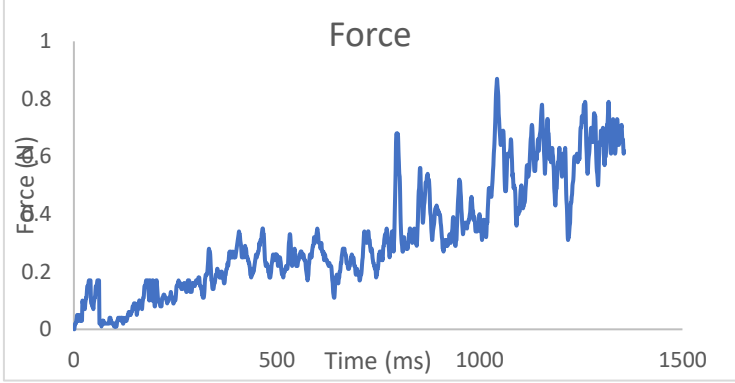
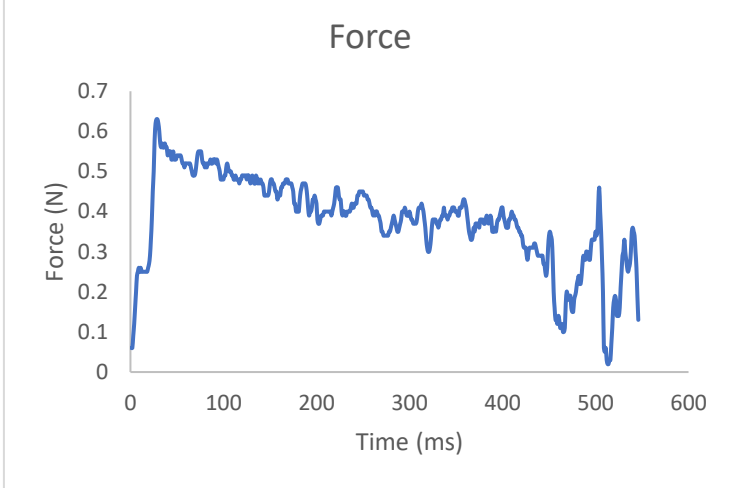
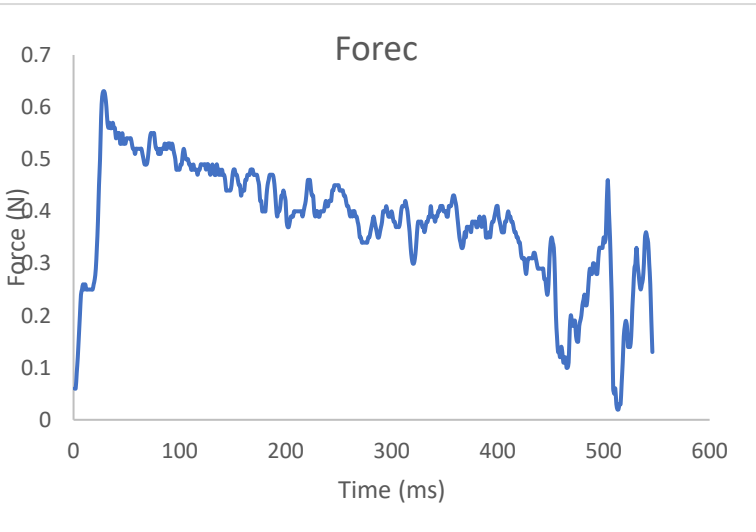
6.2 CUTTING FORCE ANALYSIS ON RSA 443

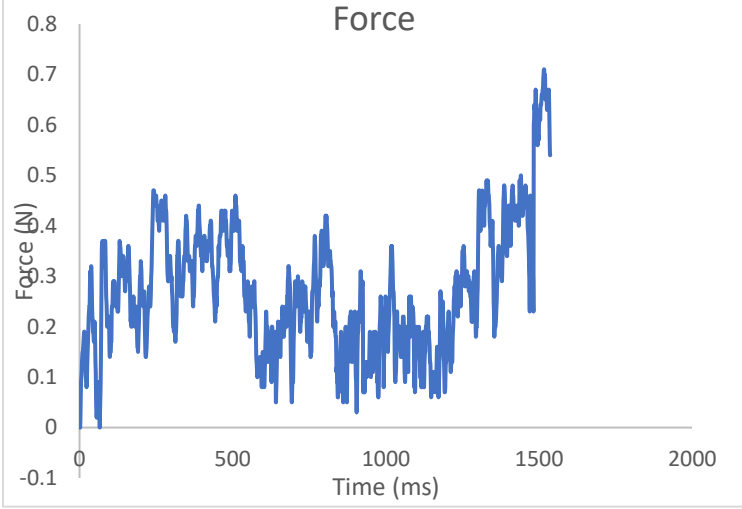
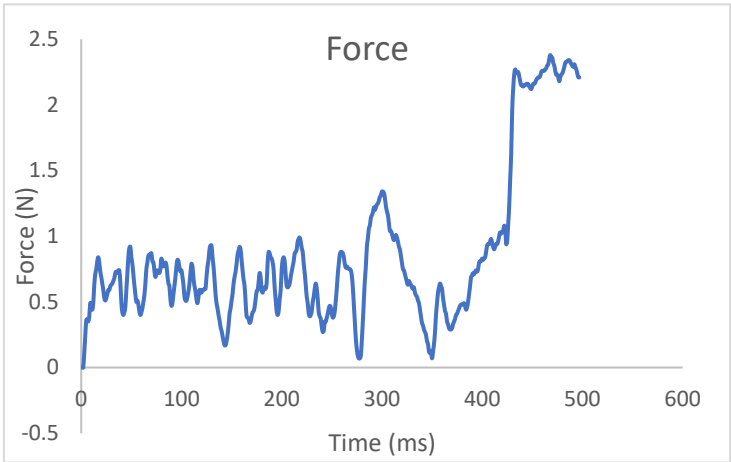
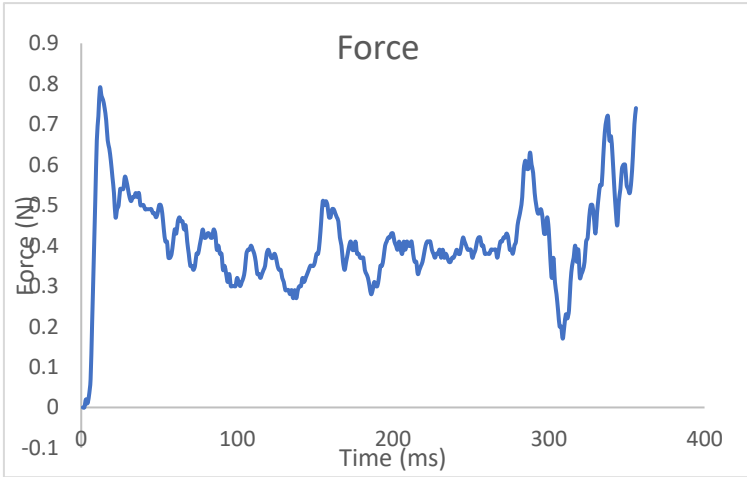
Table 6.1 represents cutting forces acquired during machining of RSA 443. This material has a refined grain structure hence an improved mechanical and thermal properties due to high composition of silicon in the alloy. This material has replaced traditional AA443 materials for manufacturing of mould inserts and precision equipment also can be used in the manufacture of radio frequency (RF) applications and some other optical components. **Table 6.1** generally, an average cutting force required to machine RSA 443 is low, we have some exceptional cases where the cutting force is around 2N. This is seen in experiment 7, where the speed is very low at 500 rpm. Hence, it will require high cutting force to break the silicon atoms in the alloy. Also, high depth of cut is associated with high cutting forces during machining process. But looking closely at the cutting force characterization of RSA 443 during machining, it appears that the feed rate is sensitive to the cutting force than the rest of cutting parameters at the engagement of cutting tool. At low feed rate of 5 mm/min (Exp 3), low cutting force is associated with the starting of cut. But at high feed rate of 25 mm/min, high force is recorded at the engagement. This can be explained by the hardness property of this newly graded aluminium alloy due to high content of silicon.

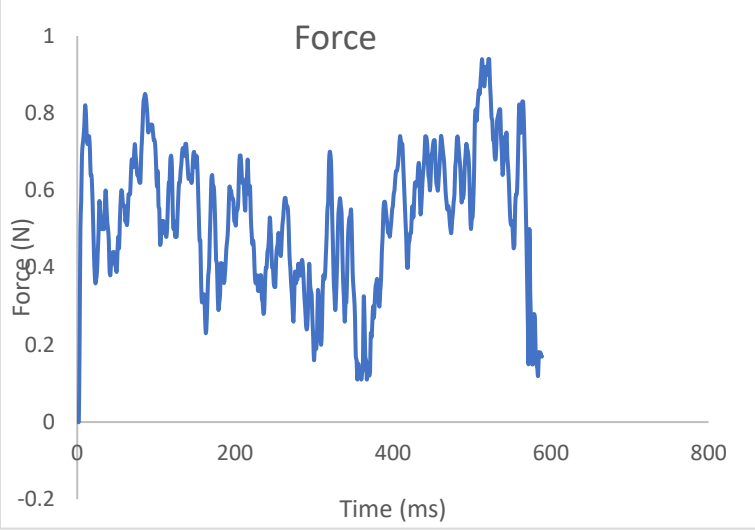
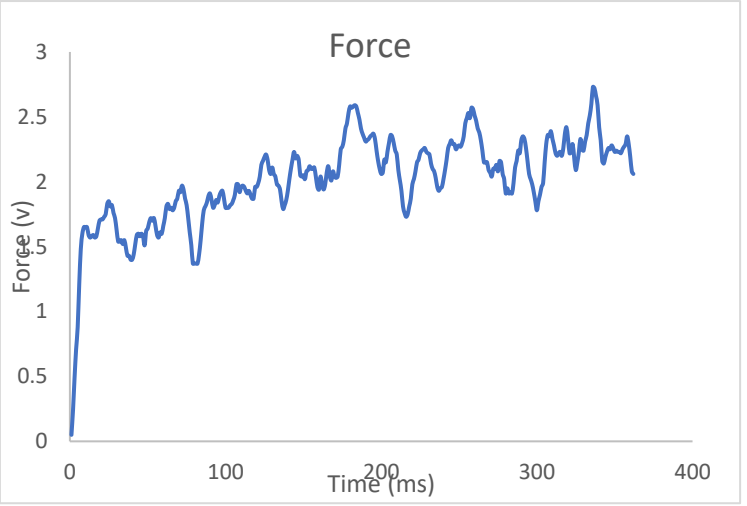
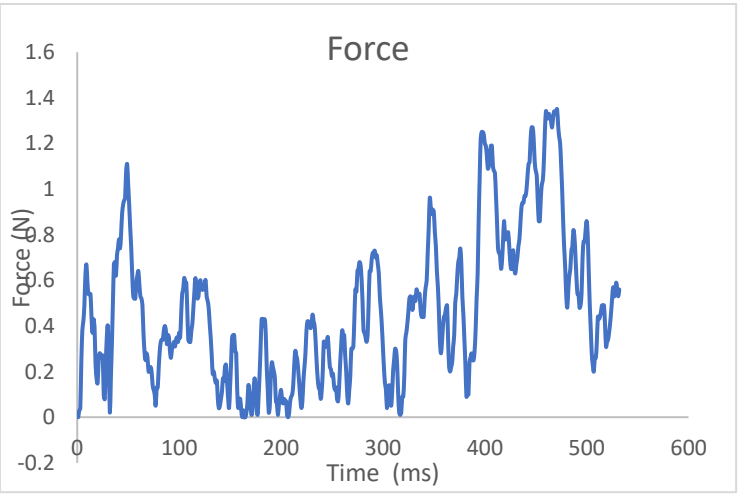
6.3 GRAPHICAL REPRESENTATION OF CUTTING FORCE CHARACTERISTICS DURING MACHINING OF RSA 443

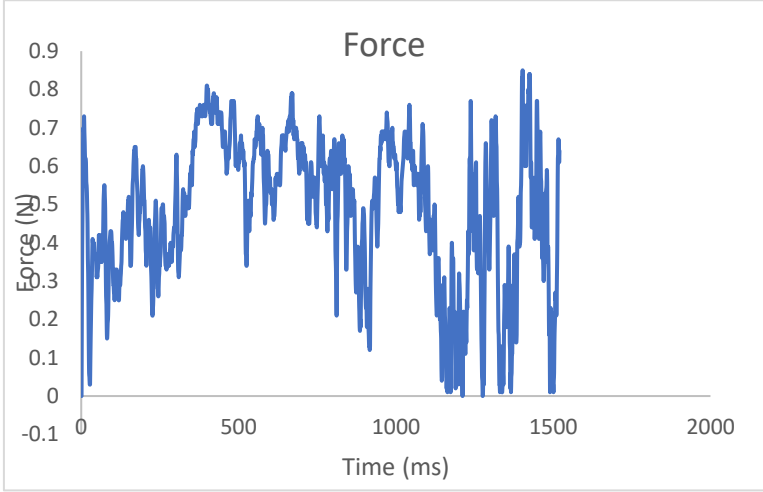
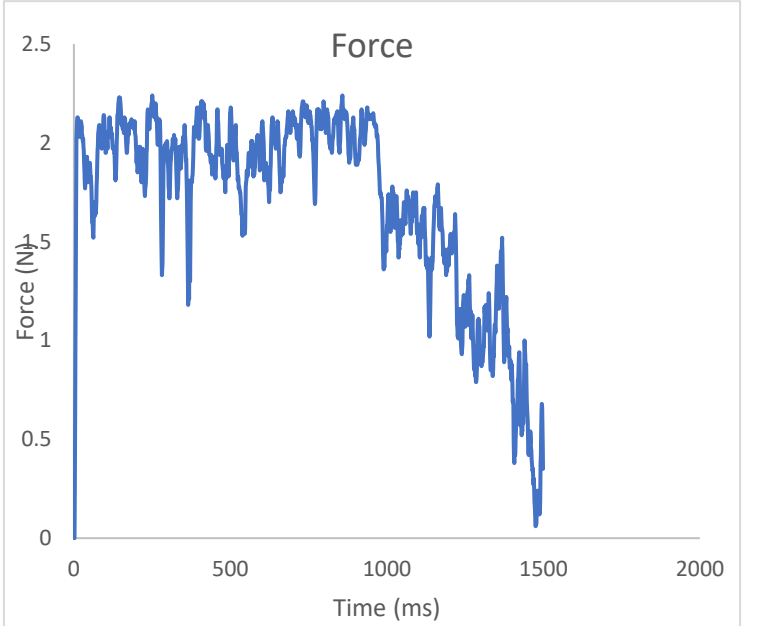
Table 6.1: Cutting force description for RSA 443

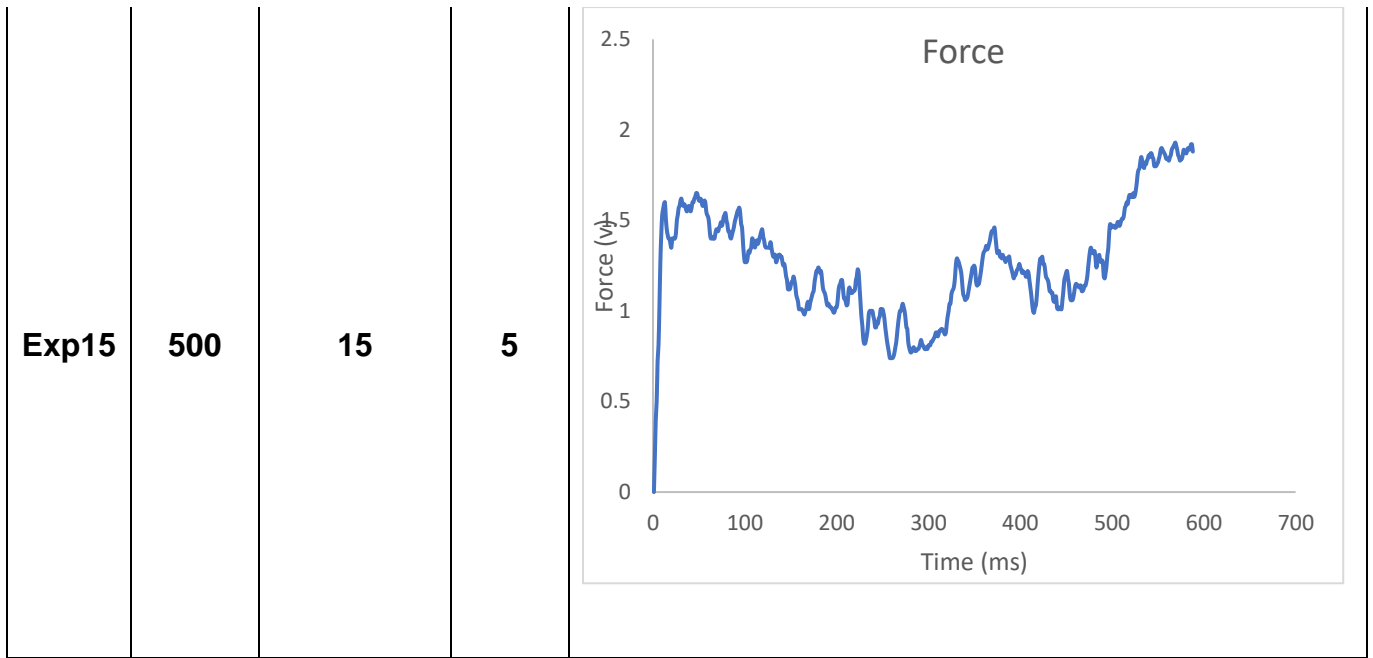
Run	V (rpm)	F (mm/min)	D (μm)	Force characteristics
Exp1	1750	25	25	<p>The graph for Exp1 shows a highly oscillatory cutting force signal. The force starts at 0 N at 0 ms, rises to about 0.2 N by 20 ms, and then continues to fluctuate with several peaks reaching up to 0.45 N, notably around 100 ms, 150 ms, and 250 ms. The signal ends at approximately 300 ms.</p>
Exp2	1750	25	5	<p>The graph for Exp2 shows a cutting force signal with significantly lower amplitude than Exp1. The force starts at 0 N at 0 ms and quickly stabilizes between 0.1 N and 0.2 N. The signal is highly oscillatory, with peaks reaching up to 0.2 N and troughs dipping to about 0.1 N. The signal ends at approximately 250 ms.</p>

<p>Exp3</p>	<p>3000</p>	<p>5</p>	<p>15</p>	
<p>Exp4</p>	<p>1750</p>	<p>15</p>	<p>15</p>	
<p>Exp5</p>	<p>1750</p>	<p>15</p>	<p>15</p>	

<p>Exp6</p>	<p>1750</p>	<p>5</p>	<p>25</p>	
<p>Exp7</p>	<p>500</p>	<p>15</p>	<p>25</p>	
<p>Exp8</p>	<p>3000</p>	<p>25</p>	<p>15</p>	

Exp9	3000	15	25	
Exp10	500	25	15	
Exp11	3000	15	5	

Exp12	500	5	15	
Exp13	1750	5	5	
Exp14	1750	15	15	Same as Experiment 4 and 5



During statistical analysis, it was discovered that a transformation is required for the raw data acquired for cutting force. Hence, a square root transformation is best suitable for the step wise regression analysis because it has the highest significant results. Detailed statistical analysis on this data **Table 6.2** were analyzed in **Table 6.3**.

Table 6.2: Experimental forces acquired for RSA 443

Run	V (rpm)	F (mm/min)	D (μm)	Vd (mm μm /min)	F ² (mm/min) ²	D ² (μm) ²	F(N)	SQRTF(N)
Exp1	1750	25	25	43750	625	625	0.6912	0.831384
Exp2	1750	25	5	8750	625	25	0.1373	0.37054
Exp3	3000	5	15	45000	25	225	0.0232	0.152315
Exp4	1750	15	15	26250	225	225	1.2121	1.100954
Exp5	1750	15	15	26250	225	225	1.2121	1.100954
Exp6	1750	5	25	43750	25	625	0.1436	0.378946
Exp7	500	15	25	12500	225	625	2.9131	1.706781
Exp8	3000	25	15	45000	625	225	0.2566	0.506557
Exp9	3000	15	25	75000	225	625	0.3716	0.60959
Exp10	500	25	15	7500	625	225	1.1120	1.054514
Exp11	3000	15	5	15000	225	25	0.3102	0.556956
Exp12	500	5	15	7500	25	225	0.3167	0.562761
Exp13	1750	5	5	8750	25	25	0.0500	0.223607
Exp14	1750	15	15	26250	225	225	1.2121	1.100954
Exp15	500	15	5	2500	225	25	0.0832	0.288444

6.4 STATISTICAL ANALYSIS FOR CUTTING FORCES ACQUIRED DURING MACHINING OF RSA 443

Table 6.3: Regression and ANOVA output summary for cutting forces of RSA 443

SUMMARY OUTPUT						
Regression Statistics						
Multiple R	0.968468					
R Square	0.937929					
Adj R Square	0.891376					
Stand Error	0.142889					
Observations	15					
ANOVA						
	df	SS	MS	F	Significance F	
Regression	6	2.468163	0.411361	20.14759	0.000201	
Residual	8	0.163339	0.020417			
Total	14	2.631502				
	Coefficients	Standard Error	t Stat	P-value	Lower 95%	Upper 95%
Intercept	-1.4537	0.273991	-5.30566	0.000723	-2.08553	-0.82188
v(rpm)	0.000231	9.48E-05	2.437198	0.040742	1.24E-05	0.00045
f (mm/min)	0.146531	0.022809	6.424263	0.000204	0.093933	0.199129
d(μ m)	0.135931	0.024906	5.457827	0.000603	0.078498	0.193364
vd	-2.7E-05	5.72E-06	-4.77888	0.001393	-4E-05	-1.4E-05
f^2	-0.00428	0.000741	-5.77561	0.000417	-0.00599	-0.00257
d^2	-0.00207	0.000741	-2.78935	0.023582	-0.00378	-0.00036

Regression analysis in **Table 6.3** shows F-value of 0.000201 confirmed the model is highly significant at p value of 0.00073 for intercept. The p-values of feed rate, speed, and depth of cut show significant contributions to the cutting force. To further assess the validity of the cutting force, stepwise backward regression analysis was performed. The R^2 from regression analysis shows 0.93799 which simply indicates that the model explains 93.79% variation of cutting force has been explained by cutting parameters in the experiment making the model a good fit. In this model, the most significant cutting parameters are feed rate that has a p-value of 0.000204 which contributed highest percentage effect.

Depth of cut as earlier noticed made a significant contribution at p-value of 0.000603 followed by speed with a p-value of 0.040704. The author saw interaction effects

between the speed and depth of cut which is significant to cutting force at p-value of 0.001393. This effect is a negative slope which means that an overall force is expected to decrease by a unit value of 0.000025 while other corresponding independent variable such as feed is kept constant. However, the model equation revealed that Feed rates contributes positive effect to square root of cutting force. **Figure 6.1** shows the scattered plot for this experiment which further validate the model standard. The model generated for the experimented conducted for RSA 443 is:

$$(F) = (-1.45 + 2.31 \times 10^{-4}V + 0.146F + 0.136 D - 2.7 \times 10^{-5} VD - 4.28 \times 10^{-3}F^2 - 2.07 \times 10^{-3}D^2)^{\frac{1}{2}}$$

Where V is the speed in rpm, F is feed rate in mm/min and D is the depth of cut in μm and Force (F) is the cutting force in Newton

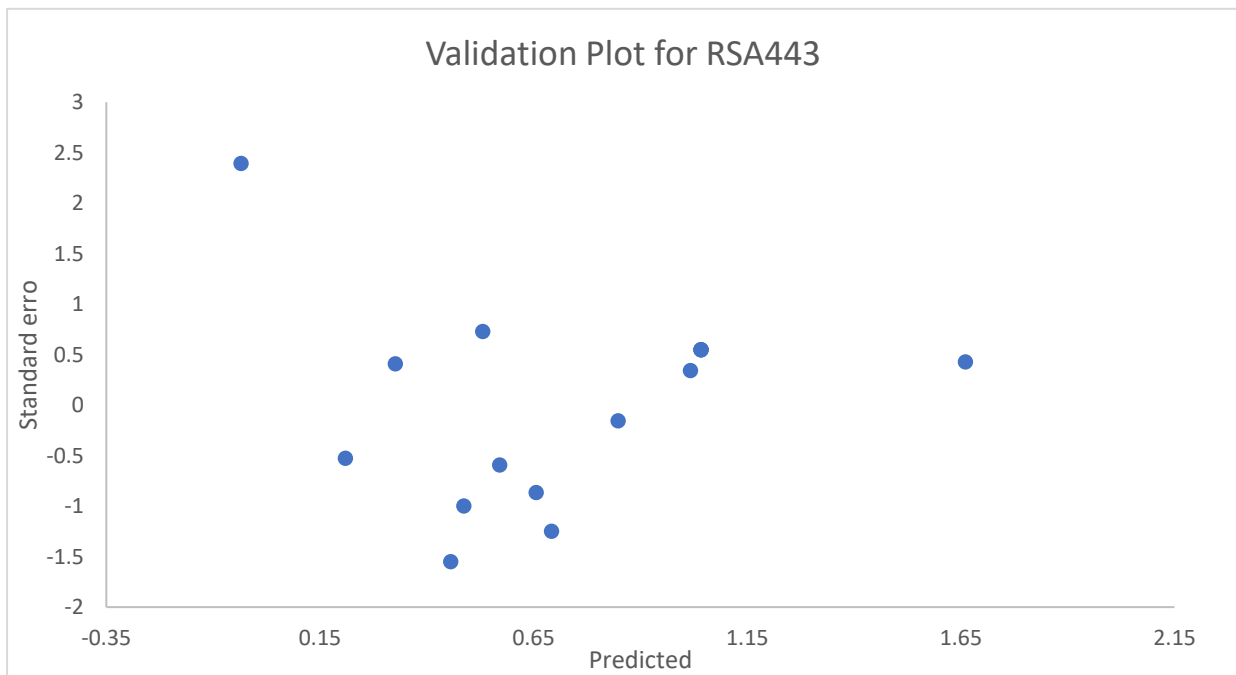


Figure 6.1: Validation plot for cutting force from the model on RSA 443

Figure 6.2 presented comparison between measured and predicted values of cutting force. **Figure 6.3** presented an interaction effect as earlier witnessed. it reveals that at low speed and depth of cut with constant feed at 15 mm/min, the square root of cutting force was low at first and later became very high as Depth of cut increases while Speed remains low. However, an increase in Depth of cut with an increased speed at 3000

rpm, the square root of force remains low. **Figure 6.4** is a 2D plot and **Figure 6.5** is a 3D plot. they present the same responses for cutting forces.

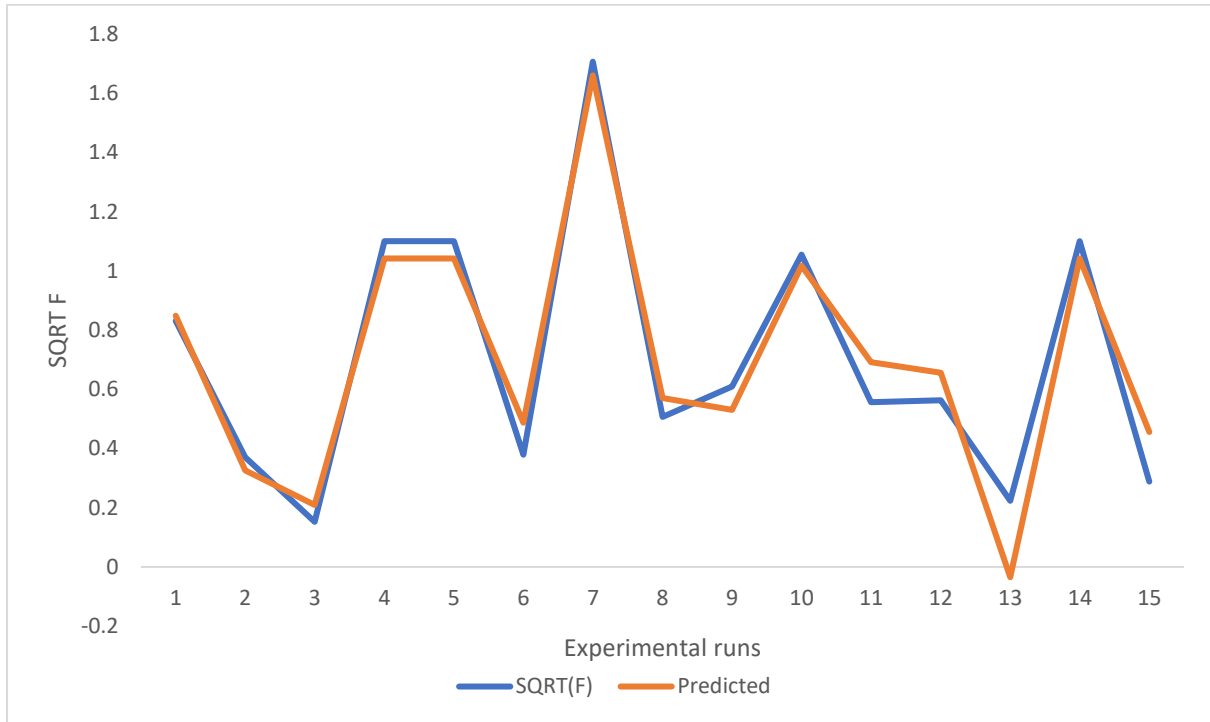


Figure 6.2: Comparison between experimental value and predicted value for cutting force on RSA 443

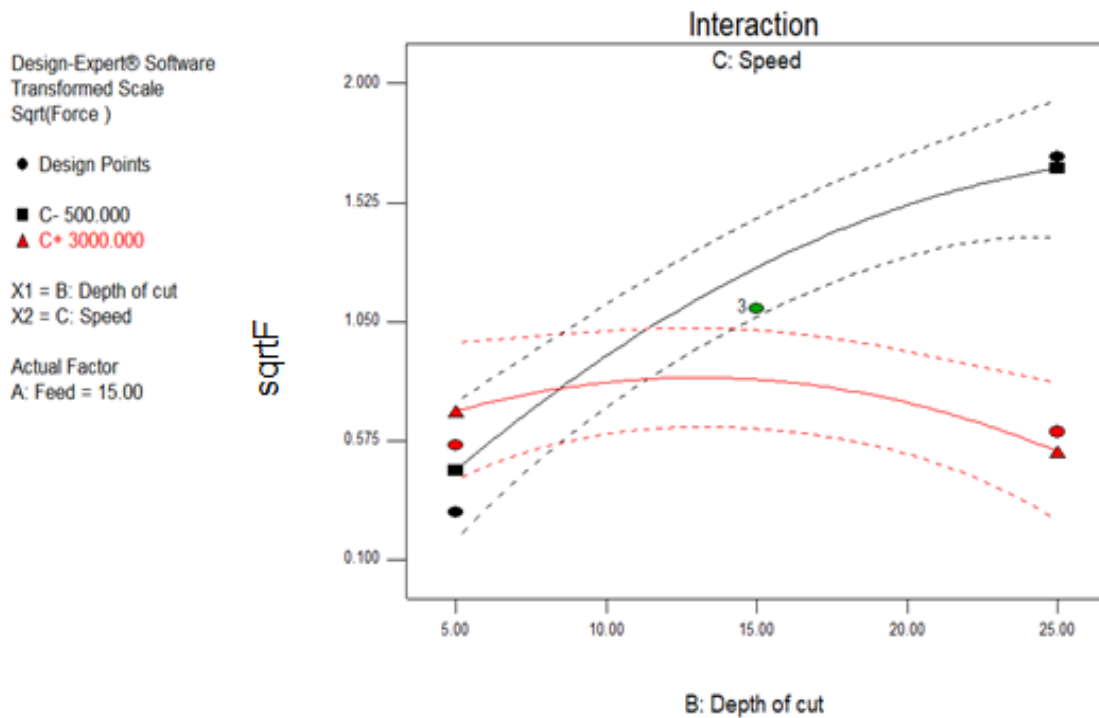


Figure 6.3: Interaction plot between cutting speed and depth of cut

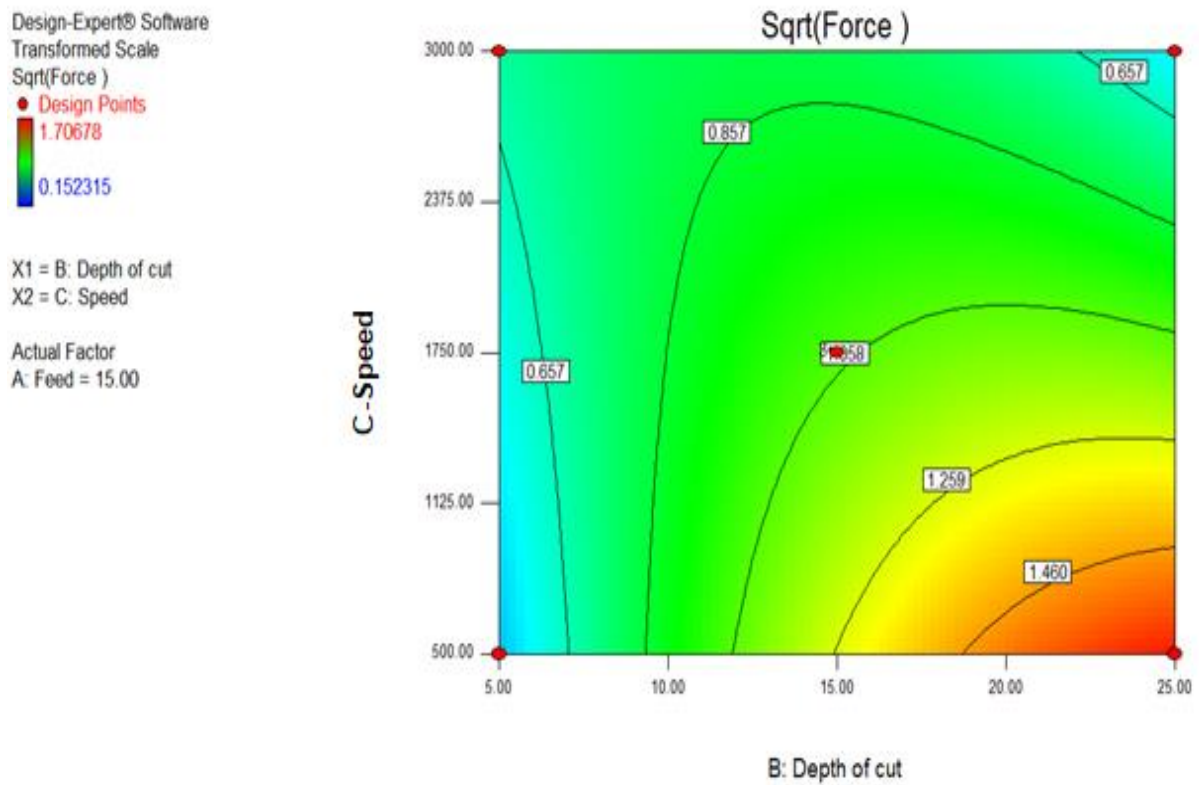


Figure 6.4: 2D plot for depth of cut and speed

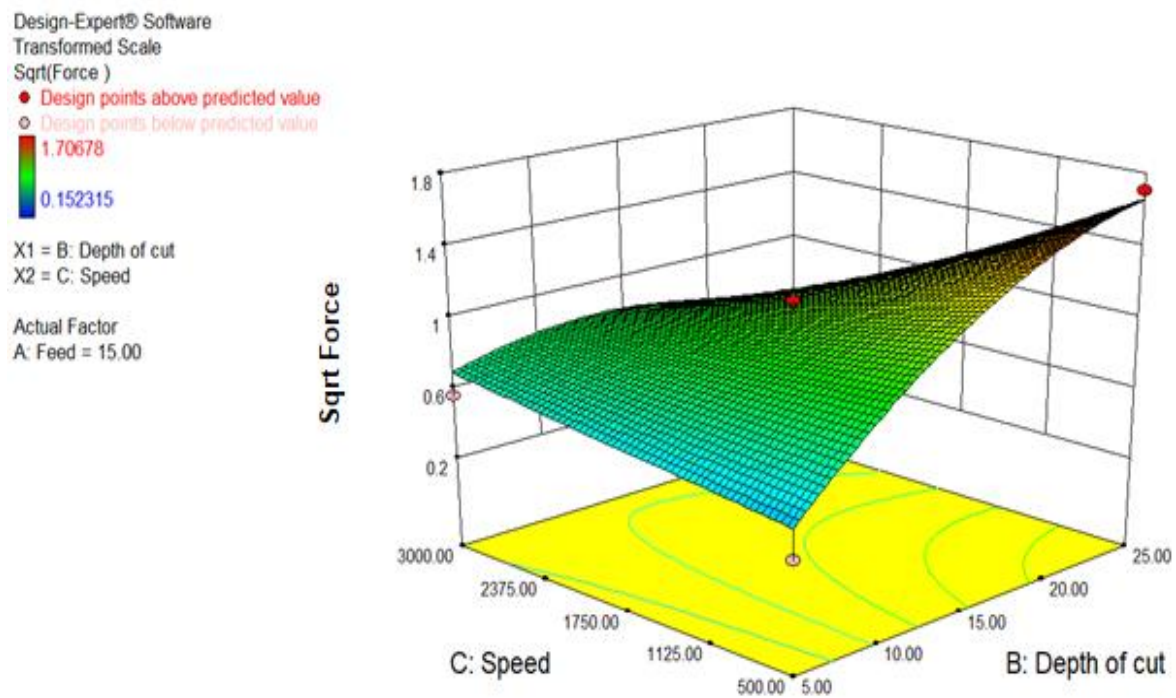


Figure 6.5: 3D plot between cutting speed and depth of cut

6.5 PROFILE PLOT OF CUTTING FORCES FOR RSA443

Profile plots in **Figures 6.6 – 6.8**, show the effect of one independent parameter on the response (cutting force) while other independent parameters are kept constant. Looking closely at **Figure 6.6**, an increase in speed at low feed rates =5 mm/min and low depth of cut = 5 μm , there is a steady increase in the square root of cutting force even though this effect is directly proportional to square root of cutting force. This could be because of increase in vibration due to increase in speed but at low feed rate. However, in generally, an increase in cutting speed will lead to a decrease in cutting force [384]. **Figure 6.7** shows the effect of feed rate on cutting force. Usually, it is expected that an increase in feed rate will cause increase in cutting force. **Figure 6.8** shows variation of depth of cut against cutting force.

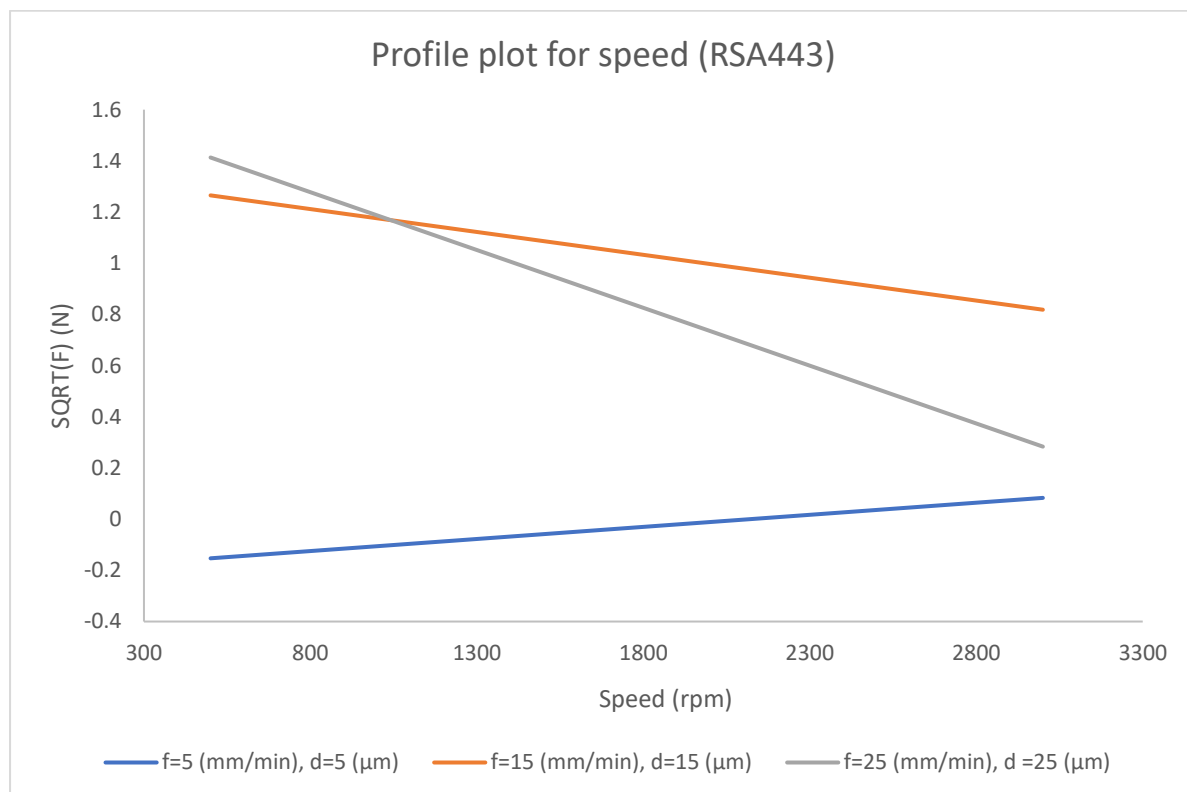


Figure 6.6: Effect of speed on cutting force during diamond turning of RSA 443

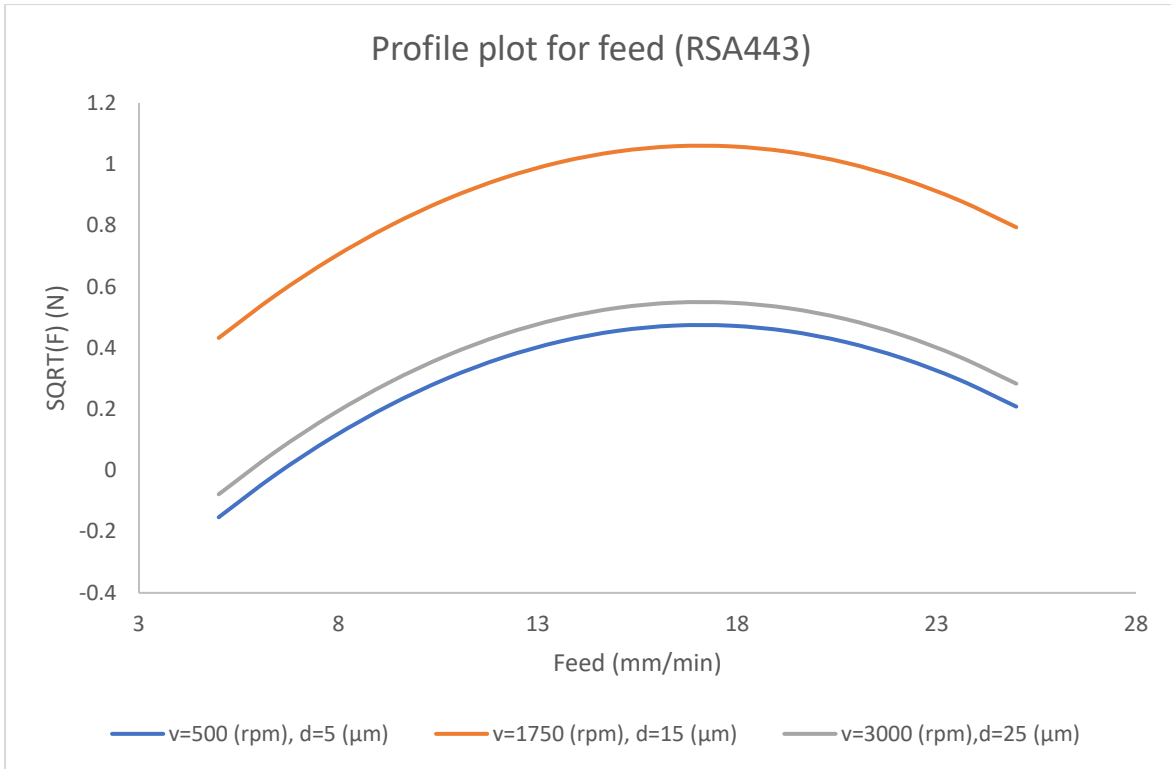


Figure 6.7: Effect of feed rate on cutting force during diamond turning of RSA 443

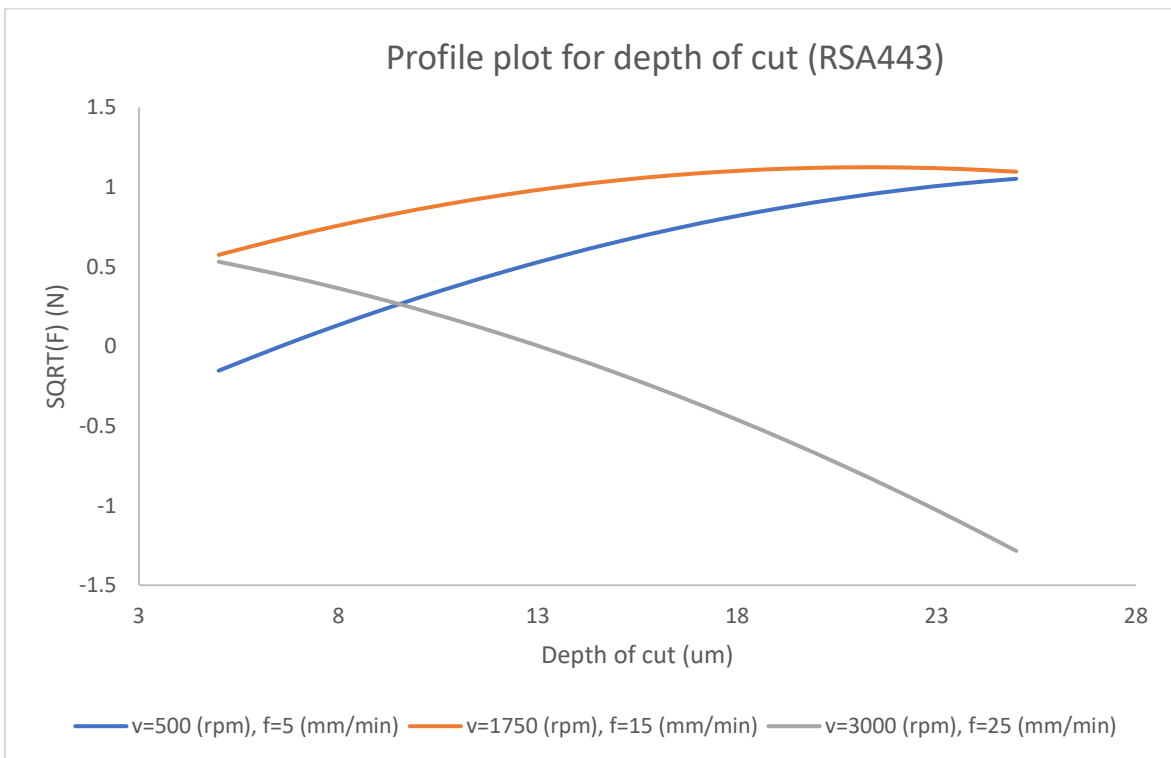


Figure 6.8: Effect of depth of cut on cutting force during diamond turning of RSA 443

6.6 OPTIMIZATION OF CUTTING PARAMETERS FOR FORCE DURING MACHINING PROCESS

Table 6.4 presents the results of an optimized analysis of the acquired data. The maximum cutting force is 2.82 N on the condition that at speed = 500rpm, feed rate = 17mm / min and cutting depth = 25 μm . This is close to **Table 6.2** of experiment 7. According to the data acquired, however, the minimum cutting force expected is 0.043N at speed = 500 rpm, feed rate = 25 mm / min and depth of cut = 5 μm . In **Table 6.4**, this prediction is similar to experiment 15.

Table 6.4: Optimization conditions for cutting force of RSA 443

	v(rpm)	f (mm/min)	d(μm)	Predicted Sqrt F(N)	Actual force (N)
Max	500	17.10959	25	1.67965	2.819
Min	500	25	5	0.208411	0.043

6.7 AE ANALYSIS FOR RSA 443

Table 6.5 shows AE Signal acquired during diamond turning of RSA 443. The responses (AE) from the effects of cutting parameters (speed, feed rate and depth of cut) on RSA 443 were recorded in volts. During statistical analysis **Table 6.6**, it was discovered that a transformation is required for the AE raw data acquired. Hence, an inverse transform is identified for the analysis.

Table 6.5: Experimental AE acquired for RSA 443

Run	V (rpm)	F (mm/min)	D (μm)	AE(v)	1/AE (v^{-1})
Exp1	1750	25	25	3.1178	0.320739
Exp2	1750	25	5	2.0867	0.479226
Exp3	3000	5	15	6.0290	0.165865
Exp4	1750	15	15	2.4318	0.411218
Exp5	1750	15	15	2.4318	0.411218
Exp6	1750	5	25	1.6269	0.614666
Exp7	500	15	25	2.3955	0.417449
Exp8	3000	25	15	3.5393	0.282542
Exp9	3000	15	25	2.8438	0.351642
Exp10	500	25	15	3.4645	0.288642
Exp11	3000	15	5	2.4520	0.40783
Exp12	500	5	15	6.5191	0.153395
Exp13	1750	5	5	2.4792	0.403356
Exp14	1750	15	15	2.4318	0.411218
Exp15	500	15	5	2.1618	0.462577

6.8 STATISTICAL ANALYSIS FOR AE ACQUIRED DURING MACHINING OF RSA 443

Table 6.6: Regression and ANOVA output for AE of RSA 443

Regression Statistics						
Multiple R	0.912659					
R Square	0.832946					
Adj R Sqr	0.665891					
Stdr Error	0.068359					
Observations	15					
ANOVA						
	df	SS	MS	F	Significance F	
Regression	7	0.163098	0.0233	4.986076	0.025116	
Residual	7	0.032711	0.004673			
Total	14	0.195808				
	Coefficients	Standard Error	t Stat	P-value	Lower 95%	Upper 95%
Intercept	0.094745	0.146839	0.645228	0.539344	-0.25248	0.441965
v(rpm)	0.00025	8.2E-05	3.046302	0.01868	5.59E-05	0.000444
f (mm/min)	0.035888	0.012084	2.969853	0.020812	0.007314	0.064463
d(μm)	-0.02132	0.012084	-1.76429	0.121042	-0.04989	0.007255
fd	-0.00092	0.000342	-2.70482	0.030426	-0.00173	-0.00012
v ²	-7.5E-08	2.28E-08	-3.27798	0.013525	-1.3E-07	-2.1E-08
f ²	-0.00072	0.000356	-2.02368	0.08268	-0.00156	0.000121
d ²	0.001153	0.000356	3.24022	0.014249	0.000311	0.001994

According to summary output of the regression analysis, the ANOVA Table 6.6 shows speed had the most influence on the AE followed by feed rate. R² from ANOVA shows 0.8329 this simply indicates the model explains 83.29% of variability of the inverse AE is explained. The most influential parameter (spindle speed) has a p-value of 0.01868. **Figure 6.9** shows scattered plot for the experiment which further validate the model equation. **Figure 6.10** also shows a plot between acquired AE signal and predicted AE signal. **Equation 6.1** represents the model generated for the experiment conducted on RSA 443:

Equation 6.1

$$\begin{aligned}
 AE = & (9.4 \times 10^{-2} + 2.5 \times 10^{-4}V + 3.5 \times 10^{-2}F - 2.1 \times 10^{-2}D - 9.2 \times 10^{-4}FD \\
 & - 7.5 \times 10^{-7} V^2 - 7.2 \times 10^{-4}F^2 \\
 & + 1.2 \times 10^{-3}D^2)^{\frac{1}{2}}
 \end{aligned}$$

Where V is the speed in rpm, F is feed rate in mm/min and D is the depth of cut in μm and AE is acoustic emission in volts.

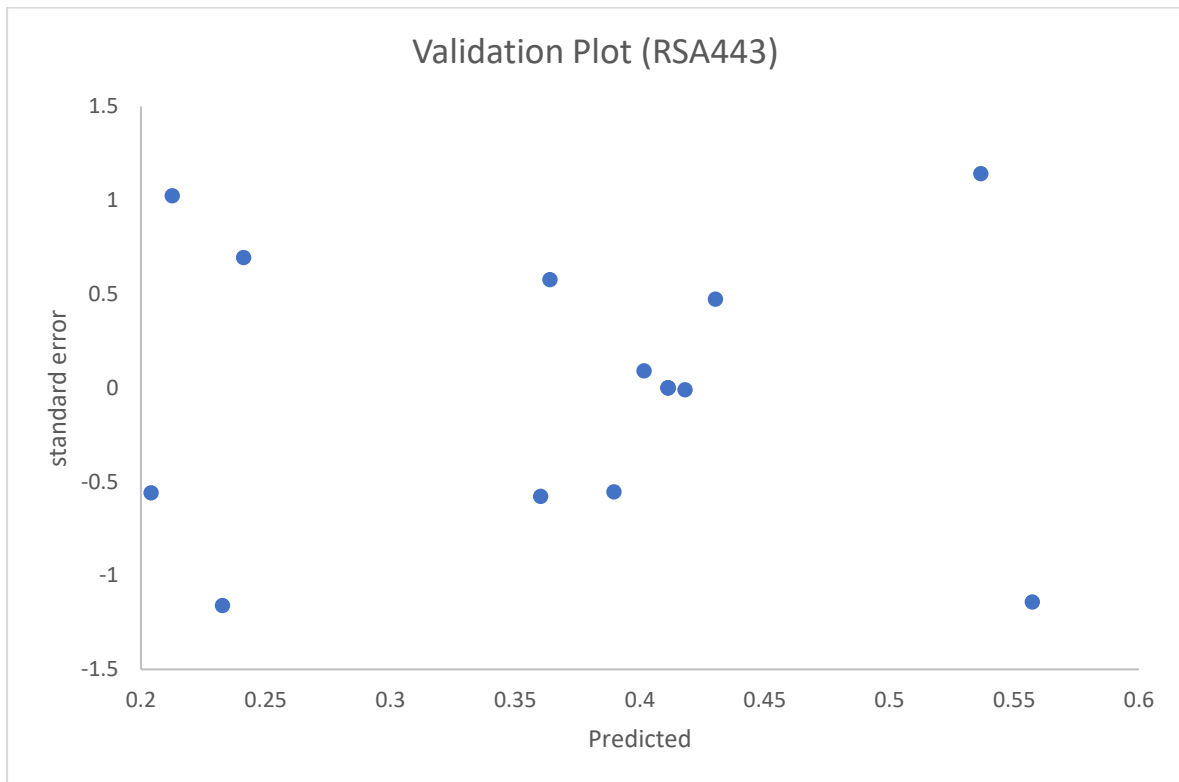


Figure 6.9: Scattered validation plot for AE on RSA 443

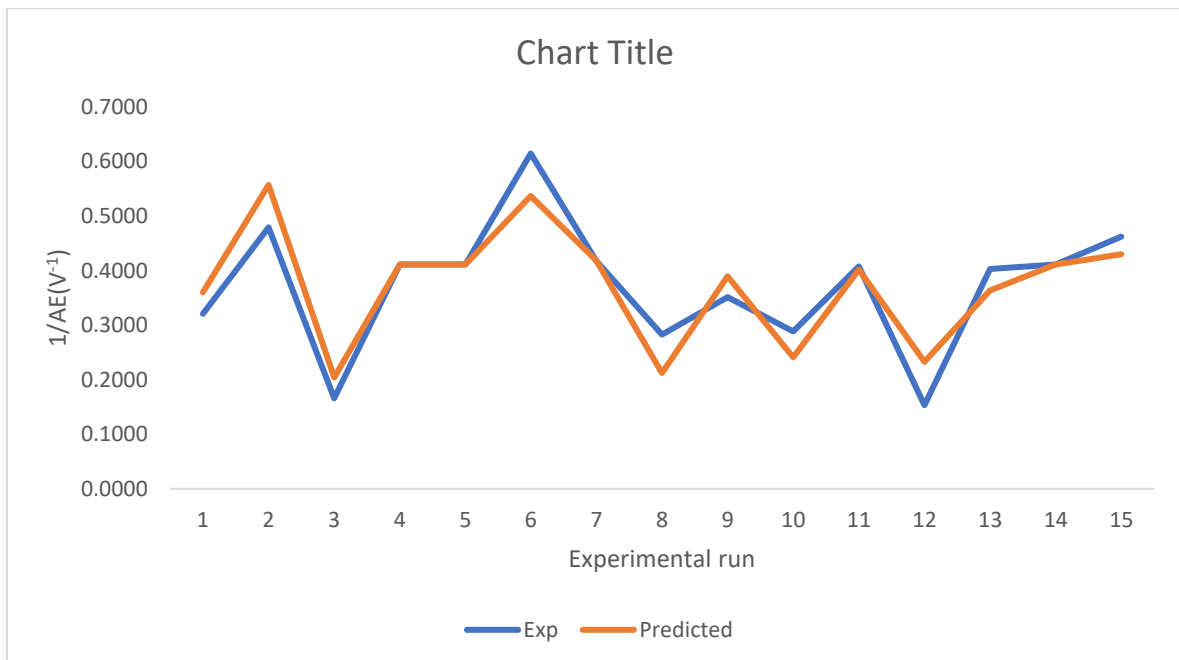


Figure 6.10: Comparison between experimental value and predicted value for AE on RSA 443

From the ANOVA table, it was revealed that an interaction exists between feed rate and Depth of cut during diamond turning of RSA 443. Here, it shows that at feed rate = 15 mm/min and depth of cut of 15 μm , an inverse AE signal between the range of 0.426 and 0.563 volts would be expected. **Figure 6.11** shows interaction plot between feed rate and depth of cut. A cross-sectional pattern was noted at a depth of cut of 15 μm and a feed rate of 15 mm/min for all three stages. This shows that at each factor level, the same acoustic signal will be sensed at these cutting parameters. This type of signal can however be used during diamond turning to monitor the efficiency of surface finish, tool wear and even cutting force of advanced optical materials.

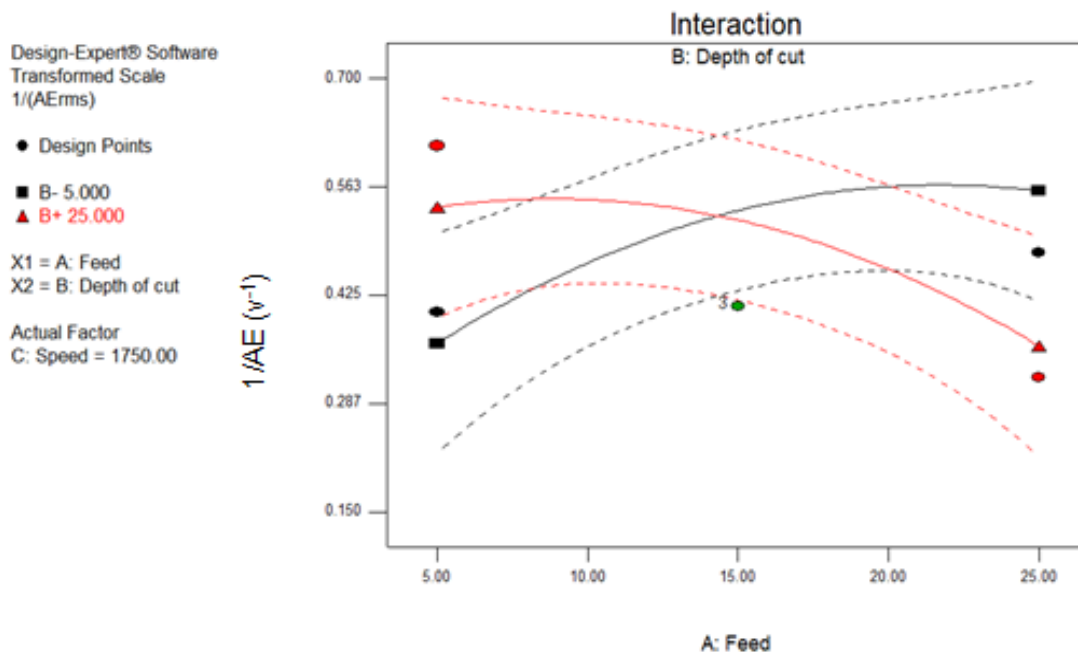


Figure 6.11: Interaction plot between feed rate and depth of cut against Inverse of AE

Further clarity can be witnessed in **Figure 6.12**, where less AE signal effects have been observed at a high feed rate and low depth of cut. Thus, vice versa, a high AE signal value was recorded for these two parameters (i.e., at low feed and high depth of cut). **Figure 6.13** is the 3-D representation of same effects at speed of 1750 rpm.

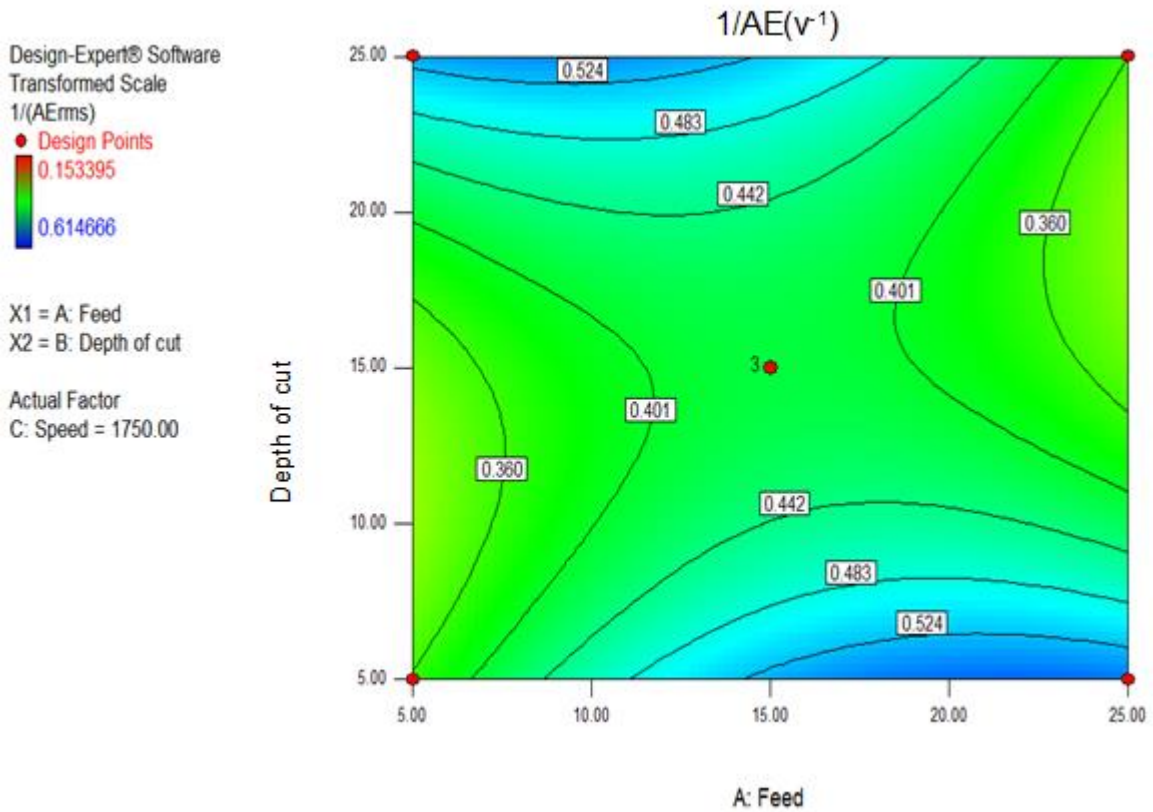


Figure 6.12: 2D response surface plot for AE on RSA 443

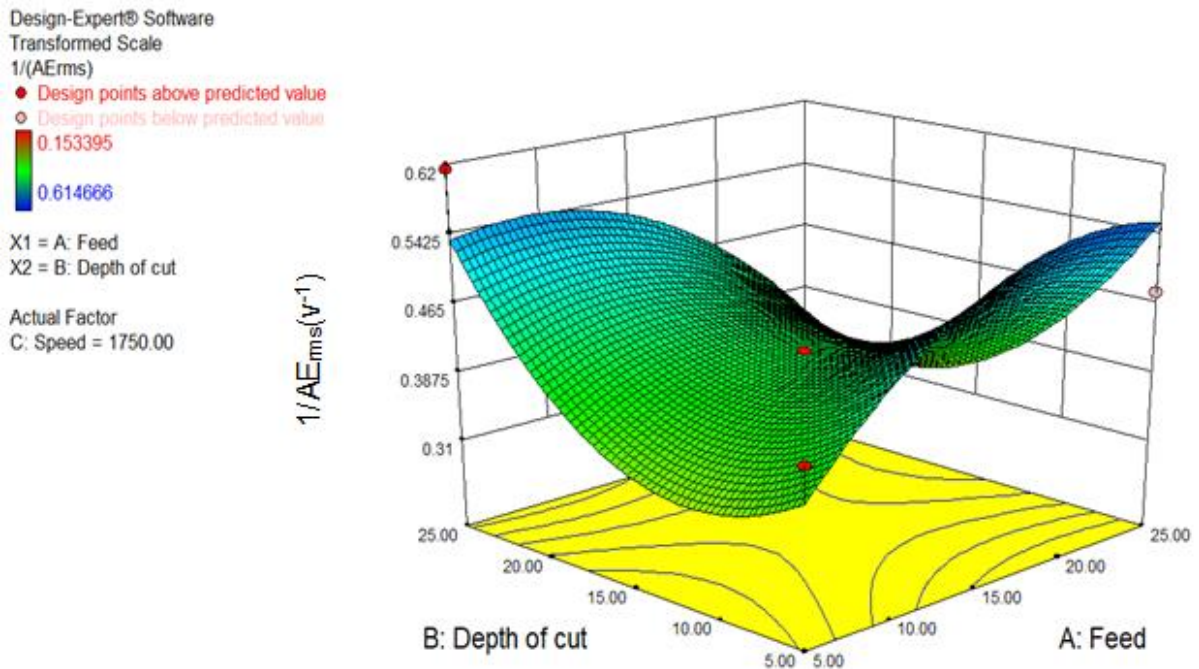


Figure 6.13: 3D response surface plot for AE on RSA 443

6.9 PROFILE PLOT FOR ACOUSTIC EMISSION OF RSA 443

The profile plots in **Figure 6.14** shows that at constant speed, even at different values of (500, 1750 and 3000) rpm for speed, the variation responses for inverse acoustic emission are identical in pattern, but different levels of quadratic relationships are observed.



Figure 6.14: Profile plot for feed rate against Inverse AE

Figure 6.15 shows different responses at constant feed rate during ultra-precision machining of RSA 443. It can be seen that the feed rates were overlapping at 12.5 mm/min for all feed rates. It shows that the same signal response will always be produced at this point in the feed rate. The basic summary shows that the feed rate relationship based on this experiment is quadratic on AE. **Figure 6.16** showed a positive quadratic relationship between the depth of the cut and the AE response.

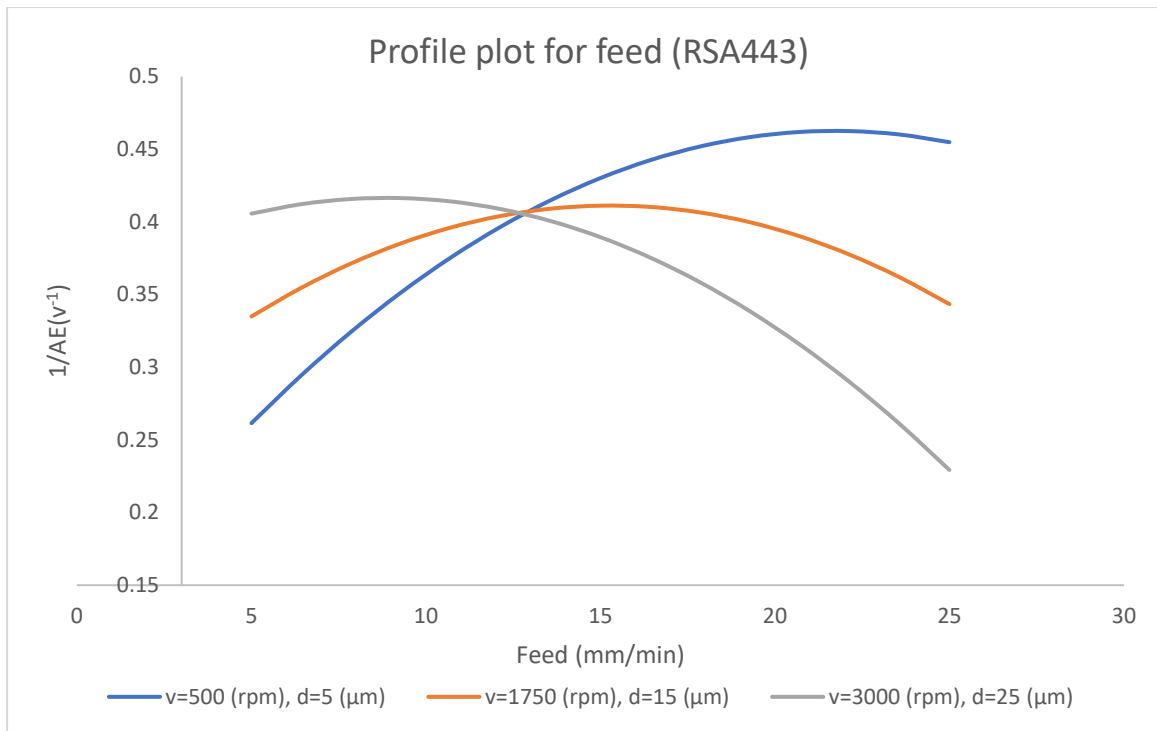


Figure 6.15: Profile plot for feed rate against Inverse AE



Figure 6.16: Profile plot for depth of cut against Inverse AE

6.10 OPTIMIZATION OF CUTTING PARAMETERS FOR AE DURING MACHINING PROCESS

Table 6.7 shows the possible ways to obtain or avoid AE of interest during the machining. For monitoring purposes e.g., cutting force, surface roughness etc. a high AE is usually a warning against catastrophe. High cutting force is an indication of possible poor surface quality which is associated with high speed and low feed rate as witnessed in the table.

Table 6.7: Optimization conditions for AE of RSA 443

	V (rpm)	F (mm/min)	D (μm)	Predicted $1/\text{AE}(\text{v}^{-1})$	Actual AE (v)
Max	1673.503	8.873252	25	0.547888	1.8252
min	1673.512	5	11.25289	0.319244	3.132

CHAPTER 7

DIAMOND TURNING OF RAPIDLY SOLIDIFIED ALUMINIUM (RSA) ALLOY 6061

7.1 INTRODUCTION

This chapter described analysis on a newly graded aluminium alloy called RSA 6061. Up till date the author has not found detailed analysis done on this material. RSA 6061 is a promising material for optical applications mostly for visual spectra range. Literature has it predicted that RSA 6061 can be machined to a very high surface quality with value less 3nm which will be good news over AA6061. More so, it has been noted that RSA 6061 could be as good as nickel plated or Alumini Plate optics that go through polishing after diamond turned but a few advantages of RSA 6061 material over the latter is reduction of production steps leading to decrease in costs and throughput time.

Secondly, its unique hardness facilitates its cleanability and high reflectivity which also good for optics applications, and finally, it allows large workpieces to be diamond turned. Hence, an in-depth analysis is carried out on RSA 6061 in this study. The first part of the analysis deals with force characteristics and analysis on this material, followed by the effect of tool geometry specifically the use of different tool nose radius on RSA 6061. The author also looks at the behaviour of different nose radius on surface quality of RSA 6061.

In this section, cutting forces applied during machining of RSA6061 is analyzed based on three different tool nose radius 0.5 mm, 1.0 mm and 1.5 mm identified. Analysis of material removal rate, chip morphology, and acoustic emission during diamond turning of this material was also investigated. Acoustic emission was also examined since AE is a good monitoring tool for surface quality during diamond turning.

7.2 FORCE ANALYSIS FOR RSA 6061 AT NOSE RADIUS (NR) 0.5 MM

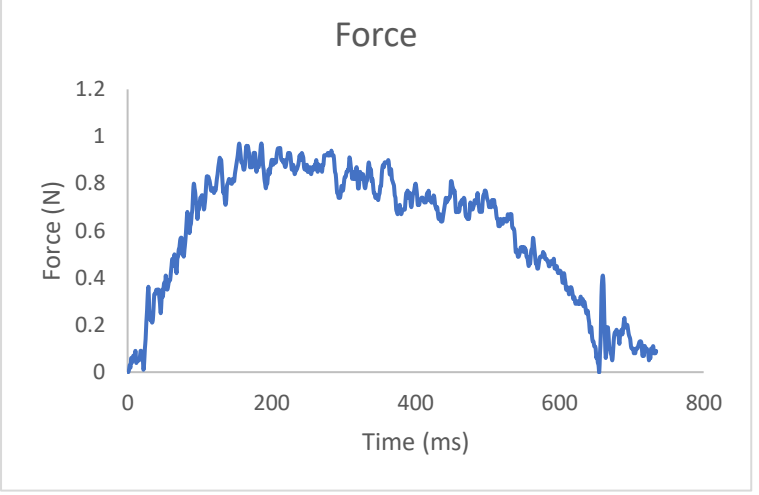
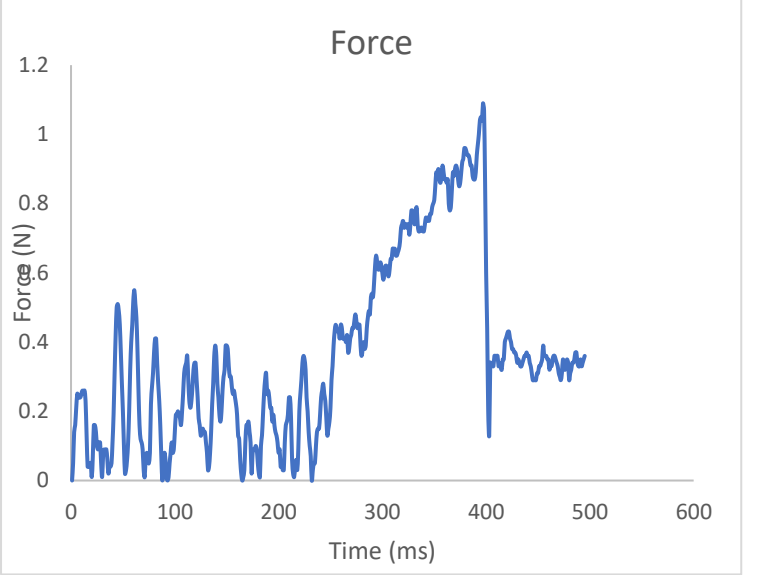
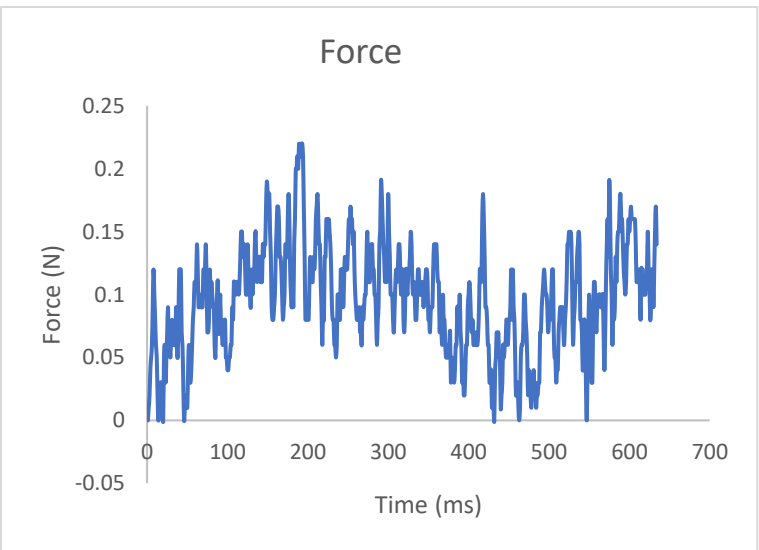
The effects of cutting parameters will be analyzed against each nose radius to observe which of the cutting parameters has most influence on cutting force. The **Table 7.1** represent force characteristics during diamond turning. The author decided to present cutting forces characteristics for nose radius 0.5 mm.

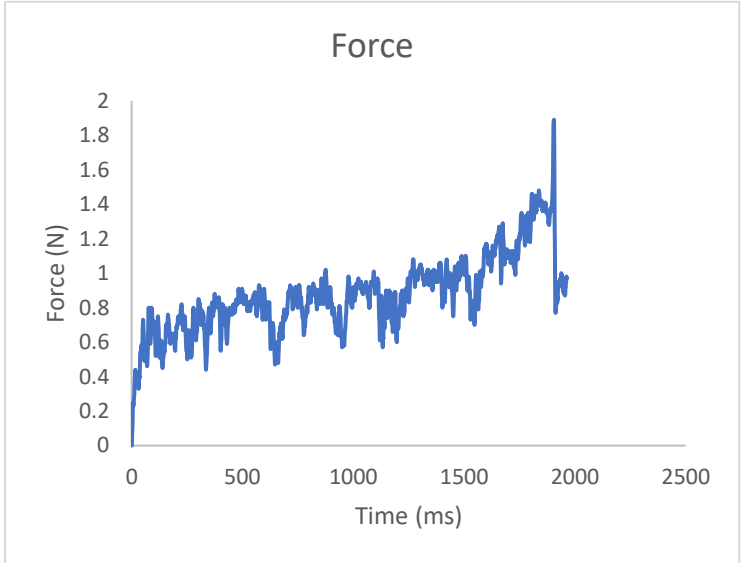
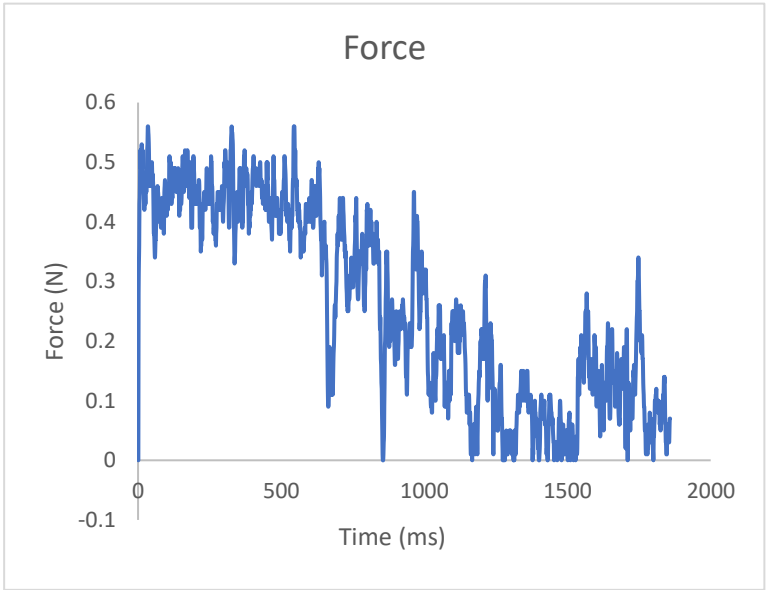
Table 7.1: Force characteristics during machining of RSA 6061

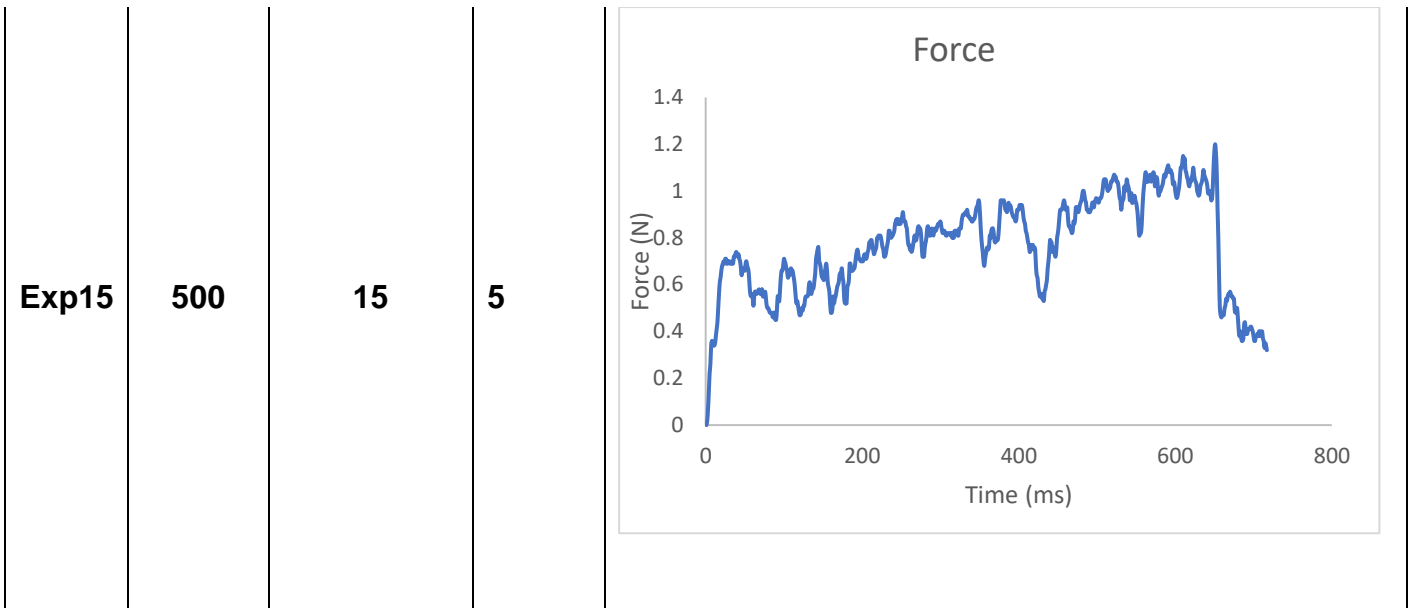
Run	V (rpm)	F (mm/min)	D (μm)	Force characteristics
Exp1	1750	25	25	<p>The graph for Exp1 shows a force signal that rises from 0 N at 0 ms to a peak of approximately 1.5 N at 150 ms. It then exhibits high-frequency oscillations between 0.8 N and 1.4 N until 400 ms, after which it drops to a lower level around 0.3 N.</p>
Exp2	1750	25	5	<p>The graph for Exp2 shows a highly oscillatory force signal. The force fluctuates between approximately 0 N and 0.15 N until 300 ms, then increases significantly to a peak of about 0.4 N at 380 ms, before dropping and oscillating again between 0 N and 0.25 N.</p>

Exp3	3000	5	15	
Exp4	1750	15	15	
Exp5	1750	15	15	

<p>Exp6</p>	<p>1750</p>	<p>5</p>	<p>25</p>	
<p>Exp7</p>	<p>500</p>	<p>15</p>	<p>25</p>	
<p>Exp8</p>	<p>3000</p>	<p>25</p>	<p>15</p>	

Exp9	3000	15	25	
Exp10	500	25	15	
Exp11	3000	15	5	

Exp12	500	5	15	 <p>The graph for Experiment 12 shows Force (N) on the y-axis (0 to 2.0) and Time (ms) on the x-axis (0 to 2500). The force starts at 0, rises to about 0.8 N by 100 ms, and then fluctuates between 0.6 N and 1.0 N until 1500 ms. After 1500 ms, the force increases steadily to a peak of approximately 1.9 N at 1900 ms before dropping to about 0.8 N.</p>
Exp13	1750	5	5	 <p>The graph for Experiment 13 shows Force (N) on the y-axis (-0.1 to 0.6) and Time (ms) on the x-axis (0 to 2000). The force starts at 0, rises to about 0.5 N by 100 ms, and then fluctuates between 0.3 N and 0.5 N until 600 ms. It then drops to about 0.1 N at 700 ms, rises to 0.45 N at 900 ms, drops to 0.1 N at 1100 ms, and then fluctuates between 0.0 N and 0.35 N until 1800 ms.</p>
Exp14	1750	15	15	Same as Experiment 4 and 5



In **Table 7.2**, the force data acquired during machining was averaged and recorded against each experimental run which can be seen tabulated as F(N). **Table 7.2** is further analyzed statistically in **Table 7.5**. However, for effective and appropriate model, it was also identified that an inverse transformation will generate high influence on the parameters.

Table 7.2: Experimental result of cutting forces for RSA 6061 during diamond turning using nose radius = 0.5 mm

Run	V (rpm)	F (mm/min)	D (μm)	FD	VD	V ²	D ²	F _{av} (N)	1/F(N ⁻¹)
Exp1	1750	25	25	625	43750	3062500	625	1.0797	0.926183
Exp2	1750	25	5	125	8750	3062500	25	0.0938	10.66098
Exp3	3000	5	15	75	45000	9000000	225	2.0841	0.479823
Exp4	1750	15	15	225	26250	3062500	225	0.3364	2.972652
Exp5	1750	15	15	225	26250	3062500	225	0.3364	2.972652
Exp6	1750	5	25	125	43750	3062500	625	0.2107	4.746084
Exp7	500	15	25	375	12500	250000	625	0.5799	1.724435
Exp8	3000	25	15	375	45000	9000000	225	0.7107	1.407063
Exp9	3000	15	25	375	75000	9000000	625	0.6606	1.513775
Exp10	500	25	15	375	7500	250000	225	0.4505	2.219756
Exp11	3000	15	5	75	15000	9000000	25	0.1052	9.505703
Exp12	500	5	15	75	7500	250000	225	0.9016	1.109139
Exp13	1750	5	5	25	8750	3062500	25	0.3065	3.262643
Exp14	1750	15	15	225	26250	3062500	225	0.3364	2.972652
Exp15	500	15	5	75	2500	250000	25	0.7965	1.255493

Table 7.3 shows the variance inflation factor (VIF) which measures how much the variance of the model is inflated by the lack of orthogonality in the design. If the factor is orthogonal to all the other factors in the model, the VIF is 1.0. VIF's exceeding 10 indicate that there is excessive correlation between the regression coefficients. Also, the Power at 5% alpha level to detect signal/noise ratios is considered in the analysis.

Table 7.3: Summary of variance inflation factor

Term	StdErr**	VIF	Ri-Squared
A	0.35	1	0
B	0.aZ35	1	0
C	0.35	1	0
AB	0.5	1	0
BC	0.5	1	0
B^2	0.52	1.01	0.0051
C^2	0.52	1.01	0.0051

Where A is speed in rpm, B is feed mm/min, D is depth of cut.

Table 7.4 shows degrees of freedom for evaluation. Here a good recommendation is a minimum of 3 lack of fit DF, this ensures a valid lack of fit test. For this experiment, we observed 5.

Table 7.4: DoF for evaluation

Model	7
Residuals	7
Lack Of Fit	5
Pure Error	2
Corr Total	14

7.2.1 Statistical analysis of cutting forces for RSA 6061 at nose radius = 0.5mm

Table 7.5: Regression and ANOVA output of cutting forces for RSA 6061 at nr = 0.5 mm

SUMMARY OUTPUT						
Regression Statistics						
Multiple R	0.953260					
R Square	0.908704					
Adj R Square	0.817408					
Std. Error	1.291509					
Observations	15					
ANOVA						
	df	SS	MS	F	Significance F	
Regression	7	116.2152	16.60217	9.953358	0.003564	
Residual	7	11.67598	1.667997			
Total	14	127.8912				
	Coefficients	Standard Error	t Stat	P-value	Lower 95%	Upper 95%
Intercept	-5.43776	2.79333	-1.9467	0.092617	-12.0429	1.167413
v(rpm)	0.006611	0.001728	3.824889	0.006501	0.002524	0.010698
f (mm/min)	0.490888	0.107086	4.584038	0.002532	0.237669	0.744107
d(μm)	-0.10181	0.245066	-0.41544	0.690261	-0.6813	0.47768
fd	-0.02805	0.006458	-4.34307	0.003383	-0.04332	-0.01278
vd	-0.00017	5.17E-05	-3.27557	0.01357	-0.00029	-4.7E-05
v^2	-9.8E-07	4.29E-07	-2.2735	0.057181	-2E-06	3.91E-08
d^2	0.020715	0.006701	3.091159	0.017538	0.004869	0.036561

Regression analysis in **Table 7.5** was carried out to establish the model and predict possible trend of cutting parameters on cutting force. R^2 from regression analysis shows 0.908704 this simply indicates that the model explains 90.08% variation of cutting force is explained by cutting parameters in the experiment making the model a good fit. F- value of 0.003564 confirmed the model is highly significant. The most influential cutting parameter is feed rate that has a p-value of 0.002532 which contributed about 24.5% effect. The interaction effect between feed rates and depth of cut has a p-value of 0.003383 contributes 24.3%. Depth of cut made less significant at p-value of 0.690261 which contributes about 3.08%. The speed with a p-value of 0.006501, this contributed about 13.9%. Squared of speed and depth of cut effects were significant with a p-value of 0.057181 contributed about 9.135% and p-value of 0.017538 contributed 6.74% respectively. Depth of cut made little or no significant value at p-value of 0.690261 and contributed about 3.08% to overall process.

Figure 7.1 shows the scattered plot for this experiment which further validate the model standard. **Figure 7.2** represent the comparison between experimental and predicted values.

The model **Equation 7.1** generated for the experiment conducted for RSA 6061 using Nose radius 0.5mm is as follows:

Equation 7.1

$$F = (-5.43 + 6.61 \times 10^{-3}V + 0.49F - 0.101D - 0.028FD - 1.7 \times 10^{-4}VD - 9.8 \times 10^{-7}V^2 + 0.021D^2)^{\frac{1}{2}}$$

Where V is the speed in rpm, F is feed rate in mm/min and D is the depth of cut in μm and Force is the cutting force in Newton

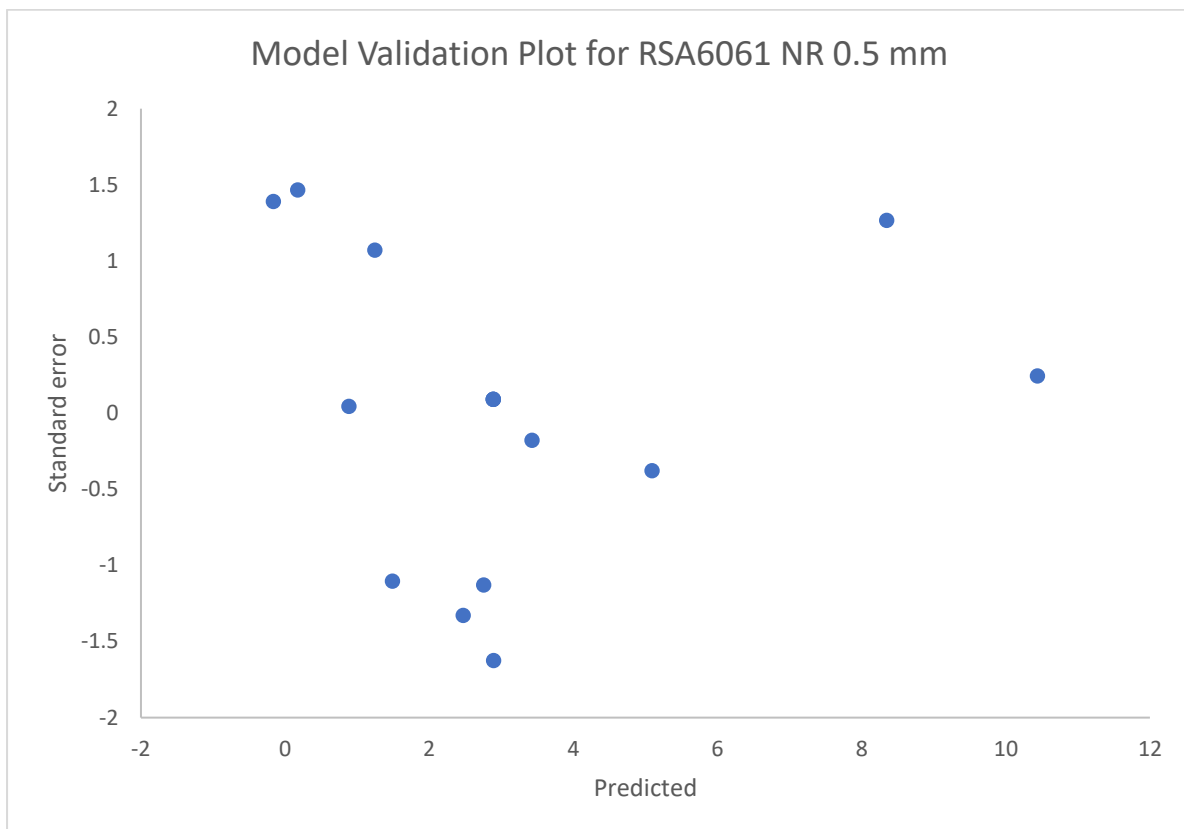


Figure 7.1: Validation plot for RSA 6061 with Nose radius 0.5 mm

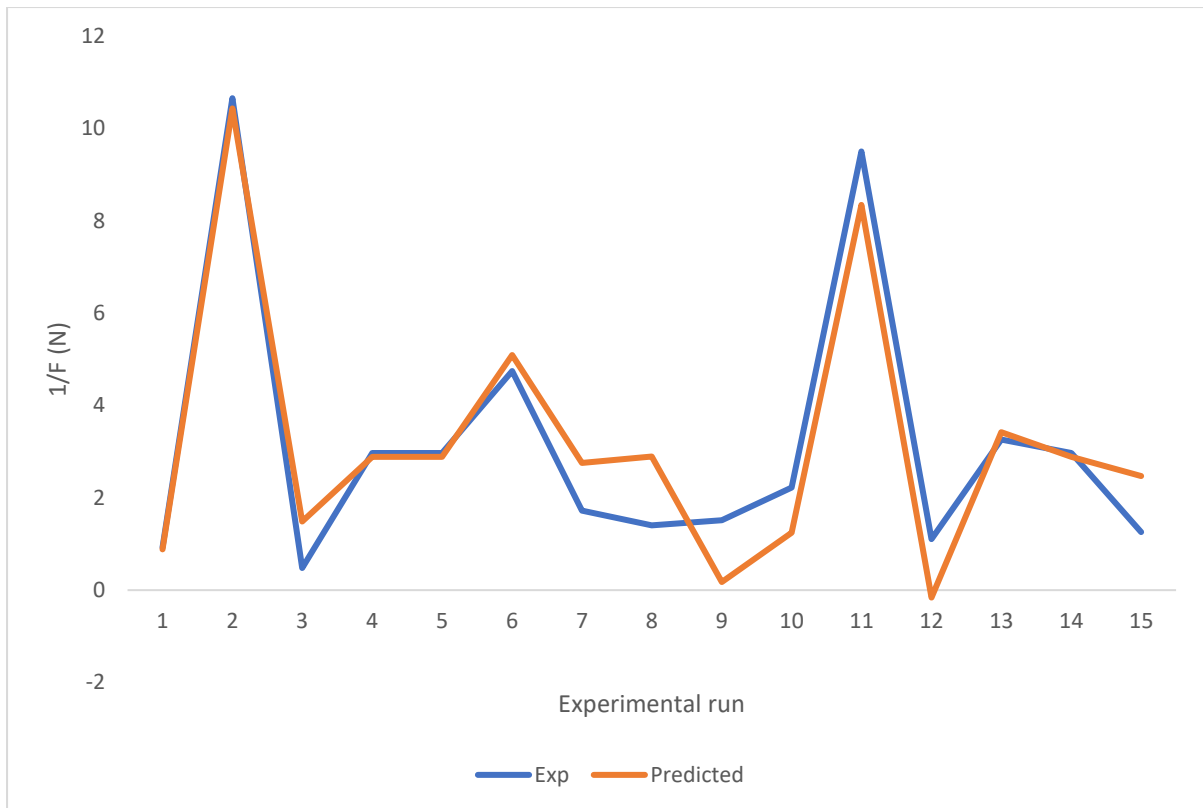


Figure 7.2: Comparison between experimental and predicted values for RSA 6061 with Nose radius = 0.5 mm

To further analyze the data, **Figure 7.3** shows some predictions that are close or the same with raw inverse cutting force data. Experimental runs 1, 2 and 14, as shown in the **Table 7.2**, confirm the predictions from the plot. **Figure 7.4** also predicted and confirmed experimental runs 4 and 5. From the model generated, two interaction effects were noticed, **Figure 7.5** show the interaction effects between feed and depth of cut at constant speed of 15rpm. Also **Figure 7.6** represents the interaction between speed and depth of cut at constant feed 15mm/min. **Figures 7.7 and 7.8** represent the 3-D contour plots.

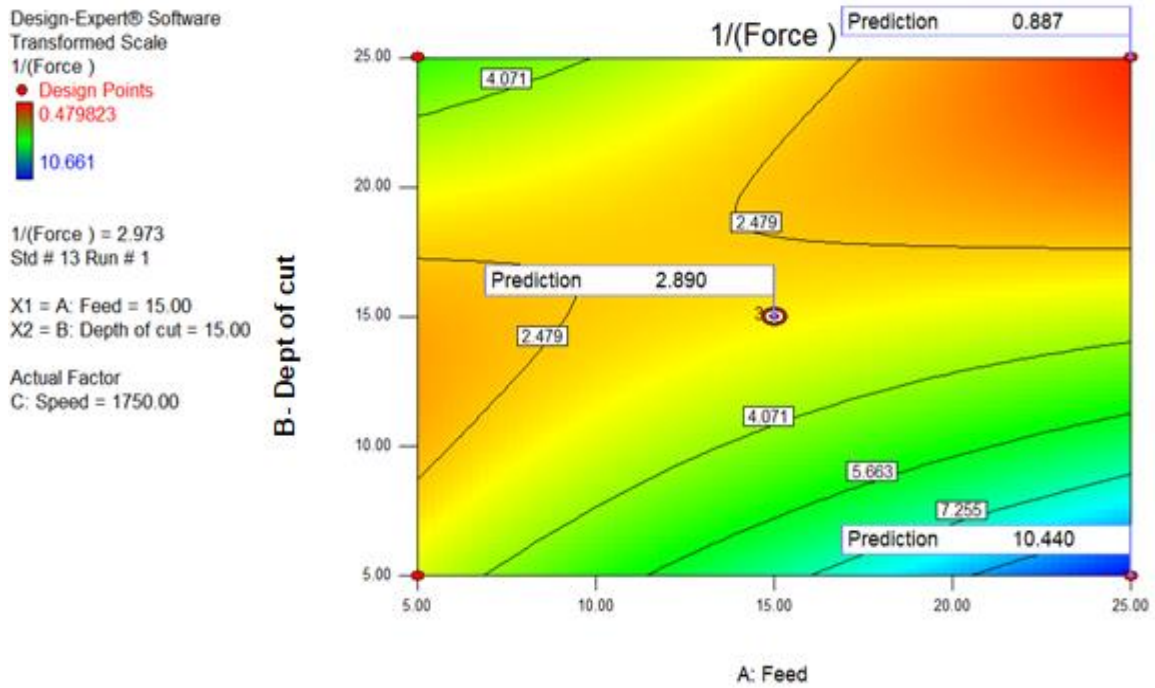


Figure 7.3: Contour plot for feed rate and depth of cut against inverse of cutting force at NR = 0.5 mm

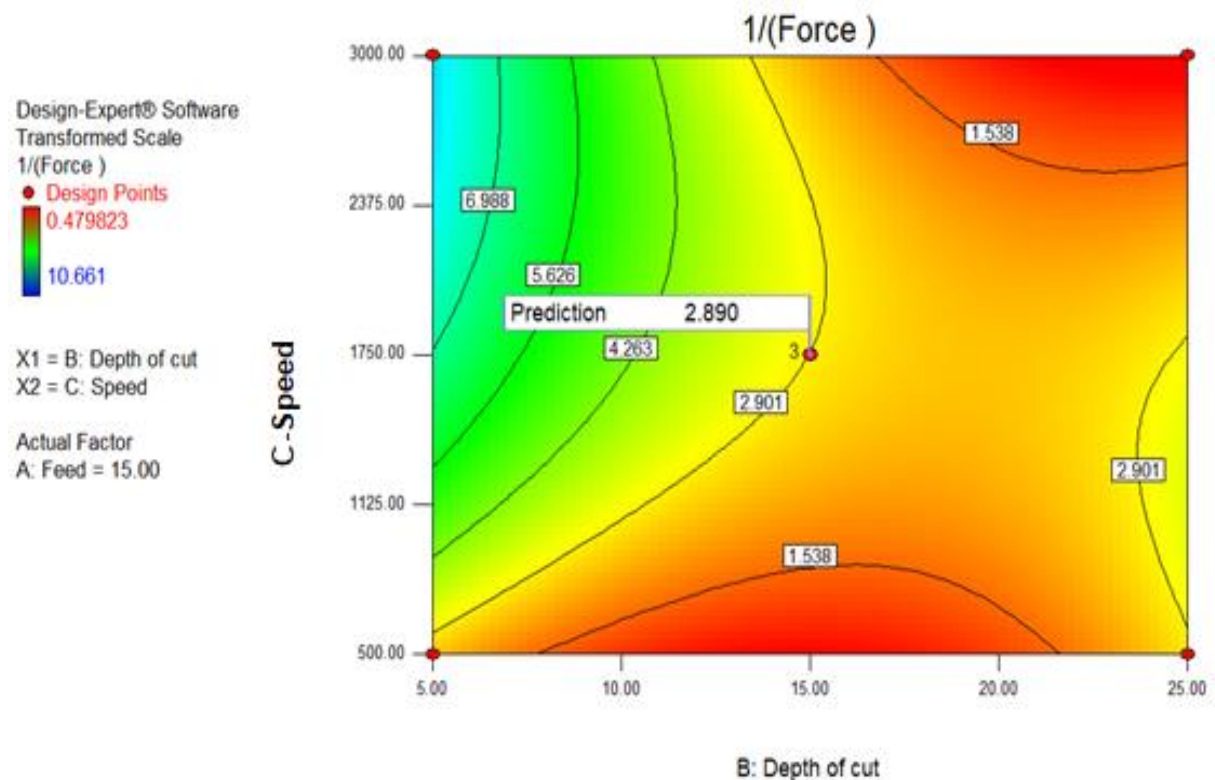


Figure 7.4: Contour plot for speed and depth of cut against inverse of cutting force at NR = 0.5 mm

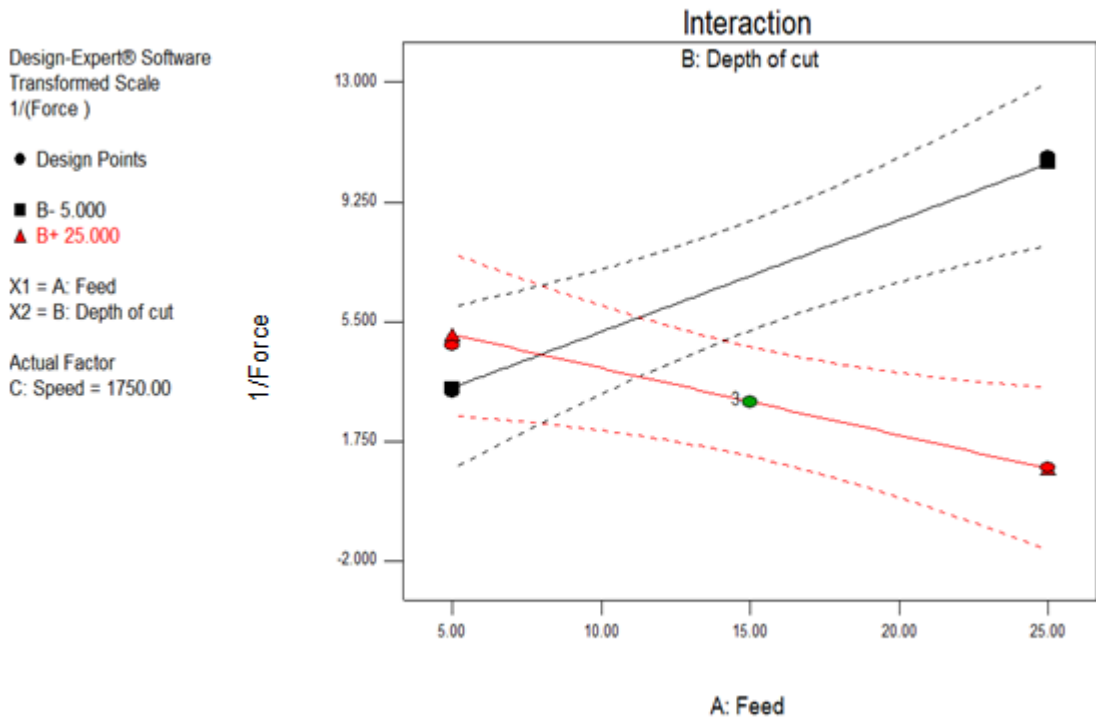


Figure 7.5: Interaction plot between feed rate and depth of cut against inverse of cutting force at NR =0.5 mm

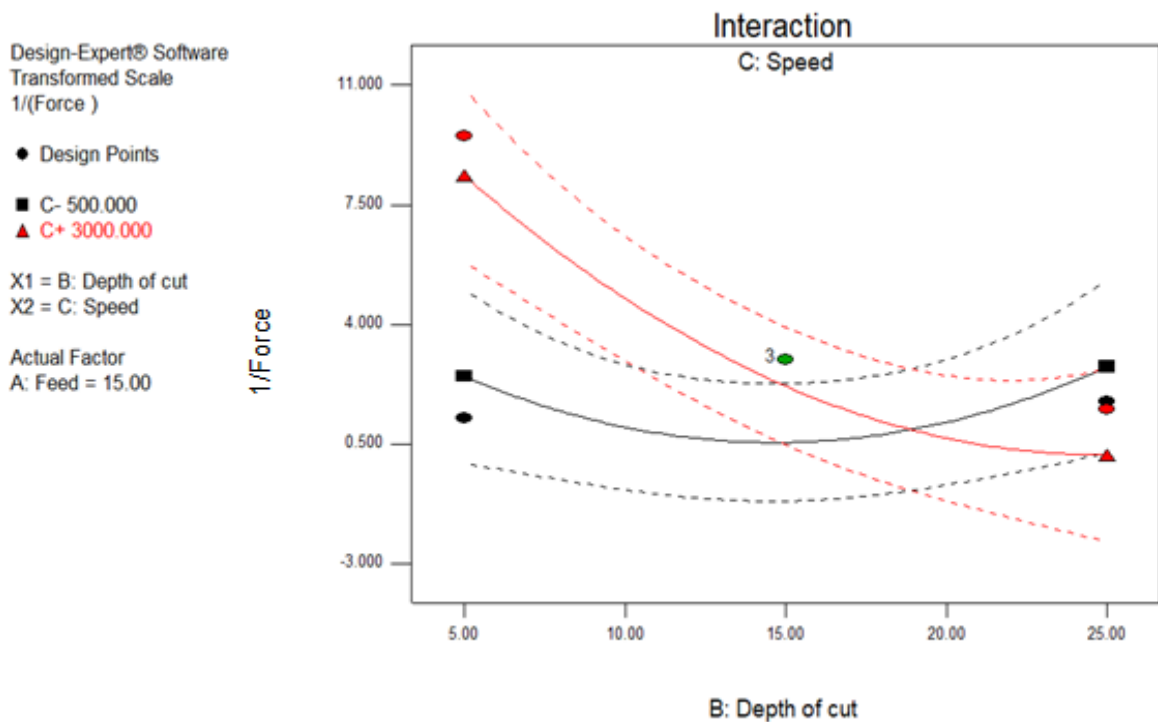


Figure 7.6: Interaction plot between speed and depth of cut against inverse of cutting force at NR =0.5 mm

Design-Expert® Software

Transformed Scale

1/(Force)

● Design points above predicted value

○ Design points below predicted value

0.479823

10.661

X1 = A: Feed

X2 = B: Depth of cut

Actual Factor

C: Speed = 1750.00

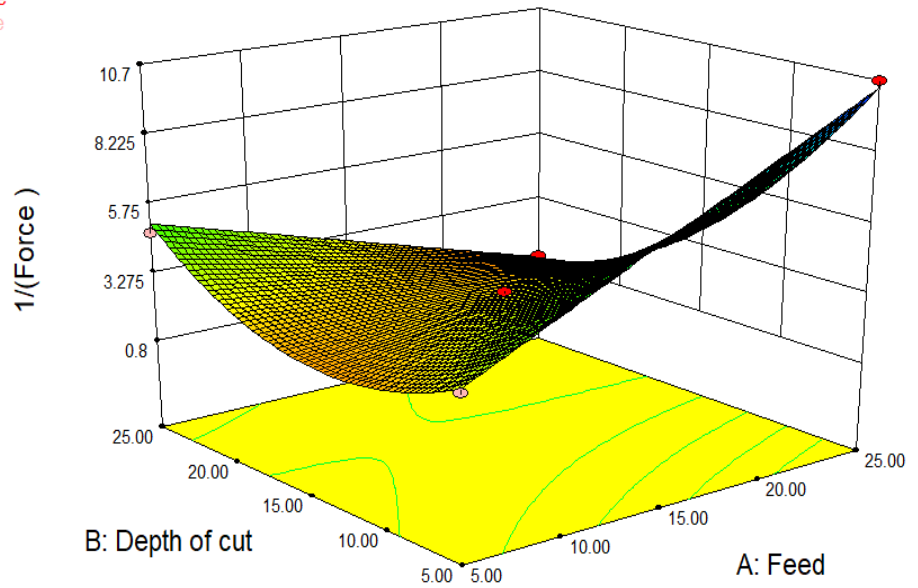


Figure 7.7: 3D plot between depth of cut and feed rate against inverse of cutting force at NR =0.5 mm

Design-Expert® Software

Transformed Scale

1/(Force)

● Design points above predicted value

○ Design points below predicted value

0.479823

10.661

X1 = B: Depth of cut

X2 = C: Speed

Actual Factor

A: Feed = 15.00

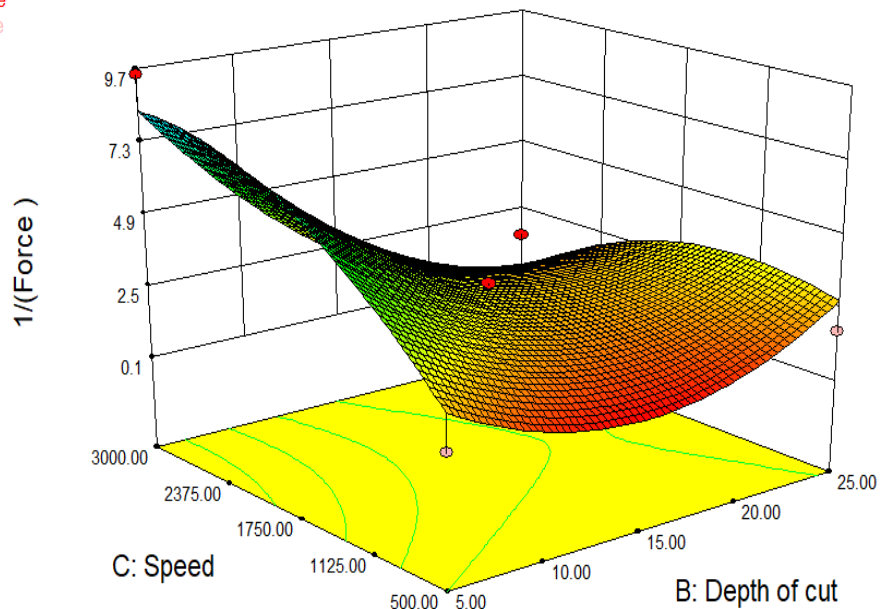


Figure 7.8: 3D plot between depth of cut and speed against inverse of cutting force at NR =0.5 mm

7.2.2 Profile plots of cutting force for RSA6061 at nose radius = 0.5 mm

Profile plots in **Figures 7.9 – 7.11**, represent effects of cutting parameters on cutting forces. In **Figure 7.9**, speed is varied against constant depth of cuts and feed rates. Looking closely, an increase in speed at low feed rates 5mm/min and low depth of cut 5mm, there is a steady increase in the inverse of cutting force even though this effect is a concave in nature. However, at moderate - high feed rates and depth of cuts, there is a sharp decrease in concavity in the inverse of cutting force while the speed is on the steady increase. **Figure 7.10** represent profile plot for feed rate. In **Figure 7.11**, depth of cut is varied, it shows an increase in depth of cut at low feed rates and low speed, there is a steady concave increase in the inverse of cutting force. However, at moderate - high feed rate and speed, there is a sharp concave decrease in inverse of cutting force while the depth of cut is on the increase.

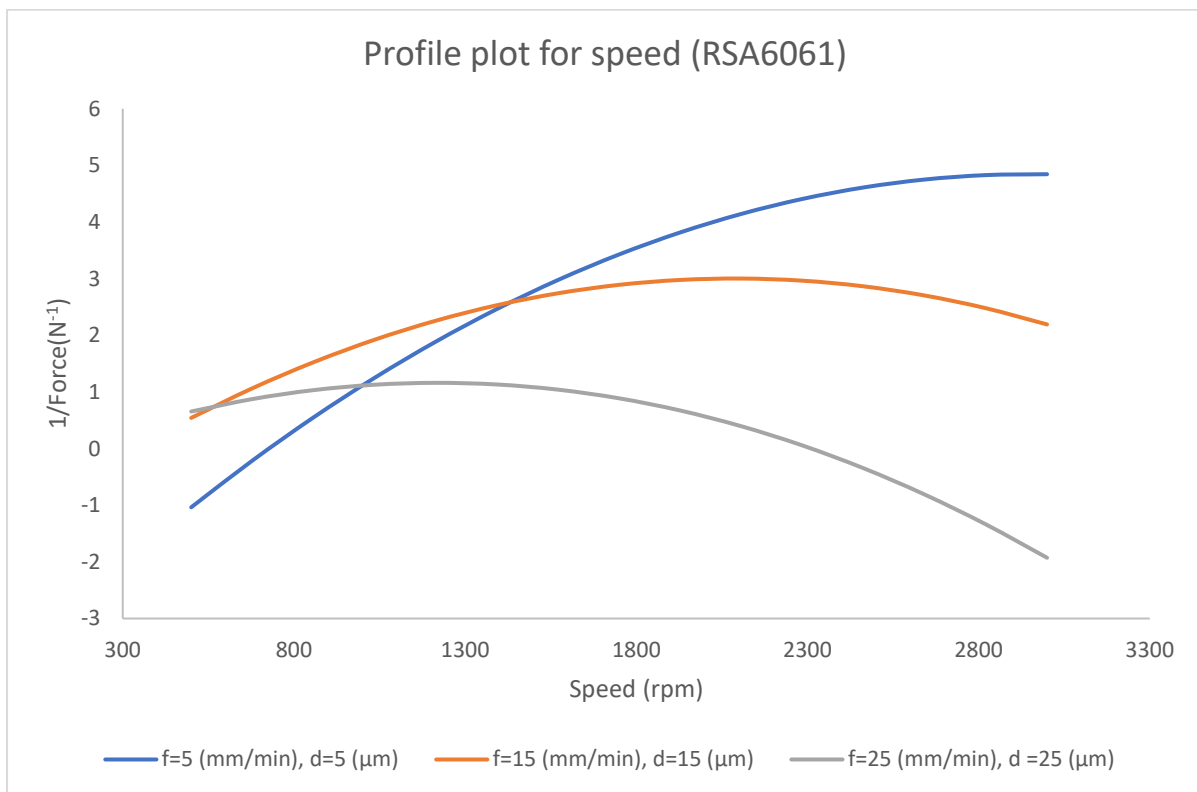


Figure 7.9: Profile plot for speed at nose radius 0.5 mm

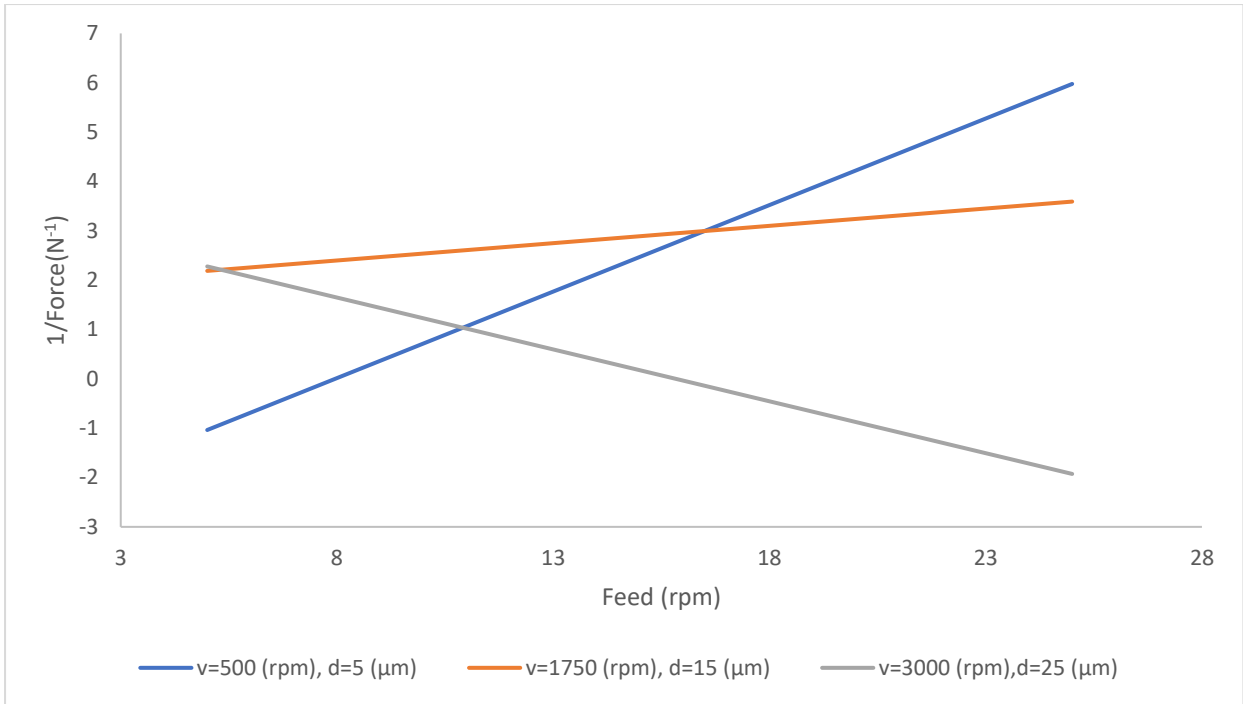


Figure 7.10: Profile plot for feed rate at nose radius 0.5 mm

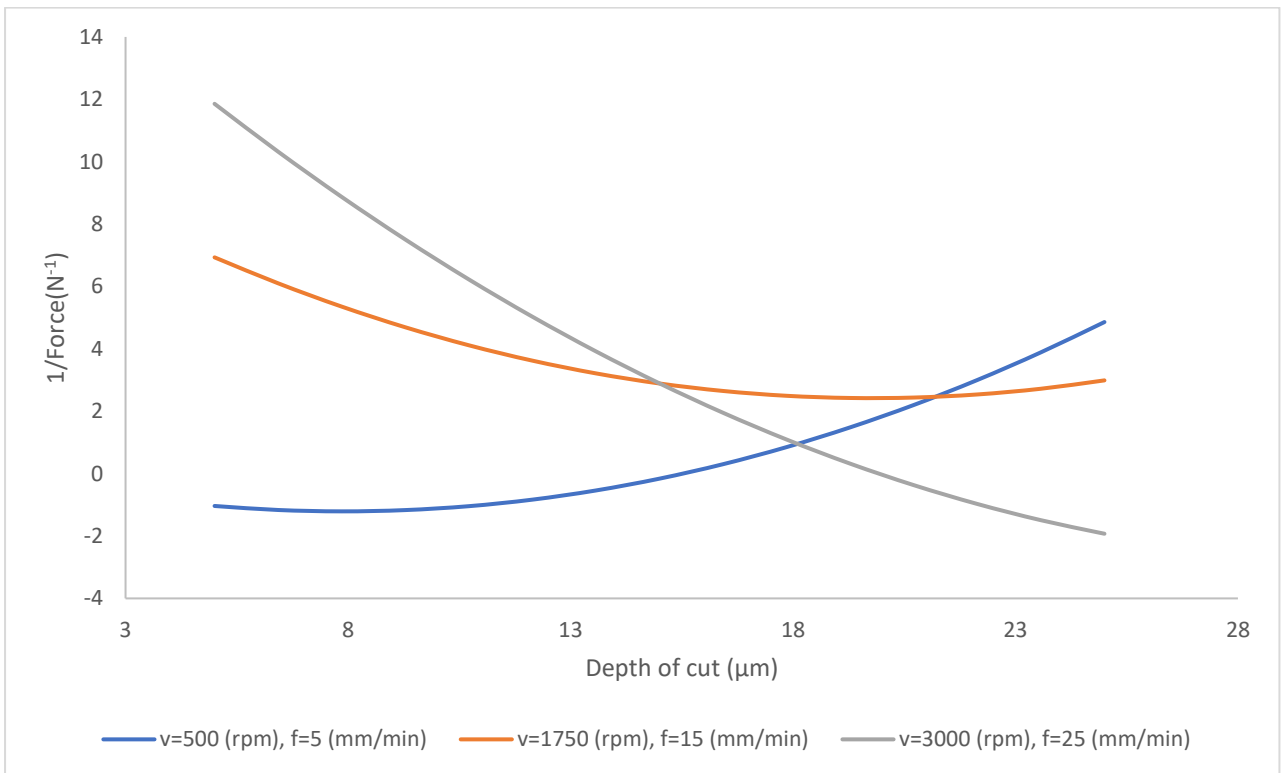


Figure 7.11: Profile plot for depth of cut at nose radius 0.5 mm

7.3 ANALYSIS OF CUTTING FORCES FOR RSA 6061 AT NOSE RADIUS = 1.0 MM

Table 7.6 represent the cutting force acquired during diamond turning of RSA 6061 with tool geometry with the following cutting-edge values: Nose radius 1.0 mm, rake angle of 0° and clearance angle of 15° cylindrical. From the raw data, experimental runs number 7, 10, 12 and 15 recorded a high cutting force, this trend is associated with very low spindle speed. The ANOVA and regression analyses explain further the raw data **Table 7.9**.

Table 7.6: Experimental results for cutting forces of RSA 6061 during diamond turning using nose radius = 1.0 mm

Run	V (rpm)	F (mm/min)	D (μm)	F _{ave} (N)
Exp1	1750	25	25	0.2030
Exp2	1750	25	5	0.2195
Exp3	3000	5	15	0.0687
Exp4	1750	15	15	0.2353
Exp5	1750	15	15	0.2353
Exp6	1750	5	25	0.3042
Exp7	500	15	25	0.5016
Exp8	3000	25	15	0.1760
Exp9	3000	15	25	0.1332
Exp10	500	25	15	0.3016
Exp11	3000	15	5	0.0671
Exp12	500	5	15	0.6233
Exp13	1750	5	5	0.3956
Exp14	1750	15	15	0.2353
Exp15	500	15	5	0.5200

Table 7.7 shows variance inflation factor (VIF) which measures how much the variance of the model is inflated by the lack of orthogonality in the design. It is established that if the factor is orthogonal to all the other factors in the model, then VIF is 1.0. But a VIF that exceed 10 indicate that there is excessive correlation between the regression coefficients also the Power at 5% alpha level to detect signal/noise ratios is considered in the analysis.

Table 7.7: Summary of VIF

Term	StdErr**	VIF	Ri-Squared
A	0.35	1	0
B	0.35	1	0
C	0.35	1	0
AC	0.5	1	0

Where A is feed in mm/min, B is depth of cut in μm , D in speed in rpm.

Table 7.8 shows Degrees of freedom for evaluation. For a good experiment, recommendation is made for a minimum of 3 lack of fit df, this ensures a valid lack of fit test. For this experiment, we observed 8.

Table 7.8: DoF for evaluation

Model	4
Residuals	10
Lack Of Fit	8
Pure Error	2
Corr Total	14

7.3.1 Statistical analysis of cutting forces for RSA 6061 at nose radius = 1.0 mm

Table 7.9: Regression and ANOVA output of cutting forces for RSA 6061 at NR =1.0 mm

SUMMARY OUTPUT						
Regression Statistics						
Multiple R	0.975313					
R Square	0.951236					
Adj R Square	0.931731					
Stdr Error	0.042869					
Observations	15					
ANOVA						
	df	SS	MS	F	Significance F	
Regression	4	0.358497	0.089624	48.76756	1.59E-06	
Residual	10	0.018378	0.001838			
Total	14	0.376875				
	Coefficients	Standard Error	t Stat	P-value	Lower 95%	Upper 95%
Intercept	0.872782	0.060272	14.48077	4.9E-08	0.738488	1.007076
v(rpm)	-0.00028	2.84E-05	-9.80611	1.9E-06	-0.00034	-0.00022
f (mm/min)	-0.02116	0.003362	-6.29443	8.97E-05	-0.02865	-0.01367
d(μm)	-0.00075	0.001516	-0.49648	0.630285	-0.00413	0.002625
vf	8.58E-06	1.71E-06	5.00357	0.000535	4.76E-06	1.24E-05

Regression statistics shows that R^2 is 0.951236 this means the model has just indicated that 95.1236% variation of cutting force is explained by cutting parameters in the experiment making the model a good fit. The most significant cutting parameter is speed with a p-value of 0.0000019 which contributed about 73.68% effect.

The interaction between speed and feed rates has a p-value of 0.000535 which contributed 12.11%. Depth of cut made less significant at p-value of 0.630285 which contributed about 0.12%. The coefficient of speed is negative which indicates that an overall cutting force is expected to decrease by a unit value of 0.00028 when other corresponding independent variable such as depth of cut and feed rate are kept constant in this statistical model even though very small. Negative coefficients of depth of cut, feed rates and interactions between speed and feed are also expected to decrease by a unit of 0.00075, 0.2116 and 0.00000858 respectively when other corresponding independent variables are kept constant.

Figure 7.12 shows the scattered plot for this experiment which establish and validate the model standard. **Figure 7.13** represent the comparison between experimental data and predicted data. The model generated from the experiment for RSA 6061 using Nose radius 1.0mm is given in **Equation 7.2** as follows:

Equation 7.2

$$F = 0.87 - 2.8 \times 10^{-4}V - 0.02F - 7.5 \times 10^{-4}D - 8.58 \times 10^{-6}VF$$

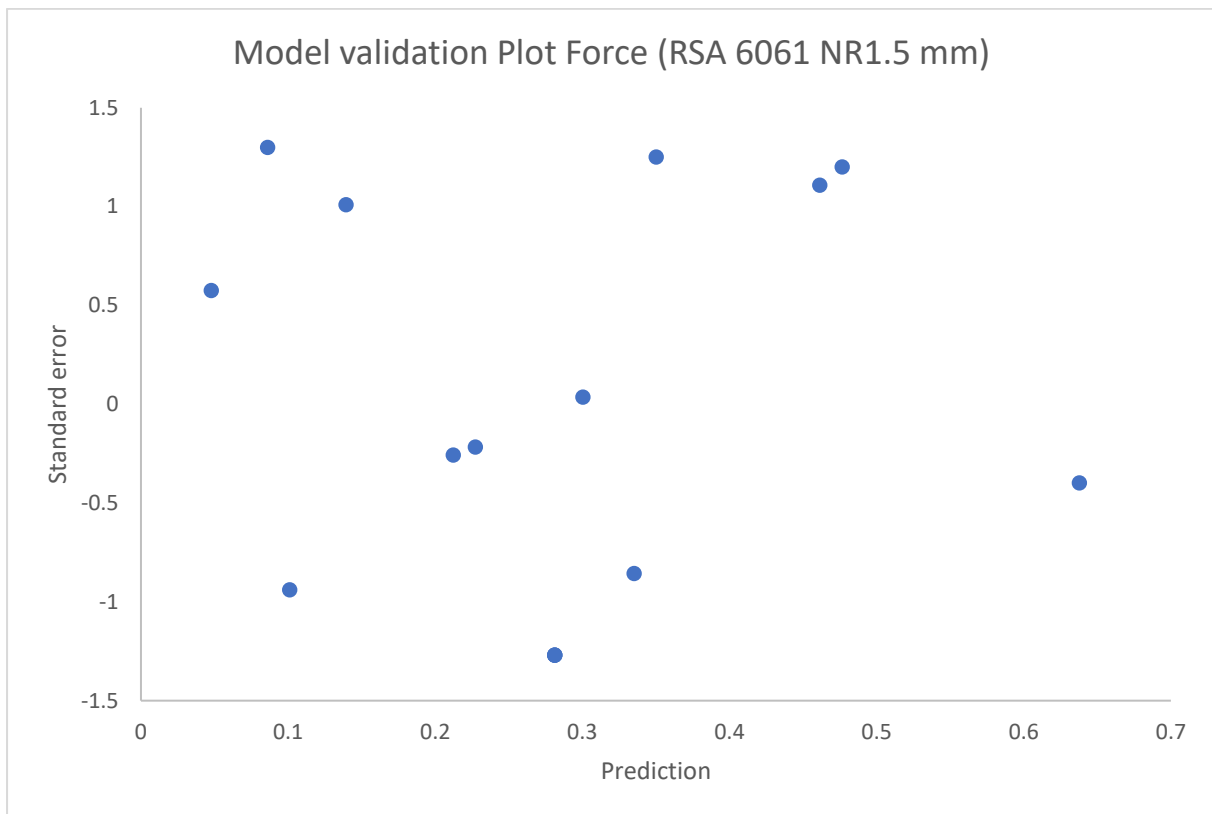


Figure 7.12: Scattered plot for cutting force on RSA 6061 at nose radius 1.0 mm

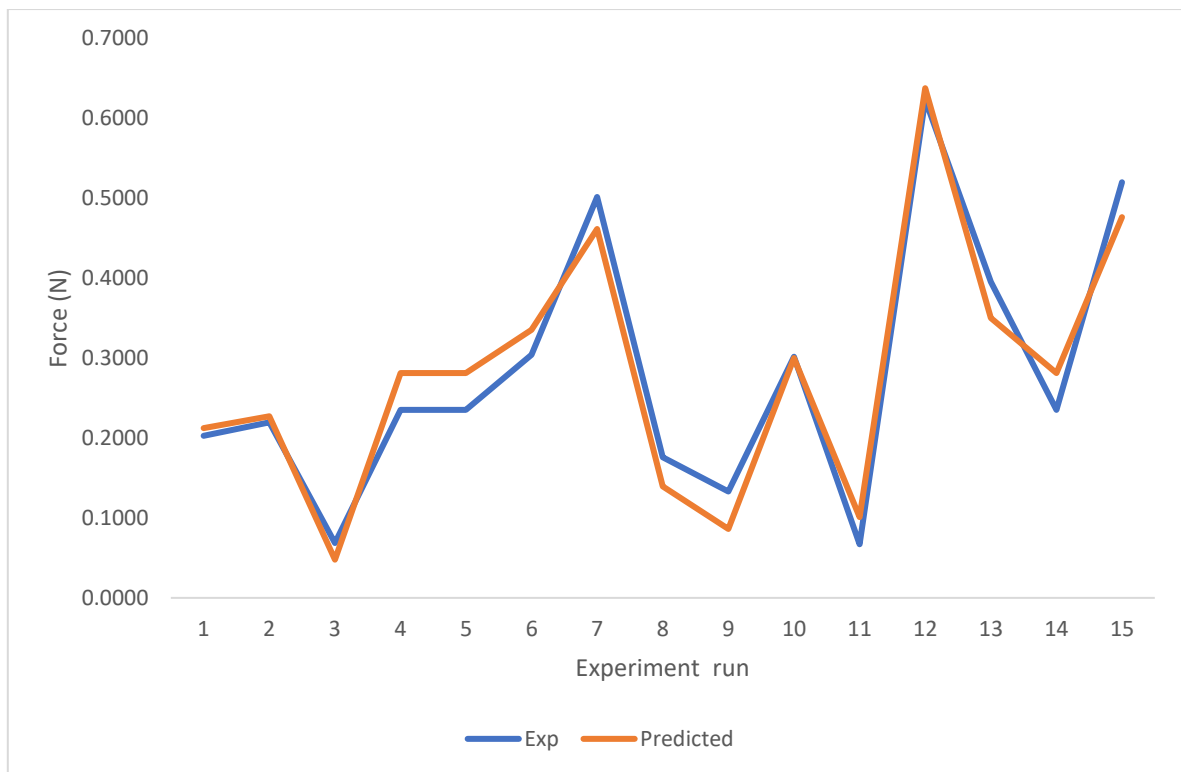


Figure 7.13: Comparison between experimental and predicted value at nose radius = 1.0 mm

To further validate the raw data, **Figures 7.14 and 7.15** present predictions that are close or the same with raw cutting force values in **Table 7.6**. as seen in Experimental runs 4, 5 and 12, it is confirmed in the predictions from the plot. From the model generated, an interaction effect between speed and feed rates were observed, **Figure 7.16** represents the interaction effect between Speed and feed rates at constant Depth of cut of 15 mm at nose radius 1.0 mm.

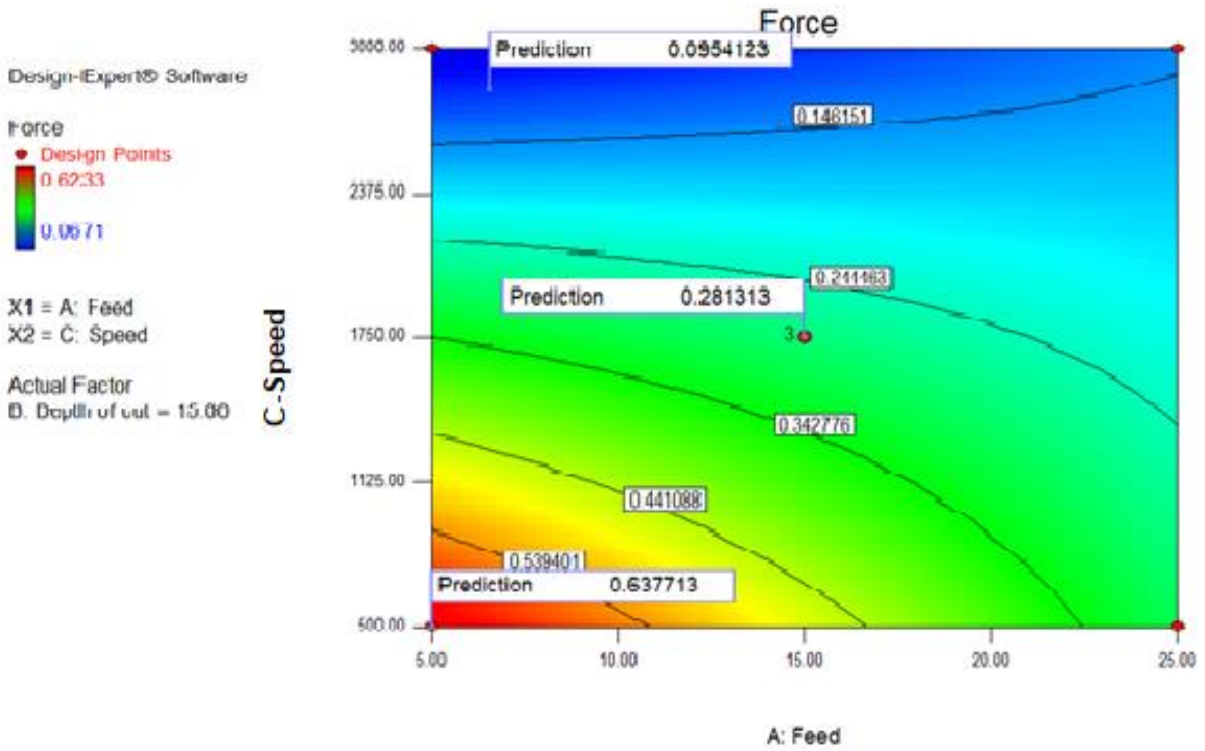


Figure 7.14: 2D Contour plot for RSA 6061 at nose radius 1.0 mm

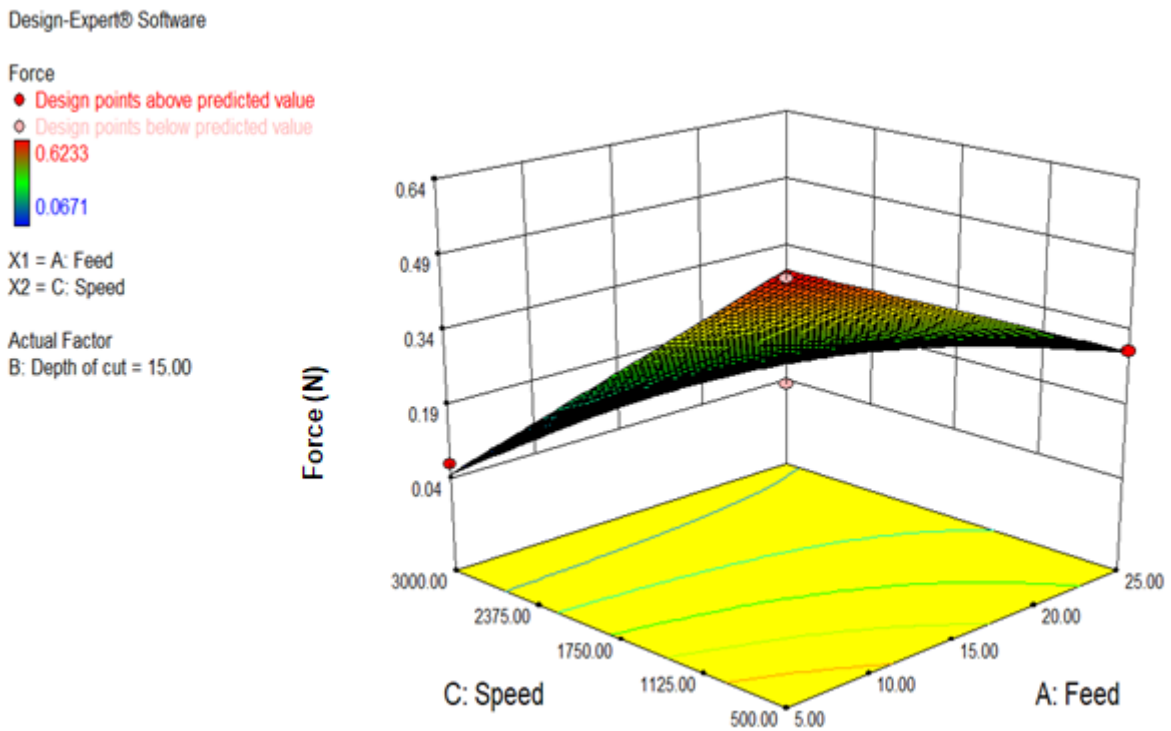


Figure 7.15: 3D Contour plot for RSA 6061 at nose radius 1.0 mm

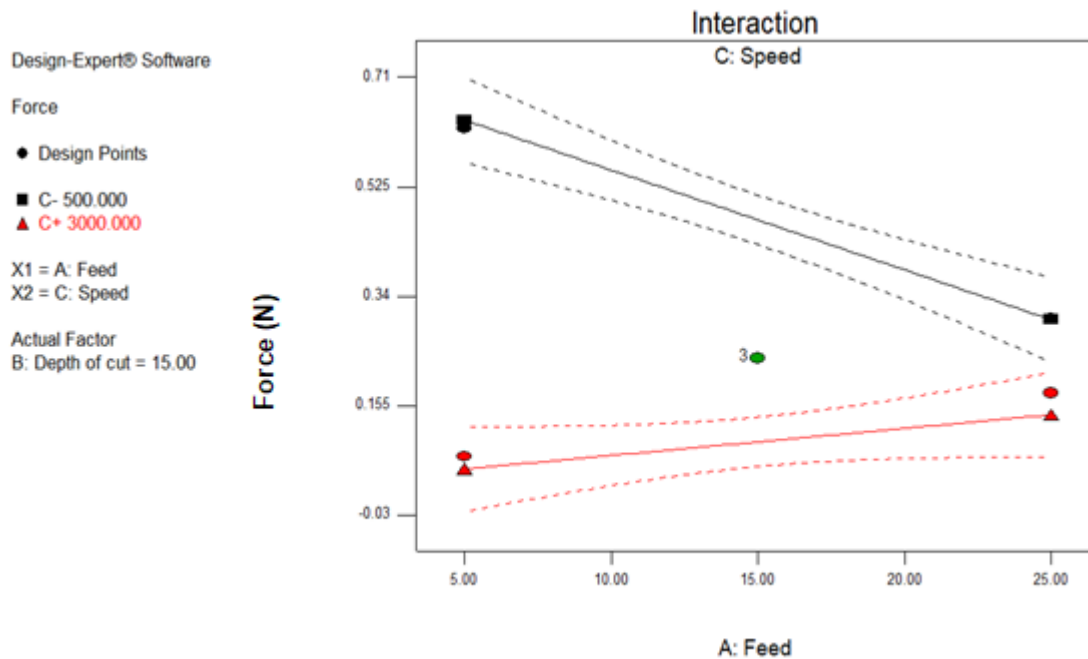


Figure 7.16: Interaction effect between speed and feed rate on cutting force at nose radius = 1.00 mm

7.3.2 Profile plot of cutting forces for RSA6061 at NR = 1.0 mm

In **Figure 7.17**, at nose radius 1.0 mm, the profile effect of cutting speed on cutting force is a negative curve. Looking closely, an increase in speed at low feed rates 5 mm/min and low depth of cut 5mm, there is a steady decrease in the cutting forces. One big disadvantage that is associated with low speed is that more raw data will be acquired during machining. **Figure 7.18**, also points out that at a cutting speed of 2645 rpm, irrespective of the level of other cutting parameters, the cutting force required to diamond turn RSA 6061 remains the same at about 0.1548 N.

In **Figure 7.19**, an increase in feed rate with high speed = 300 rpm and depth of cut = 25 mm, will result in an increase in cutting force. But negative curve was seen at low – moderate speed and depth of cut.

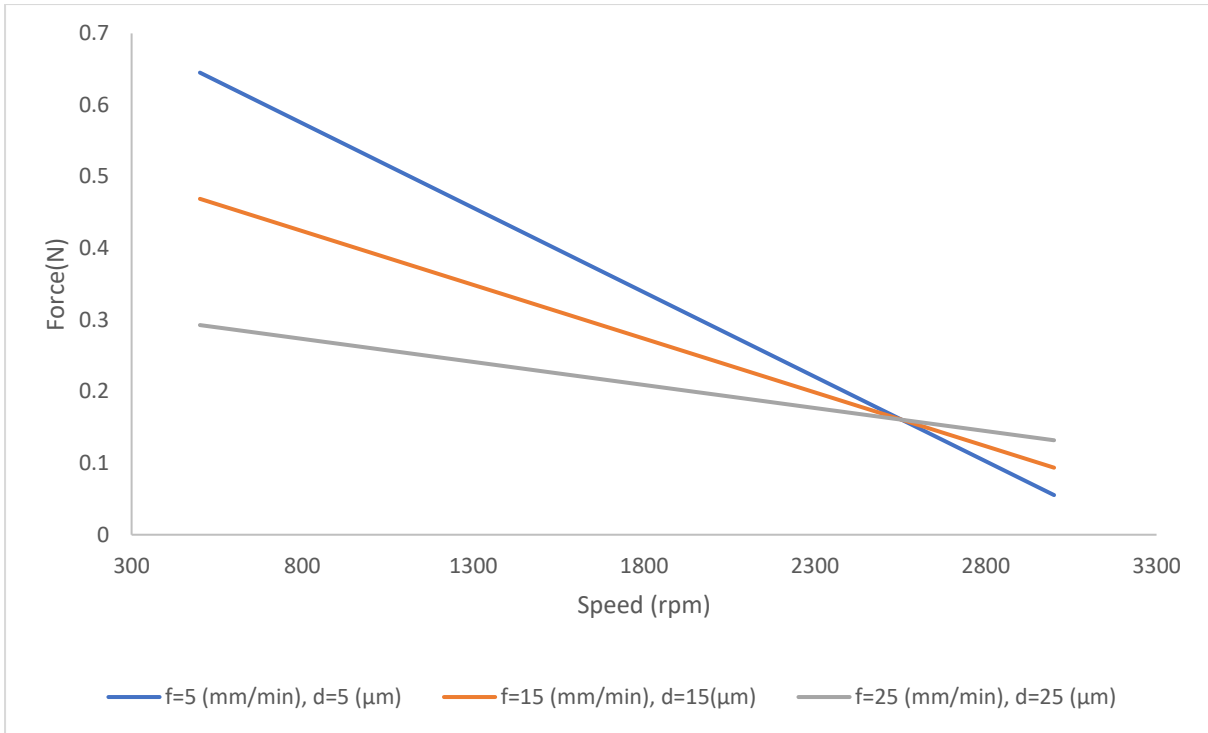


Figure 7.17: Effect of speed on cutting forces at nose radius 1.0 mm

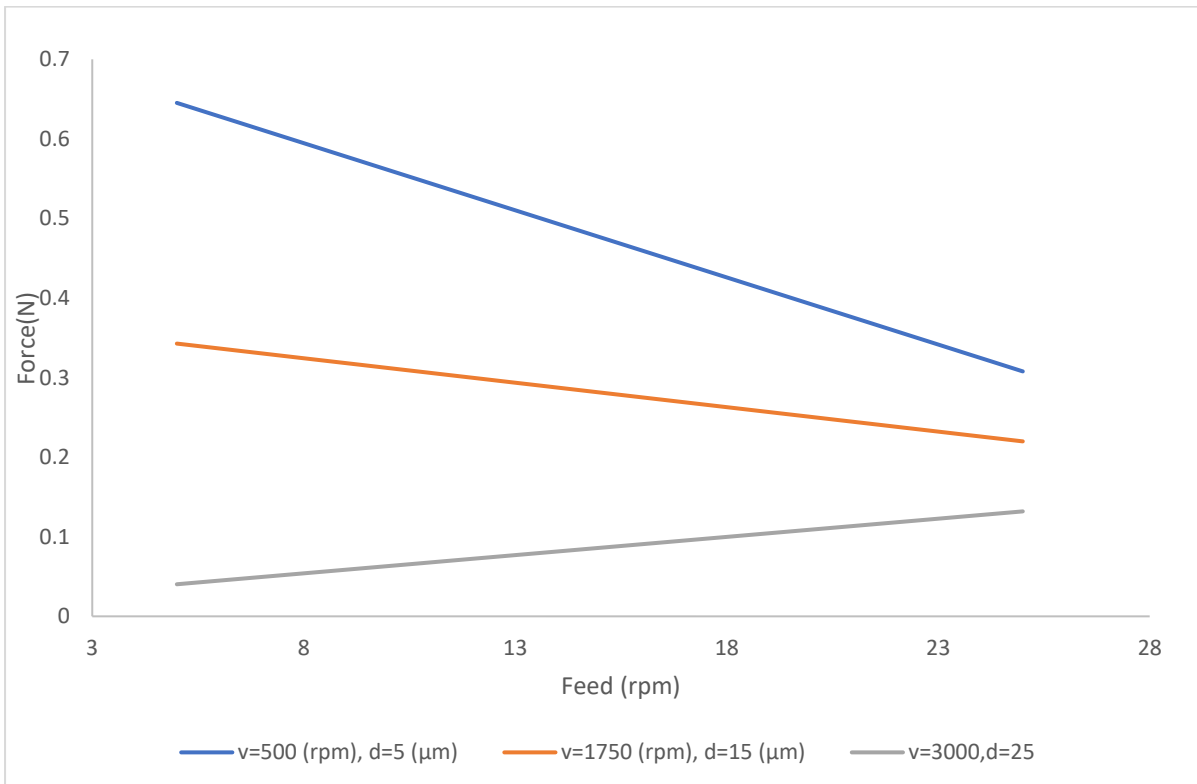


Figure 7.18: Effect of feed rate on cutting forces at nose radius 1.0 mm

According to evidence from raw data in the **Table 7.7**, the regression model in **equation 2** depicts that depth of cut has very little or negligible influence in the

experiment. **Figure 7. 19** shows effect of depth of cut on cutting for at nose radius 1.0 mm.

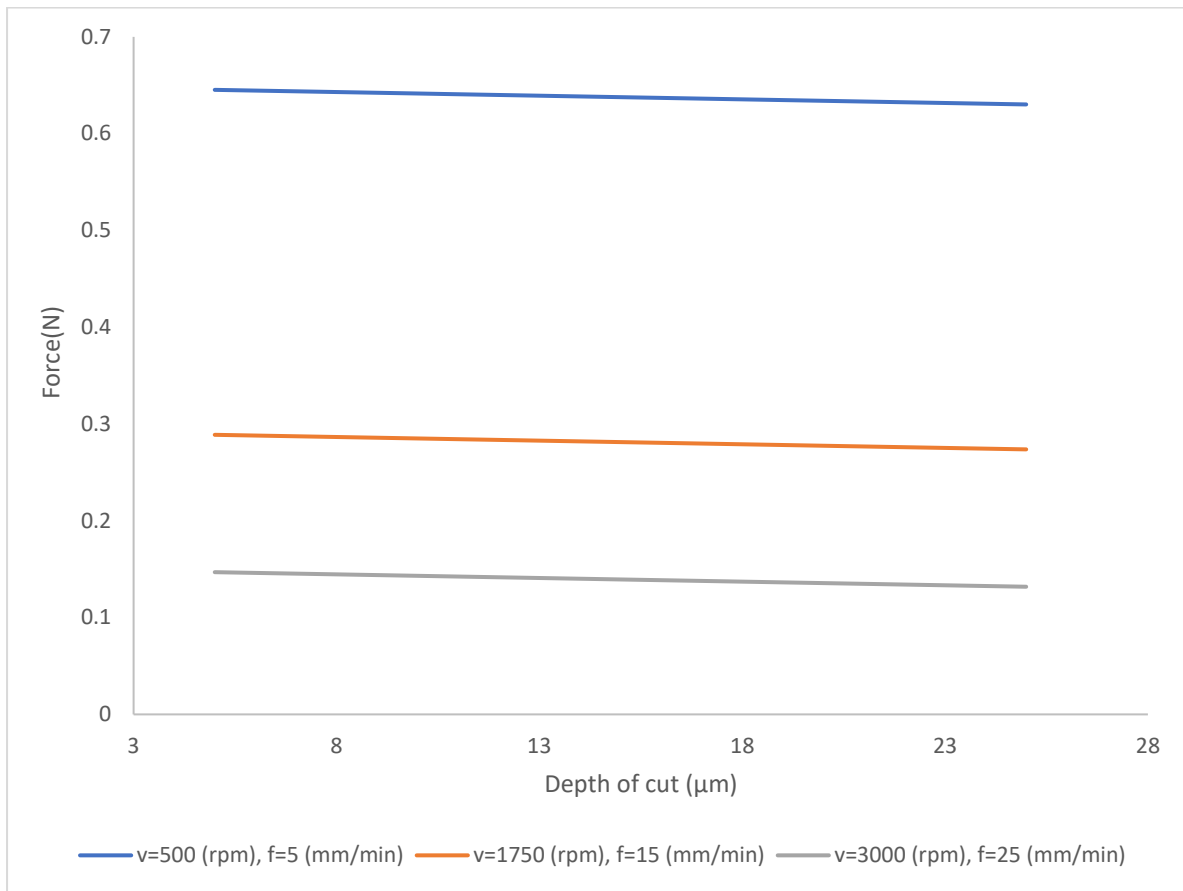


Figure 7.19: Effect of depth of cut on cutting forces at nose radius 1.0 mm

7.3.3 Optimization of cutting parameters for RSA 6061 at nose radius = 1.0 mm

Figure 7.20 confirms the optimization analysis in **Table 7.10** for maximum and minimum cutting forces. At a very low cutting parameters (feed rate, speed, and depth of cut) high cutting force is recorded. This could mean that the tool nose radius tends to exert more force on the workpiece due to low speed but at high speed and low feed rate low cutting force is expected to be noticeable.

Table 7.10: Optimization for RSA 6061 at nose radius 1.0 mm

	v(rpm)	f (mm/min)	d(μ m)	Predicted Force(N)	Actual Force (N)
Max	500	5	5	0.645238	0.416333
min	3000	5	25	0.040313	0.001625

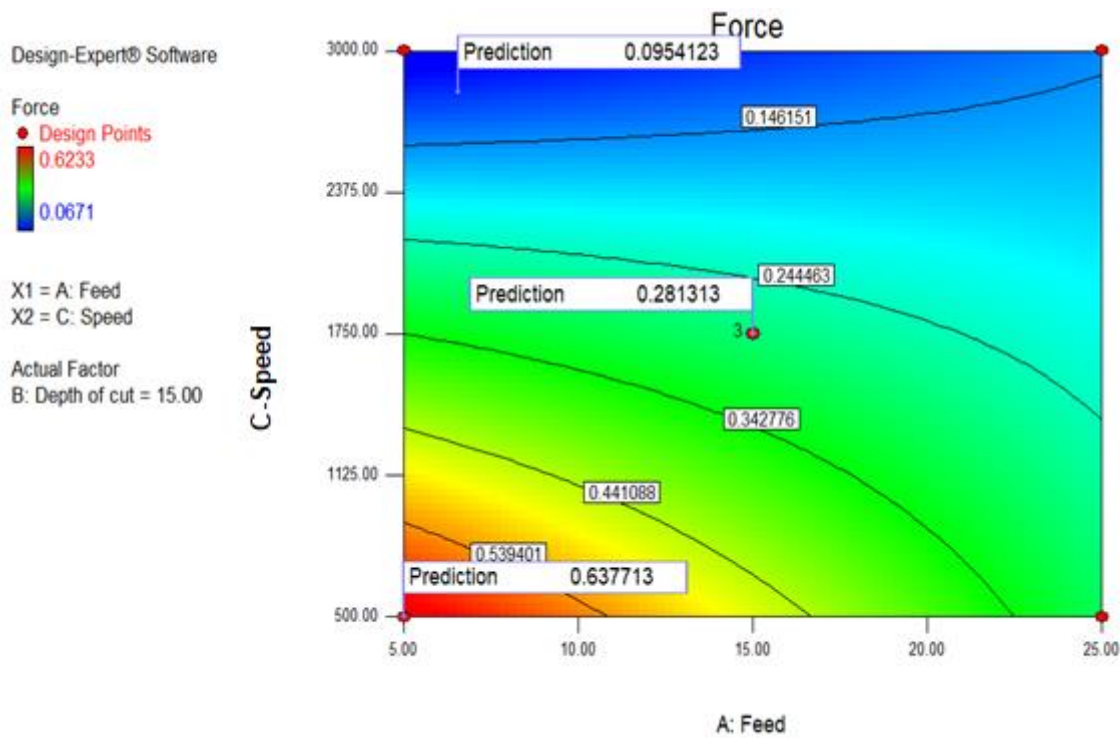


Figure 7.20: 2D contour plot for feed rate and speed on RSA 6061 at nose radius 1.5mm

7.4 FORCE ANALYSIS FOR RSA 6061 AT NOSE RADIUS OF 1.5 mm

Table 7.11 represent the force acquired at nose radius 1.5 mm. From the raw data, experimental runs 7, 10, 12 and 15 show a high cutting force, this trend witnessed is attributed to a high cutting speed. It is also observed earlier in section 7.2 with a nose radius of 1.0 mm having similar trend with a tool of nose radius 1.5 mm geometries. Further statistical analysis is carried out on the data using regression analysis and ANOVA in **Table 7. 14**.

Table 7.11: Experimental cutting forces for RSA 6061 during diamond turning using nose radius = 1.5 mm

Run	V (rpm)	F (mm/min)	D (μm)	F(N)	SQRTF(N)
Exp1	1750	25	25	0.2406	0.490510
Exp2	1750	25	5	0.0598	0.244540
Exp3	3000	5	15	0.1208	0.347563
Exp4	1750	15	15	0.1604	0.400500
Exp5	1750	15	15	0.1604	0.400500
Exp6	1750	5	25	0.0898	0.299666
Exp7	500	15	25	2.1381	1.462224
Exp8	3000	25	15	0.1427	0.377757
Exp9	3000	15	25	0.2115	0.459891
Exp10	500	25	15	1.5625	1.250000
Exp11	3000	15	5	0.3546	0.595483
Exp12	500	5	15	0.8621	0.928493
Exp13	1750	5	5	0.0333	0.182483
Exp14	1750	15	15	0.1604	0.400500
Exp15	500	15	5	0.8284	0.910165

Table 7.12 shows how much the variance inflation factor (VIF) of the model for this experiment is exaggerated by the lack of orthogonality in the design. In this experiment, the factor of orthogonal to all the other factors in the model for the VIF is 1.0. Therefore, there is no excessive correlation between the regression coefficients.

Also, the Power at 5% alpha level to detect signal/noise ratios is considered in the analysis.

Table 7.12: Summary of VIF

Term	StdErr**	VIF	Ri-Squared
A	0.35	1	0
B	0.35	1	0
C	0.35	1	0
AC	0.5	1	0
BC	0.5	1	0
A ²	0.52	1.01	0.0051
C ²	0.52	1.01	0.0051

Where A is feed in mm/min, B is depth of cut in mm, D in speed in rpm.

Table 7.13 shows Degrees of Freedom (DoF) for Evaluation. Here a good recommendation is a minimum of 3 lack of fit dF, this ensures a valid lack of fit test. For this experiment, we observed 7.

Table 7.13: DoF for evaluation

Degrees of Freedom for Evaluation	
Model	7
Residuals	7
Lack of Fit	5
Pure Error	2
Corr Total	14

7.4.1 Statistical analysis of cutting forces for RSA 6061 at nose radius = 1.5mm

Table 7.14: Regression and ANOVA output for cutting forces for RSA 6061 at NR = 1.5 mm

SUMMARY OUTPUT						
Regression Statistics						
Multiple R	0.997732					
R Square	0.995469					
Adj R Square	0.990938					
Std Error	0.036167					
Observations	15					
ANOVA						
	df	SS	MS	F	Significance F	
Regression	7	2.011756	0.287394	219.7095	1.16E-07	
Residual	7	0.009156	0.001308			
Total	14	2.020912				
	Coefficients	Standard Error	t Stat	P-value	Lower 95%	Upper 95%
Intercept	0.721803	0.076848	9.392625	3.23E-05	0.540086	0.903519
v(rpm)	-0.00096	5.3E-05	-18.1703	3.78E-07	-0.00109	-0.00084
f (mm/min)	0.052233	0.006304	8.285737	7.28E-05	0.037326	0.067139
d(μm)	0.033813	0.002836	11.92155	6.64E-06	0.027106	0.04052
vf	-5.8E-06	1.45E-06	-4.02732	0.005013	-9.2E-06	-2.4E-06
vd	-1.4E-05	1.45E-06	-9.50657	2.98E-05	-1.7E-05	-1E-05
v^2	2.8E-07	1.2E-08	23.32433	6.76E-08	2.52E-07	3.09E-07
f^2	-0.00115	0.000188	-6.1244	0.000479	-0.00159	-0.00071

From regression analysis **Table 7.14**, the value of R^2 shows 0.995469 which indicates that the model explains 99.5469% variation of cutting force explained by the cutting parameters in the experiment making the model a good fit. The F-value of 0.00000016 confirmed the model is highly significant with a p-value of 0.0000323. At a large nose radius (1.5 mm), all the cutting parameters are quite significant on the experiment. This shows that at this stage, the choice of large nose radius as cutting parameter becomes a very sensitive issue. However, since feed rate and depth of cut are operating on the same cutting domain, their effects could be misguided. Furthermore, from literature, we can be guided on how to interpret the results. From the ANOVA results, speed has highest influence with a p-value of 0.00000016 which contributed about 47.52% effect on the experiment. The squared of speed gave us the most significant value at p-value of 0.000000067 with a contribution of 35.14% total effects.

Technically, the effect of feed rate and depth of cut will always remain significant due to large pressure. For example, feed rate effect on the workpiece due to thrust force and the scratching of chip thickness of large nose radius on the machined surface. From the model in **Equation 7.3**, the coefficient of speed is negative which signifies that an overall square root of cutting force is expected to decrease by a unit value of 0.00096 when other corresponding independent variable such as depth of cut and feed rate are kept constant. Positive coefficients of depth of cut, feed rates and squared of speed are also expected to increase the square root of cutting force by a unit of 0.033813, 0.052233 and 0.0000028, respectively.

Figure 7.21 shows the scattered plot for the experiment which establishes and validates the standard of the model. **Figure 7.22** represent the comparison between experimental and predicted values. The model generated from the experiment after statistical analysis on RSA 6061 using Nose radius 1.5mm is as follows:

Equation 7.3

$$F = (-0.7218 - 9.6 \times 10^{-4}V + 0.052F + 0.033D - 5.8 \times 10^{-6}VF - 1.4 \times 10^{-5}VD + 2.8 \times 10^{-7}V^2 - 1.15 \times 10^{-3}F^2)^{\frac{1}{2}}$$

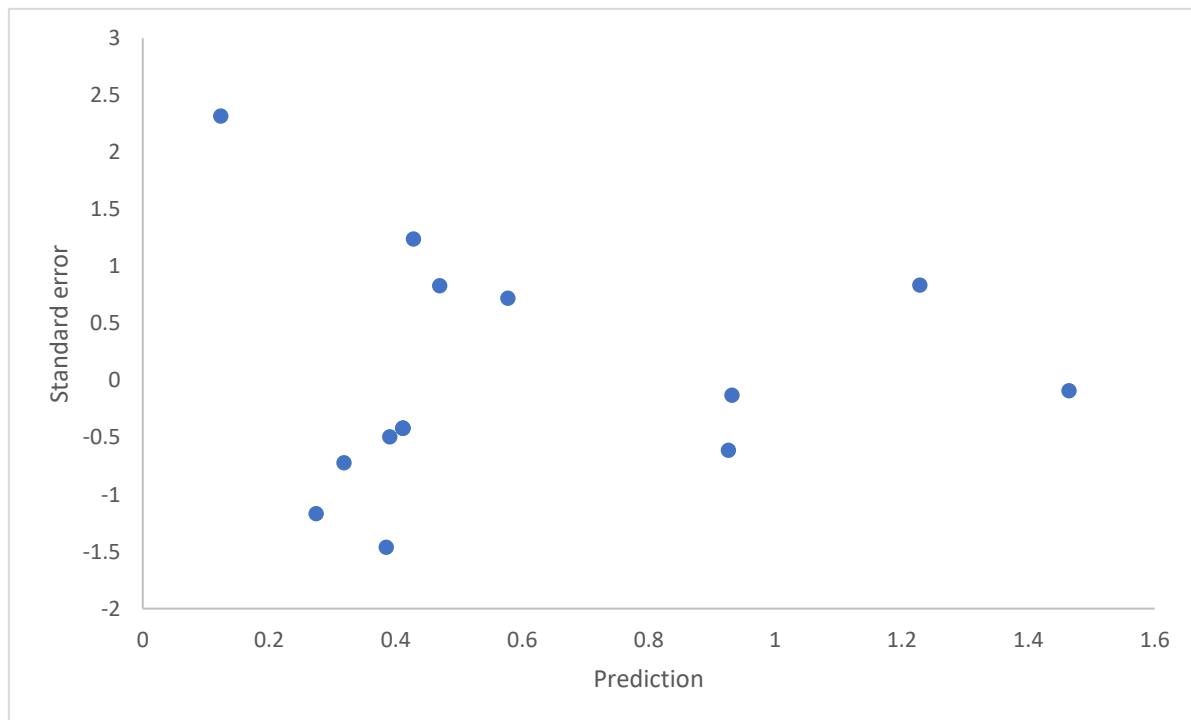


Figure 7.21: Scattered plot for RSA 6061 at nose radius 1.5mm

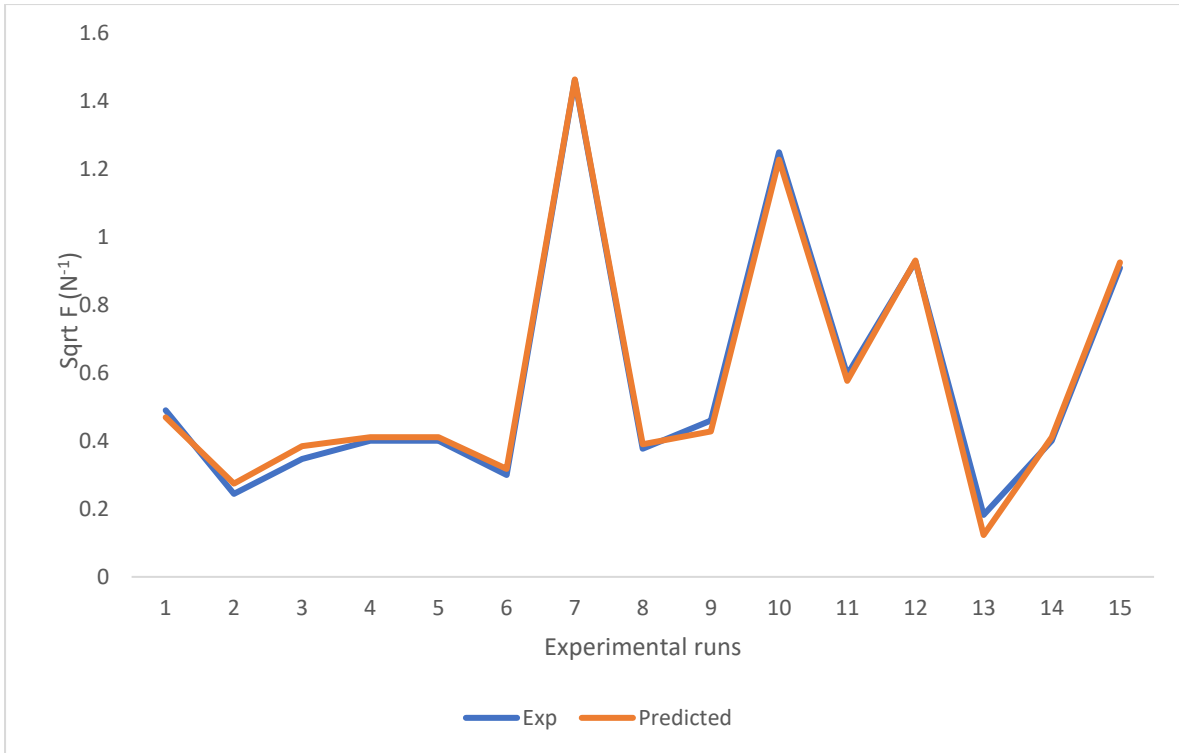


Figure 7.22: Comparison between experimental and predicted value for RSA 6061 at nose radius 1.5 mm

Figures 7.23 and 7.24 show 2D and 3D contour plots for speed and feed rates. The Flagged spots reveal some predictions that are close or the same with square root of cutting forces data in Table 7.11 in experimental runs 3, 4, 5 and 10, (Figure 7.23).

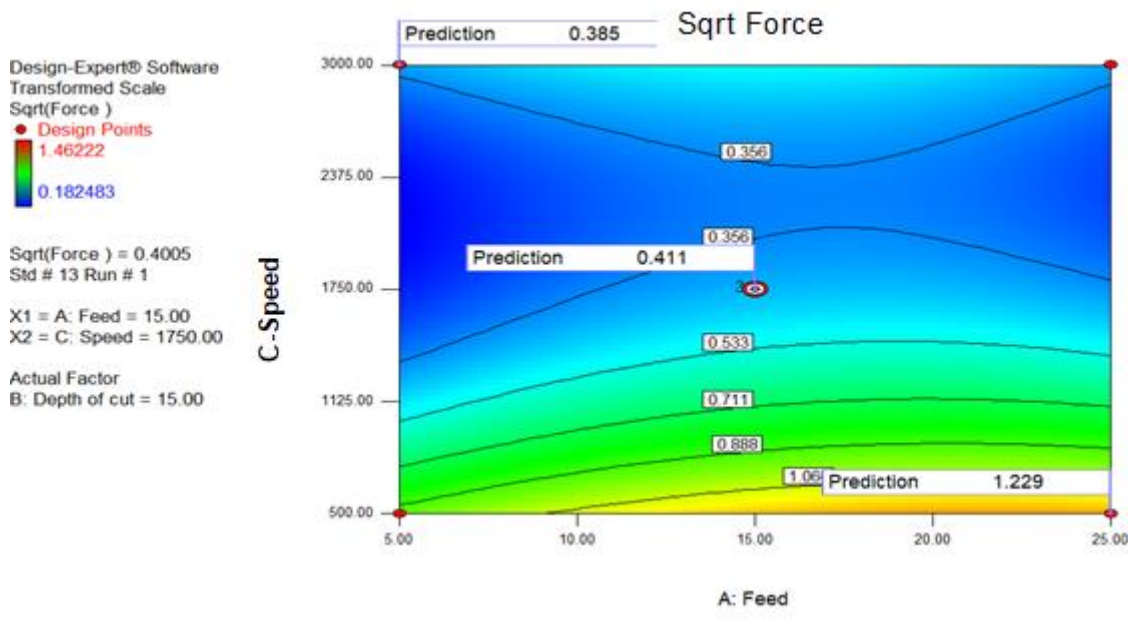


Figure 7.23: 2D contour plot speed and feed rate for RSA 6061 at nose radius 1.5 mm

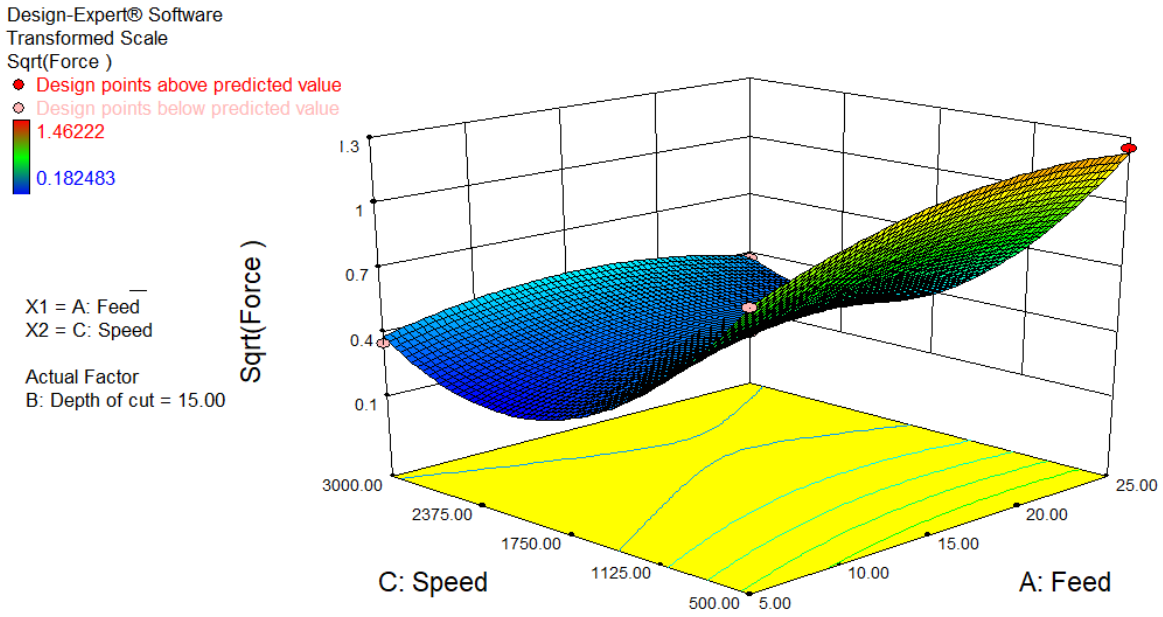


Figure 7.24: 3D contour plot between speed and feed rate for RSA 6061 at nose radius 1.5 mm

Figure 7.25 represent 2D contour plot for the interaction between speed and depth of cut at constant feed 15 mm/min. **Figure 7.26** represent the 3-D contour plots of **Figure 7.25**. They also confirm some predictions that are close or the same with values in the Experimental runs 4, 5, 7, 9 and 14 in **Table 7.11**.

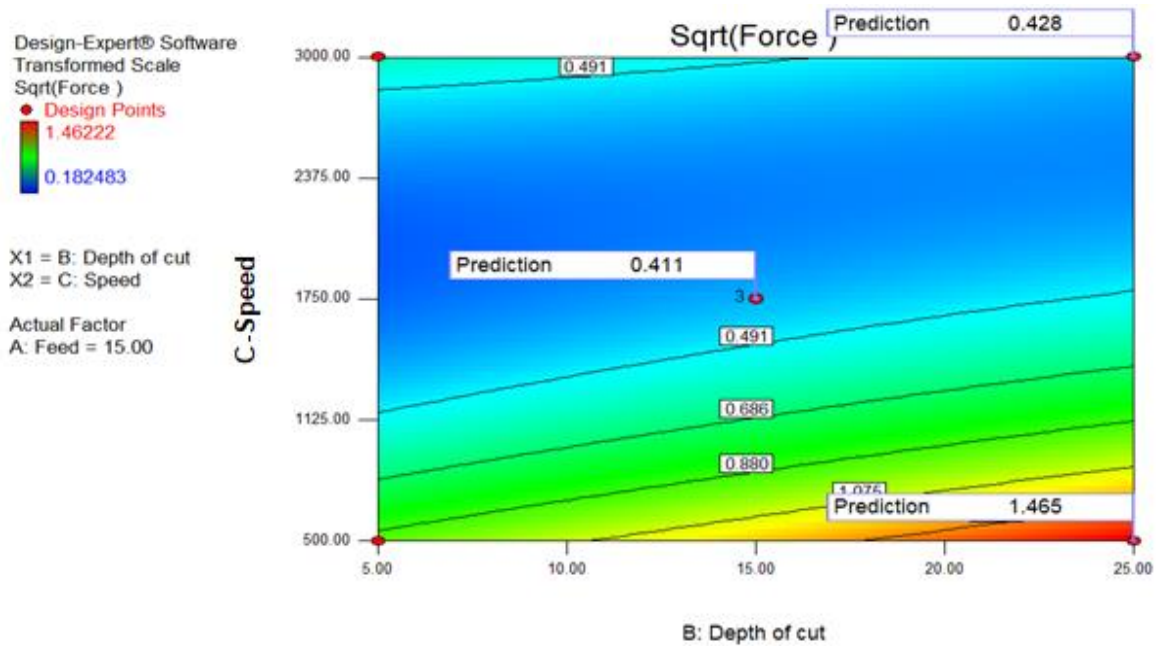


Figure 7.25: 2D contour plot between speed and depth of cut for RSA 6061 at nose radius 1.5 mm

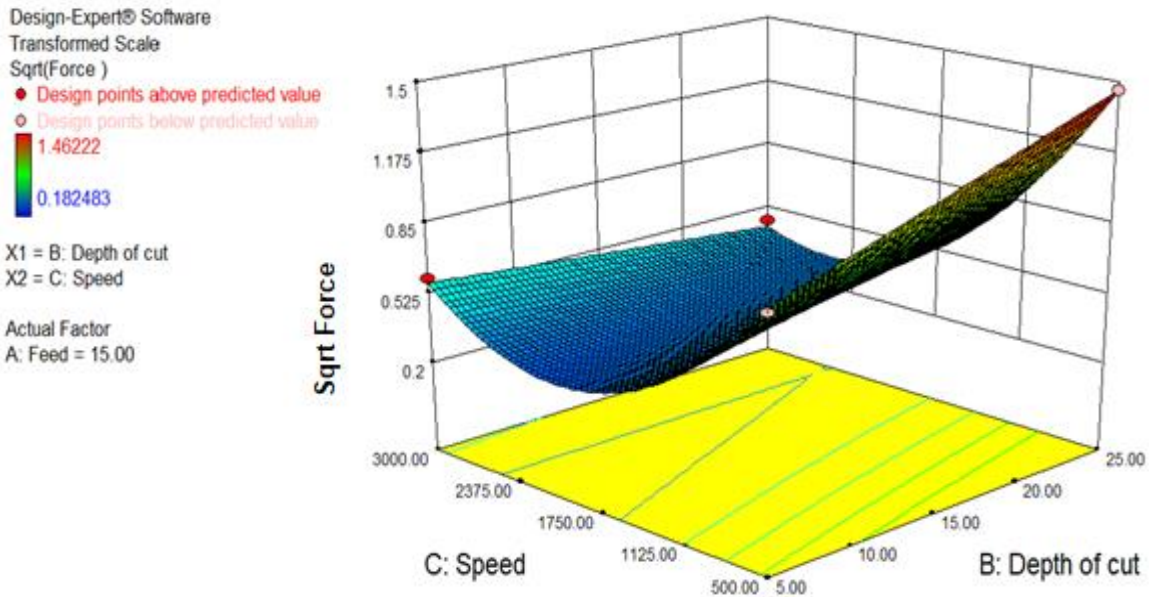


Figure 7.26: 3D contour plot between speed and depth of cut for RSA 6061 at nose radius 1.5 mm

7.4.2 Profile plot of cutting parameters for force on RSA6061 at nose radius 1.5 mm

In **Figure 7.27**, constant feed rates and depth of cut were varied against Speed at a time, the trend shows that an increase in speed leads to a decrease in cutting force. It can also be said that at this condition, a steady concave decrease in the square root of cutting force. However, at moderate - high feed rate and Depth of cut, there is a promising increase in inverse of cutting force. Also noted at cutting conditions where feed rate = 25 mm/min, depth of cut = 25 mm and Speed = 2107 rpm i.e at Point A, the same value of square root of Cutting force was observed. It was also noticed that at Point B, the same square root of cutting force was observed for feed rate = 5 mm/min and depth of cut = 25 mm.

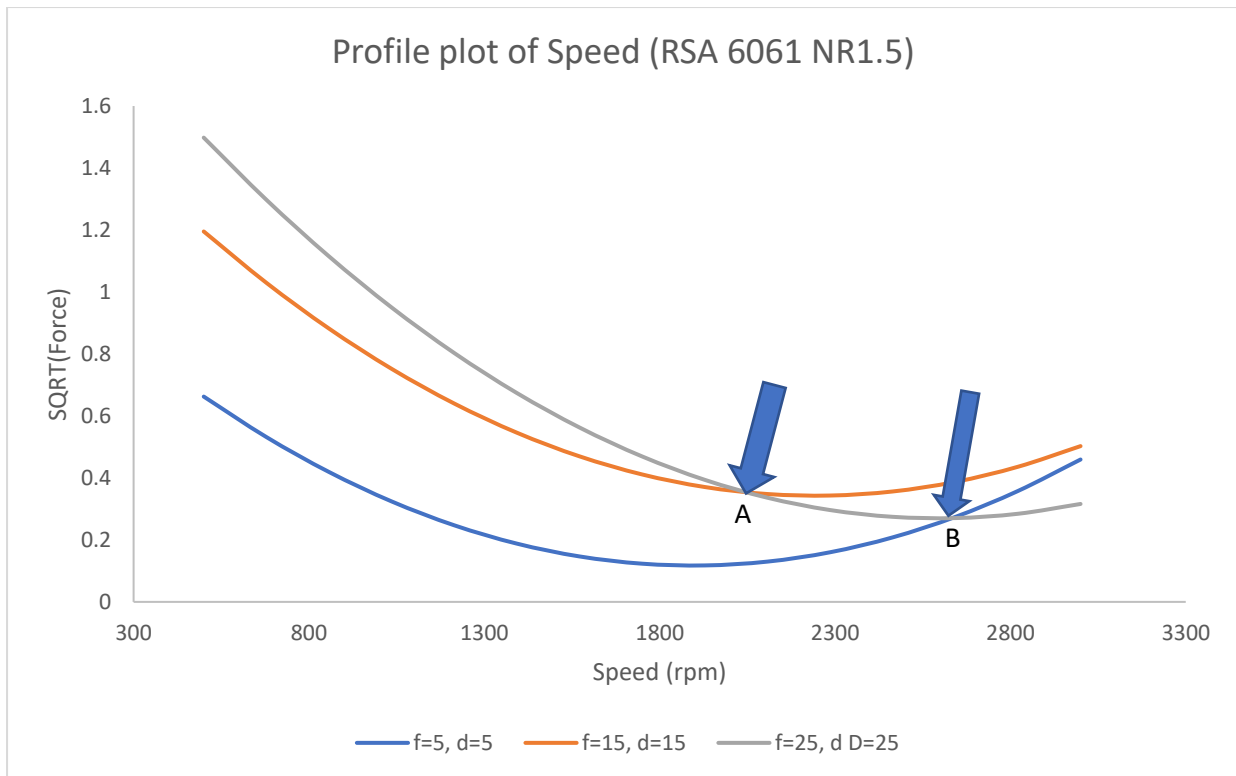


Figure 7.27: Effect of Speed on cutting forces at nose radius 1.5mm

Figure 7.28 represents the profile plot for the effects of Feed on diamond turning RSA 6061 at various level for nose radius 1.5 μ m. In **Figure 7.28**, an increase in Feed rate results in an increase in cutting force, a closer look revealed that, at low speed of 500rpm and depth of cut of 5 μ m, cutting force continue to increase as the fed rate increases. This means, at these conditions, only feed rate is dominating the cutting process and no other parameter to leverage the effect of feed during machining. However, we can witness opposite scenario at moderate - high for speed and depth of cut. At the same condition for moderate – high cutting parameters, an intersection i.e., at Point A in **Figure 7.28**, at feed rate = 17.85 mm/min, Speed = 3000 rpm and depth of cut = 25 μ m a square root of cutting force of 0.419 N was predicted which is close to what was acquired in experiment number 9 in **Table 7.11**.

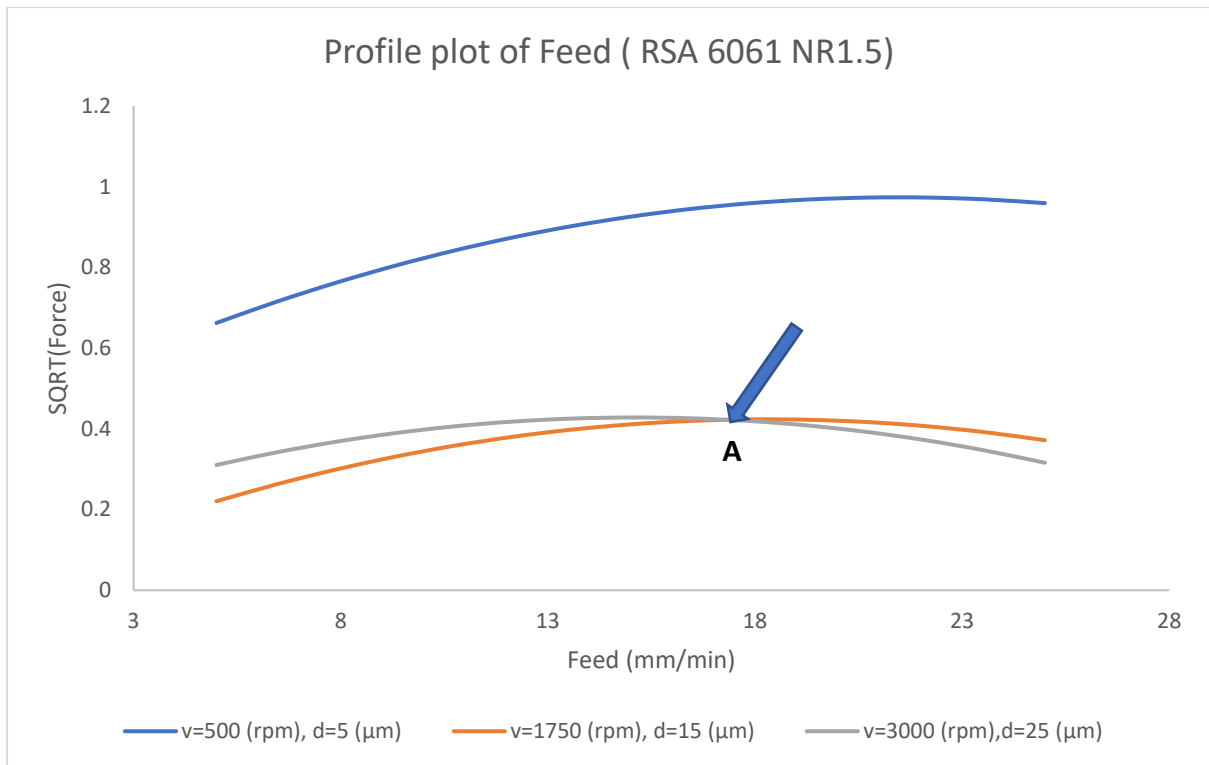


Figure 7.28: Effect of speed on feed rate at nose radius 1.5 mm

In **Figure 7.29**, the profile plot for the effects of depth of cuts on diamond turning RSA 6061 at various cutting rates. An increase in depth of cut will generally lead to an increase in square root of cutting force. Due to large nose radius, chip formation becomes fairly wide and large. Hence, continue to hit and tangle around the cutting tool on the surface of the workpiece, it scratches and contributes extra force to the cutting force. At low speed at 500 rpm and feed rates at 5 mm/min, a proportionate increase in square root of cutting Force was observed.

However, at high speed = 3000 rpm and feed rates = 25 mm/min, with varied depth of cuts, a proportionate slight decrease in square root of cutting forces were observed. At this condition, it simply confirms what was experienced or witnessed in **Figure 7.28** above. Furthermore, it was also noticeable that at moderate – high cutting parameters conditions, an intersection i.e., at Point A, when feed rate = 25 mm/min, speed = 3000 rpm and depth of cut = 13.6 μm a square root of cutting force of 0.401N was predicted.

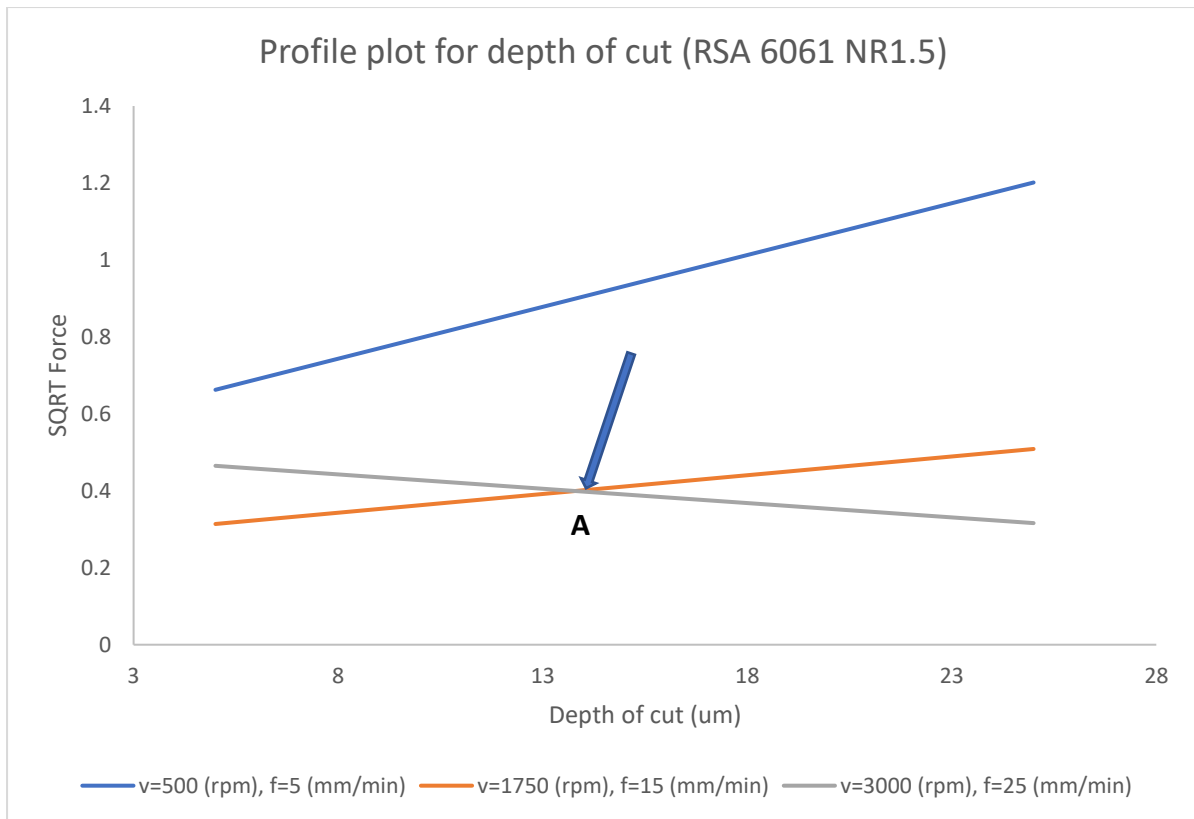


Figure 7.29: Effect of Speed on depth of cut at nose radius 1.5 mm

7.4.3 Optimization of cutting parameters for RSA 6061 at nose radius = 1.5 mm

To optimize the machining process, **Table 7.15** shows the best combination for cutting parameters.

Table 7.15: Optimization conditions for RSA 6061 at nose radius 1.5 mm

	V (rpm)	F (mm/min)	D (μm)	Predicted sqrt Force	Actual Force (N)
Max	500	21.45616	25	1.512458	2.2876
min	2102.958	25	5	0.239495	0.0574

7.5 THE EFFECTS OF TOOL GEOMETRY AND MACHINE PARAMETERS ON CUTTING FORCE DURING MACHINING OF RSA 6061.

This section investigates the effects and interactions of cutting parameters against the three different tool nose radii are used in this study. The tool geometry adopted in this study is Nose radius (NR), Rake Angle and Clearance Angle. The nose radius diameters used are 0.5 mm, 1.0 mm, and 1.5 mm. However, constant rake angle at 0° and clearance angle at 10° cylindrical were maintained. **Figures 7.30 – 7.38** reveal and depict interactive performance during diamond turning of RSA 6061.

7.5.1 Effects of speed and varied nose radius (NR) on cutting force

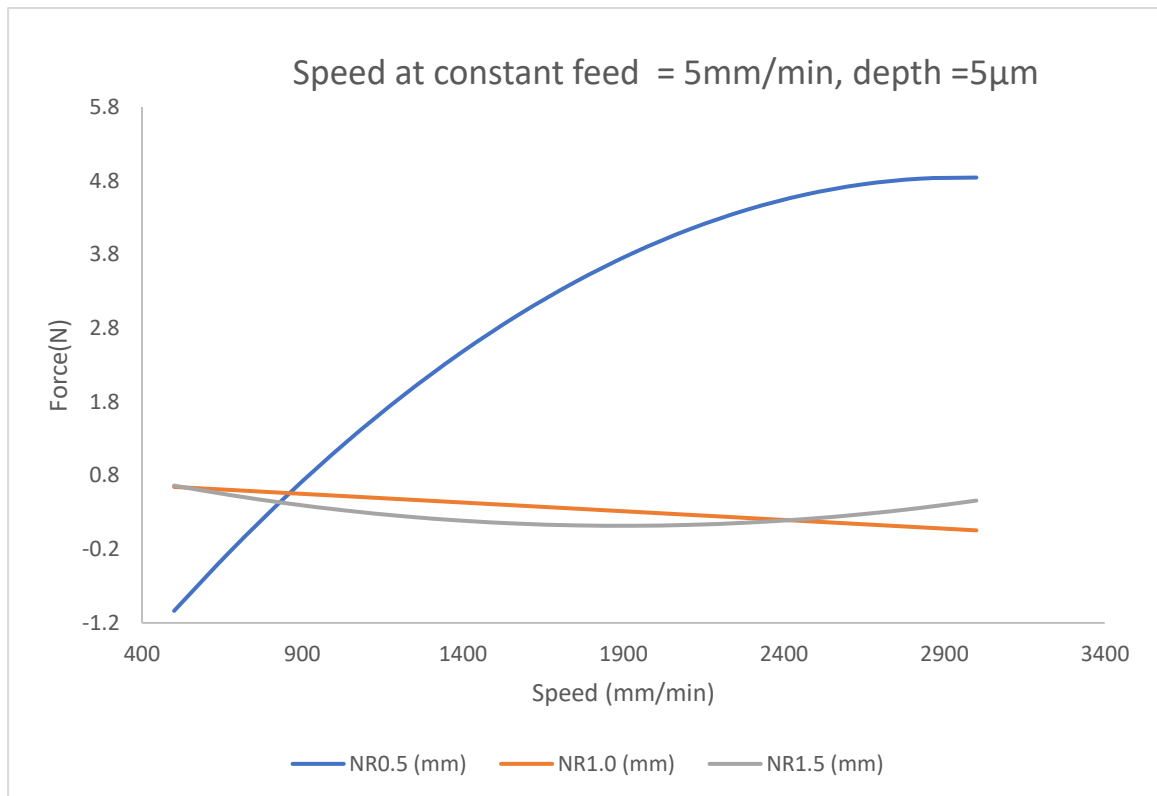


Figure 7.30: Effect of speed on cutting force at constant feed rate = 5 mm/min, Depth of cut = 5 μ m and varied nose radius (0.5 – 1.5) mm

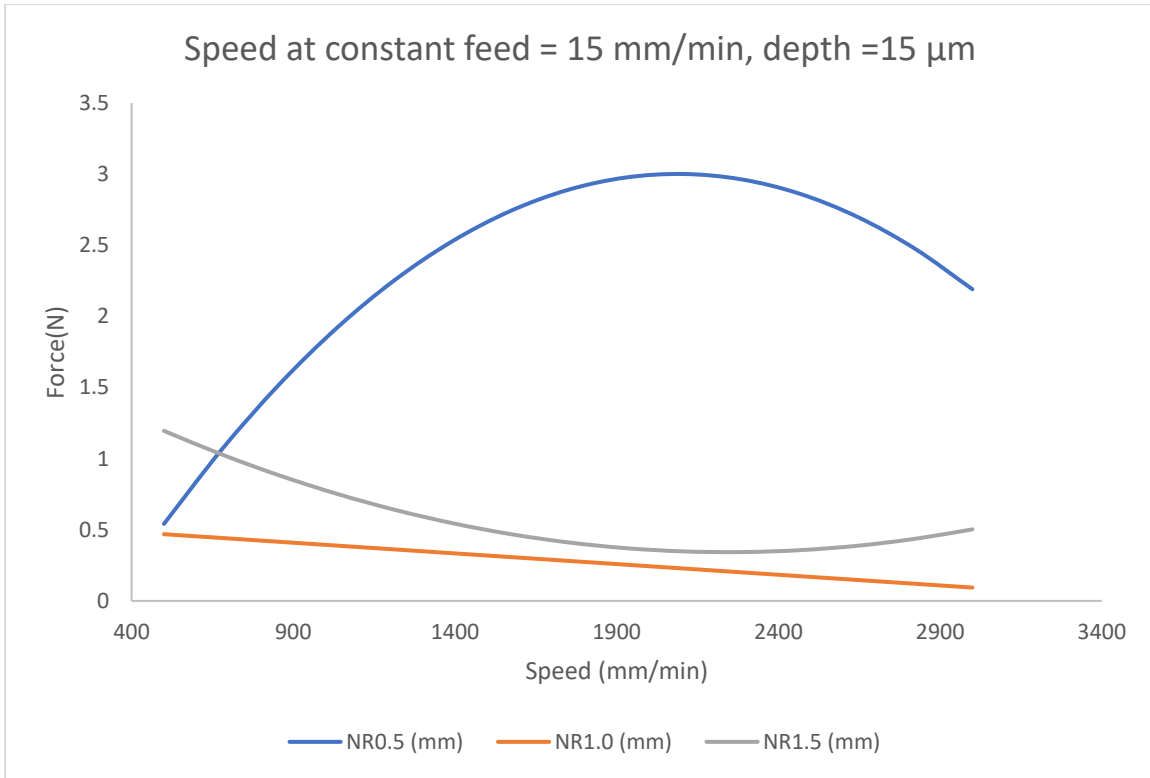


Figure 7.31: Effect of speed on cutting force at constant feed rate = 15 mm/min, depth of cut = 15 μ m and varied nose radius (0.5 – 1.5) mm

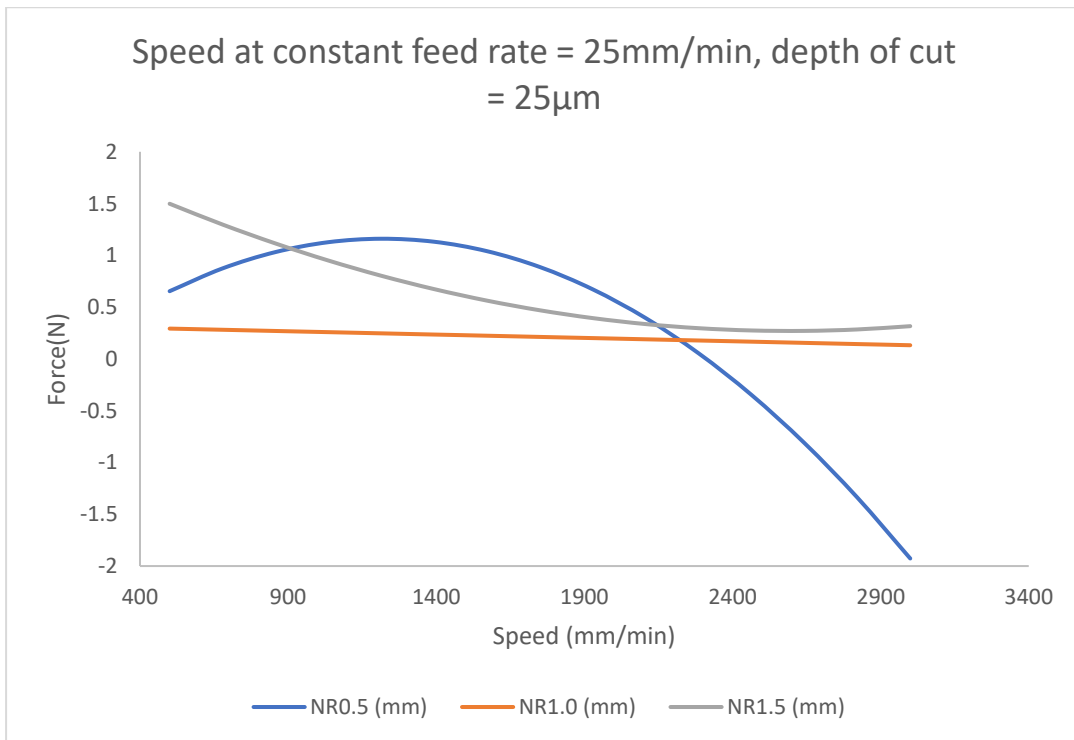


Figure 7.32: Effect of speed on cutting force at constant feed rate = 25 mm/min, Depth of cut = 25 μ m and varied nose radius (0.5 – 1.5) mm

7.5.2 Effects of feed rate and varied nose radius on cutting forces

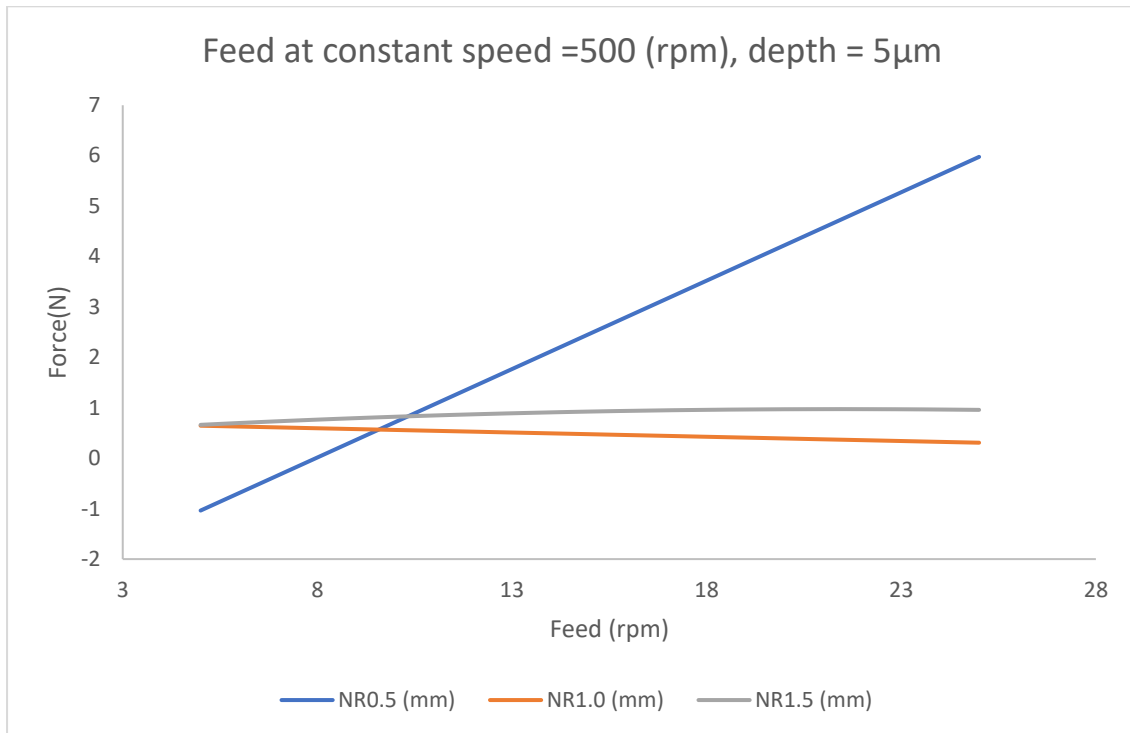


Figure 7.33: Effect of feed rate on cutting force at constant speed = 500rpm, Depth of cut = 5 μ m and varied nose radius (0.5 – 1.5) mm

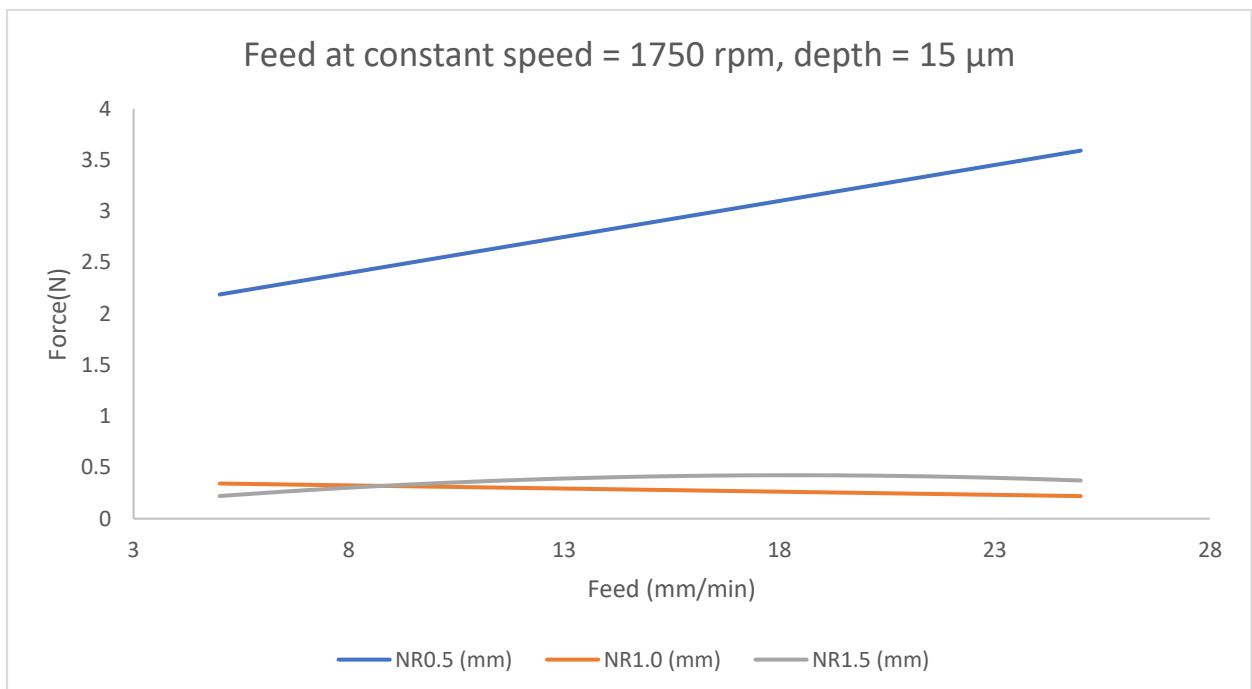


Figure 7.34: Effect of feed rate on cutting force at constant speed = 1750 rpm, depth of cut = 15 μ m and varied nose radius (0.5 – 1.5) mm

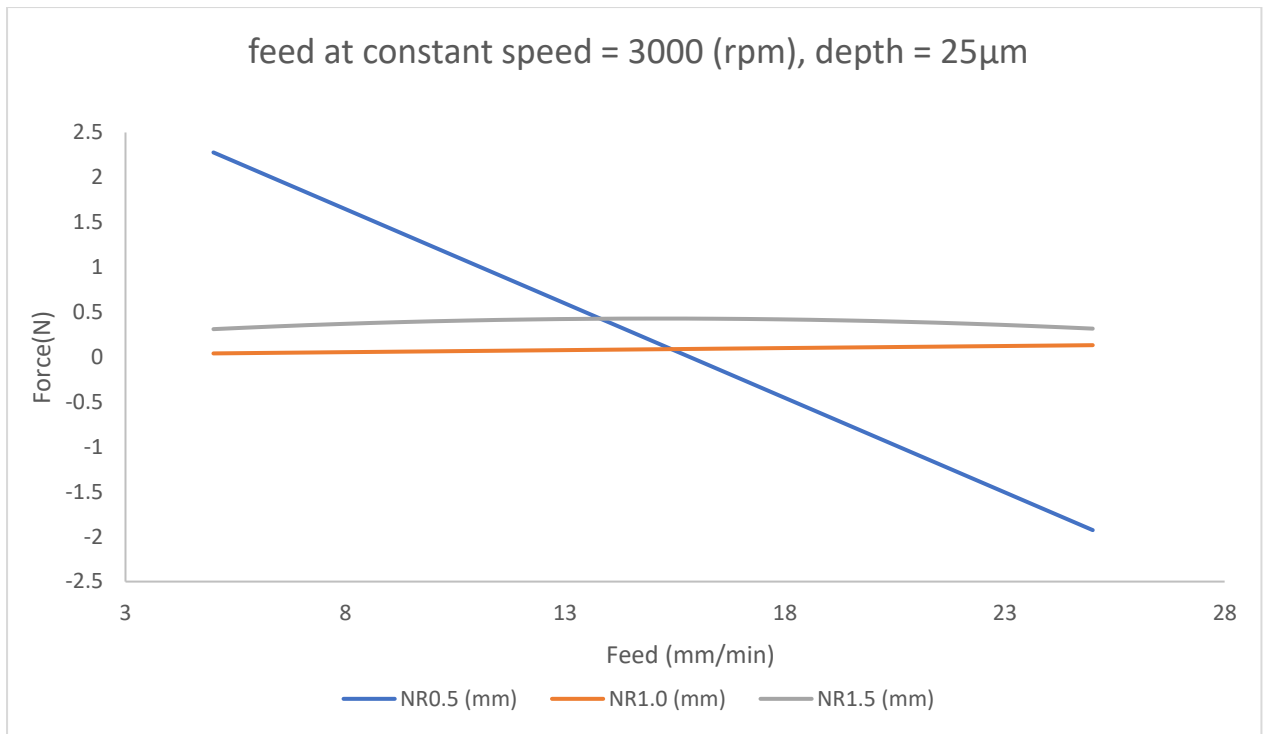


Figure 7.35: Effect of feed rate on cutting force at constant speed = 3000 rpm, Depth of cut = 5 μ m and varied nose radius (0.5 – 1.5) mm

7.5.3 Effects of depth of cut and varied nose radius (NR) on cutting forces

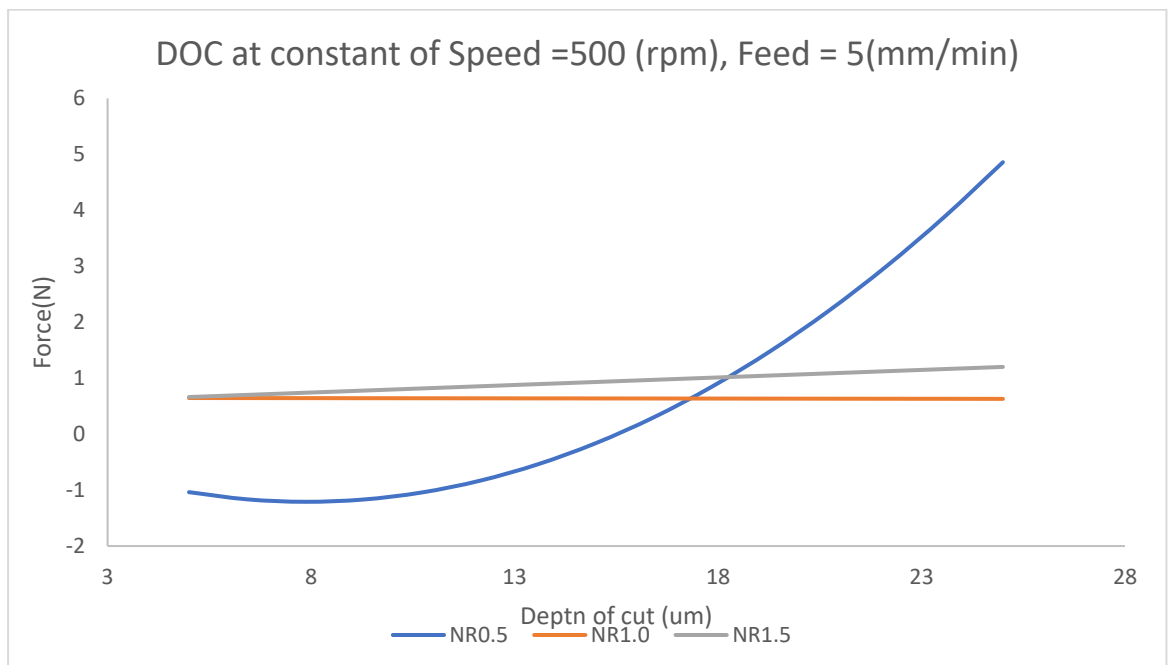


Figure 7.36: Effect of depth of cut on cutting force at constant speed = 500 rpm, feed rate = 5 mm/min and varied nose radius (0.5 – 1.5) mm

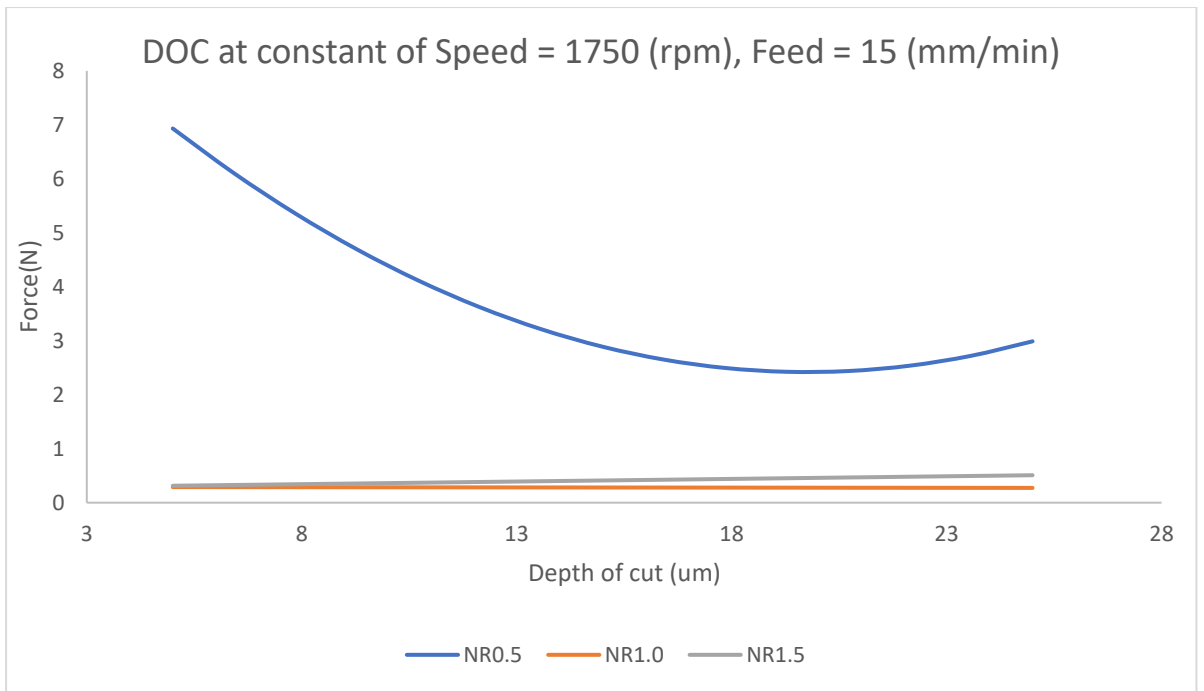


Figure 7.37: Effect of depth of cut on cutting force at constant speed = 1750 rpm, feed rate = 15 mm/min and varied nose radius (0.5 – 1.5) mm

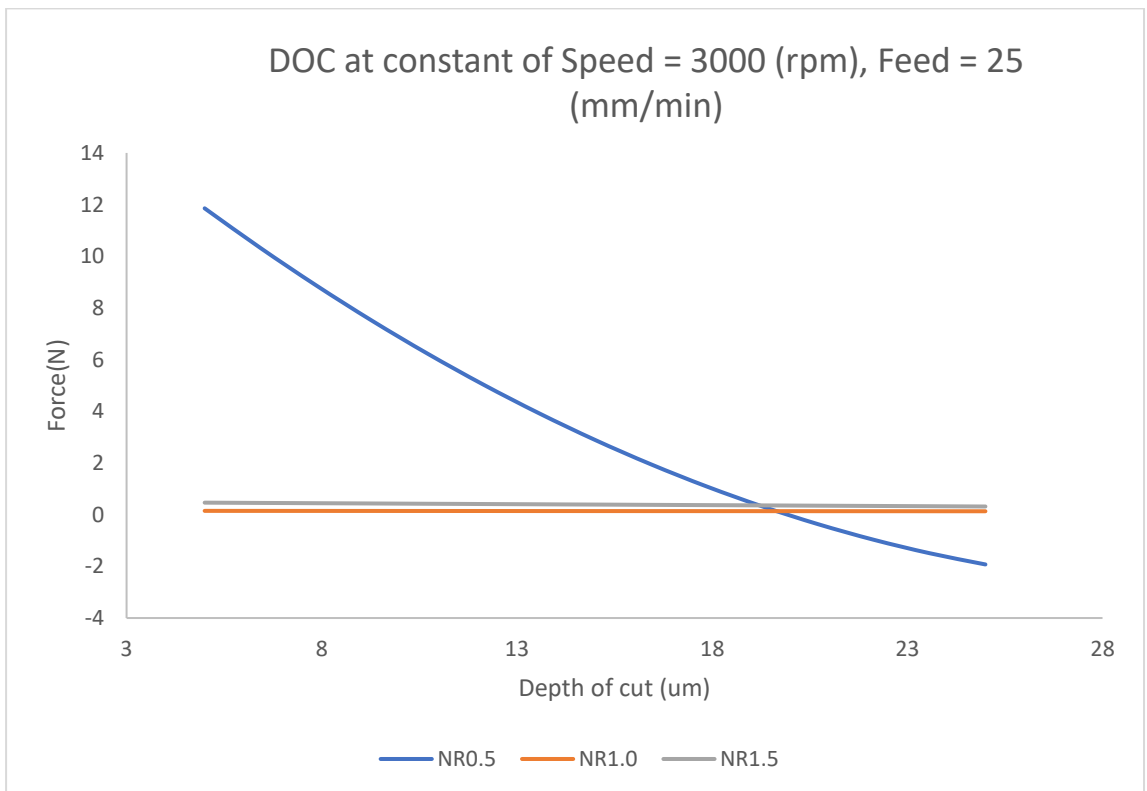


Figure 7.38: Effect of depth of cut on cutting force at constant speed = 3000 rpm, feed rate = 25 mm/min and varied nose radius (0.5 – 1.5) mm

7.6 SURFACE ROUGHNESS ANALYSIS FOR RSA 6061

7.6.1 Introduction

The focus of this section is to investigate surface roughness of the newly graded aluminium alloy namely RSA6061 that can be a potential material candidate for making advanced optical components instead of traditionally used AA 6061 optical aluminium. In this study, predictive surface roughness models are developed and optimization of the effect of cutting parameters on the surface roughness is performed. The chapter is based on conducting a series of diamond machining experiments using a monocrystalline diamond cutting tool on an ultra-high precision single-point diamond turning machine tool. Response surface methodology with Box-Behnken design is used to develop a model that may describe the influence of the diamond turning cutting parameters such as cutting speed, feed rates and depth of cut on the surface roughness. The analysis of variance (ANOVA) shows that under the optimization approach of the cutting parameters, one can attain a surface quality on RSA at levels as low as 1 nm. It is also found that the most significant parameters that affects surface quality of the RSA alloys are high feed rates and high spindle speed.

In single point diamond turning (SPDT) process, cutting parameters and tool parameters has been identified to significantly influenced the surface roughness. Analytically, the relationship can be expressed as:

Equation 7.4

$$R_a \approx \frac{0.032f^2}{RV^2}$$

Where R_a is surface roughness, f is the feed rates, R is tool nose radius, V is the rotational spindle speed and D is the depth of cut.

Considering the surface roughness value as a response and cutting parameters as input, in most cases, it is possible to attain a linear, second order (i.e., quadratic) or exponential model expressing the relationship between the output and input. In this study, an exponential equation has been established for the surface roughness of RSA 6061. The objective of this section is to investigate experimentally the influence of cutting parameters on the surface roughness during diamond turning of RSA6061 to

determine the optimal settings to improve surface quality. While the effect of depth of cut will be further investigated using molecular dynamics. The **Table 7.16** represent responses acquired during machining. **Table 7.17** presented a further statistical analysis on the experimental responses.

Table 7.16: Experiment results for surface roughness (Ra)

Run	V (rpm)	F (mm/min)	D (μm)	Ra (nm)	Ln (Ra) nm
Exp1	1750	25	25	3.0	1.098612
Exp2	1750	25	5	2.5	0.916291
Exp3	3000	5	15	2.1	0.741937
Exp4	1750	15	15	3.6	1.280934
Exp5	1750	15	15	4.0	1.386294
Exp6	1750	5	25	2.3	0.832909
Exp7	500	15	25	36.0	3.583519
Exp8	3000	25	15	2.4	0.875469
Exp9	3000	15	25	3.0	1.098612
Exp10	500	25	15	132.2	4.884315
Exp11	3000	15	5	1.6	0.470004
Exp12	500	5	15	3.0	1.098612
Exp13	1750	5	5	1.8	0.587787
Exp14	1750	15	15	3.8	1.335001
Exp15	500	15	5	37.1	3.613616

Figures 7.39 – 7.44 represent and display the profile charts for some of the worst and the best surface roughness acquired during diamond turning of RSA 6061. The filtration condition for the profilometer cut-off is 0.25 mm.

5.23.15.102

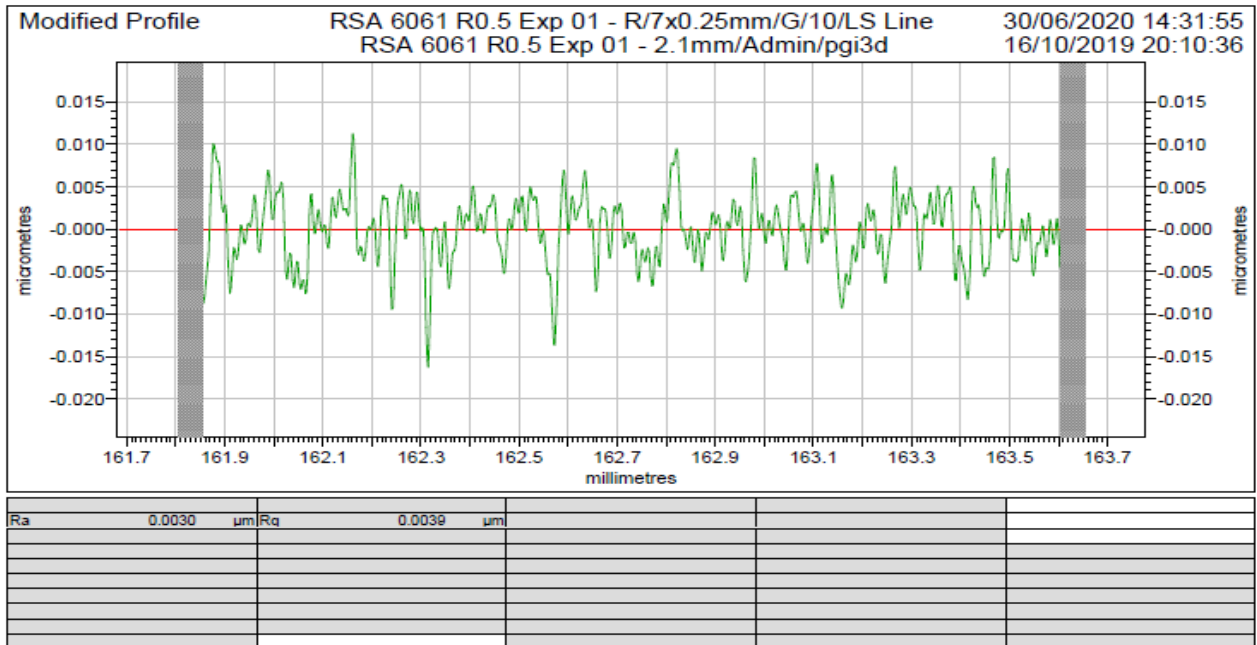


Figure 7.39: Profile chart for Experiment 1, speed = 1750 rpm, feed rate = 25 mm/min and depth of cut = 25 μm . $R_a = 0.3 \text{ nm}$

5.23.15.102

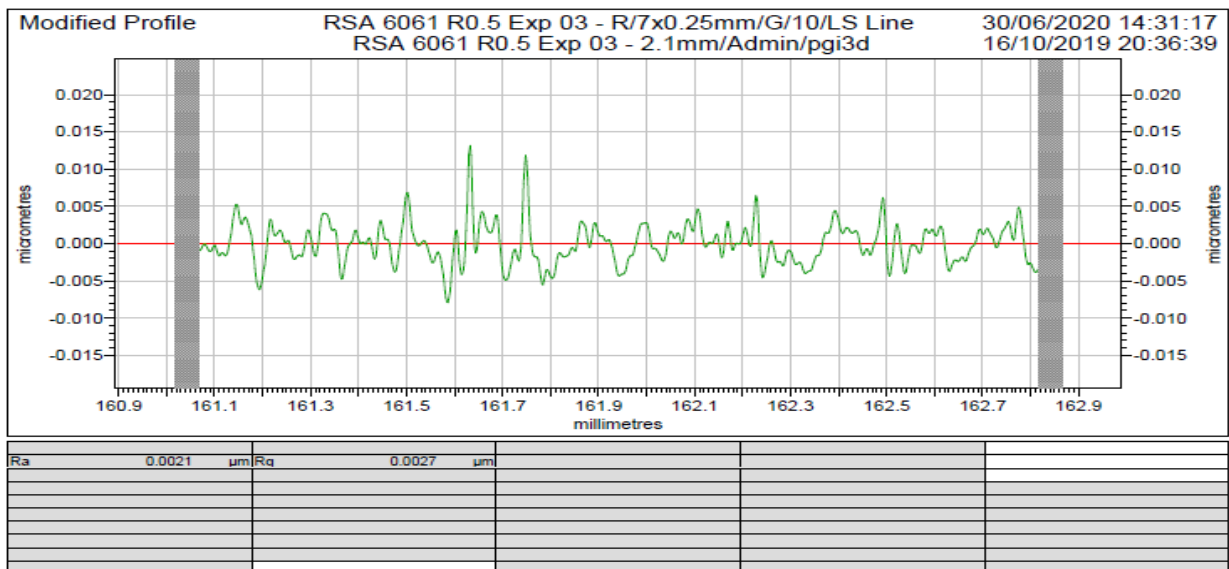


Figure 7.40: Profile chart for Experiment 3, speed = 3000 rpm, feed rate = 5 mm/min and depth of cut = 15 μm . $R_a = 2.1 \text{ nm}$

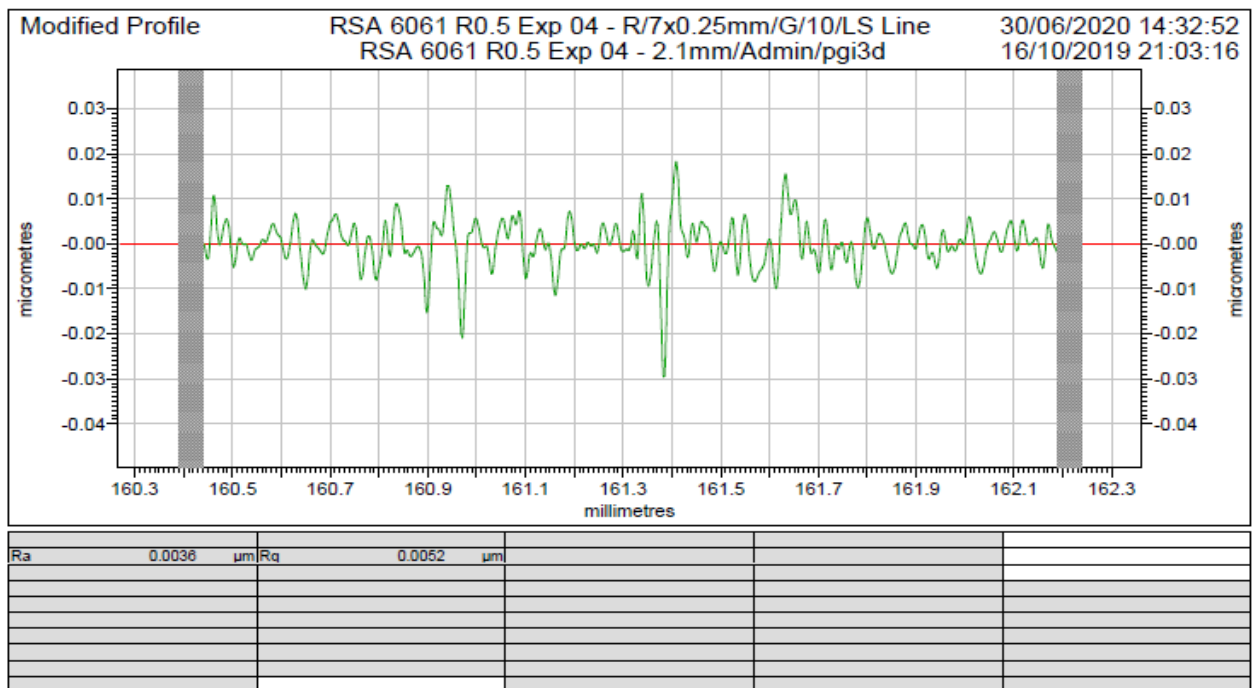


Figure 7.41 Profile chart for Experiment 4, speed = 1750 rpm, feed rate = 15 mm/min and depth of cut = 15 µm. $R_a = 3.6$ nm

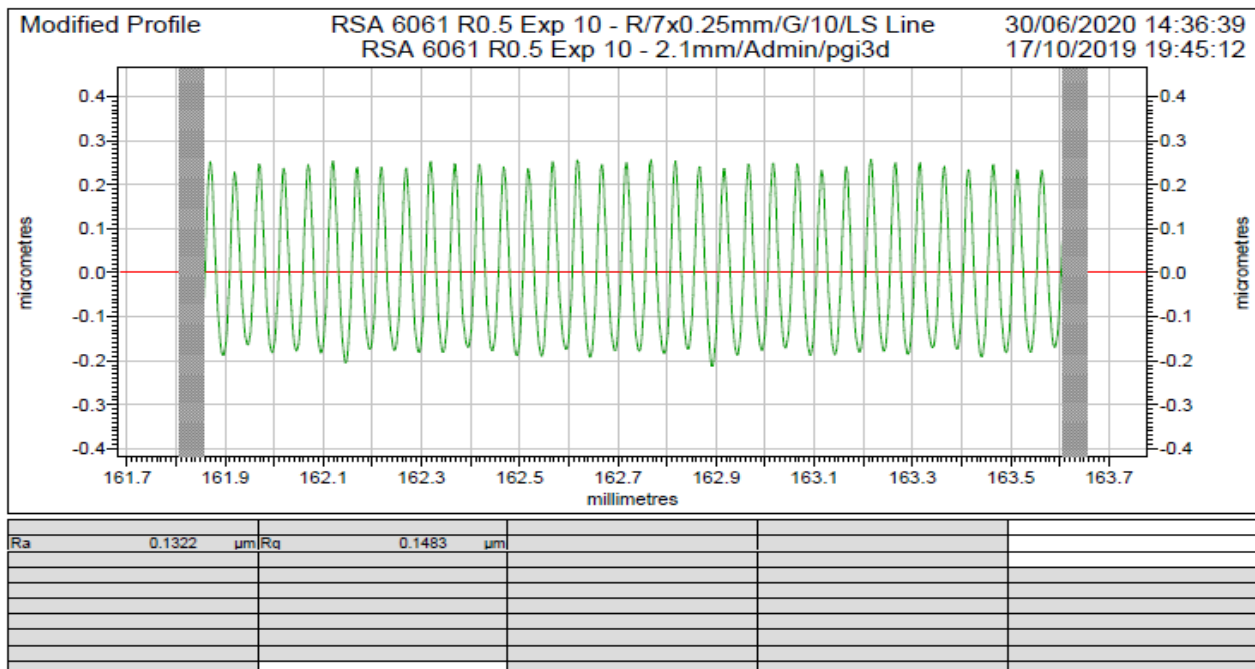


Figure 7.42: Profile chart for Experiment 10, speed = 500 rpm, feed rate = 25 mm/min and depth of cut = 15 µm. $R_a = 132.2$ nm

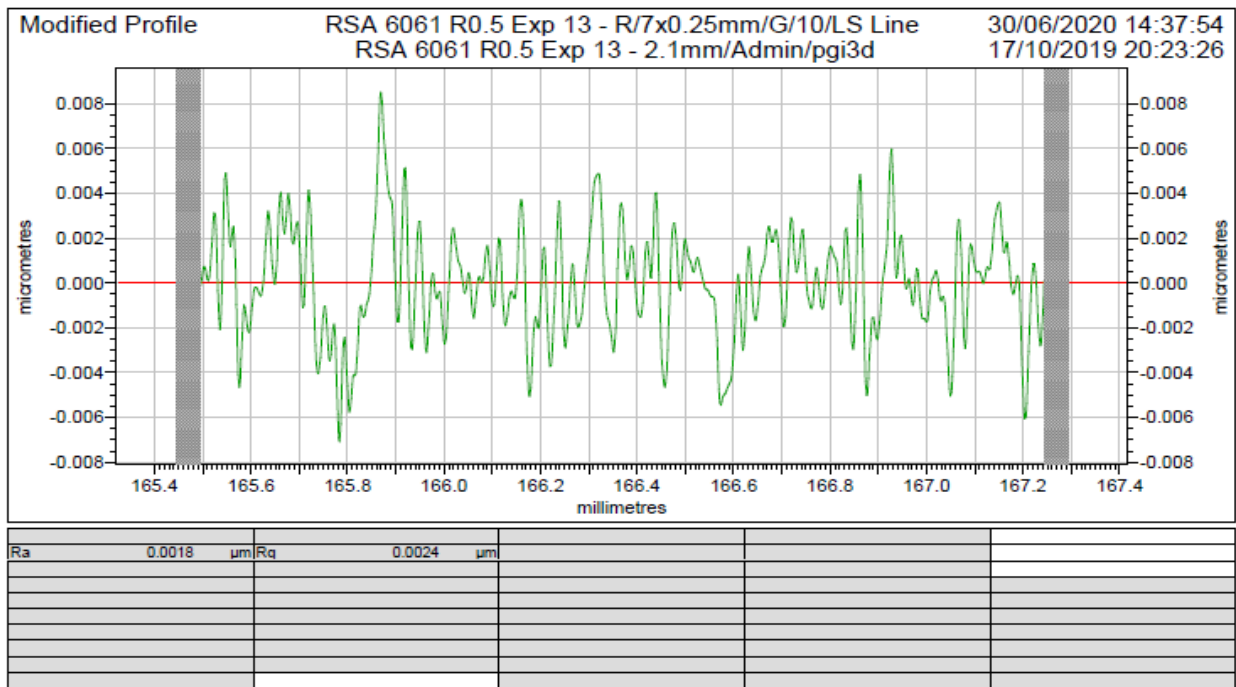


Figure 7.43: Profile chart for Experiment 13, speed = 1750 rpm, feed rate = 5 mm/min and depth of cut = 5 µm. Ra = 1.8 nm

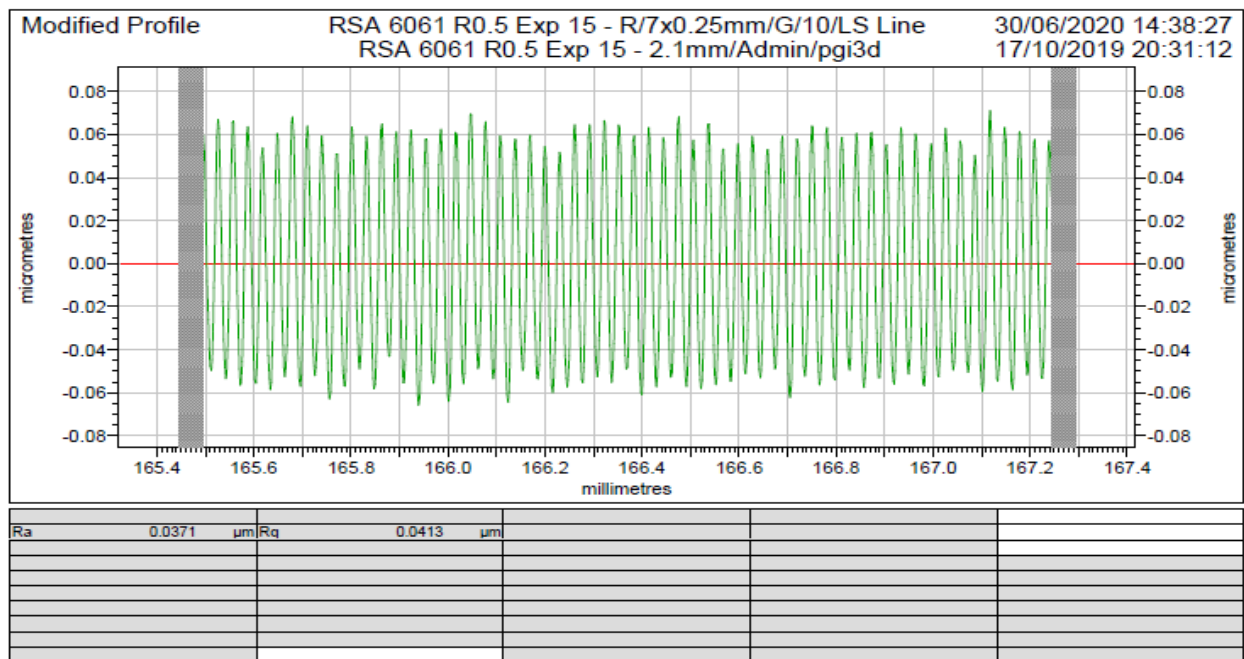


Figure 7.44: Profile chart for Experiment 17, speed = 500 rpm, feed rate = 15 mm/min and depth of cut = 5 µm. Ra = 37.1 nm

7.6.2 Statistical analysis of Ra for RSA 6061

Table 7.17: Summary output for regression and ANOVA of Ra for RSA 6061

SUMMARY OUTPUT						
Regression Statistics						
Multiple R	0.951879					
R Square	0.906073					
Adj R Square	0.853892					
Std Error	0.504907					
Observations	15					
ANOVA						
	df	SS	MS	F	Significance F	
Regression	5	22.13296	4.426591	17.36386	0.000219	
Residual	9	2.294382	0.254931			
Total	14	24.42734				
	Coefficients	Strd Error	t Stat	P-value	Lower 95%	Upper 95%
Intercept	1.794431	0.801811	2.237973	0.052015	-0.01939	3.608253
V(rpm)	-0.00211	0.000674	-3.13004	0.012121	-0.00364	-0.00059
F (mm/min)	0.183074	0.039596	4.62358	0.001248	0.093502	0.272646
D(μm)	0.012858	0.017851	0.720299	0.489625	-0.02752	0.05324
VF	-7.2E-05	2.02E-05	-3.56686	0.006054	-0.00012	-2.6E-05
V^2	6.25E-07	1.67E-07	3.737217	0.004645	2.47E-07	1E-06

Equation for the model is given as:

Equation 7.5

$$\ln Ra(nm) = 1.794431 - 0.00211D + 0.183074F + 0.012858D - 7.2^5VF + 6.25^7 V^2$$

$$Ra(nm) = e^{(1.794431 - 0.00211V + 0.183074F + 0.012858D - 7.2^5VF + 6.25^7 V^2)}$$

Where V is the speed in rpm, F is feed rate in mm/min and D is the depth of cut in μm and Ra is surface roughness in nm.

From **Table 7.17**, the model gave us an exponential equation with interaction effect. Where the F value of 0.000219 confirmed the model is highly significant with p -value of 0.052015. The p -values of feed, speed, and depth of cut show contributions to the cutting force.

The R^2 from ANOVA shows 0.906073 this shows how the model with 90.607% variation of Surface Roughness (R_a) is explained by cutting parameters in the experiment making the model a good fit. The most significant cutting parameter is feed rate that has a p-value of 0.001248 which contributed about 51.58% effect. The speed has a p-value of 0.012121 with a 10.64% contribution. However, the squared of speed gave us a high significant value at p-value of 0.004645 with a contribution of 14.57% total effects. This reveals how spontaneous the effect of speed could be on R_a of RSA 6061. Depth of cut has a p-value of 0.4896 with a contribution of 0.53% effects. Probably less significant. The interaction between speed and feed rates has a p-value of 0.006054 which contributed 13.26%.

Furthermore, from the model, the coefficient of speed is a negative value, this indicates an overall natural log of R_a is expected to decrease by a unit value of 0.00211 when other corresponding independent variables such as depth of cut and feed rate are kept constant.

Positive coefficients for depth of cut, feed rates and squared of speed are expected to increase the square root of cutting force by a unit of 0.012858, 0.0183074 and 0.000000625 respectively when other corresponding independent variables are kept constant. The negative interaction coefficients between speed and feed rate are also seen and is expected to decrease the natural log of R_a by a unit of 0.000072 provided corresponding independent variables are kept constant.

Figure 7.45 shows the scattered plot for this experiment which further validate the accuracy of the model standard. **Figure 7.46** represent the comparison between experimental and predicted values:

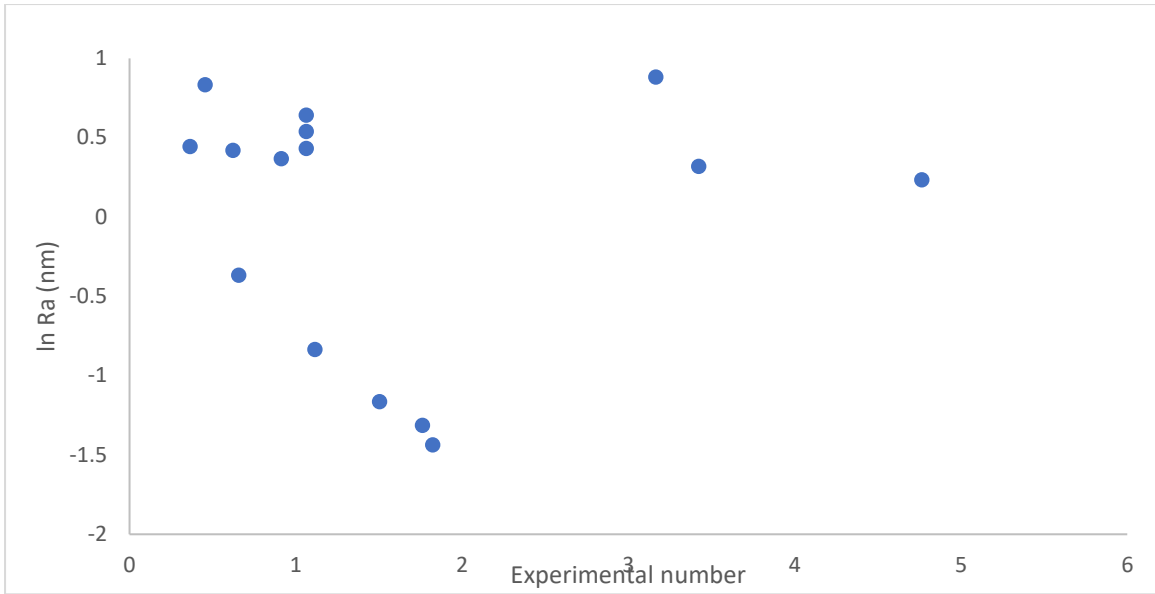


Figure 7.45: Scattered plot for surface roughness on RSA 6061

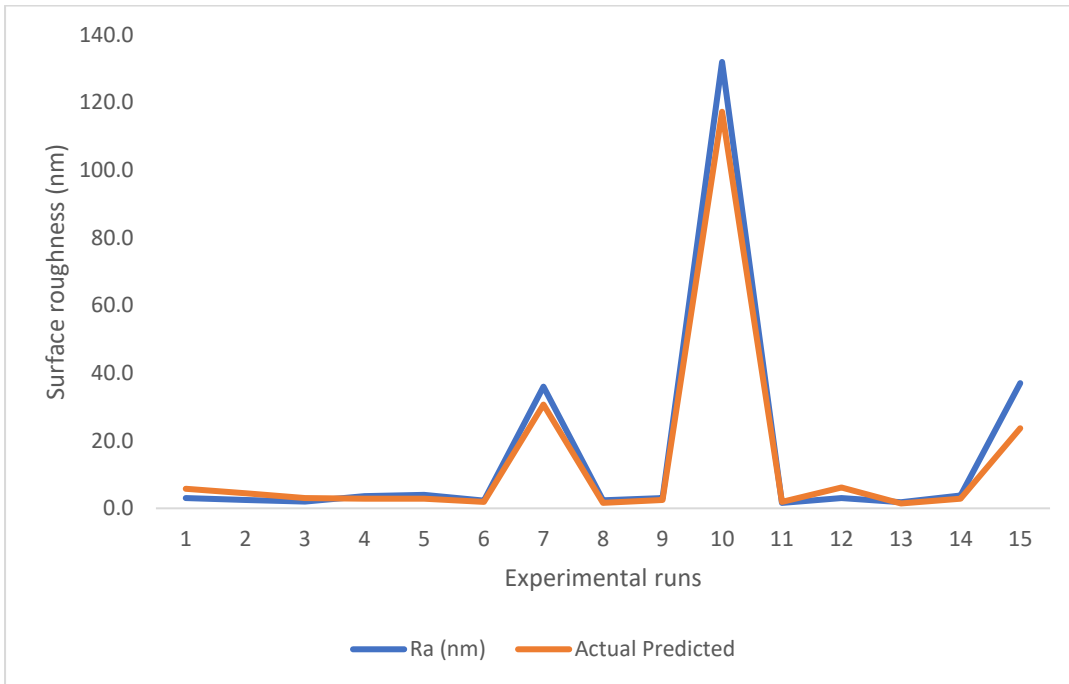


Figure 7.46: Comparison between experiment and predicted Ra

Figure 7.47 shows predictions that are close or the same with natural log of Ra data in **Table 7.16**. Looking again at experiments 7 and 10, as shown in the **Figure 7.47** (the reddest portion) confirm the predictions from the plot in **Table 7.18** below i.e., at low speed of 500 rpm and feed at 25 mm/min we have a highest surface roughness (close to what is obtained in Exp 7 and 15). This could mean that the worst surface quality will always be experienced whenever we choose to machine at low speed and high feed rate at least > 15 mm/min. From the model generated, **Figure 7.48** represent

the 3-D contour plots while the interactions between speed and feed rate is presented in **Figure 7.49**. An interaction effect between speed and feed rate was observed at constant depth of cut of 15 μm .

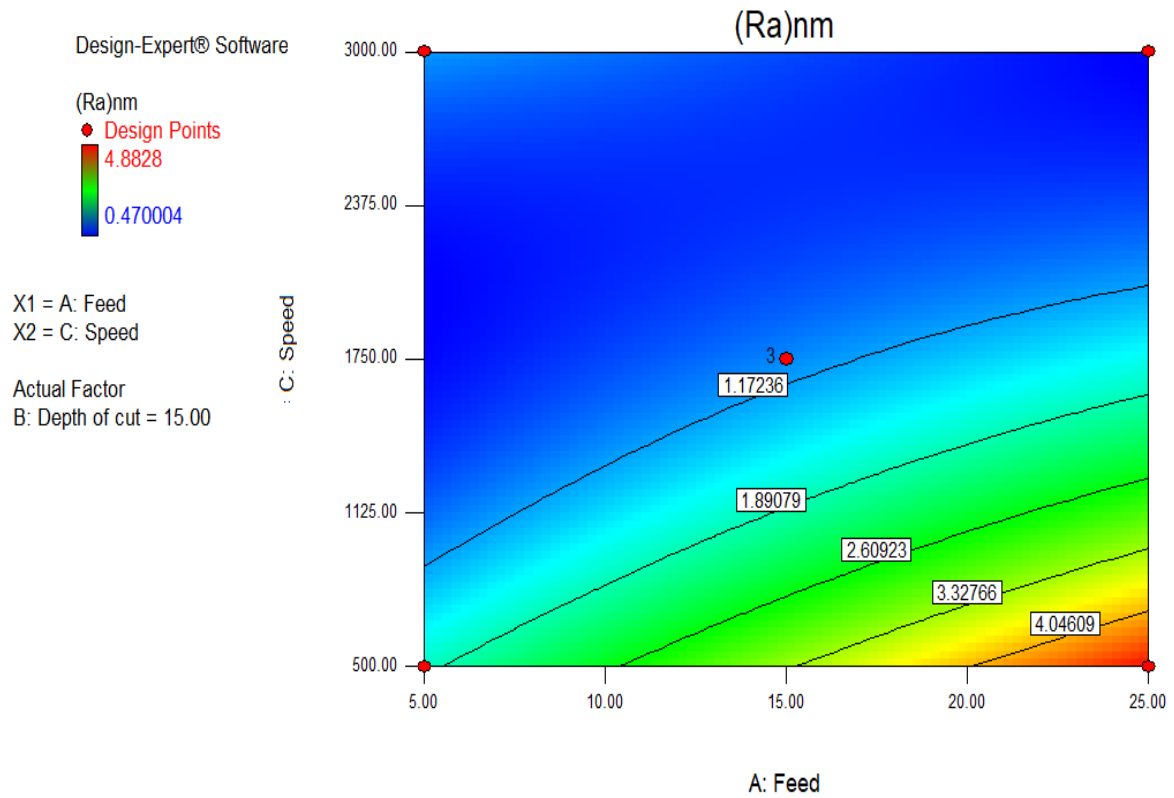


Figure 7.47: 2D contour plot for surface roughness of RSA 6061

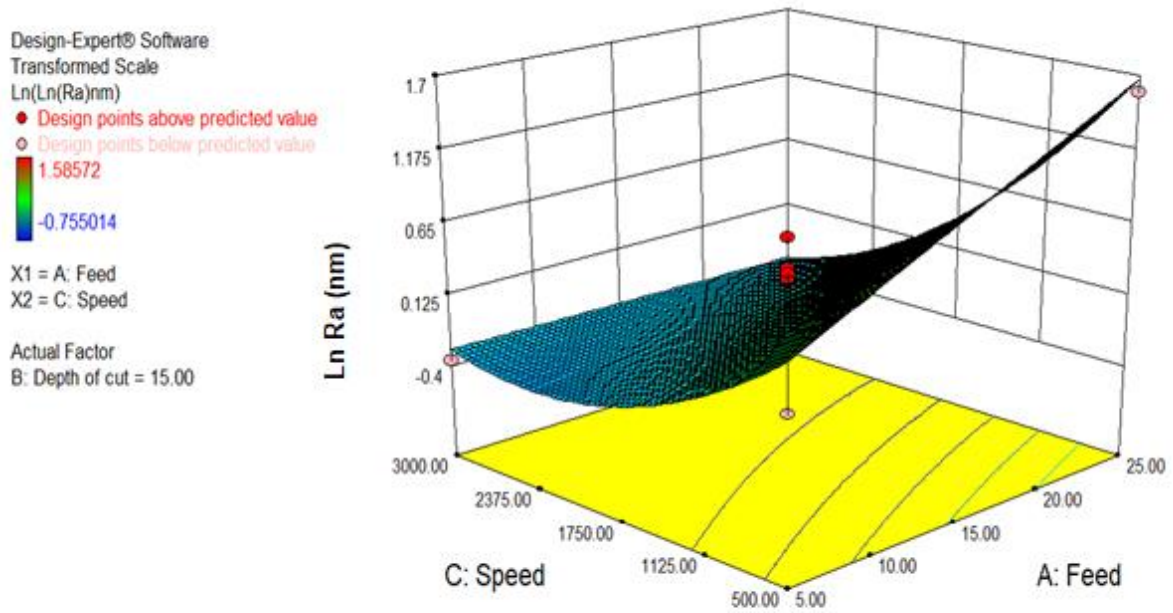


Figure 7.48: 3D plot for surface roughness of RSA 6061

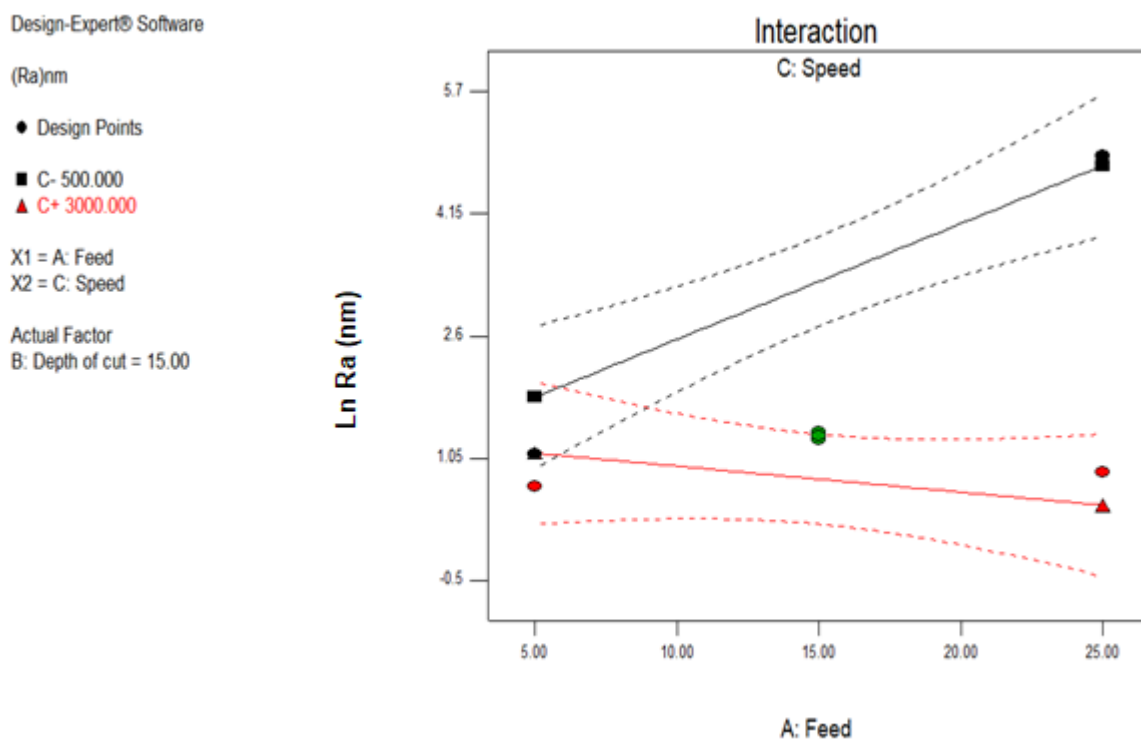


Figure 7.49: Interaction plot between feed rate and speed for surface roughness of RSA 6061

7.6.3 Profile Plot for Surface Roughness (LnRa) of RSA6061

In **Figure 7.50**, at constant feed rates and depth of cut, the patterns of the speed in the plots for the Natural log of surface roughness are the same. The speed was increased from 500 rpm – 3000 rpm while both feed rates and depth of cut were varied against speed. It is clearly shown that within this domain of machining parameters, an increase in speed leads to low surface roughness [104, 385]. This is because smallest amount of material spring back are formed due to small sizes of chips which can be blown off by coolants. Looking closely at cutting conditions for feed rates at 25 mm/min, depth of cut at 25 μm and speed at 2821.4 rpm (Point A), the same natural log of Ra, 0.63 nm was observed. This can serve as a high level of optimization condition to achieve such high surface quality for RSA 6061.

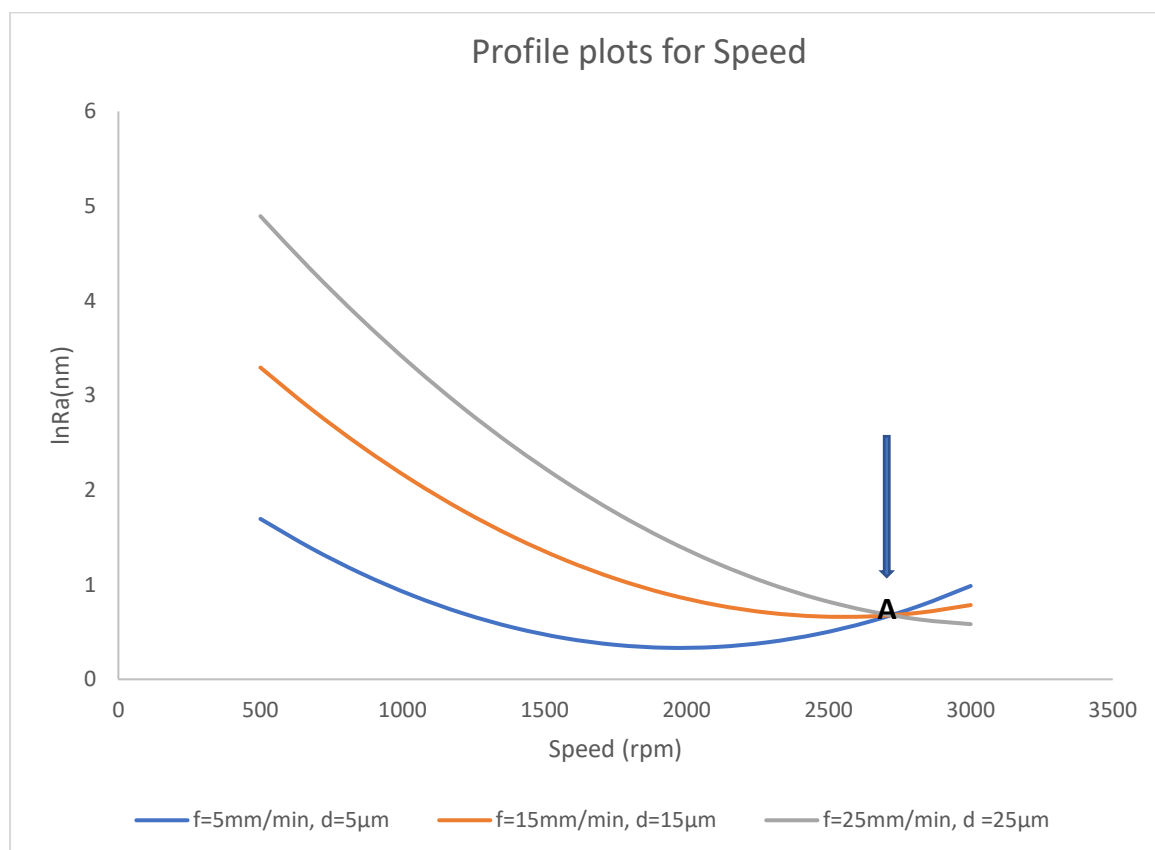


Figure 7.50: Effect of speed on surface roughness at varied feed rates and depth of cut

In **Figure 7.51** at varied speed and depth of cut, the effects of the feed in the plots for the Natural log of surface roughness shows linear relationships. This indicates that an increase in feed rate will result in high surface roughness which agrees with literature [2, 104, 253]. However, many phenomena can be responsible for this effect such as

large amount of spring back and accelerated tool damage due to friction. So, at high-speed $v = 3000$ rpm and high depth of cut $d = 25 \mu\text{m}$ an increasing feed rates was observed in order to predict negative linear relation with Natural log of Ra. This could mean that the effect of high magnitude of speed during machining has nullified any effect the size of depth of cut and feed rate may have on the machining process.



Figure 7.51: Effect of feed on surface roughness at varied speed and depth of cut

At constant speed and feed rates, the effects of depth of cuts in **Figure 7.52** plots for the Natural log of surface roughness shows positive linear relationships. At low-speed $v = 500$ rpm and low feed rate $f = 5$ mm/min, a high profile of depth of cut results in high surface finish of RSA 6061 was revealed. This can be due to large uncut chip thickness staying longer on the machined surface causing friction and scratch. However, this effect can be reduced if the condition of speed can be increased such as in the case of high speed at 3000 rpm at depth of cut of $25 \mu\text{m}$ in **Figure 7.52**.



Figure 7.52: Effect of depth of cut on surface roughness at varied feed rates and speed

7.6.4 Cutting process Optimization for surface roughness of RSA 6061

To optimize the surface roughness (Ra) of the cutting process, with the **Table 7.18** the author presents the best combination for cutting parameters that will predict worse and best surface roughness. Table 7.18 shows domain that attain Ra as low as 1nm which can be close to what was achieved in experiment 10 and 13 in **Table 7.16**. it was noted that the surface came due to the increased in cutting force and tool-workpiece contact area in UPRM, a larger depth of cut produces more heat on the machined surface.

Table 7.18: Surface roughness optimization for RRSA 6061

	V (rpm)	F(mm/min)	D (μm)	Pred Ln Ra (nm)	Actual Ra (nm)
Max	500	25	25	4.893101	133.3665
min	1976.78	5	5	0.040313	1.041137

7.7 ANALYSIS OF MATERIAL REMOVAL RATE (MRR) ON RSA 6061

In this modern age of mass manufacturing, process optimization is the key. MRR (material removal rate) is one of the primary strategies to achieve process optimization. With precision manufacturing capabilities using contemporary CNC (computer numerical controlled) machines. In ultra-precision machining of optical materials, there exist two major patterns of material removal: brittle fracture pattern and ductile pattern. Hence, in this study, diamond turning of RSA 6061 can thus be classified as the removal of metal in brittle fracture pattern due to high silicon content [369]. This was carried out from the outer diameter of a rotating cylindrical workpiece used in this study to a specified dimension. At the same time produce a smooth surface finish on the workpiece.

The MRR is often used as a tool to develop the combination of optimum cutting parameters for optimum cutting process. This section also produced a predictive equation for determining MRR with a given set of parameters in ultra-precision diamond turning of optical RSA 6061. Thus, with the proposed optimal parameters, it is possible to increase the efficiency of machining process and decrease production cost in an automated manufacturing environment. **Table 7.19** shows the calculated MRR obtained in each experimental combination during diamond turning of RSA 6061 while **Table 7.20** presents statistical analysis of the data.

Table 7.19: Experimental results for MRR of RSA 6061

Run	V (mm/min)	F (mm/rev)	D (mm)	MRR (mm ³ /min)	Ln MRR (mm ³ /min)
Exp1	439880	0.0143	0.025	157.100	5.056883
Exp2	439880	0.0143	0.005	31.420	3.447445
Exp3	754080	0.0017	0.015	18.852	2.936619
Exp4	439880	0.0086	0.015	56.556	4.035231
Exp5	439880	0.0086	0.015	56.556	4.035231
Exp6	439880	0.0029	0.025	31.420	3.447445
Exp7	125680	0.0300	0.025	94.260	4.546057
Exp8	754080	0.0083	0.015	94.260	4.546057
Exp9	754080	0.0050	0.025	94.260	4.546057
Exp10	125680	0.0500	0.015	94.260	4.546057
Exp11	754080	0.0050	0.005	18.852	2.936619
Exp12	125680	0.0100	0.015	18.852	2.936619
Exp13	439880	0.0029	0.005	6.284	1.838007
Exp14	439880	0.0086	0.015	56.556	4.035231
Exp15	125680	0.0300	0.005	18.852	2.936619

7.7.1 Statistical analysis of MRR for RSA 6061

Table 7.20: Summary output for regression and ANOVA of MRR for RSA 6061

SUMMARY OUTPUT						
Regression Statistics						
Multiple R	0.985296					
R Square	0.970808					
Adj R Sqr	0.95459					
Std Error	0.188545					
Observations	15					
ANOVA						
	df	SS	MS	F	Significance F	
Regression	5	10.64007	2.128015	59.86102	1.24E-06	
Residual	9	0.319943	0.035549			
Total	14	10.96002				
	Coefficients	Standard Error	t Stat	P-value	Lower 95%	Upper 95%
Intercept	0.819686	0.272983	3.002702	0.014891	0.202156	1.437215
Vc(mm/min)	4.63E-08	3.64E-07	0.127197	0.901581	-7.8E-07	8.69E-07
F(mm/rev)	1.162837	7.425452	0.156602	0.879015	-15.6347	17.96038
D (mm)	162.1197	30.05738	5.393675	0.000437	94.12519	230.1142
VF	0.000316	3.69E-05	8.564618	1.28E-05	0.000233	0.0004
D^2	-2721.59	976.962	-2.78577	0.0212	-4931.64	-511.552

Table 7.20 gave an exponential equation with an interaction effect. Where the F value of 0.00000124 confirmed the model is highly significant with p-value of 0.014891.

Equation 7.6 represents the model as follows:

Equation 7.6

$$\ln(MRR) = 0.819 + 4.63 \times 10^{-8}V + 1.163F + 162.11D + 3.16 \times 10^{-4}VF - 2721.59d^2$$

or

$$(MRR) = e^{(0.819+4.63 \times 10^{-8}V+1.163F+162.11D+3.16 \times 10^{-4}VF-2721.59d^2)}$$

Where *V* is the speed in rpm, *F* is feed rate in mm/min and *D* is the depth of cut in μm and MRR is material removal rate in mm³/min.

The R² from regression table shows 0.970808, this shows that the model explains 97.0808% variation of MRR in the experiment making the model a good fit. The most significant cutting parameter is the interaction between speed and feed rate that has a p-value of 0.0000128 which contributed about 41.15% effect. The speed has a p-

value of 0.90158 with a 2.74% contribution. However, the square of depth of cut gave us a high significant value at p-value of 0.0212 with a contribution of 23.91% total effects. Depth of cuts has a p-value of 0.000437 with a contribution of 27% effects. This reveals how significant the effect of depth of cut could be in MRR of RSA6061 during machining. The feed rates have a p-value of 0.879015 which contributed 4.75 %.

Figure 7.53 shows the scattered plot for this model which establishes that quadratic equation is best validate the model standard. **Figure 7.54** represents the comparison between experimental data and predicted data.

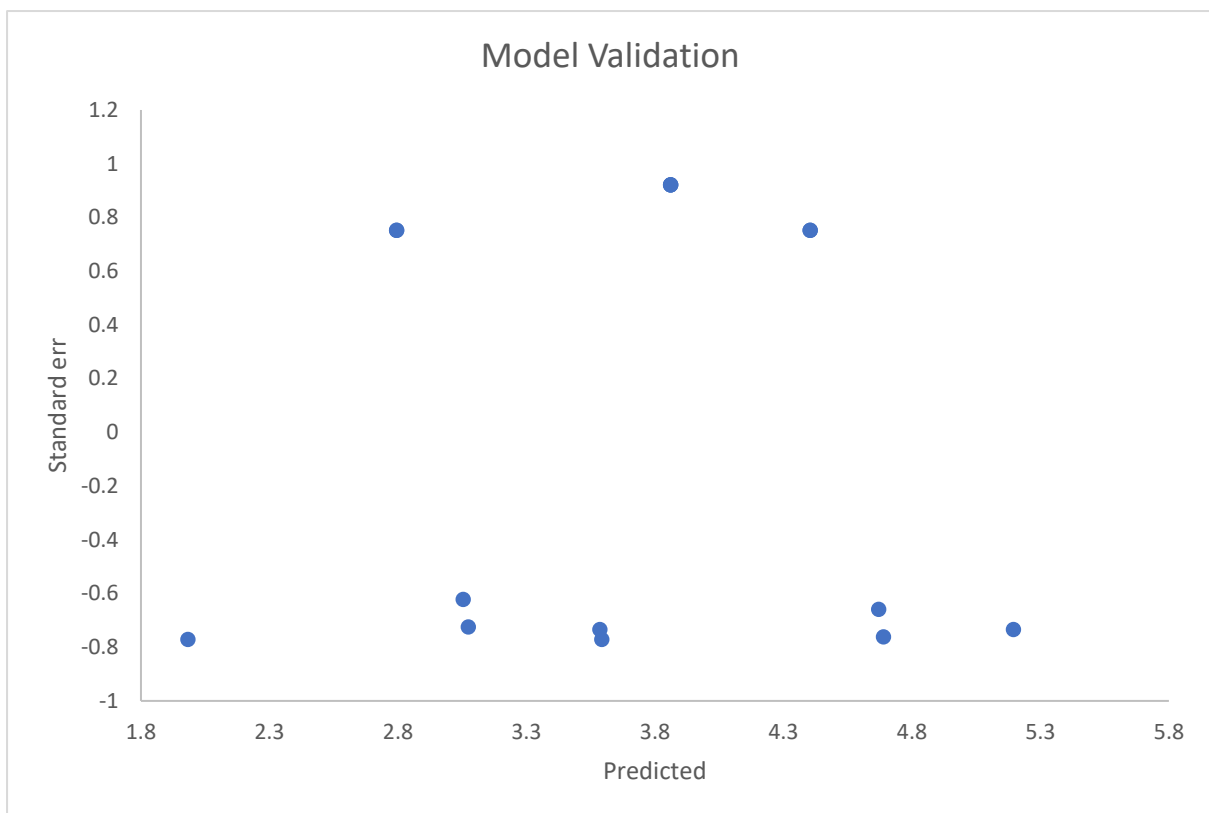


Figure 7.53: Scattered plot for MRR on RSA 6061

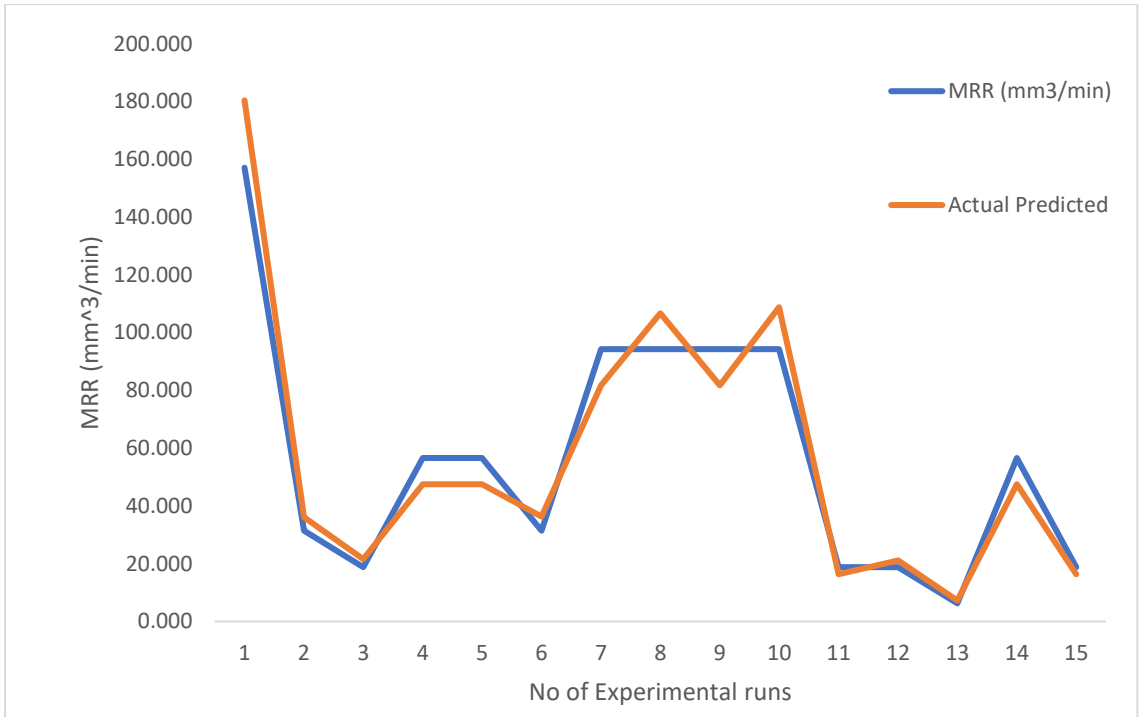


Figure 7.54: Comparison between experimental values and predicted values

Figures 7.55 – 7.57, represent 2D, 3D and interaction plots between speed and feed rate, it can be depicted that high speed and high feed rate will result in high volume of material removed which in turns save throughput time and costs. **Figure 7.57** presents a possible interaction characteristic during machining process.

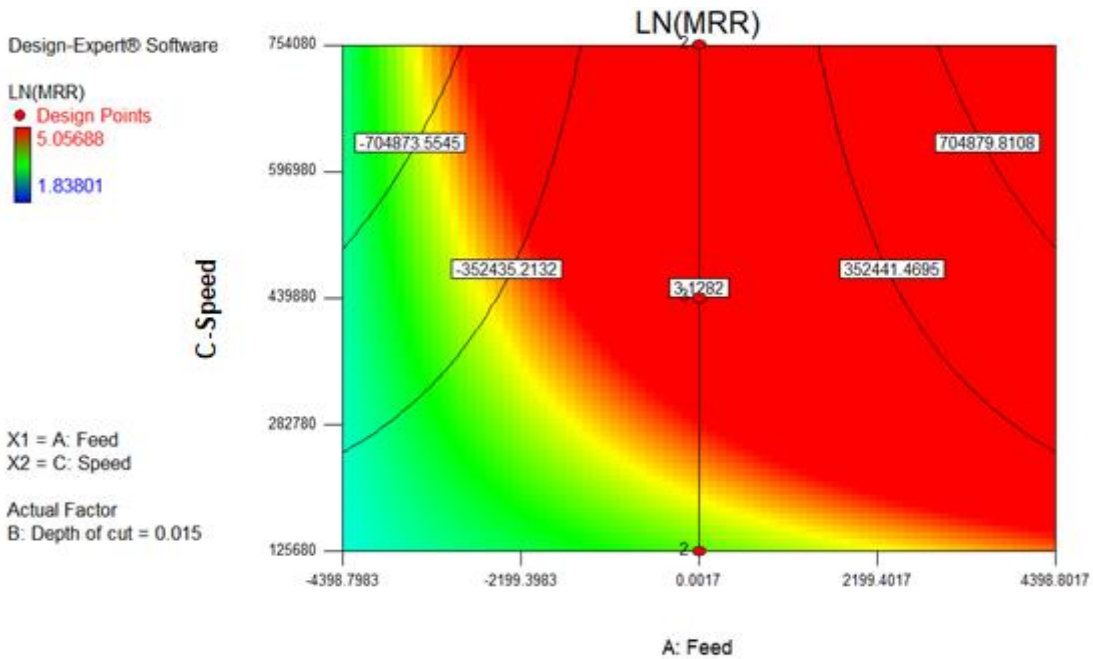


Figure 7.55: 2D contour plot showing effect of speed and feed rate on MRR on RSA 6061

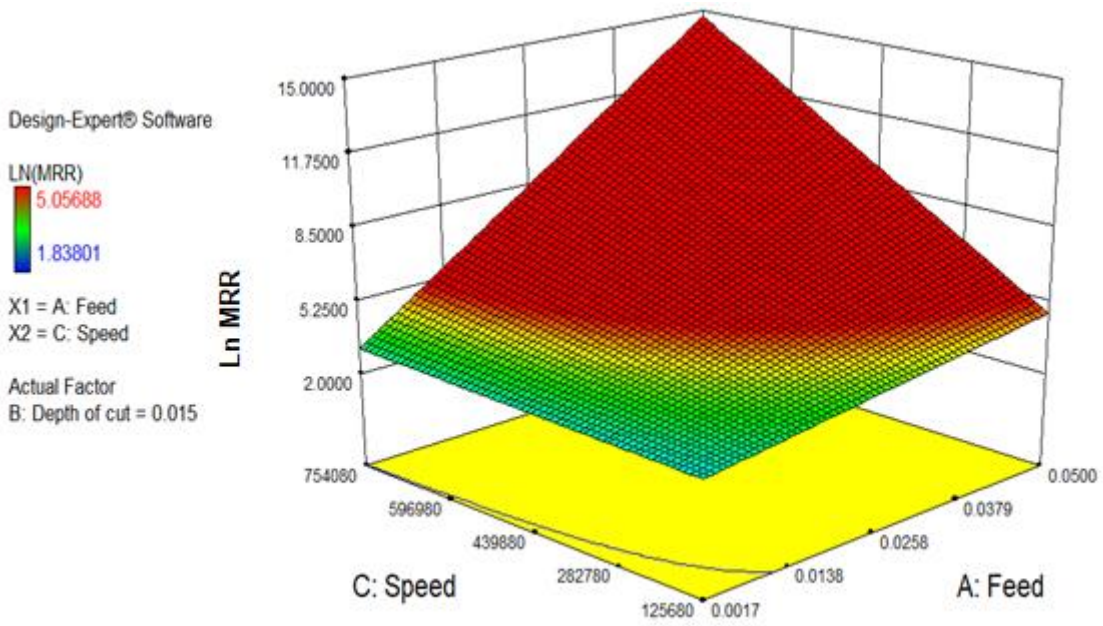


Figure 7.56: 3D-plot showing effect of speed and feed rate on MRR of RSA 6061

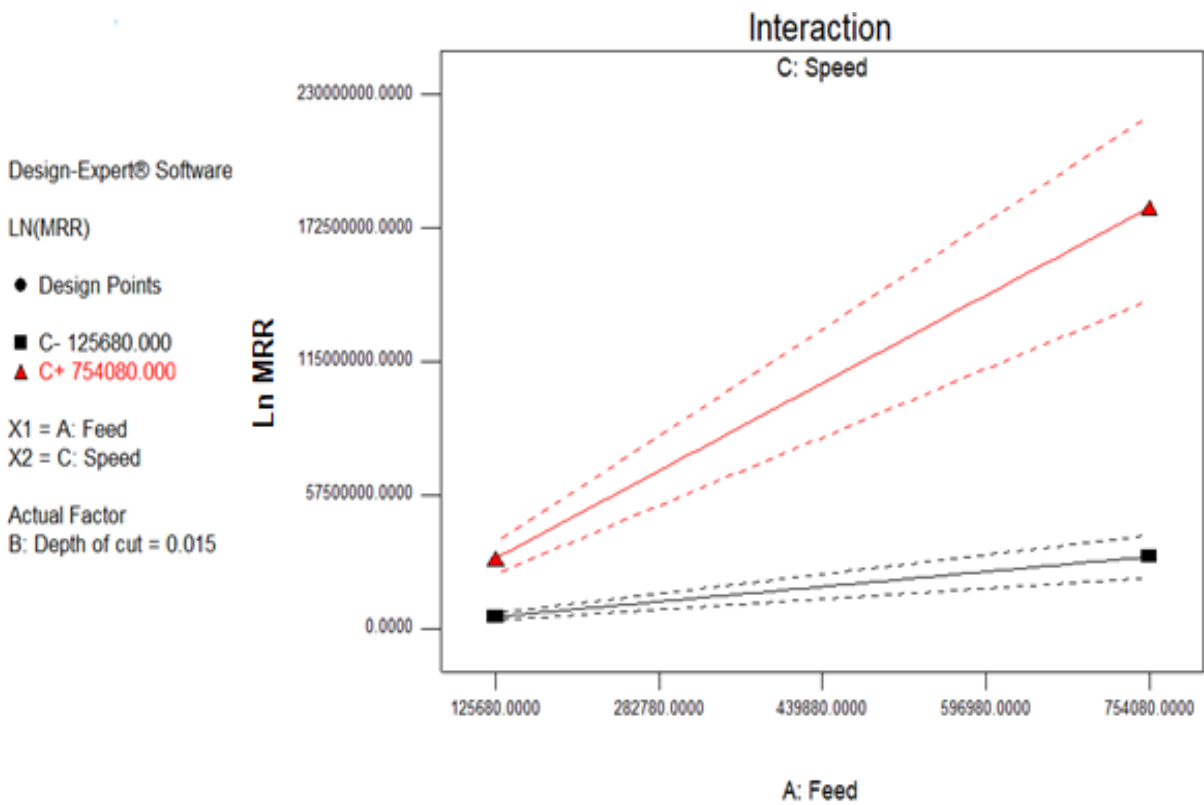


Figure 7.57: Interaction plot between feed and speed

7.7.2 Profile Plot for Material Removal Rates (Ln MRR) of RSA6061

In **Figure 7.58**, at constant feed rate and depth of cut, an increase in speed shows an increase in the Natural log of volume of material removed. **Figure 7.59** presents an increase in feed rate that will lead to an increase in the rate of material removed during diamond turning of RSA6061. The same trend was noticed in **Figure 7.60**, where an increase in depth of cut leads to an increase in MRR of RSA6061 during diamond turning. However, at a much higher depth of cut, speed and feed rate, another higher order of volume of materials were dug out per time.

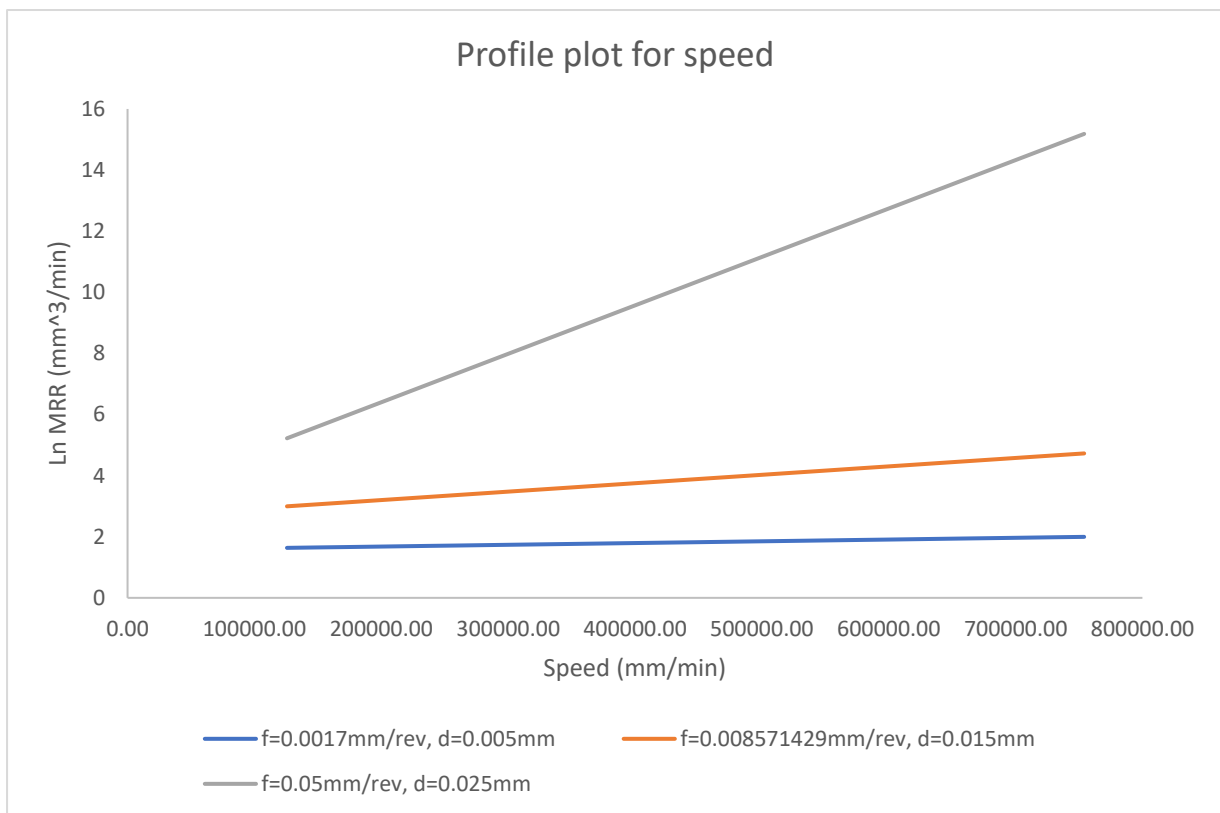


Figure 7.58: Effect of speed on MRR at varied feed rates and depth of cut

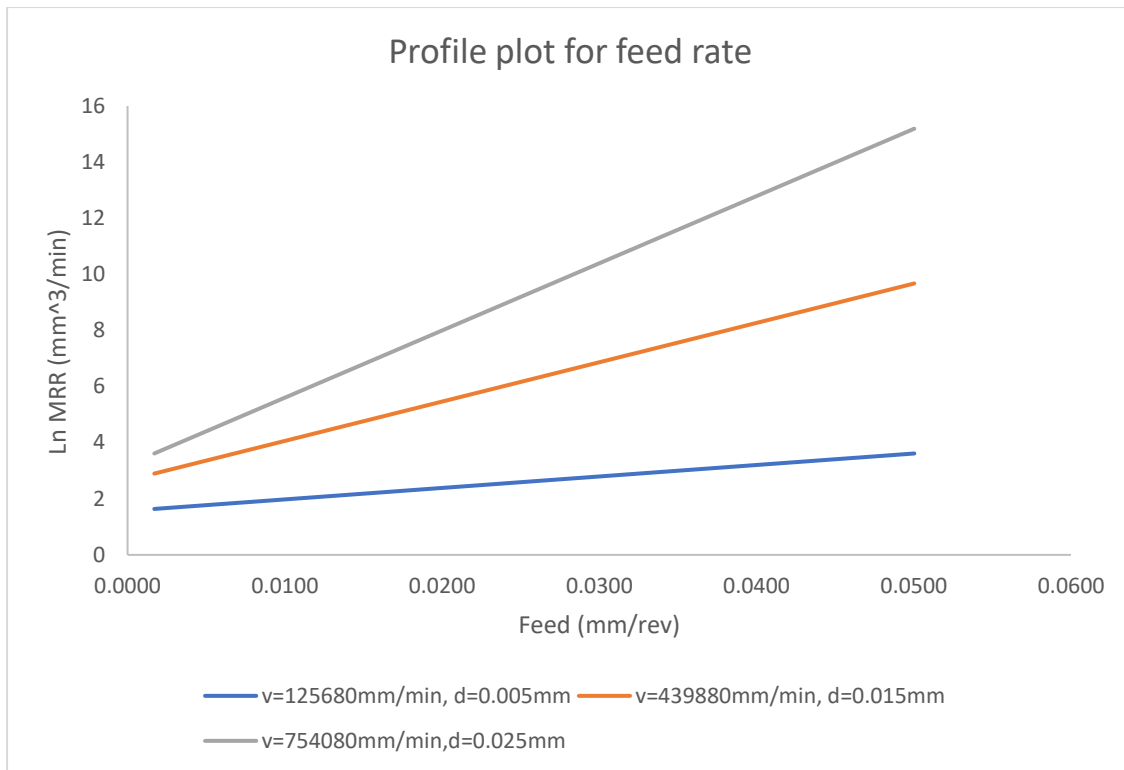


Figure 7.59: Effect of feed on MRR at varied speed and depth of cut

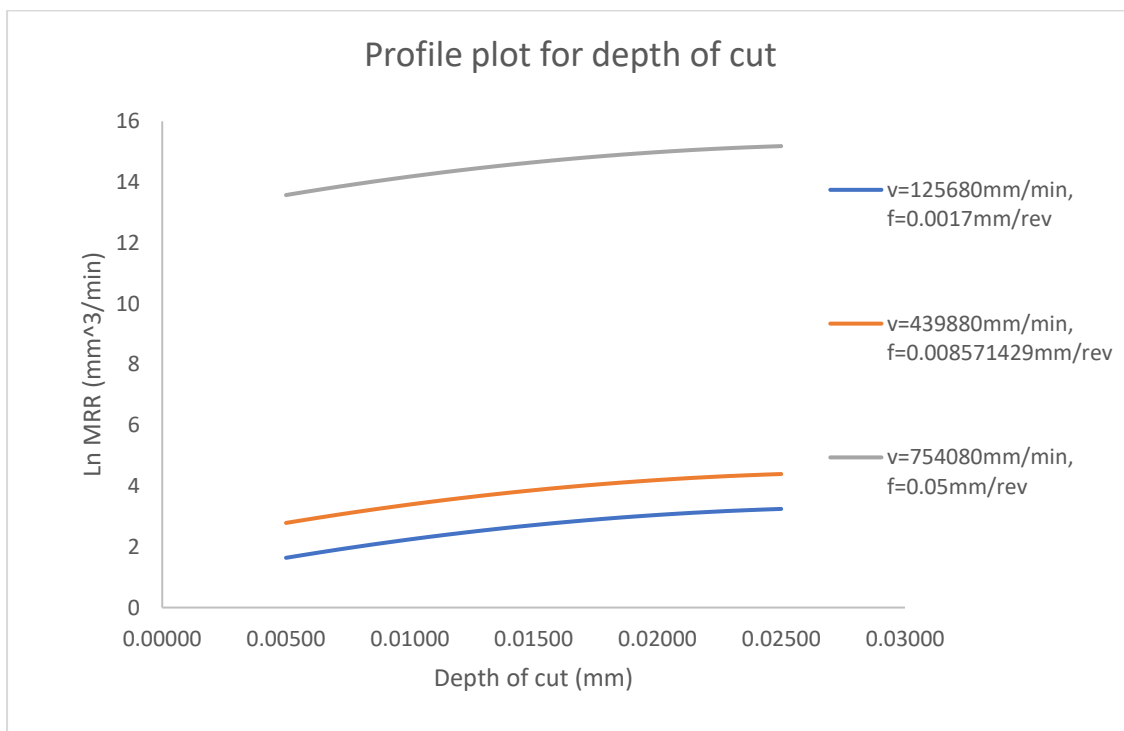


Figure 7.60: Effect of depth of cut on MRR at varied feed rates and speed

7.8 EFFECTIVE CHIP FORMATION (THICKNESS) DURING MACHINING OF RSA6061

This section intended to investigate the chip morphology during diamond turning of rapidly solidified aluminium alloys RSA 6061. In machining, chip formation is a means of generating nanostructure materials that can be used to control microstructures [386]. Chip morphologies, which could be continuous or discontinuous (sawtooth or serrated type), during ultraprecision machining depends on the combined effects of workpiece and insert material properties, depth of cut, cutting speed, feed rate, and cutting tool geometry [387, 388].

Knowledge of chip formation is very critical for surface integrity and part performance during optimization of turning process. A significant feature of chip morphology is distinguished by the style of chip shape normally observed during hard turning at high speeds [389]. Sawtooth chip forming typically happens in two-phase systems in which the workpiece material is visually warped long before the tool starts to swell. At a point where the critical strain threshold is reached, a devastating event occurs and a shear band is developed extending from the tool tip to the workpiece surface [387, 390].

However, few researchers have concentrated on the direct examination of the chip structure of advanced aluminium alloys during diamond turning. Research findings have shown that the shape and size of the chip formations have a great impact on the surface roughness during the diamond turning process [391]. Elongated chips are not needed, according to Farid et al [391], but they should be avoided because they cannot be scooped on the machined surface and thus cause scratch on the workpiece surface, however smaller broken chips can be easily swept from the surface

In the work of Farid et al [391], the effect of cutting parameters such as cutting speed has greatly enhanced the shear angle, chip thickness, size, and shape of the chips. Earlier research found that continuous chips were developed during the machining of aluminium alloys at all cutting speeds [391-394]. According to Recht [395] the formation of segmented chips in aluminium alloy machining is very poor due to the low susceptibility of adiabatic Aluminium shear localization. Despite the high thermal conductivity of aluminium alloys, these characteristics are normal. Muller and Blumke [396] suggested that continuous chips could transition to segmented chips if the speed is increased. Bartezer et al. [397] conducted an investigation and reported that seven

types of chips, conical, fan-shaped, chisel-edge, amorphous, needle, impacted, and dust-like chips, were found throughout dry drilling of cast aluminium alloys. They also observed that the feed rate is the most critical aspect influencing the size of the chip, thus increasing the cutting speed leads to a higher mass of chips creating segmented chips and an aged material state (material hardened by age hardening process).

In machining, the key distinction between the two hypotheses of crack initiation mechanism and thermo-plastic instability is the cata-strophic failure mechanism in the primary shear [398, 399]. Shaw [400], proposed that shear bands should be formed due to void propagation and within microfractures. However, if the temperature is high and the usual tension is high, the shear band will follow. Literature [400-403] further recommended that a cata-strophic breakdown be triggered first by a crack at the free surface of the tool, which extends to the tip of the tool and forms a section of the tool. Komanduri et al. [404] and Davies et al. [405] have suggested that thermoplastic inconsistency could exist inside the primary shear zone. It is worth noting that the degree of chip segmentation increases with the rise in cutting speed. As cutting speeds reach 2,400 m/min, the serrated chips are converted into fragment chips [406]. **Table 7.21** represents the effective chip volume (thickness and width) during machining of RSA6061. The Chip Thickness model generated for the experiment conducted for RSA 6061 at nose radius 0.5 mm diameter is as follows:

Effective chip formation (thickness) (t_c):

Equation 7.7

$$t_c = f \sqrt{\frac{2h}{R}}$$

Where t_c = chip thickness (μm), f = feed rate (mm/rev), h = depth of cut (μm) and R = nose radius (mm)

Table 7.21: Experimental results of chip formation for RSA 6061

Run	V (mm/min)	F (mm/rev)	D (mm)	CHIP THICKNESS (μm)
Exp1	439880	0.0143	0.025	4.52
Exp2	439880	0.0143	0.005	2.02
Exp3	754080	0.0017	0.015	0.41
Exp4	439880	0.0086	0.015	2.10
Exp5	439880	0.0086	0.015	2.10
Exp6	439880	0.0029	0.025	0.90
Exp7	125680	0.0300	0.025	9.49
Exp8	754080	0.0083	0.015	2.04
Exp9	754080	0.0050	0.025	1.58
Exp10	125680	0.0500	0.015	12.25
Exp11	754080	0.0050	0.005	0.71
Exp12	125680	0.0100	0.015	2.45
Exp13	439880	0.0029	0.005	0.40
Exp14	439880	0.0086	0.015	2.10
Exp15	125680	0.0300	0.005	4.24

7.7.3 Statistical analysis of chip thickness for RSA 6061

Table 7.22: Regression and ANOVA analysis of chip thickness

SUMMARY OUTPUT						
Regression Statistics						
Multiple R	0.999968					
R Square	0.999935					
Adj R Sqr	0.999871					
Stdr Error	0.038522					
Observations	15					
ANOVA						
	df	SS	MS	F	Significance F	
Regression	7	160.8121	22.97316	15480.91	4.03E-14	
Residual	7	0.010388	0.001484			
Total	14	160.8225				
	Coefficients	Standard Error	t Stat	P-value	Lower 95%	Upper 95%
Intercept	0.048331	0.0858	0.563299	0.59081	-0.15455	0.251215
Vc(mm/min)	-4.1E-07	1.01E-07	-3.9966	0.005212	-6.4E-07	-1.7E-07
F(mm/rev)	63.00884	5.807504	10.84956	1.25E-05	49.27628	76.7414
D (mm)	43.31692	6.728116	6.438194	0.000354	27.40745	59.22639
VF	4.91E-05	9.93E-06	4.945722	0.001664	2.56E-05	7.26E-05
FD	8740.32	127.3472	68.63377	3.66E-11	8439.192	9041.449
F^2	761.8888	82.70822	9.211767	3.67E-05	566.315	957.4627
D^2	-1443.9	212.5422	-6.79346	0.000255	-1946.48	-941.315

From the **Table 7.22**, **Equation 7.7** represents a model that was generated for an effective chip (C) thickness of RSA 6061 during diamond turning.

Equation 7.8

$$C = 0.0483 - 4.1 \times 10^{-7}V + 63F + 43.31D + 4.91 \times 10^{-5}VF + 8740.32 FD + 761F^2 - 1443D^2$$

Where C is chip thickness in μm , F is feed rates in mm/min, V is speed in rpm, and D , depth of cut μm .

R^2 from ANOVA shows 0.9999, this indicates that a model with 99.99% variation of the effective chip is explained by cutting parameters in the experiment making this model a good fit. The most significant cutting parameter is the interaction between depth of cut and feed rates that has a p-value of 0.000000000366. The feed rate is another influential cutting parameter with a p-value of 0.0000125, the square of feed rates gave us a high significant value at p-value of 0.0000367. Depth of cuts has a p-value of 0.0000354. The square of depth of cut has a p-value of 0.000255. The least

significant parameter though still made contribution is spindle Speed with a p-value of 0.005212. According to literature, it was recorded that speed is not always a significant factor for effective chip thickness.

Furthermore, from the model, the coefficient of square of depth of cut and cutting speed is a negative value, this means that an overall chip thickness is expected to decrease when another corresponding independent variable such as feed rate is kept constant.

Positive coefficients of depth of cut and feed rates are also expected to increase the chip morphology by a unit of 43.3 and 63.01 respectively when other corresponding independent variables are kept constant. The positive interaction coefficients between speed and feed rate are also expected to increase the chip thickness by a unit of 0.0000491 provided corresponding independent variables are kept constant.

Figure 7.61 shows the scattered plot for this experiment which establishes and validate the model standard. **Figure 7.62** represent the comparison between experimental data and predicted data.

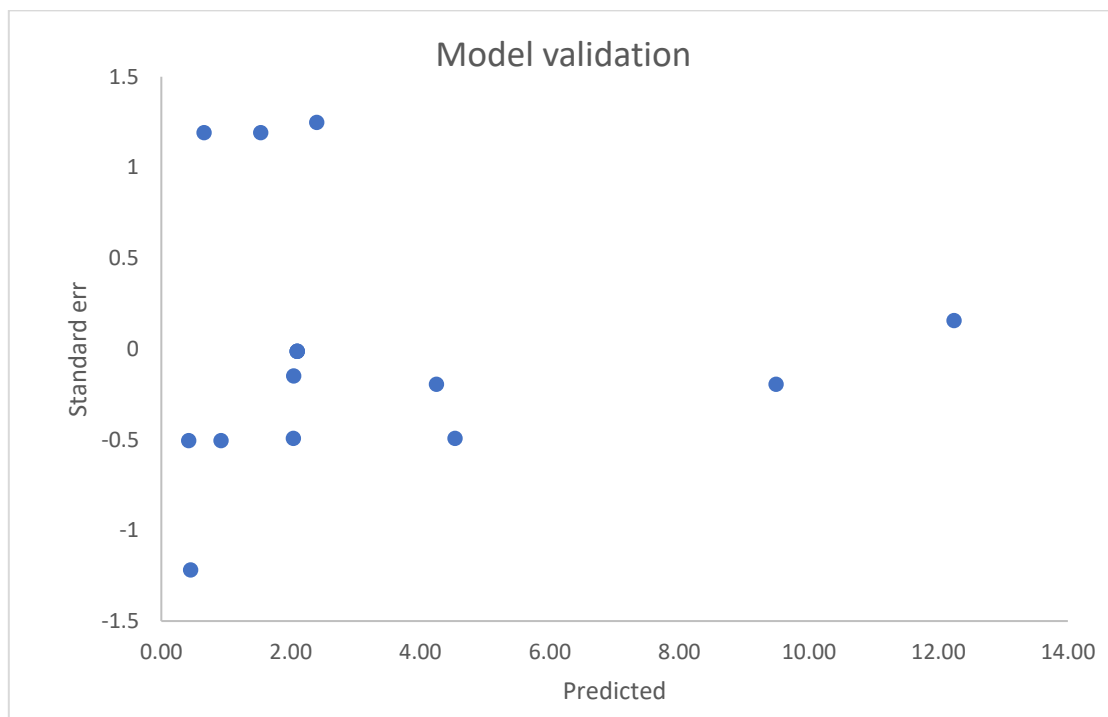


Figure 7.61: Scattered plot for effective chip thickness on RSA 6061

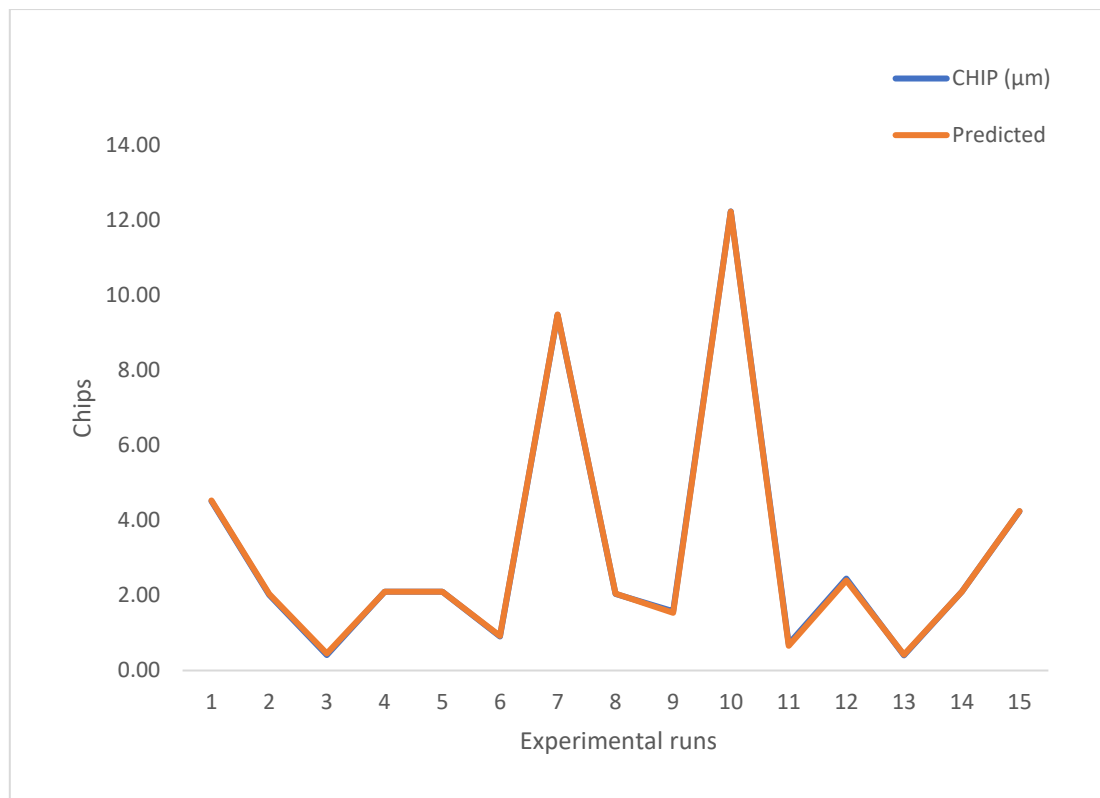


Figure 7.62: Comparison between experimental values and predicted values

7.7.4 Profile plotting for effective chip thickness of RSA6061

In **Figures 7.63 - 7.65**, the patterns of the effects of speed, feed rate and depth of cut in the plots for chip formation show that generally an increase in feed rate and depth of cut will result in a significant increase in chip width and thickness. Particularly in **Figure 7.65**, an increase in cutting speed during machining process does not necessary present a conspicuous effect on chip formation rather a stable or similar chip formation at high speed was observed. However, as the cutting speed became very high at 3000 rpm, continuous and serrated thin featherlike chips were formed. See **Table 7.23**. In Experiments 3 and 9, while chips are being collected, the chips can easily be cooled off by coolant under this condition.

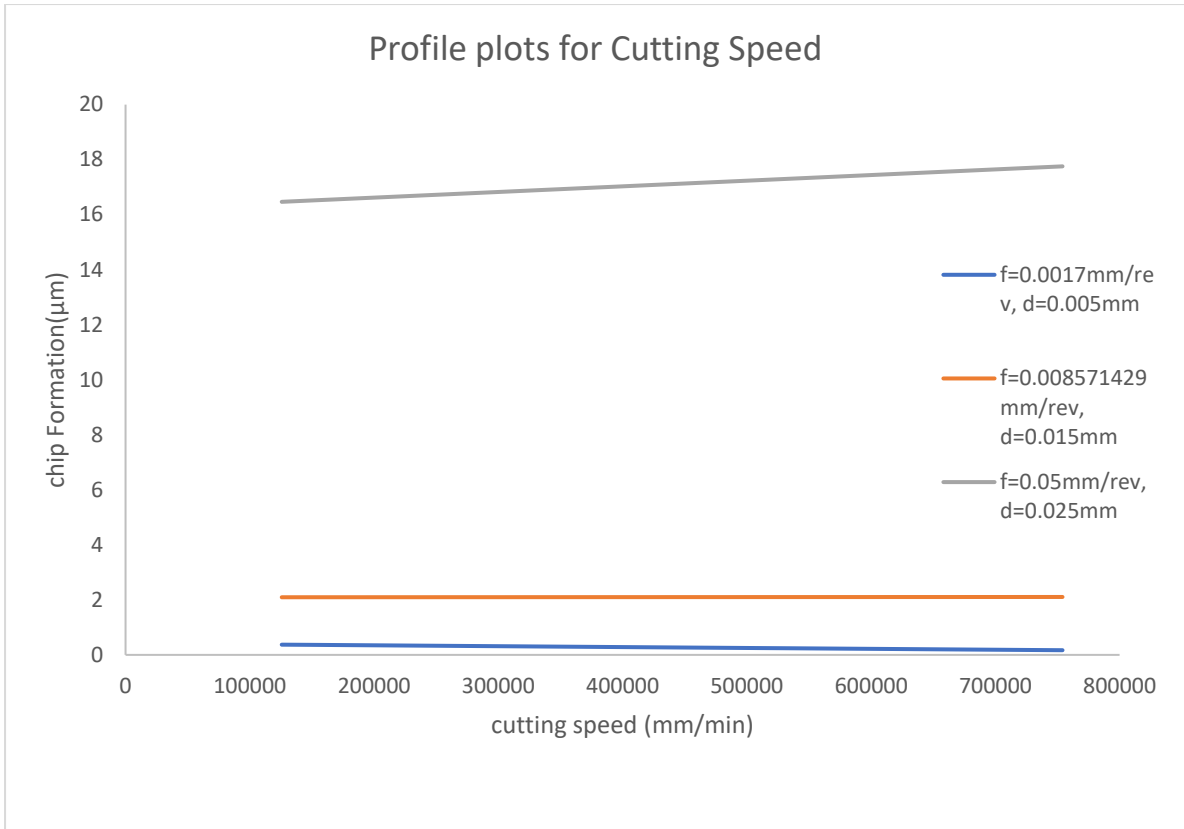


Figure 7.63: Effects of speed on chip thickness at constant feed rates and depth of cut



Figure 7.64: Effects of feed rate on chip thickness at constant speed and depth of cut

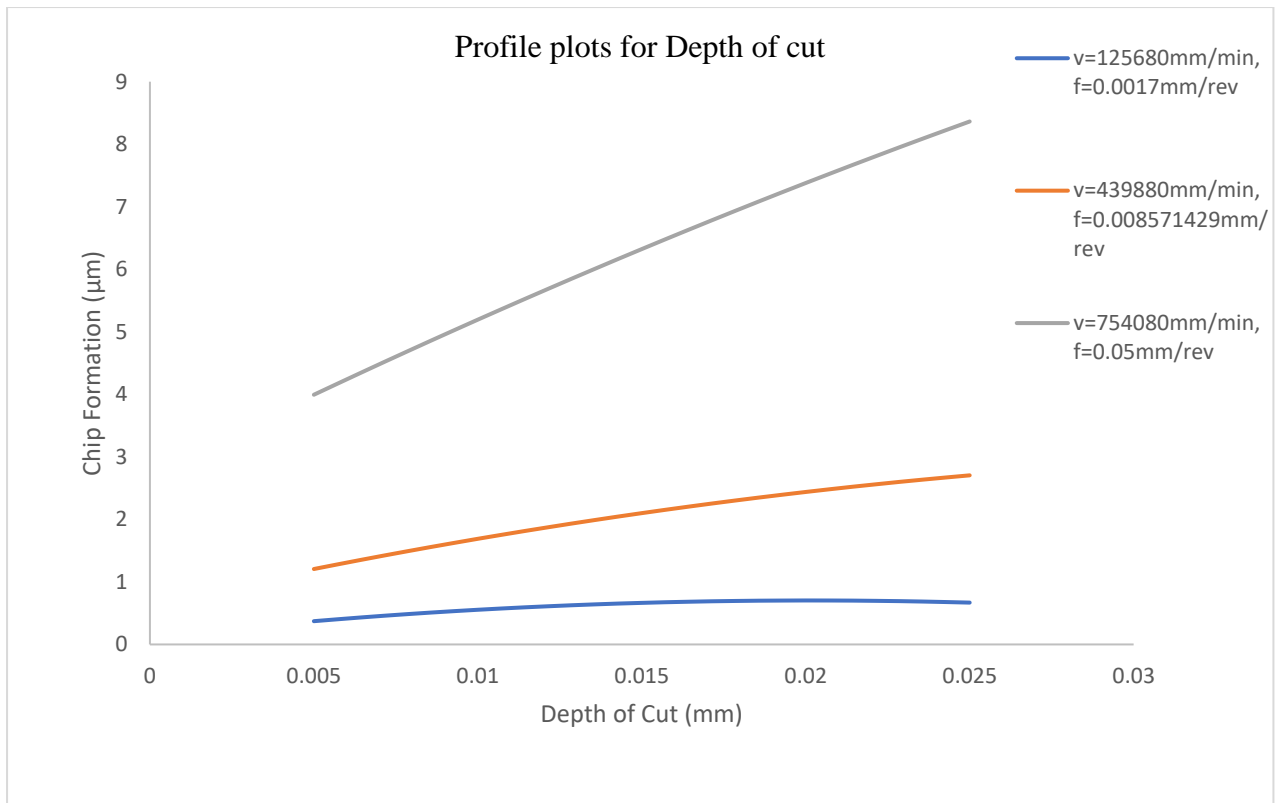


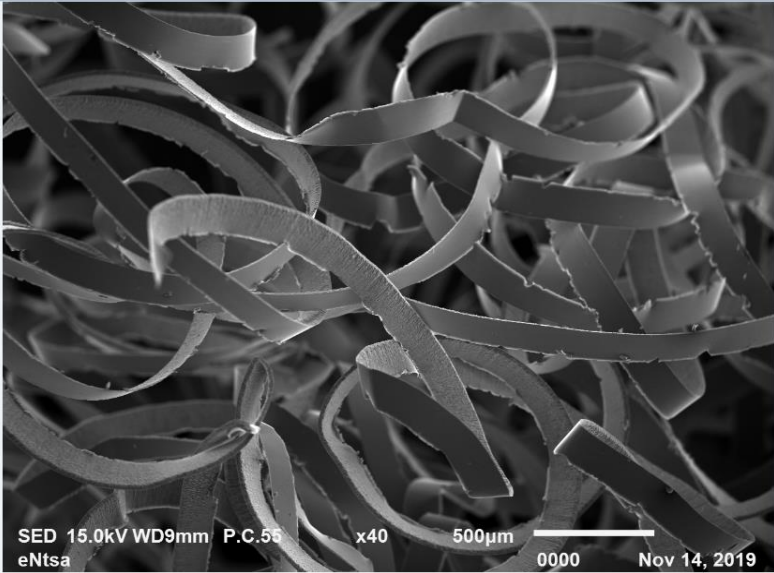
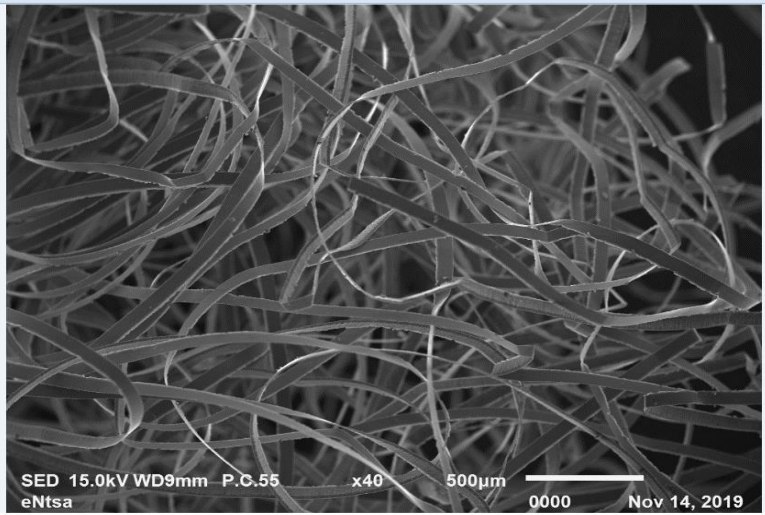
Figure 7.65: Effects of depth of cut on chip formation at constant feed rates and speed

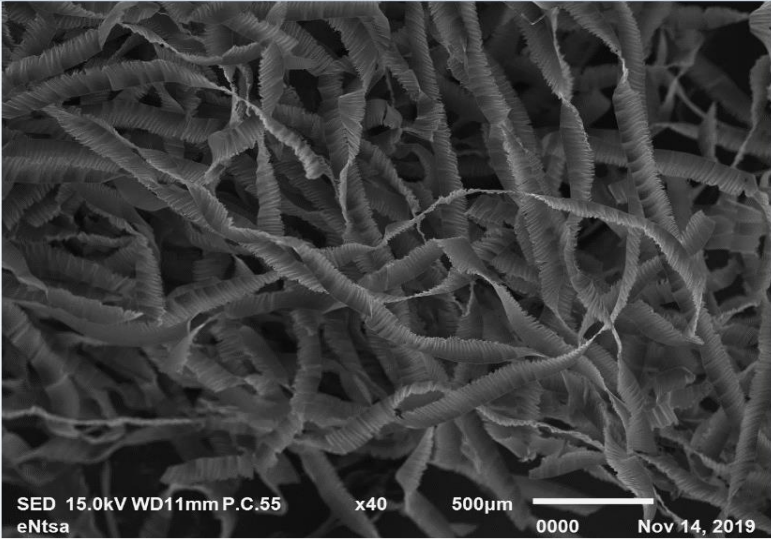
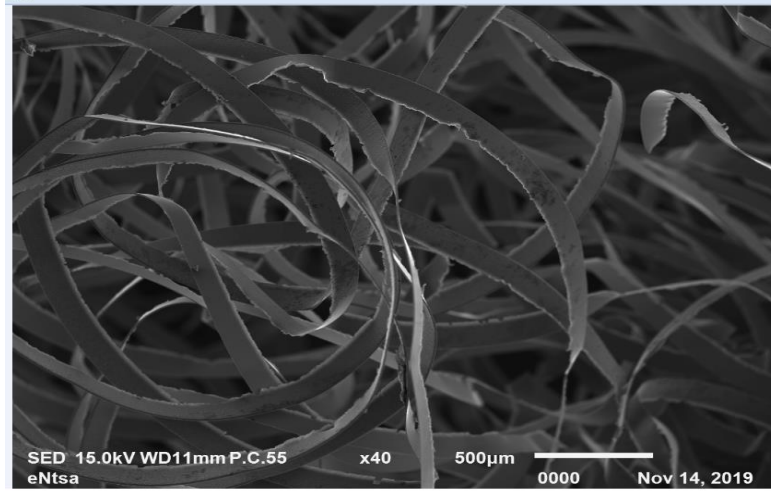
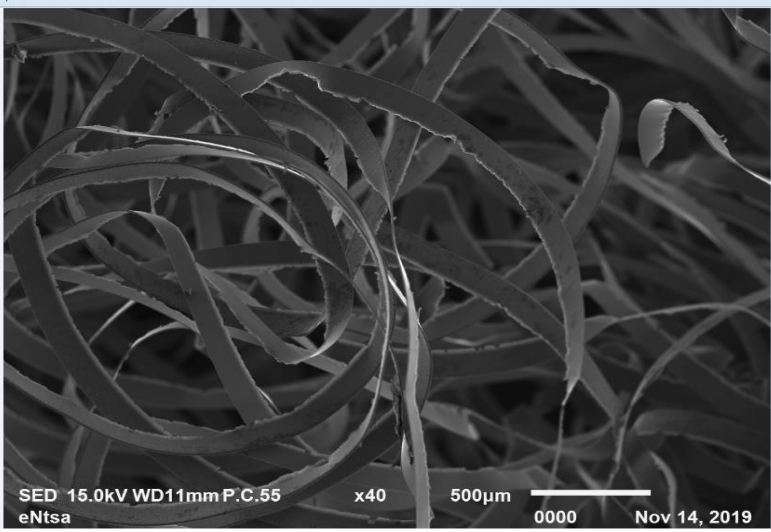
7.7.5 Chip morphology during machining of RSA6061

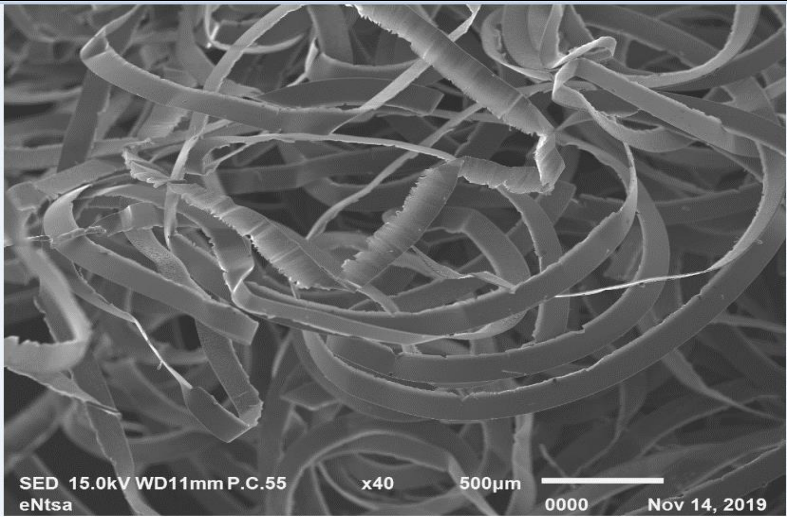
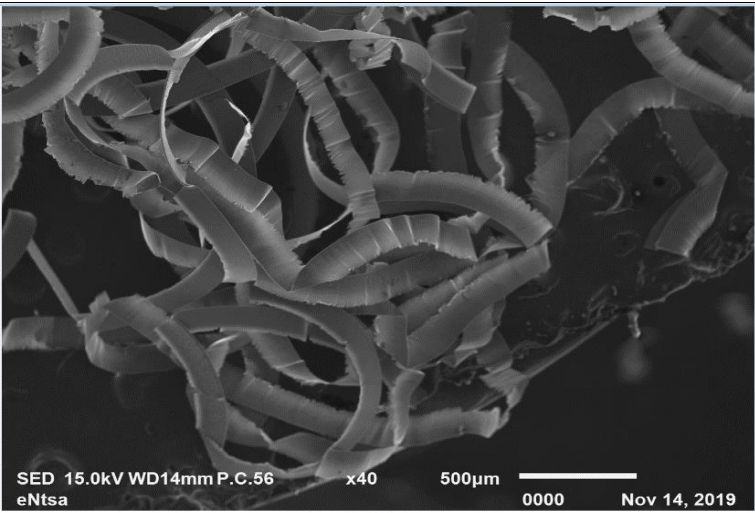
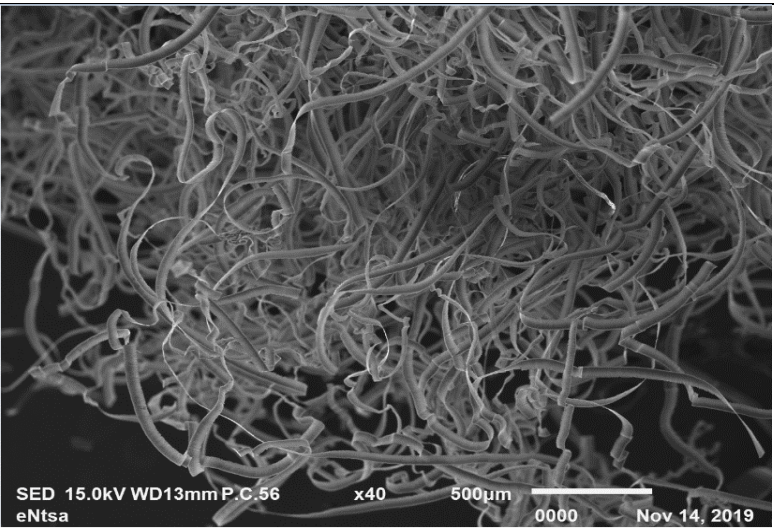
The cutting chips were collected and observed using SEM. **Table 7.23** shows high magnification of SEM. Micrographs of the chips produced using a diamond tools of clearance angle 15° , rake angle 0° nose radius 0.5mm are presented. Also, **Table 7.23** shows SEM image of typical chip morphologies at the specified cutting parameters. They are collected at the end of each experimental run. The common trend about the chip formation is that they are all continuous in nature as the chips at these cutting parameters are flowing smoothly without visible adiabatic shear. This characteristic can be attributed to very-fine microstructure melt spun of RSA 6061 alloy. More so, segmentation tendency of chip formation during diamond turning was decreased due to rearrangement of hard iron element in the alloy. The trend observed in Table 7.23 has shown that due to the presence of high content of Zn element in the alloy, high plasticity of chips which accounts for most of the continuous chip formations are witnessed. At high feed rate and low cutting speed (experiments 1, 5, 7, 10 and 15), thick and continuous chip formation are observed. This behaviour came because of low temperature with high strain rate are reached. However, at high cutting speed and

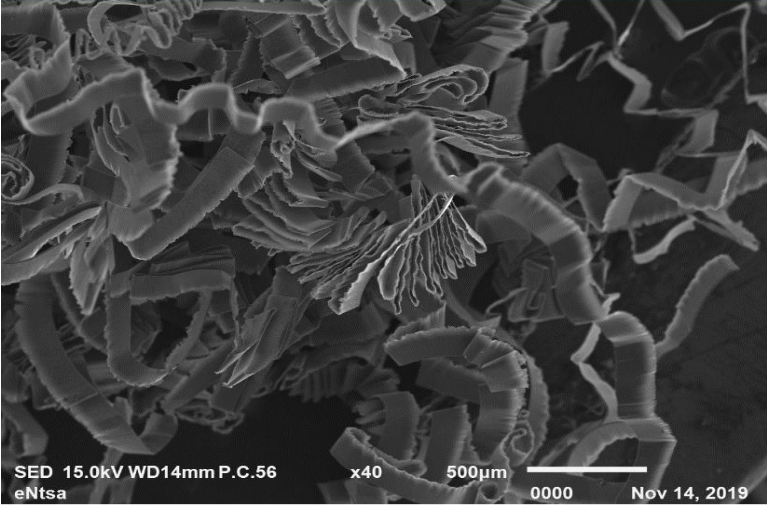
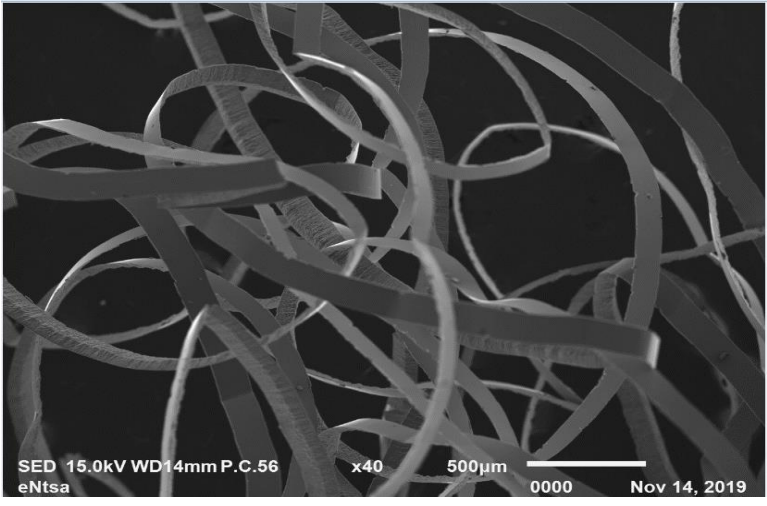
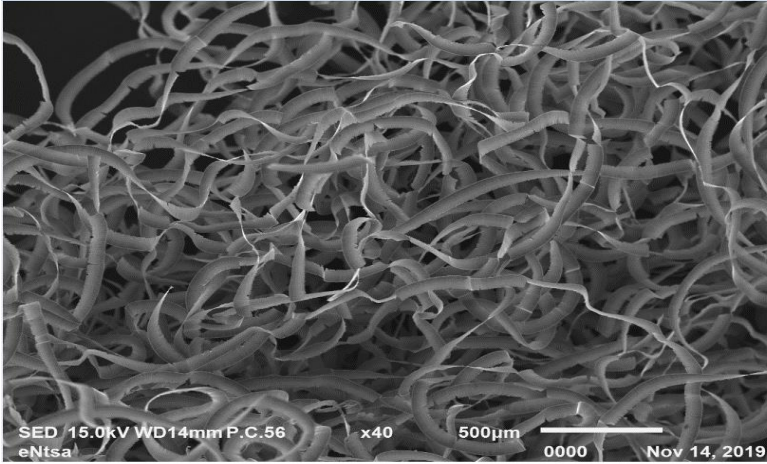
feed rates (experiments 3, 8, 9 and 11), the author noticed less thick and broken serrated chips formation. This can be because of less strain applied which requires less ultimate tensile strength and yield strength.

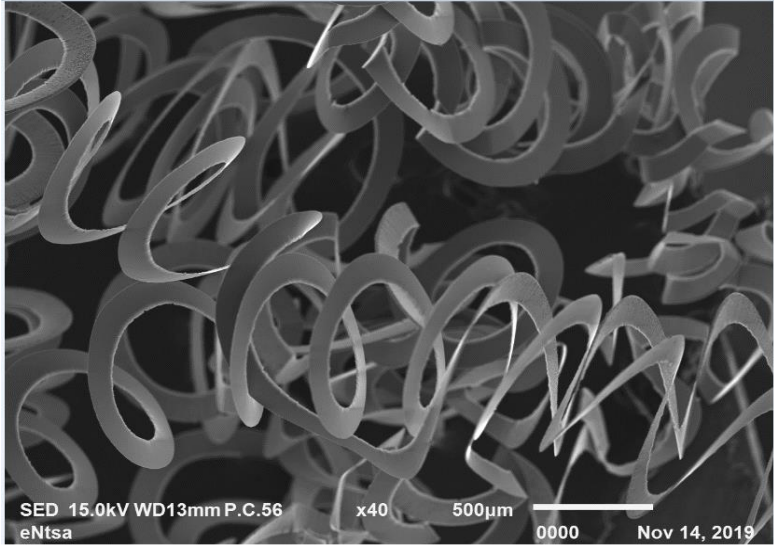
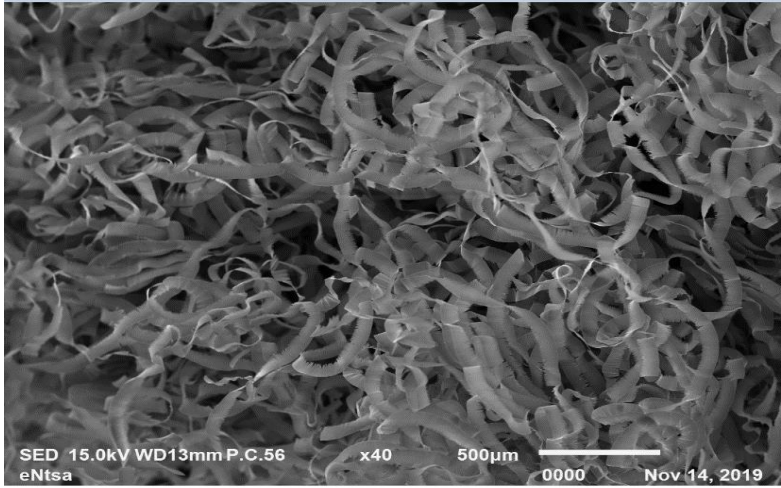
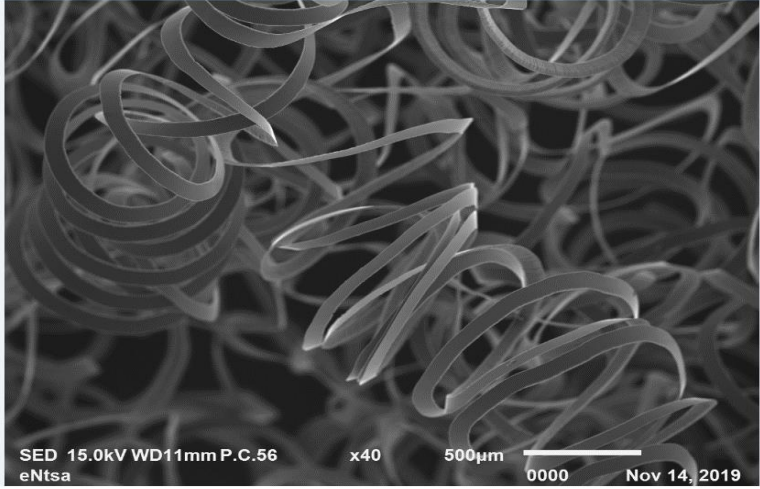
Table 7.23: Characterization of chip morphology for RSA 6061

Run	V rpm	F mm/min	D μm	CHIP MORPHOLOGY
Exp1	1750	25	25	 <p>SED 15.0kV WD9mm P.C.55 x40 500μm 0000 Nov 14, 2019 eNtSa</p>
Exp2	1750	25	5	 <p>SED 15.0kV WD9mm P.C.55 x40 500μm 0000 Nov 14, 2019 eNtSa</p>

Exp3	3000	5	15	
Exp4	1750	15	15	
Exp5	1750	15	15	

Exp6	1750	5	25	 <p>SED 15.0kV WD11mm P.C.55 x40 500µm 0000 Nov 14, 2019 eNtsa</p>
Exp7	500	15	25	 <p>SED 15.0kV WD14mm P.C.56 x40 500µm 0000 Nov 14, 2019 eNtsa</p>
Exp8	3000	25	15	 <p>SED 15.0kV WD13mm P.C.56 x40 500µm 0000 Nov 14, 2019 eNtsa</p>

Exp9	3000	15	25	
Exp10	500	25	15	
Exp11	3000	15	5	

Exp12	500	5	15	 <p>SED 15.0kV WD13mm P.C.56 x40 500µm 0000 Nov 14, 2019 eNtsa</p>
Exp13	1750	5	5	 <p>SED 15.0kV WD13mm P.C.56 x40 500µm 0000 Nov 14, 2019 eNtsa</p>
Exp14	1750	15	15	Same as Experiment 4 and 5
Exp15	500	15	5	 <p>SED 15.0kV WD11mm P.C.56 x40 500µm 0000 Nov 14, 2019 eNtsa</p>

7.8 ACOUSTIC EMISSION ANALYSIS DURING MACHINING OF RSA6061

This section presents acoustic emission which can be used as a means of monitoring tool during machining process is investigated. This monitoring techniques can be used to monitor the surface roughness as well as tool wear in ultra-precision machining. Therefore, effect of machining parameters is considered for the analysis since these same conditions operate for surface roughness prediction. A model was also generated for the AE during the process.

Acoustic emission (AE) is commonly defined as a transient elastic wave generated by the rapid release of energy from localized sources in a material or on its surface. This is caused when a component is subjected to a considerable amount of plastic deformation, dislocation, fracture, or crack propagation which occurs in metal cutting or machining [407]. The factors responsible for AE in machining are friction on the rake face and flank, plastic deformation in the shear region, cracking and propagation, effect of the chip on the workpiece, and chip breakage. These emit high-frequency elastic energy waves that can be sensed and converted to electrical signals for condition monitoring purposes in the form of voltage, such as surface finish.

During diamond turning, there are different kinds of AE signals produced. There are continuous and bursting types. In ductile materials, continuous AE signals are related to plastic deformation [408]. Burst type, commonly regarded as transient (spikes) AE signals, was observed to detect severe collisions and fractures during metal working. This burst signals are created by the interaction and disconnection of the tool with the workpiece [409, 410].

Acoustic emission (AE) is employed in this study as a precision sensing technique and further processed to correlate AE signals with the process performance. The setup for the AE sensor system exhibits excellent sensitivity to the cutting mechanism, especially for the detection of the initial engagement between the tool, workpiece, and surface finish.

Acoustic emission Signals for RSA 6061 in terms of raw data was also acquired to study the machinability of this material. The **Table 7.24** presents the cutting parameters and AE acquired in volts. During the regression analysis, for the researcher to come up with a suitable model for this experiment a transformation of

data was needed. Hence natural logarithm of the response data was the best fit to model the responses and the behaviour of the experiment which allows for further statistical analysis **Table 7.26**.

Table 7.24: Experimental results for AE during diamond turning of RSA 6061

Run	V (rpm)	F (mm/min)	D (μm)	AE(v)	Ln AE (v)
Exp1	1750	25	25	2.4497	0.895966
Exp2	1750	25	5	2.7371	1.006899
Exp3	3000	5	15	1.1274	0.119914
Exp4	1750	15	15	2.6456	0.972898
Exp5	1750	15	15	2.6456	0.972898
Exp6	1750	5	25	1.7917	0.583182
Exp7	500	15	25	1.9627	0.674321
Exp8	3000	25	15	2.6373	0.969756
Exp9	3000	15	25	2.0633	0.724307
Exp10	500	25	15	3.0897	1.128074
Exp11	3000	15	5	2.3431	0.851475
Exp12	500	5	15	1.1906	0.174457
Exp13	1750	5	5	1.4082	0.342312
Exp14	1750	15	15	2.6456	0.972898
Exp15	500	15	5	2.0930	0.738598

Table 7.25 shows the variance inflation factor (VIF) which measures how much the variance of the model is inflated by the lack of orthogonality in the design. If the factor is orthogonal to all the other factors in the model, the VIF will be 1. Table 2.25 has just

confirmed that. However, a VIF of more than 10 suggests that there is an inappropriate correlation between the regression coefficients and the 5% alpha power to detect signal/noise ratios that is considered in the study.

Table 7.25: Variance of inflation

Term	Std Err**	VIF	Ri-Squared
A	0.35	1	0
B	0.35	1	0
C	0.35	1	0
A^2	0.52	1	0.0051
C^2	0.52	1	0.0051

Where A is speed in rpm, B is feed mm/min, D is depth of cut μm .

7.8.1 Statistical analysis of AE for RSA 6061

Table 7.26: Regression analysis and ANOVA for AE of RSA 6061

SUMMARY OUTPUT						
Regression Statistics						
Multiple R	0.938409					
R Square	0.880611					
Adj R Square	0.814284					
Std Error	0.134598					
Observations	15					
ANOVA						
	df	SS	MS	F	Significan F	
Regression	5	1.202653	0.240531	13.2768	0.000623	
Residual	9	0.163049	0.018117			
Total	14	1.365703				
	Coefficients	Standard Error	t Stat	P-value	Lower 95%	Upper 95%
Intercept	-0.3401	0.20456	-1.66259	0.130758	-0.80285	0.122648
v(rpm)	0.00036	0.000161	2.235201	0.052251	-4.3E-06	0.000724
f (mm/min)	0.095654	0.021485	4.452033	0.001596	0.047051	0.144257
d(μm)	-0.00077	0.004759	-0.16157	0.875214	-0.01153	0.009996
V^2	-1E-07	4.47E-08	-2.33239	0.044572	-2.1E-07	-3.1E-09
F^2	-0.00203	0.000698	-2.90636	0.017414	-0.00361	-0.00045

ANOVA was carried out to further ascertain the validity of cutting force. R^2 from ANOVA shows 0.88061. This indicates that the achievement of 88.06% variation of natural log of AE Signal is explained by machining cutting parameters in the experiment making the model a good fit. The most influential cutting parameter is feed rate with a p-value of 0.001596 which contributed about 70% effect to the signal followed by speed with a p-value of 0.05225 during machining. The author also sees squared of feed rates effects which is significant with a p-value of 0.0174 contributing about 10.95%. Speed made a significant value as well at p-value of 0.04457 and contributed about 7% to overall process.

Figure 7.66 shows the scattered plot for this experiment which further validate the model standard. **Figure 7.67** represents the comparison between experimental data and predicted data. The model generated from AE experiment during diamond turning of RSA 6061 is as follows in **Equation 7.8 below**:

Equation 7.9

$$\ln(AE) = -0.3401 + 3.6 \times 10^{-4}V + 0.095F - 7.7 \times 10^{-4}D - 1 \times 10^{-7}V^2 - 2.03 \times 10^{-3}F^2$$

or

$$AE = e^{(-0.3401 + 3.6 \times 10^{-4}V + 0.095F - 7.7 \times 10^{-4}D - 1 \times 10^{-7}V^2 - 2.03 \times 10^{-3}F^2)}$$

where AE is acoustic emission in volts, V is the speed (rpm), F is feed rate (mm/min), and D is depth of cut (μm).

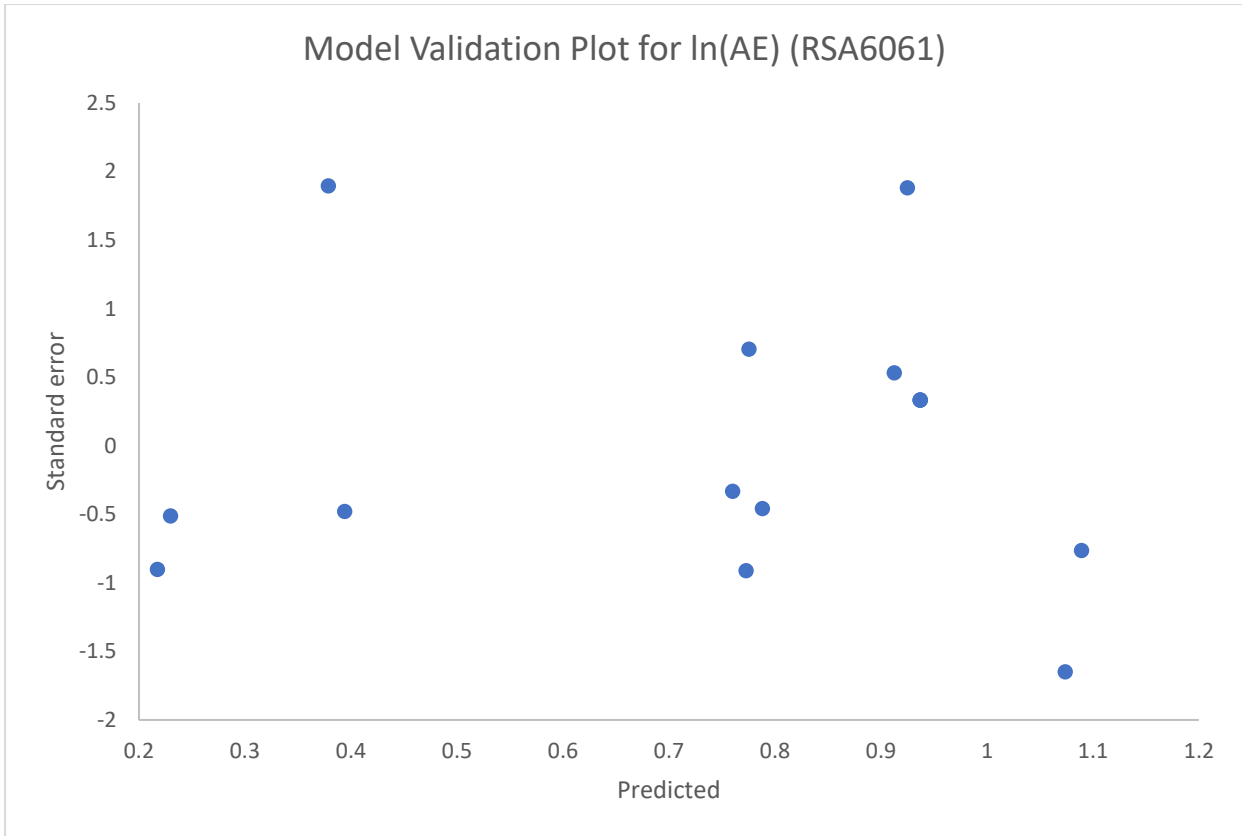


Figure 7.66: Scattered plot for AE model validation

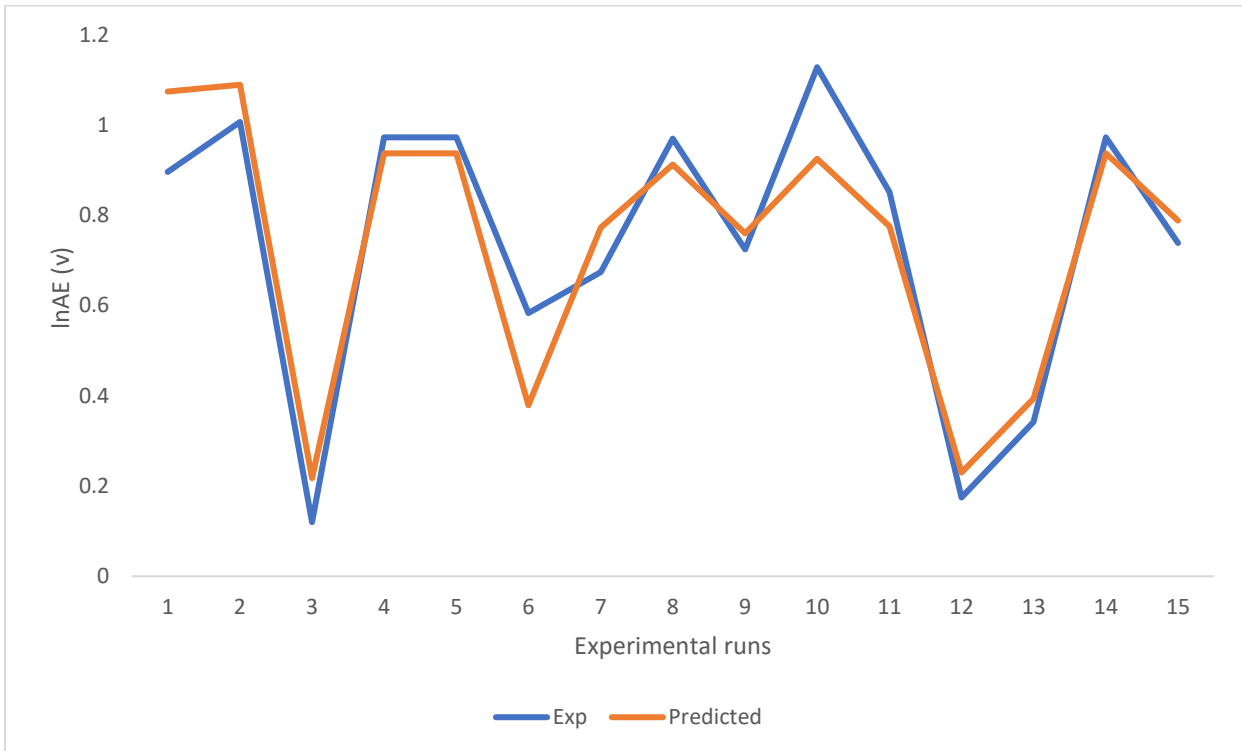


Figure 7.67: Comparison between AE experimental values and predicted values

Figures 7.68 – 7.71 show 2-D contour and 3-D plots that validates the AE signal behaviour at different combinations of cutting parameters. In **Figures 7.67 and 7.68**, two conditions are identified as the reasons for low signal which could be associated with low surface roughness (see **Table 7.16**). First, at low feed rate of 5 mm/min and speed of 500 rpm in experiment 12 (see **Table 7.16 and Table 7.24**) and secondly at very high speed of 3000 rpm and low feed rate of 5 mm/min in experiment 3 also see **Table 7.16 and Table 7.24**

On the other hand, **Figures 7.69 and 7.71** present 2-D contour plot and 3-D graph as the effects of feed rate and depth of cut on AE. It can be observed that, high feed rates (>20 mm/mins) always generate high AE signals see **Table 7.24**, Experiments 1, 2, 8, and 10. This shows that when a high AE signal is recorded during diamond turning of RSA 6061, high pressure is built up at tool tip leading to friction due to its contact with workpiece. Hence, we experience fast tool wear that will results in poor surface quality or at least compromise surface integrity.

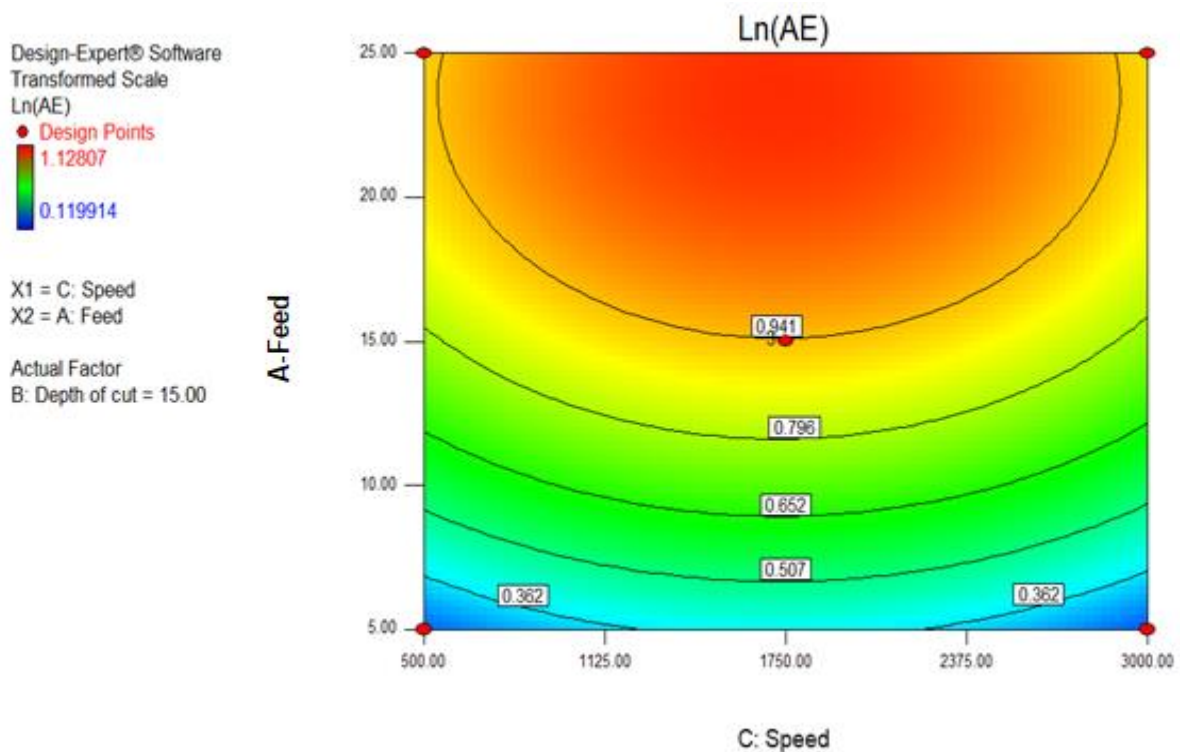


Figure 7.68: 2-D contour graph showing the effects of speed and feed rates on AE

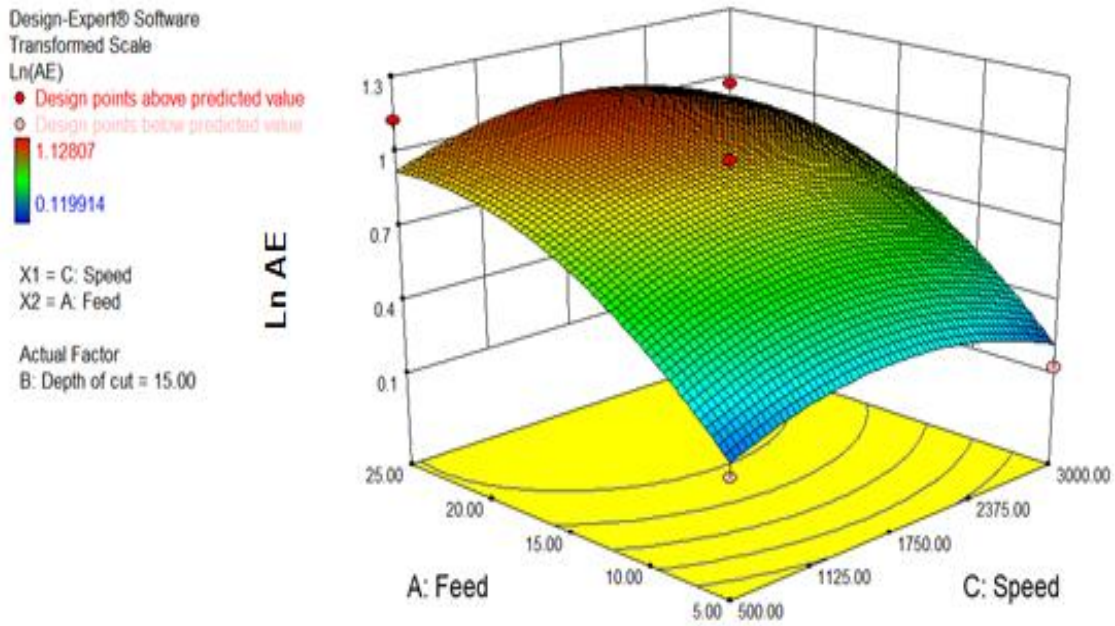


Figure 7.69: 3-D graph showing the effects of speed and feed rates on AE

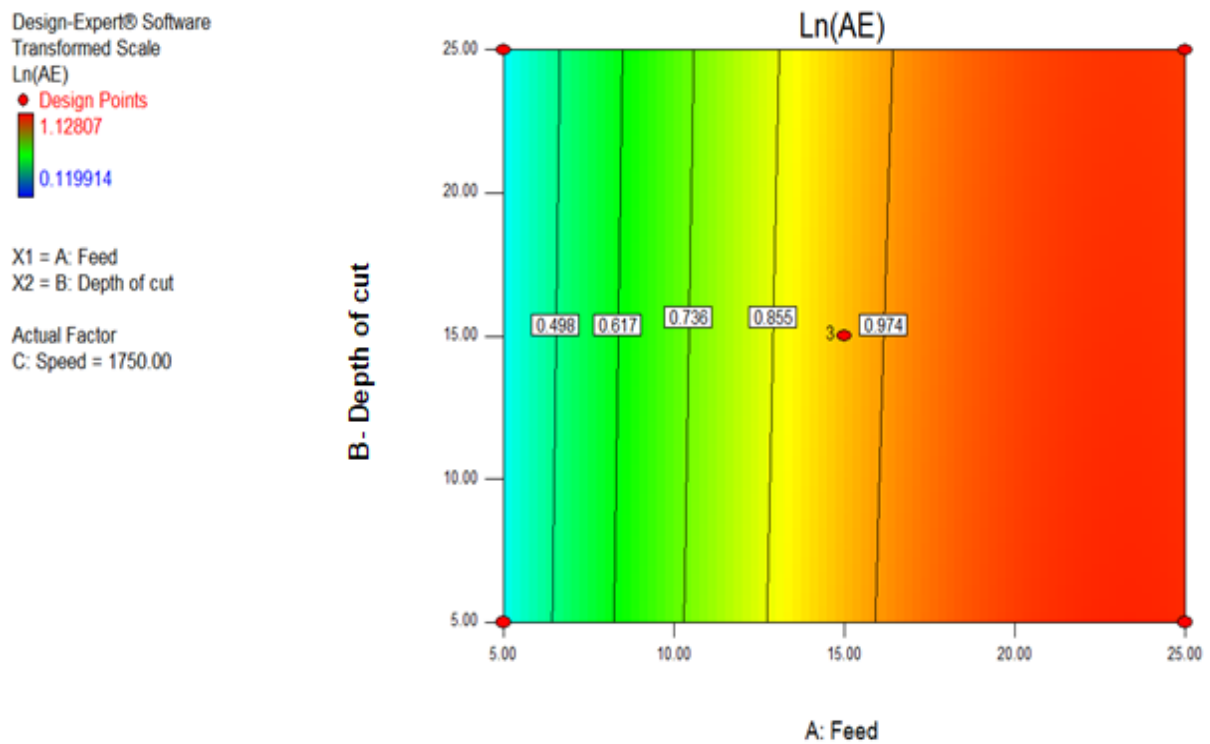


Figure 7.70: 2-D contour graph showing the effects of depth of cut and feed rates on AE

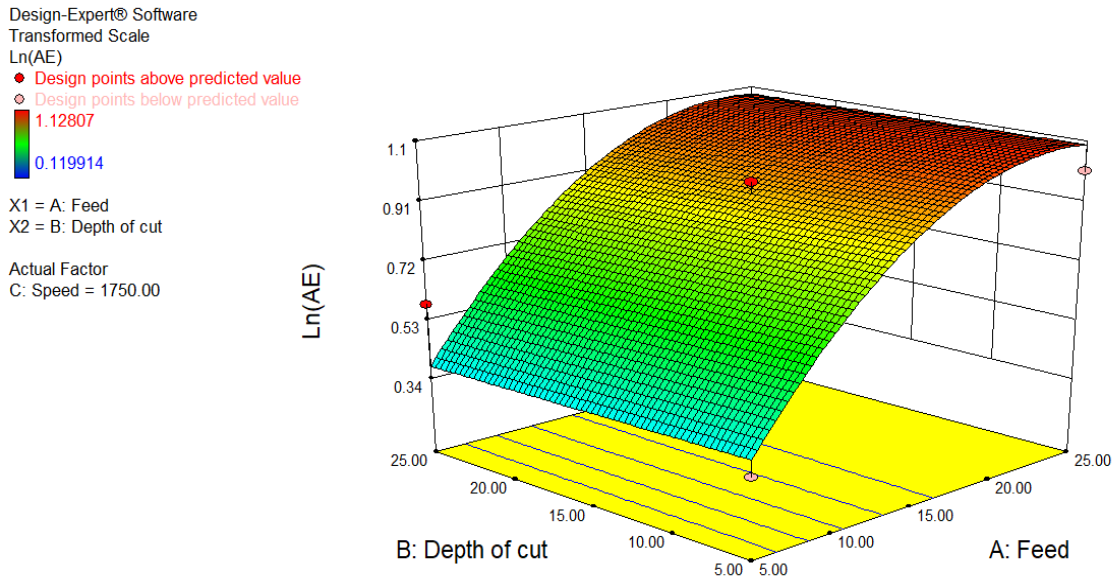


Figure 7.71: 3-D contour graph showing the effects of depth of cut and feed rates on AE

7.8.2 Profile plot for acoustic emission of RSA 6061

Figures 7.72 – 7.74 represent the profile plots for the effects of cutting parameters on AE Signal when diamond turning RSA 6061 at various level. In **Figure 7.72**, at low speed of 500 rpm and high speed of 3000 rpm, AE signals observed were minimal. But within moderate speed (1750 rpm) at constant feed rates and depth of cut, a high AE Signal was observed in all the three scenarios.

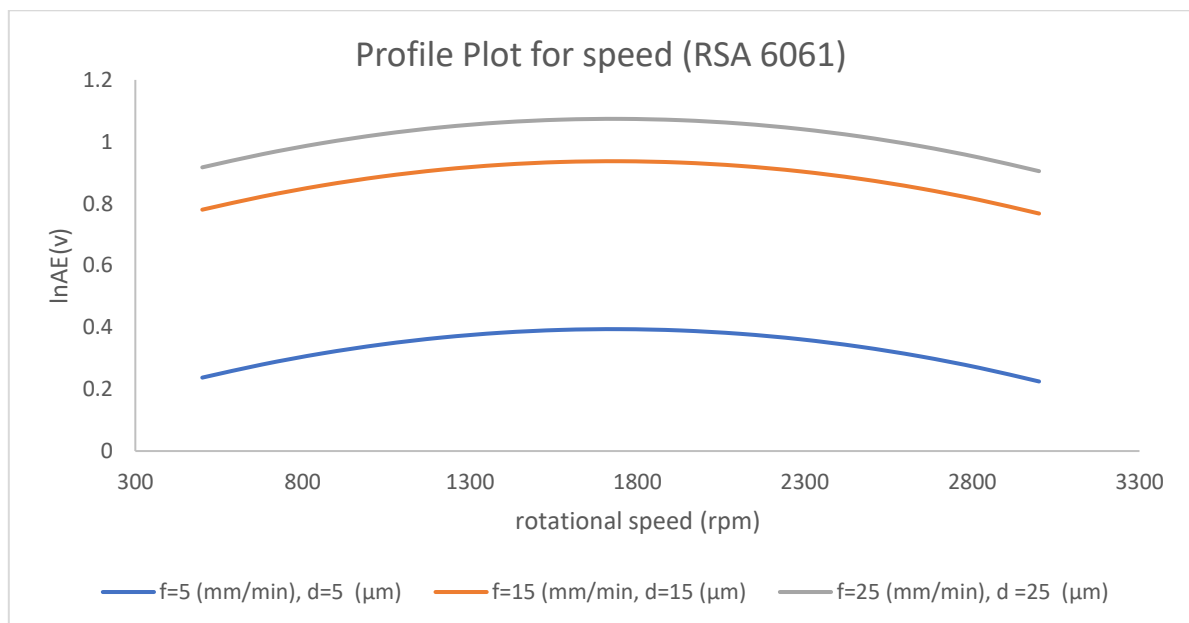


Figure 7.72: Effect of speed on AE at constant feed rates and depth of cut

From the predicted model, it was noted that feed rates made the most significant influence among the cutting parameters. It has a p-value of 0.001596 with a contribution of 70%. Furthermore, looking at experimental runs 1, 2, 8 and 10 in Table 7.24, high values of AE (volts) signals were recorded for high feed rates at 25 mm/mins. In **Figure 7.73**, the higher the feed force, the higher the AE signal. This could be a bad signal for low surface roughness.

Figure 7.74 reveals the effects of depth of cut to be slightly negative on natural log of AE signal when diamond turning of RSA 6061. At low depth of cut, we recorded low AE signal or stable signal. It can be concluded that uncut chip thickness and chip width has little or no effect on AE signal that can be used to monitor surface roughness, tool wear or machining process.

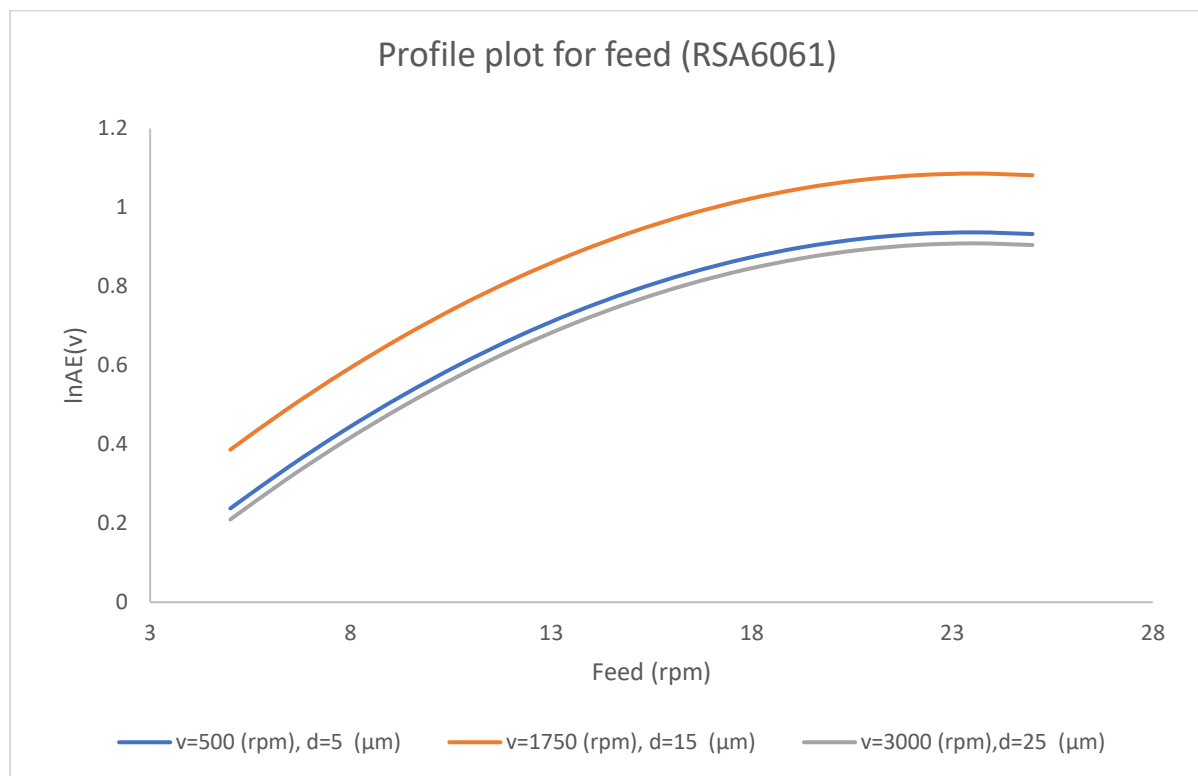


Figure 7.73: Effect of feed rates on AE at constant speed and depth of cut

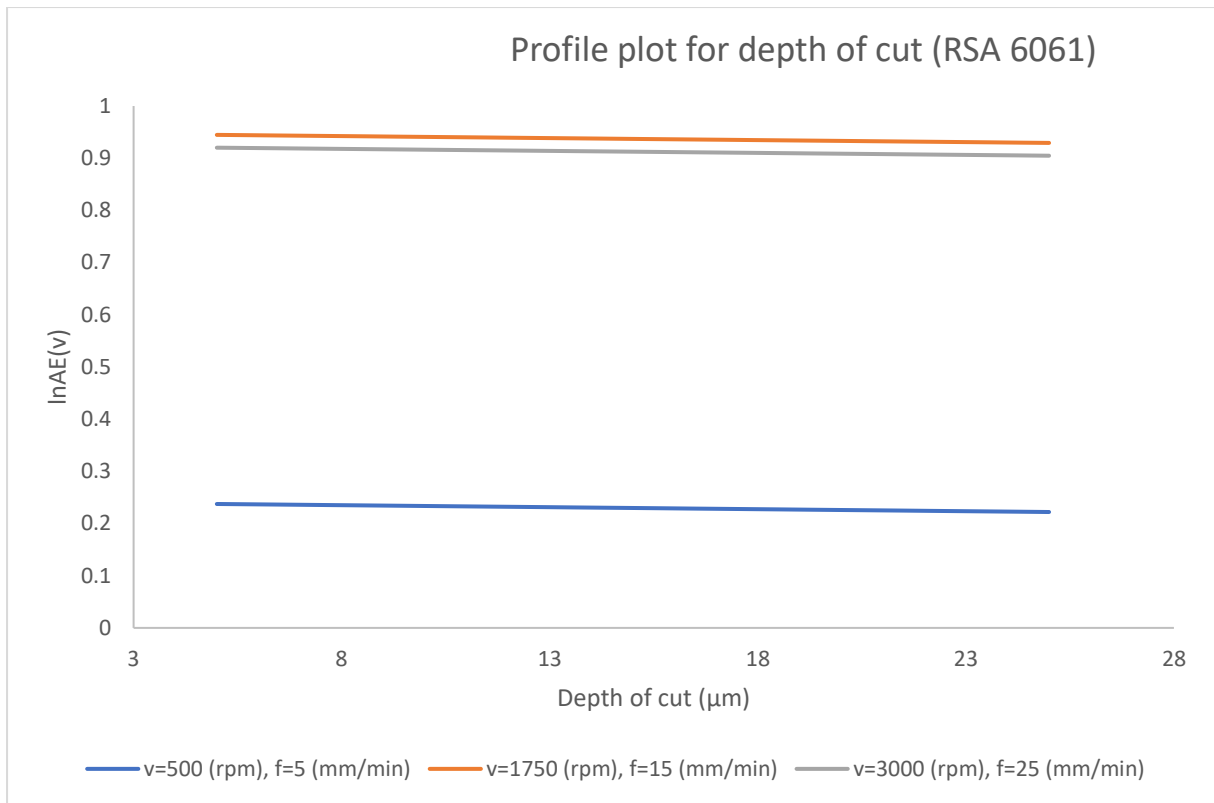


Figure 7.74: Effect of depth of cut on AE at constant feed rates and speed

CHAPTER 8

MOLECULAR DYNAMICS SIMULATION OF RSA 6061

Computation of Molecular Dynamics (MD) is the simulation of the motion of atoms/molecules in a system in order to determine each atom/force, molecule's velocities, position, stresses and energy at any point or time step. In this chapter, A simulation system for nanoscale ductile mode of Rapidly Solidified Aluminium alloys RSA 6061 was developed in this study. To better understand the ductile mode cutting process that will imitate experimental machining at the nano scale, the author used the molecular dynamics (MD) technique. Although the cutting pace of the simulation in femtoseconds remains unrealistic in the laboratory since the MD theory is based on the choice of a suitable potential energy function of the material needed to explain the material's interatomic potential energy.

Interatomic forces can be determined based on this interatomic potential energy. With the knowledge of the Newton equation of motion, we can determine the acceleration of an atom in the system. Once each atom's acceleration is known, it is therefore possible to determine the new original positions and velocities of each atom. Numerical approaches that will be described briefly below for a short time interval at femto seconds are then implemented into this Newton motion equation for ensemble atoms (1 femto sec = 10^{-15} s).

8.1 METHODOLOGY OF MOLECULAR DYNAMICS SIMULATION OF RSA 6061

In principle, molecular dynamic simulation is divided into three processes based on the molecular dynamics approach, which are:

- Pre-processing Phase
- Processing Phase
- Post-Processing phase

8.1.1 Pre-Processing phase

There are numbers of software involved for conducting MD simulation, but the choice of the software would depend on the intended implementation, the platform and

hardware of the operating system available. Some of this program is open source, i.e., free to use to mention but few, and some of them may need a licence. Furthermore, it is also important to remember that some of the functionality is only used for pre-processing, processing, and post-processing purposes. LAMMPS, AtomsK, OVITO, VMD, material studio, DL POLY, CHARMM, GROMACS, MDynaMix, Moldy etc. are some of the software. Hence for pre-processing, AtomsK, AtomEye, Material Studio are used.

A free open-source command-line program dedicated to the development, manipulation, and transfer of data files for atomic-scale simulations was used in this study by AtomsK software to create the work piece and the instrument. The file formats used by many applications, including LAMMPS, material studio and simulation tools called Atomeye, are supported by this software.

The simulation workpiece is RSA 6061, and the tool is a crystalline diamond, which is the hardest natural material known, making it suitable as a machining tool. The diamond arrangement consists of repeating units of four carbon atoms which are joined by tight covalent bonds to four other carbon atoms, see **Figure 8.1**. The chemical composition of the workpiece and chemical properties of the tool are shown in the **Tables 8.1 and 8.2**:

Table 8.1: Chemical constituents of RSA 6061

	Si	Fe	Cu	Mg	Zn	Cr	Mn	Ti	Al
RSA 6061	0.6	0.2	0.3	1	0.1	0.2	0.1	0.1	97.4

Table 8.2: Physical properties of Diamond

Chemical Symbol	C
Density	3500 kg/m ³
Melting Point	3820 K
Young Modulus	1050 GPa
Thermal Conductivity	400 W/mK
Crystal Structure	Diamond
Hardness	45 GPa

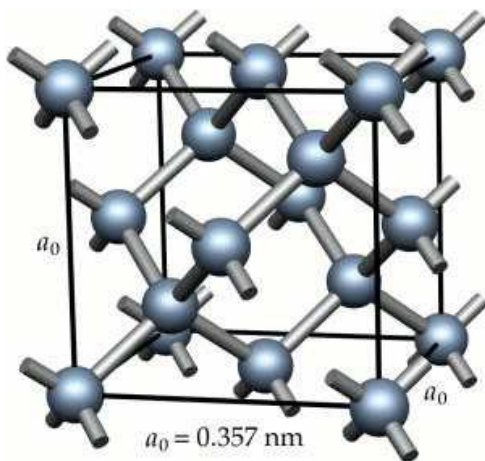


Figure 8.1: The structure of Diamond

Using atoms [411] and material studio [412], both workpiece and tool symmetry were designed, while Visual Molecular Dynamics (VMD) [413] and OVITO [414] were used for improved visualization of atomistic results. The workpiece and tool were created separately in AtomsK (Beta 0.10.6 version) and visualized using AtomEye (3 (2012) version). The size and dimension for the workpiece is $52a \times 12a \times 8a$. Both workpiece and tool were then imported into material studio for merging. After the combination, it was exported back to VMD in pbd format for visualization. **Figure 8.2** show a ready to simulate model of RSA 6061 and Crystalline diamond tool with a total of 40136 atoms together. **Table 8.3** is the 2D and 3D representation of tool geometry modelled for the simulation.

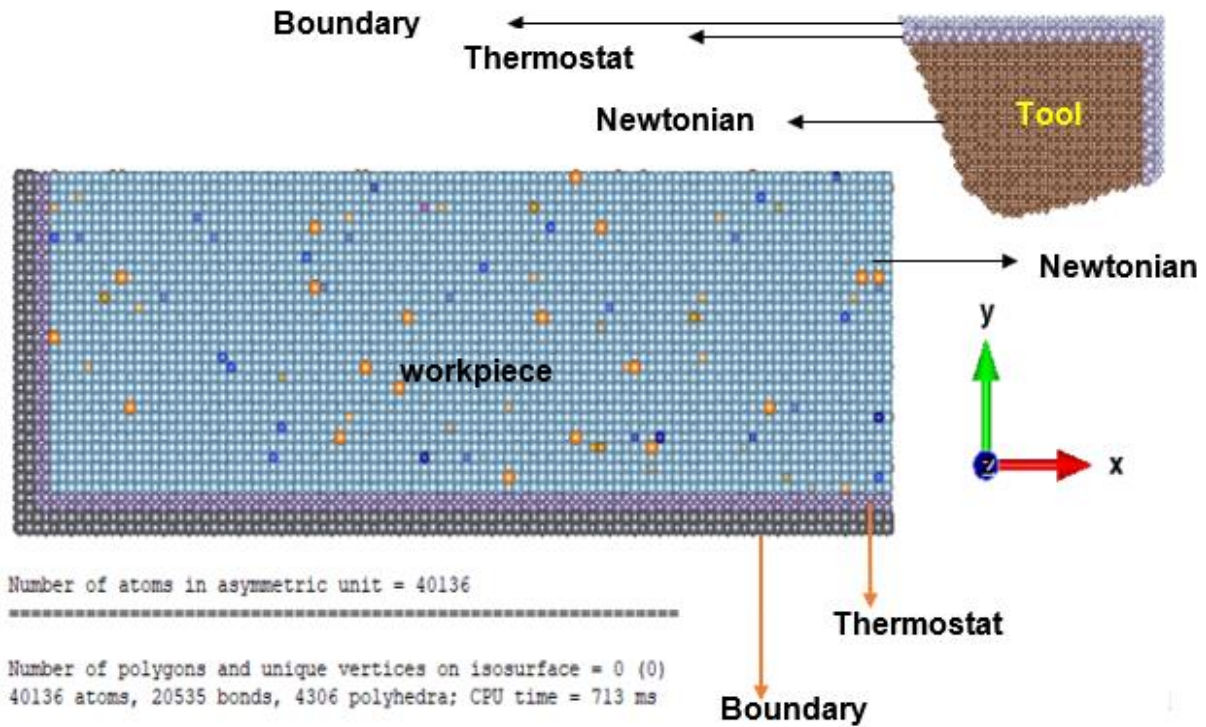


Figure 8.2: The schematic representation of the MD simulation model

Table 8.3: 2D and 3D representation of tool geometry

Rake angle	Edge radius (A)	Clearance angle (°)	2D Representation	3D Representation
25	35	10		

These same features were shared in all the configuration during the simulation which consists of the workpiece and the tool. Both are divided in Newtonian, thermostat layer and boundary layers. The Newtonian atoms follow the Newton's equation of motion. The thermostat atoms perform the heat generated during the cutting process out of the cutting region. This is achieved by the velocity scaling of the thermostat atoms, (with the conversion between the kinetic energy (KE) and temperature.

8.1.2 Processing phase

The processing phase or simulation phase is the most critical phase of the simulation and if this phase is not well planned, anything that was explained in the pre-processing phase would not work. LAMMPS is the main tool or platform for carrying out this process. LAMMPS is an MD-coded environment that is powerful, effective, parallelized, well documented, and open. In this study, LAMMPS version for 18th of March 2018 or 3rd of March 2020 are equally good and used for this simulation. The MD input scripts are simulation codes subdivided into sections such as: Initialization, atom definitions, settings and run. This approach is also represented in the MD Simulation flow chart in the **Figure 8.3**. The author will briefly explain some technical steps that are worth noted for this MD simulation.

To secure and ensure that the tool's atoms are far from the equilibrium cut-off range of the interaction of aluminium alloys - carbon, which is in the range of 2.2-2.6 Å [196, 216, 415, 416], The diamond tool was positioned at 5 Å (0.5 nm) from the workpiece to eliminate contact between the workpiece and the tool atoms at the beginning of the simulation. This distance is suggested to be greater than the cut-off distance for the potential used (e.g., $r_{cut} = 3.0$ Å for Tersoff SiC potential). Then to reach the desired temperature, the model was allowed to run for 5 ps to calm the machine. The speed of the tool was programmed to travel forward at a rate of 100 m/s (i.e., 1 Å/ps). According to the work of [69, 215, 417, 418], this knowledge was made clear that the main understanding of the cutting process and characteristics for the MD simulation of Aluminium alloys can be best illustrated at this high speed of cutting process.

The MD's motion was determined by the interatomic forces produced by the potential for interaction and the direct interpretation of Newton's equation of motion. Under the microcanonical ensemble NVE, the nanometric cutting simulation was performed for the number of time steps selected to relax the device. This is done so that the velocities of atoms initially allocated randomly would eventually enter their normal, dynamically balanced states.

Boundary layer atoms were fixed to hold the workpiece and tool in place by reducing edge effects and minimizing the motion in the workpiece beyond the range of other atoms. This is to prevent the translation caused by cutting force. This effect was resisted in the actual cutting state although in MD simulation it is highly discouraged.

Owing to the extensive gap in hardness, diamond has also been assumed to be solid by many scholars, so that diamond tip does not deform [195, 419-422] during the cutting process so that during cutting the relative positions between tool atoms are unchanged. In order to study the machining effect on both the tool and the workpiece, many other MD simulations modelled the cutting tool as deformable. In this work, the tool was modelled only as rigid with variable properties to allow efficient study without consideration of tool wear.

In order to adjust the system temperature at every 500 computational time steps, the system's thermostatic atoms must follow the theory of Berendsen thermostatic dynamics. Therefore by velocity scaling at thermostat atom temperature higher than the pre-set 293 K bulk temperature, we need to conduct heat generated from the cutting region using the relationship in **equations 8.1 and 8.2** below [255, 423]. For the time-marching process in the simulations, the velocity verlet algorithm with the single time step of 1000 fs (0.00001 ps) was used.

Equation 8.1

$$\sum_i \frac{1}{2} m_i v_i^2 = \frac{3}{2} N K_B T_i$$

$$v_{i,new} = v_i \sqrt{\frac{T_{desired}}{T_{current}}}$$

8.2 INTERATOMIC POTENTIALS AND PARAMETER SETTING FOR SIMULATION

In this simulation of nanoscale machining of advanced aluminium alloy, the dimensions of the RSA 6061 workpiece were 52a×12a×8a. The working environment temperature was set to 293 K. The cutting speed was set to 20 m/s. The undeformed chip thickness a_c was set at 2.0 nm and the radius R values of the cutting tool edge were set at 2.5 nm in the analysis of the effects of tool cutting edge radius. The undeformed chip thickness was, however, smaller than the cutting-edge radius of the tool. The tool cutting edge radius R and undeformed chip thickness a_c were 2.5 nm and 2.0 nm respectively in the study of the effects of the cutting direction. The cutting

direction [100] was used in the simulation which is along x-axis. **Table 8.4** also listed other simulation details.

Table 8.4: MD simulation parameters

Workpiece material	RSA 6061
Workpiece lattice (<i>a</i>)	0.405 nm
Workpiece dimension	52a x 12a x 8a
Tool material	Diamond
Tool lattice (<i>a</i>)	0.3567 nm
Tool rake angle	25 ⁰
Tool clearance	10 ⁰
Depth of cuts	(0.5 – 3.0) nm
Cutting speed	20 m/s
Bulk temperature	293 K
Time steps	1000 fs (0.0001ps)
Cutting direction	[100] – along x-axis
Simulation run	2000000

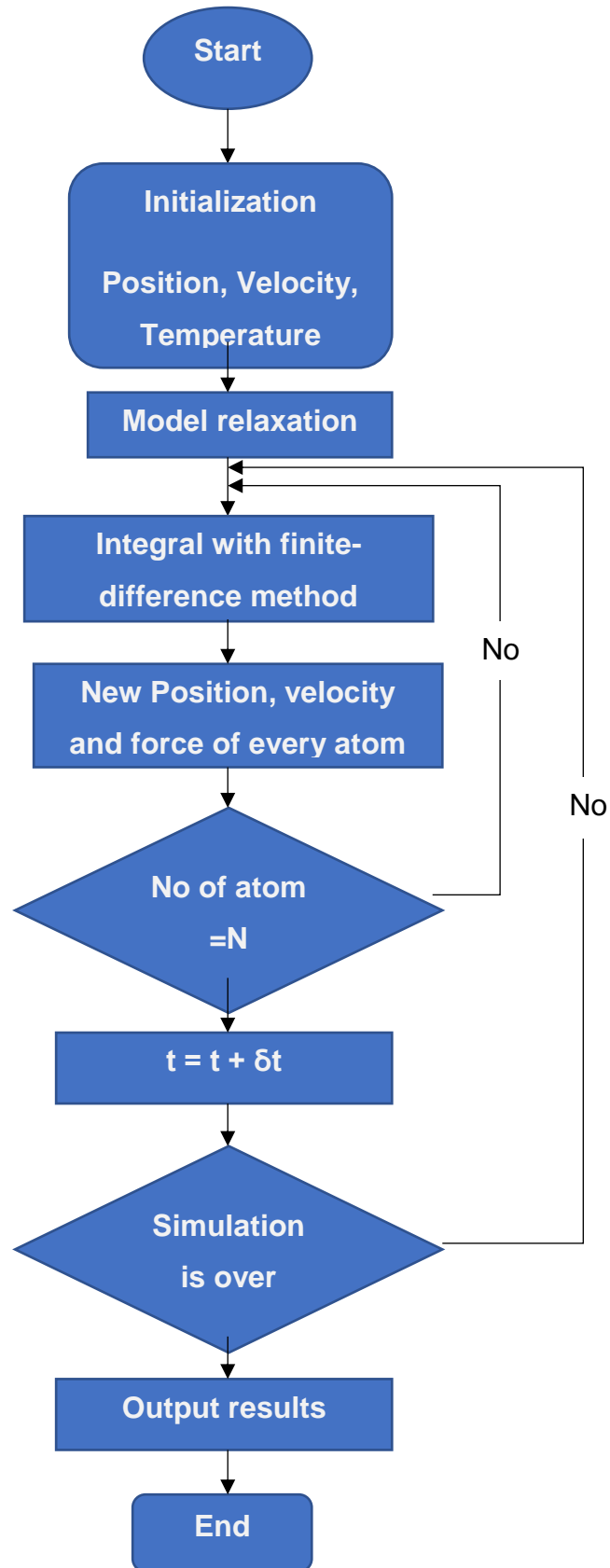


Figure 8.3: Flow chart of processing phase of MD simulation system

8.3 SELECTION OF INTERATOMIC POTENTIALS AND PARAMETERS SETTING

Due to the complexity of the constituent elements in advanced aluminium alloy, the interactions of atoms within the simulation were modelled using four interatomic potential functions. Basically, in nanomachining simulation there should be interactions within the diamond tool atoms, interactions within the workpiece alloy atoms and interactions between Tool – workpiece. Tersoff was implemented between the diamond tool atoms and silicon atoms, Morse between the tool and workpiece atoms, and MEAM within the workpiece atoms. These potentials were chosen due to the suitability to the respective materials. More so, for more suitable diatomic atomistic simulation, Morse potential function has found being used in most of the MD simulations investigated by many researchers [253, 424-427] to describe the interactions between tool-workpiece.

The cutting depth was varied depending on the actual simulation. a unique idea was carefully developed to model the potentials for this simulation because the whole functionality of the MD simulation depends on how perfect the interatomic potential would be. In this simulation, Tersoff was identified for Si and Diamond atoms (C), EAM/alloy was identified for Ti and Al, MEAM potential was identified for AL, Si, Mg, Cu and Fe. These three potentials are readily available in the LAMMPS library but not adequate for the entire interaction of all atoms in the simulation. Hence, Morse interatomic potential was calculated to take care of the remaining interactions using Morse interaction potential parameters (D_0 , α and r_0) from the relation in equations 1, 2,3. Where D_0 is the cohesion energy, α is elastic modulus and r_0 is the atomic distance at equilibrium. **Tables 8.5 and 8.6** are Morse and Tersoff potential parameters used in this study.

The Morse potential parameters for the tool-workpiece atoms interaction were calculated using the following:

Equation 8.2

$$D_{A-B} = (D_A D_B)^{\frac{1}{2}}$$

$$\alpha_{A-B} = \frac{1}{2(\alpha_A + \alpha_B)}$$

$$\sigma_{A,B} = r_{0A,B} - \ln\left(\frac{2}{\alpha_{A,B}}\right)$$

$$r_{0A-B} = \left(\left[\frac{2}{\alpha_{A-B}}\right]\right)^{\frac{1}{2}} + \ln\left(\frac{2}{\alpha_{A-B}}\right)$$

Table 8.5: Mores Potential parameters for constituent elements of RSA 6061

Elements	D _o (eV)	A (Å ⁻¹)	r _o (Å)	Literature
C	2.24300	2.55500	3.52200	[68, 428]
Al	0.27030	1.16460	3.25300	[429-432]
Fe	0.41740	1.38850	2.84500	[429, 430, 432]
Cu	0.34290	1.35880	2.86600	[151, 432]
Si	0.99560	1.36210	2.84390	[433]
Mg	0.05300	3.89050	2.04300	[434]
Ti	0.00567	1.55430	4.18784	[435]
Mn	0.00565	1.69722	4.14158	[436]
Cr	0.44140	1.57210	2.75400	[429, 430, 432]
Zn	0.17000	1.70500	2.79300	[437]

Table 8.6: Tersoff Potential Parameters

Parameter	Si	C
<i>A</i> (eV)	1.8308 x 10 ³	1.3936 x 10 ³
<i>B</i> (eV)	4.7118 x 10 ²	3.467 x 10 ²
<i>λ</i> ₁ (nm ⁻¹)	24.799	34.879
<i>λ</i> ₂ (nm ⁻¹)	17.322	22.119
<i>α</i>	0.0	0.0
<i>β</i>	1.0999 x 10 ⁻⁶	1.5724 x 10 ⁻⁷
<i>N</i>	7.8734 x 10 ⁻¹	7.2751 x 10 ⁻¹
<i>P</i>	1.0039 x 10 ⁵	3.8049 x 10 ⁴
<i>Q</i>	16.218	4.384
<i>H</i>	-5.9826 x 10 ⁻¹	-5.7058 x 10 ⁻¹
<i>λ</i> ₃ (nm ⁻¹)	17.322	22.119
<i>R</i> (nm)	0.285	0.18
<i>D</i> (nm)	0.015	0.02

8.4 MD ANALYSIS OF STRESSES, CUTTING FORCES, CUTTING KINETIC FRICTION, TEMPERATURE AND SPECIFIC CUTTING ENERGY IN THE CUTTING ZONE

MD of RSA 6061 alloy was modelled making the simulation like experimental where nanomachining was carried out on this same material. The behaviour of the MD simulation was observed, however, since roughness of material measuring package is not yet included in LAMMPS, other parameters that have been proven to determine the quality of a surface were employed as bases for comparison. These parameters

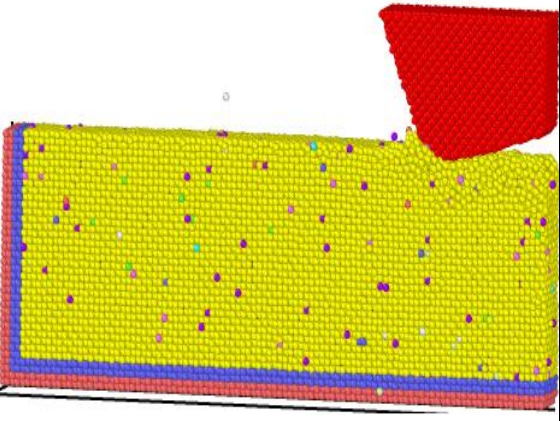
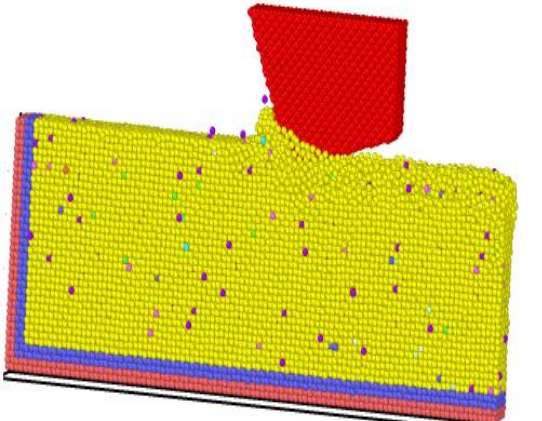
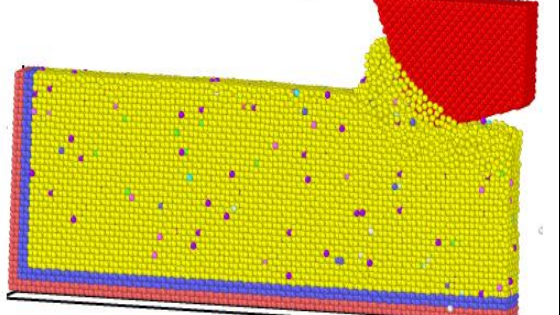
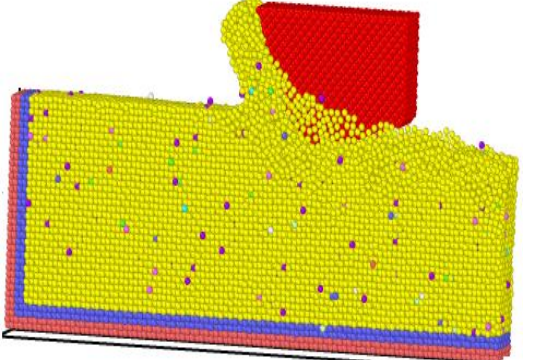
include stresses in the cutting region, cutting forces, temperature, and specific cutting energy.

The simulation was run for 2000000 steps and the behaviour of the MD system was viewed and recorded for 0.5 nm (5 Å), 2.0 nm (20 Å) and 3.0 nm (30 Å) depth of cuts at a cutting speed of 20 m/s. **Figure 8.4** shows the cutting process as the tool travels through the workpiece at different depth of cuts at stipulated speed. The workpiece atoms were seen to split and flow symmetrically along the sides of the tool, some flowed under the tool, while others piled up in front of the tool to form the chip.

8.4.1 Effect of depth of cut on stresses

Close to what is obtainable in macro and micro scale machining, the performance of nano scale machining can also be influenced by machining parameters such as Depth of cut, speed, and feed rate. Several researchers have investigated some of these parameters on different materials at nano level [438-440]. A systematic study was carried out by Zhang and Tanaka [441, 442], which offered a very fundamental understanding of machinability in copper and silicon nanomachining. They predicted minimum depth of cut that could trigger removal rate. They revealed that through four distinct regimes, surface atoms can experience deformation. Which is a defect-free regime (which can also be called a no-wear regime), adhering to the regime, ploughing regime, and cutting regime, i.e., where the removal of material has taken place.

In addition, the transformations between these regimes have been shown to be manipulated by the conditions of cutting, such as cut depth of cut. Although several authors have assessed the influence of different cutting depths in their MD simulation [443]. It has also been found that as the depth of cut increases, the amount of plastic deformation at the tip of the tool, the subsurface and the number of dislocations will increase [443, 444]. Therefore, in this study, a 3D MD simulation of nanomachining of RSA 6061 has been carried out with different depth of cuts (0.5, 2, 3) nm. **Figure 8.5** dislocation at three different depths of cut at 1million time steps and 2million time steps.

DOC	1-million-time steps	2-million-time steps
0.5 nm		
2.0 nm		

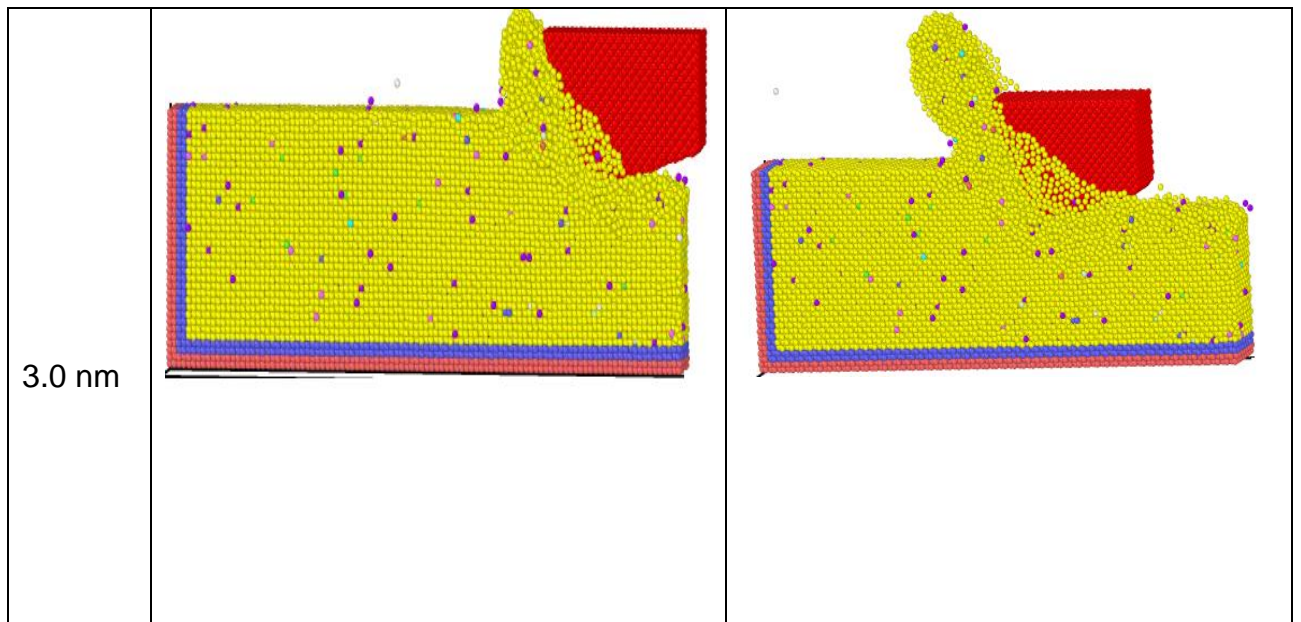


Figure 8.4: Machining simulation development showing increase in depth of cut with tool travel

Figure 8.5 are different representations that shows an increase in the cutting depth, more materials are deformed ahead of the cutting tool. Similarly, with high depth of cut, more dislocations are observed in the cutting region. It can also be observed that as the cutting depth increases, the machined surface becomes rougher. This may be due to the higher cutting forces required for the larger cutting depth [439].

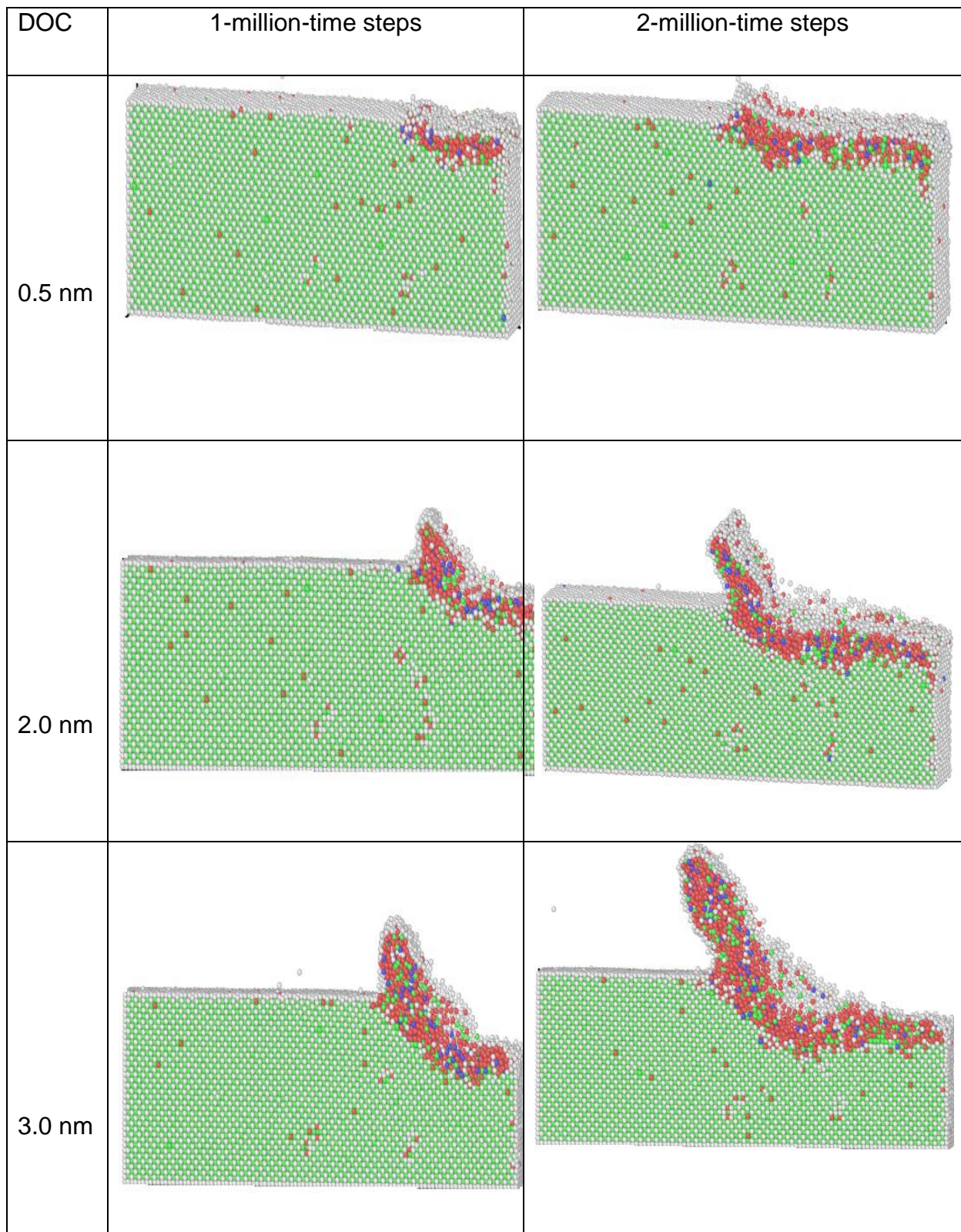


Figure 8.5: Machining simulation displaying dislocations of RSA 6061 as tool travels

It is well known about stress distribution during nano machining that an increase in depth of cut and decrease in cutting speed usually increases the effect of tensile stress, hydrostatic stress, plastic deformation, and dislocation density which could consequently turn to a radical transformation and early cracks within the workpiece and cutting tool [444-447]. In this study, depth of cut and hydrostatic stress was examined to know their effects on RSA 6061. The progression of the various component stresses at different depth of cut acting on the workpiece volume over the simulated period was observed.

In **Figures 8.6 – 8.8**, it is obvious that aluminium alloy RSA 6061 experiences constant increase in various stress components as the depth of cut increases. The highest component of the stress is along σ_{yy} . **Figures 8.9 and 8.10** show an average and maximum stresses at different depth of cut. Here, it is noticeable that average stress (**Figure 8.9**) is highest along $\sigma_{yy} = 2320.5$ (MPa) or (2.32 GPa) and maximum stress (**Figure 8.10**) along same $\sigma_{yy} = 4127.5$ MPa or (4.1275GPa). Meanwhile both average and maximum stresses along σ_{zz} tends to be constant or negligible which confirms observations in literature regarding stress along Y- component during 3D nanometric cutting.



Figure 8.6: Change in stresses with distance in RSA 6061 at depth of cut = 0.5 nm

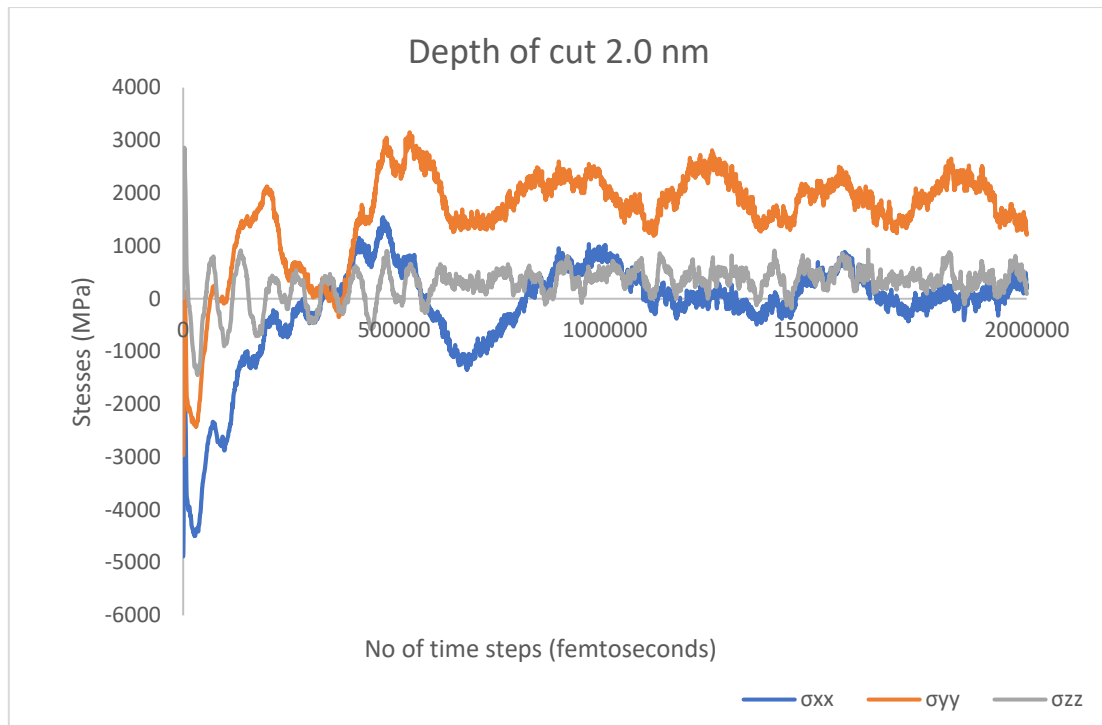


Figure 8.7: Change in stresses with distance in RSA 6061 at depth of cut = 1.0 nm

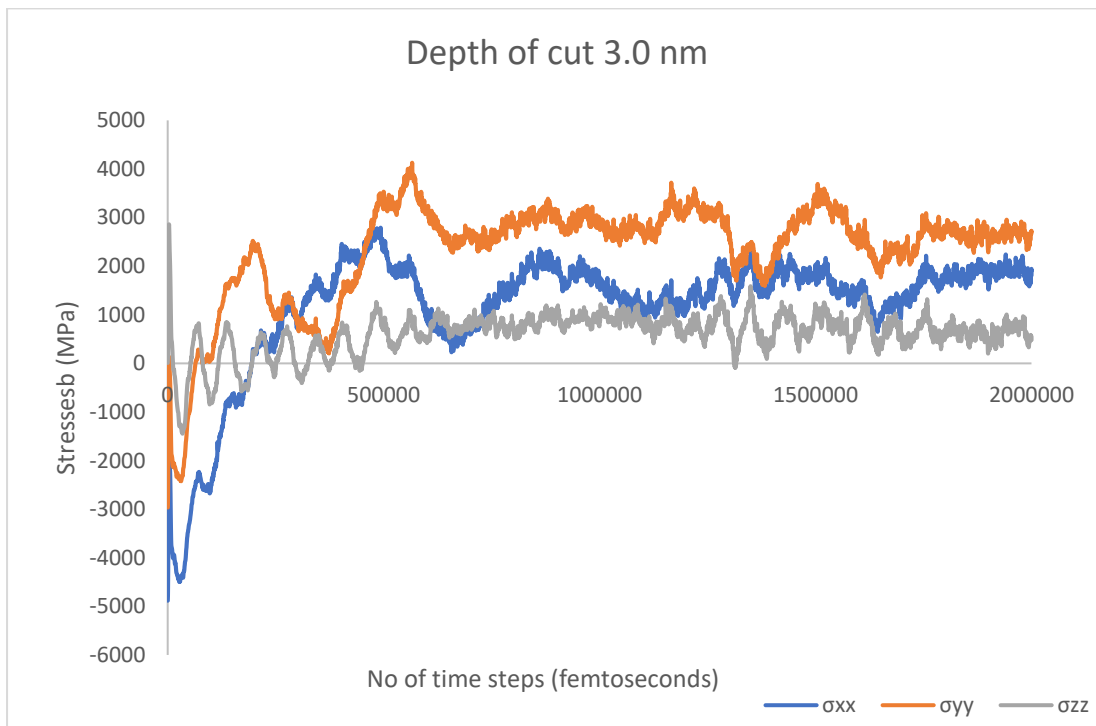


Figure 8.8: Change in stresses with distance in RSA 6061 at depth of cut = 1.5 nm

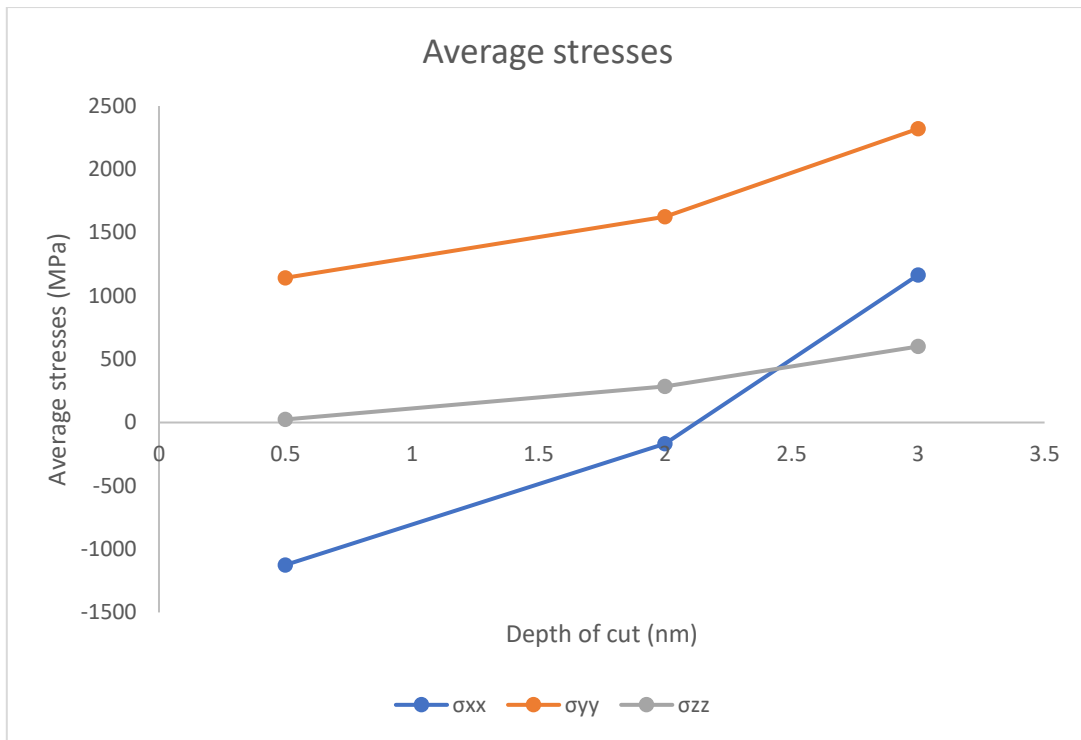


Figure 8.9: Average thrust, tangential and axial stresses against depth of cut

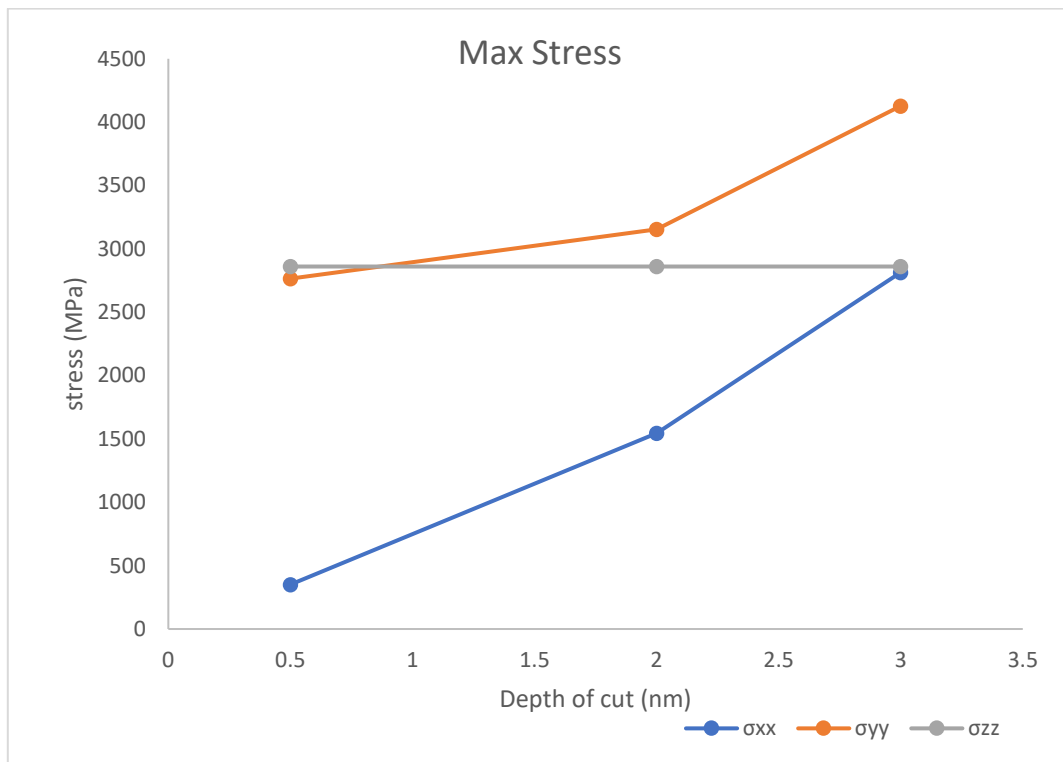


Figure 8.10: Maximum thrust, tangential and axial stresses against depth of cut

During nanometric cutting, Newtonian atoms are subjected to major stress and strain because of cutting tool movement[198], hydrostatic pressure and the maximum shear

stress. Hence, it is used to predict workpiece yield which is the plastic deformation prior to fracture [25, 444]. In addition to this, a high value of hydrostatic pressure is required for plastic flow which indirectly suggests that the smaller the hydrostatic stress, the smaller the cutting forces witnessed [215, 443, 444].

Furthermore, several previous investigations confirmed that hydrostatic stress relates to change of volume which has led to phase transformation of brittle materials in classical thermodynamics [65]. If the force applied to pull atoms of a workpiece is less than the required force to propagate the embedded micro fracture, crack is not propagated, and ductile cutting is maintained. With low cutting forces, hydrostatic stresses will reduce, and subsurface damage becomes minimal which thereby improves surface roughness.

Moreover, by increasing depth of cut, subsurface deformation also increases while generated chip formation increases due to large depth of cut. It is also widely accepted that an increase in cutting speed and depth of cut will lead to an increase in hydrostatic stress resulting in more drastic phase transformation within the workpiece and ahead the cutting tool [445, 446]. **Figure 8.11** represents hydrostatics stresses as the depth of cut increases. The average hydrostatics stresses (**Figure 8.12**) were 14.28 MPa, 580.95 MPa and 1362 MPa for 0.5 nm, 2.0 nm and 3.0 nm of depth of cuts, respectively.

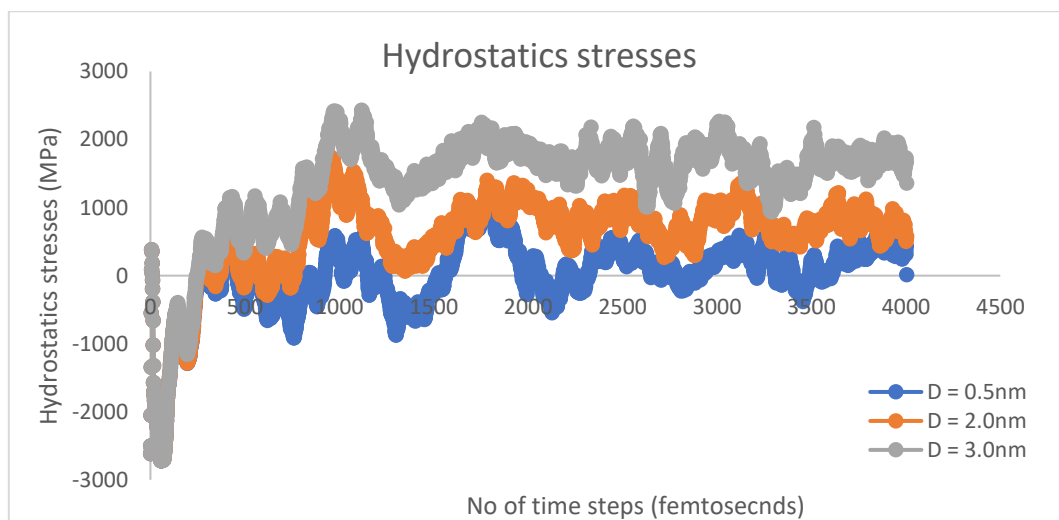


Figure 8.11: Change in hydrostatics stresses with distance in RSA 6061 at different depth of cuts

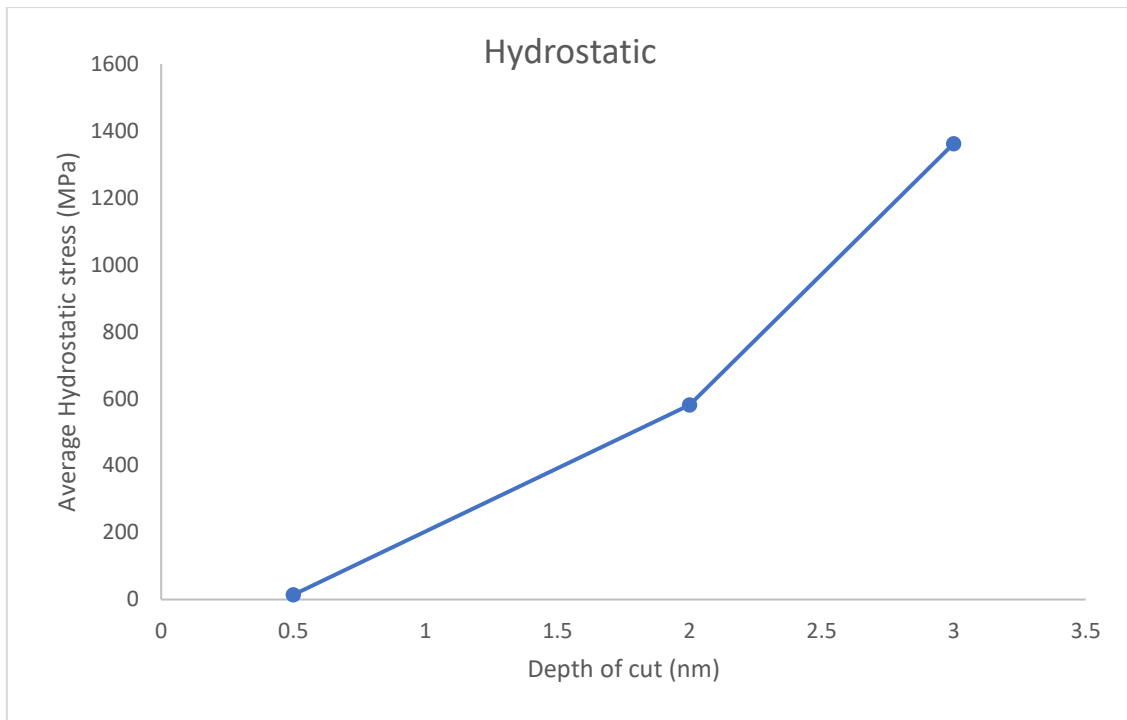


Figure 8.12: Average Hydrostatics stress against depth of cut

8.4.2 Analysis of cutting forces during MD simulation of RSA 6061

According to Luo et al. [448] cutting forces are highly significant during interactive forces between the workpiece and cutting tool atoms forms the interatomic forces in nanometric machining. In this study, the orientation of the model (F_x , F_y and F_z) is such that the force components along the direction of cut represents the tangential (F_c or F_x), while the other two axis forms the axial forces (F_z) and thrust (F_t or F_y). Both tangential (F_x) and thrust (F_y) forces rule tool action [176]. The change in cutting performance along cutting length due to cutting events such as elastic–plastic transition, material displacement, fracture, dislocation slip, heat and tool wear are responsible for force change along the length of cut. Thrust force has the tendency of separating tool from workpiece during cutting and by so doing affects surface form error. While the cut chip displacement or direction of movement determined by tangential force is responsible for chatter formation [449].

An increase in cutting force was confirmed noticeable with low cutting speed which eventually resulted in rapid increase of deep subsurface deformations where all witnessed during nanometric machining. Also, since the workpiece atoms are said to undergo series of processes such as indentation-sliding, lattice deformation, bond

fracture and chip formation by plastic removal which eventually create machined surface [450]. Then increased forces is bound to generate rough surface as seen in the experiment which was also portrayed in the MD simulation as noticed in Figures above. According to these authors [345, 451, 452], the higher the cutting speed, the smoother the surface finish of the machined surface and the higher the power consumption. With this done, average tangential cutting and thrust forces, kinetic friction (F_x/F_y) and specific cutting energy for all the different depth of cut were calculated and represented in **Figures 8.14 – 8.19**.

Further investigations revealed that increasing depth of cut increases the areas of the primary and secondary shear planes, impeding the cutting of the material and increasing the machining forces [269, 453-455]. In spite of this, because of higher temperature experienced at primary zone, the stresses on the secondary shear plane may be about 30 % lower than those on the primary shear plane [456]. Due to lower mechanical strength of aluminium alloys, cutting forces in the machining of aluminium alloys are typically low compared to those of ferrous alloys, which can produce 70% lower specific cutting pressures than in the machining of steels. [457]. **Figure 8.13** is a typical orthogonal machining nomenclature.

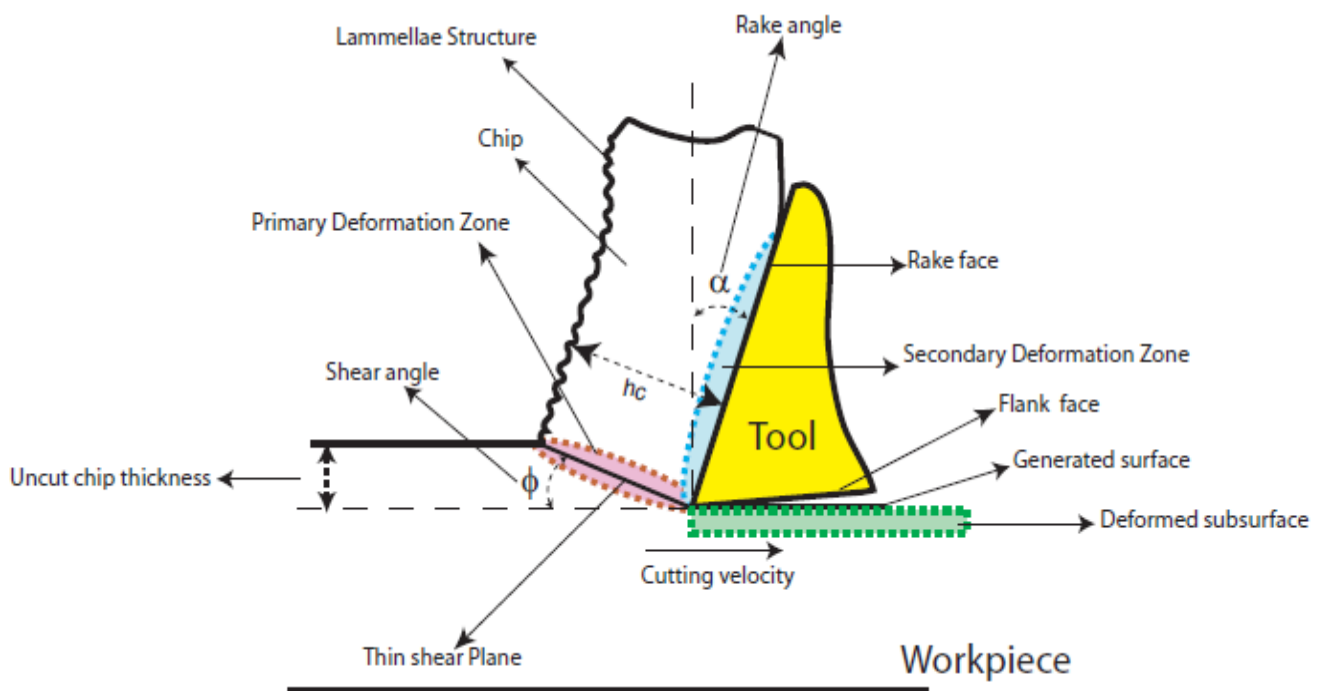


Figure 8.13: Orthogonal machining nomenclature [458]

The forces on an atom is therefore the results of the forces from its neighbouring atoms [198]. **Figures 8.14 – 8.16** illustrate cutting forces behaviour in three different depths of cut adopted in the simulation. Thrust forces in the three cases seems to be dominating among the force components. According to Goel [176], the use of high negative tool rake angle is common to any SPDT operation of brittle materials. It is worth noted that a MD simulation study stated that thrust forces dominated the tangential cutting forces is a necessary requirement to perform ductile-regime machining on brittle materials [459]. Both thrust forces and the tangential cutting forces were found significantly high during MD of RSA 6061. This suggests that the cutting resistance of RSA 6061 is significantly higher due to alloy constituents especially high silicon and Iron. Another revelation is that cutting forces increased with an increase in feed rate due to an increase in chip load making feed forces (thrust forces) to be larger than tangential forces as the depth of cut increases. Also noted by Goel is the edge radius variation that has higher effects on the cutting forces in Y- direction than X- direction. This study agreed with this observation which says the higher the depth of cut, the higher the thrust forces.

The cutting forces noted during the MD simulation indicated an increase with Depth of cut, where F_x was the primary (tangential) cutting force and F_y was the normal (thrust) force. The axial force F_z was very small or almost negligible as the tool hardly travel along the z-axis. The thrust force increased as the tool further into the workpiece and the chip built up increases for larger depth of cut. **Figures 8.17 and 8.18** represent the average and maximum forces recorded during MD simulation. it is clearly shown that an increase in the cutting depth will lead to increase in cutting forces especially in thrust forces. These results quite agreed with literature in terms of negative tool rake angle and tool edge radius during nanometric machining of aluminium alloys. **Figure 8.19** presents an average kinetic energy at various depth of cuts.

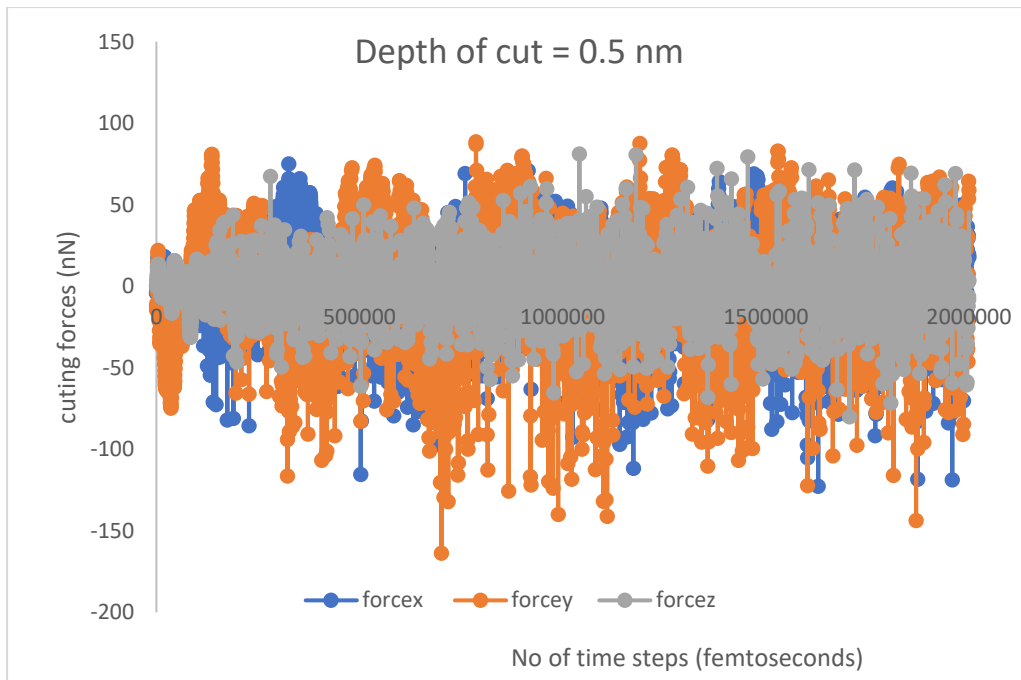


Figure 8.14: Cutting force against time steps at depth of cut = 0.5 nm

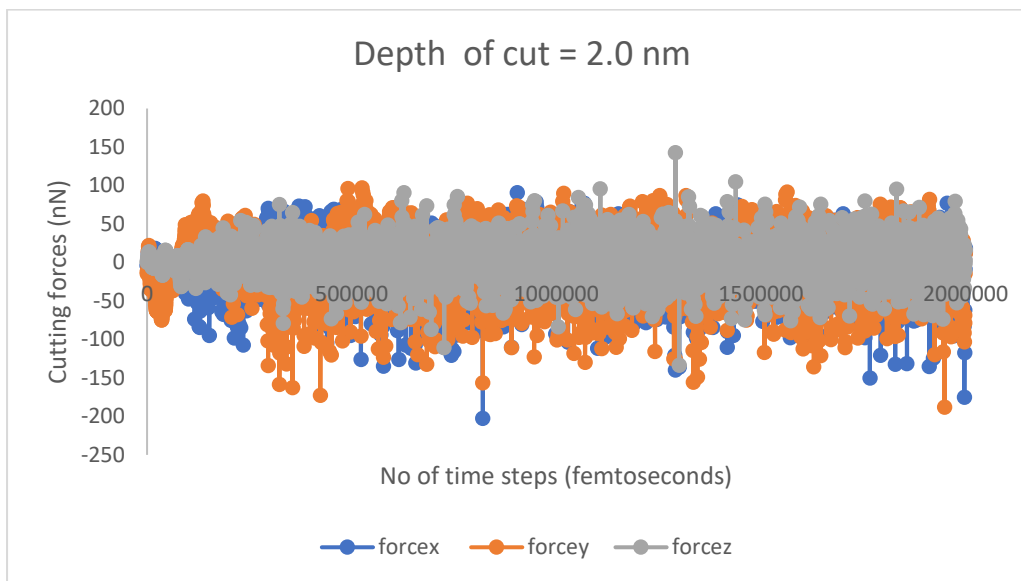


Figure 8.15: Cutting force against time steps at depth of cut = 1.0 nm

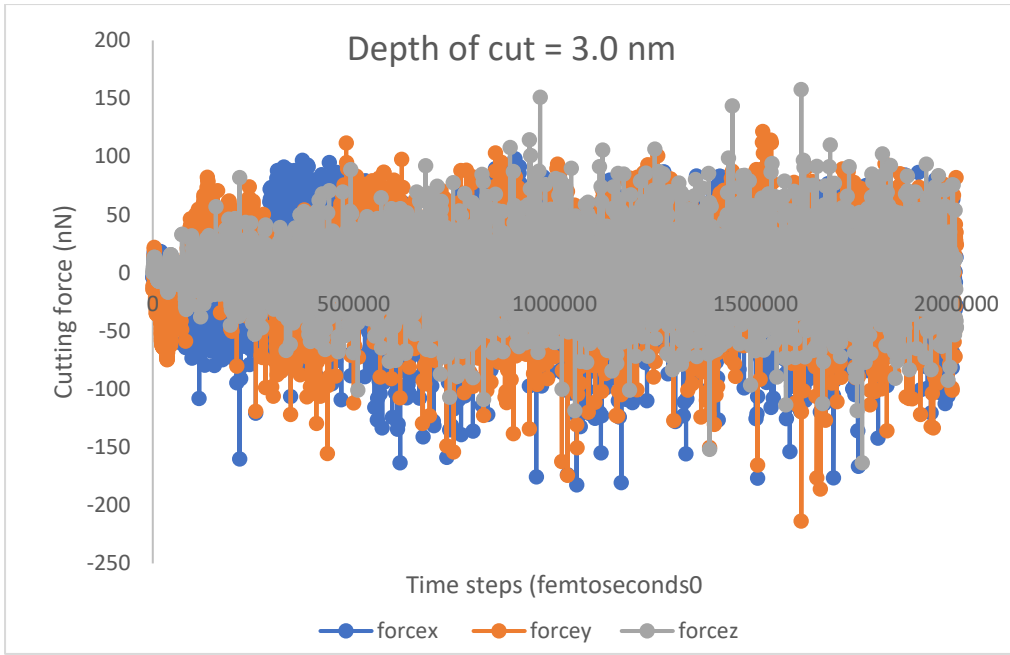


Figure 8.16: Cutting force against time steps at depth of cut = 1.5 nm

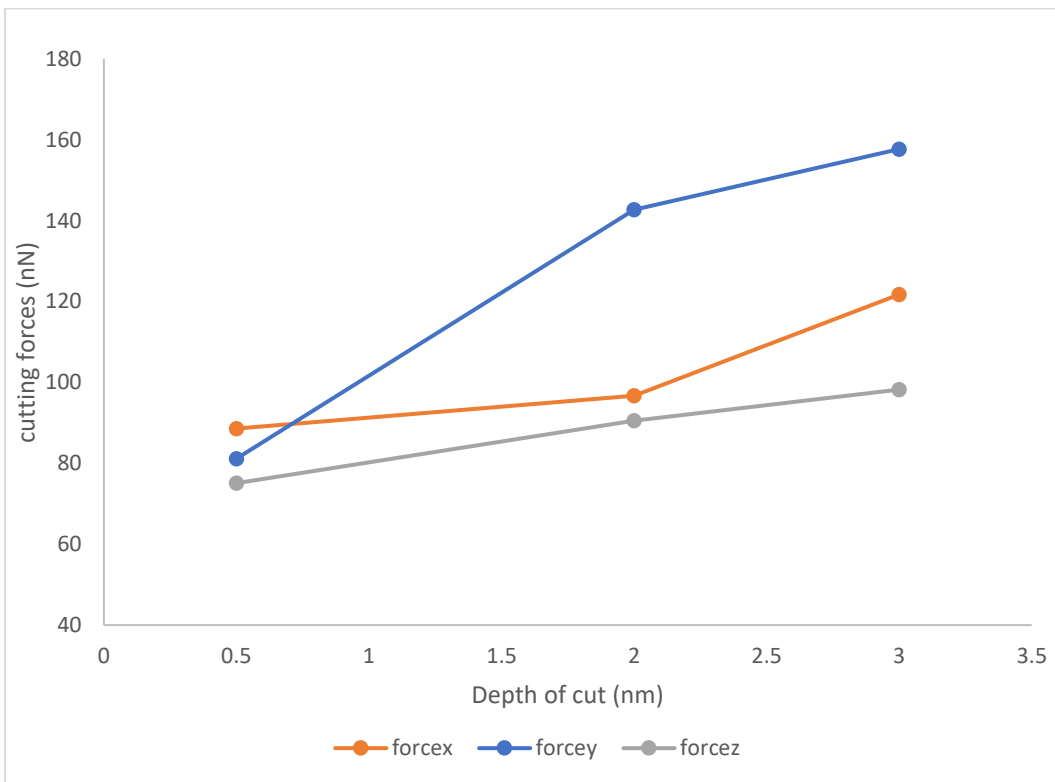


Figure 8.17: Average cutting forces

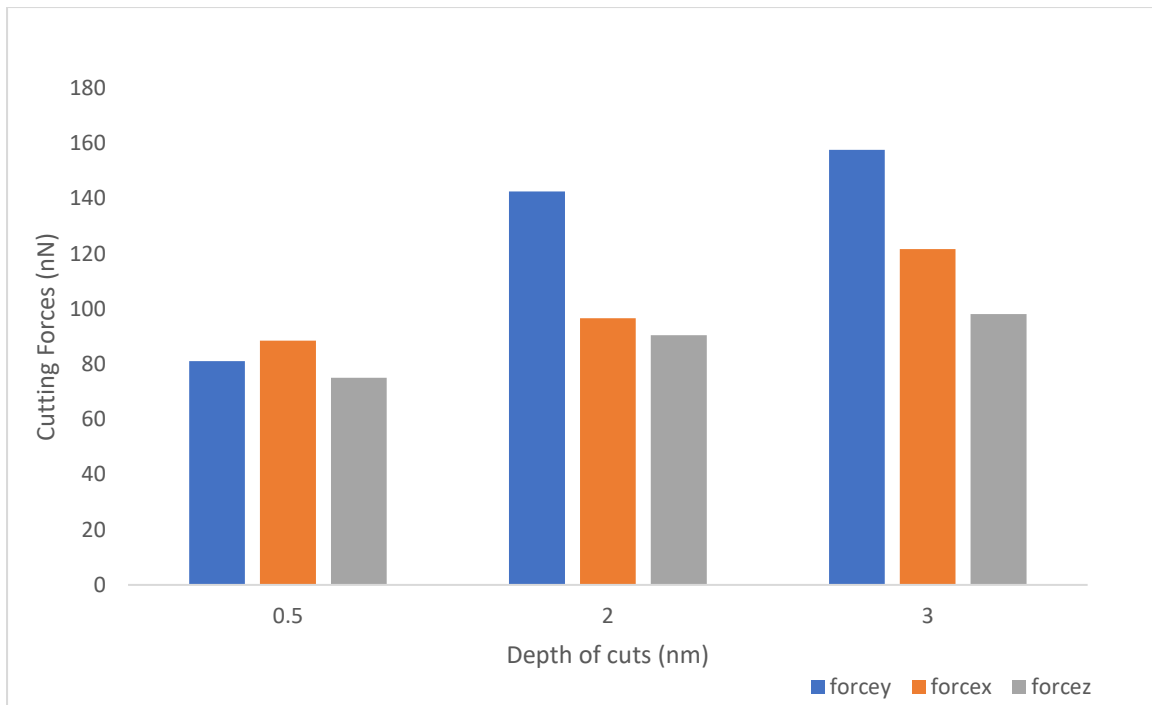


Figure 8.18: Maximum cutting forces

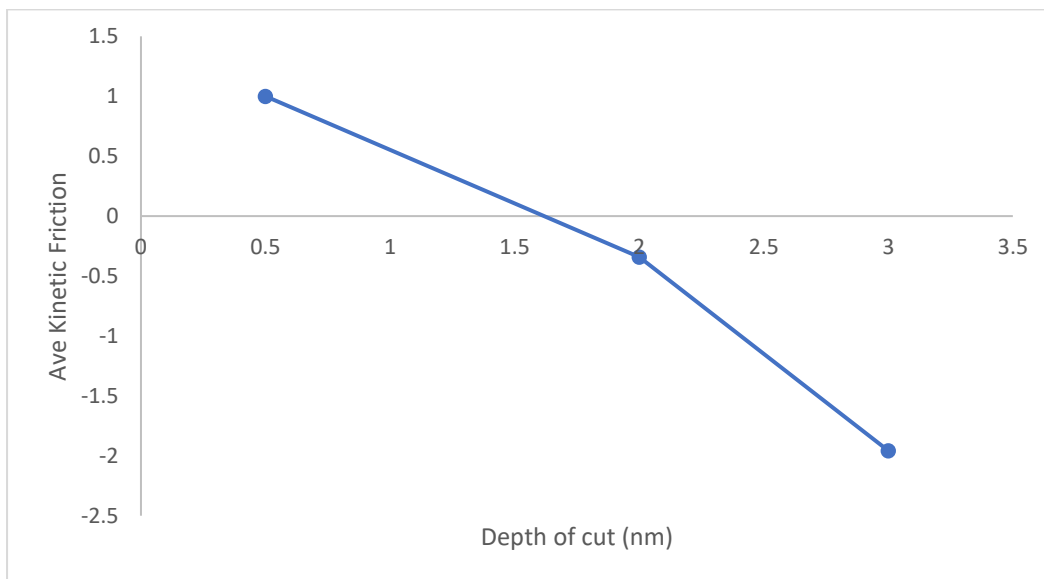


Figure 8.19: Average kinetic friction

8.4.3 Analysis of Cutting Energy

A steady state total energy that follows an increase in depth of cut was experienced in this study **Figure 8.20** represents total energy with variation in depth of cut where the energy slightly swings at the start of the simulation later become stable. The total energy remains constant and once the tool engages at approximately 5 Å distance

(this is the distance between the tool and the workpiece before tool engages the workpiece), the energy increases in a steady manner all through the cutting. As the tool cuts through the workpiece, more energy is required for material removal. The results show a sharper increase in energy with increase in depth of cut. As depth of cut increases, more layers of atoms are affected, so more energy is required for material removal. **Figure 8.20** also shows steadily increased at a constant rate with increase in depth of cut. As shown in **Figures 8.21 and 8.22**, the average total energy and maximum energy for material removal at different levels of depth of cut were reported. It can be shown that an increase in cutting depth would ultimately result in an increase in the overall energy needed for the removal of material.

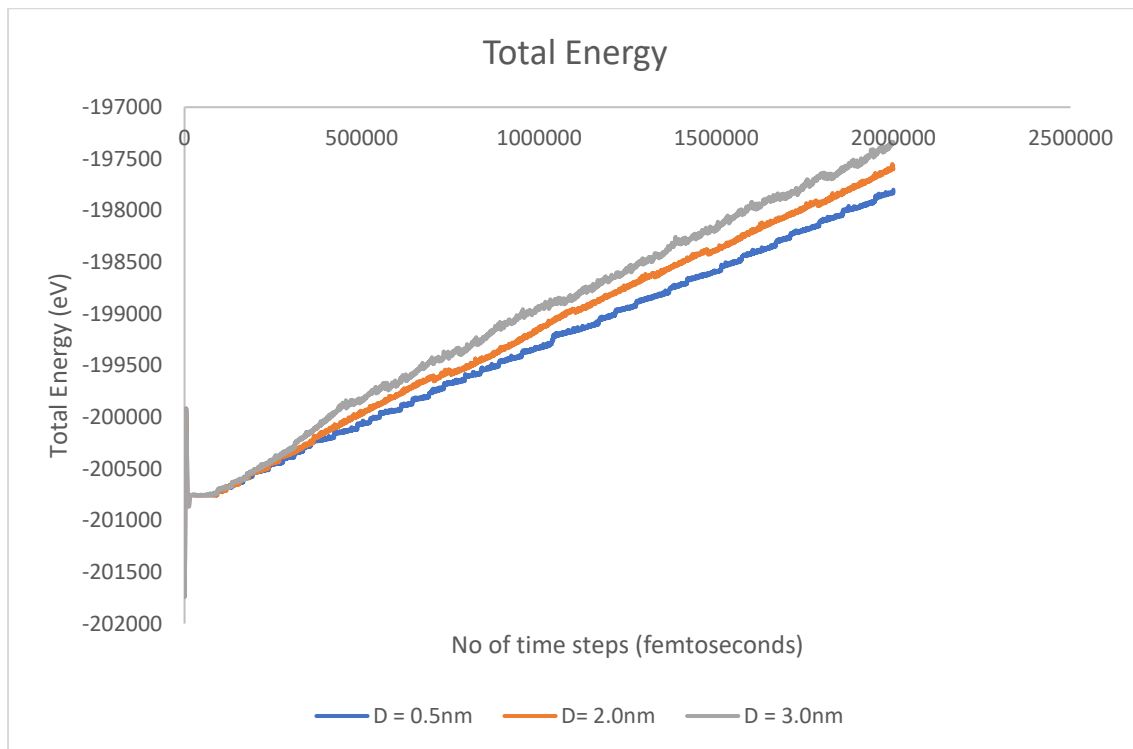


Figure 8.20: Total Energy

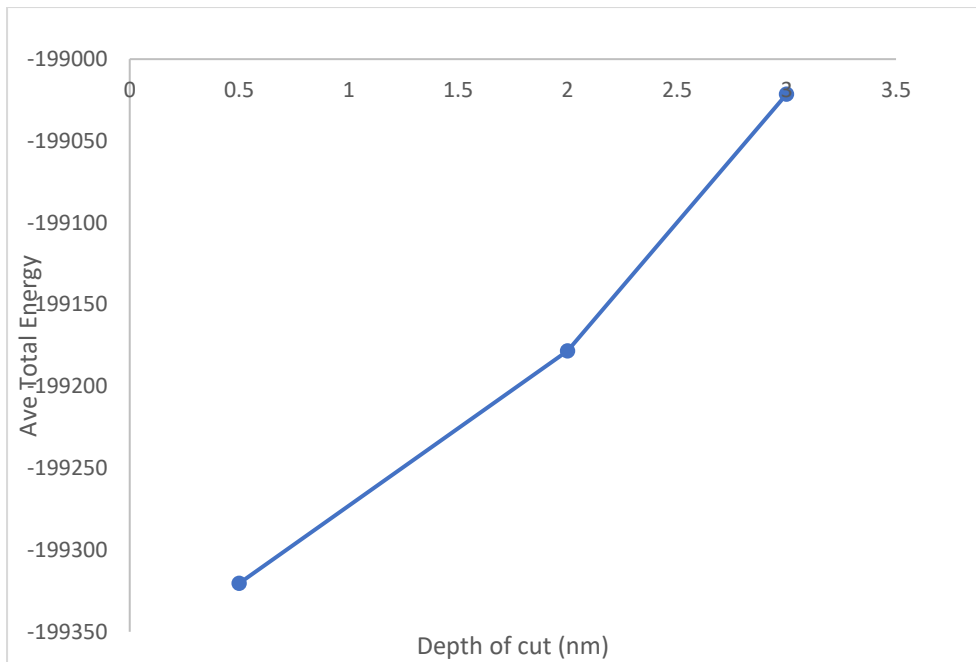


Figure 8.21: Average total energy

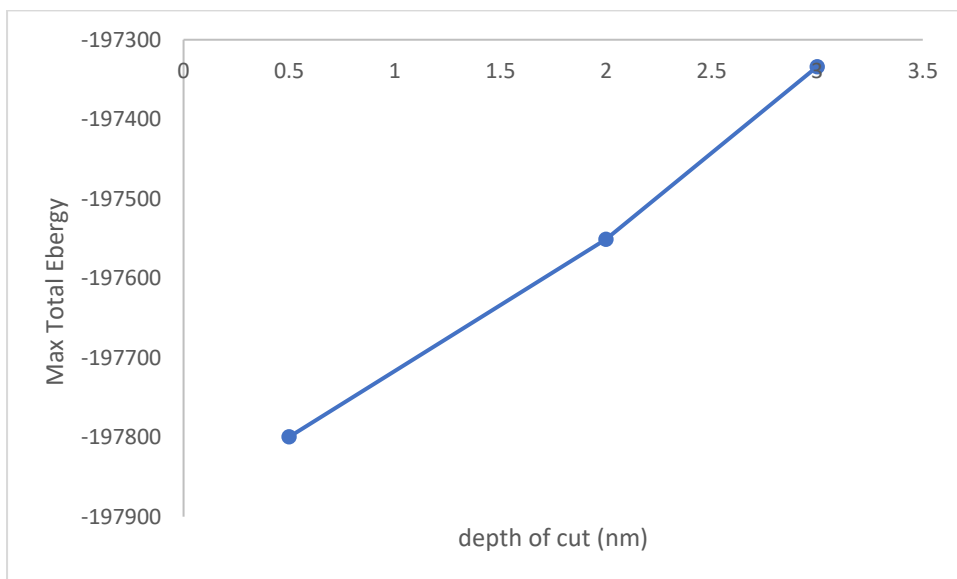


Figure 8.22: Maximum total energy

8.4.4 Specific Cutting Energy (SCE)

The machinability of a material and its cutting resistance can be predicted from its specific cutting energy. Therefore, the specific cutting energy is the energy required for the removal of a unit amount of material and it is derived by dividing the resultant force by the chip area [217]. Generally, the higher the cutting efficiency, the lower the specific cutting energy becomes [449]. This also explains the reason for large

magnitude of resultant force as an indication of low temperature during nanometric cutting, this means that at low temperature, the atoms are not excited, and the workpiece becomes so difficult to be deformed plastically.

According to previous researchers [321, 460-464] the specific energy tends to decrease with increasing depth of cut or vice versa indicating a possible size effect. The reason for this is that the rubbing or ploughing process has become dominant process instead of cutting and the resultant force vector is gradually close to thrust direction [323]. Also, the specific energy is greatly affected by both the crystal orientation of the work material and the cutting direction. In this study, the cutting orientation and direction is (100). **Figure 8.23** shows a decline in specific cutting energy for RSA 6061 alloys as depth of cut increase. This confirms the predictions in the literature [449]. The average SCE were 31.59 eV, 8.98 eV and 6.92 eV at depth of cut 0.5nm, 2.0nm and 3.0nm, respectively.

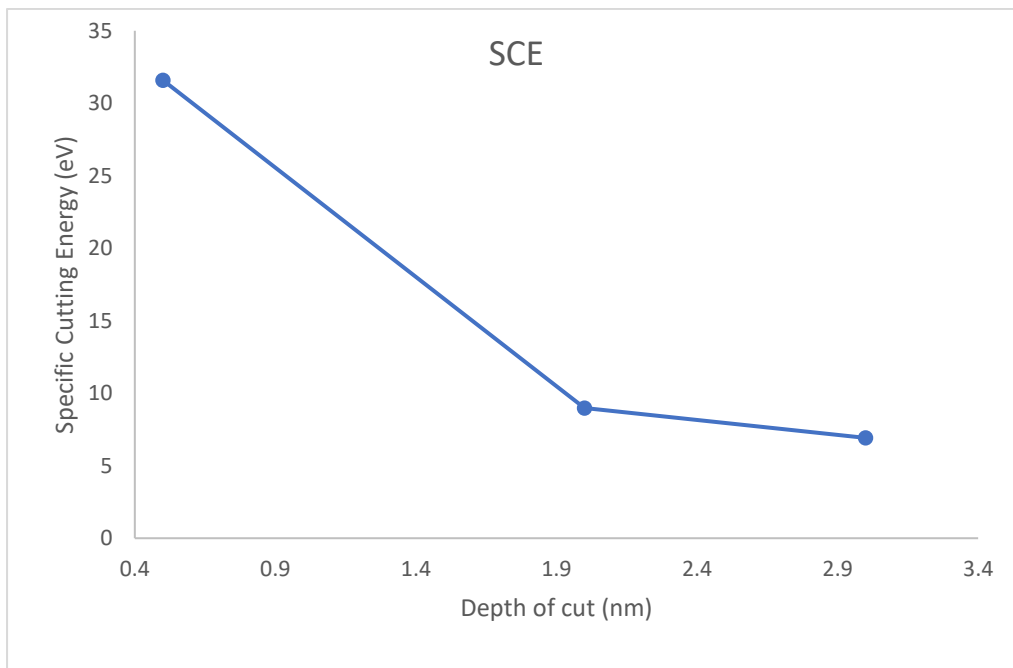


Figure 8.23: Specific cutting energy against depth of cut

8.4.5 Analysis of Temperature

During nanometric machining of aluminium alloys, it was recorded that cutting temperature does not cause key treat because of their low melting point. Making the mechanical properties of cutting tools unchanged [269, 394]; this means that the level of tool wear rates is kept at a very low [465], knowing fully that cutting temperature is

used to regulate the tool life [466]. Furthermore, an increase in temperature to certain level, it may cause microstructural alteration, residual stresses in the surface layer, and accelerate tool wear which makes the workpiece to stick to tool edges [465]. In addition, higher temperatures could also increase the ductility of the material, which generates elongated chips [467] and encourage chemical interaction between aluminium and the tool coating material to promote inter-atomic diffusion [468].

According to Yousefi and Ichida [469], an increase in the cutting speed will be experienced as a result of heat generated due to increase in the cutting temperature. Aluminium alloys that has some considerable quantity of silicon contents have experienced temperatures from 350 to 750 °C in several machining processes [470, 471]. Tang et al. [472] discovered an increase in machining temperature, led to a substantial increase in residual stresses on the surface of machined material was noticed. Also, highest cutting temperatures are recorded against the machining of aluminium alloys with higher mechanical strength [473, 474].

In **Figure 8.24** the temperature showed an increase with tool depth of cut as deformation increases. This temperature increase was high with increase in depth of cut. **Figure 8.25** shows average temperature of the workpiece against depth of cut as: 488 k, 492 k and 495 k and 693 k, 694 k and 700 k at 0.5 nm, 2.0 nm, and 3.0 nm, respectively. The maximum temperature of the workpiece (**see Figure 8.26**) against depth of cut are: 693 k, 694 k and 700 k at 0.5 nm, 2.0 nm and 3.0 nm, respectively.

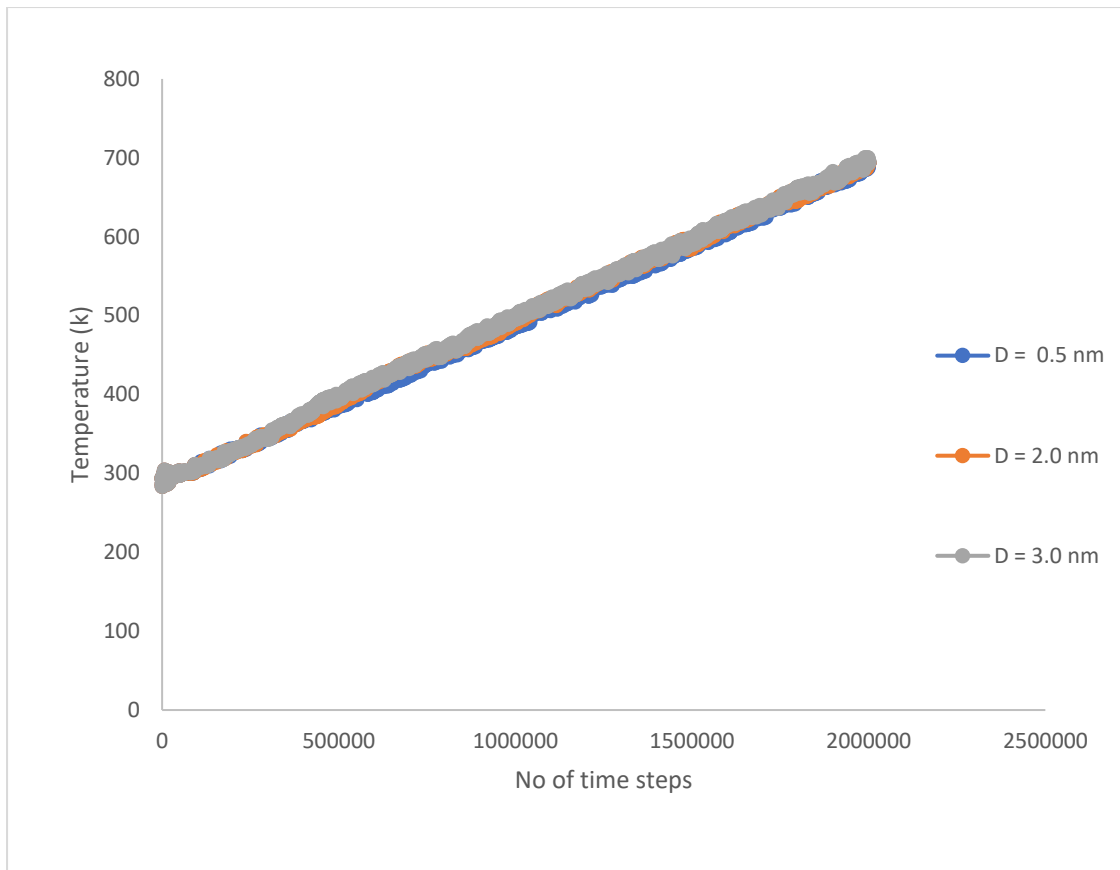


Figure 8.24: Temperature against depth of cut

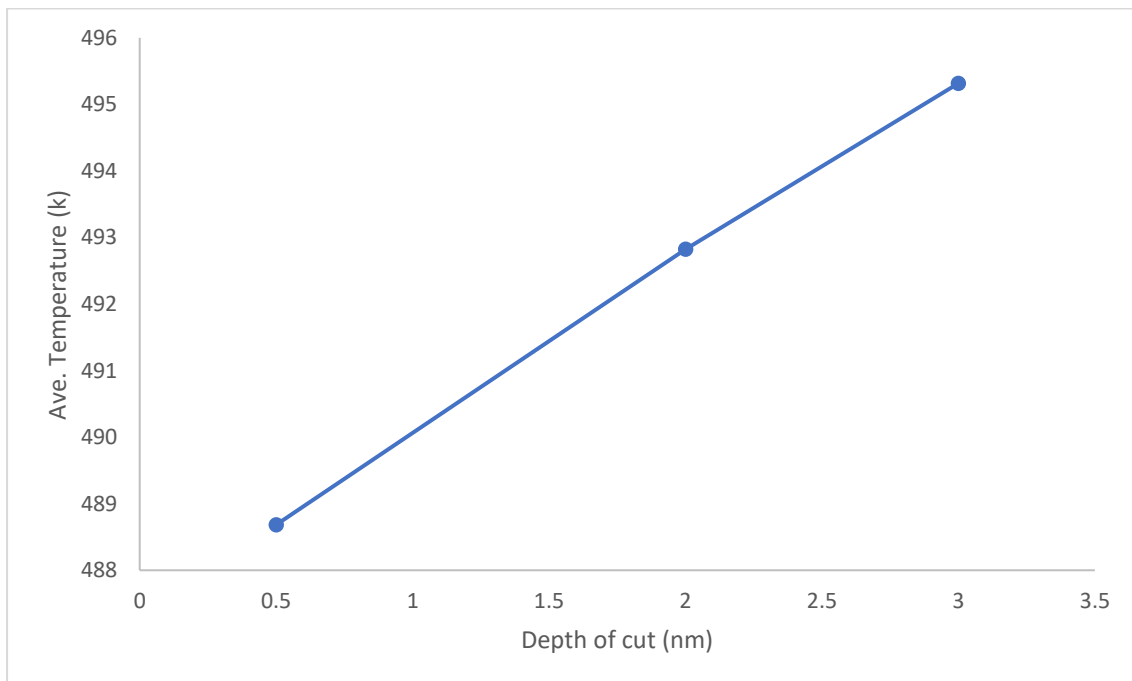


Figure 8.25: Average Temperatures versus depth of cut

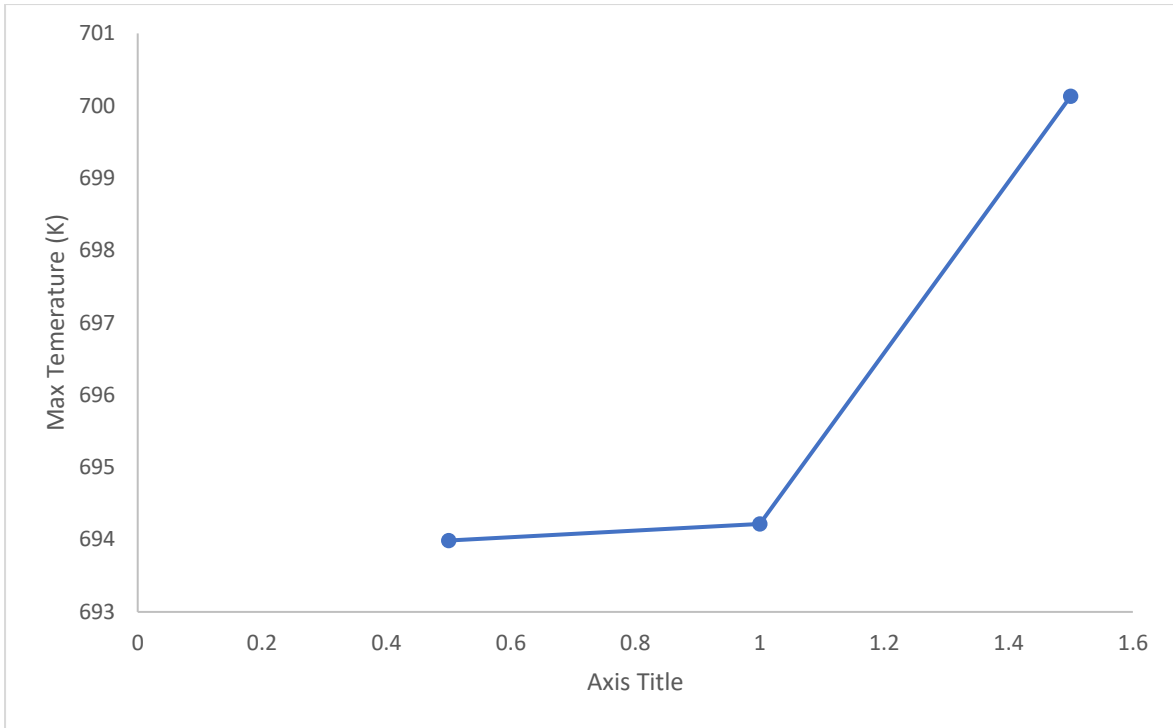


Figure 8.26: Maximum Temperature versus depth of cut

CHAPTER 9

CONCLUSIONS AND RECOMMENDATION

Classically, to identify the required and adequate conditions to maintain ductile response during a machining period that could provide a drastic improvement in the machining of brittle materials, it is important to fully understand the ductile mechanism in brittle materials. In advance machining industry, where high quality of machined surfaces is most critical, enhanced machinability can result to a better physical aspect (i.e., mechanical, optical, and electrical), superior surface quality, decreased near surface degradation, high form accuracy, increased material removal rates and minimal tool wear will be extremely crucial. This chapter offers a succinct summary of the key results in the three main investigation areas of this study. It also offers some suggestions that, if investigated, can enrich the literature available in the field of ultra-high precision machining of optical and advance materials. The three main areas of study are: self-sensing cutting force cutting tool (SSCFTH) development, ultra-precision machining of advance optical aluminium alloys (RSA 443,905, and 6061) and Molecular Dynamic Simulation of RSA 6061.

9.1 CONCLUDING REMARKS ON THE DEVELOPED SSCFTH

The main reason behind the development of SSCFTH is due to the limitations of current commercial sensor systems and the significant challenges for flexibility and reconfigurability. In this study, the principle of a cantilever beam was adopted for the force-based strain gauge sensor cutting tool holder. Cantilever which can be referred to as the beam in which one end is fixed and another end is free is a typical replication of cutting tool system in diamond turning operation. It was this simple principle (**see sections 3.10 – 3.14**) that the author capitalized on to develop force sensor that can capture force data and monitor force activities during diamond turning process using advanced data acquisition system. The following implementations and finding were established from the development:

- Implementation of proper strain gauge selection
- Implementation of the right choice of instrumentation for data collection
- Implementation of a sensor installation technique that serves as a reference and guides to the installation of strain gauges on titanium material.

- Designed a natural frequency of 807.5 Hz which is more than 4 times the frequency of the machine (50 Hz). This fulfilled the requirement that the natural frequency tool must be at least 4 times greater than the frequency of the machine.
- The sensitivity of the sensor is 0.004592 v/N while at calibration a 99.6% accuracy of design was achieved.
- The values of the three statistical indicators for SSCFTH are established as: % error is 2.19, MAPE is 17.57% and RMSE is 0.43.
- The design was able to monitor and predict the influence of cutting parameters and optimize the same during diamond turning of RSA Alloys.

9.1.1 Concluding remarks on ultra-precision machining of RSA Alloys (RSA 443, 906 and 6061)

This section of the research explores and presents the effects of cutting parameters, namely feed rate, cutting speed and depth of cut on cutting forces, surface roughness, tool geometry (nose radius), acoustic emission, chip formation and the rate of material removal, which play a major role in determining the profitability of the system and the performance of advanced optical aluminium alloy machining. Design of Experiment, which is a systematic approach of choosing the most suitable combination of machining, was used. The prediction model was developed using Box-Behnken Design in Response surface methodology. Regression and ANOVA outputs for each analysis were also carefully observed. The following contributions from the study can be identified:

- Assessment of the research contribution of Rapidly solidified aluminium (RSA) 905 alloy during diamond turning.
- A highly reliable prediction model for cutting force and acoustic emission during machining with R^2 of 96.81% and 85.97% were developed, respectively. The ANOVA revealed that feed rate and depth of cut has the most influence on both cutting force acoustic emission during machining. It was observed that the higher the cutting speed the lower the cutting force applied while higher feed rates will lead to high cutting forces and high acoustic signal. It was noted that very low cutting force can be achieved and optimized for during machining at minimum depth of cut and minimum feed rate.

- Assessment of the research contribution of Rapidly solidified aluminium (RSA) 443 alloy during diamond turning.
- In general, the cutting forces of RSA 443 during diamond turning have been found to be high, possibly due to the high silicon content in the alloy. The higher the feed rate, the higher cutting force means that brittle materials occur at high feed rates, mostly due to increased rubbing action at the tool-workpiece interface, caused by temperature rise at the cutting zone. The results presented on the optimized analysis of the acquired data showed that the maximum cutting force is 2.82 N on the basis that feed rate = 17 mm / min, depth of cut = 25 mm and speed = 500 rpm. This is similar to what was experimentally reported. According to the data obtained, however, the predicted minimum cutting force is 0.043 N at speed = 500 rpm, feed rate = 25 mm/min and depth of cut = 5 mm. This prediction is also close to what was recorded in the experiment. The acoustic signal shows highly sensitive to high cutting speed and feed rate, making it the most influential cutting parameter during cutting.
- Assessment of the research contribution of Rapidly solidified aluminium (RSA) 6061 alloy during diamond turning.
- One of the primary goals of this study is an in-depth analysis of ultra-precision manufacturing of RSA 6061. Analysis of tool geometry particularly tool nose radius (0.5, 1.0 and 1.5) mm on cutting force for RSA 6061 during machining shows that the feed rate has the highest influence cutting force with a nose radius of 0.5 mm. But for nose radius 1.0 mm and 1.5 mm, cutting speed becomes most significant on cutting force. More so, the ductile regime of RSA 6061 was facilitated by a small nose radius and shows great potential to reduce surface roughness and produce a smooth surface finish. Hence, in the experiment a connection between small nose and a high speed was noticed which establishes some of the reports we have witness so far in this study. However, in this same study, to witness a very low cutting force with a large tool nose radius (1.5 mm) on the ductile regime of RSA 6061, a high speed with an increased feed rate at a very low depth of cut would achieve this goal.
- It has been established in the literature that variation in tool geometry is one of the most significant factors to be considered in order to improve productivity in turning operations in relation to surface roughness, tool life and surface

integrity. In this study, the most significant cutting parameters at nose radius of 0.5 mm on RSA 6061 is feed rate which contributed about 51.58% effect. Which simply indicates that the higher the feed rates the bigger the surface roughness.

- The best combination for cutting parameters to optimize the surface roughness during the cutting process of RSA 6061, which will predict best surface roughness is at speed = 1976 rpm, feed rate = 5 mm / min and cut depth = 5 μ m with Ra as low as 1 nm which is similar to what was achieved experimentally, while worst surface roughness (133.6 nm) was noticed at high feed rate and depth.
- It was also observed that the largest volume that was removed during machining was recorded at highest feed rate and highest depth of cut. So, it really makes sense when depth of cut is the most influential parameter during machining and the combination of speed and feed rate will account for the rate at which this volume is been removed per minute.

9.1.2 Concluding remarks on MD simulation of RSA 6061

One of the objectives of this study was to use MD simulation to describe the atomic scale mechanisms involved in nanometric cutting at different depth of cuts of hard brittle materials such as rapidly solidified RSA 6061 aluminium alloy. To this end, using different compatible interatomic potential functions, atomistic models have been developed. This MD simulation has provided new insights into the cutting parameter dependence during nanometric cutting of hard-brittle materials of the existing mechanisms. The following contributions from this study can be outlined:

A complete workpiece for RSA 6061 alloy was model with efficient pair styles and pair coefficients that execute in LAMMPS even though literature has it that some of the constituent elements of RSA alloy cannot be modelled. A complete morse parameter for RSA 6061 workpiece was computed. MD analysis of stresses, cutting forces, cutting kinetic friction, temperature and specific cutting energy in the cutting zone were carried out. The behaviour of the MD simulation was observed, the following conclusion are drawn:

- It is established that an increase in the depth of cut, will lead to more materials deformed ahead of the cutting tool. Similarly, with increase depth of cut, more

dislocations are observed in the cutting region. It can also be observed that as the cutting depth increases, the machined surface becomes rougher. This may be due to the higher cutting forces required for the larger cutting depth. It is noted that aluminium alloy RSA 6061 experiences constant increase in various stress components as the depth of cut increases.

- In this study, both thrust forces and the tangential cutting forces were found significantly high during MD of RSA 6061. This suggests that the cutting resistance of RSA 6061 is significantly higher due to alloy constituents especially high silicon and Iron. Another revelation is that cutting forces increased with an increase in feed due to an increase in chip load making feed forces (thrust forces) to be larger than tangential forces as the depth of cut increases.
- Cutting energy outcomes indicate a sharper increase in energy with an increase in cutting depth. In other words, more layers of atoms are affected as the depth of cut increases, so more energy is required for material removal. The temperature analysis shows an increase with tool depth of cut as deformation increases. This temperature increase was sharper with increase in depth of cut. The simulation shows average temperature of the workpiece against depth of cut as: 488 k, 492 k and 495 k and 693 k, 694 k and 700 k at 0.5 nm, 2.0 nm and 3.0 nm, respectively.
- Overall, the major findings in this study will help to reduce machining costs and improve the quality during machining of RSA alloys for optical applications. The results also serve as a contribution to systematic review of the literature, developing prediction models and a resource or guide for engineers and researchers.

9.2 RECOMMENDATION FOR FUTURE INVESTIGATION

The following points were extracted from the observations made in the course of this report. Finding out what could be further known by researching the following is a matter of interest:

- A self-sensing cutting force tool holder was developed which reduces a lot of ambiguity in monitoring cutting process hence, to further improve this innovation, the designed system can be incorporated in internet of thing (IoT).

- According to literature, tool wear analysis has been carried out on RSA 905 and RSA443 but not on RSA 6061. Therefore, it is crucial to still carry out further investigation on tool wear during diamond turning of RSA 6061 in order to achieve high surface quality that will be beneficial for industry.
- The use of hybrid machining or machining assisted method is highly encouraged to further investigate the machinability of advanced optical aluminium alloys.
- To assess whether hard turning may be a useful approach to RSA machining and to check if various forms of coolant can be used during machining would have a major effect on surface roughness.
- To investigate whether different nose radius would have further influence on cutting forces and surface quality of RSA 6061 during Diamond turning.
- To carry out investigation into the effect of other cutting parameters such as feed rates and speed on RSA 6061 during MD simulation.
- To carry out further atomistic simulation studies on the effect of tool geometry of RSA 6061

REFERENCES

- [1] Zhang X, Woon K, Rahman M. "11.09-Diamond Turning," *Comprehensive Materials Processing, SHFBJVT Yilbas, Editor*, pp. 201-220, 2014.
- [2] Lee W, Cheung B C. *Surface generation in ultra-precision diamond turning: modelling and practices* vol. 12: John Wiley & Sons, 2003.
- [3] Chiu W, Lee W. "Development of ultra-precision machining technology," 1997.
- [4] Yip W S, To S, Zhou H. "Current status, challenges and opportunities of sustainable ultra-precision manufacturing," *Journal of Intelligent Manufacturing*, pp. 1-13, 2021.
- [5] Jasinevicius R G, Otoboni J A, Basso I, Dib M H. "Size effects in ultraprecision machining of aluminum alloys: Conventional AA6061-T6 and RSA 6061-T6," *Journal of Manufacturing Processes*, vol. 68, pp. 136-157, 2021.
- [6] ter Horst R, de Haan M, Gubbels G, Senden R, van Venrooy B, Hoogstrate A. "Diamond turning and polishing tests on new RSP aluminum alloys," in *Modern Technologies in Space-and Ground-based Telescopes and Instrumentation II*, 2012, p. 84502M.
- [7] Gubbels G P, van Venrooy B W, Bosch A J, Senden R. "Rapidly solidified aluminium for optical applications," in *Advanced Optical and Mechanical Technologies in Telescopes and Instrumentation*, 2008, p. 70183A.
- [8] Bosch A, Senden R, van Venrooy B, Gubbels G. "Optimization strategy for aluminium optics using the meltspinning technology," *SPIE Optifab, paper TD06-03*, 2009.
- [9] Takeuchi Y, Sakaida Y, Sawada K, Sata T. "Development of a 5-axis control ultraprecision milling machine for micromachining based on non-friction servomechanisms," *CIRP Annals*, vol. 49, pp. 295-298, 2000.
- [10] Cheung C, Lee W. "Study of factors affecting the surface quality in ultra-precision diamond turning," *Materials and Manufacturing Processes*, vol. 15, pp. 481-502, 2000.
- [11] Furukawa Y, Moronuki N. "Effect of material properties on ultra precise cutting processes," *CIRP Annals*, vol. 37, pp. 113-116, 1988.
- [12] Wada R, Kodama H, Nakamura K, Mizutani Y, Shimura Y, Takenaka N. "Wear characteristics of single crystal diamond tool," *CIRP Annals*, vol. 29, pp. 47-52, 1980.

- [13] Lee W, To S, Sze Y, Cheung C. "Effect of material anisotropy on shear angle prediction in metal cutting—a mesoplasticity approach," *International journal of mechanical sciences*, vol. 45, pp. 1739-1749, 2003.
- [14] Takasu S, Masuda M, Nishiguchi T, Kobayashi A. "Influence of study vibration with small amplitude upon surface roughness in diamond machining," *CIRP Annals*, vol. 34, pp. 463-467, 1985.
- [15] Wang S, To S, Chen X, Chen X. "An investigation on surface finishing in ultra-precision raster milling of aluminum alloy 6061," *Proceedings of the Institution of Mechanical Engineers, Part B: Journal of Engineering Manufacture*, vol. 229, pp. 1289-1301, 2015.
- [16] Wang S, To S, Chan C, Cheung C, Lee W. "A study of the cutting-induced heating effect on the machined surface in ultra-precision raster milling of 6061 Al alloy," *The International Journal of Advanced Manufacturing Technology*, vol. 51, pp. 69-78, 2010.
- [17] Cheng Y-C, Hsu W-Y, Abou-El-Hossein K, Olufayo O, Otieno T. "Investigation of diamond turning: of rapidly solidified aluminum alloys," in *Current Developments in Lens Design and Optical Engineering XV*, 2014, p. 919214.
- [18] RSP. (2019 RSP for optics). Available: <http://www.rsp-technology.com/datasheets-news.html>
- [19] Fang F, Zhang X, Gao W, Guo Y, Byrne G, Hansen H N. "Nanomanufacturing—Perspective and applications," *CIRP Annals*, vol. 66, pp. 683-705, 2017.
- [20] Corbett J, McKeown P, Peggs G, Whatmore R. "Nanotechnology: international developments and emerging products," *CIRP Annals-Manufacturing Technology*, vol. 49, pp. 523-545, 2000.
- [21] market A. (2019, 27). *Precision Market - Global Forecast 2017-2022*. Available: <https://www.arizton.com/market-reports/precision-parts-market-report>
- [22] Koenig W, Sinhoff V, Zamel S. "Manufacturing strategies for the production of ultraprecision parts," *Tutorial UME3, Aachen*, 1994.
- [23] Karaköse E, Keskin M. "Structural investigations of mechanical properties of Al based rapidly solidified alloys," *Materials & Design*, vol. 32, pp. 4970-4979, 2011.
- [24] Salehi M, Dehghani K. "Structure and properties of nanostructured aluminum A413. 1 produced by melt spinning compared with ingot microstructure," *Journal of Alloys and Compounds*, vol. 457, pp. 357-361, 2008.

- [25] Goel S, Luo X, Agrawal A, Reuben R L. "Diamond machining of silicon: a review of advances in molecular dynamics simulation," *International Journal of Machine Tools and Manufacture*, vol. 88, pp. 131-164, 2015.
- [26] Brinksmeier E, Riemer O, Schönemann L. "High performance cutting for ultra-precision machining," *International Journal of Nanomanufacturing*, vol. 11, pp. 245-260, 2015.
- [27] Taniguchi N, ARAKAWA C, KOBAYASHI T. "On the basic concept of 'nano-technology'," in *Proceedings of the International Conference on Production Engineering, 1974-8, 1974*, pp. 18-23.
- [28] Taniguchi N. "Current status in, and future trends of, ultraprecision machining and ultrafine materials processing," *CIRP annals*, vol. 32, pp. 573-582, 1983.
- [29] Sawangsri W. "An investigation on micro cutting mechanics: Modelling, simulations and experimental case studies," 2014.
- [30] Venkatachalam S. "Predictive modeling for ductile machining of brittle materials," Georgia Institute of Technology, 2007.
- [31] Keown M. "From micro to nano-machining-towards the nanometer era," *Sensor Review*, vol. 16, pp. 4-10, 1996.
- [32] Yu H, Wang Y. "Fracture performance of high strength steels, aluminium and magnesium alloys during plastic deformation," in *MATEC Web of Conferences*, 2015, p. 07001.
- [33] Neo W K, Kumar A S, Rahman M. "A review on the current research trends in ductile regime machining," *The International Journal of Advanced Manufacturing Technology*, vol. 63, pp. 465-480, 2012.
- [34] Kulshreshtha P K, Youssef K M, Rozgonyi G. "Nano-indentation: A tool to investigate crack propagation related phase transitions in PV silicon," *Solar energy materials and solar cells*, vol. 96, pp. 166-172, 2012.
- [35] Ravindra D. "Ductile mode material removal of ceramics and semiconductors," 2011.
- [36] Fang N. "Slip-line modeling of machining with a rounded-edge tool—Part II: analysis of the size effect and the shear strain-rate," *Journal of the Mechanics and Physics of Solids*, vol. 51, pp. 743-762, 2003.
- [37] Liu K, Li X, Rahman M, Liu X. "A study of the cutting modes in the grooving of tungsten carbide," *The International Journal of Advanced Manufacturing Technology*, vol. 24, pp. 321-326, 2004.

- [38] Fang F, Zhang G. "An experimental study of edge radius effect on cutting single crystal silicon," *The International Journal of Advanced Manufacturing Technology*, vol. 22, pp. 703-707, 2003.
- [39] Fang N. "Slip-line modeling of machining with a rounded-edge tool—Part I: new model and theory," *Journal of the Mechanics and Physics of Solids*, vol. 51, pp. 715-742, 2003.
- [40] Bifano T G, Dow T A, Scattergood R O. "Ductile-regime grinding: a new technology for machining brittle materials," *Journal of engineering for industry*, vol. 113, pp. 184-189, 1991.
- [41] Liu K, Li X, Liang S Y. "Nanometer-scale ductile cutting of tungsten carbide," *Journal of manufacturing processes*, vol. 6, p. 187, 2004.
- [42] Yan J, Takahashi Y, TAMAKI J i, Kubo A, Kuriyagawa T, Sato Y. "Ultraprecision machining characteristics of poly-crystalline germanium," *JSME International Journal Series C Mechanical Systems, Machine Elements and Manufacturing*, vol. 49, pp. 63-69, 2006.
- [43] Bhattacharya B, Patten J A, Jacob J, Blau P J, Howe J, Braden J D. "Ductile regime nano-machining of polycrystalline silicon carbide (6H)," *American Society of Precision Engineers*, 2005.
- [44] Yan J W, Tamaki J, Syoji K, Kuriyagawa T. "Development of a Novel Ductile-Machining System for Fabricating Axisymmetrical Aspherical Surfaces on Brittle Materials," in *Key Engineering Materials*, 2003, pp. 43-48.
- [45] Yoshino M, Ogawa Y, Aravindan S. "Machining of hard-brittle materials by a single point tool under external hydrostatic pressure," *Journal of Manufacturing Science and Engineering*, vol. 127, pp. 837-845, 2005.
- [46] Patel M T, Deshpande V A. "Optimization of machining parameters for turning different alloy steels using CNC," *Int J Innov Res Sci Eng Technol*, vol. 3, 2014.
- [47] Mir A, Luo X, Sun J. "The investigation of influence of tool wear on ductile to brittle transition in single point diamond turning of silicon," *Wear*, vol. 364, pp. 233-243, 2016.
- [48] Fang F, Liu B, Xu Z. "Nanometric cutting in a scanning electron microscope," *Precision Engineering*, vol. 41, pp. 145-152, 2015.
- [49] Blake P N. "Ductile regime diamond turning of germanium and silicon," 1989.
- [50] Blackley W, Scattergood R. "Ductile-regime machining model for diamond turning of brittle materials," *Precision engineering*, vol. 13, pp. 95-103, 1991.

- [51] Yan J, Maekawa K, Tamaki J i, Kubo A. "Experimental study on the ultraprecision ductile machinability of single-crystal germanium," *JSME International Journal Series C Mechanical Systems, Machine Elements and Manufacturing*, vol. 47, pp. 29-36, 2004.
- [52] Nakasuji T, Kodera S, Hara S, Matsunaga H, Ikawa N, Shimada S. "Diamond turning of brittle materials for optical components," *CIRP Annals-Manufacturing Technology*, vol. 39, pp. 89-92, 1990.
- [53] Jasinevicius R G. "Influence of cutting conditions scaling in the machining of semiconductors crystals with single point diamond tool," *Journal of materials processing technology*, vol. 179, pp. 111-116, 2006.
- [54] Chen J, Zhao Q. "A model for predicting surface roughness in single-point diamond turning," *Measurement*, vol. 69, pp. 20-30, 2015.
- [55] Uddin M S, Seah K, Li X, Rahman M, Liu K. "Effect of crystallographic orientation on wear of diamond tools for nano-scale ductile cutting of silicon," *Wear*, vol. 257, pp. 751-759, 2004.
- [56] Abdulkadir L N, Abou-El-Hossein K, Jumare A I, Odedeyi P B, Liman M M, Olaniyan T A. "Ultra-precision diamond turning of optical silicon—a review," *The International Journal of Advanced Manufacturing Technology*, pp. 1-36, 2018.
- [57] Navare J, Bodlapati C, Turnbull R, Zhong Y, Shahinian H. "Experimental investigation on the effect of diamond type on the performance of single-point diamond turning (SPDT) of < 111 > silicon," in *Optifab 2021*, 2021, pp. 193-199.
- [58] Buckley D H. "Influence of crystal orientation on friction characteristics of titanium single crystals in vacuum," NATIONAL AERONAUTICS AND SPACE ADMINISTRATION CLEVELAND OH LEWIS RESEARCH CENTER 1965.
- [59] Goel S, Stukowski A, Luo X, Agrawal A, Reuben R L. "Anisotropy of single-crystal 3C–SiC during nanometric cutting," *Modelling and Simulation in Materials Science and Engineering*, vol. 21, p. 065004, 2013.
- [60] Cheng K. *Machining dynamics: fundamentals, applications and practices*: Springer Science & Business Media, 2008.
- [61] Miyamoto I, Ezawa T, Nishimura K. "Ion beam machining of single-point diamond tools for nano-precision turning," *Nanotechnology*, vol. 1, p. 44, 1990.
- [62] Rao P, Bukkapatnam S, Beyca O, Kong Z J, Komanduri R. "Real-time identification of incipient surface morphology variations in ultraprecision

- machining process," *Journal of Manufacturing Science and Engineering*, vol. 136, p. 021008, 2014.
- [63] Huo D. *Micro-cutting: fundamentals and applications*: John Wiley & Sons, 2013.
- [64] Zong W, Li Z, Zhang L, Liang Y, Sun T, An C, *et al.* "Finite element simulation of diamond tool geometries affecting the 3D surface topography in fly cutting of KDP crystals," *The International Journal of Advanced Manufacturing Technology*, vol. 68, pp. 1927-1936, 2013.
- [65] Jumare A I, Abou-El-Hossein K, Abdulkadir L N. "Review of ultra-high precision diamond turning of silicon for infrared optics," *International Journal*, vol. 73, 2017.
- [66] Rodríguez C J C. *Cutting edge preparation of precision cutting tools by applying micro-abrasive jet machining and brushing*: Kassel university press GmbH, 2009.
- [67] Dornfeld D A, DeVries M. "Neural network sensor fusion for tool condition monitoring," *CIRP Annals-Manufacturing Technology*, vol. 39, pp. 101-105, 1990.
- [68] Chae J, Park S, Freiheit T. "Investigation of micro-cutting operations," *International Journal of Machine Tools and Manufacture*, vol. 46, pp. 313-332, 2006.
- [69] Dai H, Chen G, Fang Q, Yin J. "The effect of tool geometry on subsurface damage and material removal in nanometric cutting single-crystal silicon by a molecular dynamics simulation," *Applied Physics A*, vol. 122, p. 804, 2016.
- [70] Yue X, Xu M, Du W, Chu C. "Effect of cutting edge radius on surface roughness in diamond tool turning of transparent MgAl₂O₄ spinel ceramic," *Optical Materials*, vol. 71, pp. 129-135, 2017.
- [71] Fang F, Venkatesh V. "Diamond cutting of silicon with nanometric finish," *CIRP annals*, vol. 47, pp. 45-49, 1998.
- [72] Yan J, Syoji K, Tamaki J i. "Some observations on the wear of diamond tools in ultra-precision cutting of single-crystal silicon," *Wear*, vol. 255, pp. 1380-1387, 2003.
- [73] Hua Y, Liu Z. "Effects of cutting parameters and tool nose radius on surface roughness and work hardening during dry turning Inconel 718," *The International Journal of Advanced Manufacturing Technology*, vol. 96, pp. 2421-2430, 2018.

- [74] Ali M H, Ansari M. "The Effect of Nose Radius on Cutting Force and Temperature during Machining Titanium Alloy (Ti-6Al-4V)," *International Journal of Mechanical, Aerospace, Industrial, Mechatronic and Manufacturing Engineering*, vol. 8, pp. 2124-2127, 2014.
- [75] Júnior M G, de Angelo Sanchez L E, França T V, Fortulan C A, da Silva R H L, Foschini C R. "Analysis of the tool nose radius influence in the machining of a green ceramic material," *The International Journal of Advanced Manufacturing Technology*, vol. 105, pp. 3117-3125, 2019.
- [76] Shintani K, Fujimura Y. "Effective Use of CBN Tool in Fine Cutting(Continuous and Intermittent Turning)," *Strategies for Automation of Machining: Materials and Processes*, pp. 117-126, 1987.
- [77] *Aluminium history and development.* Available: <https://www.azom.com/article.aspx?ArticleID=1530>
- [78] *Aluminium statistics.* Available: <http://www.world-aluminium.org/statistics/>
- [79] Davis J R. "Aluminum and aluminum alloys," 2013.
- [80] Songmene V, Khettabi R, Zaghbani I, Kouam J, Djebara A. "Machining and machinability of aluminum alloys," *Alum. Alloys Theory Appl*, pp. 377-400, 2011.
- [81] *6061-T6 Aluminium Properties.* Available: <https://www.sapagroup.com/en-US/profiles/6061-t6-aluminum-properties/>.
- [82] To S, Lee W, Chan C. "Ultraprecision diamond turning of aluminium single crystals," *Journal of materials processing technology*, vol. 63, pp. 157-162, 1997.
- [83] Abou-El-Hossein K, Olufayo O. "Diamond machining of rapidly solidified aluminium for optical mould inserts," *Procedia materials science*, vol. 6, pp. 1077-1082, 2014.
- [84] König W. "Manufacturing strategies for the production of ultraprecision parts," *UPT, Aachen*, 1994.
- [85] Asai S, Kobayashi A. "Observations of chip producing behaviour in ultra-precision diamond machining and study on mirror-like surface generating mechanism," *Precision Engineering*, vol. 12, pp. 137-143, 1990.

- [86] Shi M, Lane B, Mooney C, Dow T, Scattergood R. "Diamond tool wear measurement by electron-beam-induced deposition," *Precision engineering*, vol. 34, pp. 718-721, 2010.
- [87] Anantharaman T R, Suryanarayana C. "Rapidly solidified metals: a technological overview," *Key Eng. Mater.*, vol. 17, pp. 1-260, 1987.
- [88] Zhang L, Jiang Y, Ma Z, Shan S, Jia Y, Fan C, *et al.* "Effect of cooling rate on solidified microstructure and mechanical properties of aluminium-A356 alloy," *Journal of materials processing technology*, vol. 207, pp. 107-111, 2008.
- [89] Wang W W, Jia B B, Yu J B. "Microstructure evolution and mechanical properties of 7A09 aluminum alloy during rapid solidifications," in *Advanced Materials Research*, 2009, pp. 1791-1794.
- [90] Mi G, Mo Y, Wang K. "Microstructure and mechanical properties of rapidly solidified Al-Cr alloys," *Journal of Wuhan University of Technology-Mater. Sci. Ed.*, vol. 24, pp. 424-427, 2009.
- [91] Otieno T. "The machinability of rapidly solidified aluminium alloy for optical mould inserts," Nelson Mandela University, 2018.
- [92] Newswander T, Crowther B, Gubbels G, Senden R. "Aluminum alloy AA-6061 and RSA-6061 heat treatment for large mirror applications," in *Material Technologies and Applications to Optics, Structures, Components, and Sub-Systems*, 2013, p. 883704.
- [93] Zhong Z, Leong M, Liu X. "The wear rates and performance of three mold insert materials," *Materials & Design*, vol. 32, pp. 643-648, 2011.
- [94] Zhang S, To S, Wang S, Zhu Z. "A review of surface roughness generation in ultra-precision machining," *International Journal of Machine Tools and Manufacture*, vol. 91, pp. 76-95, 2015.
- [95] Yang Yu G B. *Application note A150*. Available: <https://www.taylor-hobson.com/learning-zone/application-notes>
- [96] Katgerman L, Dom F. "Rapidly solidified aluminium alloys by meltspinning," *Materials Science and Engineering: A*, vol. 375, pp. 1212-1216, 2004.
- [97] Abou-El-Hossein K, Hsu W-Y, Ghobashy S, Cheng Y-C, Mkoko Z. "Diamond grooving of rapidly solidified optical aluminium," in *Optifab 2015*, 2015, p. 96331J.

- [98] Abou-El-Hossein K, Olufayo O, Mkoko Z. "Diamond tool wear during ultra-high precision machining of rapidly solidified aluminium RSA 905," *Wear*, vol. 302, pp. 1105-1112, 2013.
- [99] Cheng Y-C, Hsu W-Y, Kuo C-H, Abou-El-Hossein K, Otieno T. "Investigation of rapidly solidified aluminum by using diamond turning and a magnetorheological finishing process," in *Optical Manufacturing and Testing XI*, 2015, p. 957519.
- [100] Guo J, Wang H, Goh M H, Liu K. "Investigation on surface integrity of rapidly solidified aluminum RSA 905 by magnetic field-assisted finishing," *Micromachines*, vol. 9, p. 146, 2018.
- [101] Belgraver J, Kool W, Oomen J. "Surface Roughness and Tool Wear during Single-Point Diamond Turning of Rapidly Solidified Aluminium Alloys," in *Materials Forum*, 2004, pp. 1148-1153.
- [102] Onwuka G, Abou-El-Hossein K, Mkoko Z. "AE monitoring of diamond turned rapidly Solidified Aluminium 443," in *J Phys Conf Ser*, 2017, p. 012059.
- [103] Guo J, Zhang J, Wang H, Liu K, Kumar A S. "Surface quality characterisation of diamond cut V-groove structures made of rapidly solidified aluminium RSA-905," *Precision Engineering*, vol. 53, pp. 120-133, 2018.
- [104] Otieno T, Abou-El-Hossein K. "Surface roughness analysis when diamond turning optical grade rapidly solidified aluminium RSA 905," *Journal of Optics*, vol. 46, pp. 446-455, 2017.
- [105] Mkoko Z, Abou-El-Hossein K. "Diamond Insert Wear when Turning Rapidly Solidified Aluminium RSA 443 of High-Silicon Content," in *Materials Science Forum*, 2015, pp. 265-271.
- [106] Davim J P. *Surface integrity in machining* vol. 1848828742: Springer, 2010.
- [107] Raja J, Muralikrishnan B, Fu S. "Recent advances in separation of roughness, waviness and form," *Precision Engineering*, vol. 26, pp. 222-235, 2002.
- [108] 1 A B. "Surface Texture, Surface Roughness, Waviness, and Lay," 1995.
- [109] Lucca D, Brinksmeier E, Goch G. "Progress in assessing surface and subsurface integrity," *CIRP Annals*, vol. 47, pp. 669-693, 1998.
- [110] Bellows G, Tishler D N. "Introduction to surface integrity," *General Electric: Cincinnati, OH, USA*, 1970.
- [111] Yoshino M, Nakajima S, Terano M. "Tool wear of a single-crystal diamond tool in nano-groove machining of a quartz glass plate," *Surface Topography: Metrology and Properties*, vol. 3, p. 044007, 2015.

- [112] Sata T, Li M, Takata S, Hiraoka H, Li C, Xing X, *et al.* "Analysis of surface roughness generation in turning operation and its applications," *CIRP Annals-Manufacturing Technology*, vol. 34, pp. 473-476, 1985.
- [113] To S, Cheung C, Lee W. "Influence of material swelling on surface roughness in diamond turning of single crystals," *Materials science and technology*, vol. 17, pp. 102-108, 2001.
- [114] Kong M, Lee W, Cheung C, To S. "A study of materials swelling and recovery in single-point diamond turning of ductile materials," *Journal of materials processing technology*, vol. 180, pp. 210-215, 2006.
- [115] Zhang S, To S, Wang H. "A theoretical and experimental investigation into five-DOF dynamic characteristics of an aerostatic bearing spindle in ultra-precision diamond turning," *International Journal of Machine Tools and Manufacture*, vol. 71, pp. 1-10, 2013.
- [116] Lee W, To S, Chan C. "Deformation band formation in metal cutting," *Scripta materialia*, 1999.
- [117] Liu K, Melkote S N. "Effect of plastic side flow on surface roughness in micro-turning process," *International Journal of Machine Tools and Manufacture*, vol. 46, pp. 1778-1785, 2006.
- [118] Cheung C, Chan K, To S, Lee W. "Effect of reinforcement in ultra-precision machining of Al6061/SiC metal matrix composites," *Scripta Materialia*, vol. 47, pp. 77-82, 2002.
- [119] Simoneau A, Ng E, Elbestawi M. "Surface defects during microcutting," *International Journal of Machine Tools and Manufacture*, vol. 46, pp. 1378-1387, 2006.
- [120] Gupta A, Ramagopal S, Batish A, Bhattacharya A. "Surface roughness and profile error in precision diamond turning of C18000," *Materials and Manufacturing Processes*, vol. 29, pp. 606-613, 2014.
- [121] Ulutan D, Ozel T. "Machining induced surface integrity in titanium and nickel alloys: A review," *International Journal of Machine Tools and Manufacture*, vol. 51, pp. 250-280, 2011.
- [122] Wang S. "Modelling and optimization of cutting strategy and surface generation in ultra-precision raster milling," The Hong Kong Polytechnic University, 2011.

- [123] Nalbant M, Gökkaya H, Sur G. "Application of Taguchi method in the optimization of cutting parameters for surface roughness in turning," *Materials & design*, vol. 28, pp. 1379-1385, 2007.
- [124] Zain A M, Haron H, Sharif S. "Prediction of surface roughness in the end milling machining using Artificial Neural Network," *Expert Systems with Applications*, vol. 37, pp. 1755-1768, 2010.
- [125] Grzenda M, Bustillo A. "The evolutionary development of roughness prediction models," *Applied Soft Computing*, vol. 13, pp. 2913-2922, 2013.
- [126] Davim J P, Gaitonde V, Karnik S. "Investigations into the effect of cutting conditions on surface roughness in turning of free machining steel by ANN models," *Journal of materials processing technology*, vol. 205, pp. 16-23, 2008.
- [127] Modi K P, Joshi S, George P. "" IMPROVEMENT IN SURFACE FINISH BY LAPPING PROCESS"-A REVIEW," *International Journal of Engineering, Science and Mathematics*, vol. 2, p. 175, 2013.
- [128] Ikawa N, Donaldson R, Komanduri R, König W, McKeown P, Moriwaki T, *et al.* "Ultraprecision metal cutting—the past, the present and the future," *CIRP Annals-Manufacturing Technology*, vol. 40, pp. 587-594, 1991.
- [129] Dornfeld D, Min S, Takeuchi Y. "Recent advances in mechanical micromachining," *CIRP Annals-Manufacturing Technology*, vol. 55, pp. 745-768, 2006.
- [130] Zong W, Huang Y, Zhang Y, Sun T. "Conservation law of surface roughness in single point diamond turning," *International Journal of Machine Tools and Manufacture*, vol. 84, pp. 58-63, 2014.
- [131] Zhongxiang H, Lei Z, Jiaxu T, Xuehong M, Xiaojun S. "Evaluation of three-dimensional surface roughness parameters based on digital image processing," *The International Journal of Advanced Manufacturing Technology*, vol. 40, pp. 342-348, 2009.
- [132] Thomas T. "Characterization of surface roughness," *Precision Engineering*, vol. 3, pp. 97-104, 1981.
- [133] Correa M, Bielza C, Pamies-Teixeira J. "Comparison of Bayesian networks and artificial neural networks for quality detection in a machining process," *Expert systems with applications*, vol. 36, pp. 7270-7279, 2009.

- [134] Sato H, O-hori M, Tsuwa H. "Characteristics of two dimensional surface roughness—taking self-excited chatter marks as objective," *CIRP Annals*, vol. 30, pp. 481-486, 1981.
- [135] Kalpakjian S, Vijai Sekar K, Schmid S R. *Manufacturing engineering and technology*. Pearson, 2014.
- [136] Shaw M C. "Metal cutting principles—Oxford series on advanced manufacturing," *Publ. Oxford University Press, New York (USA)*, 2005.
- [137] Munoz-Escalona P. "Surface Roughness Prediction When Milling With Square Inserts," University of Bath, 2010.
- [138] Plaza E G, López P N. "Surface roughness monitoring by singular spectrum analysis of vibration signals," *Mechanical Systems and Signal Processing*, vol. 84, pp. 516-530, 2017.
- [139] Lu C. "Study on prediction of surface quality in machining process," *Journal of materials processing technology*, vol. 205, pp. 439-450, 2008.
- [140] Chang H-K, Kim J-H, Kim I H, Jang D Y, Han D C. "In-process surface roughness prediction using displacement signals from spindle motion," *International Journal of Machine Tools and Manufacture*, vol. 47, pp. 1021-1026, 2007.
- [141] Huang B P, Chen J C, Li Y. "Artificial-neural-networks-based surface roughness Pokayoke system for end-milling operations," *Neurocomputing*, vol. 71, pp. 544-549, 2008.
- [142] Franco P, Estrems M, Faura F. "Influence of radial and axial runouts on surface roughness in face milling with round insert cutting tools," *International Journal of Machine Tools and Manufacture*, vol. 44, pp. 1555-1565, 2004.
- [143] Ryu S H, Choi D K, Chu C N. "Roughness and texture generation on end milled surfaces," *International Journal of Machine Tools and Manufacture*, vol. 46, pp. 404-412, 2006.
- [144] Özel T, Karpuz Y. "Predictive modeling of surface roughness and tool wear in hard turning using regression and neural networks," *International Journal of Machine Tools and Manufacture*, vol. 45, pp. 467-479, 2005.
- [145] Ali S, Dhar N. "Tool Wear and Surface Roughness Prediction using an artificial Neural Network in Turning Steel under Minimum Quantity Lubrication," in *International Conference on Industrial Engineering-ICIE-2010, WASET Conference Proceedings*, 2010, pp. 607-616.

- [146] Zeng W, Jiang X, Blunt L. "Surface characterisation-based tool wear monitoring in peripheral milling," *The International Journal of Advanced Manufacturing Technology*, vol. 40, pp. 226-233, 2009.
- [147] Xu A-P, Qu Y-X, Zhang D-W, Huang T. "Simulation and experimental investigation of the end milling process considering the cutter flexibility," *International Journal of Machine Tools and Manufacture*, vol. 43, pp. 283-292, 2003.
- [148] Abburi N, Dixit U. "A knowledge-based system for the prediction of surface roughness in turning process," *Robotics and Computer-Integrated Manufacturing*, vol. 22, pp. 363-372, 2006.
- [149] Jiao Y, Pei Z, Lei S, Lee* E, Fisher G. "Fuzzy adaptive networks in machining process modelling: dimensional error prediction for turning operations," *International journal of production research*, vol. 43, pp. 2931-2948, 2005.
- [150] Ahmad N, Janahiraman T V, Tarlochan F. "Modeling of surface roughness in turning operation using extreme learning machine," *Arabian Journal for Science and Engineering*, vol. 40, pp. 595-602, 2015.
- [151] Pei Q, Lu C, Fang F, Wu H. "Nanometric cutting of copper: A molecular dynamics study," *Computational Materials Science*, vol. 37, pp. 434-441, 2006.
- [152] Woon K, Rahman M, Fang F, Neo K, Liu K. "Investigations of tool edge radius effect in micromachining: a FEM simulation approach," *Journal of materials processing technology*, vol. 195, pp. 204-211, 2008.
- [153] Asiltürk I, Çunkaş M. "Modeling and prediction of surface roughness in turning operations using artificial neural network and multiple regression method," *Expert systems with applications*, vol. 38, pp. 5826-5832, 2011.
- [154] Reddy B S, Padmanabhan G, Reddy K V K. "Surface roughness prediction techniques for CNC turning," *Asian Journal of Scientific Research*, vol. 1, pp. 256-264, 2008.
- [155] Kumar G P, Narayana R L. "Prediction of surface roughness in turning process using soft computing techniques," *International Journal of Mechanical Engineering and Robotics Research*, vol. 4, p. 561, 2015.
- [156] Makadia A J, Nanavati J. "Optimisation of machining parameters for turning operations based on response surface methodology," *Measurement*, vol. 46, pp. 1521-1529, 2013.

- [157] Lee D-E, Hwang I, Valente C M, Oliveira J, Dornfeld D A. "Precision manufacturing process monitoring with acoustic emission," in *Condition Monitoring and Control for Intelligent Manufacturing*, ed: Springer, 2006, pp. 33-54.
- [158] Marfo A, Chen Z, Li J. "Acoustic emission analysis of fatigue crack growth in steel structures," *Journal of Civil Engineering and Construction Technology*, vol. 4, pp. 239-249, 2013.
- [159] Prickett P, Johns C. "An overview of approaches to end milling tool monitoring," *International Journal of Machine Tools and Manufacture*, vol. 39, pp. 105-122, 1999.
- [160] Hase A, Wada M, Koga T, Mishina H. "The relationship between acoustic emission signals and cutting phenomena in turning process," *The International Journal of Advanced Manufacturing Technology*, vol. 70, pp. 947-955, 2014.
- [161] Bhaskaran J, Murugan M, Balashanmugam N, Chellamalai M. "Monitoring of hard turning using acoustic emission signal," *Journal of mechanical science and technology*, vol. 26, pp. 609-615, 2012.
- [162] Sutowski P, Nadolny K, Kaplonek W. "Monitoring of cylindrical grinding processes by use of a non-contact AE system," *International Journal of Precision Engineering and Manufacturing*, vol. 13, pp. 1737-1743, 2012.
- [163] Li H, Li J, Liu X, Fok A. "Non-Destructive Examination of Interfacial Debonding in Dental Composite Restorations Using Acoustic Emission," in *Composites and Their Applications*, ed: InTech, 2012.
- [164] Available: <https://www.crosswalk.com/faith/prayer/the-prayer-of-jabez-5-inspiring-lessons.html>
- [165] Lindberg R A. "Processes and materials of manufacture," *Allyn and Bacon, Inc., Boston, Mass. 1977, 704 p(Book)*. 1977.
- [166] Dornfeld D, Lee Y, Chang A. "Monitoring of ultraprecision machining processes," *The International Journal of Advanced Manufacturing Technology*, vol. 21, pp. 571-578, 2003.
- [167] Dornfeld D, König W, Kettler G. "Present state of tool and process monitoring in cutting," *Proc. New Developments in Cutting*, pp. 363-376, 1993.
- [168] Tlusty J, Andrews G. "A critical review of sensors for unmanned machining," *CIRP Annals-Manufacturing Technology*, vol. 32, pp. 563-572, 1983.

- [169] Tönshoff H, Wulfsberg J, Kals H, König W, Van Luttervelt C. "Developments and trends in monitoring and control of machining processes," *CIRP Annals-Manufacturing Technology*, vol. 37, pp. 611-622, 1988.
- [170] Byrne G, Dornfeld D, Inasaki I, Ketteler G, König W, Teti R. "Tool condition monitoring (TCM)—the status of research and industrial application," *CIRP Annals-Manufacturing Technology*, vol. 44, pp. 541-567, 1995.
- [171] Iwata K. "Sensing technologies for improving the machine tool function," in *Proc. 3rd Int'l Machine Tool Engineer's Conference*, 1988, pp. 87-109.
- [172] Liu J-J B. *Monitoring the precision machining process: sensors, signal processing and information analysis*: University of California, Berkeley, 1991.
- [173] Chen X, Tang J, Dornfeld D. "Monitoring and analysis of ultraprecision metal cutting with acoustic emission," in *Mechanical Engineering Congress and Exposition, ASME, Atlanta, GA*, 1996, p. 387.
- [174] Olufayo O A. "Acoustic Emission Monitoring in Ultra-High Precision Machining of Rapidly Solidified Aluminium," in *COMA'13*, 2013.
- [175] Keffer D. "The working person's guide to molecular dynamics simulations," *University of Tennessee*, 2002.
- [176] Goel S. "An atomistic investigation on the nanometric cutting mechanism of hard, brittle materials," Heriot-Watt University, 2013.
- [177] Rapaport D C, Rapaport D C R. *The art of molecular dynamics simulation*: Cambridge university press, 2004.
- [178] Alder B. "BJ Alder and TE Wainwright, J. Chem. Phys. 27, 1208 (1957)," *J. Chem. Phys.*, vol. 27, p. 1208, 1957.
- [179] Promyoo R, El-Mounayri H, Yang X. "Molecular dynamics simulation of nanometric cutting," *Machining Science and Technology*, vol. 14, pp. 423-439, 2010.
- [180] Komanduri R, Raff L. "A review on the molecular dynamics simulation of machining at the atomic scale," *Proceedings of the Institution of Mechanical Engineers, Part B: Journal of Engineering Manufacture*, vol. 215, pp. 1639-1672, 2001.
- [181] Abdulkadir L N, Abou-El-Hossein K, Jumare A I, Liman M M, Olaniyan T A, Odedeyi P B. "Review of molecular dynamics/experimental study of diamond-silicon behavior in nanoscale machining," *The International Journal of Advanced Manufacturing Technology*, vol. 98, pp. 317-371, 2018.

- [182] Shimizu J, Zhou L, Eda H. "Molecular dynamics simulation of vibration-assisted cutting: influences of vibration, acceleration and velocity," *International journal of nanomanufacturing*, vol. 1, pp. 105-116, 2006.
- [183] MINBO C. "Study of nanoscale ductile mode cutting of silicon using molecular dynamics simulation," 2008.
- [184] Notman R, Anwar J. "Breaching the skin barrier—Insights from molecular simulation of model membranes," *Advanced drug delivery reviews*, vol. 65, pp. 237-250, 2013.
- [185] Frenkel D, Smit B. *Understanding molecular simulation: from algorithms to applications* vol. 1: Elsevier, 2001.
- [186] LeSar R. *Introduction to computational materials science: fundamentals to applications*: Cambridge University Press, 2013.
- [187] Brenner D. "The art and science of an analytic potential," *physica status solidi (b)*, vol. 217, pp. 23-40, 2000.
- [188] Oluwajobi A. "Molecular Dynamics Simulation of Nanoscale Machining," in *Molecular Dynamics-Studies of Synthetic and Biological Macromolecules*, ed: InTech, 2012.
- [189] Oluwajobi A O. "Nanomachining technology development," University of Huddersfield, 2012.
- [190] Oluwajobi A O, Chen X. "The effect of depth of cut on the molecular dynamics (MD) simulation of multi-pass nanometric machining," in *Automation and Computing (ICAC), 2011 17th International Conference on*, 2011, pp. 40-45.
- [191] Camprubí G S. "Mechanical properties at nano-level," Universitat Politècnica de Catalunya. Escola Tècnica Superior d'Enginyeria ..., 2010.
- [192] Tien C L, Lienhard J H. "Statistical thermodynamics/ revised printing," *wdch*, 1979.
- [193] Oluwajobi A O, Chen X. "The effect of interatomic potentials on nanometric abrasive machining," ed: Chinese Automation and Computing Society in the UK, 2010.
- [194] Han X, Hu Y-Z, Yu S. "Molecular dynamics analysis micro-mechanism of ductile machining single crystal silicon by means of nanometric cutting technology," *The European Physical Journal-Applied Physics*, vol. 42, pp. 255-262, 2008.
- [195] Olufayo O, Abou-El-Hossein K. "Molecular dynamics modeling of nanoscale machining of silicon," *Procedia CIRP*, vol. 8, pp. 504-509, 2013.

- [196] Tersoff J. "Modeling solid-state chemistry: Interatomic potentials for multicomponent systems," *Physical review B*, vol. 39, p. 5566, 1989.
- [197] Justo J F, Bazant M Z, Kaxiras E, Bulatov V V, Yip S. "Interatomic potential for silicon defects and disordered phases," *Physical review B*, vol. 58, p. 2539, 1998.
- [198] Wang Y, Shi J, Ji C. "A numerical study of residual stress induced in machined silicon surfaces by molecular dynamics simulation," *Applied Physics A*, vol. 115, pp. 1263-1279, 2014.
- [199] Li X-P, Chen G, Allen P, Broughton J. "Energy and vibrational spectrum of the Si (111)(7× 7) surface from empirical potentials," *Physical Review B*, vol. 38, p. 3331, 1988.
- [200] Porter L J, Yip S, Yamaguchi M, Kaburaki H, Tang M. "Empirical bond-order potential description of thermodynamic properties of crystalline silicon," *Journal of applied physics*, vol. 81, pp. 96-106, 1997.
- [201] Tersoff J. "New empirical approach for the structure and energy of covalent systems," *Physical Review B*, vol. 37, p. 6991, 1988.
- [202] Ishimaru M, Yoshida K, Motooka T. "Application of empirical interatomic potentials to liquid Si," *Physical Review B*, vol. 53, p. 7176, 1996.
- [203] Tersoff J. "Empirical interatomic potential for carbon, with applications to amorphous carbon," *Physical Review Letters*, vol. 61, p. 2879, 1988.
- [204] Nordlund K, Keinonen J, Mattila T. "Formation of ion irradiation induced small-scale defects on graphite surfaces," *Physical review letters*, vol. 77, p. 699, 1996.
- [205] Nakayama K, Tamura K. "Size effect in metal-cutting force," *Journal of Engineering for Industry*, vol. 90, pp. 119-126, 1968.
- [206] Pastewka L, Klemenz A, Gumbsch P, Moseler M. "Screened empirical bond-order potentials for Si-C," *Physical Review B*, vol. 87, p. 205410, 2013.
- [207] Dai H, Li S, Chen G. "Comparison of subsurface damages on mono-crystalline silicon between traditional nanoscale machining and laser-assisted nanoscale machining via molecular dynamics simulation," *Nuclear Instruments and Methods in Physics Research Section B: Beam Interactions with Materials and Atoms*, vol. 414, pp. 61-67, 2018.

- [208] Bocchetti V, Diep H T, Enriquez H, Oughaddou H, Kara A. "Thermal stability of standalone silicene sheet," in *Journal of Physics: Conference Series*, 2014, p. 012008.
- [209] Yamaguchi K, Itagaki K. "Measurement of high temperature heat content of silicon by drop calorimetry," *Journal of thermal analysis and calorimetry*, vol. 69, pp. 1059-1066, 2002.
- [210] Fang K-C, Weng C-I. "An investigation into the melting of silicon nanoclusters using molecular dynamics simulations," *Nanotechnology*, vol. 16, p. 250, 2005.
- [211] Dozhdikov V, Basharin A Y, Levashov P. "Two-phase simulation of the crystalline silicon melting line at pressures from -1 to 3 GPa," *The Journal of chemical physics*, vol. 137, p. 054502, 2012.
- [212] Li S, Qi W. "Unification of two different melting mechanisms of nanovoids," *The Journal of Physical Chemistry C*, vol. 119, pp. 6843-6851, 2015.
- [213] Li H, Xu R, Bi Z, Shen X, Han K. "Melting properties of medium-sized silicon nanoclusters: a molecular dynamics study," *Journal of Electronic Materials*, vol. 46, pp. 3826-3830, 2017.
- [214] Wang Y, Shi J. "Effects of water molecules on tribological behavior and property measurements in nano-indentation processes-a numerical analysis," *Nanoscale research letters*, vol. 8, p. 389, 2013.
- [215] Dai H, Chen G, Li S, Fang Q, Hu B. "Influence of laser nanostructured diamond tools on the cutting behavior of silicon by molecular dynamics simulation," *RSC advances*, vol. 7, pp. 15596-15612, 2017.
- [216] Agrawal P M, Raff L M, Komanduri R. "Monte Carlo simulations of void-nucleated melting of silicon via modification in the Tersoff potential parameters," *Physical Review B*, vol. 72, p. 125206, 2005.
- [217] Chavoshi S Z, Goel S, Luo X. "Influence of temperature on the anisotropic cutting behaviour of single crystal silicon: A molecular dynamics simulation investigation," *Journal of Manufacturing Processes*, vol. 23, pp. 201-210, 2016.
- [218] Moura C S, Amaral L. "Molecular dynamics simulation of silicon nanostructures," *Nuclear Instruments and Methods in Physics Research Section B: Beam Interactions with Materials and Atoms*, vol. 228, pp. 37-40, 2005.
- [219] Baskes M. "Modified embedded-atom potentials for cubic materials and impurities," *Physical review B*, vol. 46, p. 2727, 1992.

- [220] Kim Y-M, Lee B-J. "Modified embedded-atom method interatomic potentials for the Ti–C and Ti–N binary systems," *Acta materialia*, vol. 56, pp. 3481-3489, 2008.
- [221] Lee B-J, Jang J-W. "A modified embedded-atom method interatomic potential for the Fe–H system," *Acta Materialia*, vol. 55, pp. 6779-6788, 2007.
- [222] Shimada S, Ikawa N, Tanaka H, Ohmori G, Uchikoshi J, Yoshinaga H. "Feasibility study on ultimate accuracy in microcutting using molecular dynamics simulation," *CIRP annals*, vol. 42, pp. 91-94, 1993.
- [223] Oluwajobi A. *Molecular dynamics simulation of nanoscale machining*: InTech, 2012.
- [224] Verlet L. "Computer" experiments" on classical fluids. I. Thermodynamical properties of Lennard-Jones molecules," *Physical review*, vol. 159, p. 98, 1967.
- [225] Beeman D. "Some multistep methods for use in molecular dynamics calculations," *Journal of computational physics*, vol. 20, pp. 130-139, 1976.
- [226] Gear C, Tu K. "The effect of variable mesh size on the stability of multistep methods," *SIAM Journal on Numerical Analysis*, vol. 11, pp. 1025-1043, 1974.
- [227] Rahman A. "Correlations in the motion of atoms in liquid argon," *Physical review*, vol. 136, p. A405, 1964.
- [228] Cheong W C D, Zhang L C, Tanaka H. "Some essentials of simulating nano-surfacing processes using the molecular dynamics method," in *Key Engineering Materials*, 2001, pp. 31-42.
- [229] "Cutting Forces Model," in *CIRP Encyclopedia of Production Engineering*, Laperrière L, Reinhart G, Eds., ed Berlin, Heidelberg: Springer Berlin Heidelberg, 2014, pp. 329-329.
- [230] Karpát Y, Bahtiyar O, Değer B. "Mechanistic force modeling for milling of unidirectional carbon fiber reinforced polymer laminates," *International Journal of Machine Tools and Manufacture*, vol. 56, pp. 79-93, 2012.
- [231] Dang J-W, Zhang W-H, Yang Y, Wan M. "Cutting force modeling for flat end milling including bottom edge cutting effect," *International Journal of Machine Tools and Manufacture*, vol. 50, pp. 986-997, 2010.
- [232] Min W, Zhang W-h, Gang T, Qin G-h. "New cutting force modeling approach for flat end mill," *Chinese Journal of Aeronautics*, vol. 20, pp. 282-288, 2007.
- [233] Smith S, Tlusty J. "An overview of modeling and simulation of the milling process," 1991.

- [234] Bayoumi A, Yucesan G, Kendall L. "An analytic mechanistic cutting force model for milling operations: a theory and methodology," 1994.
- [235] Fuh K-H, Hwang R-M. "A predicted milling force model for high-speed end milling operation," *International Journal of Machine Tools and Manufacture*, vol. 37, pp. 969-979, 1997.
- [236] Zheng L, Li Y, Liang S Y. "A generalised model of milling forces," *The International Journal of Advanced Manufacturing Technology*, vol. 14, pp. 160-171, 1998.
- [237] Zheng L, Liang S Y, Melkote S N. "Angle domain analytical model for end milling forces," 1998.
- [238] Hadi Y. "Dynamic Deflection of Periodic Cutting Tool Holder Based on Passive Model," *International Journal of Mechanical & Mechatronics Engineering*, vol. 11.
- [239] Montgomery D, Altintas Y. "Mechanism of cutting force and surface generation in dynamic milling," 1991.
- [240] Yücesan G, Altıntaş Y. "Improved modelling of cutting force coefficients in peripheral milling," *International Journal of Machine Tools and Manufacture*, vol. 34, pp. 473-487, 1994.
- [241] Jiang F, Zhang T, Yan L. "Analytical model of milling forces based on time-variant sculptured shear surface," *International Journal of Mechanical Sciences*, vol. 115, pp. 190-201, 2016.
- [242] Arrazola P, Özel T, Umbrello D, Davies M, Jawahir I. "Recent advances in modelling of metal machining processes," *CIRP Annals*, vol. 62, pp. 695-718, 2013.
- [243] Yoon H-S, Lee J-Y, Kim M-S, Ahn S-H. "Empirical power-consumption model for material removal in three-axis milling," *Journal of Cleaner Production*, vol. 78, pp. 54-62, 2014.
- [244] Newby G, Venkatachalam S, Liang S. "Empirical analysis of cutting force constants in micro-end-milling operations," *Journal of Materials Processing Technology*, vol. 192, pp. 41-47, 2007.
- [245] Jiang F, Yan L, Rong Y. "Orthogonal cutting of hardened AISI D2 steel with TiAlN-coated inserts—simulations and experiments," *The International Journal of Advanced Manufacturing Technology*, vol. 64, pp. 1555-1563, 2013.

- [246] Chang C-S. "Prediction of the cutting temperatures of stainless steel with chamfered main cutting edge tools," *Journal of materials processing technology*, vol. 190, pp. 332-341, 2007.
- [247] Malakizadi A, Cedergren S, Sadik I, Nyborg L. "Inverse identification of flow stress in metal cutting process using Response Surface Methodology," *Simulation Modelling Practice and Theory*, vol. 60, pp. 40-53, 2016.
- [248] Zhou L, Peng F, Yan R, Yao P, Yang C, Li B. "Analytical modeling and experimental validation of micro end-milling cutting forces considering edge radius and material strengthening effects," *International Journal of Machine Tools and Manufacture*, vol. 97, pp. 29-41, 2015.
- [249] Soo S, Aspinwall D, Dewes R. "3D FE modelling of the cutting of Inconel 718," *Journal of Materials Processing Technology*, vol. 150, pp. 116-123, 2004.
- [250] Özel T, Altan T. "Process simulation using finite element method—prediction of cutting forces, tool stresses and temperatures in high-speed flat end milling," *International Journal of Machine Tools and Manufacture*, vol. 40, pp. 713-738, 2000.
- [251] Jiang F, Li J, Sun J, Zhang S, Wang Z, Yan L. "Al7050-T7451 turning simulation based on the modified power-law material model," *The International journal of advanced manufacturing technology*, vol. 48, pp. 871-880, 2010.
- [252] Niesłony P, Grzesik W, Chudy R, Habrat W. "Meshing strategies in FEM simulation of the machining process," *Archives of Civil and Mechanical Engineering*, vol. 15, pp. 62-70, 2015.
- [253] Abdulkadir L N, Abou-EI-Hossein K, Jumare A I, Odedeyi P B, Liman M M, Olaniyan T A. "Ultra-precision diamond turning of optical silicon—a review," *The International Journal of Advanced Manufacturing Technology*, vol. 96, pp. 173-208, 2018.
- [254] Cai M, Li X, Rahman M, Tay A. "Crack initiation in relation to the tool edge radius and cutting conditions in nanoscale cutting of silicon," *International Journal of Machine Tools and Manufacture*, vol. 47, pp. 562-569, 2007.
- [255] Cai M, Li X, Rahman M. "Molecular dynamics modelling and simulation of nanoscale ductile cutting of silicon," *International Journal of Computer Applications in Technology*, vol. 28, pp. 2-8, 2007.

- [256] Cai M, Li X, Rahman M. "Study of the temperature and stress in nanoscale ductile mode cutting of silicon using molecular dynamics simulation," *Journal of materials processing technology*, vol. 192, pp. 607-612, 2007.
- [257] Shaw M C, Cookson J. *Metal cutting principles* vol. 2: Oxford university press New York, 2005.
- [258] Zhang H, Wang X, Pang S. "A mathematical modeling to predict the cutting forces in microdrilling," *Mathematical Problems in Engineering*, vol. 2014, 2014.
- [259] Kim J-D, Kim D S. "Theoretical analysis of micro-cutting characteristics in ultra-precision machining," *Journal of materials processing technology*, vol. 49, pp. 387-398, 1995.
- [260] Fetecau C, Stan F. "Study of cutting force and surface roughness in the turning of polytetrafluoroethylene composites with a polycrystalline diamond tool," *Measurement*, vol. 45, pp. 1367-1379, 2012.
- [261] Kim B, Schmittiel M C, Degertekin F L, Kurfess T R. "Scanning grating microinterferometer for MEMS metrology," *J. Manuf. Sci. Eng.*, vol. 126, pp. 807-812, 2004.
- [262] Budak E, Kops L. "Improving productivity and part quality in milling of titanium based impellers by chatter suppression and force control," *CIRP Annals*, vol. 49, pp. 31-36, 2000.
- [263] Dow T A, Miller E L, Garrard K. "Tool force and deflection compensation for small milling tools," *Precision engineering*, vol. 28, pp. 31-45, 2004.
- [264] Kim C-J, Mayor J R, Ni J. "A static model of chip formation in microscale milling," *J. Manuf. Sci. Eng.*, vol. 126, pp. 710-718, 2004.
- [265] Bao W, Tansel I. "Modeling micro-end-milling operations. Part III: influence of tool wear," *International Journal of Machine Tools and Manufacture*, vol. 40, pp. 2193-2211, 2000.
- [266] Tlustý J, Andrews G. "A critical review of sensors for unmanned machining," *CIRP annals*, vol. 32, pp. 563-572, 1983.
- [267] Tlustý J. "Dynamics of cutting forces in end milling," *Annals of CIRP*, vol. 24, pp. 22-25, 1975.
- [268] Stru M N O, Uporabo E Z, Podlagi T. "Multi-objective optimization of the cutting forces in turning operations using the grey-based Taguchi method," *Materiali in tehnologije*, vol. 45, pp. 105-110, 2011.

- [269] Santos M C, Machado A R, Sales W F, Barrozo M A, Ezugwu E O. "Machining of aluminum alloys: a review," *The International Journal of Advanced Manufacturing Technology*, vol. 86, pp. 3067-3080, 2016.
- [270] Zhu D, Zhang X, Ding H. "Tool wear characteristics in machining of nickel-based superalloys," *International Journal of Machine Tools and Manufacture*, vol. 64, pp. 60-77, 2013.
- [271] M'Saoubi R, Axinte D, Soo S L, Nobel C, Attia H, Kappmeyer G, *et al.* "High performance cutting of advanced aerospace alloys and composite materials," *CIRP Annals*, vol. 64, pp. 557-580, 2015.
- [272] Yao Q, Luo M, Zhang D, Wu B. "Identification of cutting force coefficients in machining process considering cutter vibration," *Mechanical Systems and Signal Processing*, vol. 103, pp. 39-59, 2018.
- [273] Huo D, Cheng K. "Machining dynamics. Fundamentals, applications and practices," ed: Springer-Verlag London Limited. Londres, Inglaterra, 2009.
- [274] Stein J L, Huh K. "Monitoring cutting forces in turning: a model-based approach," *J. Manuf. Sci. Eng.*, vol. 124, pp. 26-31, 2002.
- [275] SUKVITTAYAWONG S, Inasaki I. "Optimization of turning process by cutting force measurement," *JSME international journal. Ser. 3, Vibration, control engineering, engineering for industry*, vol. 34, pp. 546-552, 1991.
- [276] Weck M. "Machine diagnostics in automated production," *Journal of Manufacturing Systems*, vol. 2, pp. 101-106, 1983.
- [277] Spiewak S. "Acceleration based indirect force measurement in metal cutting processes," *International Journal of Machine Tools and Manufacture*, vol. 35, pp. 1-17, 1995.
- [278] Shiraishi M, Aoshima S. "Sensorless in-process measurement of instantaneous depth of cut and cutting force in turning," in *Proceedings of the 1997 American Control Conference (Cat. No. 97CH36041)*, 1997, pp. 155-159.
- [279] Stein J L, Huh K S. "Design procedure for model-based monitoring systems. Cutting force estimation as a case study," in *Winter Annual Meeting of the American Society of Mechanical Engineers*, 1991, pp. 45-57.
- [280] Huh K, Jung J-J, Lee K-K. "A cutting force monitoring system based on AC spindle drive," in *Proceedings of the 1998 American Control Conference. ACC (IEEE Cat. No. 98CH36207)*, 1998, pp. 3013-3017.

- [281] Kurihara D, Kakinuma Y, Katsura S. "Cutting force control applying sensorless cutting force monitoring method," *Journal of Advanced Mechanical Design, Systems, and Manufacturing*, vol. 4, pp. 955-965, 2010.
- [282] Shinno H, Hashizume H, Yoshioka H. "Sensor-less monitoring of cutting force during ultraprecision machining," *CIRP Annals*, vol. 52, pp. 303-306, 2003.
- [283] Ibaraki S. "On the monitoring of cutting forces in end milling processes: An estimation method by geometrically combining force vectors of servo motors and a spindle motor," *Journal of JSPE*, vol. 70, pp. 1091-1095, 2004.
- [284] Li X, Djordjevich A, Venuvinod P K. "Current-sensor-based feed cutting force intelligent estimation and tool wear condition monitoring," *IEEE Transactions on Industrial Electronics*, vol. 47, pp. 697-702, 2000.
- [285] Chang Y-C. "Cutting force estimation of spindle motor," *Journal of Control Systems and Technology*, vol. 3, pp. 145-152, 1995.
- [286] Li Y, Zhao Y, Fei J, Zhao Y, Li X, Gao Y. "Development of a tri-axial cutting force sensor for the milling process," *Sensors*, vol. 16, p. 405, 2016.
- [287] Shin B-C, Ha S-J, Cho M-W, Seo T-I, Yoon G-S, Heo Y-M. "Indirect cutting force measurement in the micro end-milling process based on frequency analysis of sensor signals," *Journal of mechanical science and technology*, vol. 24, pp. 165-168, 2010.
- [288] Auchet S, Chevrier P, Lacour M, Lipinski P. "A new method of cutting force measurement based on command voltages of active electro-magnetic bearings," *International Journal of Machine Tools and Manufacture*, vol. 44, pp. 1441-1449, 2004.
- [289] Tuysuz O, Altintas Y, Feng H-Y. "Prediction of cutting forces in three and five-axis ball-end milling with tool indentation effect," *International Journal of Machine Tools and Manufacture*, vol. 66, pp. 66-81, 2013.
- [290] Tsai C-L, Liao Y-S. "Cutting force prediction in ball-end milling with inclined feed by means of geometrical analysis," *The International Journal of Advanced Manufacturing Technology*, vol. 46, pp. 529-541, 2010.
- [291] Fussell B K, Jerard R B, Hemmett J G. "Modeling of cutting geometry and forces for 5-axis sculptured surface machining," *Computer-Aided Design*, vol. 35, pp. 333-346, 2003.

- [292] Ferry W, Altintas Y. "Virtual five-axis flank milling of jet engine impellers—Part I: mechanics of five-axis flank milling," *Journal of manufacturing science and engineering*, vol. 130, 2008.
- [293] Rao B C, Gao R, Friedrich C. "Integrated force measurement for on-line cutting geometry inspection," *IEEE transactions on instrumentation and Measurement*, vol. 44, pp. 977-980, 1995.
- [294] Kim J, Chang H, Han D, Jang D, Oh S. "Cutting force estimation by measuring spindle displacement in milling process," *CIRP annals*, vol. 54, pp. 67-70, 2005.
- [295] Kim J-D, Kim D-S. "Development of a combined-type tool dynamometer with a piezo-film accelerometer for an ultra-precision lathe," *Journal of materials processing technology*, vol. 71, pp. 360-366, 1997.
- [296] Jin W, Venuvinod P, Wang X. "An optical fibre sensor based cutting force measuring device," *International Journal of Machine Tools and Manufacture*, vol. 35, pp. 877-883, 1995.
- [297] Liang Q, Zhang D, Ge Y, Song Q. "A novel miniature four-dimensional force/torque sensor with overload protection mechanism," *IEEE Sensors Journal*, vol. 9, pp. 1741-1747, 2009.
- [298] Liang Q, Zhang D, Coppola G, Wang Y, Wei S, Ge Y. "Multi-dimensional MEMS/micro sensor for force and moment sensing: A review," *IEEE Sensors Journal*, vol. 14, pp. 2643-2657, 2014.
- [299] Park S S. "High frequency bandwidth cutting force measurements in milling using the spindle integrated force sensor system," University of British Columbia, 2003.
- [300] Jantunen E. "A summary of methods applied to tool condition monitoring in drilling," *International Journal of Machine Tools and Manufacture*, vol. 42, pp. 997-1010, 2002.
- [301] Bayo E, Stubbe J. "Six-axis force sensor evaluation and a new type of optimal frame truss design for robotic applications," *Journal of Robotic Systems*, vol. 6, pp. 191-208, 1989.
- [302] Svinin M M, Uchiyama M. "Optimal geometric structures of force/torque sensors," *The International journal of robotics research*, vol. 14, pp. 560-573, 1995.
- [303] Liu M, Zhou Z, Tao X, Tan Y. "A dynamometer design and analysis for measurement the cutting forces on turning based on optical fiber Bragg Grating

- sensor," in *Proceedings of the 10th World Congress on Intelligent Control and Automation*, 2012, pp. 4287-4290.
- [304] Yıldız S, Ünsaçar F. "A dynamometer design for measurement the cutting forces on turning," *Measurement*, vol. 39, pp. 80-89, 2006.
- [305] Liang Q, Zhang D, Coppola G, Mao J, Sun W, Wang Y, *et al.* "Design and analysis of a sensor system for cutting force measurement in machining processes," *Sensors*, vol. 16, p. 70, 2016.
- [306] Liang Q, Zhang D, Wu W, Zou K. "Methods and research for multi-component cutting force sensing devices and approaches in machining," *Sensors*, vol. 16, p. 1926, 2016.
- [307] Li X, Wu W, Cheng Y, Liu L. "Structure design and optimization for a cutting force measurement tool with embedded nickel–chromium film sensor," *Advances in Mechanical Engineering*, vol. 10, p. 1687814018759887, 2018.
- [308] Stein J, Colvin D, Clever G, Wang C-H. "Evaluation of dc servo machine tool feed drives as force sensors," 1986.
- [309] Altintas Y. "Prediction of cutting forces and tool breakage in milling from feed drive current measurements," 1992.
- [310] Altintas Y, Dong C. "Design and analysis of a modular CNC system for machining control and monitoring," in *Modeling of Machine Tools: Accuracy, Dynamics, and Control American Society of Mechanical Engineers, Production Engineering Division (Publication) PED*. vol. 45, ed: ASME, 1990, pp. 199-208.
- [311] Kim T-Y, Woo J, Shin D, Kim J. "Indirect cutting force measurement in multi-axis simultaneous NC milling processes," *International Journal of Machine Tools and Manufacture*, vol. 39, pp. 1717-1731, 1999.
- [312] Kim T-Y, Kim J. "Adaptive cutting force control for a machining center by using indirect cutting force measurements," *International Journal of Machine Tools and Manufacture*, vol. 36, pp. 925-937, 1996.
- [313] Santochi M, Dini G, Tantussi G, Beghini M. "A sensor-integrated tool for cutting force monitoring," *Cirp Annals*, vol. 46, pp. 49-52, 1997.
- [314] Zhao Y, Zhao Y, Wang C, Liang S, Cheng R, Qin Y, *et al.* "Design and development of a cutting force sensor based on semi-conductive strain gauge," *Sensors and Actuators A: Physical*, vol. 237, pp. 119-127, 2016.
- [315] Zhao Y, Zhao Y, Liang S, Zhou G. "A high performance sensor for triaxial cutting force measurement in turning," *Sensors*, vol. 15, pp. 7969-7984, 2015.

- [316] Albrecht A, Park S S, Altintas Y, Pritschow G. "High frequency bandwidth cutting force measurement in milling using capacitance displacement sensors," *International Journal of Machine Tools and Manufacture*, vol. 45, pp. 993-1008, 2005.
- [317] Liu M, Zhang Z, Zhou Z, Peng S, Tan Y. "A new method based on Fiber Bragg grating sensor for the milling force measurement," *Mechatronics*, vol. 31, pp. 22-29, 2015.
- [318] Bartow M J, Calvert S G, Bayly P V. "Fiber Bragg grating sensors for dynamic machining applications," in *Sixth Pacific Northwest Fiber Optic Sensor Workshop*, 2003, pp. 21-31.
- [319] Totis G, Sortino M. "Development of a modular dynamometer for triaxial cutting force measurement in turning," *International Journal of Machine Tools and Manufacture*, vol. 51, pp. 34-42, 2011.
- [320] Totis G, Wirtz G, Sortino M, Veselovac D, Kuljanic E, Klocke F. "Development of a dynamometer for measuring individual cutting edge forces in face milling," *Mechanical Systems and Signal Processing*, vol. 24, pp. 1844-1857, 2010.
- [321] Moriwaki T. "Machinability of copper in ultra-precision micro diamond cutting," *CIRP Annals*, vol. 38, pp. 115-118, 1989.
- [322] Liu X, DeVor R, Kapoor S G, Ehmann K. "The mechanics of machining at the microscale: assessment of the current state of the science," *J. Manuf. Sci. Eng.*, vol. 126, pp. 666-678, 2004.
- [323] Huang P, Lee W. "Cutting force prediction for ultra-precision diamond turning by considering the effect of tool edge radius," *International Journal of Machine Tools and Manufacture*, vol. 109, pp. 1-7, 2016.
- [324] Magdum V B, Naik V R. "Evaluation and optimization of machining parameter for turning of EN 8 steel," *International Journal of Engineering Trends and Technology (IJTT)*, vol. 4, pp. 1564-1568, 2013.
- [325] Baldoukas A, Soukatzidis F, Demosthenous G, Lontos A. "Experimental investigation of the effect of cutting depth, tool rake angle and workpiece material type on the main cutting force during a turning process," in *Proceedings of the 3rd International Conference on Manufacturing Engineering (ICMEN)*, 2008.

- [326] Günay M, Korkut I, Aslan E, Şeker U. "Experimental investigation of the effect of cutting tool rake angle on main cutting force," *Journal of materials processing technology*, vol. 166, pp. 44-49, 2005.
- [327] Waldorf D J, DeVor R E, Kapoor S G. "A slip-line field for ploughing during orthogonal cutting," 1998.
- [328] Vogler M P, Kapoor S G, DeVor R E. "On the modeling and analysis of machining performance in micro-endmilling, Part II: Cutting force prediction," *J. Manuf. Sci. Eng.*, vol. 126, pp. 695-705, 2004.
- [329] Liu X, Jun M B, DeVor R E, Kapoor S G. "Cutting mechanisms and their influence on dynamic forces, vibrations and stability in micro-endmilling," in *ASME 2004 international mechanical engineering congress and exposition*, 2004, pp. 583-592.
- [330] Bissacco G, Hansen H N, Slunsky J. "Modelling the cutting edge radius size effect for force prediction in micro milling," *CIRP annals*, vol. 57, pp. 113-116, 2008.
- [331] Saglam H, Unsacar F, Yaldiz S. "Investigation of the effect of rake angle and approaching angle on main cutting force and tool tip temperature," *International Journal of machine tools and manufacture*, vol. 46, pp. 132-141, 2006.
- [332] Korkut I, Donertas M. "The influence of feed rate and cutting speed on the cutting forces, surface roughness and tool–chip contact length during face milling," *Materials & design*, vol. 28, pp. 308-312, 2007.
- [333] Bartarya G, Choudhury S. "Effect of cutting parameters on cutting force and surface roughness during finish hard turning AISI52100 grade steel," *Procedia CirP*, vol. 1, pp. 651-656, 2012.
- [334] Biddut A, Rahman M, Neo K, Rahman K R, Sawa M, Maeda Y. "Performance of single crystal diamond tools with different rake angles during micro-grooving on electroless nickel plated die materials," *The International Journal of Advanced Manufacturing Technology*, vol. 33, pp. 891-899, 2007.
- [335] Pramanik A, Neo K, Rahman M, Li X, Sawa M, Maeda Y. "Ultra-precision turning of electroless-nickel: Effect of phosphorus contents, depth-of-cut and rake angle," *Journal of materials processing technology*, vol. 208, pp. 400-408, 2008.

- [336] Shih A J. "Finite element analysis of the rake angle effects in orthogonal metal cutting," *ASME PROD ENG DIV PUBL PED, ASME, NEW YORK, NY,(USA)*, 1993, vol. 64, pp. 475-483, 1993.
- [337] Lee W K. "Detection of chipping in ceramic cutting inserts from workplace profile signature during turning process using machine vision," Universiti Sains Malaysia, 2017.
- [338] DeVries W R. *Analysis of material removal processes*: Springer Science & Business Media, 1991.
- [339] Huang W, Yu D, Zhang M, Cao Q, Yao J. "Predictive cutting force model for ductile-regime machining of brittle materials," *The International Journal of Advanced Manufacturing Technology*, vol. 98, pp. 781-790, 2018.
- [340] Ma L-j, Yu A-b, Chen J. "Theoretical model of cutting force in turning the lithium disilicate glass-ceramic," *The International Journal of Advanced Manufacturing Technology*, vol. 92, pp. 4355-4366, 2017.
- [341] Ma L, Li C, Chen J, Li W, Tan Y, Wang C, *et al.* "Prediction model and simulation of cutting force in turning hard-brittle materials," *The International Journal of Advanced Manufacturing Technology*, vol. 91, pp. 165-174, 2017.
- [342] Ma L, Li C, Chen J, Li W, Tan Y, Wang C, *et al.* "Prediction model and simulation of cutting force in turning hard-brittle materials," *The International Journal of Advanced Manufacturing Technology*, vol. 91, pp. 165-174, 2017.
- [343] Ezilarasan C, Velayudham A. "Theoretical predictions and experimental validations on machining the Nimonic C-263 super alloy," *Simulation Modelling Practice and Theory*, vol. 40, pp. 192-207, 2014.
- [344] Coroni D A, Croitoru S M. "Prediction of cutting forces at 2D titanium machining," *Procedia Engineering*, vol. 69, pp. 81-89, 2014.
- [345] Dogra M, Sharma V, Dureja J. "Effect of tool geometry variation on finish turning-A Review," *Journal of Engineering Science & Technology Review*, vol. 4, 2011.
- [346] Duong T H, Chul K H, Yoon L D. "Study on the Effect of Rake Angle on Cutting Forces in Ultra-precision Machining," in *Key Engineering Materials*, 2012, pp. 551-556.
- [347] Croitoru S M, Constantin G. "Simulation of titanium parts manufacturing," in *Proceedings of the 1-st WSEAS International Conference on VISUALIZATION, IMAGING and SIMULATION (VIS'08)*, 2008, pp. 121-126.

- [348] Coroni D. "Prelucrarea implanturilor dentare din titan si aliajele sale (Manufacturing of Dental Implants Made of Titanium and Its Alloys)," Dissertation Paper, Machine and Manufacturing Systems Department, University ..., 2011.
- [349] Ceretti E, Lucchi M, Altan T. "FEM simulation of orthogonal cutting: serrated chip formation," *Journal of materials processing technology*, vol. 95, pp. 17-26, 1999.
- [350] Kim W K, Kim B H. "A molecular dynamics study on atomistic mechanisms of nano-scale cutting process of sapphire," *Journal of Mechanical Science and Technology*, vol. 31, pp. 4353-4362, 2017.
- [351] Abdulkadir L N, Abou-El-Hossein K. "Observed edge radius behavior during MD nanomachining of silicon at a high uncut chip thickness," *The International Journal of Advanced Manufacturing Technology*, vol. 101, pp. 1741-1757, 2019.
- [352] Singh K, Vaishya R O, Singh H, Mishra V, Ramagopal S. "Investigation of tool life & surface roughness during single point diamond turning of silicon," *Int J Sci Res*, vol. 2, pp. 265-267, 2013.
- [353] Otieno T, Abou-El-Hossein K. "Cutting forces and acoustic emission in the diamond turning of rapidly-solidified aluminium," *Insight-Non-Destructive Testing and Condition Monitoring*, vol. 60, pp. 11-18, 2018.
- [354] Jang H W, Lee S E, Hong J-W. "Molecular dynamics evaluation of the effects of zinc on the mechanical properties of aluminum alloys," *Computational Materials Science*, vol. 159, pp. 66-72, 2019.
- [355] Xie Z, Lu Y, Li J. "Development and testing of an integrated smart tool holder for four-component cutting force measurement," *Mechanical Systems and Signal Processing*, vol. 93, pp. 225-240, 2017.
- [356] Byrne G, O'Donnell G. "An integrated force sensor solution for process monitoring of drilling operations," *CIRP annals*, vol. 56, pp. 89-92, 2007.
- [357] Jun M B, Ozdoganlar O B, DeVor R E, Kapoor S G, Kirchheim A, Schaffner G. "Evaluation of a spindle-based force sensor for monitoring and fault diagnosis of machining operations," *International Journal of Machine Tools and Manufacture*, vol. 42, pp. 741-751, 2002.

- [358] Ma L, Melkote S N, Morehouse J B, Castle J B, Fonda J W, Johnson M A. "Thin-film PVDF sensor-based monitoring of cutting forces in peripheral end milling," *Journal of dynamic systems, measurement, and control*, vol. 134, 2012.
- [359] Ma L, Melkote S N, Castle J B. "PVDF sensor-based monitoring of milling torque," *The International Journal of Advanced Manufacturing Technology*, vol. 70, pp. 1603-1614, 2014.
- [360] Guo K, Zhao Y, Zan Z, Sun J. "Development and testing of a wireless rotating triaxial vibration measuring tool holder system for milling process," *Measurement*, p. 108034, 2020.
- [361] Rizal M, Ghani J A, Nuawi M Z, Haron C H C. "Development and testing of an integrated rotating dynamometer on tool holder for milling process," *Mechanical systems and signal processing*, vol. 52, pp. 559-576, 2015.
- [362] Suprock C A, Nichols J S. "A low cost wireless high bandwidth transmitter for sensor-integrated metal cutting tools and process monitoring," *International Journal of Mechatronics and Manufacturing Systems*, vol. 2, pp. 441-454, 2009.
- [363] Nichols J S. "Design and application of a wireless torque sensor for CNC milling," 2009.
- [364] Khan A S, Wang X. *Strain measurements and stress analysis*, 2001.
- [365] Ayomoh M, Abou-El-Hossein K, Olufayo O. "Model for cutting force prediction in high precision single-point diamond turning of optical silicon," *African Journal of Science, Technology, Innovation and Development*, vol. 9, pp. 111-120, 2017.
- [366] Zhu Z, To S, Zhu W-L, Huang P, Zhou X. "Cutting forces in fast-/slow tool servo diamond turning of micro-structured surfaces," *International Journal of Machine Tools and Manufacture*, vol. 136, pp. 62-75, 2019.
- [367] Shaw M. "Metal cutting principles. Clarendon," ed: Oxford, 1984.
- [368] Silva A L, Varanis M, Mereles A G, Oliveira C, Balthazar J M. "A study of strain and deformation measurement using the Arduino microcontroller and strain gauges devices," *Revista Brasileira de Ensino de Física*, vol. 41, 2019.
- [369] Wzorek Ł, Wiewióra M, Wędrychowicz M, Skrzekut T, Noga P, Wiewióra J, *et al.* "Effect of rapid solidification aluminum alloys with different Si contents on mechanical properties and microstructure," *Metallurgy and Foundry Engineering*, vol. 42, 2016.

- [370] Horst R t, Haan M d, Gubbels G, Senden R, van Venrooy B, Hoogstrate A. "Diamond turning and polishing tests on new RSP aluminium alloys," 2012.
- [371] Tong Z. "A systematic research on diamond turning using nanoscale multi-tip diamond tools," University of Strathclyde, 2015.
- [372] Ting H, Abou-El-Hossein K, Chua H. "Application of design of experiment for modelling of etching of ceramics," *Proceedings of EnCon2008*, 2008.
- [373] MOHRUNI A S, Sharif S, Noordin M, Venkatesh V C. "Performance evaluation of uncoated and coated carbide tools when end milling of titanium alloy using response surface methodology," Universiti Teknologi Malaysia, 2008.
- [374] Khanna N, Davim J. "Design-of-experiments application in machining titanium alloys for aerospace structural components," *Measurement*, vol. 61, pp. 280-290, 2015.
- [375] Veiga C, Davim J, Loureiro A. "Properties and applications of titanium alloys: a brief review," *Rev. Adv. Mater. Sci*, vol. 32, pp. 133-148, 2012.
- [376] Telford J K. "A brief introduction to design of experiments," *Johns Hopkins apl technical digest*, vol. 27, pp. 224-232, 2007.
- [377] "Design of Experiments," 2020.
- [378] Dean A, Voss D, Draguljić D. *Design and analysis of experiments* vol. 1: Springer, 1999.
- [379] Gupta A K. "Predictive modelling of turning operations using response surface methodology, artificial neural networks and support vector regression," *International Journal of Production Research*, vol. 48, pp. 763-778, 2010.
- [380] Dikshit M K, Puri A B, Maity A. "Empirical Modelling of Dynamic Forces and Parameter Optimization Using Teaching-Learning-Based Optimization Algorithm and RSM in High Speed Ball-End Milling," *Journal of Production Engineering*, vol. 19, pp. 11-21, 2016.
- [381] Myers R H, Montgomery D C, Anderson-Cook C M. *Response surface methodology: process and product optimization using designed experiments*: John Wiley & Sons, 2016.
- [382] Bosque-Sendra J M, Pescarolo S, Cuadros-Rodríguez L, García-Campaña A M, Almansa-López E M. "Optimizing analytical methods using sequential response surface methodology. Application to the pararosanine determination of formaldehyde," *Fresenius' journal of analytical chemistry*, vol. 369, pp. 715-718, 2001.

- [383] Ferreira S C, Bruns R, Ferreira H S, Matos G D, David J, Brandao G, *et al.* "Box-Behnken design: an alternative for the optimization of analytical methods," *Analytica chimica acta*, vol. 597, pp. 179-186, 2007.
- [384] Thandra S, Choudhury S. "Effect of cutting parameters on cutting force, surface finish and tool wear in hot machining," *International Journal of Machining and Machinability of Materials*, vol. 7, pp. 260-273, 2010.
- [385] Kartal F, Yerlikaya Z, Gökkaya H. "Effects of machining parameters on surface roughness and macro surface characteristics when the machining of Al-6082 T6 alloy using AWJT," *Measurement*, vol. 95, pp. 216-222, 2017.
- [386] Mann J, Chandrasekar S, Compton W, Trumble K, Saldana C, Swaminathan S, *et al.* "Severe plastic deformation and the production of nanostructured alloys by machining," in *Nanostructured Metals and Alloys*, ed: Elsevier, 2011, pp. 178-210.
- [387] Jin D, Liu Z. "Effect of cutting speed on surface integrity and chip morphology in high-speed machining of PM nickel-based superalloy FGH95," *The International Journal of Advanced Manufacturing Technology*, vol. 60, pp. 893-899, 2012.
- [388] Aykut Ş, Bağcı E, Kentli A, Yazıcıoğlu O. "Experimental observation of tool wear, cutting forces and chip morphology in face milling of cobalt based superalloy with physical vapour deposition coated and uncoated tool," *Materials & Design*, vol. 28, pp. 1880-1888, 2007.
- [389] Ning Y, Rahman M, Wong Y. "Investigation of chip formation in high speed end milling," *Journal of materials processing technology*, vol. 113, pp. 360-367, 2001.
- [390] Cotterell M, Byrne G. "Dynamics of chip formation during orthogonal cutting of titanium alloy Ti-6Al-4V," *CIRP annals*, vol. 57, pp. 93-96, 2008.
- [391] Farid A A, Sharif S, Idris M H. "Chip morphology study in high speed drilling of Al-Si alloy," *The International Journal of Advanced Manufacturing Technology*, vol. 57, pp. 555-564, 2011.
- [392] Komanduri R, Flom D, Lee M. "Highlights of the DARPA advanced machining research program," 1985.
- [393] Flom D. "Implementation of high speed machining," *High Speed Machining*, ASME, New York, 1984.

- [394] Kishawy H, Dumitrescu M, Ng E-G, Elbestawi M. "Effect of coolant strategy on tool performance, chip morphology and surface quality during high-speed machining of A356 aluminum alloy," *International Journal of Machine Tools and Manufacture*, vol. 45, pp. 219-227, 2005.
- [395] Recht R. "Catastrophic thermoplastic shear," 1964.
- [396] Müller C, Blümke R. "Influence of heat treatment and cutting speed on chip segmentation of age hardenable aluminium alloy," *Materials science and technology*, vol. 17, pp. 651-654, 2001.
- [397] Batzer S, Haan D, Rao P, Olson W, Sutherland J. "Chip morphology and hole surface texture in the drilling of cast aluminum alloys," *Journal of Materials Processing Technology*, vol. 79, pp. 72-78, 1998.
- [398] Bejjani R, Balazinski M, Attia H, Plamondon P, L'Espérance G. "Chip formation and microstructure evolution in the adiabatic shear band when machining titanium metal matrix composites," *International Journal of Machine Tools and Manufacture*, vol. 109, pp. 137-146, 2016.
- [399] Marchand A, Duffy J. "An experimental study of the formation process of adiabatic shear bands in a structural steel," *Journal of the Mechanics and Physics of Solids*, vol. 36, pp. 251-283, 1988.
- [400] Shaw M, Vyas A. "Chip formation in the machining of hardened steel," *CIRP annals*, vol. 42, pp. 29-33, 1993.
- [401] Nakayama K. "On the formation of" saw-toothed chip" in metal cutting," *J Japan Soc Prec Eng*, vol. 43, pp. 117-122, 1977.
- [402] Nakayama K, Arai M, Kanda T. "Machining characteristics of hard materials," *CIRP Annals*, vol. 37, pp. 89-92, 1988.
- [403] König W, Berkold A, Koch K-F. "Turning versus grinding—a comparison of surface integrity aspects and attainable accuracies," *CIRP annals*, vol. 42, pp. 39-43, 1993.
- [404] Komanduri R, Schroeder T, Hazra J, Von Turkovich B, Flom D. "On the catastrophic shear instability in high-speed machining of an AISI 4340 steel," 1982.
- [405] Davies M A, Chou Y, Evans C J. "On chip morphology, tool wear and cutting mechanics in finish hard turning," *CIRP annals*, vol. 45, pp. 77-82, 1996.
- [406] Komanduri R. "Some clarifications on the mechanics of chip formation when machining titanium alloys," *Wear*, vol. 76, pp. 15-34, 1982.

- [407] Guo Y, Ammula S. "Real-time acoustic emission monitoring for surface damage in hard machining," *International Journal of Machine Tools and Manufacture*, vol. 45, pp. 1622-1627, 2005.
- [408] Inasaki I. "Application of acoustic emission sensor for monitoring machining processes," *Ultrasonics*, vol. 36, pp. 273-281, 1998.
- [409] Jemielniak K, Otman O. "Catastrophic tool failure detection based on acoustic emission signal analysis," *CIRP Annals*, vol. 47, pp. 31-34, 1998.
- [410] Olufayo O A. "Tool wear monitoring in end milling of mould steel using acoustic emission," Masters, Mechatronics, 2011.
- [411] Hirel P. "Atomsk: a tool for manipulating and converting atomic data files," *Computer Physics Communications*, vol. 197, pp. 212-219, 2015.
- [412] Module F. "Material Studio 6.0," *Accelrys Inc., San Diego, CA*, 2011.
- [413] Humphrey W, Dalke A, Schulten K. "VMD: visual molecular dynamics," *Journal of molecular graphics*, vol. 14, pp. 33-38, 1996.
- [414] Stukowski A. "Visualization and analysis of atomistic simulation data with OVITO—the Open Visualization Tool," *Modelling and Simulation in Materials Science and Engineering*, vol. 18, p. 015012, 2009.
- [415] Tersoff J. "Erratum: Modeling solid-state chemistry: Interatomic potentials for multicomponent systems," *Physical Review B*, vol. 41, p. 3248, 1990.
- [416] Erhart P, Albe K. "Analytical potential for atomistic simulations of silicon, carbon, and silicon carbide," *Physical Review B*, vol. 71, p. 035211, 2005.
- [417] Dai H, Chen G, Zhou C, Fang Q, Fei X. "A numerical study of ultraprecision machining of monocrystalline silicon with laser nano-structured diamond tools by atomistic simulation," *Applied Surface Science*, vol. 393, pp. 405-416, 2017.
- [418] Goel S, Luo X, Reuben R L, Pen H. "Influence of temperature and crystal orientation on tool wear during single point diamond turning of silicon," *Wear*, vol. 284, pp. 65-72, 2012.
- [419] Marshall D, Lawn B, Evans A. "Elastic/plastic indentation damage in ceramics: the lateral crack system," *Journal of the American Ceramic Society*, vol. 65, pp. 561-566, 1982.
- [420] Dai H, Chen G. "A molecular dynamics investigation into the mechanisms of material removal and subsurface damage of nanoscale high speed laser-assisted machining," *Molecular Simulation*, vol. 43, pp. 42-51, 2017.

- [421] Oluwajobi A. "Molecular Dynamics Simulation of Nanoscale Machining, Molecular Dynamics—Studies of Synthetic and Biological Macromolecules," *Prof. Lichang Wang (Ed.)*, 2012.
- [422] Cardarelli F. "Polymers and elastomers," *Materials Handbook: A Concise Desktop Reference*, pp. 691-750, 2008.
- [423] Guo Y, Liang Y, Chen M, Bai Q, Lu L. "Molecular dynamics simulations of thermal effects in nanometric cutting process," *Science China Technological Sciences*, vol. 53, pp. 870-874, 2010.
- [424] Yingfei G, Jihua X, Hui Y. "Diamond tools wear and their applicability when ultra-precision turning of SiCp/2009Al matrix composite," *Wear*, vol. 269, pp. 699-708, 2010.
- [425] Feng Z, Field J. "The friction and wear of diamond sliding on diamond," *Journal of Physics D: Applied Physics*, vol. 25, p. A33, 1992.
- [426] Cai M, Li X, Rahman M. "Study of the mechanism of groove wear of the diamond tool in nanoscale ductile mode cutting of monocrystalline silicon," 2007.
- [427] Wang Z, Liang Y, Chen M, Tong Z, Chen J. "Analysis about diamond tool wear in nano-metric cutting of single crystal silicon using molecular dynamics method," in *5th International Symposium on Advanced Optical Manufacturing and Testing Technologies: Advanced Optical Manufacturing Technologies*, 2010, p. 765500.
- [428] Maekawa K, Itoh A. "Friction and tool wear in nano-scale machining—a molecular dynamics approach," *Wear*, vol. 188, pp. 115-122, 1995.
- [429] Pamuk H, Halicioğlu T. "Evaluation of morse parameters for metals," *physica status solidi (a)*, vol. 37, pp. 695-699, 1976.
- [430] Girifalco L A, Weizer V G. "Application of the Morse potential function to cubic metals," *Physical Review*, vol. 114, p. 687, 1959.
- [431] Fang T-H, Wu J-H. "Molecular dynamics simulations on nanoindentation mechanisms of multilayered films," *Computational Materials Science*, vol. 43, pp. 785-790, 2008.
- [432] Komanduri R, Chandrasekaran N, Raff L. "Molecular dynamics simulation of atomic-scale friction," *Physical Review B*, vol. 61, p. 14007, 2000.

- [433] Van Hung N, Toan N C, Trung N B, Giang N H. "Calculation of Morse Potential for Diamond Crystals. Application to Anharmonic Effective Potential," *VNU Journal of Science: Mathematics-Physics*, vol. 24, 2008.
- [434] Teik-Cheng L. "Relationship and discrepancies among typical interatomic potential functions," *Chinese Physics Letters*, vol. 21, p. 2167, 2004.
- [435] Swamy V, Gale J D. "Transferable variable-charge interatomic potential for atomistic simulation of titanium oxides," *Physical Review B*, vol. 62, p. 5406, 2000.
- [436] Fleming S D, Morton J R, Rohl A L, Ward C B. "Interatomic potentials for simulating MnO₂ polymorphs," *Molecular Simulation*, vol. 31, pp. 25-32, 2005.
- [437] Hung N V. "A method for calculation of morse potential for fcc, bcc, hcp crystals applied to debye-waller factor and equation of state," *CPhy*, vol. 14, p. 7, 2007.
- [438] Komanduri R, Chandrasekaran N, Raff L. "MD simulation of indentation and scratching of single crystal aluminum," *Wear*, vol. 240, pp. 113-143, 2000.
- [439] Pei Q, Lu C, Lee H. "Large scale molecular dynamics study of nanometric machining of copper," *Computational Materials Science*, vol. 41, pp. 177-185, 2007.
- [440] Cui D-D, Zhang L-C. "Nano-machining of materials: understanding the process through molecular dynamics simulation," *Advances in Manufacturing*, vol. 5, pp. 20-34, 2017.
- [441] Zhang L, Tanaka H. "Towards a deeper understanding of wear and friction on the atomic scale—a molecular dynamics analysis," *Wear*, vol. 211, pp. 44-53, 1997.
- [442] Zhang L, Tanaka H. "Atomic scale deformation in silicon monocrystals induced by two-body and three-body contact sliding," *Tribology international*, vol. 31, pp. 425-433, 1998.
- [443] Komanduri R, Chandrasekaran N, Raff L. "Effect of tool geometry in nanometric cutting: a molecular dynamics simulation approach," *Wear*, vol. 219, pp. 84-97, 1998.
- [444] Han X, Lin B, Yu S, Wang S. "Investigation of tool geometry in nanometric cutting by molecular dynamics simulation," *Journal of materials processing technology*, vol. 129, pp. 105-108, 2002.

- [445] Kumbera T G, Cherukuri H P, Patten J A, Brand C J, Marusich T D. "Numerical simulations of ductile machining of silicon nitride with a cutting tool of defined geometry," 2001.
- [446] El-Gallab M S, Sklad M P. "Machining of aluminum/silicon carbide particulate metal matrix composites: Part IV. Residual stresses in the machined workpiece," *Journal of materials processing technology*, vol. 152, pp. 23-34, 2004.
- [447] Xiao G, To S, Zhang G. "Molecular dynamics modelling of brittle–ductile cutting mode transition: case study on silicon carbide," *International Journal of Machine Tools and Manufacture*, vol. 88, pp. 214-222, 2015.
- [448] Luo X, Cheng K, Guo X, Holt R. "An investigation on the mechanics of nanometric cutting and the development of its test-bed," *International Journal of Production Research*, vol. 41, pp. 1449-1465, 2003.
- [449] Chavoshi S Z, Luo X. "Atomic-scale characterization of occurring phenomena during hot nanometric cutting of single crystal 3C–SiC," *RSC advances*, vol. 6, pp. 71409-71424, 2016.
- [450] Guichun T, Zigong Z, Zhaosheng L. "Advance in Processing Technology of Engineering Plastics of China in 2011," *Engineering Plastics Application*, vol. 5, p. 028, 2012.
- [451] Valera H Y, Bhavsar S N. "Experimental investigation of surface roughness and power consumption in turning operation of EN 31 alloy steel," *Procedia Technology*, vol. 14, pp. 528-534, 2014.
- [452] Zare Chavoshi S, Luo X. "Molecular dynamics simulation investigation of hot nanometric cutting of single crystal silicon," in *16th euspen International Conference*, 2016, pp. 249-250.
- [453] Ng C K, Melkote S N, Rahman M, Kumar A S. "Experimental study of micro- and nano-scale cutting of aluminum 7075-T6," *International Journal of Machine Tools and Manufacture*, vol. 46, pp. 929-936, 2006.
- [454] Fuh K-H, Chang H-Y. "An accuracy model for the peripheral milling of aluminum alloys using response surface design," *Journal of Materials Processing Technology*, vol. 72, pp. 42-47, 1997.
- [455] Manna A, Bhattacharyya B. "A study on different tooling systems during machining of Al/SiC-MMC," *Journal of Materials Processing Technology*, vol. 123, pp. 476-482, 2002.

- [456] Zaghbani I, Songmene V. "A force-temperature model including a constitutive law for dry high speed milling of aluminium alloys," *Journal of Materials Processing Technology*, vol. 209, pp. 2532-2544, 2009.
- [457] Johne P. "Machining of products," *European Aluminium Association*, p. 38, 1994.
- [458] Kota N. "Mechanical Micromachining-Effect of Crystallographic Anisotropy on Machining Forces," 2011.
- [459] Cai M, Li X, Rahman M. "Study of the mechanism of nanoscale ductile mode cutting of silicon using molecular dynamics simulation," *International Journal of Machine Tools and Manufacture*, vol. 47, pp. 75-80, 2007.
- [460] Komanduri R, Chandrasekaran N, Raff L. "MD Simulation of nanometric cutting of single crystal aluminum—effect of crystal orientation and direction of cutting," *Wear*, vol. 242, pp. 60-88, 2000.
- [461] Komanduri R, Chandrasekaran N, Raff L. "Some aspects of machining with negative-rake tools simulating grinding: a molecular dynamics simulation approach," *Philosophical Magazine B*, vol. 79, pp. 955-968, 1999.
- [462] Nakayama K, Tamura K. "Size effect in metal-cutting force," 1968.
- [463] Komanduri R. "Some aspects of machining with negative rake tools simulating grinding," *International journal of machine tool design and research*, vol. 11, pp. 223-233, 1971.
- [464] Lucca D, Rhorer R, Komanduri R. "Energy dissipation in the ultraprecision machining of copper," *CIRP annals*, vol. 40, pp. 69-72, 1991.
- [465] Kelly J, Cotterell M. "Minimal lubrication machining of aluminium alloys," *Journal of Materials Processing Technology*, vol. 120, pp. 327-334, 2002.
- [466] Nouari M, List G, Girot F, Coupard D. "Experimental analysis and optimisation of tool wear in dry machining of aluminium alloys," *Wear*, vol. 255, pp. 1359-1368, 2003.
- [467] Ozcatalbas Y. "Chip and built-up edge formation in the machining of in situ Al₄C₃-Al composite," *Materials & design*, vol. 24, pp. 215-221, 2003.
- [468] Roy P, Sarangi S, Ghosh A, Chattopadhyay A. "Machinability study of pure aluminium and Al-12% Si alloys against uncoated and coated carbide inserts," *International Journal of Refractory Metals and Hard Materials*, vol. 27, pp. 535-544, 2009.

- [469] Yousefi R, Ichida Y. "A study on ultra–high-speed cutting of aluminium alloy:: Formation of welded metal on the secondary cutting edge of the tool and its effects on the quality of finished surface," *Precision engineering*, vol. 24, pp. 371-376, 2000.
- [470] Dasch J M, Ang C C, Wong C A, Cheng Y T, Weiner A M, Lev L C, *et al.* "A comparison of five categories of carbon-based tool coatings for dry drilling of aluminum," *Surface and Coatings Technology*, vol. 200, pp. 2970-2977, 2006.
- [471] Sánchez J, Rubio E, Álvarez M, Sebastián M, Marcos M. "Microstructural characterisation of material adhered over cutting tool in the dry machining of aerospace aluminium alloys," *Journal of Materials Processing Technology*, vol. 164, pp. 911-918, 2005.
- [472] Tang Z, Liu Z, Pan Y, Wan Y, Ai X. "The influence of tool flank wear on residual stresses induced by milling aluminum alloy," *Journal of Materials Processing Technology*, vol. 209, pp. 4502-4508, 2009.
- [473] Coelho R, Yamada S, Aspinwall D, Wise M. "The application of polycrystalline diamond (PCD) tool materials when drilling and reaming aluminium based alloys including MMC," *International Journal of Machine Tools and Manufacture*, vol. 35, pp. 761-774, 1995.
- [474] Dwivedi D, Sharma A, Rajan T. "Machining of LM13 and LM28 cast aluminium alloys: Part I," *Journal of Materials Processing Technology*, vol. 196, pp. 197-204, 2008.